Electrochemical Techniques in Corrosion Science and Engineering

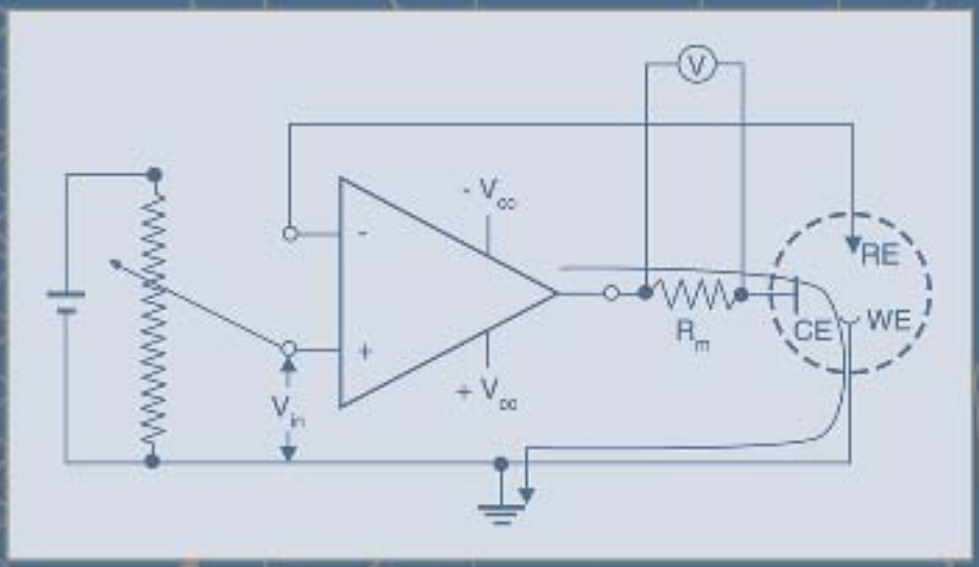

Robert G. Kelly
John R. Scully
David W. Shoesmith
Rudolph G. Buchheit

Electrochemical Techniques in Corrosion Science and Engineering

Robert G. Kelly and John R. Scully
University of Virginia
Charlottesville, Virginia, U.S.A.

David W. Shoesmith
University of Western Ontario
London, Ontario, Canada

Rudolph G. Buchheit
The Ohio State University
Columbus, Ohio, U.S.A.

Marcel Dekker, Inc. New York • Basel

ISBN: 0-8247-9917-8

This book is printed on acid-free paper.

Headquarters
Marcel Dekker, Inc.
270 Madison Avenue, New York, NY 10016
tel: 212-696-9000; fax: 212-685-4540

Eastern Hemisphere Distribution
Marcel Dekker AG
Hutgasse 4, Postfach 812, CH-4001 Basel, Switzerland
tel: 41-61-260-6300; fax: 41-61-260-6333

World Wide Web
http://www.dekker.com

The publisher offers discounts on this book when ordered in bulk quantities. For more information, write to Special Sales/Professional Marketing at the headquarters address above.

Current printing (last digit):
10 9 8 7 6 5 4 3 2 1

PRINTED IN THE UNITED STATES OF AMERICA

CORROSION TECHNOLOGY

Editor
Philip A. Schweitzer, P.E.
Consultant
York, Pennsylvania

1. *Corrosion and Corrosion Protection Handbook: Second Edition, Revised and Expanded*, edited by Philip A. Schweitzer
2. *Corrosion Resistant Coatings Technology*, Ichiro Suzuki
3. *Corrosion Resistance of Elastomers*, Philip A. Schweitzer
4. *Corrosion Resistance Tables: Metals, Nonmetals, Coatings, Mortars, Plastics, Elastomers and Linings, and Fabrics: Third Edition, Revised and Expanded (Parts A and B)*, Philip A. Schweitzer
5. *Corrosion-Resistant Piping Systems*, Philip A. Schweitzer
6. *Corrosion Resistance of Zinc and Zinc Alloys*, Frank C. Porter
7. *Corrosion of Ceramics*, Ronald A. McCauley
8. *Corrosion Mechanisms in Theory and Practice*, edited by P. Marcus and J. Oudar
9. *Corrosion Resistance of Stainless Steels*, C. P. Dillon
10. *Corrosion Resistance Tables: Metals, Nonmetals, Coatings, Mortars, Plastics, Elastomers and Linings, and Fabrics: Fourth Edition, Revised and Expanded (Parts A, B, and C)*, Philip A. Schweitzer
11. *Corrosion Engineering Handbook*, edited by Philip A. Schweitzer
12. *Atmospheric Degradation and Corrosion Control*, Philip A. Schweitzer
13. *Mechanical and Corrosion-Resistant Properties of Plastics and Elastomers*, Philip A. Schweitzer
14. *Environmental Degradation of Metals*, U. K. Chatterjee, S. K. Bose, and S. K. Roy
15. *Environmental Effects on Engineered Materials*, edited by Russell H. Jones
16. *Corrosion-Resistant Linings and Coatings*, Philip A. Schweitzer
17. *Corrosion Mechanisms in Theory and Practice: Second Edition, Revised and Expanded*, edited by Philippe Marcus
18. *Electrochemical Techniques in Corrosion Science and Engineering*, Robert G. Kelly, John R. Scully, David W. Shoesmith, and Rudolph G. Buchheit
19. *Metallic Materials: Physical, Mechanical, and Corrosion Properties*, Philip A. Schweitzer

ADDITIONAL VOLUMES IN PREPARATION

Preface

Corrosion science and engineering have benefited tremendously from the explosion in the use of electrochemical methods that can probe the thermodynamic and kinetic aspects of corrosion, including the rate of corrosion. These methods have proved of great utility to corrosion engineers and scientists in predicting the performance of materials and devising corrosion mitigation strategies, understanding the effects of changes in process and environment conditions, and assessing the accuracy of corrosion monitoring techniques. Enhanced prevention and understanding of corrosion has been achieved over the past several decades by applying these methods in both the laboratory and field. Electrochemical methods for corrosion, when used properly, have distinct advantages over exposure techniques. Some of these advantages are speed, nondestructiveness, high resolution, and ability to provide mechanistic information. Unfortunately, few engineers and scientists tasked with corrosion problems have been trained in electrochemical fundamentals and their application to corrosion phenomena.

The goal of this book is to present a framework for understanding the principles of electrochemistry and the methods derived from these principles in a clear manner and ready-to-apply format. The book emphasizes practical fundamentals that make it possible to determine whether electrochemical techniques are of use for a given problem, choose the correct electrochemical method, and intelligently interpret the results, including the limitations of the methods and analyses.

Chapter 1 provides an introduction to some of the basic terms and concepts of electrochemistry and corrosion and provides a detailed overview of the remainder of the book. Chapter 2 provides an overview of the important thermodynamic and kinetic parameters of relevance to corrosion electrochemistry. Chapter 3 focuses on what might be viewed as an aberration from normal dissolution kinetics: passivity. This aberration—or "peculiar condition," as Faraday referred to it—is critical to the use of stainless steels, aluminum alloys, and all the so-called corrosion resistant alloys (CRAs).

Chapter 4 describes how the electrical nature of corrosion reactions allows the interface to be modeled as an electrical circuit, as well as how this electrical circuit can be used to obtain information on corrosion rates. Chapter 5 focuses on how to characterize flow and how to include its effects in the test procedure. Chapter 6 describes the origins of the observed distributions in space and time of the reaction rate. Chapter 7 describes the applications of electrochemical measurements to predictive corrosion models, emphasizing their use in the long-term prediction of corrosion behavior of metallic packages for high-level nuclear waste. Chapter 8 outlines the electrochemical methods that have been applied to develop and test the effectiveness of surface treatments for metals and alloys. The final chapter gives experimental procedures that can be used to illustrate the principles described.

"Electrochemical techniques, when conducted intelligently and interpreted knowledgeably, are valuable tools for solving, understanding, and preventing corrosion problems." This has been the mantra of a short course on electrochemical methods applied to corrosion that has been conducted annually since 1984. The overall goal of the course is to provide practicing corrosion engineers with an introduction to the use of electrochemical techniques. This book, based on the lectures and laboratories of that short course, shows how to use electrochemical methods to understand corrosion phenomena and solve corrosion problems.

ACKNOWLEDGMENTS

More than 50 people have contributed to the success of the course that spawned this book. These include both faculty members and graduate student assistants who have taken to heart the desire to constantly improve the quality of the instruction. The father of the short course is Pat Moran (U.S. Naval Academy). He not only designed the original course but also served as a mentor for many graduate students in corrosion, including two of the authors of this book. The graduate students listed below have made critical contributions to the experiments described in Chapter 8. The written experimental procedures reflect only a small portion of the time they devoted to designing these labs and making them work during the course. Their influence permeates the book.

The course has enjoyed outstanding support from our sponsors throughout its history. The local sections of NACE International (Baltimore/Washington from 1985–1990; Old Dominion from 1991–present) provided advertising support and their good name. Perkin-Elmer Instruments provided excellent equipment and outstanding technical support from the start. Their steadfast assistance was instrumental in the success of the course.

Many of the figures in Chapters 1 through 5 were created by Jean Reese, who was also critical in the organization of the short course, and the Center for Electrochemical Science and Engineering at the University of Virginia.

The patience and pleasant persistence of the team at Marcel Dekker, Inc., especially Rita Lazazzaro and Eric Stannard, have been instrumental in making this book a reality. Most importantly, we acknowledge our families, who made all the work worthwhile.

Lecturers

Bob Baboian	Jerry Kruger	John R. Scully
Bill Eggers	Chip Lee	David W. Shoesmith
Gary Greczek	Pat Moran	Theresa Simpson
Robert G. Kelly	Geoff Prentice	Glenn Stoner

Lab Instructors

Chris Brodrick	Ron Holser	Sheldon Pride
Sean Brossia	Sudesh Kannan	James Scanlon
Noah Budiansky	Robert G. Kelly	Louie Scribner
Brendan Coffey	Karen Ferrer	Steve Smith
Brian Connolly	Jason Lee	Chris Streinz
Kevin Cooper	Scott Lillard	Doug Wall
Lisa DeJong	Daryl Little	Chris Weyant
Ron Dombro	Greg Makar	Jackie Williams
Susan Ehrlich	Lysle Montes	Todd Wilson
Michelle Gaudett	Leigh Ann Pauly	Steve Yu
Steve Golledge	Jeff Poirier	

Robert G. Kelly
John R. Scully
David W. Shoesmith
Rudolph G. Buchheit

Contents

1
Introduction

Corrosion can be defined as the deterioration of a material's properties due to its interaction with its environmnet. The demands for long-term performance of engineering structures over a wide size scale continue to increase. As microelectronic structures decrease in size, smaller amounts of dissolution on interconnects in integrated circuits can lead to the failure of large computer systems. The long-term storage of nuclear waste may represent man's most compelling engineering challenge: containment of high-level radioactive material for thousands of years. In both cases, as well as in many in between, the corrosion engineer has a primary responsibility to provide guidance throughout the design, construction, and life process in terms of material selection, environment alteration, and life prediction. Over the past thirty years, the use of electrochemical methods for probing corrosion processes has increased to the point where they represent an indispensable set of tools. The overarching goal of this book is to provide the foundation for corrosion engineers to use electrochemical techniques as part of the tool kit they apply to corrosion concerns.

This introduction briefly reviews topics that underlie the remainder of the book. Most of these topics will be familiar from high school or college chemistry. Nonetheless, the topics are generally given short shrift in standard chemistry syllabi, so their importance with respect to corrosion is emphasized here.

I. CHEMICAL VS. ELECTROCHEMICAL REACTIONS

Chemical reactions are those in which elements are added or removed from a chemical species. Purely chemical reactions are those in which none of the species undergoes a change in its valence, i.e., no species is either oxidized or reduced. Electrochemical rections are chemical reactions in which not only may elements be added or removed from a chemical species but also at least one species undergoes a change in the number of valence electrons. For example, the precipitation of iron hydroxide, $Fe(OH)_2$, is a pure chemical reaction:

$$Fe^{2+} + 2OH^- \rightarrow Fe(OH)_2 \quad (1)$$

None of the atoms involved have changed its valence; the iron and oxygen are still in the divalent state, and the hydrogen is still univalent. One way to produce the ferrous ion needed in the above reaction is via the oxidation of metallic (zero valent) iron:

$$Fe \rightarrow Fe^{2+} + 2e^- \quad (2)$$

In order for this reaction to occur, the two electrons produced must be consumed in a reduction reaction such as the reduction of dissolved oxygen:

$$O_2 + 2H_2O + 4e^- \rightarrow 4OH^- \quad (3)$$

If the two reactions are not widely physically separated on a metal surface, the chemical reaction between the hydroxide and ferrous ions can produce a solid on the surface. Thus chemical and electrochemical reactions can be (and often are) coupled.[1] The electrochemical methods described in this book can be used to study directly the wide range of reactions in which electrons are transferred. In addition, some chemical reactions can also be studied indirectly using electrochemical methods.

The vast majority of engineering materials dissolve via electrochemical reactions. Chemical processes are often important, but the dissolution of metallic materials requires an oxidation of the metallic element in order to render it soluble in a liquid phase. In fact, there are four requirements for corrosion: an anode (where oxidation of the metal occurs), a cathode (where reduction of a different species occurs), an electrolytic path for ionic conduction between the two reaction sites, and an electrical path for electron conduction between the reaction sites. These requirements are illustrated schematically in Fig. 1.

All successful corrosion control processes affect one or more of these requirements. For example, the use of oxygen scavengers affects the cathodic reaction rate possible. Isolating dissimilar metals with insulating materials attempts to remove the electrical path. Most organic coatings serve to inhibit the formation of an electrolytic path. Thus, when evaluating a corrosion process or proposed mitigation method, a first-pass analysis of the effects of it on the four requirements can serve to structure one's thinking.

A simple calculation demonstrates the tremendous power of electrochemical reaction rate measurements due to their sensitivity and dynamic range. Dissolution current densities of 10 nA/cm^2 are not tremendously difficult to measure.

[1] Bard and Faulkner (1) is an excellent source of information on the intricacies of such coupling.

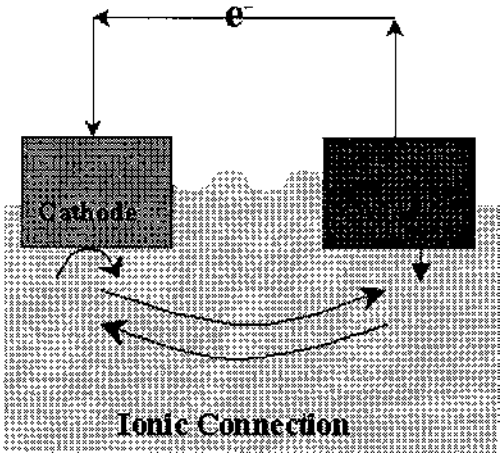

Figure 1 Schematic diagram of four requirements for corrosion. Note that the anode and cathode can be on the same piece of material.

A metal corroding at this rate would lose 100 nm of thickness per year.[2] On the other end of the spectrum, measurements of reaction rates of several to hundreds of A/cm^2 are needed in some transient studies of localized corrosion. A dissolution rate of 100 A/cm^2 corresponds to a penetration rate of 1 km/s. Fortunately for modern society, such penetration rates last in practice for far less than one second! Thus modern instrumentation allows the measurement of dissolution rates over more than 10 orders of magnitude with accuracy on the order of a few percent.

The issues of accuracy and precision are often controversial in discussions of corrosion electrochemistry. Analytical electrochemists can achieve high accuracy and precision through the strict control of variables such as temperature, solution composition, surface condition, and mass transport. Throughout this book, the effects of these and other variables on corrosion processes are highlighted. Unfortunately, in practice, close control of such important parameters is often impossible. In addition, corrosion systems are generally time-varying in practice, further complicating reproducibility. This situation can be disturbing for physical scientists new to electrochemical corrosion measurements who are used to more control and thus more reproducibility in instrumental measurements.

[2] In most applications, this would be considered outstanding corrosion resistance, but for a nuclear waste storage vessel needing 100,000 years of service, the corrosion allowance would need to be at least 10 cm.

Nonetheless, they become more comfortable with experience, as they realize that in most cases, getting the first digit in the corrosion rate right is both a necessary and a sufficient condition for job security.

II. FARADAY'S LAWS OF ELECTROLYSIS

In the early 1800s, Michael Faraday performed superb quantitative experimental studies of electrochemical reactions. He was able to demonstrate that electrochemical reactions follow all normal chemical stoichiometric relations and in addition follow certain stoichiometric rules related to charge. These additional rules are now known as Faraday's laws. They can be written as follows:

Faraday's First Law: The mass, m, of an element discharged at an electrode is directly proportional to the amount of electrical charge, Q, passed through the electrode.

Faraday's Second Law: If the same amount of electrical charge, Q, is passed through several electrodes, the mass, m, of an element discharged at each will be directly proportional to both the atomic mass of the element and the number of moles of electrons, z, required to discharge one mole of the element from whatever material is being discharged at the electrode. Another way of stating this law is that the masses of the substances reacting at the electrodes are in direct ratio to their equivalent masses.

The charge carried by one mole of electrons is known as 1 faraday (symbol F). The faraday is related to other electrical units because the charge on a single electron is 1.6×10^{-19} C/electron. Multiplying the electronic charge by the Avogadro number 6.02×10^{23} electrons/mole electrons tells us that 1 F equals 96,485 C.

These empirical laws of electrolysis are critical to corrosion as they allow electrical quantities (charge and current, its time derivative) to be related to mass changes and material loss rates. These laws form the basis for the calculations referenced above concerning the power of electrochemical corrosion measurements to predict corrosion rates. The original experiments of Faraday used only elements, but his ideas have been extended to electrochemical reactions involving compounds and ions.

By combining the principles of Faraday with an electrochemical reaction of known stoichiometry permits us to write Faraday's laws of electrolysis as a single equation that relates the charge density (charge/area), q, to the mass loss (per unit area), Δm:

$$\Delta m = \frac{q(AM)}{nF} \tag{4}$$

Taking the time derivative of the equation allows the mass loss rate to be related to the dissolution current density:

$$\dot{m} = \frac{i(\mathrm{AM})}{nF\rho} \tag{5}$$

In many cases, a penetration rate, in units of length/time, is more useful in design. The inclusion of corrosion allowances in a structure requires an assumption of uniform penetration rate. The most common engineering unit of penetration rate is the mil per year (mpy). One mil of penetration equates to a loss in thickness of 0.0001″. Corrosion rates of less than 1 mpy are generally considered to be excellent to outstanding, although such adjectives are highly dependent on the details of the engineering scenario. A rule of thumb is that 1μA/cm^2 is approximately equivalent to 0.5 mpy for a wide range of structural materials, including ferrous, nickel-, aluminum-, and copper-based alloys. For more extract calculations, the following formula can be used:

$$\mathrm{mpy} = \frac{129(\mathrm{AM})(i)}{n\rho} \tag{6}$$

where

mpy = penetration rate (mils per year)
AM = atomic mass (g)
i = corrosion current density (mA/cm^2)
ρ = density (g/cm^3)
n = number of electrons lost per atom oxidized

Throughout the text, distinctions are made between current, i.e., the rate of a reaction, and current density, i.e., the area-specific reaction rate. The combination of Faraday's laws described above involves current density rather than current. The current, usually symbolized with a capital I, has units of amperes and represents an electrical flux. The current density, usually symbolized with a lower case i, has units of amperes per unit area, e.g., A/cm^2. Under a given set of conditions (i.e., potential, metal and solution composition, temperature, etc.), the current density is fixed. Thus, although doubling the area of the electrode will double the measured current, the current density will remain unchanged.

The most direct example of the importance of differentiating between i and I is in the application of the conservation of charge to corrosion. In this case, the conservation of charge means that in a isolated system,[3] all electrons that are liberated in oxidation reactions (at anodes must be consumed in reduction reac-

[3] Isolated means that there are no external sources or sinks of electrons.

tions (at cathodes). In terms of charge, the total anodic charge must equal the total cathodic charge (each in coulombs):

$$\sum_i Q_a = \sum_j Q_c \tag{7}$$

Taking the time derivative converts the law to a rate expression:

$$\sum_i I_a = \sum_j I_c \tag{8}$$

For each reaction, the current density is the current for that reaction divided by the area over which it occurs:

$$i_i = \frac{I_i}{A_i} \tag{9}$$

Thus combining these expressions demonstrates that only in the cases in which the areas on which the anodic and cathodic reactions occur are equal can the anodic and cathodic current densities be equal:

$$\sum_i i_a A_a = \sum_j i_c A_c \tag{10}$$

In other cases, a push-me-pull-you situation arises; the faster (as defined by the current density) reaction cannot produce current any faster than the slower reaction can consume it. Corrosion engineers use this principle in several ways including sacrificial anodes and corrosion inhibitors. Examples can be found throughout the text.

III. OVERVIEW OF THE REMAINDER OF THIS BOOK

A. What Is Covered

This book consists of nine chapters. The second chapter provides an overview of the important thermodynamic and kinetic parameters of relevance to corrosion electrochemistry. This foundation is used in the third chapter to focus on what might be viewed as an aberration from normal dissolution kinetics, passivity. This aberration, or ''peculiar condition'' as Faraday called it, is critical to the use of stainless steels, aluminum alloys, and all of the so-called corrosion resistant alloys (CRAs). The spatially discrete failure of passivity leads to localized corrosion, one of the most insidious and expensive forms of environmental attack. Chapter 4 explores the use of the electrical nature of corrosion reactions to model the interface as an electrical circuit, allowing measurement methods originating in electrical engineering to be applied to nondestructive corrosion evaluation and

inspection. Convective flow of the environment can have substantial effects on corrosion processes. The fifth chapter focuses on how to characterize flow and how to include its effects in test procedures. In many systems, there are distributions in space and time of the reaction rate due to distributions in the electrochemical potential. The origins of such distributions and their effects on measurements and interpretations are explored in the sixth chapter of the book. Chapter 7 describes the applications of electrochemical measurements to predictive corrosion models, emphasizing their use in the long-term prediction of the corrosion behavior of metallic packages for high-level nuclear waste. Chapter 8 outlines how electrochemical methods have been applied to develop and test the effectiveness of surface treatments for metals and alloys. The final chapter contains descriptions of experimental procedures that can be used to illustrate the principles described. Throughout the book, example from the literature are provided in order to ground the discussions and to provide the interested reader with access to more in-depth discussions of certain topics.

B. What Is Not Covered

We have chosen to focus this text on the use of electrochemical techniques. Thus there are many important areas in corrosion engineering that are excluded. For example, space constraints prevent any direct coverage of environment-assisted cracking, although some of the concepts considered in localized corrosion can be easily extended to the conditions inside occluded cracks. Details of corrosion mechanisms are not described. Fundamental corrosion information is provided only to the extent necessary to understand the origin of signals measured by the electrochemical methods under consideration. Similarly, nonelectrochemical methods are not described in any detail. In general, high-temperature gaseous oxidation does not involve a liquid phase and thus falls outside the purview of this book.

C. Importance of the Motto

The motto found in the front of this book was coined by Pat Moran, currently Chairman of the Department of Mechanical Engineering at the U.S. Naval Academy and the Ph.D. advisor of two of the authors (RGK, JRS). It includes the key elements in electrochemical testing that will be emphasized throughout this book. In order to conduct tests intelligently, one needs to perform the tests in a relevant environment, on a relevant material surface, under relevant experimental conditions. Although this advice sounds obvious, there is always a tension between the proper choices for experimental parameters for accurate simulations and the proper choices for experimental convenience. Such tradeoffs must be carefully

considered. In order to interpret knowledgeably one must be well-read in the appropriate literature, bring one's engineering experience to bear on the results, and use complementary methods for data verification wherever possible. The power of electrochemical methods is substantial as long as their limitations are kept in mind.

REFERENCE

1. A. J. Bard, L. R. Faulkner. *Electrochemical Methods: Fundamentals and Applications*. John Wiley, New York, 1980.

2

Electrochemical Thermodynamics and Kinetics of Relevance to Corrosion

I. ELECTROCHEMICAL THERMODYNAMICS

A. Utility of Thermodynamics in Electrochemistry

Thermodynamic considerations in electrochemistry allow the determination of whether a reaction can occur spontaneously, i.e., without the input of external energy. If metal dissolution is unfavorable thermodynamically in a given set of circumstances, the job of the corrosion engineer is generally done. For example, copper will not corrode in pure, deoxygenated water at any pH. Although this example is one of the few in which corrosion can be excluded on thermodynamic grounds, the use of such principles can be used to understand the effects of some variables on corrosion tendencies. In addition, thermodynamics provides the basis for many of the electrochemical measurements made in corrosion science and engineering.

The three goals of the thermodynamic section are (1) to relate the thermodynamics of corrosion-related electrochemistry to concepts with which the reader may be familiar, (2) to describe the need for and characteristics of reference electrodes, and (3) to describe the origin, use, and limitations of electrochemical phase diagrams (a.k.a., *E*-pH or Pourbaix diagrams).

B. Relation of ΔG to E_r

All processes in nature that occur spontaneously have a Gibbs free energy change (ΔG) associated with them that is negative. A negative free energy change indicates that the stability of the products is greater than that of the reactants. The nature of the process determines the components of the free energy change that contribute.

In electrochemistry, the ΔG is related to the change in the energy of charge as it passes through the potential difference (E_r) at the metal/solution interface by the relation

$$\Delta G = -nFE_r \tag{1}$$

where ΔG is the free energy change, n is the number of electrons transferred in the reaction, and E_r is the reversible potential differences across the interface. This equation relates the amount of energy required to move a charge of nF reversibly through a potential difference E_r. If the energy change is negative, no external source of energy is required; the reaction will proceed spontaneously, just as a ball will roll spontaneously down a hill.

One can think of the reversible (i.e., equilibrium) potential for a reaction across an interface as a battery with a value of E_r, as shown schematically in Fig. 1. Thus, at equilibrium, our metal/solution interface can be modeled as a battery. Because the system is at equilibrium, no net reaction is occurring under these conditions.

Each electrochemical reaction has its own reversible potential, just as each element has its own melting temperature. A list of these reversible potentials under standard conditions is called an electromotive (emf) series.

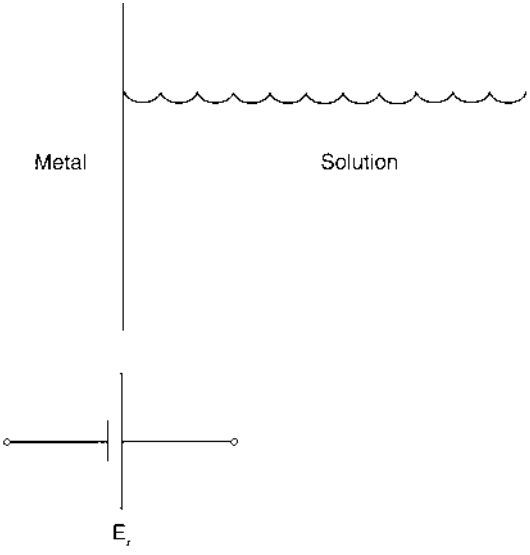

Figure 1 Schematic of an equilibrium metal–solution interface as battery with a voltage of magnitude E_r.

Table 1 Partial List of Standard Electrochemical Potentials

Reaction	Standard Potential (V vs. NHE)
$Au^{3+} + 3e^- = Au$	1.42
$Cl_2 + 2e^- = 2Cl^-$	1.36
$O_2 + 4H^+ + 4e^- = 2H_2O$	1.229
$Cu^2 + 2e^- = Cu$	0.34
$2H+ + 2e^- = H_2$	0.000
$Ni^{2+} + 2e^- = Ni$	−0.23
$Fe^{2+} + 2e^- = Fe$	−0.44
$Zn^{2+} + 2e^- = Zn$	−0.763
$A1^{3+} + 3e^- = A1$	−1.706
$Mg^{2+} + 2e^- = Mg$	−2.375
$Na^+ + e^- = Na$	−2.712

Two aspects of Table 1 are important. The "standard conditions" are 298 K and all reactants and products are at unity activity.* The second key is the selection of the hydrogen reaction as having a standard reversible potential of 0.0 V. The table allows the first use of thermodynamics in corrosion. For a metal in a 1 M solution of its salt, the table allows one to predict the electrochemical potential below (i.e., more negative) which net dissolution is impossible. For example, at +0.337 V(NHE), copper will not dissolve to cuprous ion if the solution is 1 M in Cu^{2+}. In fact, at more negative potentials, there will be a tendency at the metal/solution interface to reduce the cuprous ions to copper metal on the surface.

The concept of interfacial potential difference can be a major stumbling block for those new to electrochemistry. The measurement of voltage and its analogy to pressure in fluid flow is reasonable, but the reference point of zero volts and the sign conventions can be confusing. Moran and Gileadi wrote an excellent article on these topics to which the interested reader is referred (1). The key issues are summarized here.

Measurements of voltages within electrical circuits are familiar to many. One connects the lead from the positive terminal of the voltmeter to the point in the circuit of interest, and the lead from the negative terminal of the voltmeter to the point known as the ground. The ground is often in some way connected

* In most cases in corrosion, we ignore activity coefficients. Thus activity and concentration are used interchangeably. Strictly, this approach is flawed, but the lack of information concerning the values of activity coefficients in most cases makes it necessary.

electrically to the earth. In an ideal world, all grounds are the same voltage and are interchangeable. In electrochemical measurements, the idea of a ground as a reference point is more complicated.

Consider Fig. 2. In Fig. 2a, the connections for a standard measurement of voltage in an electrical circuit are shown. In Fig. 2b, the connections for an electrochemical measurement are started; connecting the lead from the positive terminal of the voltmeter to the electrode of interest is straightforward, but what is to be done with the negative lead? We need the electrochemical equilivalent of a ground. Despite many attempts, it has proved impossible to measure the

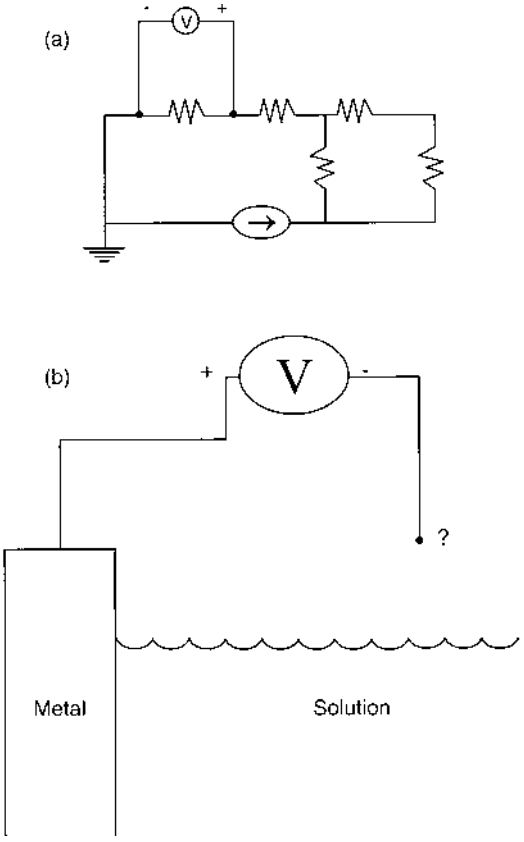

Figure 2 (a) Connections to measure potential difference in an electrical circuit. (b) Impossibility of measuring the potential across an electrochemical interface without introducing a second interface.

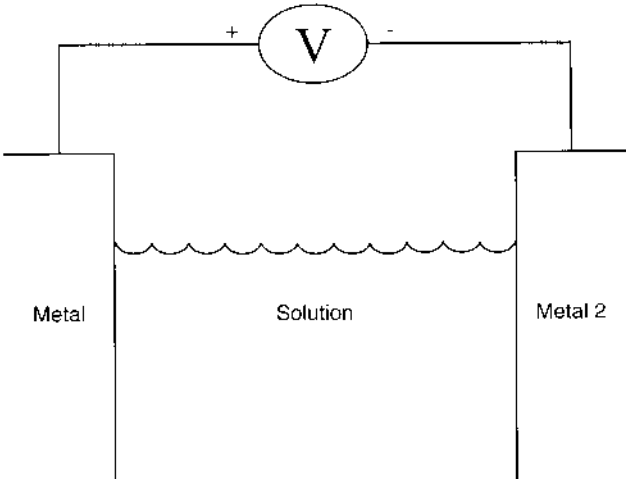

Figure 3 Inclusion of a second interface allows combined voltage of the two interfaces to be measured with a voltmeter.

potential across an electrochemical interface without introducing *another* electrochemical interface as shown in Fig. 3.

C. Reference Electrodes

By introducing another electrochemical interface, it would seem that the problem of measurement has been doubled. In fact, if the additional interface is at thermodynamic equilibrium, then the practical problem of measurement is solved. By maintaining a reaction in equilibrium at the interface, the potential across it is constant (and calculable). Thus any changes in the measurement of the potential between the two interfaces can be attributed to the electrode of interest (typically referred to as the *working electrode*).

Theoretically, any of the reactions shown in Table 1 could be used as reference electrodes (along with many others). Many years ago, the hydrogen reaction was selected as the reaction to which a value of zero volts is ascribed. Thus the standard for all reference electrodes is the hydrogen electrode in which a Pt (or other catalytic but corrosion-free surface) is exposed to a pH 0 solution saturated with hydrogen gas at room temperature. Its value is zero as the reaction is at equilibrium in a 1 M solution of the ion of interest (H^+) with the other reactant at unit activity (a partial pressure of 1 atm for H_2, generally achieved by bubbling hydrogen gas into the solution). It is sometimes called the standard hydrogen

electrode (SHE) or the normal hydrogen electrode (NHE). Thus voltages of other electrodes referred to this electrode are labeled in V(SHE) or V(NHE).

The perfect reference electrode (RE) is one for which the value depends solely on the concentration of one species, is in thermodynamic equilibrium, does not contaminate the solution of interest, is cheap to acquire, and is easy to maintain. Although the NHE electrode has a value of zero volts, it has some practical disadvantages. Chief among these is the need to maintain a source of hydrogen gas. Ever since the Hindenburg, many individuals have shied away from routinely having large volumes of hydrogen in close proximity to possible ignition sources. Fortunately, many more practical RE have been developed and are commercially available.

Most RE have the components shown in Fig. 4. In order to maintain the RE at equilibrium, a glass or polymeric body separates the inner, or fill, solution from the test environment. The ionic communication with the test solution needed is controlled, often through a porous frit. The electrode interface itself is often composed of a metal coated with a metal salt. This arrangement often leads to a robust equilibrium condition; as long as some metal salt is present on the electrode surface, the potential of the RE is independent of the *amount* of salt. The composition of the fill solution is important in maintaining the RE at equilibrium.

A large variety of reference electrodes has been reviewed by Ives and Janz

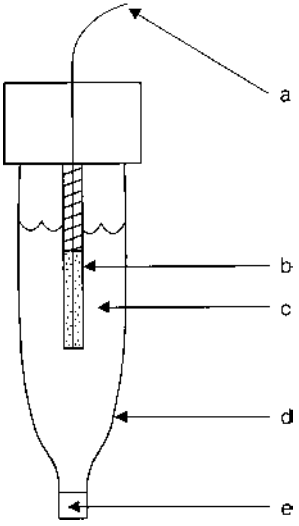

Figure 4 Components of typical commercial reference electrode: (a) electrical connection, (b) metal–metal salt electrode, (c) filling solution that maintains electrode interface equilibrium, (d) glass or polymeric electrode body, (e) porous frit.

(2). There are commercial suppliers for many of these. Three of the most commonly used in aqueous solutions are the saturated calomel electrode (SCE), the Ag/AgCl electrode, and the Hg/Hg_2SO_4 electrode. For soil, concrete, and other partially aqueous systems, other RE have been found to be better suited.

Selection of the type of RE is determined in large part by the composition of the fill solution. The fill solution can have two major effects on the electrochemical measurement. Along with the metal electrode, it controls the value of the RE potential. In addition it is generally concentrated (i.e., on the order to 0.5 to 5 M salt). Thus it can act as a source for ionic contamination of the test solution. Because the most popular reference electrodes contain chloride ion, a known aggressive species, this contamination source must be considered carefully. The rate at which the fill solution contaminates the solution (and vice versa) is strongly dependent on the leak rate of the frit. If the frit (or valve) prevented all movement of ionic species, then the RE would not function as a complete electrical circuit, which is required to allow a potential to be measured. Thus frits are generally designed to leak at rates on the order of 1μL/h.

A simple calculation shows the effects of such a leak rate. Consider a 0.5 1L test solution volume having 4 μL/h of 4 M Cl^- added (the KCl concentration in a saturated calomel electrode). In a 24 h test the initial Cl^--free solution will develop a concentration of 7.7×10^{-5} M Cl^-. Although low, this concentration will lead to pitting in many alloys (3), confounding interpretation of the results. A second effect of filling solution leakage into the bulk solution involves the cations that are released. In the case of the SCE, there is a small concentration of Hg^{2+} that makes its way into the bulk. Once in the bulk solution, the mercurous ions can be deposited electrochemically onto any surface at a potential below the reversible potential for Hg deposition. This deposition of metallic mercury can cause dramatic changes in the surface behavior.

Whereas the discussion of filling solution leakage has focused on the effects of the filling solution leaking out, there can also be effects of the bulk solution leaking into the reference electrode. Some compounds can foul the metal–solution interface within the RE or displace/convert the metal salt. The important effect of such processes is the disturbance of the equilibium at the interface, rendering our assumption of constant interfacial potential in the RE invalid. Unfortunately no warning signal is emitted from the RE under these conditions. Periodic checking of the RE to a laboratory standard is the only means of ensuring valid measurements.

In some cases, the physical size of a reference electrode can be important when space is constrained either in a laboratory cell or in a field monitoring application. The success of microdevices for monitoring environmental, physiological, and corrosivity variables has been greatly impeded by the lack of a robust, inexpensive RE. As discussed in Chapter 5, a RE placed too close to a surface can affect the current distribution and lead to erroneous potential measurements.

Rules of thumb are discussed in Chapter 5 that allow minimization of this problem.

Care and feeding of the RE is often neglected. Nonetheless, due to the nature of electrochemical potential measurements, confidence in one's reference electrode is critical. To maintain such confidence, establish a laboratory reference reference electrode. This standard can be most easily established by purchasing an extra reference electrode of choice and placing it in a two-necked flask containing the same solution that is used as the filling solution within the RE. For example, at UVa we have a "lab standard SCE" that is exposed to a saturated solution of KCl. On a regular basis, the RE to be used in an experiment can be compared to the lab standard. Be sure to clean the outer surface of the to-be-tested RE before immersion in the two-necked flask. If the value of the potential difference between the two nominally identical RE is steady and small (e.g., < 3 mV), the tested RE passes. For high-precision meaurements, the difference measured can be used to correct the measured potentials in the experiment. Periodic refurbishment of RE used in experiments according to the manufacturer's instructions is also good practice and will keep RE cost under control.

Protection of the lab standard is clearly of paramount importance. Use of the lab standard for any measurement in a real cell is considered a capital offense in our center. Every year or so the lab standard is introduced into experimental service and replaced with a new lab standard.

Independent of the RE chosen for a measurement, there is often a need to convert the measured values to a difference reference scale. For example, although the measurements may have been made with an SCE, the investigator may want to make a comparison with thermodynamic data that are referenced to NHE. The most foolproof means of conversion is the number line. Even the most algebraically challenged can use a number line flawlessly to convert readings from one scale to another. Figure 5 shows a number line containing the most common RE.

An example will serve to illustrate the use of the number line. If a measure-

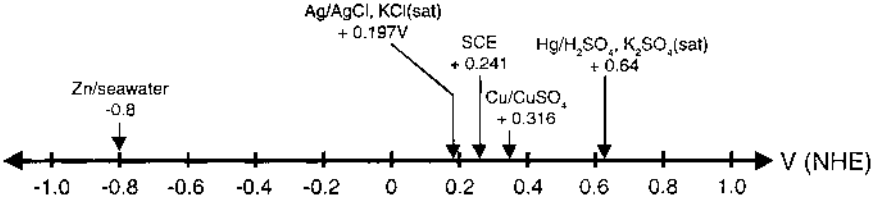

Figure 5 Number line for conversion of electrode potentials among different reference electrode scales.

ment of the potential of steel in seawater shows that it is −0.5 V(SCE), what is the potential on the NHE scale? On the $Cu/CuSO_4$ scale? By placing a tick at the measured value (see arrows) we can see that the measured value would be −0.259 V(NHE) and −0.68 V($Cu/CuSO_4$).

D. Nernst Equation

As electrochemical reactions are, at their heart, chemical reactions, their thermodynamics depend on the concentrations of the species involved, as well as the temperature. The Nernst equation describes this dependence. Derivations of the Nernst equation are available in many standard texts (4–6). For our purposes, it will be simply stated that for a reaction described by

$$aRd + mH^+ + ne^- = bOx + cH_2O \tag{2}$$

The reversible potential can be calculated according to

$$E_r = E_o - \frac{RT}{nF}\ln\frac{\{Ox\}^b\ \{H_2O\}^c}{\{Rd\}^a\ \{H^+\}^m} \tag{3}$$

where E_r = reversible potential (V), E_o = standard reversible potential (i.e., E_r for unit activity of all reactants/products), and $\{i\}^j$ = activity of species *i*, raised to the stoichiometric coefficient *j*.

The standard reversible potential is that listed in the EMF series of Table 1 and represents a special case of the Nernst equation in which the second term is zero. The influence of the solution composition manifests itself through the logarithmic term. The ratio of activities of the products and reactants influences the potential above which the reaction is thermodynamically favorted toward oxidation (and conversely, below which reduction is favored). By convention, all solids are considered to be at unit activity. Activities of gases are equal to their fugacity (or less strictly, their partial pressure).

Note that the effects of solution composition on E_r are fairly weak as they appear in the logarithm term. Thus an order of magnitude change in the concentration of oxidized form (i.e., Ox in the equation above), while keeping the concentration of the reduced form constant, changes the reversible potential by *RT/nF* (typically 30 to 60 mV). Although small, these changes can be important in corrosion situations. Figure 6 shows a graphical representation of the Nernst equation.

E. Pourbaix Diagrams

In 1945, Marcel Pourbaix submitted a Ph.D. dissertation entitled "Thermodynamics in dilute solutions: graphical representation of the role of pH and potential." It was initially rejected, or so the legend goes. Fortunately for corrosion scientists

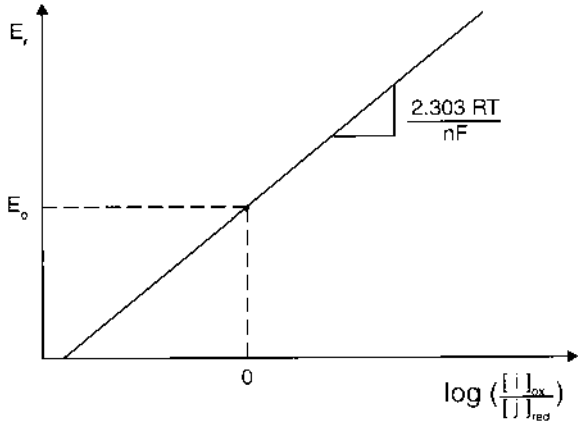

Figure 6 Semilogarithmic plot of Nernst equation showing dependence of reversible potential on ratio of activities of oxidized and reduced species for cases in which both stoichiometric coefficients are unity.

and engineers everywhere, Pourbaix continued his development of graphical representations of electrochemical thermodynamics. The work of the institute that M. Pourbaix founded continues through both additions and updates to his *Atlas of Electrochemical Equilibria in Aqueous Solution*, a must-have for all corrosionists (7). These diagrams are to electrochemistry what temperature–composition phrase diagrams are to materials science. In both cases, the plots identify the phases that have the lowest Gibbs free energy for various values of the external variables. In this way the spontaneous directions of all reactions can be determined.

Pourbaix diagrams are plots of (reversible) potential vs. pH for elements in pure water. They consist of regions of stability defined by lines as borders. Three types of lines exist on Pourbaix diagrams. Horizontal lines describe reactions that are dependent only on potential (e.g., $Fe = Fe^{2+} + 2e^-$). Vertical lines describe reactions that are dependent only on pH (e.g., $Fe^{2+} + 2OH^- = Fe(OH)_2$). Angled lines correspond to reactions that depend on both potential and pH (e.g., $O_2 + 4H^+ + 4e^- = 2H_2O$).

The most simple Pourbaix diagram is that for water shown in Fig. 7. All Pourbaix diagrams contain the two lines that bound the regions of stability for water, known as the reversible hydrogen and reversible oxygen lines, and labeled as "a" and "b," respectively. For corrosionists the importance of these lines should not be underestimated. As noted in the introduction, for metal dissolution to occur, a reduction reaction must occur. In aqueous solution, the most common reduction reactions are the reduction of dissolved oxygen and the reduction of water

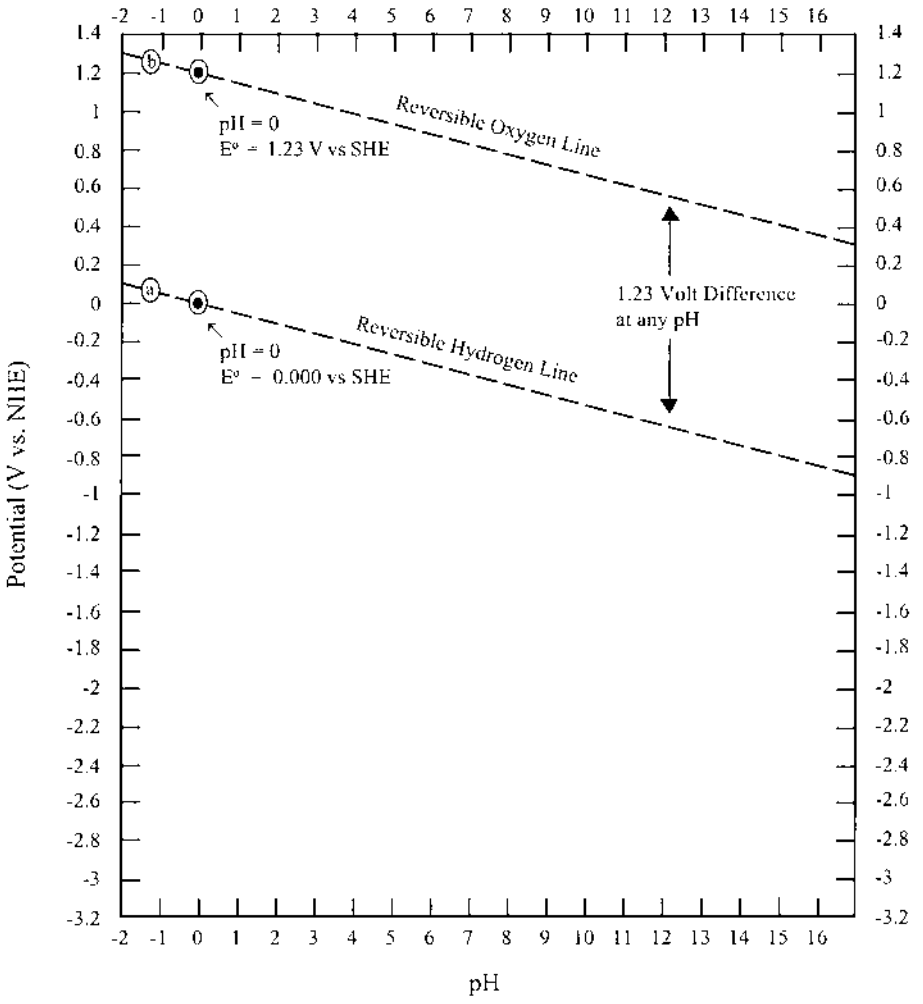

Figure 7 *E*–pH (Pourbaix) diagram for water. Water is stable between lines ''a'' and ''b.''

(also known as hydrogen evolution). Lines "a" and "b" define the regions of pH and potential where these two cathodic reactions can occur. The lines are dotted as an indication that all the species in the reaction are dissolved rather than solid. Oxygen can be reduced only at potentials below the line "b," conditions for which the oxygen reduction reaction (ORR),

$$O_2 + 4H^+ + 4e^- \rightarrow 2H_2O \quad (4)$$

is favored to proceed as written. Similarly, the reduction of water can only occur at potentials more negative than line "a," under which conditions the hydrogen evolution reaction (HER),

$$2H_2O + 2e^- \rightarrow H_2 + 2OH^- \quad (5)$$

is favored to proceed as written. When the metal surface is at a potential where one or both of these reactions can occur, the possibility of corrosion exists as long as the metal dissolution reaction is thermodynamically favorable. For example, the reversible potential for copper metal oxidation reaction is above line "a" for all pH. Thus, in the absence of oxygen, metallic copper is thermodynamically favored in pure water over all dissolved or other solid copper species. The Pourbaix diagram can be used to illustrate why gold is useful for wedding bands as shown in Fig. 8. As (generally) marriage is considered to be permanent state, the selection of gold is fortuitous; the reversible potential for the oxidation of pure gold is above the oxygen line for all pH. Thus gold is absolutely stable at room temperature in pure water. If only all marriages were.

The Nernst equations for ORR and HER are simplified due to their dependence only on pH, which is itself the negative logarithm of the activity of H^+:

$$\text{For ORR:} \quad E_r = 1.23 - 0.059\text{pH} \quad (6)$$

$$\text{For HER:} \quad E_r = -0.059\text{pH} \quad (7)$$

As with all Pourbaix diagrams, the potential scale is referenced to NHE. Thus, line "a" at pH 0 (i.e., 1 M H^+) has a value of 0 V(NHE), and line "b" at pH 0 has a value of 1.23 V (NHE).

A slightly more complicated diagram is that for Al as shown in Fig. 9. Many valve metals have such fairly simple E–pH diagrams. Lines "a" and "b" are present, as always. The solid lines represent three reactions: oxidation of Al metal to Al^{3+}, the equilibrium between Al^{3+} and Al_2O_3, and the equilibrium between AlO_2^- and Al_2O_3. The latter two are purely chemical reactions, so there is no potential dependence. The oxidation of Al at low pH does not involve water, whereas it does at higher pH.

$$\text{At low pH:} \quad Al \rightarrow Al^{3+} + 3e^- \quad (8)$$

$$\text{At high pH:} \quad Al + 2H_2O \rightarrow AlO_2^- + 4H^+ + 3e^- \quad (9)$$

The involvement of both electrons and hydrogen ion in the high pH reaction explains the slope of the line. Because both reactions involve at least one solid species, the lines are solid, by convention. The diagram in Fig. 9a assumes that the concentration of all dissolved species except H^+ and O_2 is 10^{-6} M. Such simplified diagrams have pedagogical uses, but the dependence of the Nernst

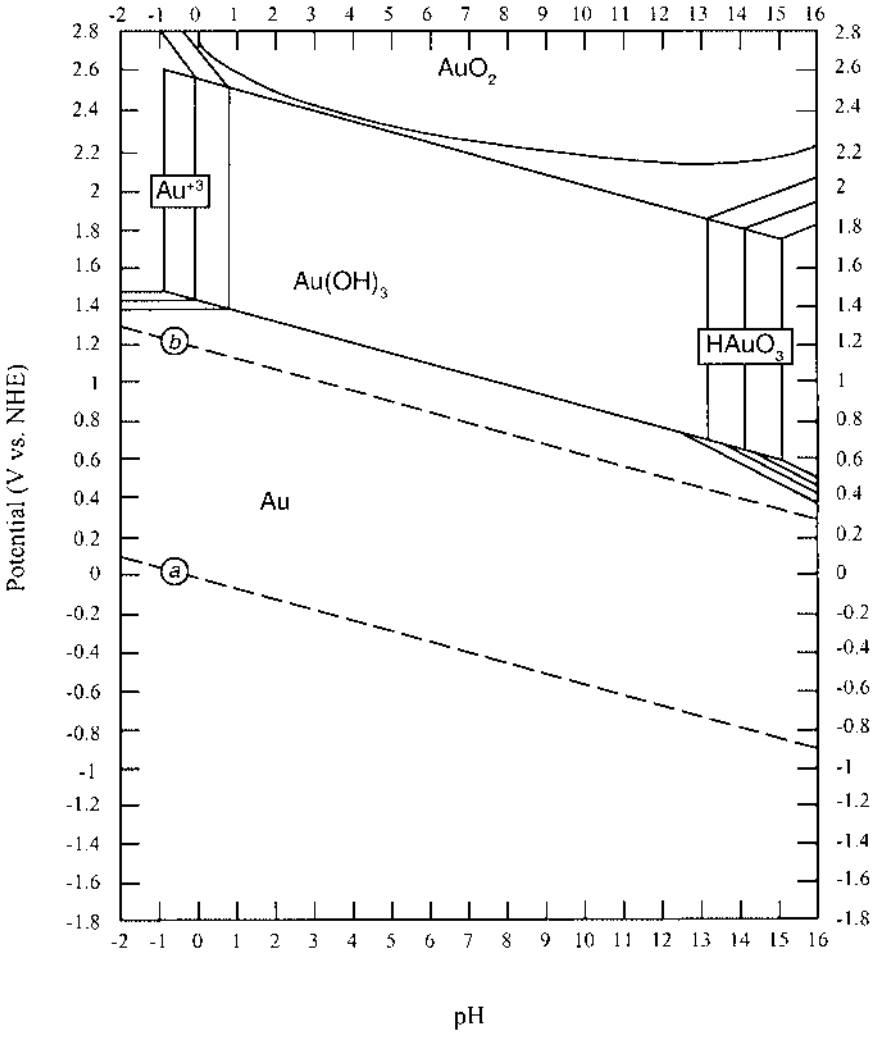

Figure 8 *E*–pH diagram for Au. Note that Au is stable at all pH in pure water at room temperature, as the reversible potential for Au oxidation is greater than the reversible potential for oxygen reduction (line ''b'').

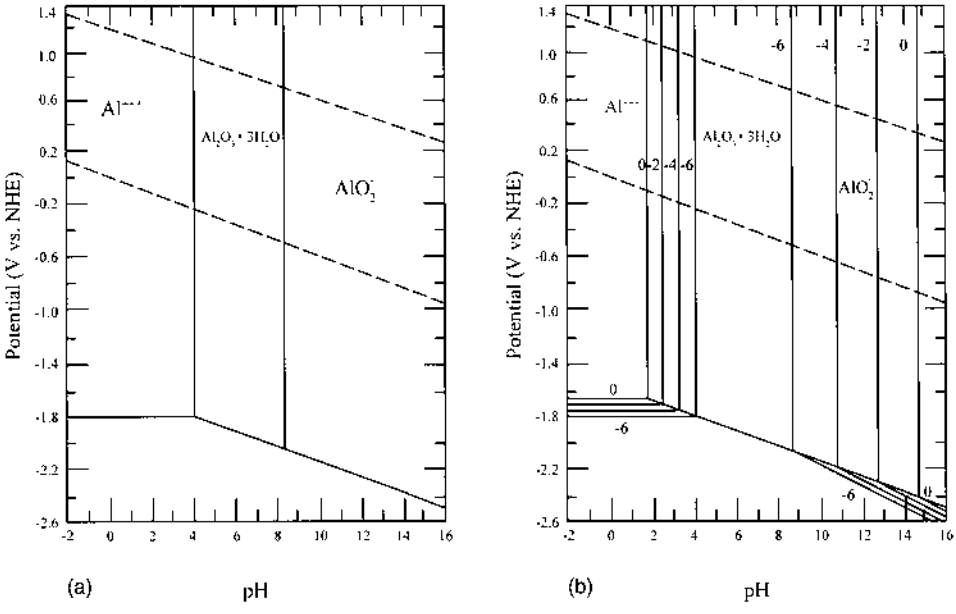

Figure 9 (a) Simplified *E*–pH diagram for Al, which is typical of many valve metals such as Ti, W, and Zn. Al is expected to show amphoteric behavior, i.e., corrode at both high and low pH, because soluble species are more stable than metallic Al under such conditions. (b) *E*–pH diagram for Al showing effects of dissolved ion concentration on the boundaries of the phase diagram. Numbers next to boundary lines are the logarithms of the concentration of the species involved.

equation on concentration must generally be considered. A more extensive *E*–pH diagram for Al is shown in Figure 1-9b.

The Pourbaix diagram for Cu represents one of the more complicated sets of *E*–pH behavior as shown in Fig. 10. All three kinds of lines are possible due to the large number of reactions to be considered. Nonetheless, the same principles apply to the diagrams as for the more simple Pourbaix diagrams. The *Atlas* (7) and the literature continue to refine and extend the *E*–pH concept for a concise graphical approach to electrochemical equilibria. Some current issues in this regard include:

1. Higher Temperature

All of the diagrams in Pourbaix's original atlas were calculated for room temperature. To develop Pourbaix diagrams under higher temperature conditions, several aspects need to be considered. Not only does the temperature affect the logarith-

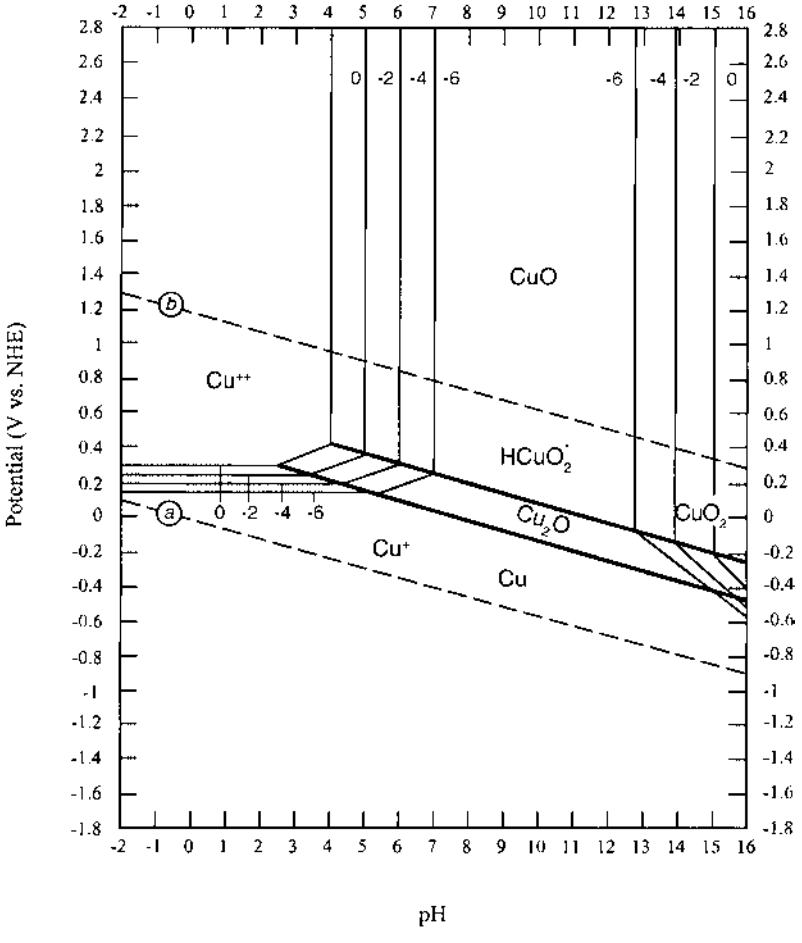

Figure 10 *E*–pH diagram for Cu showing all three types of lines along with the effects of dissolved copper concentration.

mic term but also the effects on the standard potentials (including the effect on the NHE) must be included. In recent years there has been increasing work for high-temperature conditions in pure water driven by the need for nuclear reactor materials (8–10).

2. Metastable Species

Metastable species (such as thiosulfate, $S_2O_3^{2-}$) have been shown to be important in some corrosion scenarios (11–13). Such species are not represented on stan-

dard Pourbaix diagrams. For example, Marcus (14,15) has published diagrams that consider metastable sulfur species. The most significant challenge in these studies is the determination of accurate thermodynamic data.

3. Alloys

Alloys represent special problems for *E*–pH diagrams. Overlaying of the diagrams for the individual elements has shown some, albeit limited, promise (16). The problem may indicate that the effects of alloying are manifested more in the kinetics than in the thermodynamics of corrosion and electrochemistry. For example, passivity of pure iron in acid is not predicted from *E*–pH diagrams; it is a kinetic effect.

F. Applications

Despite the limitations inherent in *E*–pH diagrams, the approach can be extremely useful in understanding and overcoming corrosion problems in solutions more complicated than pure water. Two examples illustrate the power of this approach.

Figure 11 shows an *E*–pH diagram developed by Silverman (17,18). This diagram differs from that in the *Atlas* (7) in the use of more recent, more accurate thermodynamic data for the species involved, including several titanium chloride species expected because of the presence of several molar chloride, and because it was calculated for a temperature of 75°C. The conditions represent a process stream in which Grade 2 Ti was exposed to acidic chloride solutions containing an organic molecule that had acid–base and thermodynamic properties very similar to those of aspartic acid. There was concern that the Grade 2 Ti might corrode at sufficiently low pH, but the critical pH was unknown. Although details are available in the original work (17,18), the key results can be seen in Fig. 11, in which the corrosion potentials (E_{corr}) measured for several possible process solutions are indicated. The open symbols are for conditions in which the thermodynamics predict dominance of TiO_2, suggesting that low corrosion rates are likely, whereas the solid symbols are in a region in which Ti^{3+} dominates, indicating the likely absence of any protective film. The *E*–pH diagram indicates a threshold pH of approximately zero, below which corrosion rates would be expected to increase rapidly. Short-term (two-day) experiments were conducted. For solutions of pH 0.05 and greater, corrosion rates of < 1 mpy were observed, whereas for pH values of -0.55 and -0.9, penetration rates of 20 and 100 mpy, respectively, were measured. By taking into account complexation and using the best thermodynamic data avilable, Silverman showed that a rapid assessment of process limitations can be made and handed off to the production line.

A second example of the utility of *E*–pH diagrams comes from the work of Walter at the University of Wollongong in Australia. Hot-dipped Al–Zn-

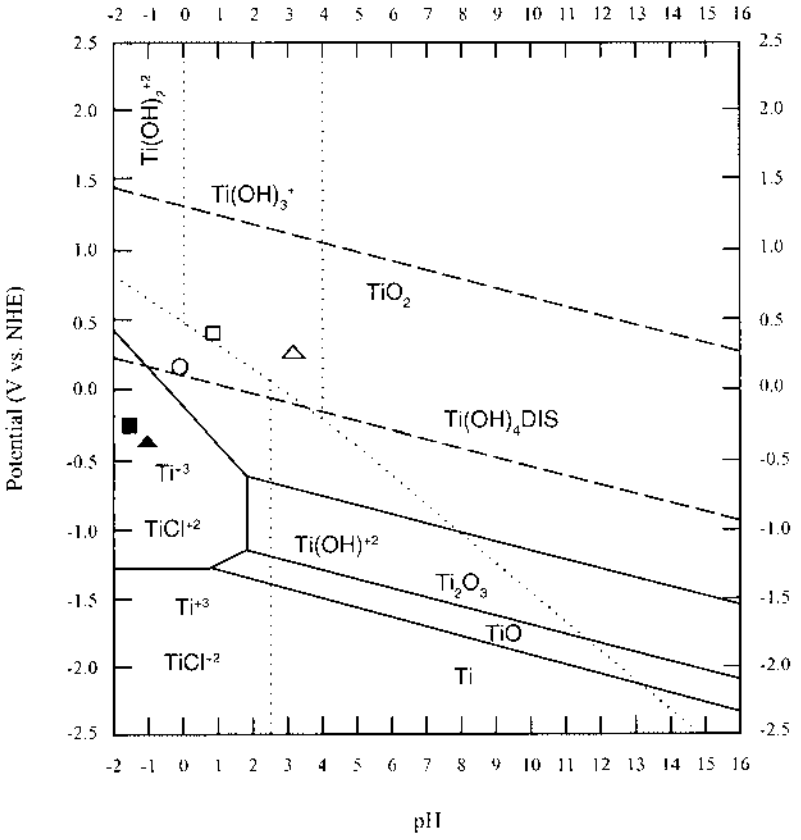

Figure 11 *E*–pH diagram for Ti developed by Silverman for 75°C and 10 M Cl^-. Symbols represent measured E_{corr} of Grade 2 Ti alloy in a simulated process solution. Solid symbols indicate conditions that led to rapid corrosion ($>$ 20 mpy), whereas open symbols represent conditions that led to very low corrosion rates ($\ll$ 1 mpy).

coated steel is widely used for fences and roofs after painting. Their expected service life is in the 20 to 30 year range. Unfortunately, in some geographical locations, so-called "bleedthrough rusting" occurred in which rust stains appeared (i.e., "bled through") coatings in only a few years. The hot-dipped coatings were designed to be sacrificial to the steel, but failure analyses showed that although the metallized coatings were still present, the underlying steel had corroded at defects. Figure 12 shows a photograph of such a system after service in the field. Walter used Pourbaix diagrams in order to assess what types of environmental conditions could lead to such a phenomenon.

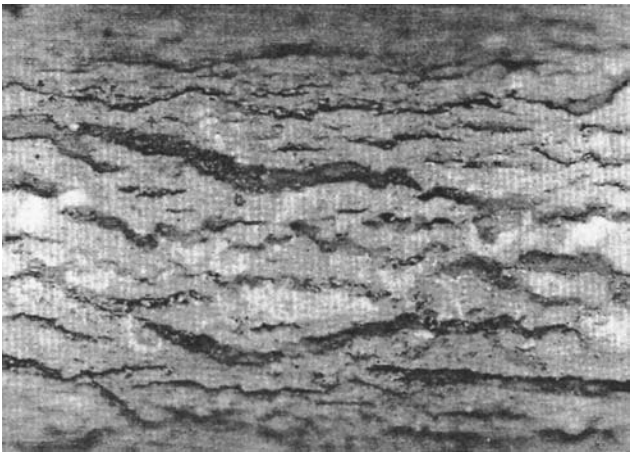

Figure 12 Photomicrograph of bleedthrough rust phenomenon. Red areas represent corroded steel that was not protected by the hot-dipped Al-Zn coating. (From Ref. 22.)

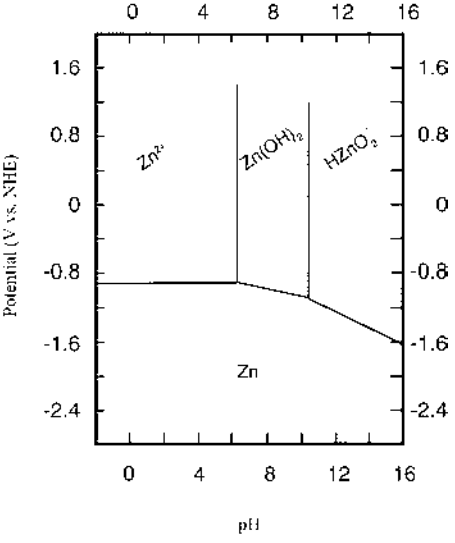

Figure 13 Simplified E–pH for Zn. (From Ref. 22.)

To approach the problem, the complex system was modeled as a galvanic couple amongst pure Al, pure Zn, and pure Fe. Figure 13 shows the *E*–pH diagram for Zn. Qualitatively, it is similar to the Al diagram shown in Fig. 9. Figure 14 shows an overlay of the *E*–pH diagrams for Al, Zn, and Fe. In order for material to function as a sacrificial anode, it must remain active/unfilmed. In fact, prevention of passivation of Al anodes continues to be an area of interest for marine applications owing to its many advantages over conventional zinc anodes. Careful inspection of Fig. 14 shows that there exists a narrow region of potential and pH in which both Al and Zn would be expected to (possibly) form protective films, but in which metallic Fe is thermodynamically unstable. In these neutral, but oxidizing, solutions, it would be expected that the hot-dipped Al–Zn would not provide sacrificial protection to the steel.

II. ELECTROCHEMICAL KINETICS

A. Types of Electrochemical Cells

1. Driving and Driven Cells

The kinetics of electrochemical reactions at a metal–solution can best be studied when the electrode of interest is part of an electrochemical system or cell. The polarity of electrochemistry conventions can be confusing, but the application of a few simple rules can alleviate much of the uncertainty. Electrochemical cells are two-terminal devices that can be classified as either driving or driven according to their function. A driving electrochemical cell is a power producer, converting chemical energy into electrical power. In some cases this power can be used externally to the cell. A driven electrochemical cell is a power consumer. When used to power an electrical device, a battery is a driving system. When a battery is being recharged, it becomes a driven system. Corrosion systems in the absence of external influence are short-circuited, driving systems.

Consider the driving system shown in Fig. 15a. A battery is connected to a resistor. Convention states that positive current (defined as the flow of positive charge) leaves the positive terminal of a discharging battery and enters the positive terminal of a resistor.* A voltmeter would read a positive value if its positive lead were connected to the positive end of the resistor (or battery) and its negative lead attached to the negative side of the resistor.

Now consider just the battery in Fig. 15b. It is acting as a driving system. The positive electrode is called the *cathode* and the negative electrode is the *anode*. Four rules can be used to assist in determining polarity and the location of the different reactions.

* Of course, it is now known that electrons are the charge carriers and hence their flow is in the opposite direction of conventional current.

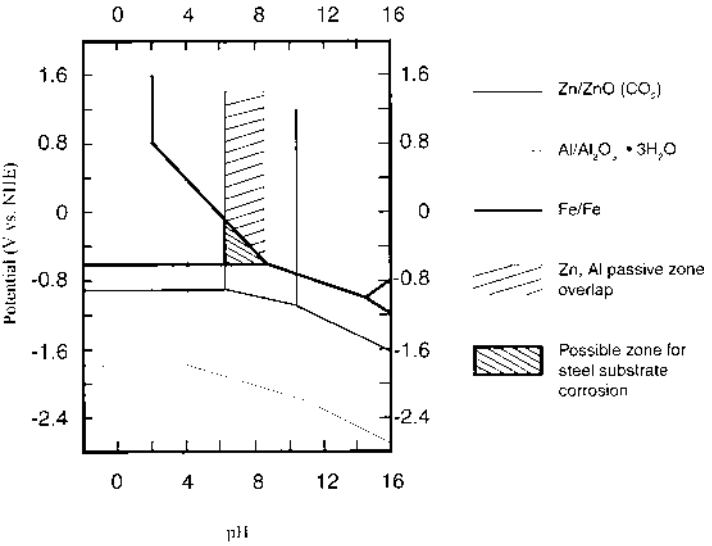

Figure 14 Overlay of Pourbaix diagrams for Al, Fe, and Zn, showing that there exists a region of potential and pH within which Al and Zn would be expected to form solid films (i.e., passivate) and lose their ability to corrode sacrificially and protect the steel. (From Ref. 22.)

Rule 1: Gain of electrons is reduction.
Rule 2: Reduction always occurs at the cathode.
Rule 3: Loss of electrons is oxidation.
Rule 4: Oxidation always occurs at the anode.

These rules applied to Fig. 15b imply that the reduction reaction (at the cathode) produces positive current (i.e., it consumes electrons), whereas the oxidation reaction (at the anode) consumes positive current. The resistor is blissfully unaware of these goings on. It simply removes some of the energy from the electrons for its own purposes, such as running a watch, calculator, or laptop computer. In the case of a driving system, the cathode is at a potential more positive than the anode.

In Fig. 15c, the resistor has been replaced by an electrochemical cell. This cell could be a recharging battery or a corrosion cell that is being studied electrochemically. In either case, it will be a driven system. The driving is being done by the battery just discussed, or a power supply, or a potentiostat (more on this option below). Nonetheless, replacing the resistor with an electrochemical cell does nothing to change the polarity of the driven system. The electrode on the

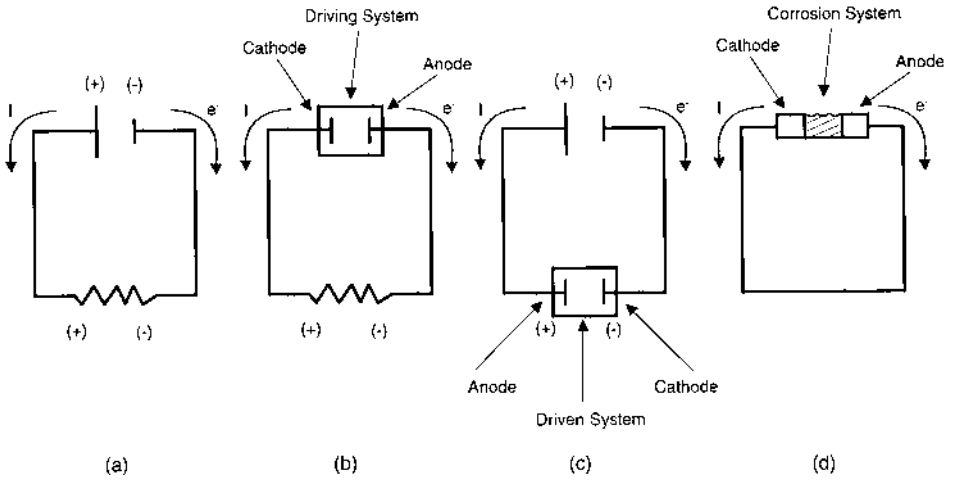

Figure 15 Types of electrical/electrochemical cell with polarity conventions shown: (a) power supply driving a resistor, (b) battery driving resistor, (c) power supply recharging a driven battery, (d) corrosion cell as a nearly short-circuited driving system. The resistance represents the electrical resistance in the metal between anode and cathode sites.

left is at a more positive potential than the electrode on the right, allowing positive current to continue to pass through the cell. Consider the electrode on the left. Positive current enters it from the electrical lead and leads it into the solution. Electrons must be being liberated by a reaction at the interface and moving into the lead. Thus an electrochemical oxidation is occurring on that positive electrode, making it an anode. Similarly, electrochemical reduction occurs on the opposite electrode, making it a cathode. Note that in the case of the driven cell, the anode is positive whereas the cathode is negative, opposite the case of the driving cell. Test your understanding by using these concepts to determine if the terminals in your car battery are labeled correctly under both charge and discharge. See the footnote below* for the answer.

A corrosion cell is represented in this manner as shown in Fig. 15d. It is a driving cell, but one that is short-circuited. The anodic and cathodic reactions occur on the same metal surface. If the sites at which the two reactions occur could be physically separated, then the cathodic reactions would be occurring at a higher potential than the anodic reactions.

---

* The labels on your car battery (or any other rechargeable battery) are always correct. During use (discharge), the positive terminal is the cathode and the negative terminal is the anode; it is a driving system. During recharge, the positive terminal is the anode and the negative terminal is the cathode; it is a driven system.

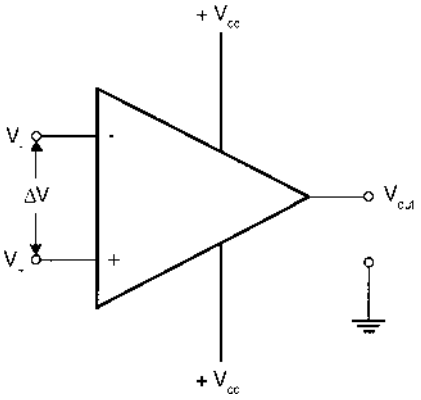

Figure 16 Terminal connections for operational amplifier. V_{cc} represent the positive and negative power supplies needed. The input terminals are labeled as ''−'' and ''+''.

2. Potentiostats

In most electrochemical measurements of corrosion kinetics a potentiostat is used. This description will cover the rudimentary operation of a potentiostat using the concept of an ideal operational amplifier (op amp) as a basis. An op amp is a three-terminal device as shown in Fig. 16 with two input terminals and one output terminal. A perfect op amp follows five basic rules (19):

1. When the voltage difference ΔV ($= V_+ - V_-$) is zero, the output voltage V_{out} (relative to ground) is zero. That is, a perfect device acts as a differential amplifier.
2. When a small ΔV is applied between the input terminals, the output voltage tends towards plus or minus infinity depending upon the polarity of ΔV. That is, the gain of a perfect op amp is infinite.
3. The current between the two input terminals is zero because the resistance (impedance) between them is infinite. That is, the input impedance is infinite.
4. The output current depends only on the output voltage and the resistance (impedance) of the load. That is, the output impedance is zero.
5. If ΔV undergoes changes, the output voltage follows these changes exactly. That is, the bandwidth of a perfect device is infinite.

Fig. 17 shows how such an ideal op amp can be configured as a potentiostat and connected to an electrochemical cell to study kinetics. First consider the electrochemical cell in the schematic. Unlike the cells discussed above, this cell has three electrodes. The working elecrode (WE) represents the interface of inter-

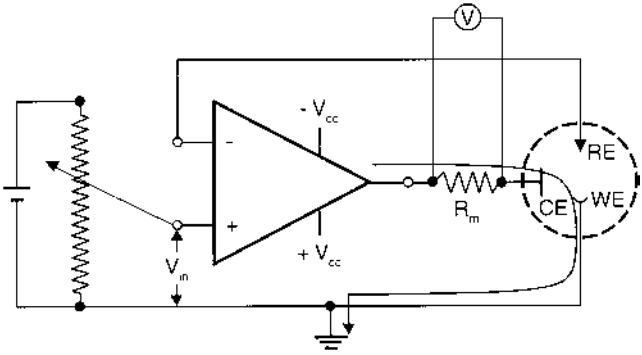

Figure 17 Configuration of op amp to function as a potentiostat. The desired V_{in} is set by the experimenter via the voltage divider on the left, which consists of a battery and a variable resistor. The path of the current is shown, indicating that no current passes through the RE.

est; the reference electrode (RE) has been introduced earlier in Chapter 2 and acts as our standard for potential measurements. The counter electrode (CE) is an additional interface whose sole purpose is to act as an anode or a cathode (electron sink or source) for our driven electrochemical cell via reactions that occur on its surface. In order to study the corrosion kinetics of the WE, the potential of the WE is controlled with respect to the RE at a constant value, and the reaction rate (i.e., current density) under those conditions is determined. A series of potentials may be studied in order to determine the effect of changes in potential on the corrosion rate, for example.

The potentiostat accomplishes this feat by simply following the five rules. If the ΔV between the RE and the WE is not V_{in} (set by the battery and variable resistor), the output voltage will be nonzero until ΔV goes to zero. The application of a V_{out} other than zero allows current to pass through the ammeter, through the CE interface, through the solution, through the WE interface, and to electrical ground. This current path is shown in Fig. 17. Because of the infinite input impedance of the assumed perfect negative input (see Rule 3), no current passes through the RE, allowing it to remain at equilibrium and to serve as a potential standard. If the current needed to maintain V_{in} changes because of alterations in conditions at the WE surface (e.g., formation of a film), then V_{out} changes instantaneously to accommodate. By changing the polarity and magnitude of V_{in}, the kinetic behavior of an interface in terms of the i–E relationship over a wide range of potential can be determined. Of course, the effects of external variables such as temperature, solution composition, and solution flow can also be studied under constant electrochemical conditions.

The WE and CE combination represents a driven electrochemical cell. The presence of the RE allows the separation of the applied potential into a controlled portion (between the RE and the WE) and a controlling portion (between the RE and the CE). The voltage between the RE and the CE is changed by the potentiostat in order the keep the controlled portion at the desired value. Consider the application of a potential V_{in} to the WE that is more positive than its rest potential, V_{rest}, with respect to RE. By definition, polarization of the WE anodically (i.e., in a positive direction) would lead to an anodic current through the WE–solution interface and a release of electrons to the external circuit. These electrons would be transported by the potentiostat to the CE. A reduction reaction would occur at the CE–solution interface facilitated by a more negative potential across it. The circuit would be completed by ionic conduction through the solution.

For simplicity, assume that the WE and the CE are identical and therefore, in the absence of external polarization, have the same interfacial potential. As shown in Fig. 18a, application of a potential that encourages oxidation on the WE surface would cause reduction on the CE surface. The WE potential would

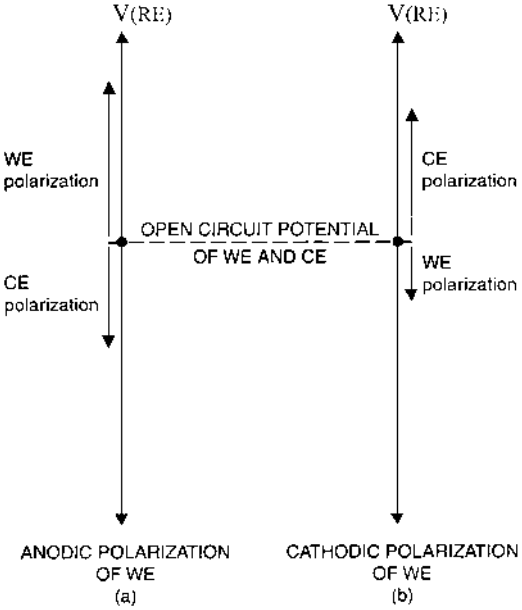

Figure 18 Number lines representing change in the potential of the WE and CE under conditions of (a) anodic polarization of the WE and (b) cathodic polarization of the WE. The extent of the polarization of each is determined by the kinetics of the reactions occurring.

become more positive, and the CE potential would become more negative. The current passing through the WE at a given level of polarization ($V_{in} - V_{rest}$) is a measure of the reaction kinetics at the WE–solution interface. The amount of polarization of the CE would depend on its kinetics. Changing the polarity of $V_{in} - V_{rest}$ would result in changes in interfacial potentials in the directions shown in Fig. 18b.

B. Tafel Behavior and Evans Diagrams

Consider the electrochemical system shown in Fig. 19 consisting of three Pt–solution interfaces in room-temperature solutions. The middle chamber is separated from the outer chambers by a porous membrane that limits mass transport, allowing the solutions to remain at different pH. Chamber A represents a NHE reference electrode: the pH is zero and hydrogen gas is present at 1 atm. At this Pt–solution interface, the HER reaction is in thermodynamic equilibrium. A

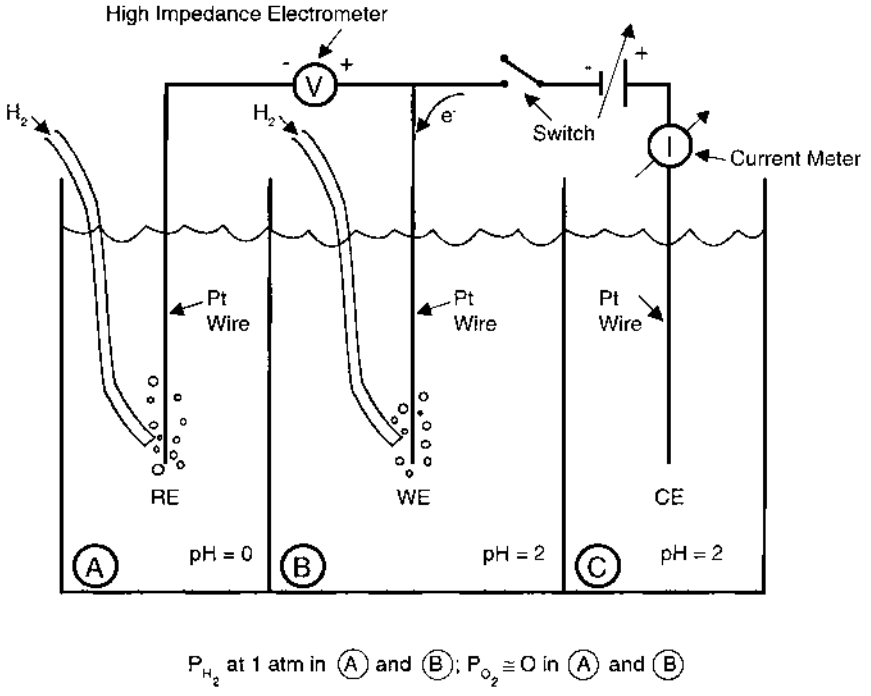

Figure 19 Three-compartment cell for studies of the kinetics of the hydrogen evolution reaction on Pt. The lines between the chambers prevent mixing but allow ionic conduction.

nearly identical situation exists in chamber B; the only difference is that the solution is at pH 2. Both chambers are deaerated (thus removing the reduction of dissolved oxygen as a possibility). In chamber C, a Pt wire is immersed in a pH 2 solution. The presence or absence of oxygen or hydrogen gas is immaterial in chamber C, as will be discussed below. The WE wire in chamber B is connected to the positive terminal of a voltmeter, whereas the RE wire in chamber A is connected to the negative terminal. The WE can also be connected (via a switch) to a variable current source that is connected to the CE wire in chamber C through an ammeter.

With the switch open, the potential measured by the high-impedence* voltmeter would be −0.118 V. This value can be calculated from the Nernst equation. The reversible potential of the Pt wire in chamber A would be zero relative to NHE as it is itself an NHE, the reversible potential of the WE in chamber B would be

$$E_{WE} = -0.059\ \text{pH} = -0.059(2) = -0.118\ \text{V (NHE)} \tag{10}$$

As long as the two electrodes are in equilibrium (i.e., no current is passing through the interfaces), the reversible potentials will follow the Nernst equation.

The variable current source can be used to supply electrons to the WE at a constant current of 100 $\mu A/cm^2$. The source of these electrons is an oxidation reaction occurring at the CE–solution interface. The most likely is water oxidation,

$$2H_2O \rightarrow O_2 + 4H^+ + 4e^- \tag{11}$$

also known as oxygen evolution. According to the Nernst equation, the potential of the CE must be at least 1.05 V(NHE)† for this reaction to occur. At the WE, water reduction occurs, producing hydrogen gas at the prescribed rate (which is about 1 nanomole of hydrogen per second = about 600 trillion hydrogen atoms per second). To give this net rate of hydrogen production, the interfacial potential of the WE must move in the negative direction. Assume that it does so by 100 mV, so that the potential of the WE becomes −0.218 V(NHE). Increasing the applied cathodic current by an order of magnitude 1 mA leads to another 100 mV movement in potential more negative, so that the WE potential becomes −0.318 V(NHE). Continued measurements result in the plot of Fig. 20.

Figure 20a is a plot of the data on semilogarithmic axes; the potential is on a linear scale, whereas the current is on a logarithmic scale. The data form a straight line with a slope of *b*, referred to as the Tafel slope, in honor of Henrik Tafel, who studied the HER in the early 1900s (20). The data shown have a Tafel

* If the voltmeter did not have a high impedance (resistance) between its terminals, current would pass between the WE and RE, polarizing both and rendering the RE a useless standard for potential.

† $E_{r,02} = 1.23 - 0.059\ \text{pH} = 1.05$ V(NHE).

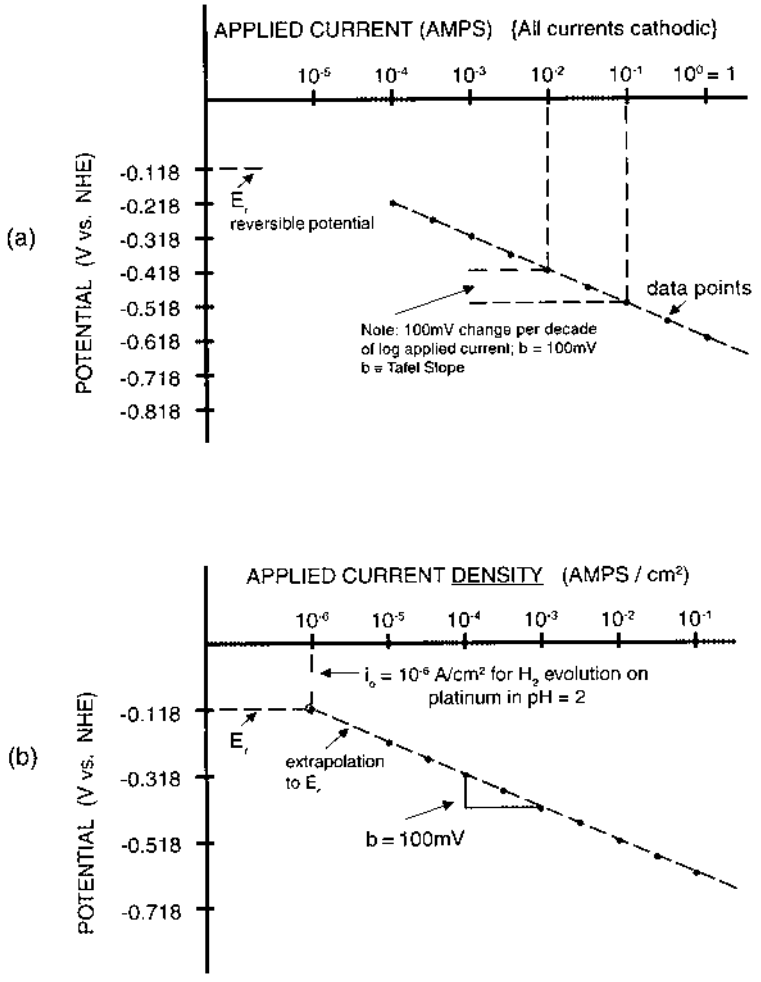

Figure 20 Schematic results from apparatus in Fig. 19: (a) cathodic polarization data in terms of current, (b) normalized polarization data assuming an area of 10 cm^2. Also included is an extrapolation of the data to E_r in order to determine i_o.

slope of 100 mV/decade, a value in the middle of the 30–200 mV/decade range typical of such slopes. As was noted previously, current densities are generally of more interest than currents, so the data in Fig. 20b represent an area correction assuming an area of 10 cm^2. Note that the Tafel slope is independent of the electrode area.

Included in Fig. 20b is an extrapolation of the data to lower applied current densities back to the reversible potential for the WE (−0.118 V(NHE)). At the reversible potential, no net reaction occurs; the system is in thermodynamic equilibrium. Nonetheless, this equilibrium is a dynamic one. Both hydrogen evolution and hydrogen oxidation are occurring on the Pt surface, albeit at the same rate so that no net production or consumption of hydrogen occurs. It is somewhat analogous to the idle rate of an engine; there is no net movement, but the automobile is ready to go as soon as the gear is engaged. In the case of electrochemistry, engaging the gear is achieved by applying a potential or current. The electrochemical analogue to the idle rate is referred to as the exchange current density, i_0. For the data in Fig. 20, the exchange current density for the hydrogen reaction is 10^{-6} A/cm^2. Current densities for electrochemical reactions usually range between 10^{-2} and 10^{-12} A/cm^2.

The difference between the potential applied and the reversible potential for a reaction is known as the overpotential. It represents the driving force for the kinetics of the reaction. Anodic overpotentials are associated with oxidation reactions, and cathodic overpotentials are associated with reduction reactions. The relationship between the overpotential and the reaction rate defines the kinetics. Mathematical relationships exist for many instances, but in corrosion situations, the data are generally experimentally derived.

During this polarization of the WE, qualitatively similar effects have occured on the CE as shown in Fig. 21, which includes the data from Fig. 20a. The current passing through the CE must be the same as that passing through the WE in order to satisfy the conservation of charge. As mentioned above, oxidation of water occurs on the CE surface in order to change the electronic condition to ionic conduction.* The Tafel slope for this reaction is shown as 50 mV/decade for illustration purposes. Thus, for every 100 mV of polarization of the WE with respect to the RE, the CE is polarized 50 mV in the opposite direction. Note that the difference in potential between the WE and the CE is termed the cell voltage. One rating for potentiostats is the maximum cell voltage (called the compliance voltage) that can be applied and is usually in the range of 10 to 100 V.

Consider now the dissolution of iron by replacing the Pt WE with an Fe wire and adding 1 M Fe^{2+} to the solution in chamber B (via dissolution of $FeSO_4$, for example), as shown in Fig. 22. Calculation of the reversible potential for iron dissolution indicates that it would be the same as the standard reversible potential, −0.44 V (NHE), as the ferrous ion is at unit activity. We will assume that only iron oxidation/reduction can occur in this cell. Changing the polarity of the variable voltage supply allows removal of electrons from the WE, forcing net oxidation to occur there and net reduction to occur on the Pt CE in chamber C. Figure

* The description of an interface acting as a transducer from ionic to electronic conduction is due to Eliezer Gileadi.

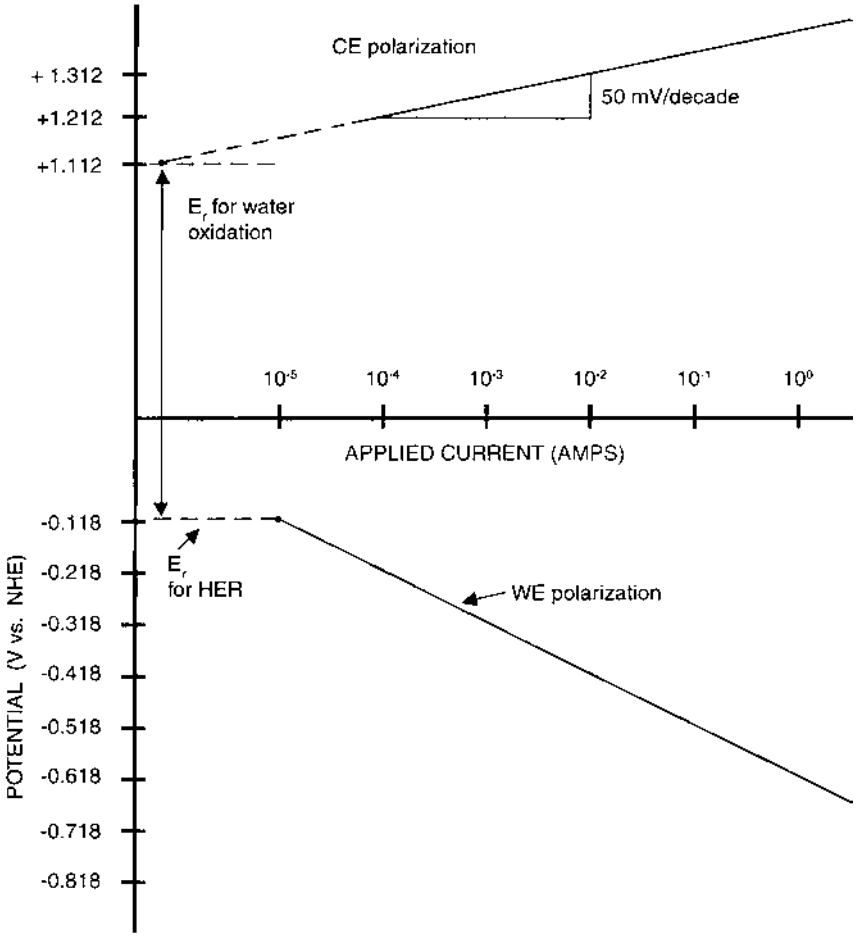

Figure 21 Polarization data for both the CE and the WE for the experiment discussed in Fig. 19 and 20. In order to allow net reduction to occur on WE, net oxidation must occur on the CE at the same rate (i.e., current).

23a shows illustrative data for the WE. A Tafel slope of 100 mV is calculated, and an exchange current density for iron dissolution is found to be 10^{-7} A/cm^2. The anodic kinetics of the iron dissolution reaction are thus determined. Faraday's laws can be used to show that a dissolution rate of 100 μA/cm^2 (=0.1 mA/cm^2 = 10^{-4} A/cm^2) represents a penetration rate of 46 mpy.

In Fig. 23b, the cell voltage as a function of applied current density for our illustrative example is shown. At zero applied current density, the cell voltage

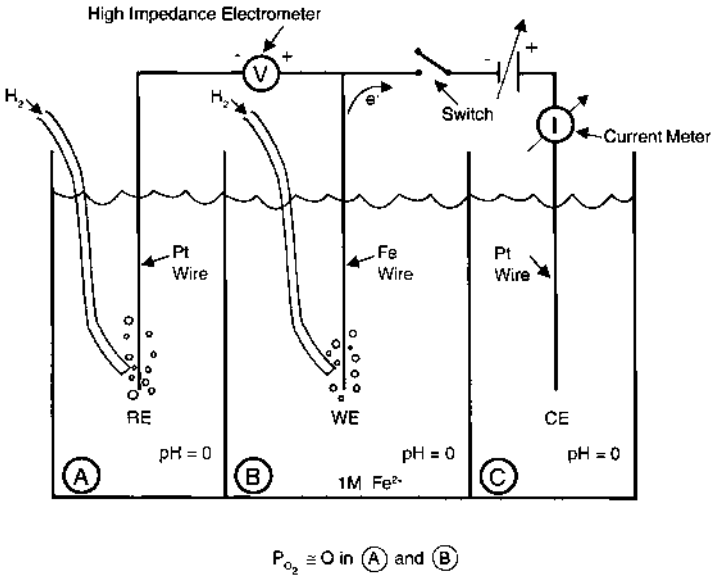

Figure 22 Three-compartment cell for studies of the kinetics of iron dissolution in acid.

is the difference between reversible potentials. During anodic polarization of the WE, the cell voltage actually *decreases*. In other words, a controlled short-circuiting of the two electrodes occurs. At an applied current of 3×10^{-4} A/cm^2 the cell voltage is zero. The potential of both the WE and the CE is -0.13 V(NHE). As discussed below, this condition represents a galvanic coupling between the Pt CE and the Fe WE. In order to polarize the WE above -0.13 V(NHE), the voltage supply must do electrical work, and the magnitude of the cell voltage increases.

Throughout this discussion, the behavior of the RE has been ignored. One might question how the RE maintains its standard value with applied voltages and currents everywhere else. In a well-built instrumental arrangement, the impedance of the electrical connection to the RE (i.e., the input impedance of the voltmeter) is so high that the current passing through the RE is truly negligible ($\ll 1$ nA). Very high impedance voltage measuring devices used in commercial potentiostats are known as electrometers, with input impedances of 10^{13} Ω or more. Thus, with a voltage between the CE and the RE of the 100 V, the current through the RE is 10 pA. Assuming a Tafel slope of 100 mV/decade and an exchange current density of 10^{-11} A/cm^2 (both worst-case conditions for a RE), the RE would be polarized 10 mV, which would be a significant problem. In

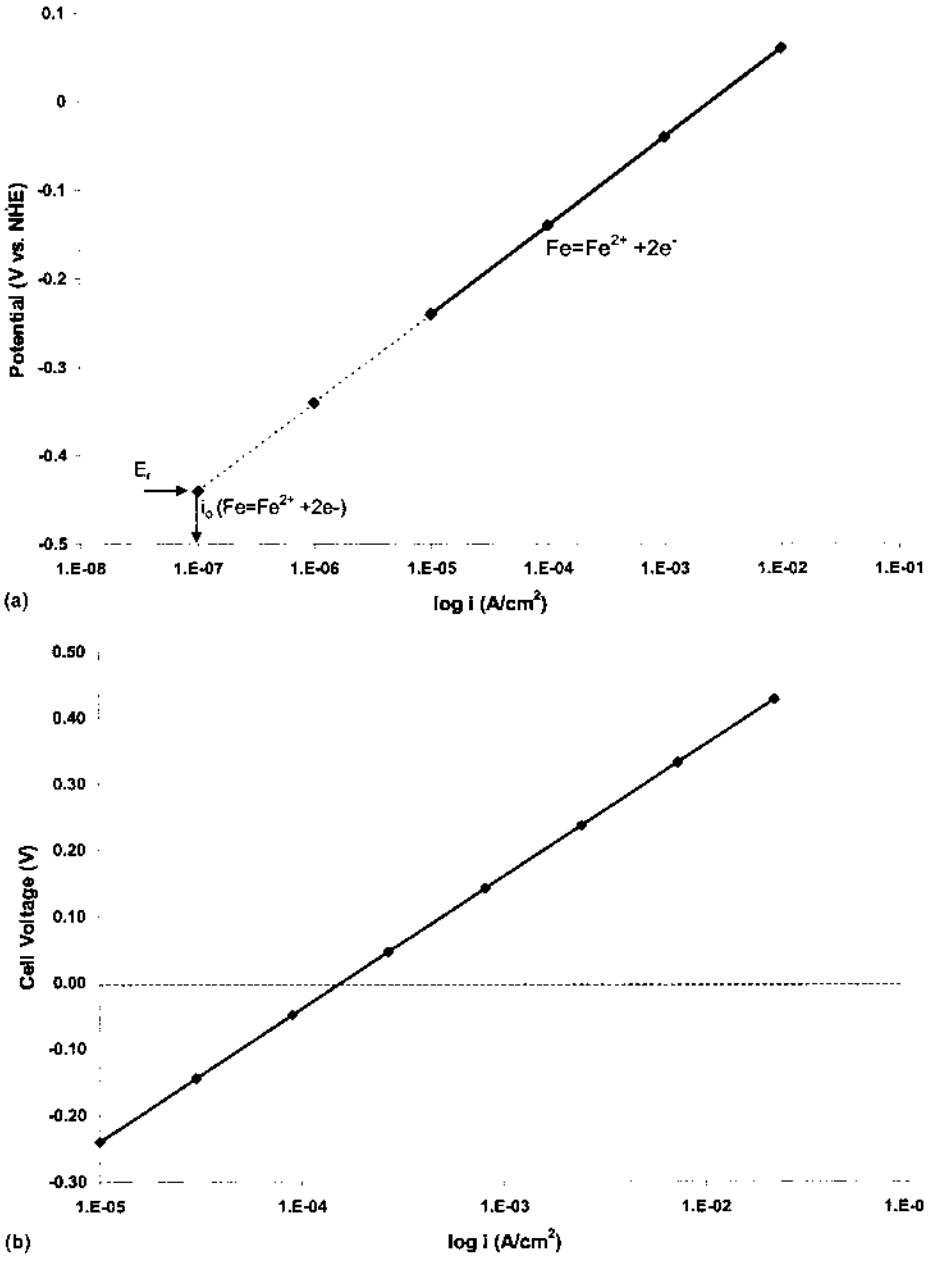

Figure 23 Schematic results from apparatus in Fig. 22. (a) Anodic polarization data normalized for the exposed area; (b) cell voltage (V_{CE}-V_{WE}) as a function of applied current density.

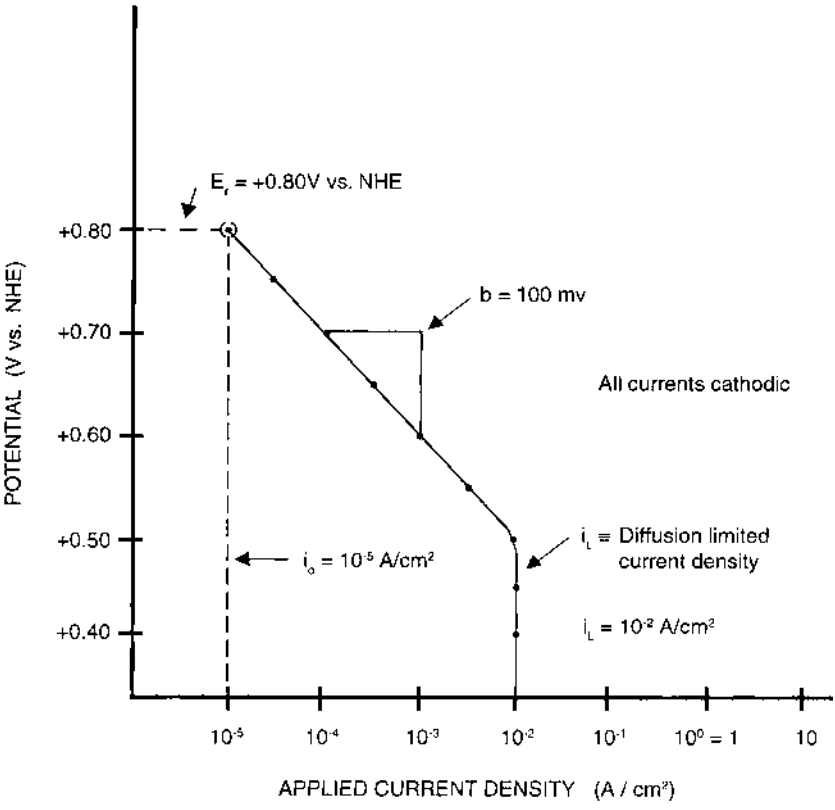

Figure 24 Schematic polarization data for oxygen reduction reaction (ORR) in neutral (pH 7.2) solution. Diffusion-limited current density (i_L) is present due to mass transport limitations on dissolved oxygen.

practice, exchange current densities are closer to mA/cm^2, so pA currents have no effect on the RE potential. Nonetheless, keeping the possibility of such effects in mind is important.

A final example of electrochemical kinetics will consider a return of the Pt WE from before but now exposed to a neutral (pH 7.2) solution into which oxygen is bubbled. The kinetics of the oxygen reduction reaction (ORR) will be studied. The data generated might appear as shown in Fig. 24. The reversible potential for the ORR in pH 7 solution, according to the Nernst equation, is

$$E_{\mathrm{ORR,pH2}} = 1.23 - 0.059\mathrm{pH} = 1.23 - 0.059(7.2) = +0.80\ \mathrm{V(NHE)}. \quad (12)$$

As before, polarization in the cathodic direction yields a straight line on the semi-

logarithmic scales at low overpotentials (i.e., within 200 mV of the reversible potential). At more negative potentials, a region of potential-independent kinetics appears. As discussed in detail in Chapter 5, this behavior represents a diffusion-limited current density. The rate of oxygen reduction under these conditions is controlled by the rate at which dissolved oxygen diffuses to the Pt surface, not by the potential across the interface. Transport of oxygen and electrochemical reduction occur in series, so the slowest step controls the rate. At low overpotentials, diffusion is rapid compared to the electrochemical reaction rate, so a potential dependence is observed.

Many corrosion systems are controlled by diffusion limitations on oxygen because of its low solubility in aqueous solution (0.25 mM at room temperature). The diffusion-limited current density, i_L, can be described mathematically by

$$i_L = \frac{Kc_b}{\delta} \tag{13}$$

where K = constant that includes the diffusion coefficient of oxygen, c_b = bulk concentration of oxygen, and δ = diffusion layer thickness.

The diffusion layer thickness is controlled by the hydrodynamics (fluid flow). Although more details on mass transfer effects are discussed in Chapter 5, it is worthwhile to point out here that the diffusion-limited current density is independent of the substrate material.

C. Polarization Curves

Metallic corrosion occurs because of the coupling of two different electrochemical reactions on the material surface. If, as assumed in the discussion of iron dissolution kinetics above, only iron oxidation and reduction were possible, the conservation of charge would require that in the absence of external polarization, the iron be in thermodynamic equilibrium. Under those conditions, no net dissolution would occur. In real systems, that assumption is invalid, and metallic dissolution occurs with regularity, keeping corrosionists employed and off the street.

Return to the Fe dissolution experiment discussed above, altering the solution to contain 5 μM M Fe^{2+}. In addition, allow hydrogen evolution to occur on the iron surface with an exchange current density of 10^{-5} A/cm^2, whereas the exchange current density for the iron reaction is 10^{-6} A/cm^2. Assume that both reactions have Tafel slopes of 100 mV/decade. These conditions are illustrated graphically in the *Evans diagram,* named in honor of its creator, U. R. Evans, shown in Fig. 25. The lines represent the reaction kinetics of the two reactions considered.

The corrosion rate of the iron can be directly predicted from the Evans diagram by considering two facts:

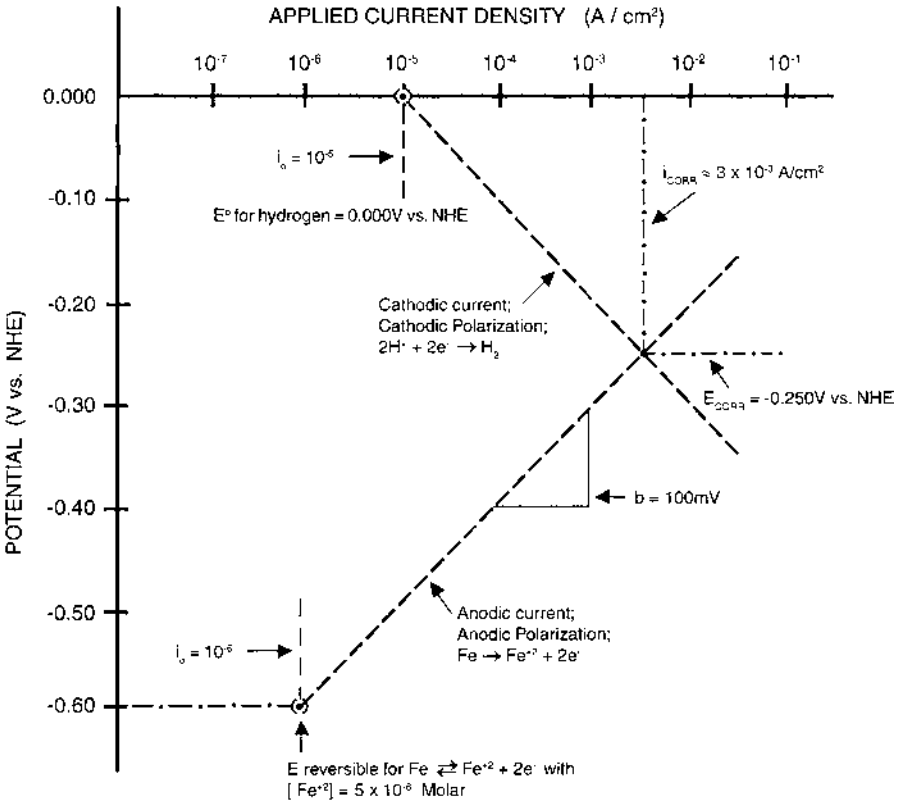

Figure 25 Evans diagram for Fe in acid showing use of conservation of charge to determine E_{corr} and corrosion rate (i_{corr}), given complete knowledge of the kinetic parameters involved.

1. Measurement of a material immersed in solution gives a single potential value at any instant. Thus all reactions must be occurring at the same potential.
2. The conservation of charge demands that under rest conditions (the absence of any applied potential or current), all of the electrons produced in oxidation reactions must be consumed in reduction reactions.

The two facts imply that the rest, or corrosion, potential (E_{corr}) of the system must be -0.25 V(NHE) as this is the only potential at which the rates of two reactions are identical. The common rate of the two reactions, known as the corrosion rate, i_{corr}, is approximately 3 mA/cm^2. Thus iron is dissolving at 3 mA/cm^2 and hydro-

gen is being evolved on the iron surface at 3 mA/cm^2. These data could be used to predict the long-term performance of iron in this environment if they were representative of the steady state conditions. This example is an illustration of the application of mixed potential theory, the framework that underlies virtually all electrochemical corrosion science.

Given sufficient quantitative information about the electrochemical processes occurring, mixed potential theory can be used to predict a corrosion rate. Unfortunately, in the vast majority of cases, there are few data that can be applied with any confidence. In general, experimental measurements must be made that can be interpreted in terms of mixed potential theory. The most common of these measurements in electrochemical corrosion engineering is the polarization curve.

The data discussed in Figs. 20 through 24 represent the type of data in a polarization curve: combinations of potential and applied current density. Figure 26 shows a complete polarization curve for the iron in acid systems for which the Evans diagram is shown in Fig. 25. The Evans lines are included as dotted lines in the figure. The difference between the Evans diagram and the polarization curve is that the polarization curve data display applied current densities, whereas the Evans diagram displays the reaction rates in terms of current densities.

The applied current density is the difference between the total anodic and the total cathodic current densities (reaction rates) at a given potential:

$$i_{app} = i_a - |i_c| \tag{14}$$

using the convention in which the cathodic current density is defined as negative. At the corrosion potential (E_{corr}), the anodic and cathodic rates are exactly equal; thus the applied current density is zero. No external device is needed to supply or remove electrons from the reactions; all of the electrons generated by oxidation reactions (iron dissolution in the case under consideration) are consumed by reduction reactions (HER) on the same metal surface. Note that the corrosion rate is not zero; it is simply not directly measurable because of the presence of the HER on the same surface. The logarithm of zero is negative infinity. As this is tough to plot on finite-sized paper, the applied current density forms a sharp point as the electronics of the current converter output a large negative voltage to the recording device.

Imposing an anodic current density on the iron with an external device results in the generation of the anodic branch of the polarization curve. Increasing the applied anodic current decreases the reduction reaction rate as the surface is polarized in the positive direction. At small anodic current densities, the HER current density is still an appreciable fraction of the anodic current density. Under these conditions the applied current density is less than anodic current density. For example, at a potential of -0.225 V(NHE), i_c is 2×10^{-3} A/cm^2, i_{app} is 6×10^{-3} A/cm^2, and i_a is 8×10^{-3} A/cm^2. At sufficiently large anodic current densities (e.g., 10^{-2} A/cm^2 in Fig. 26), the cathodic reaction is insignificant rela-

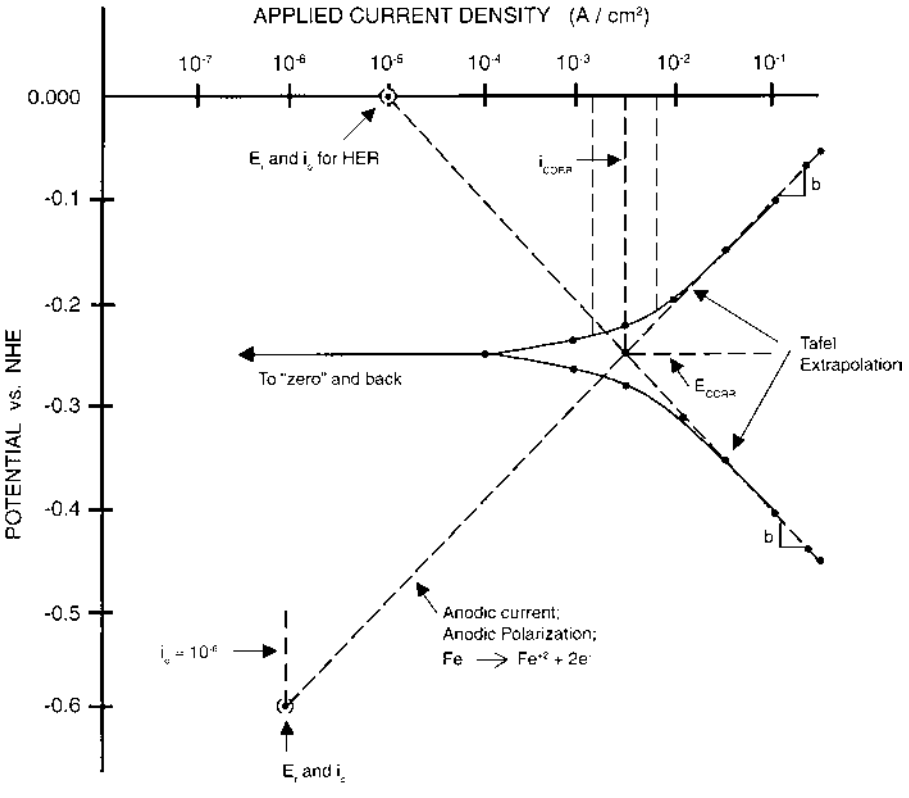

Figure 26 Polarization curve that would result for Evans diagram of Fig. 25. The Evans lines are included as well.

tive to the anodic current density, so the applied current density is virtually equal to the anodic current density. Measurements under these conditions allow the Tafel slope to be determined. The development of the cathodic branch of the polarization curve can be described in a qualitiatively similar manner.

The impossibility of a direct measurement of corrosion rate using electrochemical testing would seem to be discouraging. Application of mixed potential theory allows determination of the corrosion rate using a method known as Tafel extrapolation.

D. Tafel Extrapolation

The Evans lines in Fig. 26 are key to the method of Tafel extrapolation. At potentials well away from the corrosion potential, the applied current density

reflects the kinetics of only one of the reactions. Extrapolating the linear portions of the polarization curve found at potentials well away from E_{corr} leads to an intersection at E_{corr}. This intersection corresponds to i_{corr}, the corrosion rate. Assuming uniform dissolution across the surface, Faraday's laws can be used to convert it to penetration rate for engineering design. Note that extrapolation to the reversible potentials can, in theory, be used to determine the exchange current densities for the two reactions.

1. Analysis Issues

The logarithmic nature of the current density axis amplifies errors in extrapolation. A poor selection of the slope to be used can change the corrosion current density calculated by a factor of 5 to 10. Two rules of thumb should be applied when using Tafel extrapolation. For an accurate extrapolation, at least one of the branches of the polarization curve should exhibit Tafel (i.e., linear on semilogarithmic scale) over at least one decade of current density. In addition, the extrapolation should start at least 50 to 100 mV away from E_{corr}. These two rules improve the accuracy of manual extrapolations.

Commercial corrosion electrochemistry software applies nonlinear least squares fitting to fit the entire polarization curve, which can improve accuracy. Nonetheless users are wise to check periodically the software-generated corrosion rates with manual fits. Not all computation algorithms are created equally robust against noise and other realities of corrosion measurements. In addition, the use of Tafel extrapolation invokes the implicit assumption that the dissolution is uniformly spread over the entire specimen surface. Figure 27 shows a polarization curve for which it might be tempting to apply Tafel extrapolation, ignoring the portion of the anodic region very close to E_{corr}. In actuality this polarization curve represents a system in which pitting is occurring at E_{corr}. The area over which the anodic current is distributed is much less than 5% of the total area. Using Tafel extrapolation on these data would lead to highly erroneous conclusions. More on the interpretation of polarization curves in passive systems undergoing localized corrosion is presented in Chapter 3.

There are several factors that can lead to non-Tafel behavior. Diffusion limitations on a reaction have already been introduced and can be seen in the cathodic portion of Fig. 27. Ohmic losses in solution can lead to a curvature of the Tafel region, leading to erroneously high estimations of corrosion rate if not compensated for properly. The effects of the presence of a buffer in solution can also lead to odd-looking polarization behavior that does not lend itself to direct Tafel extrapolation.

2. Interpretation Issues

The generation and analysis of polarization curve data has become increasingly straightforward with the increasing computerization of electrochemical instru-

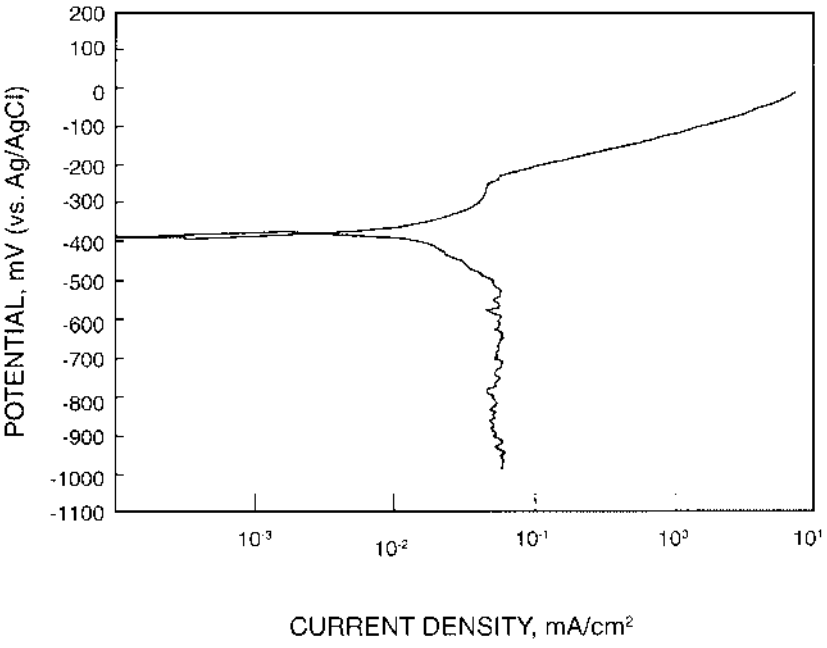

Figure 27 Example of real polarization data illustrating problems associated with analysis of limited or false Tafel regions.

mentation. Nonetheless the interpretation of the data can be a tremendous challenge. Rarely do polarization curves look as classic as those presented here. Thus several cautions regarding interpretation should be added to those presented concerning data analysis.

The assumption of a steady-state system has been implicit throughout all of the discussion of polarization curves. Note the difference between steady state and equilibrium. No corroding system can be in equilibrium; if it were, it would not be corroding. Corrosion is a nonequilibrium process that may occur at steady state. Steady state corrosion occurs when the rate of corrosion does not change with time. Knowledge that a given system is and will remain in steady state is of great value. In many cases steady state is only approached and never achieved. No universally agreed upon rule exists concerning a means to establish whether an elecrochemical system has achieved a steady state. The most popular means of monitoring the approach to steady state of a corrosion system is the measurement of the corrosion potential with time. Generally, the E_{corr} changes most rapidly at the beginning of immersion. As the conditions at the metal/solution inter-

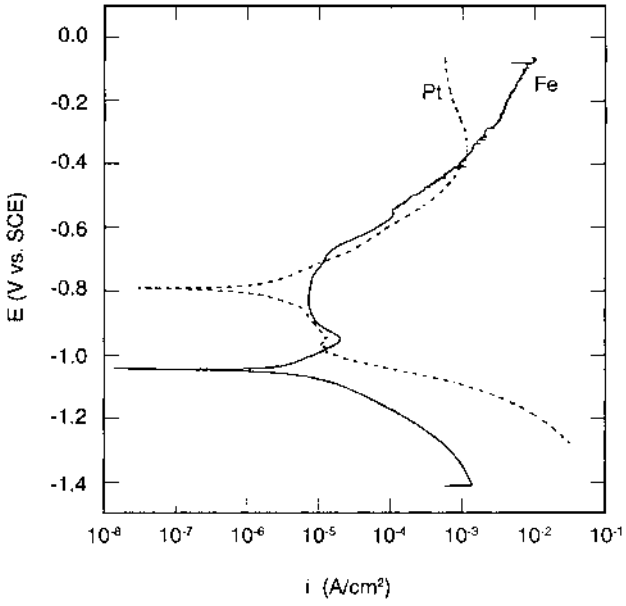

Figure 28 Polarization curves on Pt and Fe in alkaline sulfide solution at 65°C illustrating danger of interpreting all anodic current as due to metal dissolution. Above approximately −0.7 V(SCE), the anodic current on both Pt and Fe is dominated by sulfide oxidation.

face approach steady state, the time-rate of change in E_{corr} decreases. A reasonable criterion for steady state would be a change of less than 5 mV in E_{corr} over a 10 minute period.

An additional interpretation issue involves the presence of oxidation reactions that are not metal dissolution. Figure 28 shows polarization curves generated for platinum and iron in an alkaline sulfide solution (21). The platinum data show the electrochemistry of the solution species; sulfide is oxidized above −0.8 V(SCE). Sulfide is also oxidized on the iron surface, its oxidation dominating the anodic current density on iron above a potential of approximately −0.7 V(SCE). Without the data from the platinum polarization scan, the increase in current on the iron could be mistakenly interpreted as increased iron dissolution. The more complex the solution in which the corrosion occurs, the more likely that it contains one or more electroactive species. Polarization scans on platinum can be invaluable in this regard.

Finally, even the most skilled interpretation of electrochemical data is akin to the best photograph in that it contains only a portion of the information avail-

able. Correlation of electrochemical measurements to as many varied measurements as possible is good practice. Whereas electrochemical measurements may be the most rapid, they are also the most susceptible to variations in conditions. Corrosion rate estimations based on Tafel extrapolation should be compared to weight loss measurements whenever possible. Often decisions need to be made regarding material selection in a narrow time window that precludes such information. In these cases, postselection weight loss measurements in the actual environment are invaluable checks on the applicability of the electrochemically derived corrosion rates.

E. Polarization Curve Measurements for Galvanic Corrosion Prediction

One example of the application of polarization curves in a predictive manner involves their use in galvanic corrosion. Galvanic corrosion occurs when two dissimilar metals are in electrical and ionic contact as is schematically shown in Fig. 29. Galvanic corrosion is used to advantage in sacrificial anodes of zinc in seawater and magnesium in home water heaters. It slows corrosion of millions of tons of structural materials. The darker side of galvanic corrosion is that it also causes major failures by the accelerated dissolution of materials that are accidentally linked electrically to more noble materials.

Galvanic series are well known to many. These listings of corrosion potentials for materials (generally structural alloys) in a given environment are often

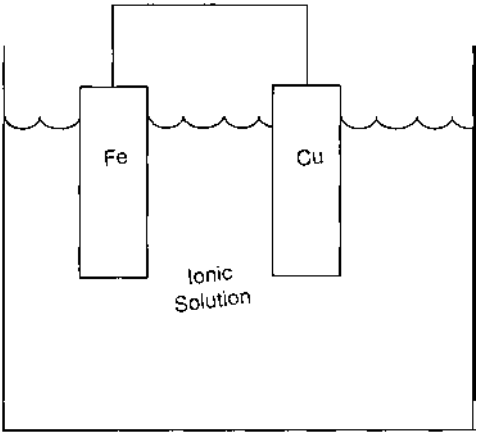

Figure 29 Schematic of galvanic corrosion arrangement.

used to avoid damaging combinations. One example is shown in Fig. 30 for materials in seawater. Conventional corrosion engineering would suggest avoiding combinations with widely different corrosion potentials, such as Ti and Al alloys. If this combination of alloys were electrically in contact in seawater, the galvanic series would predict that the corrosion rate of the Al alloy would increase, whereas that of the Ti alloy would decrease. The galvanic series does not allow even an estimation of the changes in the corrosion rates. The magnitude of the potential differences does not always correlate with the changes in corrosion rate, nor can the effects of anode-to-cathode area ratio (a key parameter in galvanic corrosion) be predicted accurately. There is no direct correlation between the value of the corrosion potential of different materials and their relative corrosion rates, even when exposed to the same environment. Polarization curves allow generation not only of the galvanic series in the environment of interest but also information on the effects of area ratio on the changes in corrosion rate of both materials.

Consider the two materials whose polarization curves are shown in Fig. 31. Both the polarization curves and the Evans lines are shown for both materials. Material 1 is the more noble material (i.e., it has a more positive E_{corr}) and has a lower circuit corrosion rate when it is uncoupled. If the surface area of the two materials is the same and the materials are coupled, then the two material–solution interfaces must come to the same potential. In a manner identical to that used for the example of iron in acid used to introduce Evans diagrams, the potential and current at which this condition is met can be found by applying the conservation of charge to the sysytem:

$$\sum I_A = \sum I_C \tag{15}$$

Note that it is the currents, not the current densities, that are involved in the statement of charge conservation.

The intersection of the total anodic and total cathodic lines is at the (E_{couple}, i_{couple}) pair. The E_{couple} represents the potential measured (vs. a RE) for the case of the two metals in electrical contact in the test environment. The potential of the more noble material (Metal 1) has been moved from its own circuit E_{corr} in the negative direction, which would generally lead to a lower dissolution rate. The potential of the more active material (Metal 2) has been moved from its open circuit E_{corr} in the positive direction, which would generally lead to a higher dissolution rate.

The open circuit E_{corr} values for each metal are the entries in the traditional galvanic series. Kinetic information is also available via analysis of the polarization curves. The i_{couple} can be used to calculate the increased corrosion rate of Metal 2. Because of the coupling to Metal 1, the dissoultion rate has increased from $i_{corr,2}$ to i_{couple}. The rate has increased because the cathodic kinetics on Metal 1 must now be satisfied. In addition to determining the increase in the corrosion

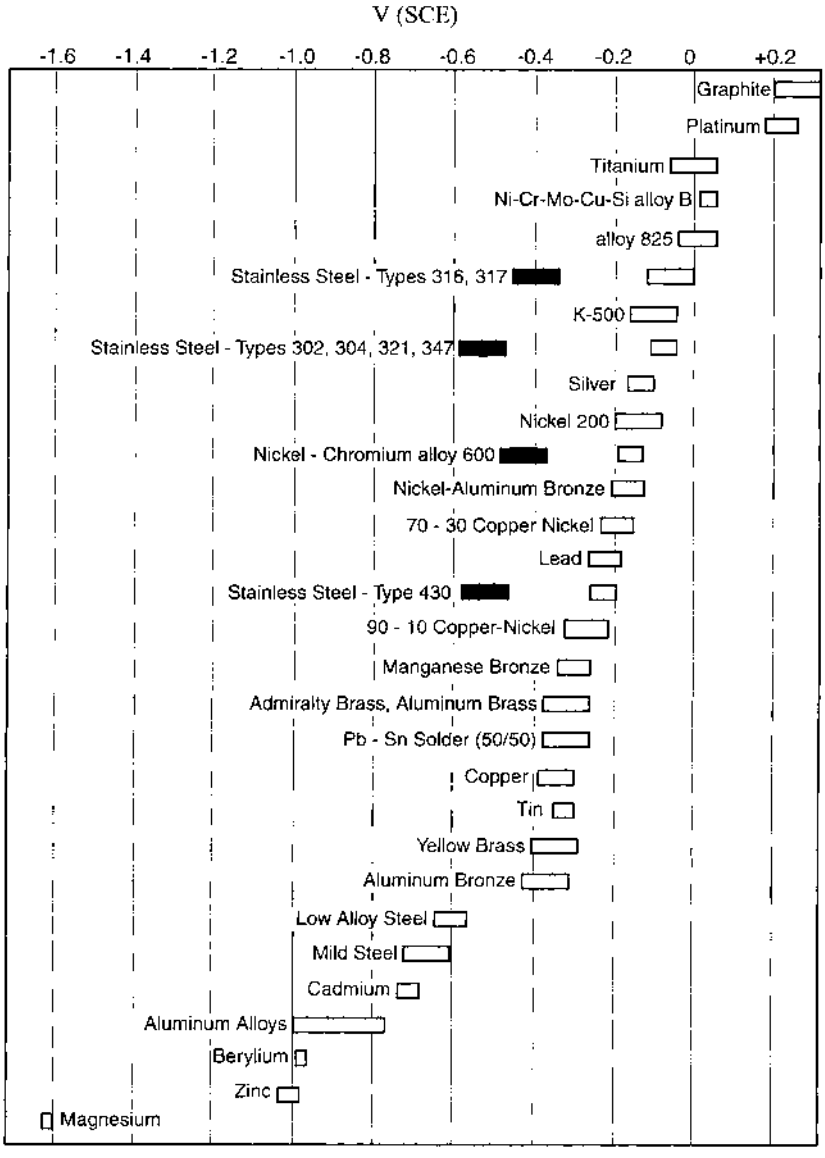

Figure 30 Partial list of galvanic series in seawater. (From H.P. Hack, *Metals Handbook*, Vol. 13, Corrosion, 9th ed., ASM, Metals Park, OH, p. 234, 1987.)

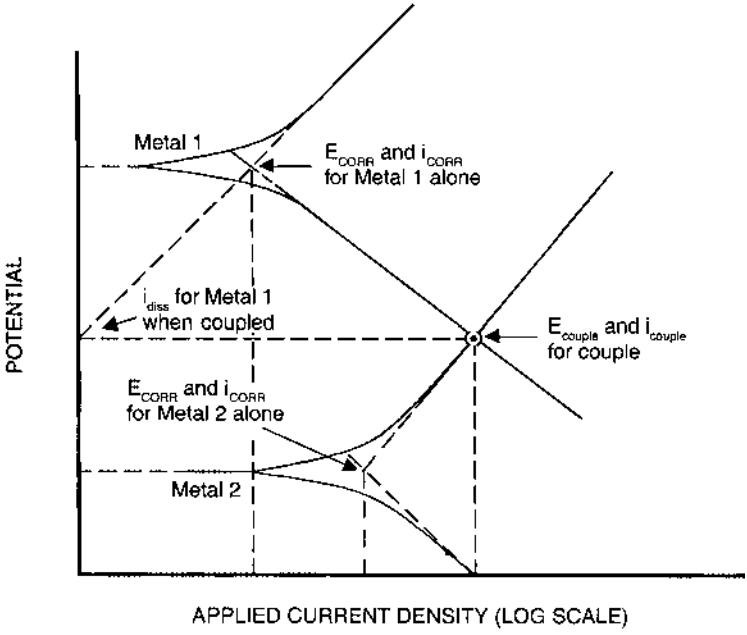

Figure 31 Polarization curves of Metals 1 and 2 that are to be analyzed for their behavior in a galvanic couple.

rate of Metal 2, the decrease in the corrosion rate of Metal 1 can also be estimated by extrapolating the Metal 1 anodic line to E_{couple}. Recall that the Evans lines describe the reaction rate as a function of the interfacial potential independent of the means by which that potential is achieved. Thus the application of a sacrificial anode (Metal 2) serves to reduce the corrosion rate of Metal 1. The predictive ability of corrosion electrochemistry can be used to investigate the effect of changing the relative areas of Metal 1 and Metal 2, i.e., changing the cathode-to-anode area ratio. In Fig. 32 the polarization data are reconfigured with the assumption of two different area ratios: in part (a) the anode area is 10 cm^2 and the cathode area 1 cm^2, whereas in part (b) the cathode area is considered to be 10 cm^2 and the anode area 1 cm^2. Note that no additional experiments are needed to perform this analysis, as all the unit-area data are applicable.

Experience shows that increasing the cathode-to-anode area ratio increases the rate of consumption of the anode and decreases the corrosion rate of the cathode, but the galvanic series alone would not allow a quantitative analysis of these effects. Inspection of Fig. 32 reveals that the abscissa has been changed to current from current density. When dealing with unequal areas, such a transfor-

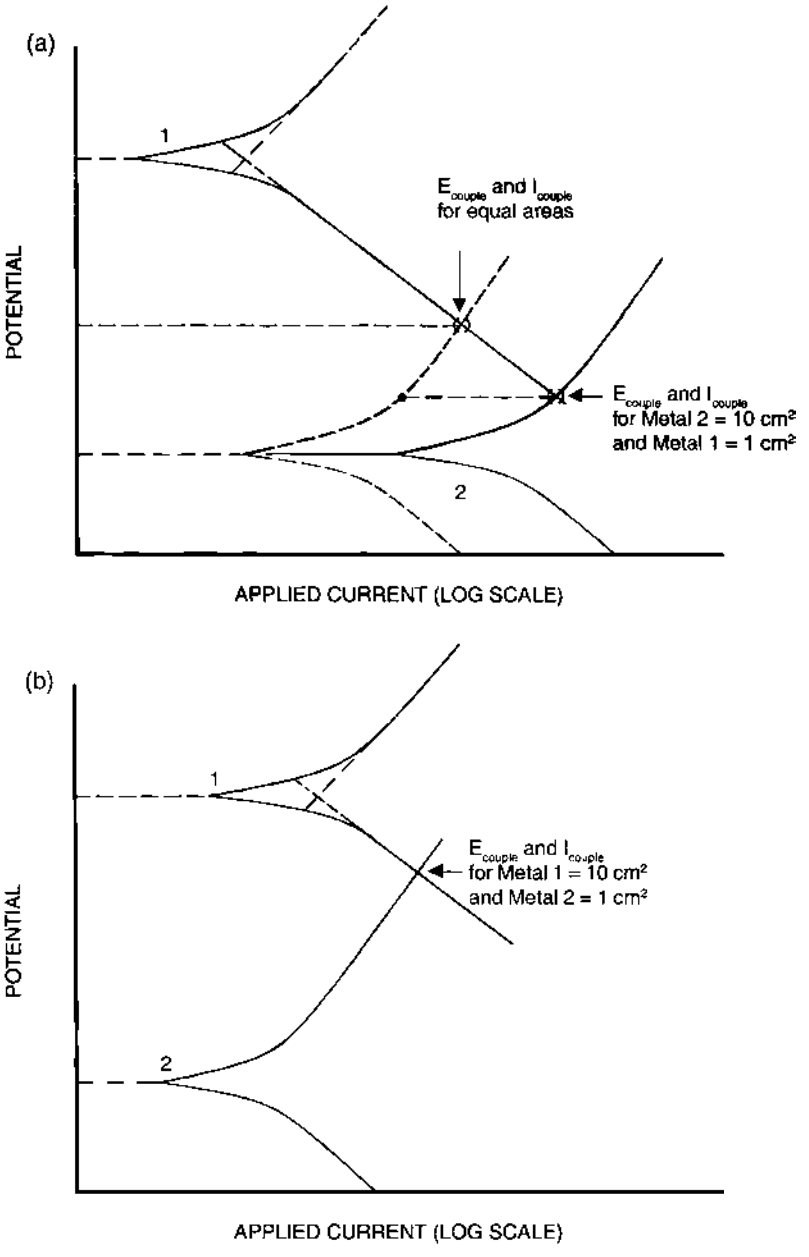

Figure 32 Shift in polarization curves on a current basis for cases in which (a) the anode area is considered to be 10 cm^2 and the cathode area 1 cm^2, (b) the cathode area is considered to be 10 cm^2 and the anode area 1 cm^2.

mation is needed, as it is currents that must be balanced rather than current densities. In the case of Fig. 32a, the increase in the area of the anode leads to a decrease in E_{couple} relative to the equal area case. Two other effects can also be noted. The corrosion rate of the cathodes (Metal 1) has decreased (the interfacial potential is more negative, reducing the driving force for oxidation). In addition, the dissolution rate of the anode (Metal 2) has also decreased. The anodic current is higher, but the area-averaged dissolution rate is lower once the increased area is taken into account (by moving from the E_{couple}, I_{couple} point to the point on the Metal 2 unit area line at E_{couple}).

This paradox of lowering both corrosion rates can be understood by considering the accounting of the electrons. By simply increasing the anode area, the number of electrons per second (i.e., the anodic current) that is produced is increased at all potentials more positive than the open circuit E_{corr} of Metal 2. To accommodate this increased production, the cathodic reaction on Metal 1 must increase the rate at which it consumes electrons (i.e., the cathodic current). Increased cathodic current can only be achieved by moving the system to more negative potentials. The more negative the potential, the lower the dissolution rate of both materials.

The converse situation regarding area ratio is shown in Fig. 32b, in which the area of the cathode has increased by a factor of 10 relative to the anode. The effect on E_{couple} and the corrosion rate of both materials is opposite that of increasing the area of the anode, although the I_{couple} has increased in both cases, (a and b). From Fig. 32b the widsom of avoiding large cathode-to-anode area ratios is clear. Not only is the corrosion rate of the material to be protected higher the higher the ratio but also the dissolution rate of the anode material is higher. Because of the impossibility of producing and/or maintaining pinhole-free coatings, noble metal coatings are generally avoided. The gold-plated electrical connectors used in the electronics industry are an exception. The gold plating is deposited onto copper layers that are connected into circuit boards. Problems have indeed developed in some atmospheric environments in which thin moisture layers lead to galvanic corrosion of the copper and resulting loss of electrical continuity between the connector and the electrical device.

REFERENCES

1. P. J. Moran, E. Gileadi. J. Chem. Educ. 66, 912 (1989).
2. D. J. G. Ives, J. G. Janz, eds. *Reference Electrodes: Theory and Practice.* Academic Press, New York (1961).
3. Z. Szklarska-Smialowska. *Pitting Corrosion of Metals.* NACE International, Houston, 203 (1986).
4. A. J. Bard, L. R. Faulkner. *Electrochemical Methods: Fundamentals and Applications.* John Wiley, New York, 50 (1980).

5. P. W. Atkins, *Physical Chemistry,* 2nd ed., W. H. Freeman and Co., San Francisco, 1982, p. 355.
6. E. Gileadi. *Electrode Kinetics for Chemists, Chemical Engineers, and Materials Scientists.* VCH, New York, 19 (1993).
7. M. Pourbaix. *Atlas of Electrochemical Equilibria in Aqueous Solutions.* NACE International, Houston (1974).
8. J. B. Lee. Corrosion, 37, 467 (1981).
9. J. T. Atkinson. In: Equilibrium Diagrams. Proc. Int. Symp. Electrochem. Soc. (R. P. Frankenthal, J. Kruger, eds.) Electrochemical Society, Pennington, NJ, 175 (1984).
10. L. B. Kriksunov, D. D. Macdonald. Corrosion 53, 605 (1997).
11. A. Garner, Corrosion 41, 587 (1985).
12. S. J. Mulford, D. Tromans. Corrosion 44, 891 (1988).
13. D. B. Wells, J. Stewart, R. Davidson. Corrosion Sci. 33, 39 (1992).
14. P. Marcus, E. Protopopoff. J. Electrochem. Soc. 144, 1586 (1997).
15. P. Marcus, E. Protopopoff. J. Electrochem. Soc. 140, 1571 (1993).
16. E. D. Verink, Jr. In: *Electrochemical Techniques for Corrosion Engineering* (R. Baboian, ed.). NACE International, Houston, 101 (1986).
17. D. Silverman. Corrosion 38, 541 (1982).
18. D. C. Silverman. In: *Electrochemical Techniques for Corrosion Engineering* (R. Baboian, ed.). NACE International, Houston, 117 (1986).
19. E. Gileadi, E. Kirowa-Eisner, J. Penciner. *Interfacial Electrochemistry: An Experimental Approach.* Addison-Wesley, Reading, MA, 151 (1975).
20. H. Tafel. Z. Physik. Chem. 50, 641 (1905).
21. S. Kannan, R. G. Kelly. Corrosion Sci. 38, 1051 (1996).
22. G. Walter, personal communication (1999).

3
Passivity and Localized Corrosion

The objectives of this chapter are to provide a basic explanation of the chemical and physical processes involved in localized corrosion and to explain the test techniques that are commonly used to determine the resistance of alloys to localized corrosion.

I. INTRODUCTION

While localized corrosion occurs in many forms, the results are the same: the accelerated loss of material at discrete sites on a material's surface. The amount of metal lost would usually be considered insignificant if uniformly distributed across the entire surface. However, since current density is important in assessing penetration rates, the same amount of material lost, when confined to a discrete site, can result in perforation or other failure. More than one-third of the corrosion failures in a major chemical plant were due to localized corrosion (including stress-corrosion cracking) (1). One can usually design around uniform corrosion, by the choice of alloy, by the application of a corrosion control program, or by the inclusion of a corrosion allowance. Localized corrosion often appears to have a stochastic (or purely random) nature. Thus it is very difficult to design a structure with a corrosion allowance for localized corrosion. Another difficulty with localized corrosion is that associated with its detection and monitoring under service conditions. Since the vast majority of the surface is unaffected, thickness monitoring is generally unhelpful. In addition, many forms of localized corrosion occur in areas that are difficult to access such as at flanges and under deposits. Another important aspect of localized corrosion is the fact that it most often occurs in highly alloyed materials that were chosen specifically for their corrosion resistance.

The same aspects of localized corrosion that make it such an engineering nuisance also make it difficult to study. Since it has a stochastic nature, Murphy's law applies, and the sample never seems to pit at the time or in the place that

suits the experimenter and his or her apparatus. The existence of an incubation time, during which no measurable attack occurs, can also make such studies very time-consuming. The sensitivity of the phenomenon to seemingly small changes in environmental, metallurgical, and experimental conditions adds to the confusion.

The phenomenology of localized corrosion helps to define certain requirements for localized corrosion that can be expressed in terms of the concepts already discussed in Chapter 2. In order for localized corrosion to occur, there must be a spatial variation in the electrochemical or metallurgical conditions. The occurrence of discrete sites of attack demonstrates that passivity must be able to coexist on the same surface with active regions. In fact, this is one of the scientifically interesting aspects of localized corrosion. Under "normal" circumstances, one would expect that a surface would either be completely passive or completely active, not a mixture of the two. Finally, there is a physical separation of the anodic and cathodic reaction sites during localized corrosion. In order to understand localized corrosion and thus how to test for resistance to localized corrosion, we must understand each of these aspects and their interrelations.

A. Chapter Overview

The goal of this chapter is to provide a basic understanding of the processes involved in localized corrosion in terms of what has been covered in Chapters 1 and 2. In addition, the different test techniques that are used to determine the resistance of alloys to pitting and crevice corrosion will be reviewed and discussed.

The first section briefly introduces the concepts behind passivity. The ability of the material to passivate in an environment is a necessary condition for localized corrosion. While volumes have been written on the subject (2,3), this section provides the basic framework for understanding how passivity develops and how it can be characterized electrochemically. The next section discusses the breakdown of passivity that leads to localized corrosion. A basic understanding of the underlying causes of localized corrosion aids in understanding currently used tests as well as in the design of new tests. More details of the phenomenology of the different types of localized corrosion are presented, including the electrochemical manifestations of this phenomenology. The final section discusses the various test techniques that can be used both to characterize the resistance of material to localized corrosion and to understand the factors that control it. A description of the manner in which each test is performed is followed by a discussion of why each works as well as its advantages, disadvantages, and limitations. From this discussion, the parameters of the test that can be modified by a user to make it more applicable to an individual case of interest will become clear.

Owing to space constraints, stress-corrosion cracking (SCC) will not be

treated as a specific subject in this chapter. However, information that impacts SCC will be highlighted. While we will concentrate on pitting and crevice corrosion, the basic phenomenology presented is applicable to other forms of localized corrosion including integranular attack, weld- or heat-affected zone attack, and exfoliation. While each of these has particular details that are unique (e.g., exfoliation occurs in wrought, precipitation-hardened aluminum alloys), much of the basic approach to understanding the process is the same. The main differences are the origin of the heterogeneity that leads to the localized attack and the details of the electrochemistry. Since the focus of this chapter is to introduce electrochemical techniques rather than a study of corrosion, we will concentrate on pitting and crevice corrosion as generic examples.

II. PASSIVITY

Passivity is the origin of the utility of all corrosion resistant alloys (CRAs). While passivity can be defined in a number of ways, two have become generally accepted:

1. A metal is passive if it substantially resists corrosion in an environment where there is a large thermodynamic driving force for its oxidation (also known as thick film passivity). The Evans diagram for this type of behavior is shown in Fig. 1.

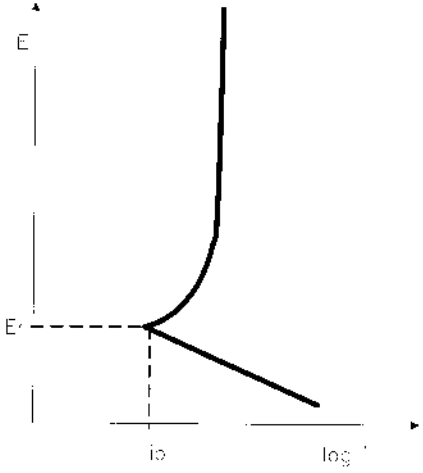

Figure 1 Schematic Evans diagram for a material that exhibits thick film passivity.

2. A metal is passive if, on increasing its potential to more positive values, the rate of dissolution decreases, exhibiting low rates at high potentials (also known as thin film passivity). The anodic Evans diagram for this type of behavior is shown in Fig. 2.

Examples of material–solution combinations that fall within the first definition are Pb in H_2SO_4 and Mg or Al in water. These materials can be considered to have very high (near infinite) anodic Tafel slopes in these solutions. Thus large increases in potential do not cause significant increases in dissolution rate. On the other hand, metal–solution combinations such as nickel, molybdenum, or chromium in sulfuric acid would be classified as passive according to the second criterion. For these materials, the Tafel slope can be thought of as having a strong potential dependence. At potentials in the vicinity of the reversible (equilibrium) potential, the Tafel slope is similar to that of the materials discussed in Chapter 2, with values on the order of 40 to 100 mV/decade. The Tafel slope increases

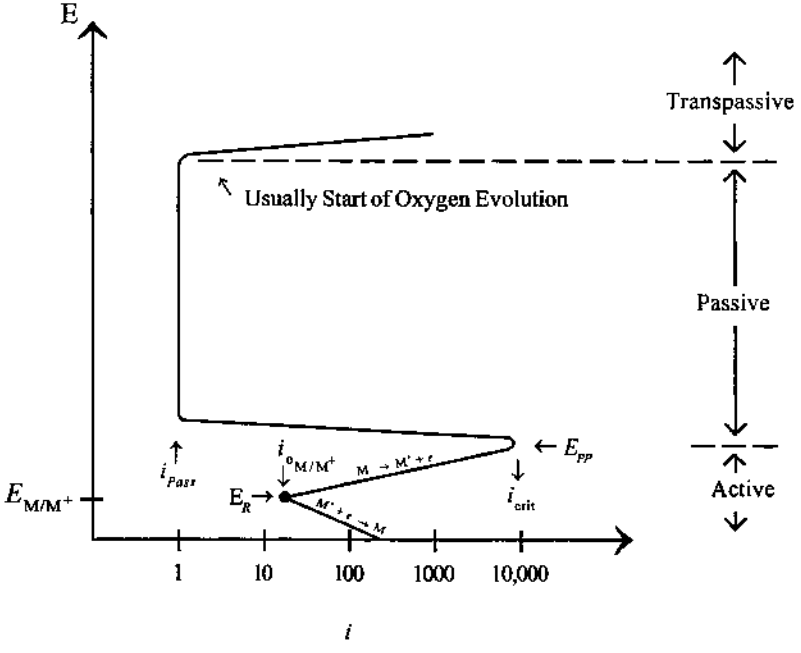

Figure 2 Typical anodic dissolution behavior of an active–passive metal. E_{PP} = primary passivation potential, i_{crit} = critical anodic current density, and i_{pass} = passive current density. (After Ref. 71.)

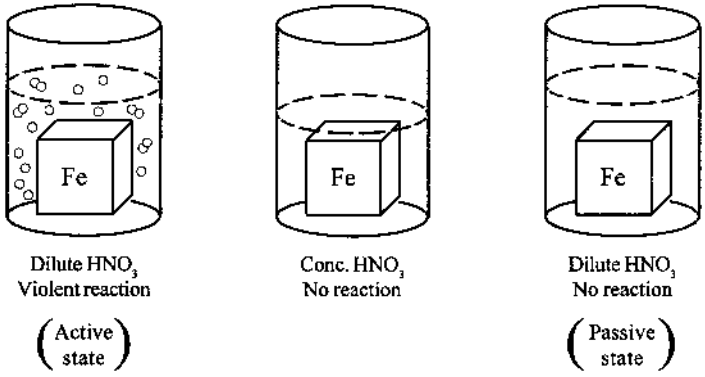

Figure 3 Faraday's experiments on the passivity of Fe. In dilute nitric acid, Fe corrodes at a high rate. In concentrated nitric acid, the reaction rate slows to almost zero. Upon a return to dilute acid, the reaction rate remains low, i.e., it is passive, until the surface is disturbed, at which point it begins to corrode at a high rate again. (After Ref. 21.)

dramatically near E_{pp}, approaching infinity after a short range of potential in which it is actually negative.

Kier first observed the passivity of Fe in 1790. A set of experiments by Michael Faraday have become a standard method for demonstrating the phenomena involved. In this experiment, shown in Fig. 3, a piece of Fe is placed in dilute (~30%) nitric acid. It dissolves at a high rate, with simultaneous generation of NO_2 by the reduction of nitrate. Placing the same specimen in more concentrated (70%) HNO_3 results in only a momentary reaction followed by no observable reaction. Upon moving the sample back into the dilute acid, no increase in rate occurs until the sample is scratched. Beginning at the point of the scratch and quickly engulfing the entire surface, the dissolution increases to a high rate again.

One would normally expect that placing the sample into the concentrated acid would cause the reaction to occur even faster than in the dilute acid, based upon Le Châtlier's principle. In addition, one would not expect that exposure to the concentrated acid would alter the behavior of the Fe in the dilute acid, but it does. This alteration was called "passivity" by Schöenbien in 1836. The electrochemical explanation of the Faraday experiment is discussed below. While a large body of literature exists concerning the underlying mechanisms, for our purposes only a brief review of the fundamental origins will be required.

A. Origins of Passivity

Thick film passivity (i.e., protection of a metal surface by a film of visible thickness) can be due either to oxide formation or salt film precipitation. Salt film

precipitation can in some cases be either a precursor for a thin passive film (4) or provide adequate protection alone. For example, Mg passivates in fluoride-containing solutions by the precipitation of MgF_2, which forms an effective barrier coating. Precipitation of $FeSO_4$ as a precursor to Fe_2O_3 has been observed for Fe in acid (4). In addition, Beck showed that Ti initially passivates via precipitation of $TiCl_3$ in HCl (5), while Carraza and Galvele have (6) postulated a similar mechanism for Type 304 SS in acidic chloride solutions. Mayne and Menter (7) showed that the passive film on Fe in 0.1 N Na_2HPO_4 consists of ferric oxide with particles of $FePO_4$ embedded within it, showing that in some cases, mixed thick film and thin film passivity can occur.

While thick film passivity has been documented and understood for many years, the difficulties in studying thin film passivity were daunting. It took many years to determine that indeed a film was responsible for the effect, as these films are so thin that they are invisible to the eye (i.e., transparent to radiation in the visible region). Two main types of theories were developed in order to explain the phenomena observed: theories based upon the idea of adsorption reducing the corrosion rate, and theories based upon the formation of a new phase, an oxide of the base metal, on the surface. In all cases, an increased barrier to dissolution results upon the increase in potential. This increased kinetic barrier upon anodic polarization contrasts with the exponentially decreased barrier which develops during anodic polarization of an active material.

B. Electrochemical Phenomenology

Independent of the mechanism of passivity, its electrochemical manifestations can be best understood on the basis of mixed potential theory presented in Chapter 2. A schematic Evans diagram for a passivating metal is shown in Fig. 4. If there are no strong oxidizing agents in the solution, the corrosion potential is E_{corr}, and the metal corrodes uniformly in a film-free condition. As the potential is raised in this *active region* (either by the application of an external current or by the introduction of oxidizing species into the environment), the dissolution rate of the metal increases until a potential of E_{pp} is reached. Above this *passivation potential*, a dramatic decrease in the dissolution rate occurs. Further increases in potential usually have little effect on the passive current density, i_{pass}. In some cases, the difference between the critical anodic current density for passivation, i_{crit}, and i_{pass} can be over four orders of magnitude. As shown in Chapter 1, these current densities are directly related to the dissolution rate of the material. In solutions without aggressive species such as Cl^-, further increases in potential will eventually lead to an increase in the current due to a combination of oxygen evolution and transpassive dissolution of the passivating film for most metals. For the valve metals (e.g., aluminum, tantalum, lead, titanium), certain solutions

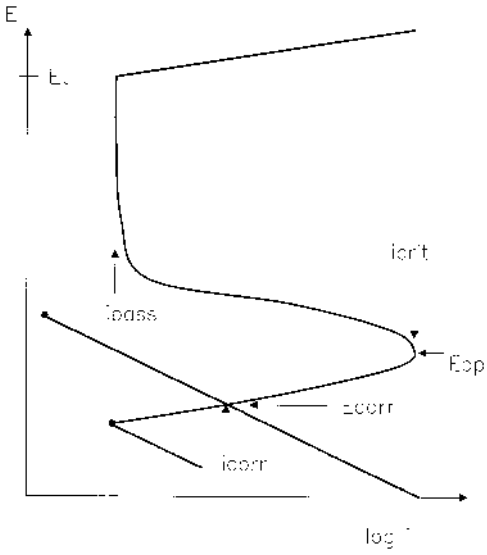

Figure 4 Schematic Evans diagram for a material that undergoes an active–passive transition. Important parameters that characterize this behavior are indicated.

will allow a thick, insulating oxide film to grow on which oxygen evolution does not occur. Under these conditions, *anodization* occurs. The electrochemical parameters that characterize passivity (E_{pp}, E_t, i_{crit}, and i_{pass}) depend upon both the metal and the environment to which it is exposed.

In order to determine the corrosion state of an active–passive system, the position of the corrosion potential relative to E_{pp} must be determined. According to Fig. 4, if E_{corr} is below E_{pp}, the material will undergo uniform dissolution under film-free conditions. If E_{corr} is above E_{pp} but below E_t, the material will be passive and will dissolve at its passive current density, which is often on the order of 0.01 mpy. Corrosion-resistant alloys are designed to operate under such conditions. For situations in which E_{corr} is above E_t, the material will dissolve transpassively, i.e., uniformly.

As discussed in detail in Chapter 2, the corrosion potential is determined by the intersection of the sum of the anodic Evans lines and the sum of the cathodic Evans lines. For active–passive materials, the only new wrinkle is the increased complexity of the anodic line. Since the anodic line is not single-valued with respect to current density, three distinct cases can be considered. In all cases, the condition $\sum I_a = \sum I_c$ determines the position of the corrosion potential, and the condition $i_{app} = i_a - i_c$ determines the appearance of the polarization curve

for each case. Thus the nature and kinetics of the cathodic reaction(s) are critical in determining the corrosion state and rate of dissolution of an active–passive material.

Under reducing conditions (e.g., in acids such as HCl), the predominant cathodic reaction is hydrogen evolution as shown in Fig. 5. This combination results in a polarization curve in which all of the parameters characterizing passivity can be measured as shown in Fig. 5. If a material were to be used under these conditions, nothing would be gained from its ability to passivate.

In the presence of oxidizing species (such as dissolved oxygen), some metals and alloys spontaneously passivate and thus exhibit no active region in the polarization curve, as shown in Fig. 6. The oxidizer adds an additional cathodic reaction to the Evans diagram and causes the intersection of the total anodic and total cathodic lines to occur in the passive region (i.e., E_{corr} is above E_{pp}). The polarization curve shows none of the characteristics of an active–passive transition. The open circuit dissolution rate under these conditions is the passive current density, which is often on the order of 0.1 μA/cm^2 or less. The increased costs involved in using CRAs can be justified by their low dissolution rate under such oxidizing conditions. A comparison of dissolution rates for a material with the same anodic Tafel slope, E_o, and i_o demonstrates a reduction in corrosion rate

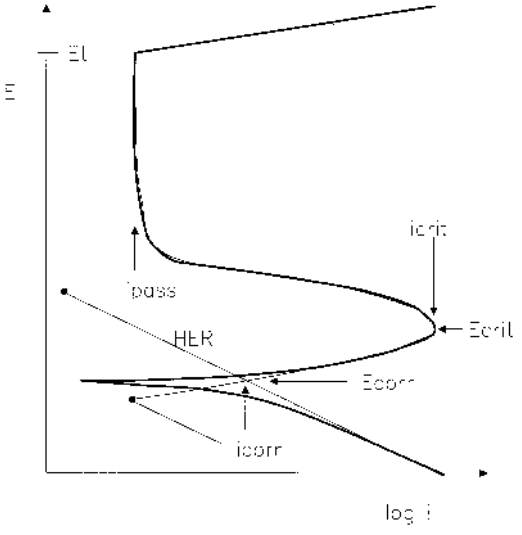

Figure 5 Schematic Evans diagram and resulting potential-controlled polarization curve for a material that undergoes an active–passive transition and is in a reducing solution. The heavy line represents the applied currents required to polarize the sample.

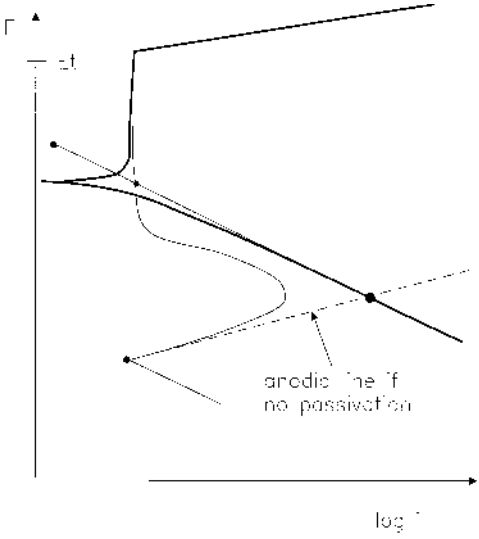

Figure 6 Schematic Evans diagram and resulting potential-controlled polarization curve for a material that undergoes an active–passive transition and is in an oxidizing solution. The heavy line represents the applied currents required to polarize the sample. If the sample did not undergo an active–passive transition, it would corrode at a much higher rate in this solution, as is indicated by the intersection of the dotted line and the cathodic curve.

by many orders of magnitude.

Examples of materials whose "active nose" is hidden are stainless steel in dilute aerated acid and carbon steel in alkaline solution containing strong oxidizers. In the case of materials that are passive only in the presence of oxidizers stronger than water, removal of those oxidizers (e.g., by deaeration in the case of oxygen) reveals the presence of the active–passive transition as shown in Fig. 7. Note the lower E_{corr} after deaeration. Oxidizers are not always good; if the oxidizing power of the solution raises the potential too much, transpassive dissolution or pitting (if an aggressive species is present) can occur.

For the case shown in Fig. 8, the anodic and cathodic Evans lines intersect at three points. The polarization curve for this situation appears unusual, although it is fairly commonly observed with CRAs. At low potentials, the curve is identical to that shown in Fig. 5. However, just above the active–passive transition, another E_{corr} appears followed by a "loop" and yet a third E_{corr} before the passive region is observed. The direction (anodic or cathodic) of the applied current density for each region shown in the polarization curve of Fig. 8 is indicated, showing that the loop consists of cathodic current. The origin of the cathodic loop is the

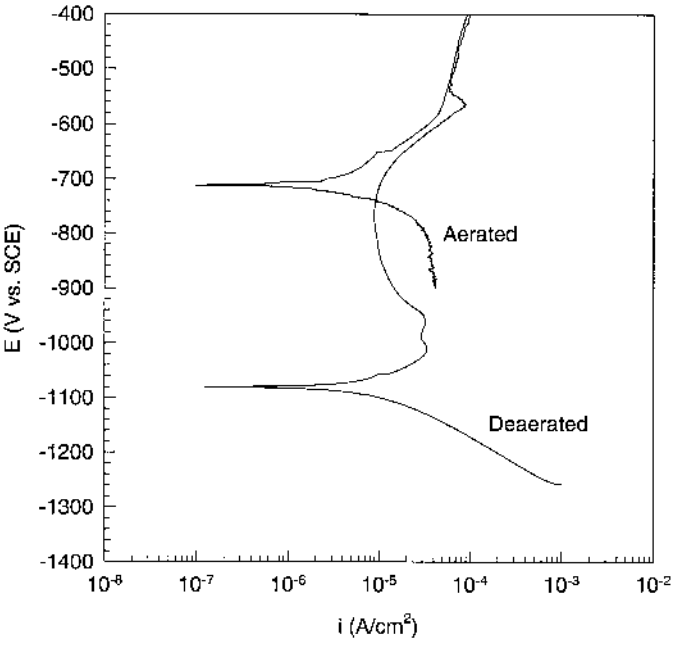

Figure 7 Polarization curves for carbon steel in pH 11.5 solution at 65°C containing 10 g/L Na_2S, 1 g/L catechol under (a) deaerated and (b) aerated conditions. Upon aeration, quinones are formed, which act as strong oxidizing agents. Note the higher E_{corr} of the steel under aerated conditions. (Data courtesy of S. Kannan, University of Virginia.)

fact that at these potentials, the rate of the cathodic reaction is greater than the passive current density. Thus the net current is cathodic over that range of potential. An example of this behavior is seen in Fig. 9 (8). Generally, either the uppermost or lowermost E_{corr} is the most stable, and the material exhibits that corrosion potential spontaneously.

Such cathodic loop behavior is often observed on the reverse scans of polarization curves in which pitting does not occur as shown in Fig. 10 (9). During the initial anodic scan, the oxide is thickening and the anodic line is moving to the left. Thus, upon the return scan, the unchanged cathodic line now intersects the anodic line at several places, leading to the appearance of cathodic loops. Cathodic loops do not pose fundamental problems; they merely conceal the passive current density at potentials near the active–passive transition.

The cathodic reaction kinetics thus play an important role in determining the corrosion state for an active–passive material. The introduction of additional cathodic reactions to an environment or the change in the kinetics of one already present can dramatically affect the state of the material's surface. Figure 11 shows

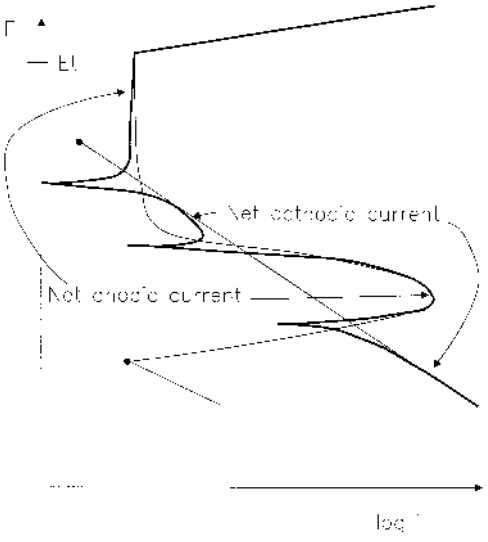

Figure 8 Schematic Evans diagram and potential-controlled polarization curve for a material/environment combination that exhibits a cathodic loop. Note that the direction of the applied current changes three times in traversing the curve.

schematically the effects of changes in the kinetics of a single cathodic reaction (modeled as changes in the exchange current density). From the different corrosion potentials established, one can see the key role of cathodic reaction kinetics in establishing the corrosion state of active–passive metals.

Based upon the above descriptions, the Faraday experiment can now be explained. Figure 5 shows the polarization curve and Evans diagram for a passivating metal in a reducing acid such as dilute H_2SO_4. Figure 12 shows the Evans diagram for this case. The anodic curve in the Evans diagram is independent of the acid (to a first approximation). In the dilute acid, the rate of reduction of nitric acid is not higher than i_{crit}, so the sample does not passivate, but the presence of the nitric acid reduction as an additional cathodic reaction raises the potential above what it would be if hydrogen evolution were dominant. With the concentrated nitric acid, not only is the E_r raised, but also the i_{dl} increases owing to the higher concentration, so i_{crit} and E_{pp} are exceeded, and the sample passivates. Upon returning the passivated sample to the dilute acid, the nitric acid reduction is able to maintain the passivity because only a small current is necessary. However, when bare surface is exposed, the passivation process must start again, and soon the passive film is undermined, as the entire surface subsequently dissolves at the high rate, since the low nitric acid concentration is insufficient to raise the E_{corr} above E_{pp}.

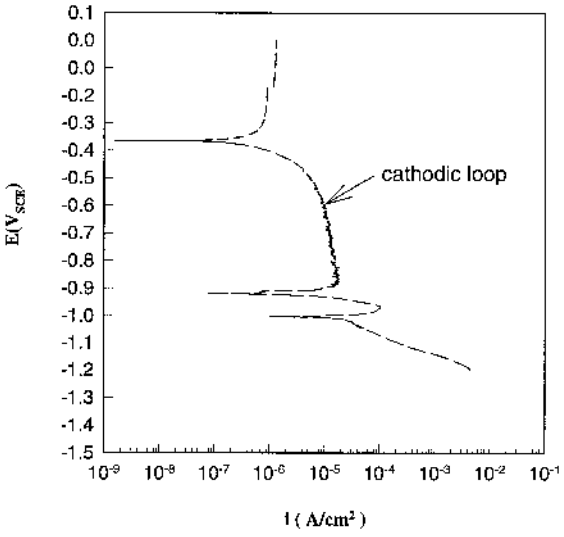

Figure 9 Polarization curve of carbon steel in deaerated, pH 13.5 solution at 65°C. Sample was initially held potentiostatically at −1.2 V(SCE) for 30 min before initiation of the potentiodynamic scan in the anodic direction at 0.5 m V/s. The cathodic loop results from the fact that the passive current density is only 1 μA/cm^2, which is less than the diffusion-limited current density for oxygen reduction for the 0.5 ppm of dissolved oxygen present. (From Ref. 8.)

The i_{dl} of the cathodic reaction can be of critical importance in the passivation of a material. The effects of increasing i_{dl} by increasing solution velocity are shown in Fig. 13a for both passivating and nonpassivating metals. The Evans diagram in Fig. 13b shows that for both types of materials, the corrosion potential and corrosion rate initially increase with increasing velocity. However, for the passivating metal, a critical velocity is reached at which the i_{crit} is exceeded and the sample passivates (i.e., the dissolution rate decreases dramatically). Higher velocities have no effect on the corrosion rate. For the nonpassivating metal, the increased cathodic reaction rate increases the corrosion rate until the sample is under complete activation control. It should be stressed that these velocities are at much lower values than those under which erosion corrosion occurs.

1. Galvanic Couples

The presence of galvanic couples can affect passivity in three ways (two of which are bad), as demonstrated in Fig. 14: (**1**) increasing the potential of the active–

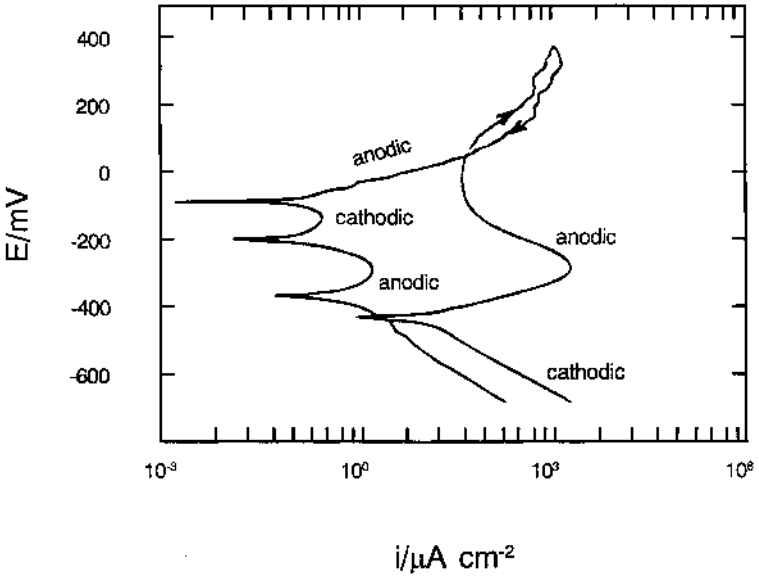

Figure 10 Polarization curve for Type 302 stainless steel in 0.5% HCl. Note the presence of a cathodic loop on the return scan due to the greatly reduced passive current density. Also, note the lowered critical current density on the reverse scan due to incomplete activation of the surface. (From Ref. 9.)

passive material so that passivity can occur for conditions under which it otherwise would not, (**2**) increasing the potential of the active–passive material to the point that localized corrosion can occur, and (**3**) decreasing the potential of the previously spontaneously passive material so that passivity cannot be maintained and active dissolution occurs on the (previously) passive metal. In case **1** the cathodic material must be able to deliver a cathodic current density higher than the i_{crit} of the active–passive material. Case **2** is similar to the case discussed above in which the cathodic reaction raises the corrosion potential above E_t, leading to transpassive corrosion. If an aggressive species such as chloride ion is present, the dissolution can become nonuniform. This phenomenon will be discussed in greater detail in the section on localized corrosion. Though rare, case **3** is an example of a sacrificial anode that is causing, rather than solving, problems. While the idea of cathodic protection by galvanic coupling might be appealing, in the schematic shown this would lead to rapid uniform dissolution of the cathode (active–passive) material. Thus galvanic couples involving active–passive materials must be considered carefully.

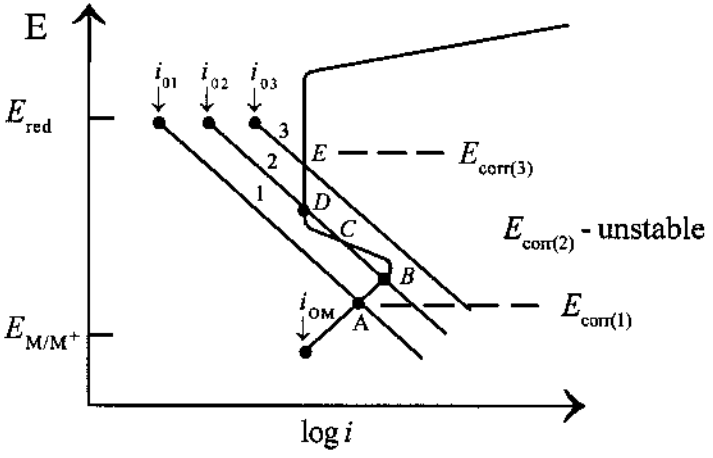

Figure 11 Schematic Evans diagram illustrating the effect of a change in the cathodic reaction kinetics on the corrosion conditions. Case 1 would be representative of Fig. 5. Case 3 would lead to the polarization behavior described in Fig. 6. Case 2 would lead to the polarization behavior shown in Fig. 8. (After Ref. 71.)

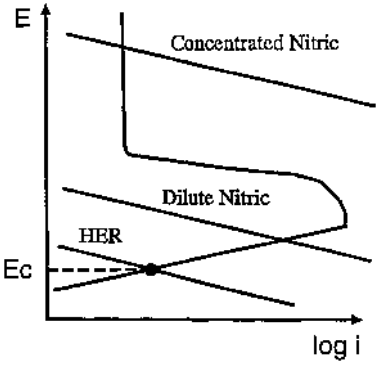

Figure 12 Schematic Evans diagrams for the three conditions of the Faraday experiment.

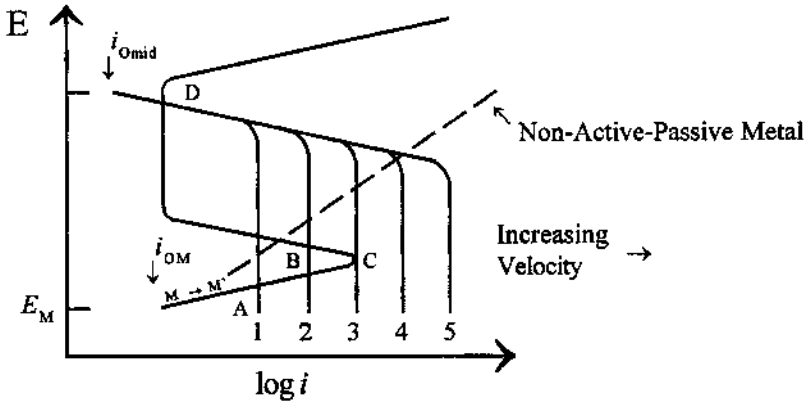

(a)

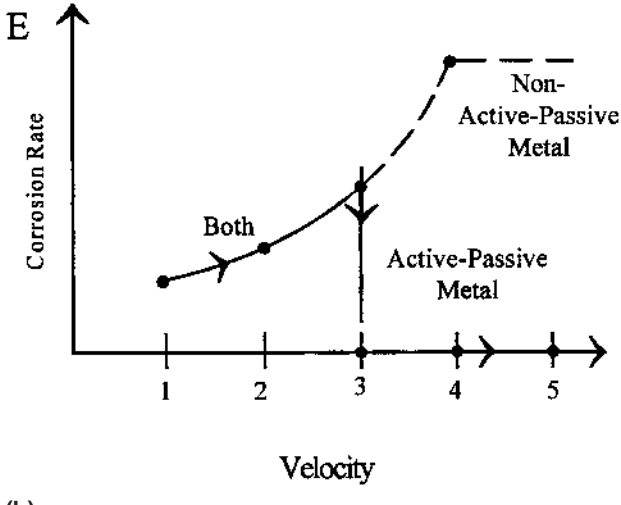

(b)

Figure 13 (a) Effect of fluid velocity on the electrochemical behavior of both active–passive and nonactive–passive materials. (b) Effect of fluid velocity on corrosion rate of these materials. (After Ref. 71.)

2. Anodic Protection

Corrosion control using external polarization usually operates by reducing the driving force for the metal dissolution reaction, as in cathodic protection. For passivating metals, an alternative is to reduce the kinetics of the dissolution process by raising the potential. This is known as anodic protection and has been

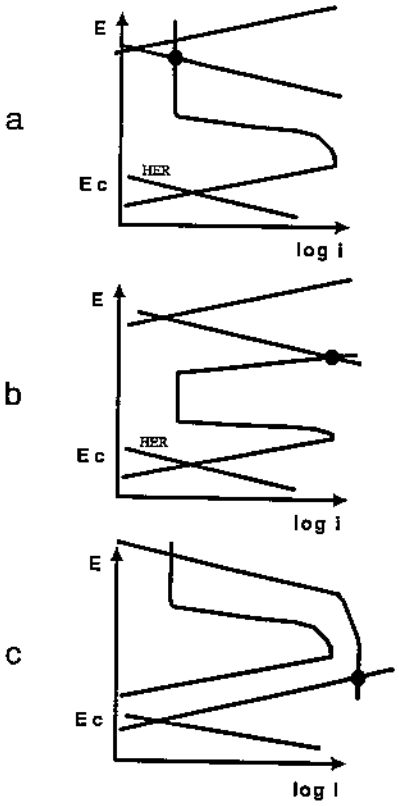

Figure 14 Evans diagrams for active–passive metal when coupled to (a) a metal that holds E_{corr} in a passive region, (b) a metal that holds E_{corr} above pitting or transpassive potential, and (c) a metal that causes a passive–active transition.

applied with success in the pulp and paper industry, particularly for the mitigation of stress-corrosion cracking. The operating principles are shown in Figs. 15 and 16. Recall that $i_{app} = i_a - i_c$. Therefore at E_{corr}, $i_{app} = 0$, by definition. In order to polarize the surface to E_i, i_{appi} must be applied:

E_c requires $i_{app,c} = 10{,}000\ \mu A/cm^2$ (cathodic)
E_3 requires $i_{app3} = 0.9\ \mu A/cm^2$ (anodic)
E_4 requires $i_{app4} = 1.0\ \mu A/cm^2$ (anodic)

At E_4, the sample is dissolving at $1\ \mu A/cm^2$. In order to protect cathodically the structure to the same dissolution rate, the potential must be E_c. To polarize the surface to E_c would require $10{,}000\ \mu A/cm^2$, a value five orders of magnitude

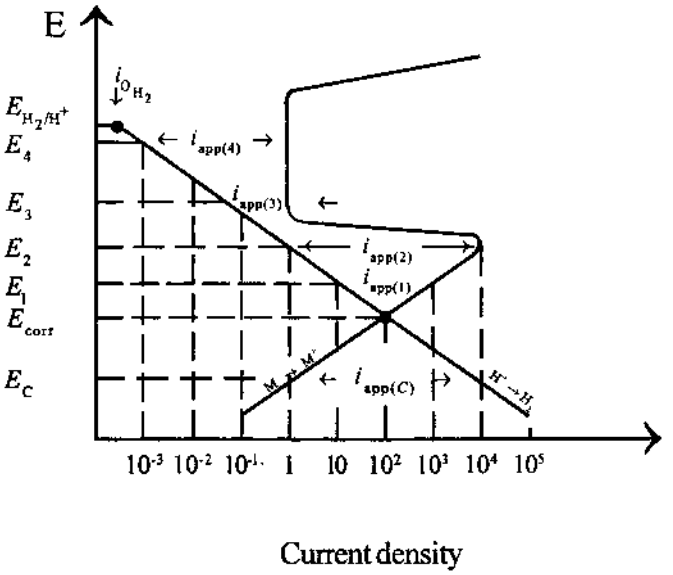

Figure 15 Applied current densities required for different applied potentials for an active–passive material in acid. If there is a dissolution rate of 1 μA/cm^2, cathodic protection to E_c would require an applied current density of 10,000 μA/cm^2, while anodic protection to E_4 would require only 1 μA/cm^2. (After Ref. 21.)

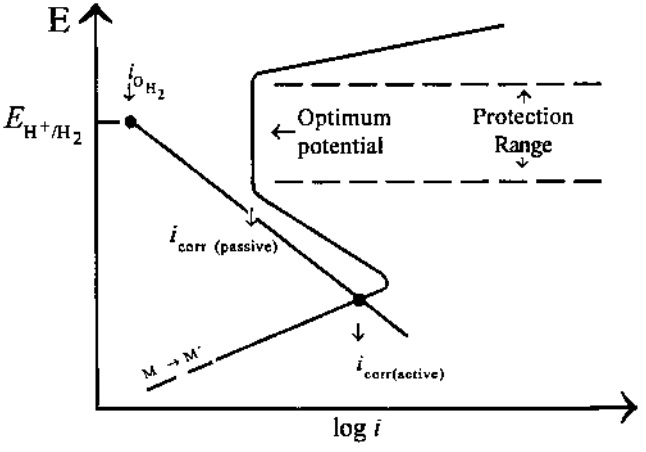

Figure 16 Schematic diagram showing protection range and optimum potential for anodically protecting an active–passive metal. (After Ref. 21.)

higher than that required for anodic protection. Since current costs money, there are cases when it is cheaper to use anodic protection.

One must be wary of the use of anodic protection, in that any area that is not polarized completely into the passive region will dissolve at a high rate. The optimum protection range is shown in Fig. 16. Therefore anodic protection is more susceptible to the presence of crevices, deposits, or poor placement of polarizing electrodes than is cathodic protection. If a component is cathodically under protected, the maximum rate at which the unprotected area corrodes is the "normal" open circuit corrosion rate; in anodic protection, underprotection results in *high* rate dissolution of the unprotected area and can therefore can lead to unexpected career changes. Understanding the manner in which current from an anodic protection system is distributed across a surface is important in such installations. The issues involved in current distribution are discussed in detail in Chapter 4.

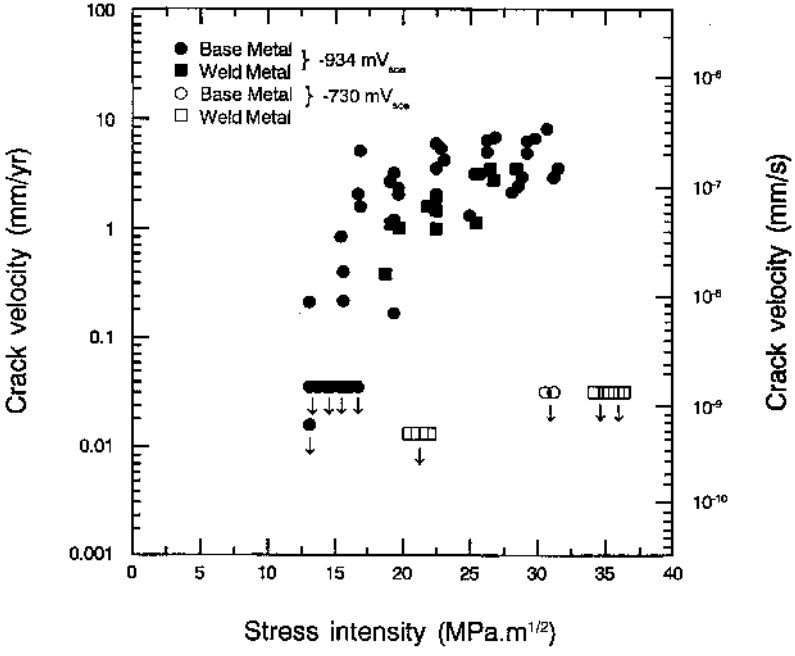

Figure 17 Fracture mechanics data plotted as log apparent crack velocity vs. stress intensity. Each point represents the exposure of a single specimen. The specimens were immersed in a simulated impregnation zone liquor at 115°C for 151 days. No crack propagation was observed at anodic protection potentials (-730 mV_{SCE}). (From Ref. 10.)

Singbeil and Garner (10) showed that the use of anodic protection can prevent stress-corrosion cracking in the pressure vessel steels exposed to alkaline solutions used in digesters in the pulp and paper industry, as shown in Fig. 17. The 200 mV anodic polarization placed the material above the active–passive transition where cracking had been shown to occur (10).

III. LOCALIZED CORROSION

Localized corrosion is the direct result of the breakdown of passivity at discrete sites on the material surface. As was stated above, once passivity is established on a surface, one might expect either that it would remain passive or that a complete activation of the surface would occur. However, what is often observed in practice is the appearance of discrete areas of attack that begin to corrode actively while the vast majority of the surface remains passive. These isolated regions of attack are more than mere annoyances; the local penetration rates can be on the order of 10 mpy or higher, leading to rapid perforation of any reasonably sized container. Since the original intent in using passive materials (e.g., CRAs) in any application is to exploit their low dissolution rates, localized corrosion can be a major operational problem.

This section provides a basic explanation of the underlying physical processes that control localized corrosion in order to lay the foundation for an understanding of the tests that are discussed in the next section. The manifestations of these physical processes through electrochemically measurable quantities are then discussed. Some generalized phenomenology is presented through illustrative examples from the literature. Full mechanistic understanding of localized corrosion has not yet been achieved. Information on the various models proposed can be found in review articles (11,12) and corrosion texts (13,14).

While there are a variety of types of localized corrosion phenomena (e.g., crevice corrosion, pitting, intergranular attack, stress-corrosion cracking, filiform corrosion), they share a number of common features. Foremost among these is the development of an extremely aggressive solution locally which causes high-rate localized attack. It is becoming increasingly clear that much can be understood about the different types of localized corrosion by considering them as manifestations of the same set of basic phenomena (15–17). For example, pitting can be viewed as crevice corrosion on a smaller scale, with either micropores or surface heterogeneities acting to form the crevice.

A. Important Physical Processes

The important physical processes that control localized corrosion do so through their impact on three key aspects: (**1**) the development of a local solution chemis-

try that is sufficiently aggressive to destroy passivity, (**2**) the physical separation and ionic/electrical communication of anodic and cathodic sites, and (**3**) the stability of the high-rate dissolution. For localized corrosion to occur, the local conditions must become substantially more aggressive than those across the majority of the surface. While some controversy remains, it is generally accepted that during the growth of a localized corrosion site, a highly aggressive solution develops in which the material undergoes active dissolution. Mears and Evans (18) originally proposed the development of what has become known as the critical crevice solution (CCS) (19–22). Oldfield and Sutton (19,20) were the first to construct a mathematical model based upon the CCS concept formulated by Fontana and Greene (21), and it is in this context that the important physical processes will be discussed.

While the Fontana and Greene model was developed specifically for crevice corrosion of stainless steel in neutral halide solutions, it has been traditionally accepted as qualitatively describing the phenomena that occur during the initiation and propagation in most alloys, with minor modifications. The model identifies four stages in the crevice corrosion of stainless steel in neutral Cl^- solution as shown in Fig. 18. In the first stage, the model predicts that the alloy will dissolve stoichiometrically, with Fe, Ni, and Cr entering the solution in proportion to their presence in the alloy. This dissolution occurs over the entire surface and constitutes the passive current. The cathodic reaction (oxygen reduction) also occurs both inside and outside the crevice. However, owing to the restricted diffusion to the occluded site, oxygen becomes depleted inside the crevice, and the physical separation of anode and cathode develops that is necessary for localized corrosion to occur. This marks the beginning of stage II. As the passive dissolution of the alloy continues, the accumulation of cations inside the crevice (due to the production of Fe^{2+}, Cr^{3+}, Ni^{2+} by dissolution and the mass transport restrictions inherent in the geometry) is balanced by the electromigration of Cl^- into the crevice from the bulk solution. Chloride dominates the anion migration into the crevice owing to its high mobility and concentration compared to other anions. The Cl^- forms complexes with the metal ions, which are then quickly hydrolyzed. This hydrolysis lowers the pH of the crevice through the production of hydrogen ion. As the pH drops, the passive current in the crevice increases, which acts to increase the amount of Cl^- migration, which increases the amount of hydrolysis, leading to further decreases in pH. The limited concentration of OH^- (0.1 μM at neutral pH) in the bulk prevents its migration into the crevice from having a substantial effect on the local pH. Due to the large stability constant for Cr^{3+} hydrolysis (23), it is generally thought that this reaction path determines the final occluded site pH for stainless steels.

The self-sustaining nature of the process leads to a drastic reduction in the stability of the passive film. Stage III is characterized by the breakdown of the passive film due to the attainment of what has become known as the critical crevice solution. This solution has a low pH [typically 1 or less (23)] and a high Cl^-

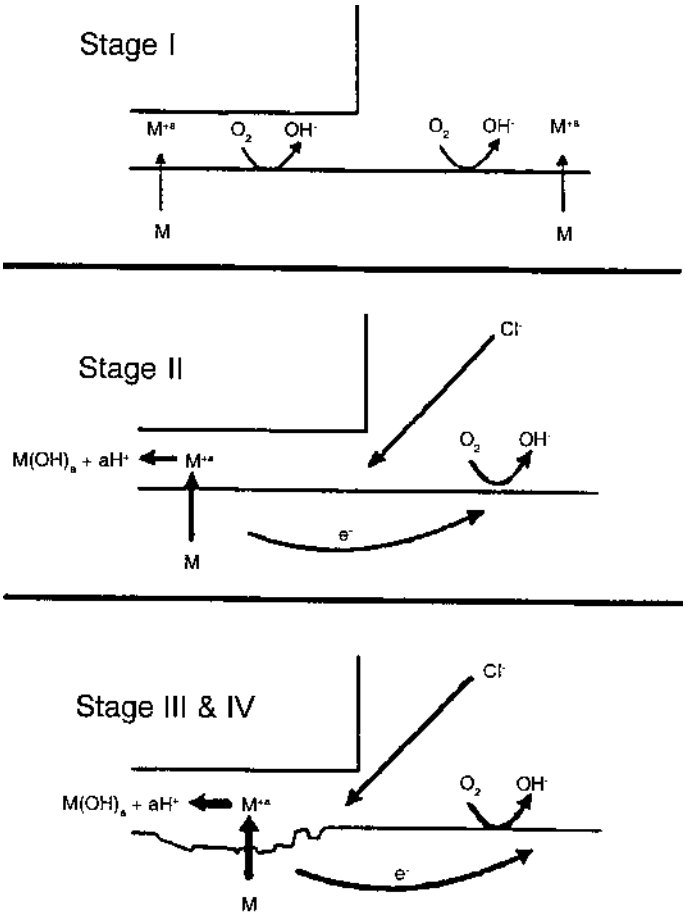

Figure 18 Schematic of Fontana and Greene model for crevice corrosion initiation of stainless steels in aerated Cl^- solution. (After Ref. 21.)

concentration [typically on the order of several M (24)] that results from the continual ingress of Cl^- into the crevice. These concentrated solutions form in the localized corrosion site even if the bulk solution Cl^- concentration is low. Stainless steel is not able to remain passive in this solution and begins to dissolve actively. In stage IV, propagation is stabilized owing to the large cathode-to-anode area ratio that exists. The large freely exposed surface acts as a large cathode (with oxygen reduction supplying the current), while the creviced area acts as an anode.

Both calculations and measurements have indicated that it is possible to develop very concentrated metal chloride solutions within occluded sites. For example, stainless steel pits would be expected to contain 5 N Cl^-, 4 N Fe^{2+}, 1 N Cr^{3+}, 0.5 Ni^{2+}, and 0.007 N Na^+ and have a pH of 0.5. The low sodium ion concentration develops as the Na^+ migrates out of the crevice due to the electric field but is not replaced by any reaction in the crevice. Recent measurements (24) of active crevice sites on Type 316L stainless steel showed the following concentrations: 2.9M Fe^{2+}, 0.77 M Cr^{3+}, 0.24 M Ni^{2+}, and 0.06 M Mn^{2+}. As was stated above, stainless steel will not remain passive in such a solution and can dissolve at a high rate. The autocatalytic nature of the process stabilizes the environment by exceeding the rate at which diffusion can disperse the concentrated solution. Initial dissolution rates of the order of 1 A/cm^2 ($\approx$ 440 in./yr) can be reached.

In order for these rates to be maintained, the anodic dissolution current must be balanced with a cathodic current according to $\sum I_a = \sum I_c$. The cathodic current comes from reduction reaction(s) occurring on the outer surface of the sample. Since this has a large surface area associated with it, it is a classic galvanic corrosion problem of large cathode and small anode. In this case, they are on the same surface, as shown in Fig. 19. However, as the pit deepens, it becomes more and more isolated from the outside environment, both chemically and in terms of potential control. There are three limitations on the dissolution rate at a localized corrosion site: (**1**) diffusional effects at the cathode (e.g., increases in the boundary layer thickness with time limits the cathodic current), (**2**) salt film precipitation at the anode (i.e., exceeding the solubility of the metal salts causes a porous film to form across which some of the driving force drops), and (**3**) ohmic effects in the solution between anode and cathode. Together these decrease the steady-state penetration rates to values of between 0.5 and 10 mm/yr. Figure 20 shows how each of these effects can act to limit the pit dissolution rate in terms of Evans diagrams. Figures 21 and 22 show data for pit depth deter-

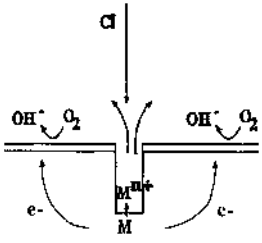

Figure 19 Location of anodic and cathodic reactions in pitting, showing the "galvanic" nature of the process.

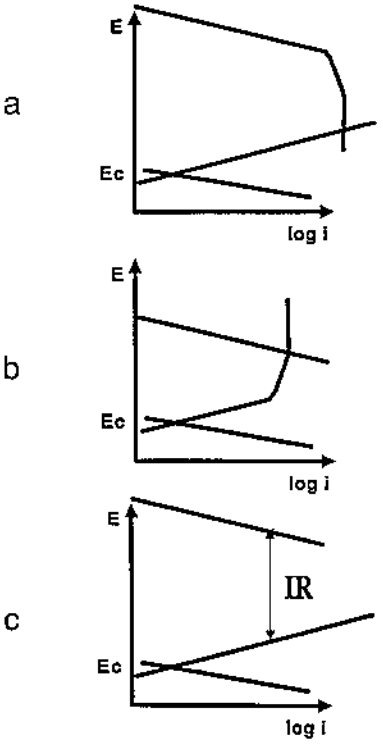

Figure 20 Evans diagrams showing limitations to pit growth: (a) diffusion limitation at cathode, (b) salt film formation at anode, and (c) IR limitations between anode and cathode.

mined from long-term exposures of alloys to seawater. The pitting rate can be crudely estimated from the slope of the curves. In the cases shown of copper and two aluminum alloys in seawater, the rate of pit propagation falls off dramatically after the first year. Such behavior is typical in localized corrosion, due to the effects discussed above, which limit the local current density.

The propagation of localized corrosion thus becomes an issue of stability. For the localized corrosion site to exist, the CCS must be maintained locally. However, the solution inside the localized corrosion site is constantly diffusing away. The higher the concentrations required in the CCS, the larger the Fickian driving force. In order to maintain the CCS within the localized corrosion site, the anodic reactions inside the localized corrosion site must occur at a high rate and must be balanced by cathodic reactions either inside or outside the localized corrosion site. Any process that upsets this balance will cause the diffusion of

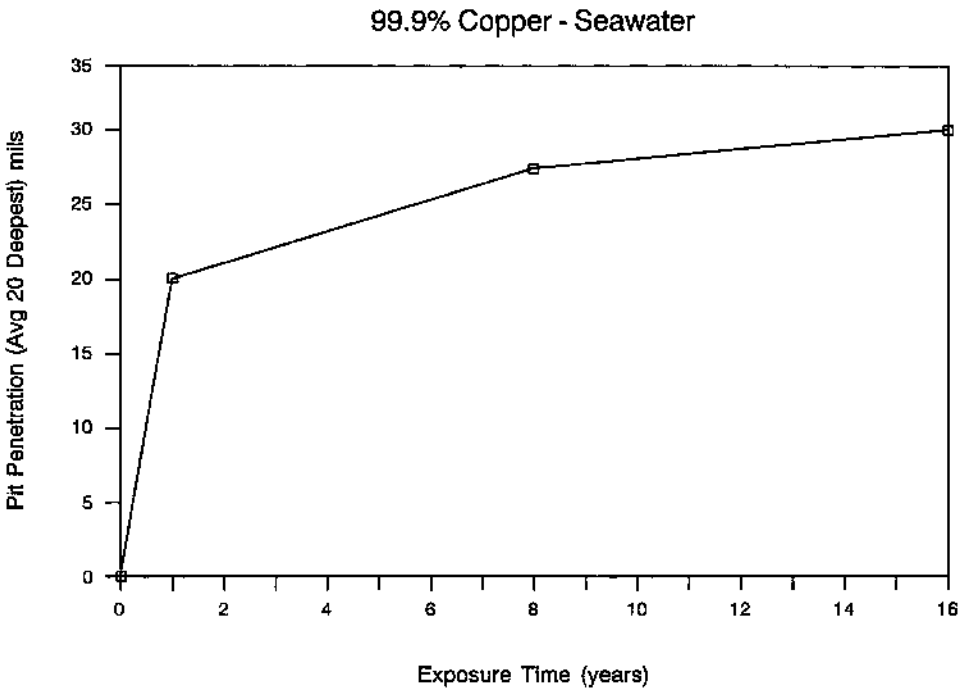

Figure 21 Pit penetration as a function of time for pure copper exposed to natural seawater. The pit penetration rate can be estimated from the slope of the line. While the initial pit penetration rate is rapid, it decreases substantially after the first year. (Data from C. R. Southwell, J. D. Bultman, A. L. Alexander, Materials Performance, 15 (1976).)

CCS to dominate and the localized corrosion site to repassivate. In studying the localized corrosion test techniques, these three aspects of localized corrosion, the CCS, the separation of anode and cathode, and the stability of these processes, should be kept in mind.

The initiation of localized corrosion is one of its most important and least understood aspects. While theories of initiation abound (10–15), a full under-

Figure 22 Maximum pitting depth as a function of time for (a) AA3003-H14 and (b) AA6061-T6 exposed to natural seawater at Halifax, Nova Scotia. The pit penetration rate can be estimated from the slope of the line. While the initial pit penetration rate is rapid, it decreases substantially after the first year. (Data from H. P. Godard et al., The Corrosion of Light Metals, John Wiley, New York (1967).

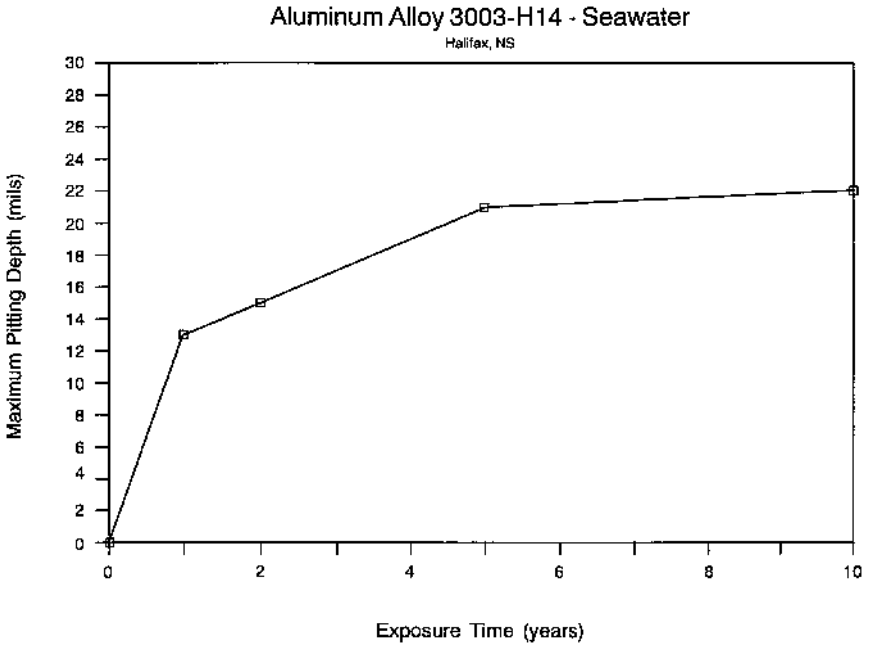
Aluminum Alloy 3003-H14 - Seawater
Halifax, NS
Maximum Pitting Depth (mils)
0
2
4
6
8
10
12
14
16
18
20
22
24
26
28
30
0
2
4
6
8
10
Exposure Time (years)

(a)

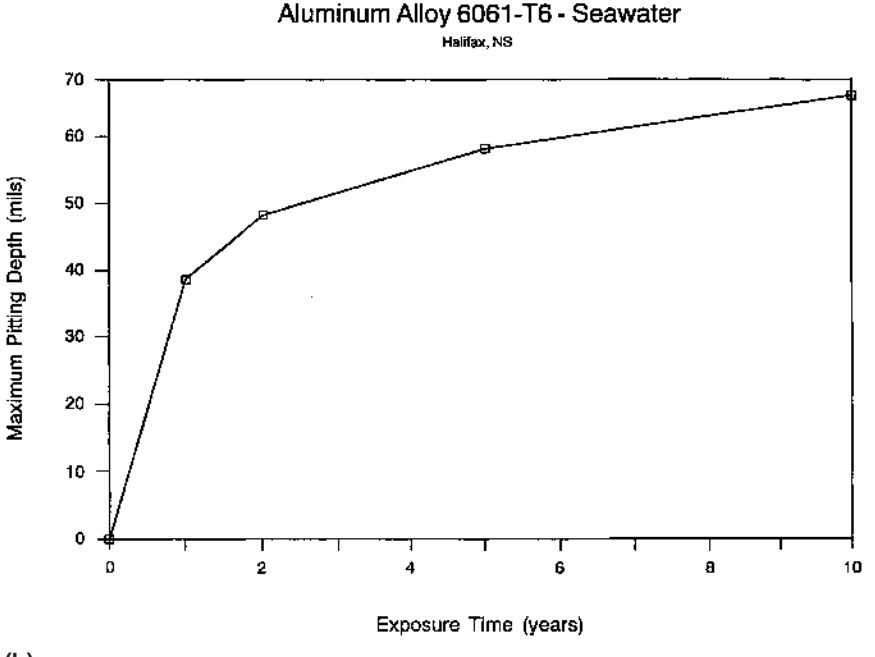
Aluminum Alloy 6061-T6 - Seawater
Halifax, NS
Maximum Pitting Depth (mils)
0
10
20
30
40
50
60
70
0
2
4
6
8
10
Exposure Time (years)

(b)

standing of the atomistics of the process(es) involved has remained elusive. The model described above has a number of drawbacks and shortcomings. In engineering terms, propagation of localized corrosion sites is often considered more problematic, though there are situations where even very small pits constitute failure (e.g., interconnections on integrated circuits).

B. Electrochemical Phenomenology

Armed with an understanding of the underlying physical processes, the electrochemical phenomenology of localized corrosion can be better understood. Figure 23 shows three schematic polarization curves for a metal in an environment in which it spontaneously passivates and (**1**) can be anodized, (**2**) transpassively dissolves at higher potentials, and (**3**) pits upon further anodic polarization. We have discussed cases **1** and **2** in the section on passivity. For case **3**, the region of passivity extends from E_{corr} to a potential labeled E_{bd} at which point the current increases dramatically at higher potentials.

Inspection of the specimen surface at the points labeled "a" and "b" on curves **2** and **3** would show the difference in the physical processes causing the identical current densities to be measured. In the case of curve **2**, the surface would have undergone uniform dissolution; in some cases, the dissolution is so slight that it is imperceptible without magnification. In the case of curve **3**, the

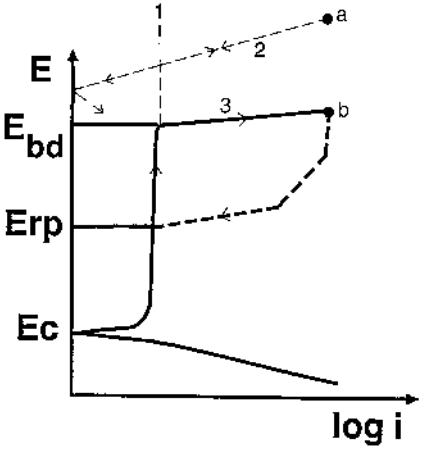

Figure 23 Schematic polarization curve for metal that spontaneously passivates but pits upon anodic polarization. A hysteresis loop, which can appear during a reverse scan, is shown ending at Erp. One dotted line shows behavior for anodizing conditions, while the other shows transpassive dissolution.

vast majority of the surface would appear unaffected as well. However, one or more areas would have suffered severe localized attack. Note that without physical inspection of the surface, determination of the origins of the applied currents cannot be made.

The dotted lines in Fig. 23 show the applied current densities observed if, after reaching points a and b respectively, the direction of the potential scan is reversed. In both cases, a hysteresis loop is generated. For case **2**, a negative loop occurs, i.e., the current densities in the passive region on the reverse scan are less than those on the forward scan at the same potential. For case **3**, a positive hysteresis develops. In both cases, the current eventually changes polarity (note the new "E_{corr}'s"). Inspection of the two surfaces would reveal that while the case **2** surface remains virtually unaffected, the localized corrosion sites on the case **3** surface will have increased in size dramatically.

The physical origins behind the negative hysteresis of case **2** lie in the effect of passive film thickness on potential and subsequent dissolution rate. Passive films grow thicker at higher potentials and after longer times at a constant potential. As the potential of the material of case **2** is scanned anodically, its film thickens and becomes more protective. If the scan were stopped at any potential and held, the current would decrease with time. However, in the experiment shown, the potential is constantly being increased until the vertex current density (point a) is reached. On the reverse scan, the currents are lower at all potentials because of the thickened passive film. The effect can also be understood by assuming that at the end of the forward scan, the surface with the thickened film has an anodic Evans line that is displaced to lower current densities compared to the Evans line for the forward scan. Assuming no change in the kinetics of the reduction reaction, the applied currents will be lower and the potential at which $\sum I_a = \sum I_c$ is also more positive, as shown in Fig. 24.

The physical origins behind the positive hysteresis of case **3** lie in the connection among the CCS, the stability of localized corrosion sites, and the competition between diffusion and dissolution at localized corrosion sites. As was discussed in the section on localized corrosion phenomenology, CRAs will actively corrode only in aggressive, concentrated solutions. These concentrated solutions can be generated locally by hydrolysis of dissolution products, but there will be a large Fickian driving force to disperse them. An open pit is subject to hemispherical diffusion that is quite rapid. In order to maintain the aggressive CCS, the dissolution rate and subsequent hydrolysis must be able to overcome the diffusional processes even as the pit grows. At high applied potentials (near point b on curve 3), the local dissolution rate can be quite high (ca. A/cm^2), the diffusion is overwhelmed and an aggressive solution is maintained. During the initial portion of the reverse scan, the driving force for dissolution is decreasing, but the CCS has not had sufficient time to diffuse away. As the reverse scan continues, the driving force for dissolution continues to decrease, and eventually the CCS

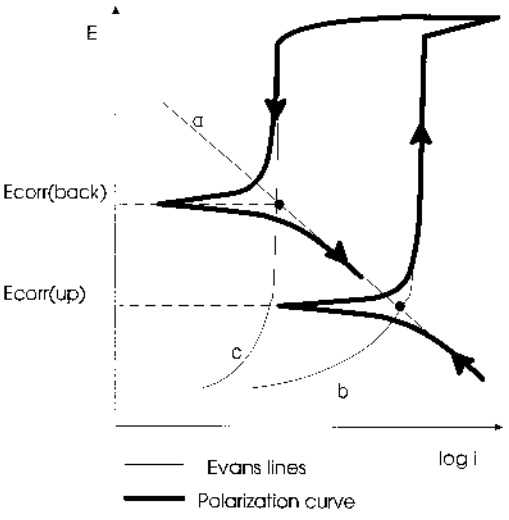

Figure 24 Schematic Evans diagram and polarization curve illustrating the origin of the negative hysteresis observed upon cyclic polarization for materials that do not pit. Line a represents the (unchanging) cathodic Evans line. Line b represents the anodic Evans line during the anodically directed polarization, while line c represents the anodic Evans line for the material after its passive film has thickened because of the anodic polarization. The higher corrosion potential observed for the return scan (E_{corr} (back)) is due to the slowing of the anodic dissolution kinetics.

cannot be maintained against diffusion. At this point, the localized corrosion site repassivates, and the anodic current falls. Throughout the scan, the areas on the surface that were not dissolving at high rate were having the passive films covering them thicken, as in case **2**. Thus the E_{rp} is a convolution of the loss of the critical crevice solution from the localized corrosion site and the raising of the E_{corr} of the surrounding passive surface due to a decrease in anodic kinetics.

From polarization curves of the type shown in case **3**, three important parameters can be determined: E_{corr}, E_{bd}, and E_{rp}. In the literature there exists a nearly infinite number of variations of nomenclature, many of which are shown in Table 2. The interpretation of cyclic polarization curves has been and continues to be a subject of great controversy. The classic interpretation of case **3** would be that the potential of a material must exceed E_{bd} for new pits (or localized corrosion sites) to nucleate, but that at potentials between E_{bd} and E_{rp}, existing pits can propagate. At potentials below E_{rp}, all localized corrosion sites repassivate. Thus, from a design or material selection perspective, a material will perform well if its E_{corr} is kept below E_{rp}. This criterion can be met by environment

Table 1 Partial List of Terminology Used to Define Characteristic Pitting Potentials

Symbol	Name
E_b	Breakdown potential, breakthrough potential
E_c	Critical potential
E_i	Initiation potential
E_p, E_{pit}	Pitting potential
E_{np}	Nucleation potential
E_{cp}	Critical pitting potential
E_z	Potential of pit precursor
E_{prot}	Protection potential
E_{rp}	Repassivation potential
E_u	Unique pitting potential

treatment (e.g., the removal of oxidizers) and/or cathodic protection. More discussion of the controversy surrounding the interpretation of cyclic polarization data can be found in Section IV.B.3, p. 104.

Two other aspects of electrochemical phenomenology associated with localized corrosion should be appreciated before we discuss individual test techniques: common observations during potentiostatic testing and common observations during open circuit testing. Careful interpretation of these tests can provide useful information on the processes that control localized corrosion.

Three cases of potentiostatic testing can be considered: potentiostatic holds above E_{bd}, potentiostatic holds between E_{bd} and E_{rp}, and potentiostatic holds between E_{rp} and E_{corr}. In these tests, the applied current is measured versus time. Generally, at potentials above the E_{bd} found in potentiodynamic scans, large initial current will be observed, which is due to a combination of double layer charging, passive film growth, and pit initiation. The current will then decay before increasing in an erratic manner to values on the order of 1 to 10 mA/cm^2 (higher for higher potentials above E_{bd}). These currents represent both the propagation of the first pits and the initiation of new pits. The erratic nature of the currents is due to the repeated birth and death of pits. Deconvolution of the signal into components for individual pits is not possible without deterministic laws for initiation and propagation.

For potentiostatic holds between E_{rp} and E_{bd}, the current vs. time signal will typically look like Fig. 25a. After the initial decay from a high current, there will be an incubation time during which the current will remain low (e.g., on the order of 1 μA/cm^2 or less for stainless steels in neutral solution). Often, transient bursts of current will be observed. These currents are due to the initiation and

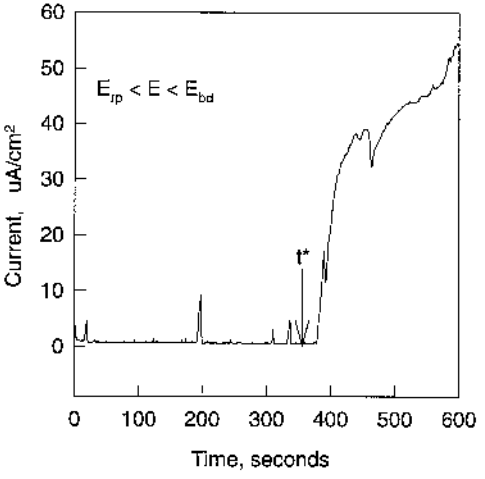

(a)

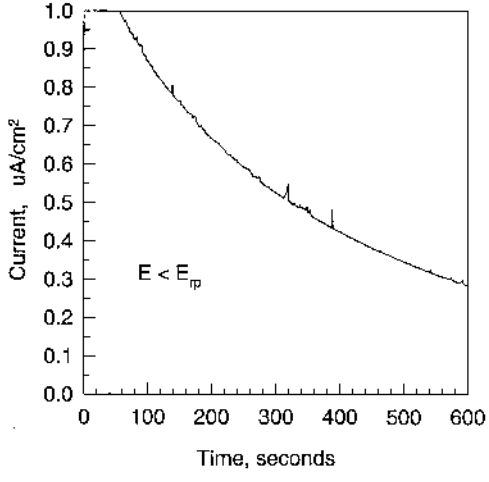

(b)

Figure 25 Current versus time behavior for Type 302 stainless steel in 1,000 ppm NaCl at (a) a potential between its repassivation and breakdown potentials, and (b) at a potential below its repassivation potential. Note the existence of an incubation time before stable localized corrosion occurs in (a). The small, short-lived current spikes during the first 400 s are due to the formation and repassivation of metastable pits, which can also be observed in (b), although they are of a smaller magnitude.

short-term propagation of metastable pits. The only difference between these pits and the stable pits is that the metastable ones repassivate in a short time (1 to 20 s, typically). If the test were interrupted at time t^* and the surface inspected, a series of small pits would be observed. The number would be less than or equal to the number of transients, as some of the repassivated metastable pits may reinitiate (e.g., if they are located at an inclusion stringer). Eventually, the current will increase as shown and stable pitting will commence. One or more metastable pits will stabilize (possibly by the formation of deposits of corrosion products from previous metastable pitting activity), the current will increase to values on the order of mA/cm^2, and the pits will propagate. For potentiostatic holds below E_{rp}, the currents will remain low, though metastable pitting activity may still occur, with the peak currents for each pit being smaller, as shown in Fig. 25b.

Due to their separation in time, it is possible to analyze the metastable pit transients in terms of the electrochemical processes occurring. If each transient is considered to be from a single, hemispherical pit, the dissolution current density in that pit can be calculated:

$$i_{\text{diss}} = \frac{I_{\text{peak}}}{A_{\text{pit}}} \qquad A_{\text{pit}} = \pi r_{\text{pit}}^2 \qquad r_{\text{pit}} = \left(\frac{3V_{\text{pit}}}{4\pi}\right)^{1/3} \qquad V_{\text{pit}} = \frac{(EW)\int_{t_0}^{t_{peak}} I(t)\,dt}{F\rho}$$

where I_{peak} is the peak current of the transient, EW and ρ are the equivalent weight and density of the material, F is Faraday's constant, and the integral of $I(t)$ is the charge passed during the transient. In addition to the assumption of a hemispherical geometry, these calculations assume that all of the dissolution is electrochemical and that all of the cathodic reaction supporting the anodic dissolution occurs on the counter electrode (i.e., no reduction reactions take place within the pit or on the boldly exposed surface). Such calculations on actual data (see the laboratory experiments associated with this chapter) demonstrate that the dissolution current density inside pits can reach the order of A/cm^2. By studying how these current densities are affected by potential, solution, alloy composition, and other experimental variables, insights into the factors that control the stabilization of pitting for any given material can be gained.

Upon immersion of CRAs into solution, their E_{corr}'s tend to rise with time as shown in Fig. 26. This rise in potential occurs as the passive film thickens or otherwise improves, moving the anodic Evans line to lower current densities. These circumstances lead to a rise in E_{corr}, in an analogous manner to the higher E_{corr} observed during a return scan of the transpassively dissolved material (Fig. 24). In a solution containing aggressive species, this rise in potential can eventually result in the E_{corr} exceeding the critical potential for localized attack, as shown in Fig. 26. Once localized corrosion can occur, a new Evans diagram must be considered. Figure 27 shows the Evans diagram for an initiated localized corrosion site. The cathodic line is that for the reduction of oxygen on the boldly

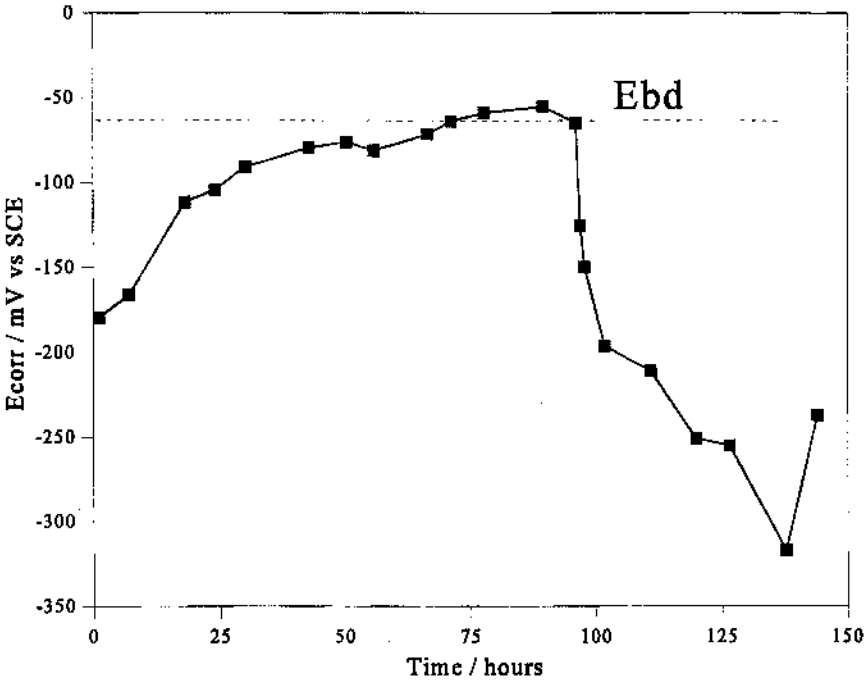

Figure 26 Corrosion potential vs. time for Type 410 stainless steel in 0.5 M NaCl + 0.01 M H_2O_2. The breakdown potential is indicated by the dotted line. Once this potential is exceeded, the potential falls as stable, localized corrosion begins to propagate.

exposed, nonlocally corroding surface. The anodic line is that for the dissolution of material in an aggressive CCS. Note that the abscissa is in terms of current rather than current density, since we must take area effects into account. At all times, the sum of the anodic currents must equal the sum of the cathodic currents. In the presence of the newly initiated pit, the new corrosion potential is lower. Our observation is a drop in the E_{corr}. If this is a metastable pit and it repassivates, the potential will rise again as the anodic line for the pit returns to its previously passive condition. This change can be viewed as an increase in Tafel slope. Once completely repassivated, the E_{corr} has regained its prepit initiation value. This process can be repeated at other sites on the surface, leading to a series of corrosion potential excursions as shown in Fig. 27 (line c). These transients will be discussed in more detail in the section on electrochemical noise.

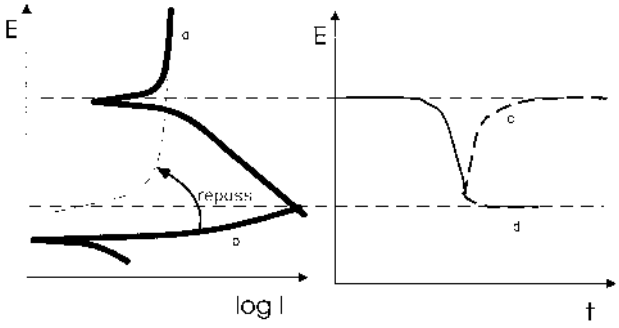

Figure 27 Schematic (a) Evans diagram and (b) corrosion potential vs. time behavior for localized corrosion stabilization. Line a on the Evans diagram represents the electrochemical behavior of the material before localized corrosion initiates, while line b represents the electrochemical behavior of the material in the localized corrosion site. Due to the low Tafel slope of the active site, the corrosion potential of the passive surface/localized corrosion site falls. If repassivation occurs, the anodic behavior reverts back to line a, and the corrosion potential increases again (line c). If repassivation does not occur, the corrosion potential will remain low (line d).

IV. TEST TECHNIQUES

The ultimate goal of any corrosion test technique is the ability to quantitatively predict rate of corrosion attack, whether it be uniform dissolution, pitting, intergranular corrosion, or stress-corrosion cracking. This objective has been achieved for uniform corrosion in most instances as discussed in Chapters 1 and 2. However, the complexity of localized corrosion has prevented the achievement of this goal. Instead, the test techniques generally are used as a means of ranking the resistance of alloys to a particular type of attack. A second goal of many test programs is the study of the effects of changes in environmental variables due, for example, to intentional changes in chemical process conditions or transients.

Often, the tests are conducted in specified environments. Extrapolation of the results obtained under those conditions to others is fraught with uncertainty. Electrochemical testing can usually be performed in the solution of interest, making the results more applicable. Nevertheless, a common theme throughout this book is the need for the user of electrochemical tests to ensure that both the environment and the material surface are relevant to the corrosion problem of interest.

This section will focus on explaining the electrochemical bases for two generic types of testing: accelerated coupon testing and electrochemical testing.

Several accelerated coupon tests described in ASTM standards will serve as examples of the use of chemical potentiostats as accelerating agents. The bulk of the section will focus on electrochemical testing. Some of the problems involved in sample preparation for electrochemical testing for localized corrosion will be discussed first. Electrochemical potentiokinetic reactivation (EPR) testing for the quantitative analysis of susceptibility of stainless steels to intergranular attack will be reviewed and compared to ASTM accelerated coupon tests. The issues surrounding the use of cyclic polarization for determining resistance to pitting will be discussed. Several applications of potentiostatic testing to localized corrosion studies will be presented, along with two examples of the use of galvanostatic testing. Finally, a review of the present understanding of the basis and utility of electrochemical noise measurements for localized corrosion will be presented.

A. Accelerated Coupon Testing

The use of highly aggressive environments and elevated temperatures for the accelerated testing of materials has a long and successful history in the ranking of the relative resistance of materials to localized corrosion. Numerous ASTM standards have been developed that fall within this classification. This section will review four tests that are representative of this type: the ferric chloride test for pitting and crevice corrosion in stainless steels, the Huey and Streicher tests for the susceptibility to intergranular corrosion in stainless steels, and the NAMLT test for intergranular corrosion in aluminum alloys.

1. Chemical Potentiostats

All four of these accelerated tests rely on the introduction of a redox couple into the solution that serves to poise the potential of the specimen surface in a region where localized attack will commence if and only if the material is susceptible. This redox couple is termed a chemical potentiostat. Figure 28 shows an Evans diagram for a generic chemical potentiostat that would test if a material is susceptible to pitting in that solution. In the absence of the redox couple O/R, the open circuit potential of the material would be E_{corr} (1), and the material would not undergo localized attack. Upon introduction of O/R, the corrosion potential for a material that is resistant to localized attack would rise to E_{corr} (2), since the kinetics of both the oxidation and the reduction reaction of O/R are faster than the other reactions present. Thus the kinetics of O/R would dominate the criterion for establishing the corrosion potential. A resistant material would remain passive under these conditions as its pitting potential is much higher. The open circuit potential of a less resistant material, whose pitting potential is at or below the reversible potential for O/R, would rise up towards the E_r (O/R) until it exceeded

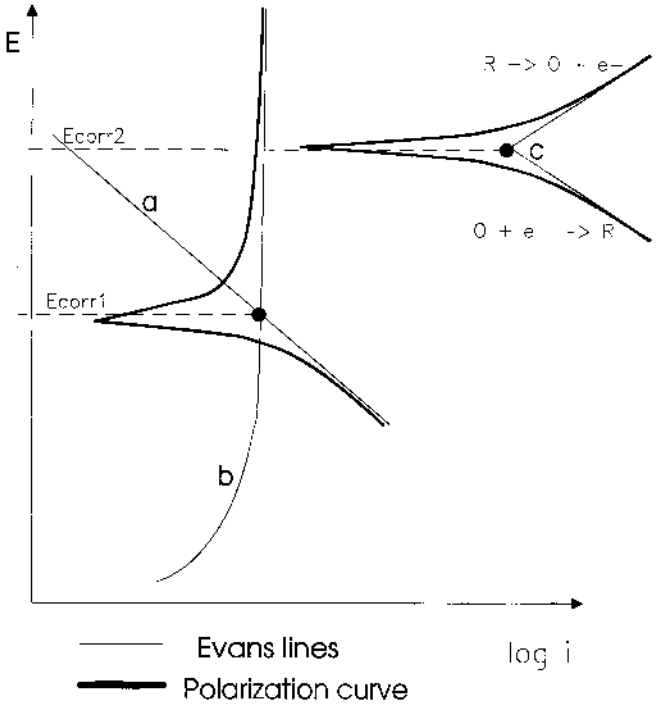

Figure 28 Schematic Evans diagrams and polarization curves for a material in a solution containing a redox couple that acts as a chemical potentiostat. The i_o used in the Evans diagram for the O/R redox couple is that relevant to the material of interest. In the absence of the redox couple, the material obtains E_{corr1}. In the presence of the redox couple, the material obtains E_{corr2}. If E_{corr2} is above the pitting potential, the material will be rapidly attacked.

the material pitting potential. At that point, pitting would commence, and the potential would fall, as was discussed above for Fig. 27. The presence of the O/R redox couple would accelerate the attack by providing a fast cathodic reaction on the passive surface.

The choice of the redox couple for an accelerated test will depend on factors such as its thermodynamics and kinetics, its compatibility with other accelerating factors (e.g., temperature, aggressive anion concentration), and its ease of use. Rarely is the relevance of the redox couple to the service environment of interest considered.

2. Ferric Chloride Test

Described in ASTM G 48 (25), this type of test for stainless steels (including Ni-base alloys containing a large amount of Cr) involves exposure of the material to a highly oxidizing, highly acidic, concentrated metal chloride solution. Briefly, a material is exposed to a 10 wt% $FeCl_3 \cdot 6H_2O$ solution for a relatively short time (24 to 72 hours) at either ambient or elevated (usually 50°C) temperature. At the end of the test, the sample is examined for weight loss and localized attack. If pitting and crevice corrosion are of concern, artificial crevices can be applied by the use of Teflon blocks held tightly to the sample surface by rubber bands, though a superior method for forming a crevice is discussed below.

The chemical potentiostat in this test is the ferric salt that forms a Fe^{3+}/Fe^{2+} redox couple with a potential of approximately +0.45 V(SCE). The high concentration of ferric ion (0.4 M) allows the couple to provide a large current without an appreciable change in potential (approaching an ideally nonpolarizable electrode). The cathodic reaction (reduction of ferric to ferrous ion) occurs on the boldly exposed passive surface. The high potential in turn increases the probability of exceeding the pitting potential on a given material, especially in such a concentrated Cl^- solution (and even more so if the test temperature is raised to 50°C). Other accelerating factors include the high chloride concentration (1.2 M) and the low pH of the solution (typically about 1.3), which inhibits repassivation and lowers the stability of the passive film. Thus the ferric chloride test is a test of the resistance of an alloy to propagation of localized corrosion for most alloys, since their pitting potentials are well below +0.45 V(SCE) in this solution. However, more highly alloyed materials can resist initiation in this solution, and thus the time of the test is often extended to a period of many days.

This very popular test does have a number of drawbacks. Very few industries operate in 10 wt% $FeCl_3$ (thankfully). Thus the relation of the results of this test to performance in real service environments that are profoundly different is questionable, and in fact, a number of cases where reversals in alloy ranking has occurred have been documented. Part of the problem lies in the use of Fe^{3+} to act as the chemical potentiostat. Inside pits in stainless steels, it is well established that anaerobic conditions exist, and thus the concentration of ferric ion is small, though the concentration of ferrous (Fe^{2+}) can be very high. For Ni-base materials, the use of an iron-base solution is also of questionable value. In addition, the effects of other alloying elements in determining the chemistry of the localized corrosion site are not addressed with this type of test. The fact that crevice corrosion can occur in such an aggressive solution indicates that the accumulation of other types of compounds at the localized corrosion site is of importance. Despite these limitations, the $FeCl_3$ test will continue to be an important tool in alloy development and screening for historical, if for no other, reasons.

A variety of modifications can be made to the ferric chloride test and still

fall within the spirit of the method. The exposure time and temperature can be altered, as can the surface finish. Since surface finish can have important impact on the localized corrosion behavior by providing occluded sites and, in some cases, surface area for cathodic reactions, it is important that this be chosen with care.

Since crevice corrosion can occur under more mild conditions than pitting, it often limits the operating envelope for highly alloyed materials. Thus a variety of exposure tests for crevice corrosion resistance have been developed. The most important part of a testing program for crevice corrosion is the ability to inflict a tight, reproducible crevice. Many designs have been tried, but the multiple crevice assembly, shown in Fig. 29 and discussed in detail by Kearns (26), has emerged as the crevice former of choice. This nonmetallic (usually Teflon™ or Delrin™) segmented washer addresses a number of issues in crevice corrosion testing. Since each washer contains 20 individual crevice formers, a large number of potential crevice sites can be tested simultaneously, allowing a statistically significant number of sites to be evaluated on a small number of specimens. For example, triplicate specimens would provide three specimens $\times$ 20 sites per washer $\times$ 2 washers per specimen = 120 sites. The wealth of information that can result from such a test, in terms of initiation probability and depth of attack, allows a great deal to be learned about the service limitations of a material. In addition, the use of torque wrenches allows a reproducible force to be applied and thus reproducible crevice dimensions to be realized. Finally, the low cost and ease of application makes this arrangement amenable to large scale testing.

Other designs do exist, and may be more applicable in certain situations. For example, O-rings or Tygon™ tubes may provide a more realistic crevice arrangement for material in pipe form. Dissimilar metal–metal crevices may be more appropriate in some circumstances (24,27), and such arrangements can be easily fabricated as well. One of the major advantages of crevice corrosion testing using crevice formers is that acceleration of the process can often be accomplished by applying a tighter crevice than would be expected to exist in service (this is another advantage of nonmetallic deformable crevice formers). The tighter the crevice gap, the more severe the problem. Solution ingress will always occur at practical gaps by capillary action. To accelerate the process further, daily increases in temperature of 5°C, with periodic inspection for initiation, can result in the determination of the critical crevice temperature.

3. Intergranular Corrosion Tests

Intergranular attack occurs due to a difference in the metallurgical condition of the material at (or near) the grain boundaries. Exposure solutions that magnify the differences in corrosion resistance between the grain boundary areas and the

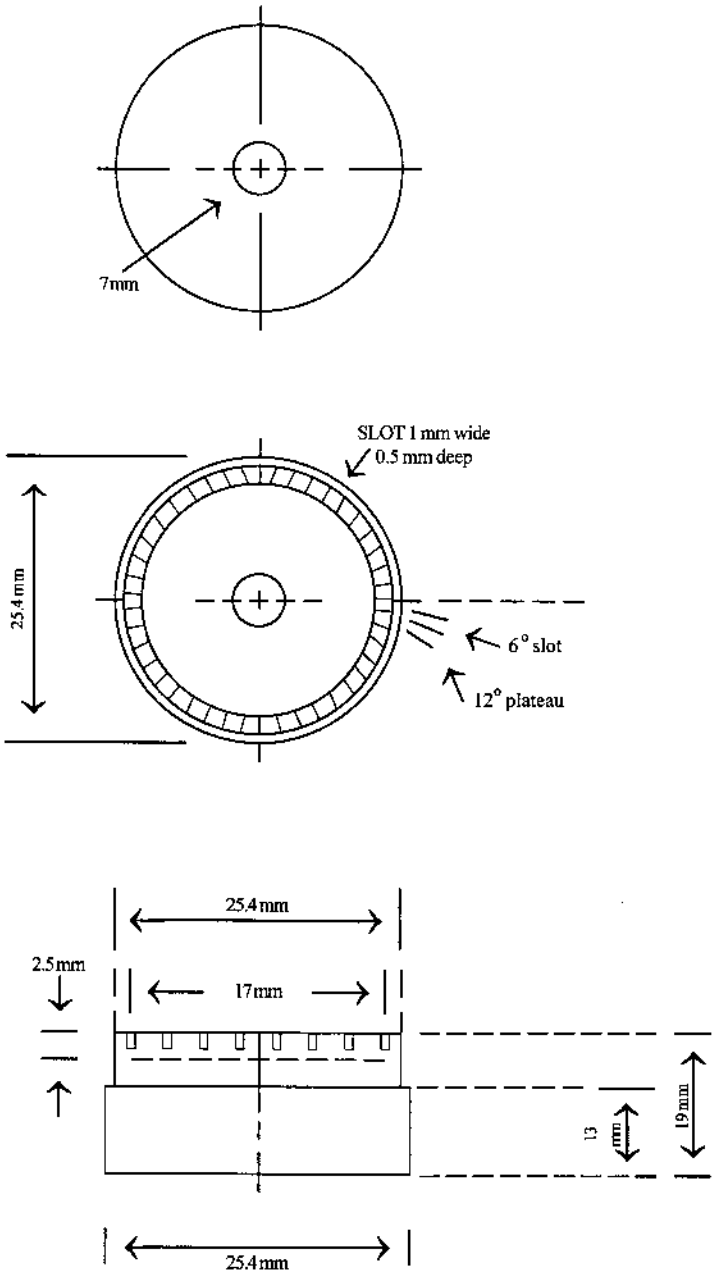

Figure 29 Details of multiple crevice washer (not to scale).

bulk grain are therefore useful in evaluating the extent to which sensitization has occurred. The more that is known about the metallurgy behind the sensitization, the more efficient can be the test designed. Due to differences in the metallurgy and the effects of hot and cold work on the distribution of the precipitates at the grain boundaries, separate tests must be developed for different alloys and even for cast and wrought materials of the same composition.

Over the years, a number of standard practices have developed to evaluate the susceptibility of austenitic stainless steels to intergranular attack, especially as the result of heat treatment and welding. The most popular have been compiled into ASTM standard A262. The oxalic acid test (Practice A) is an excellent screening test and is discussed below under galvanostatic testing. The accelerated coupon tests (Practices B through E) are aimed at evaluating the degree of sensitization in more detail with a more severe test. They vary in the details of their solution composition, test temperature, and length. These tests include the Streicher test (ferric sulfate–sulfuric acid) and the Huey test (boiling nitric acid). Each has applicability to the detection of susceptibility among certain classes of alloys, since each attacks different types of precipitates (or the depleted areas adjacent to the precipitates).

The Huey and Streicher tests rely on the effect of a material's Cr content on its electrochemical behavior in acid. Figure 30 shows polarization curves for two materials in acid, one representing the unsensitized grain interiors containing 18% Cr and the other representing the sensitized grain boundary material containing 10% (less than the 13% required for "stainless" behavior). Both tests rely on the differences between the passive behavior of sensitized and unsensitized material, the main electrochemical difference being the potentials to which the materials are driven by the respective chemical potentiostats (Fe^{3+}/Fe^{2+} for the Streicher, NO_3^-/NO for the Huey). The corrosion potentials in the Streicher test reach approximately +0.6 V(SCE), while those in the Huey test reach +0.75 to +1.0 V(SCE). The sensitized material has dissolution rates two orders of magnitude higher than the unsensitized material. Since this attack is focused at the grain boundaries, the grains eventually fall out, and substantial weight losses can be observed for sensitized products. The advantages and disadvantages of the different sensitization tests are reviewed by Streicher (28).

Another good example of the importance of understanding the metallurgy involved is the use of ASTM G-67 for IGA resistance of the 5XXX series alloys (Al–Mg and Al–Mg–Mn) known as the NAMLT test. It is known that the precipitation of AlMg, an intermetallic compound, leads to the susceptibility of these alloys. The AlMg precipitate is anodic to the base material and is thus susceptible to removal. By exposing the alloy to nitric acid (which acts as the chemical potentiostat), the AlMg is quickly removed while the base metal remains passive. The more precipitates present, the higher the weight loss in the 24 hour exposure to concentrated (70%) nitric acid, with losses on the order of 50 mg/cm^2 possible

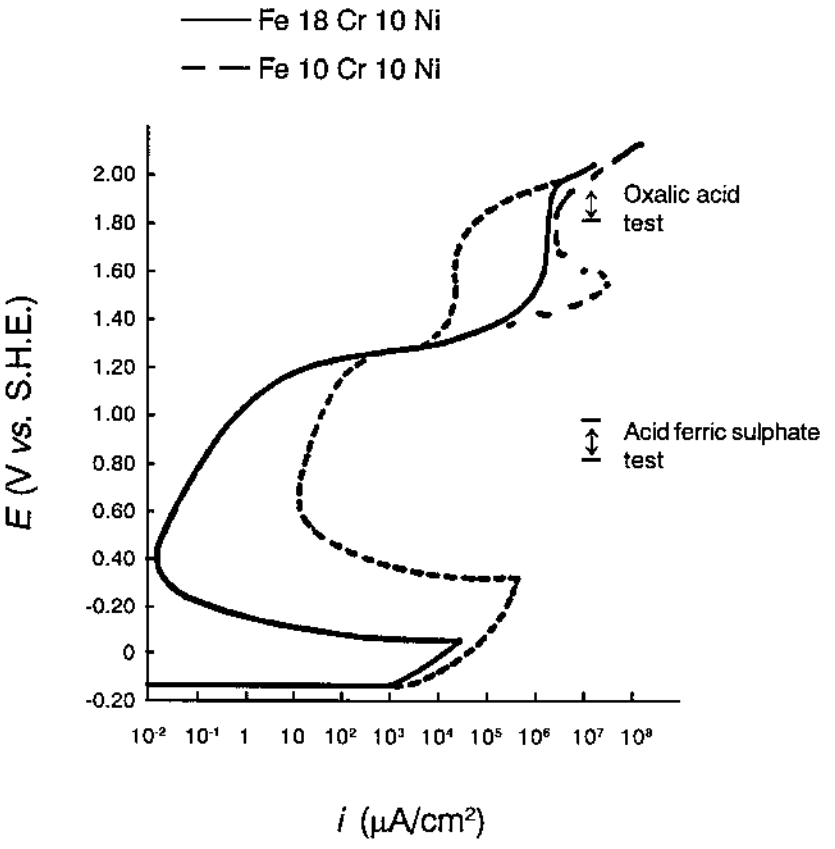

Figure 30 Schematic polarization curves illustrating the origins of the ability of the oxalic etch test and acid ferric sulfate test to differentiate sensitized (represented by the Fe-10Cr-10Ni) from unsensitized (represented by the Fe-18Cr-10Ni) material.

resulting from grain fallout. This high mass loss occurs when the precipitates form a continuous path around the grains. It should be noted that electrochemical measurements of grain fallout are impossible, since no charge is passed that accounts for the material lost.

Each practice indicates its limitations, and these are important to keep in mind. As with all accelerated tests, what is actually tested is the resistance of these alloys to IGA in the specific test environment. One must be very careful to be sure that these results correlate with longer term exposures to the field environment of interest. In addition, these tests are only useful for evaluating the susceptibility of these alloys to IGA, not to pitting or general corrosion or SCC.

Finally, it is difficult to quantify many of these tests to compare alloys whose resistance is intermediate. That is, these tests are excellent at weeding out very good material from very bad material, but provide no means by which the infinite shades of grey can be fairly ranked. Electrochemical tests such as the EPR test described below fill such a need.

B. Electrochemical Testing

The main advantage of electrochemical testing is the opportunity to investigate corrosion phenomena in the solution of interest rather than in a more aggressive and probably less relevant environment. In addition, a great deal of information can be gained about the dependence of the phenomena on external variables in a short time. Finally, the determination of critical potentials for initiation and propagation of localized corrosion can be useful in design decisions. For example, the use of mixed potential theory can allow the prediction of the protection (either anodic or cathodic) criteria, as well as galvanic couples to avoid. However, misinterpretation of electrochemical test results occurs regularly; this section has been designed to explain the commonly used tests and possible interpretation pitfalls.

1. Specimen Mounting

Probably the main problem with electrochemical testing for localized corrosion resistance is sample mounting. It can be extremely difficult to mount a sample with an insulated electrical contact and a controlled surface area without introducing a crevice at the sample–mount interface as shown in Fig. 31. Since crevice corrosion will occur at lower potentials than pitting, the sample invariably begins to be attacked at the crevice, leading to an underestimation of the resistance of the sample to pitting. Some may argue that for the same reason, this type of testing is not overly conservative, as in service, one wants to know the potential at which any localized corrosion can occur, not just pitting. The drawback is that most crevices formed during sample preparation are not reproducible either in position or geometry, making comparisons extremely difficult. In addition, there may be applications where crevice corrosion is not the limiting performance factor, but pitting is. Such testing would lead one to choose a more resistant (and therefore expensive) alloy than one would actually need.

A number of solutions have been suggested for sample mounting, including the use of "knife-edge" PTFE washers, other mounting compounds and procedures, the use of wire loops, and flag geometries. All of these have their limitations, and one must choose the most appropriate for the particular alloy–environment combination. The knife-edge PTFE washer (as shown in Fig. 32) has been used successfully in a number of applications in which a tight seal can be formed that prevents ingress of any electrolyte. The success of this approach is closely

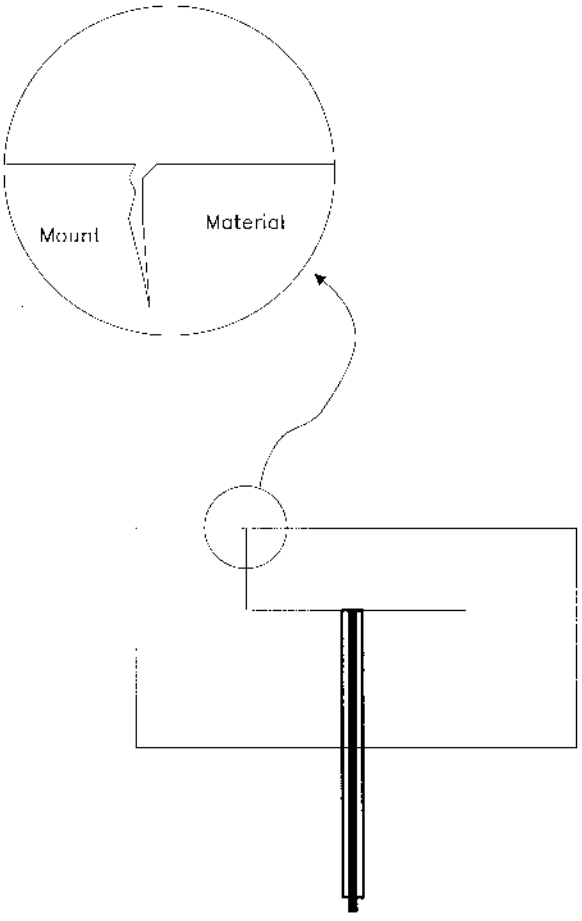

Figure 31 Schematic of crevice formed at mount–sample interface. Mounting material is used to insulate the electrical contact to the sample.

related to the quality of the surface finish both in terms of its fineness (i.e., final polishing step particle size) and its uniformity. One large scratch can allow capillary action to draw electrolyte into an otherwise impervious crevice and start the sample down the slippery slope to crevice corrosion. This intolerance of polishing faults is the prime reason for the failings of this type of approach. In addition, due to the cost of the PTFE washers, many experimenters tend to try to reuse them. This recycling works occasionally, though unpredictably. The knife-edge PTFE washer is actually a second generation of the Stern–Makrides approach

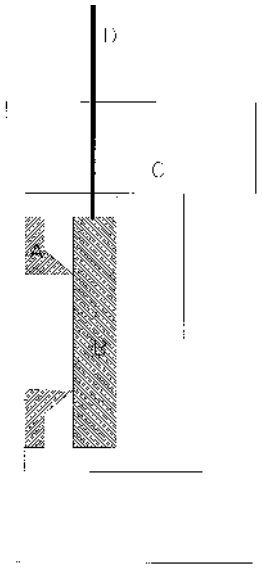

Figure 32 Schematic of cross section of arrangement used with knife-edge PTFE washer for definition of sample area. A represents the PTFE washer, B represents the sample, C represents the assembly, including the backing plate that generally is screwed against the sample to press it against the PTFE washer, and D represents the insulated electrical contact.

(Fig. 33) in which a cylinder of PTFE is forced onto the top of a generally cylindrical sample. The Stern-Makrides washer suffers from same problems as does the knife-edge, but to a greater degree due to the larger surface area involved.

One example of the effect of crevices is shown in Fig. 34 for a solution in which propagating crevice corrosion will not occur. In this case, the higher passive current densities are observed for the insulating materials that perform poorly. In a Cl^--containing solution, this would translate into a lower E_{bd}. As can be seen from Fig. 34, some mounting materials perform well in this solution, though it should be pointed out that this is not so for other solutions. For example, the alkyd varnish is used in electroplating to mask off areas. While it works well in acid solutions, it performs very poorly in neutral or basic solutions, especially on materials with passive films such as stainless steel. One mounting compound that has been found to work well is a mixture of five parts of Armstrong A-12 adhesive to 1 part of T-146 hardener by weight.[1] After mixing well, the epoxy

[1] Armstrong Products Co., Argonne Road, Warsaw, IA.

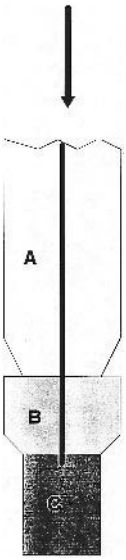

Figure 33 Schematic of cross section of Stern–Makrides arrangement. A represents the glass tube which protects the threaded rod, which acts as an electrical contact. A is pressed onto B, a machined PTFE cylinder that seals against the sample C.

can be poured over the previously well-cleaned sample. After setting overnight, the sample can be polished and used in electrochemical studies. It has been used successfully for stainless steel, Ni-base alloys, magnesium, aluminum, and steel at room temperature. It has been found to degrade in propylene carbonate–water mixtures. Other mounting compounds have also been found to form very good seals, such as the Interlux 404 base/414 Reactor combination.[2]

Qvarfort (29) developed a cell in which the creviced area of the sample is continuously washed with deionized water in order to prevent the development of the critical crevice solution. As shown schematically in Fig. 35, the purified water enters the creviced area via a groove machined in the cell base. In order to disperse the flow throughout the occluded region, a fine porosity filter paper ring is placed between the groove and the specimen. The water flow rate is typically 4 to 5 mL/h. Thus dilution of the solution inside the cell should not be an issue in most electrochemical testing (e.g., after 4 h, a 1 M NaCl solution will become a 0.98 M solution). Named the Avesta cell for Qvarfort's employer, this approach has been used to study pitting and intergranular corrosion at tempera-

[2] Courtlauds Coatings, Inc., Morris Avenue, Union, NJ.

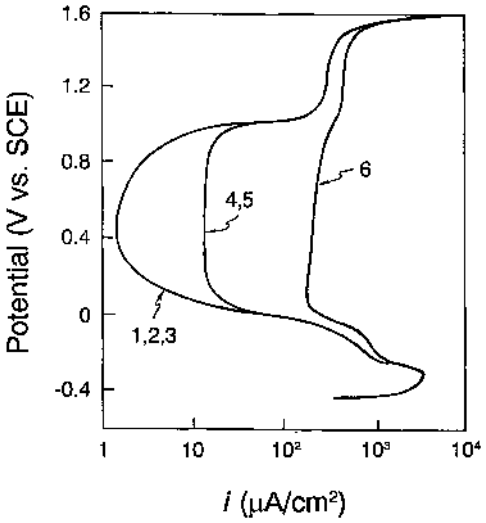

Figure 34 Potentiostatic anodic polarization curves of a Fe 10% Cr 10% Ni alloy in a 1 N H_2SO_4 solution at 25°C as a function of electrode mounting technique. (From Greene et al., France, and Wilde.)

tures up to 100°C (29,30). Avesta has not copyrighted the design and has made it generally available to the corrosion community.

If mounting cannot be accomplished, two other approaches can be used. The first is the use of a wire loop electrode, as shown in Fig. 36. Böehni (31) has used this approach to study pitting without the complications of crevice corrosion. This approach works extremely well if one can obtain the material in wire form, though there is always the concern of metallurgical differences between material in wire form and that in plate or tube form, which is more likely to be used in actual applications. A related approach is the use of a flag electrode configuration, as shown in Fig. 36b. This design works well with plate material by minimizing the shaft size and thereby minimizing any effects of the waterline. If localized corrosion at the waterline continues to be a problem, deaeration of the air space above the solution can be of help as well. However, edge attack can be an issue, particularly in wrought products.

2. EPR Testing

Sensitization of stainless steel can occur owing to improper heat treatment, welding, or long-term exposure in service to elevated temperatures (28). While there

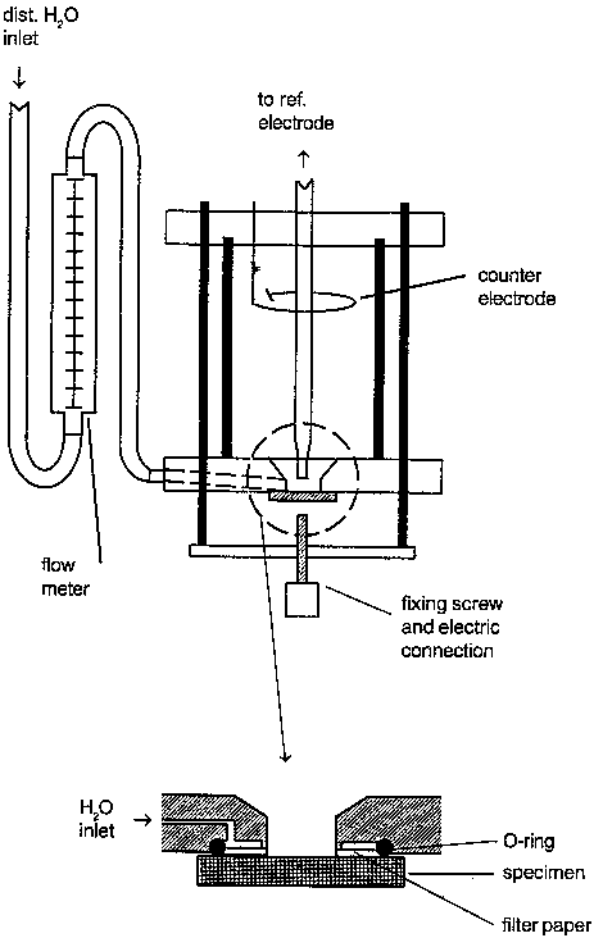

Figure 35 Schematic diagram of the Avesta cell. Note that some details such as the thermometer have been omitted. (From Ref. 29.)

are a number of exposure tests to evaluate sensitization, as discussed above, none of these allows a quantitative comparison of the degree of sensitization (DOS), especially for lightly sensitized materials. Electrochemical potentiokinetic reactivation (EPR) tests have been developed as rapid nondestructive tools for assessing the DOS of stainless steels. All types of EPR testing involve polarization of a sample (which could be, for example, the wall of a pipe in a chemical plant) in a solution of deaerated sulfuric acid containing a depassivator (KSCN). Sensi-

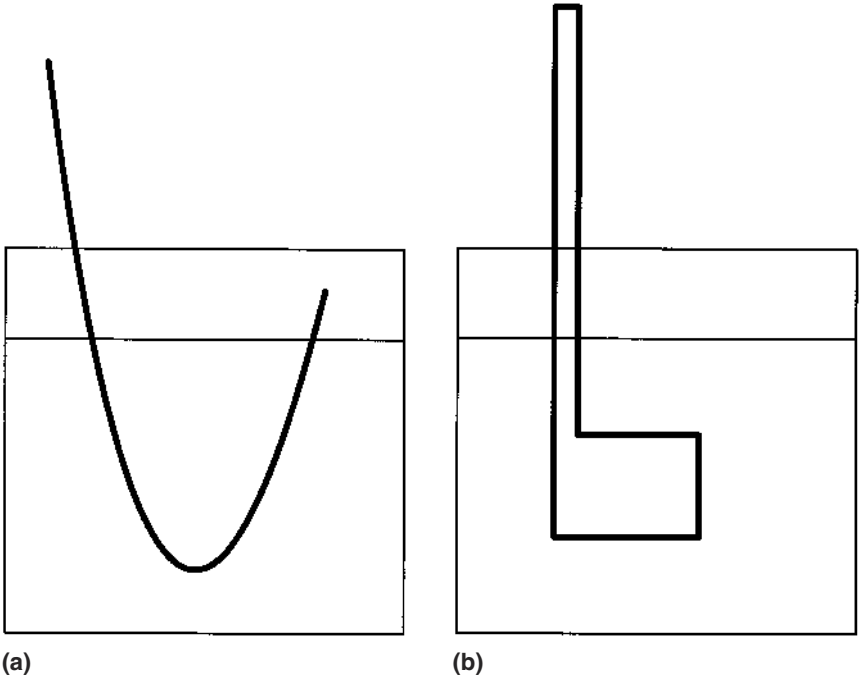

Figure 36 (a) Wire loop and (b) flag sample configurations used to prevent crevice corrosion during electrochemical testing.

tized grain boundaries will activate to a stronger degree than unsensitized boundaries, and therefore a greater current will be measured. The magnitude of the current is a quantitative measure of the DOS. The single loop (SL-EPR) test (32) is shown schematically in Fig. 37. After allowing the sample (previously polished to a 1 μm finish) to establish a steady-state E_{corr}, the potential is stepped into the passive region and then scanned in the cathodic direction. The passive–active transition involves the passage of a certain amount of charge. This charge is then normalized to the grain boundary area to establish a P_a value (a measure of DOS):

$$P_a = \frac{Q}{\text{GBA}}$$

where:

P_a = degree of sensitization
Q = charge passed during test
GBA = grain boundary area = $A_s[5.09544 \times 10^{-3}\exp(0.34696X)$

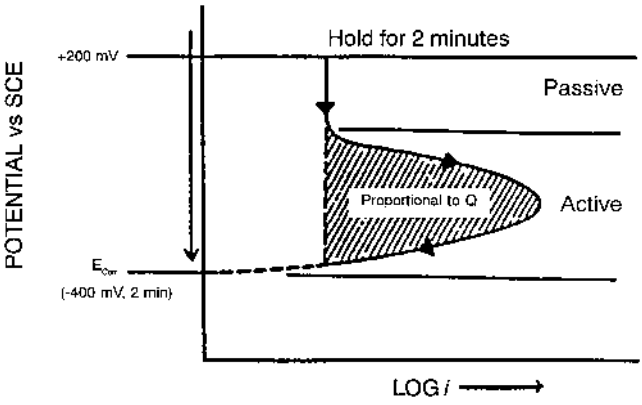

Figure 37 Schematic SL-EPR polarization curve. (From Ref. 32.)

A_s = specimen surface area
X = ASTM micrograin size number [per ASTM Practice E 112 (33)].

The grain interiors will have a characteristic charge density associated with their passive–active transition. Unsensitized material will exhibit this low value of P_a. Sensitized grain boundaries will activate more vigorously, resulting in higher currents and therefore larger amounts of charge passed. However, since the amount of grain boundary area will have a direct influence on the amount of charge passed, it is important to take this into account when comparing materials that have been exposed to different heat treatments.

The SL-EPR test was pioneered by Clark (32). Figure 38 shows the results from an extensive study by Majidi and Streicher (32) that compared the results of SL-EPR testing to those from the ASTM ferric sulfate test. One can see that at low levels of sensitization, the SL-EPR test is much more discriminating, though for severely sensitized steel, the electrochemical test results saturate. Since it is usually more important to find low levels of sensitization, EPR tests are becoming increasingly popular.

An improvement on the SL-EPR test is the double loop, or DL-EPR, test, which is shown schematically in Fig. 39. In this test, the potential is first scanned in the anodic direction from E_{corr} to a point in the middle of the passive region before the scan is reversed. The ratio of the two peak current densities, L/I_a, is used as the degree of sensitization indicator. During the anodic sweep, the entire surface is active and contributes to the peak current. During the reactivation sweep, only the sensitized grain boundaries contribute to the passive–active transition. Thus in unsensitized specimens there is a small I_r, and therefore a small ratio, while in heavily sensitized specimens, I_r approaches I_a, as shown in

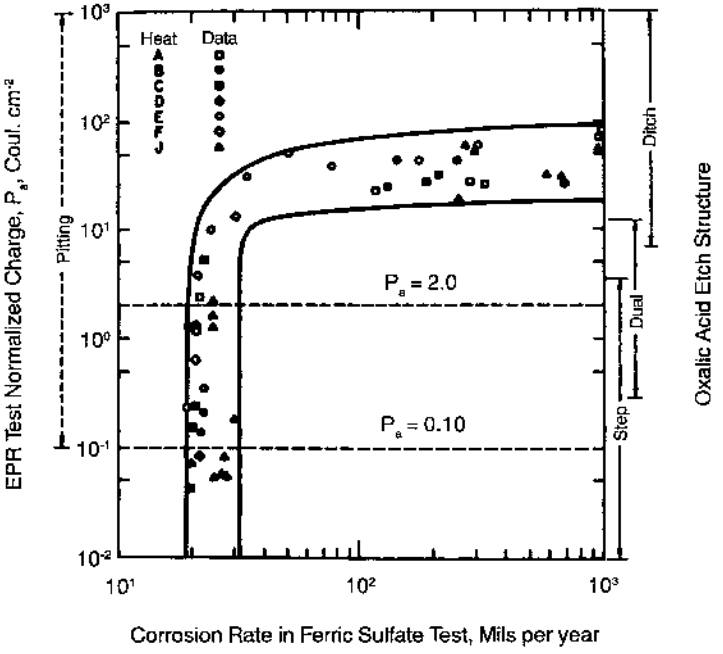

Figure 38 Comparison of data from SL-EPR, acid ferric sulfate, and oxalic acid etch test for seven separate heats of Type 304 and 304L stainless steel. Note that for low levels of sensitization, the SL-EPR can quantitatively distinguish among degrees of sensitization. At higher levels, the coupon exposure tests are more discriminating. (From Ref. 32.)

Fig. 40. The advantages of the DL-EPR are (**1**) only a 100 grit finish is necessary, as the anodic sweep "cleans" the surface, (**2**) intragrain pitting does not affect the ratio, and (**3**) no measurement of either surface area or grain size is necessary. The anodic sweep essentially gives an internal calibration for the method. Majidi and Streicher have shown excellent correlation between SL- and DL-EPR tests for Type 304 SS (32). DOS values measured by EPR have been included in models of intergranular SCC of sensitized stainless steel (34,35).

The EPR technique has been used for other alloys as well, including cast (36) and wrought (37,38) duplex stainless, as well as Ni-base alloys (39). Lee (38) used DL-EPR testing to determine the minimum amount of Ti and/or Nb required to render Type 430 SS immune from intergranular attack. In some cases, the details of the experimental method (i.e., solution temperature, KCNS and H_2SO_4 concentrations, scan range) must be modified to differentiate best the levels of sensitization of interest. For example, Scully and Kelly doubled the

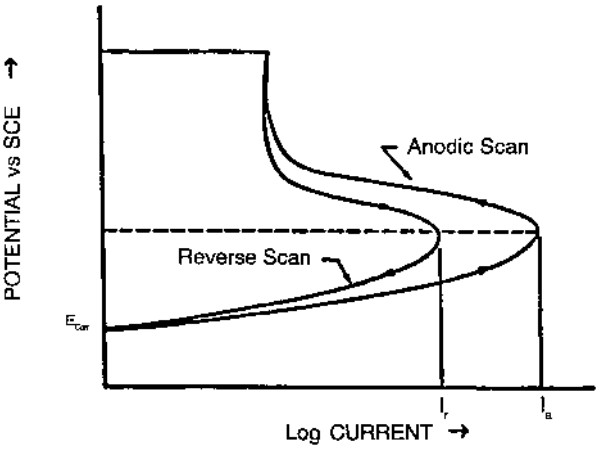

Figure 39 Schematic diagram of the double loop (DL) EPR test. Sensitization is evaluated from the current ratio, I_r/I_a.

KCNS concentration and increased the peak potential for their study of sensitization of duplex alloy 2205 (40).

Intergranular stress-corrosion cracking (IG-SCC) can occur in some sensitized materials when placed under tensile stress. Thus DL-EPR has been used to study the effects of aging time on the susceptibility of Alloy 600 to IGSCC, as shown in Fig. 41 (39). This work also shows the need to modify the experimental parameters of the test to achieve optimal correlation for alloys other than Type 304SS, in this case lowering the KCNS concentration and the temperature while raising the peak potential and the scan rate.

3. Cyclic Potentiodynamic Polarization

The most common electrochemical test for localized corrosion susceptibility is cyclic potentiodynamic polarization. As was discussed briefly in the section on the electrochemical phenomenology of localized corrosion, this test involves polarizing the material from its open circuit potential (or slightly below) anodically until a predetermined current density (known as the vertex current density) is achieved, at which point the potential is scanned back until the current reverses polarity, as shown in Fig. 42. The curve is generally analyzed in terms of the breakdown (E_{bd}) and repassivation potentials (E_{rp}). Very often, metastable pits are apparent by transient bursts of anodic current. The peaks in current shown in Fig. 42 for a potentiodynamic scan are due to the same processes as those shown in Fig. 25 for a potentiostatic hold.

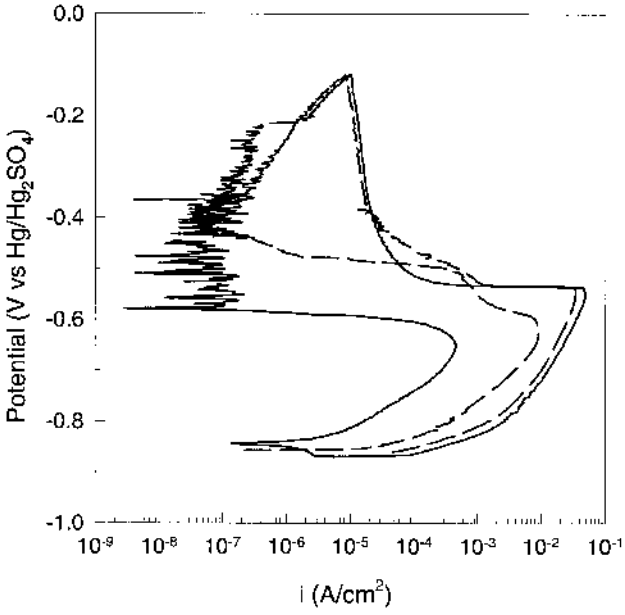

Figure 40 Double loop EPR data for Type 304 stainless steel heated at 600°C for 100 h (solid line) and 1 h (dotted line). The extremely sharp active–passive transition at −0.5 V(SCE) is due to ohmic drop effects. Note the much larger i_r for the sensitized (100 h) material. (Data courtesy of M. A. Gaudett, University of Virginia.)

Controversy concerning the interpretation of cyclic polarization curves has raged for many years. Of particular interest is which (if either) of the two potentials can be used for material selection and mitigation strategy decisions. The classic interpretation is that a material's potential must exceed E_{bd} in order to initiate pits, but if flaws were introduced into the surface in any way, they could propagate at all potentials above E_{rp}. Thus E_{rp} could be used in design as a protection potential.

There are those who feel that there are not two distinct potentials. These workers propose that, when measured correctly, E_{bd} and E_{rp} are one and the same. In standard testing, the nucleation of pits occurs at E_{rp}, but owing to the time necessary for pits to become established, the probability that pits will repassivate, and the finite potential scan rate used, pits do not cause a dramatic increase in the current until E_{bd}. This explanation would rationalize the often-observed effect that increasing the scan rate increases E_{bd} but not E_{rp}. If E_{rp} is properly measured, these workers feel that it can be used as a go–no go potential for applications, i.e., if the potential of the alloy is always below E_{rp}, then pitting cannot occur.

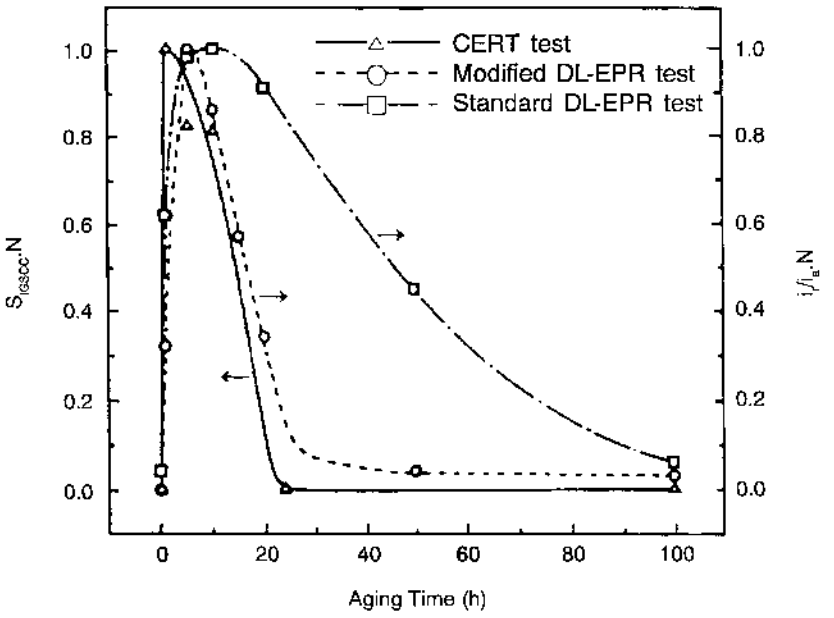

Figure 41 Comparison in normalized condition between the results of EPR tests and S_{IGSCC} of Alloy 600 aged at 700°C. (From Ref. 39.)

The E_{rp} could be an important design parameter for engineering structures if it can be shown to be a material property like yield strength, for example. If the E_{rp} were known accurately, preventing localized corrosion would be possible by maintaining the potential of the structure below that value, either by chemical treatments designed to lower the E_{corr} or via external polarization (cathodic protection). The difficulty has been in determining if a proper method exists for measuring E_{rp}. Since the early 1970s, there has been disagreement concerning the utility of E_{rp}, since it was shown to depend upon the maximum current density used in the forward scan, as shown in the result of Wilde in Fig. 43. However, a recent evaluation of both the literature and long-term experiments by Sridhar and Cragnolino (41) and Sridhar and Dunn (42) have clarified the situation somewhat.

Sridhar and Cragnolino (41) showed that the repassivation potential decreased with increasing pit depth for shallow pits but became independent of the degree of attack for deep pits, as shown in Fig. 44. Sridhar and Cragnolino (41) showed that for Alloy 825 and Type 316L SS, E_{rp} became independent of charge passed above 10 C/cm^2. This charge density corresponded to a maximum pit depth of about 100 μm (42). In Wilde's work (43), the charge density passed was less than 0.7 C/cm^2 in all cases studied. Such charge densities are typical

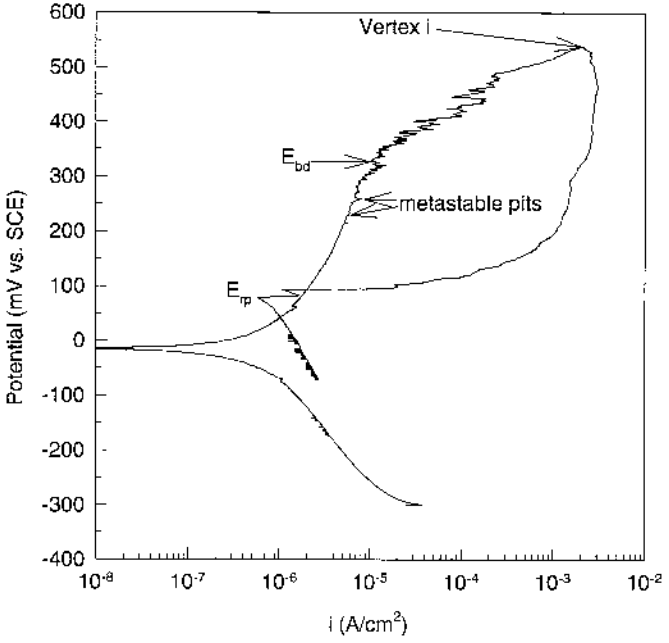

Figure 42 Cyclic polarization curve for Type 302 stainless steel in 1,000 ppm NaCl. Note the definition of the breakdown and repassivation potentials, the vertex current density, and the appearance of metastable pits.

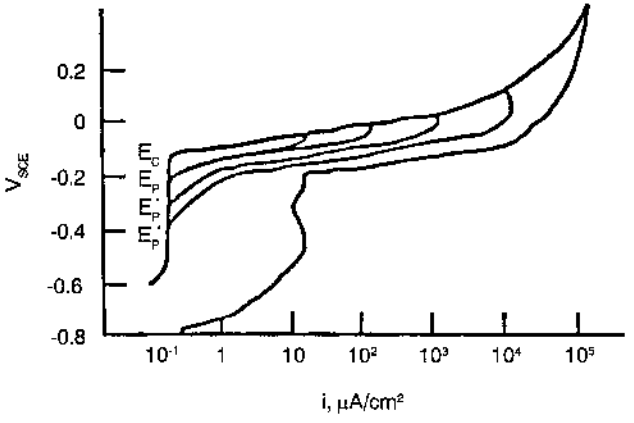

Figure 43 Cyclic polarization behavior of 430 stainless steel in 1 M NaCl, demonstrating the striking effect of pit propagation on E_{prot}. (From Ref. 43.)

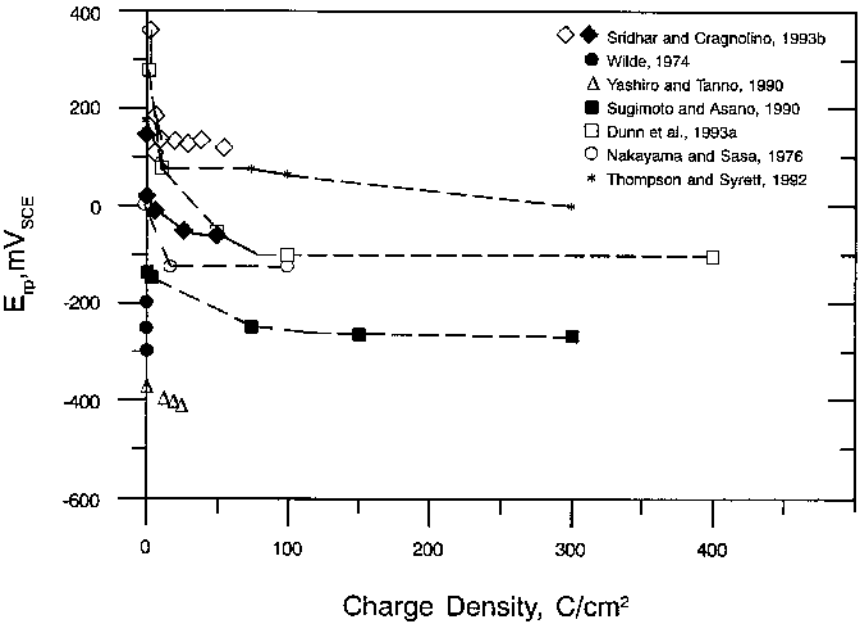

Figure 44a A compendium of repassivation potential versus charge density data from the literature for various Ni–Fe–Cr–Mo alloys in Cl^- solutions. Some of the charge densities were calculated from the data provided in the original references. (From Ref. 41.)

of results using the standard cyclic polarization method. Not surprisingly, a dependence of E_{rp} on vertex current density or pit depth has been observed by a number of workers (44–46) using low charge densities, as would be expected from Fig. 44. Those workers who have used larger localized corrosion charge densities to determine E_{rp} have observed its independence of charge passed.

Important evidence supporting the application of E_{rp} is the long-term potentiostatic data of Dunn and Sridhar (47), in which potentiostatic holds of alloy 825 in 1000 ppm Cl^- at 95°C have been performed for up to 18 months. They found that the repassivation potential determined for deep pits at short times corresponded well to the potential below which localized attack did not occur over long times. Localized attack did occur only 10 mV above the highest observed repassivation potential.

A third approach to critical localized corrosion potentials is emerging in which no single critical potential is accepted as a material property. In this school of thought, E_{rp} is the potential at which pits will most probably (in a statistical sense) repassivate. However, pit initiation and propagation can occur below this

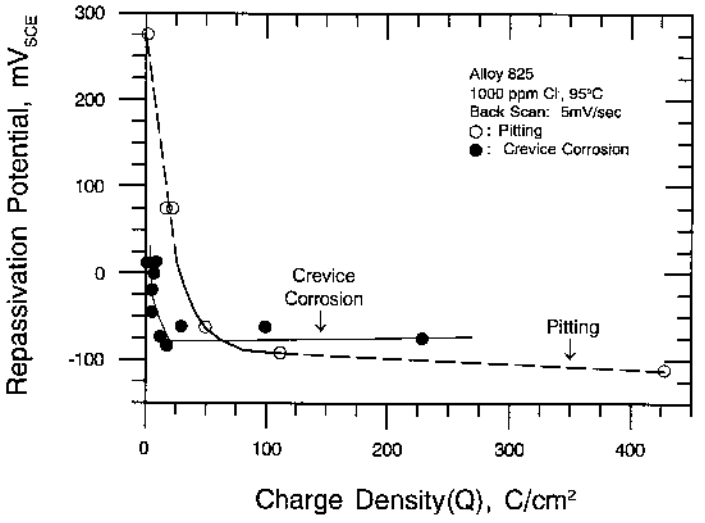

Figure 44b Effect of charge density on the repassivation potential for pitting and crevice corrosion.

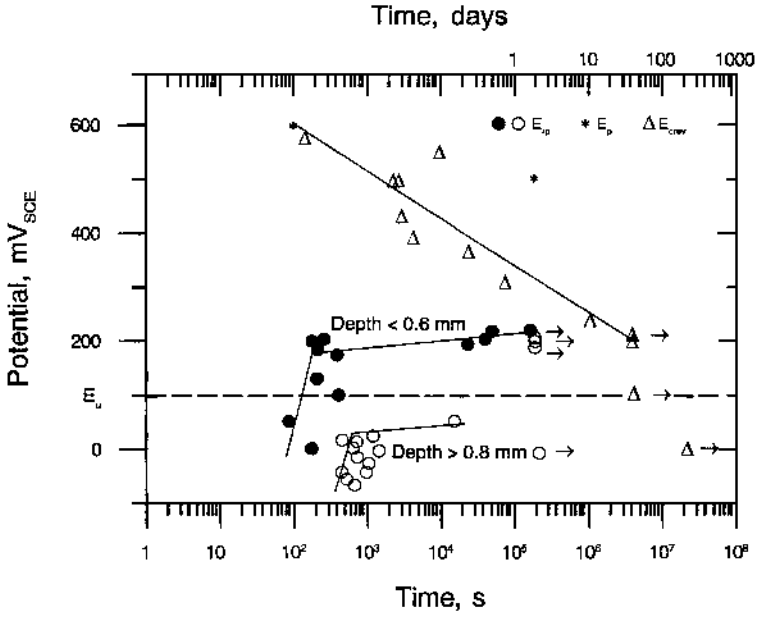

Figure 44c Effect of applied potential on the initiation and repassivation of localized corrosion in Alloy 825 in 1,000 ppm Cl^- at 95°C.

potential. The probabilities that a pit will initiate or propagate decrease as the potential of the surface decreases below E_{rp}. In most applications, the most probable E_{rp} is usable as a guide for material selection or process alteration. However, in critical applications, a more statistical approach is needed. For example, even a 1 μm pit will cause a failure of a connection on an integrated circuit, and thus pits that form at this size are considered failures. Such pits can occur at potentials below E_{rp}.

Shibata and Takeyama (48) and Williams et al. (49) have applied such statistical arguments to pitting of stainless steel. In order to develop these models, a large amount of data that can be treated as an ensemble must be gathered. In other words, variations in results from test to test are expected, even for nominally identical tests. This variation is used to develop the cumulative probability curve for pitting under a certain set of conditions. Both groups used multiple specimen testing apparatus to gather up to 12 data points for critical potentials and metastable pit nucleation rates simultaneously. The results for one set of 30 tests is shown in Fig. 45. This shows that the breakdown potential, E_{bd}, follows a distribution. Thus, for this alloy–environment combination, there is a 20% chance that the breakdown potential of commercial 304 SS will be below +160 mV(SCE) in 1000 ppm NaCl. The argument is that there was nothing wrong with those tests

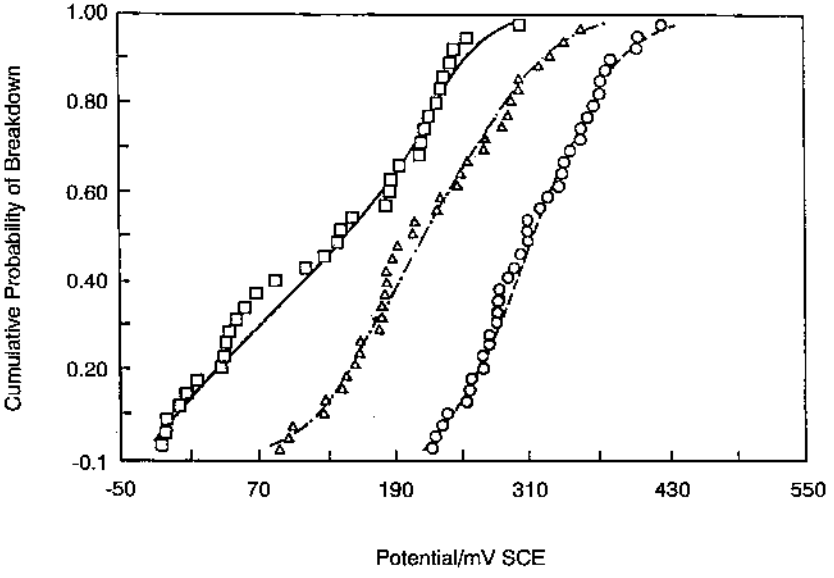

Figure 45 Cumulative distributions of pitting breakdown potentials for the commercial purity (CP), high sulphur (HiS), and high purity (HiP) 304L steels. (From Ref. 50.)

whose E_{bd} was less than + 160 mV(SCE), but that the variation reflects the stochastic nature of the pitting process. Such information could then be used to estimate component lifetimes, which could then be used to make design decisions based upon the consequences of a failure. For example, a 30% chance of perforation may be acceptable for an easily shut down and repaired vessel if it allows a cheaper alloy to be used, but such a probability would not be acceptable for a critical component in an inaccessible submersible. Fujimoto et al. (51) have also recently applied this type of approach to the initiation of crevice corrosion.

4. Potentiostatic Testing

While long-term potentiostatic tests can be useful, they are extremely time-consuming and expensive. Potentiostaircase tests can be performed in lieu of potentiodynamic tests, though at equivalent potential scan rates, the results should be identical. In addition, the time frames involved are usually still very short compared to the projected life. Thus a number of approaches have been developed for accelerating the process of initiation in order to determine the potential below which initiated sites will repassivate (i.e., E_{rp}).

Mechanical scratching is favored by some as a means by which a bare surface can be created. In this technique, one is ascribing no importance to (or taking any engineering credit for) initiation time. The surface is held at a constant potential and then a portion of it is scratched, usually with a diamond-tipped point. The current is monitored with time. For potentials below E_{rp}, the surface will repassivate rather rapidly, as shown in Fig. 46. Just above E_{rp}, the surface

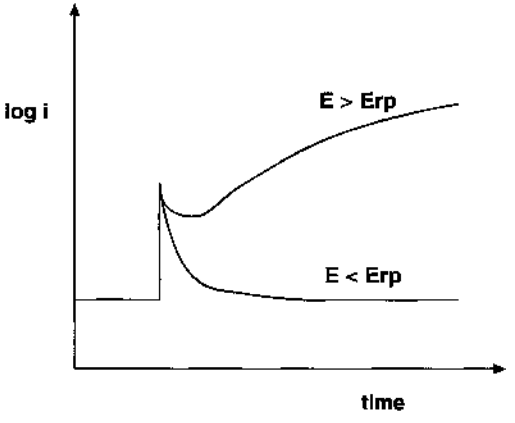

Figure 46 Schematic of applied current density vs. time observed for mechanical scratching of a surface exposed to a solution above and below its repassivation potential.

will try to repassivate, but it will fail, and the current will eventually increase. The closer the potential to E_{rp}, the longer is the time before the current increases. Thus, in most cases, the E_{rp} measured by this method is not conservative, as usually no more than 10 minutes is spent at any one potential. If one had waited long enough at the potential used just before the measured E_{rp}, localized corrosion might have occurred. However, this does not denigrate its utility as a screening test. One problem with scratching tests of this type is the dependence on the weight of the scratch. For hand scratching, the E_{rp} decreases with increasing damage. A mechanical system improves the reproducibility. A more damning problem concerns the site of pitting. In many (if not most) cases, pitting occurs in practice at inclusions or second phase particles of one type or another. Such inclusions are usually present at small volume fractions, so the probability of hitting one (or more) with a fine diamond tip is extremely small. Thus this approach can lead to erroneously high values of E_{rp} that reflect the pitting susceptibility of the matrix material but ignore the susceptibility of the weakest link, the inclusions.

A second method of producing a bare surface is what has become known as the electrochemical scratch. In this technique, the entire exposed surface is activated by a large positive voltage excursion that is followed by a voltage step back to (or towards) E_{corr}. In this way, any likely pitting sites are initiated, and the test measures the ability of the material to resist propagation and to repassivate. One version of the test (see Fig. 47) involves a step to +2 V for 3 s followed by a step back to E_{corr}, during which time the current is monitored. The potential is held there for 5 minutes before it is again stepped to +2 V for 3 s to reinitiate localized corrosion. At this point, the potential is stepped back to a potential 50 mV above E_{corr} and the current is monitored for 5 minutes. The process is repeated until the current does not decay upon the step in the negative direction. In this way, an estimate of E_{rp} can be made, with better estimates resulting from the use of smaller increments in the test potential (i.e., 25 mV instead of 50 mV). Sridhar et al. (41,42,47) used a variation of this technique to determine the repassivation potentials discussed previously. They found excellent correlation from these tests and the long-term performance of materials. Tsujikawa and coworkers (52,53) have also used repassivation potentials measured via potentiostatic tests that focused on the stability of the localized corrosion process (i.e., measured the conditions under which a material would repassivate once activated and allowed to grow).

Temperature has been used in conjunction with electrochemical control to quantify the resistance of materials to localized corrosion. Kearns (26) has reviewed the different critical temperature tests in some detail. Electrochemical critical temperature testing consists of holding a material exposed to a solution of interest potentiostatically at a potential in its passive region while increasing the temperature of the solution either intermittently (54) or continuously (55). An example of the results of the latter type of testing is shown in Fig. 48. In this

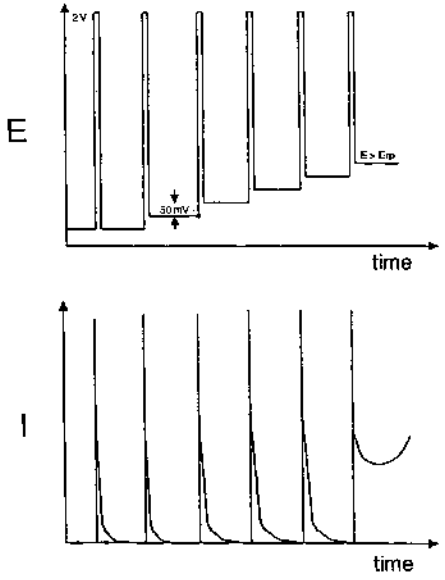

Figure 47 Schematic E_{app} (t) and I_{app} (t) for the electrochemical scratch test. Once the return potential exceeds E_{rp}, the current increases. The size of the step (50 mV in this case) will define the uncertainty of the measurement of E_{rp}.

case, a localized corrosion site is stabilized and the current increases dramatically. Parameters of importance in such testing include the potential at which the sample is held, the rate of temperature increase, and the criterion for the current that establishes the critical temperature. This method allows a quantitative ranking of a wide variety of alloys by a single parameter that can be related to actual process conditions.

5. Galvanostatic Testing

The vast majority of electrochemical testing involves controlling the potential of the working electrode and measuring the applied current required. This bias has development for two main reasons: (**1**) the easier applicability of critical potentials, rather than critical current densities in mitigation strategies, (**2**) the exponential dependence of dissolution rate on potential. There are situations in which galvanostatic tests (in which a constant applied current is maintained) can be more discriminating. These are most often coupled with post-test visual examination of the specimen. The posttest examination allows a determination of the sites from which the current was emitted in cases where the polarization behavior itself is

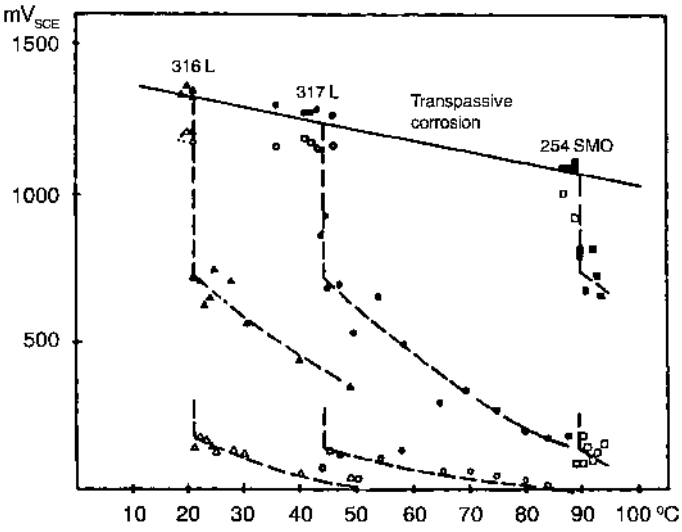

Figure 48 Plot of breakdown and repassivation potentials vs. temperature for different steel grades in 1 M NaCl. Filled symbols for breakdown and open symbols for repassivation potentials. (From Ref. 30.)

not discriminating. Galvanostatic tests also require less advanced equipment than potentiostatic tests.

The most widely-used galvanostatic test is Practice A of ASTM A262, the oxalic etch test. In this screening test for sensitization of stainless steels, an applied anodic current density of 1 A/cm^2 polarizes the specimen to high potentials for 1.5 min in 10% oxalic acid. Posttest examination reveals whether the charge passed went to uniform dissolution or localized attack along the grain boundaries. Unsensitized materials show a "step" structure in which the individual grains are uniformly dissolved. As shown in the cross section, the different grains dissolve at different rates owing to the dependence of the kinetic parameters on crystallographic orientation. Slightly sensitized materials have localized attack of some grain boundary areas superimposed on the uniform dissolution, while heavily sensitized materials have entire grains circled. This test allows a rapid estimation of sensitization with a minimum of equipment.

A second example of the utility of galvanostatic testing is from an investigation of surface treatments and alloying on the dealloying of aluminum bronzes. Kelly and Scully (56) used a 150 μA/cm^2 applied anodic current density for 7 days in simulated ocean water followed by cross-sectional metallography to differentiate the susceptibilities of five aluminum- and nickel–aluminum–

bronzes. They found that the test led to dealloying morphologies and relative susceptibilities that correlated well to those developed in natural seawater over 36 months, though the depths of attack were less.

6. Electrochemical Noise

Recently, electrochemical noise has been promoted as a tool for both corrosion science and corrosion engineering. The basics behind the concept for localized corrosion have already been outlined above; by monitoring the galvanic current between two nominally identical electrodes, or by monitoring the corrosion potential of a single electrode carefully, metastable pitting can be detected. The localization of the dissolution inherent in localized corrosion implies a separation of the anodic and cathodic reactions that constitute the corrosion couple. This physical separation of reactions distinguishes localized corrosion from uniform corrosion, in which it is traditionally thought that the anodic and cathodic sites are in very close proximity to one another. The majority of the anodic (oxidative dissolution) reaction occurs inside the localized corrosion site, while the majority of the cathodic (reduction) reaction occurs on the boldly exposed surface. Thus a galvanic couple is created (see Fig. 19). The spatial separation of the processes necessitates the passage of current between the two sites. This passage of current leads to the various electrochemical noise signals measured.

Under open circuit conditions, bursts of dissolution at localized corrosion sites require the generation of bursts of cathodic current from the surrounding boldly exposed surface. This increased demand typically causes a decrease in the measured open circuit potential (see Fig. 49). Localized corrosion sites are typically very small (<100 μm in diameter). However, the current densities inside these cavities during transient bursts can be on the order of 1 A/cm^2. These rates are possible because of the extremely aggressive environments that develop inside localized corrosion sites. Thus, even though the sites are geometrically small, they can influence the electrochemical potential of the much larger boldly exposed surface on which the kinetics are far slower. This difference in relative current densities on separated anodes and cathodes is what accounts for the ability to detect the electrochemical noise associated with localized corrosion. When the potential of the surface is controlled with an external device, the same burst of dissolution requires the device to supply a burst of current, which can be recorded (see Fig. 25). Usually, these bursts are transient, with temporary repassivation of the localized corrosion site occurring and allowing the system to return to the previous steady-state condition. On a metal surface of appreciable size (>1 cm^2), there can be many localized corrosion sites. They will usually propagate individually, so that a series of current (or potential) fluctuations are observed because of the summation of the signals from the individual sites. These fluctuations are referred to as electrochemical noise. Since electrochemical noise can often be

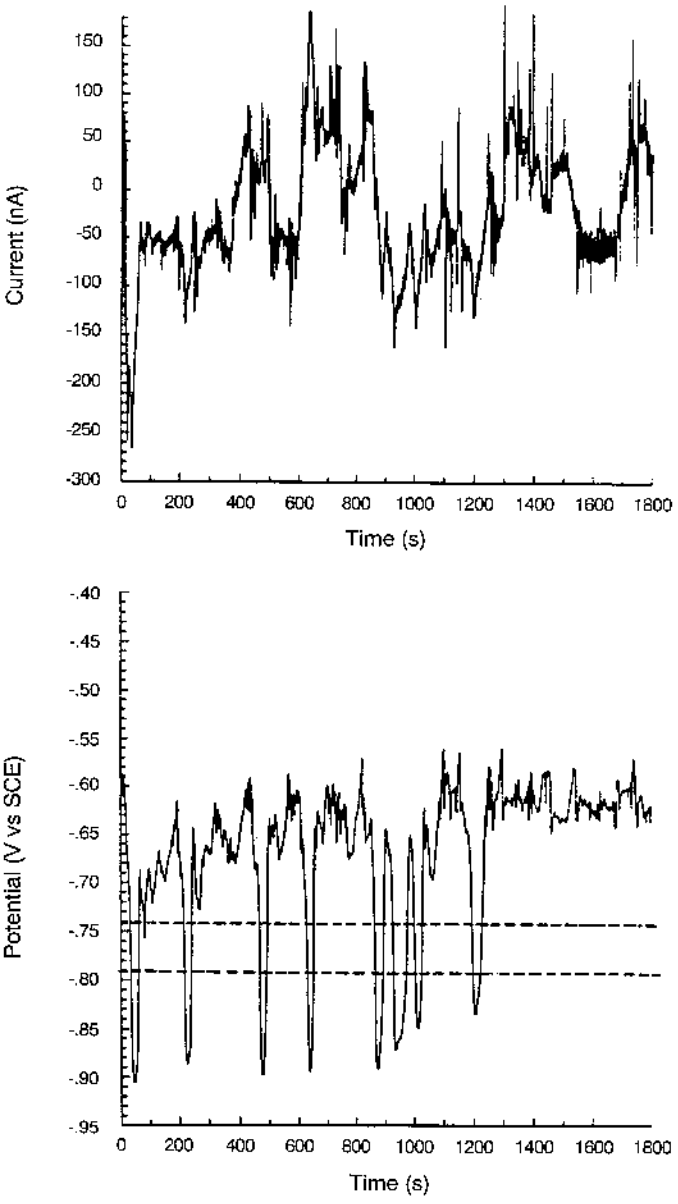

Figure 49 Electrochemical time series of galvanically coupled AA2024-T3 (ST) in 1 M NaCl. No deaeration and 0.01 cm^2 exposure area. (a) Current and (b) open circuit potential. The horizontal dashed lines represent the mean pitting (top) and transition (bottom) potentials of high purity Al at this Cl^- concentration. (Data courtesy of Sheldon T. Prude, University of Virginia.)

observed under open circuit conditions, it has been hailed as the only truly noninvasive electrochemical method. An example of electrochemical noise associated with the pitting of stainless steel is shown in Fig. 50.

Changes in the noise signal are often taken as indications that conditions are favorable for pit initiation to occur. Thus, if one is monitoring corrosion of a material in a process stream, corrective action can be taken. The disadvantage of noise monitoring is that it does not give sufficient information about what level of metastable pitting is acceptable. For example, there may be literally millions of metastable pits forming and repassivating in a vessel wall, but only one needs to penetrate completely. It is impossible to differentiate between conditions that will allow this and those in which the extent of pitting is negligible. In addition, the noise from crevice corrosion is often extremely hard to detect owing to the shielding associated with its formation. Experience and correlations with coupon exposures are critical factors in the use of noise for localized corrosion monitoring.

One way to divide the types of electrochemical noise is by the manner in which it is collected. *Potential noise* refers to measurements of the open circuit potential of an electrode versus either a reference electrode or a nominally identical electrode. While measurements with a conventional reference electrode have the advantage of being relatable to thermodynamic conditions, these reference electrodes have their own noise associated with them that could complicate analysis. In addition, the application of noise monitoring to field conditions would be

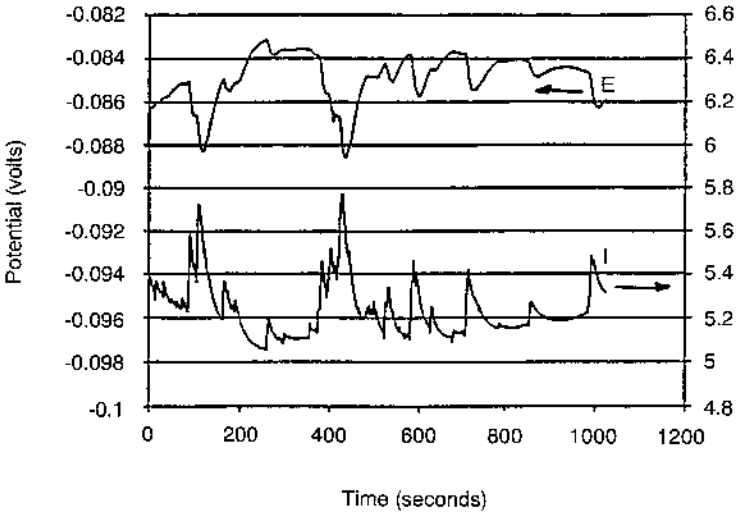

Figure 50 Electrochemical noise (spontaneous potential and current fluctuations) associated with the metastable pitting of austenitic stainless steel. (From Ref. 57.)

much more attractive if maintenance of the reference electrode were not required. Since typically the fluctuations of the signal are the most important aspect, rather than the absolute value of the potential, the use of an electrode nominally identical to the working electrode has become popular. Current noise can occur with two types of experimental arrangements. In one, measurements are made of the current that passes between two nominally identical electrodes that are exposed to the same environment and connected through a zero resistance ammeter (ZRA). The fluctuations in this coupling current are due to each electrode becoming more or less anodic with respect to the other as a function of time. The initiation, short-term propagation, and repassivation of a pit on one electrode, while the other remains passive, is one example. A second situation in which current noise can be generated is during a potentiostatic experiment in which the current necessary to hold the interfacial potential constant fluctuates. The origin of these fluctuations is the same as those in the ZRA arrangement, but in this case it is the potentiostat that supplies the current, and the transients are only of one polarity (since the potentiostat never "pits"). All types of measurements of electrochemical noise described have been used to study corrosion processes. Most field applications have involved a three-electrode probe system. Two electrodes are connected via a ZRA and the current noise is measured. The potential of this couple is then measured against the third electrode in order to monitor the potential noise associated with the same processes. This approach has been found useful in that it allows an additional correlation (between the two types of noise measurements) to be made.

7. Analysis Methods and Precautions

Analysis methods for electrochemical noise data can be separated into three categories, (**1**) deterministic, (**2**) statistical, and (**3**) spectral. Deterministic methods involve the use of mixed potential theory to explain the oscillations that occur. For example, if the ZRA current increases suddenly while the potential difference between the two current electrodes and the potential electrode increases, localized corrosion has likely initiated on one of the current electrodes. A common pitfall in such a measurement is that if a nominally identical "reference" electrode is used, it could pit as well, leading to no change in potential versus the coupled electrodes. Due to the need for careful interpretation, deterministic methods are not widely used.

Statistical methods are the most popular techniques for EN analysis. The potential difference and coupling current signals are monitored with time. The signals are then treated as statistical fluctuations about a mean level. Amplitudes are calculated as the standard deviations root-mean-square (rms) of the variance according to (for the potential noise)

$$\sigma_E = \sqrt{\frac{\sum_i (E_i)^2}{N - 1}}$$

By taking the ratio of the standard deviation of the potential signal to that of the coupling current signal, a parameter with the units of resistance (or Ω-cm^2 when corrected for area) can be calculated. This ratio has been termed the noise resistance, R_n, by Eden and Rothwell (57) and has been found to correlate to the polarization resistance, R_p, to be discussed in Chapter 4. Localized corrosion indices have also been proposed (58), though none have been sufficiently correlated with other measurements to allow generalizations to be made.

Spectral analysis of EN generally uses the fast Fourier transform (FFT) or other algorithm to convert the signal from the time domain to the frequency domain. This transformation displays the frequency content of the signal, i.e., the amount of the signal power as a function of frequency. Generally, EN of interest to corrosion studies has most of its power in the range of 0.01 to 1 Hz. A typical FFT spectrum for potential noise is shown in Fig. 51 for carbon steel pitting. As with the pitting index, a number of workers have published correlations between parameters describing the FFT spectra and localized corrosion behavior, but the correlations are not extendable to other systems.

Correlations between noise measurements and corrosion processes have been reported for uniform corrosion as well as pitting, crevice corrosion, and stress corrosion cracking in individual systems. Dawson et al. (59) found that the ratio of the root-mean-square (rms) amplitudes of the potential and current noise (which they termed the noise resistance, R_n) correlated well with both the polarization resistance determined by conventional methods and by weight loss of steel in acid. By using different solution compositions, different types of attack were created, and they found qualitative differences between the electrochemical noise signatures for uniform, pitting, and crevice corrosion. A number of workers have correlated noise measurements to the occurrence of localized corrosion. Pitting has been the most studied, with applications with steels (60), stainless steels in Cl^- (61–63), and aluminum alloys (64,65). Crevice corrosion of stainless steel has also received some attention, especially in differentiating it from pitting (61). A number of applications of noise to stress corrosion cracking have been published (66–69). For example, the group at Harwell Lab in the UK has shown that current noise can be correlated with the nucleation and growth of stress-corrosion cracks in stainless steel exposed to thiosulfate at room temperature (67) as well as in BWR conditions (pure water, 288°C) (68). Newman et al. (69) correlated electrochemical noise with acoustic emission and discontinuous crack growth in brass exposed to nitrite solution. Eden et al. (66) correlated the shape, frequency, and magnitude of both current and potential noise of steel exposed to CO/CO_2 solutions with the observed cracking. Loto and Cottis (70) found that

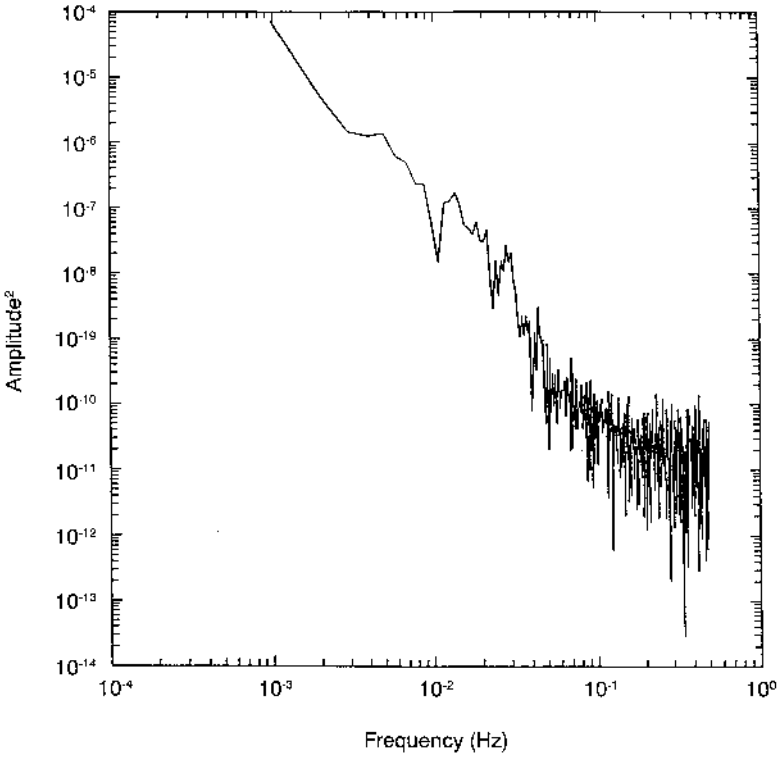

Figure 51 Fast Fourier transform of the potential noise from two nominally identical carbon steel electrodes exposed to 0.2 M HCl + 0.5 M NaCl + 0.15 M $NaNO_2$. (Data courtesy of J. Yuan, M. Inman, T. Lunt, J. Hudson, University of Virginia.)

not only did the amplitude of the potential noise increase during the cracking of aluminum alloy 7075 in chloride solution, but also the standard deviation calculated from the noise signal increased as well.

In the absence of a fundamentally based theory of electrochemical noise that has been thoroughly tested, the utility of the technique should be demonstrated on a case-by-case basis. For example, the reliance upon purely empirical correlations leaves open the possibility of changes in some process variable causing changes in the noise signal but not in the corrosion process or vice versa. Of utmost importance is the correlation of noise data to other measurements such as conventional electrochemical measurements and coupon testing. Recently, Huet and Bertocci (72) have made important progress in putting noise resistance measurements on a firmer theoretical basis.

V. SUMMARY AND CONCLUSIONS

The goals of this chapter were (1) to provide an introduction to the science behind passivity and its breakdown, (2) to furnish a framework for understanding the conditions under which localized corrosion occurs and how external variables affect it, (3) to give a brief overview of the accelerated coupon exposure tests used to determine localized corrosion susceptibility, including the reasons why each works, and (4) critically to introduce a variety of electrochemical techniques that can provide important information concerning localized corrosion susceptibility if they are used correctly. None of the methods discussed is perfect or a panacea, but when they are used judiciously and in combination with each other, a better picture of the localized corrosion process can be gained, even in complicated solutions. This allows for better informed decisions on alloy selection, process alteration, or failure analysis. While prediction of localized penetration rate remains a goal of electrochemical testing, recent applications of statistics to the process appear promising.

REFERENCES

1. J. A. Collins, M. L. Monack. Mats. and Perf. 12, 11 (June 1973).
2. R. P. Frankenthal, J. Kruger, eds. Passivity of Metals, Electrochem. Soc. Pennington, NJ (1978).
3. M. Froment, ed. Passivity of Metals and Semiconductors, Elsevier, Amsterdam (1983).
4. W. J. Muller. Trans. Faraday Soc. 27, 737 (1931).
5. T. R. Beck. J. Electrochem. Soc. 129, 2500 (1982).
6. R. M. Carraza, J. R. Galvele. Corr. Sci. 28, 233 (1988).
7. J. E. O. Mayne, J. W. Menter. J. Chem. Soc. 103 (1954).
8. S. Kannan, R. G. Kelly. Corr. Sci., in press (1995).
9. A. Legat, V. Doleček. J. Electrochem. Soc. 142, 1851 (1995).
10. D. Singbeil, A. Garner. Materials Performance 31 (April 1987).
11. Z. Szklarska-Smialowska. In: Advances in Localized Corrosion (H. Isaacs, U. Bertocci, J. Kruger, S. Smialowska, eds). NACE, Houston, 41 (1990).
12. A. J. Sedricks. Intl. Metals Review 27, 321 (1982).
13. Z. Szklarska-Smialowska. Pitting Corrosion of Metals. NACE, Houston (1986).
14. D. A. Jones. Principles and Prevention of Corrosion. Macmillan, New York, 198 (1992).
15. H. H. Uhlig. Corrosion and Corrosion Control. John Wiley, New York, 272 (1963).
16. Z. Szlarska-Smialowska, J. Mankowski. Corros. Sci. 18, 953 (1978).
17. J. R. Galvele. Proc. 4th Intl. Symp. Passivity. TMS, Warrendale, PA, 285 (1977).
18. R. B. Mears, U. R. Evans. Trans. Faraday Soc. 30, 417 (1934).
19. J. W. Oldfield, W. H. Sutton. Brit. Corr. J. 13, 13 (1978).
20. J. W. Oldfield, W. H. Sutton. Brit. Corr. J. 13, 104 (1978).

21. M. G. Fontana, N. D. Greene. Corrosion Engineering. McGraw-Hill, New York, 41 (1967).
22. J. L. Crolet, J. M. Defranoux, L. Seraphin, R. Tricot. Mem. Sci. Rev. Metall. 71, 797 (1974).
23. A. Turnbull, M. K. Gardner. Brit. Corros. J. 16, 140 (1981).
24. G. Salamat, G. A. Juhl, R. G. Kelly. Corrosion, in press (Nov. 1995).
25. ASTM G 48, 1995 Annual Book of Standards, Section 3.02, American Society for Testing and Materials, Philadelphia (1985).
26. J. R. Kearns. In: Corrosion Tests and Standards: Application and Interpretation (R. Baboian, ed.). ASTM, Philadelphia, 175 (1995).
27. J. R. Kearns, M. J. Johnson, J. F. Grubb. Paper 228, Corrosion/86 Conference, NACE, Houston (1986).
28. M. A. Streicher. In: Corrosion Tests and Standards: Application and Interpretation (R. Baboian, ed.). ASTM, Philadelphia, 197 (1995).
29. R. Qvarfort. Corr. Sci. 28, 135 (1988).
30. R. Qvarfort. Corr. Sci. 29, 987 (1989).
31. L. Stockert, F. Hunkeler, H. Bohni. Corrosion 41, 676 (1985).
32. A. P. Majidi, M. A. Streicher. In: Electrochemical Techniques for Corrosion Engineering (R. Baboian, ed.). NACE, Houston, 217 (1986).
33. ASTM E112, 1995 Annual Book of Standards, American Society for Testing and Materials, Philadelphia (1985).
34. F. P. Ford, P. L. Andresen. Paper 83, Corrosion/87. NACE, Houston (1987).
35. P. L. Andresen, F. P. Ford. Proc. ASME Symp. on Predictive Capabilities in Environmentally Assisted Cracking, Miami, 17 (Nov. 1985).
36. D. L. Reichert, G. E. Stoner. J. Electrochemical Soc. 137, 411 (1990).
37. A. P. Majidi, M. A. Streicher. Corrosion 40, 584 (1984).
38. J. B. Lee. Corrosion 42, 106 (1986).
39. M.-K. Ahn, H.-S. Kwon, J.-H. Lee. Corrosion 51, 441 (1995).
40. J. R. Scully, R. G. Kelly. Corrosion 42, 537 (1986).
41. N. Sridhar, G. A. Cragnolino. Corrosion 49, 885 (1993).
42. N. Sridhar, D. Dunn. Corrosion 50, 857 (1994).
43. B. E. Wilde. In: Localized Corrosion (Staehle, Brown, Kruger, Agarwal, eds.). NACE, Houston, 342 (1974).
44. H. Yashiro, K. Tanno. Corros. Sci. 33, 735 (1992).
45. K. Sugimoto, K. Asano. In: Advances in Localized Corrosion (H. Isaacs, U. Bertocci, J. Kruger, S. Smialowska, eds.). NACE, Houston, 375 (1990).
46. N. G. Thompson, B. C. Syrett. Corrosion 48, 649 (1992).
47. D. Dunn, N. Sridhar. Paper 347, Corrosion/94. NACE, Houston (1994).
48. T. Shibata, T. Takeyama. Corrosion 33, 243 (1977).
49. D. E. Williams, C. Westcott, M. Fleischman. J. Electrochem. Soc. 132, 1796 (1985).
50. J. Stewart. Ph.D. thesis, Department of Chemistry, University of Southampton, UK (1990).
51. S. Fujimoto, T. Shibata, M. Minamida, S. Ukada. Corros. Sci. 36, 1575 (1994).
52. S. Tsujikawa, S. Okayama. Corros. Sci. 31, 441 (1990).
53. S. Tsujikawa, Y. Sone, Y. Hisamatsu. In: Corrosion Chemistry Within Pits, Crevices and Cracks (A. Turnbull, ed.). Her Majesty's Stationary Office, London, 171 (1987).

54. R. J. Brigham, E. W. Tozer. Corrosion 29, 33 (1973).
55. J. M. Drugli, R. Johnsen. Paper 410, Corrosion/88, NACE. Houston (1988).
56. R. G. Kelly, J. R. Scully. An evaluation of the susceptibility of laser surface-melted aluminum bronze to dealloying via an accelerated electrochemical test, NSRDC TM-28-83-189. David Taylor Naval Ship R & D Center, Annapolis, MD (Sept. 1983).
57. D. A. Eden, A. N. Rothwell. Paper 292, Corrosion '92. NACE, Houston (1992).
58. D. A. Eden, D. G. John, J. L. Dawson. Intl. Patent WO 87/07022, World Intellectual Property Organization, 1987.
59. J. L. Dawson, D. M. Farrell, P. J. Aylott, K. Hladky. Paper 31, Corrosion '89. NACE, Houston (1989).
60. K. Hladky, J. L. Dawson. Corros. Sci. 23, 231 (1982).
61. S. Magaino, A. Kawaguchi, A. Hirata, T. Osaka. J. Electrochem. Soc. 134, 2993 (1987).
62. N. Stolica. Corros. Sci. 9, 205 (1969).
63. W. Schwenk. Corrosion 20, 129t (1964).
64. S. Magaino. Boshoku Gijutsu 32, 712 (1983).
65. S. Magaino, M. Yasuda, H. Yamada. Boshoku Gijustu 34, 157 (1985).
66. D. A. Eden, A. N. Rothwell, J. L. Dawson. Paper 444, Corrosion '91. NACE, Houston (1991).
67. D. B. Wells, J. Stewart, R. Davidson, P. M. Scott, D. E. Williams. Corros. Sci. 33, 39 (1992).
68. J. Stewart, D. B. Wells, P. M. Scott, D. E. Williams. Corros. Sci. 33, 73 (1992).
69. R. C. Newman, K. Sieradzki, J. Woodward. In: Corrosion Chemistry Within Pits, Crevices and Cracks (A. Turnbull, ed.). HMSO, 203 (1987).
70. C. A. Loto, R. A. Cottis. Corrosion 45, 136 (1989).
71. M. G. Fontana, N. D. Greene, Corrosion Engineering, McGraw-Hill, New York (1978), p. 321.
72. U. Bertocci, F. Huet, J. Electrochem. Soc., 144(8), 2786–2793 (1997).

4

The Polarization Resistance Method for Determination of Instantaneous Corrosion Rates

OVERVIEW

The polarization resistance method utilized for determination of instantaneous corrosion rates of metals is reviewed. The fundamental assumptions in electrode kinetics that govern the technique are restated. Error-producing factors such as high excitation voltage amplitude, insufficiently slow scan rate or inadequate polarization hold period, high solution resistance, presence of competing reduction–oxidation reactions, and nonuniform current and potential distributions are discussed with the goal of defining conditions and circumstances where these complicating factors are important.

I. INTRODUCTION

A variety of methods such as electrical resistance, gravimetric-based mass loss, quartz crystal microbalance-based mass loss, electrochemical, and solution analysis methods enable the determination of the corrosion rates of metals. The polarization resistance method, based on electrochemical concepts, enables determination of *instantaneous* interfacial reaction rates such as corrosion rates and exchange current densities from a single experiment. In contrast, electrical resistance change, gravimetric and quartz crystal microbalance mass loss, as well as solution analysis for metallic cations all provide historical or integrated mass loss information from corrosion that has occurred over some period of time. Therefore instantaneous rates cannot be determined from a single measurement using these other methods. Instead, the derivative of multiple measurements over time provides rate information.

II. POLARIZATION RESISTANCE METHOD

A. Review of the Governing Electrode Kinetics in Corrosion Processes

The following relationship is experimentally observed between applied electrochemical current density and potential for a corroding electrode in the absence of competing reduction–oxidation reactions (1,2). The applicability of this relationship relies on the presence of a single charge transfer controlled cathodic reaction and a single charge transfer controlled anodic reaction.

$$i_{app} = i_{corr}\left(\exp\left[\frac{2.3(E - E_{corr})}{\beta_a}\right] - \exp\left[\frac{-2.3(E - E_{corr})}{\beta_c}\right]\right) \quad (1)$$

where β_a and β_c are the anodic and cathodic Tafel parameters ($\partial E/\partial \log i_{app}$) given by the slopes of the polarization curves in the anodic and cathodic Tafel regimes, respectively. E-log(i_{app}) data govern by such kinetics are shown in Fig. 1. E_{corr} is the corrosion potential. E is an applied potential such that $E - E_{corr}$ is ΔE, and i_{corr} is the corrosion current density. This relationship provides the basis for the electrochemical polarization technique as applied to a corroding electrode at its corrosion potential.

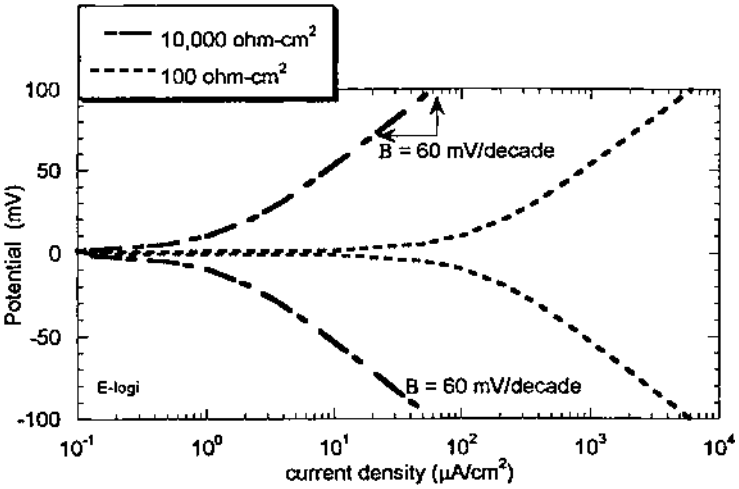

Figure 1 E–log(i_{app}) data for hypothetical corroding interfaces with $R_p = 100$ and 10,000 ohm-cm^2 and $\beta_a = \beta_c = 60$ mV/decade. The two cases produce corrosion current densities of 130.4 and 1.3 μA/cm^2, respectively. The Tafel slope is obtained from E–log(i_{app}) data at high overpotential. The open circuit potential is arbitrarily selected to be 0 mV.

B. The Derivation of the Polarization Resistance

Many investigators have experimentally observed that i_{app} was approximately linearly related to applied potential within a few millivolts of polarization from E_{corr} (3). Stern and Geary simplified the kinetic expression to provide an approximation to the charge transfer controlled reaction kinetics given by Eq. (1) for the case of small overpotentials with respect to E_{corr} (4–6). Equation (1) can be mathematically linearized by taking its series expansion (e.g., $e^x = 1 + x + x^2/2! + x^3/3! + x^4/4! \ldots$) and by neglecting higher terms when $\Delta E/\beta < 0.1$. This simplified relationship has the form

$$R_p(\text{ohm} - \text{cm}^2) = \left[\frac{\Delta E}{\Delta i_{app}}\right]_{(E-E_{corr})\to 0} = \left(\frac{\beta_a\beta_c}{2.3 i_{corr}(\beta_a + \beta_c)}\right) \tag{2}$$

Rearranging, we obtain

$$i_{corr} = \frac{1}{(2.3R_p)}\left(\frac{\beta_a\beta_c}{\beta_a + \beta_c}\right) = \frac{B}{R_p} \tag{3}$$

where R_p is the polarization resistance given by $(\partial E/\partial i)$ at $t = \infty$, $\Delta E = 0$ (ohm-cm^2), and B is a proportionality constant. Note that R_p in units of ohms is obtained from E–I data if current is not normalized by electrode area. Such data must be multiplied by electrode area to yield R_p (ohm-cm^2). If electrode area is doubled then the measured R_p value in ohms is halved, but R_p (ohm-cm^2) would be the same since the electrode area is doubled. This gives the result that corrosion rate per unit area is independent of electrode surface area. However, the working electrode area must be known to calculate corrosion rate. Note also that the proportionality constant, B, is dominated by the smaller of the two anodic and cathodic Tafel slopes, if unequal. Therefore cathodic mass transport control such that $\beta_c \to \infty$ results in $B = \beta_a/2.3$. Similarly, anodic mass transport control results in $B = \beta_c/2.3$ (7). Knowledge of R_p, β_a, and β_c enables direct determination of the corrosion rate at any instant in time using Eq. (3) (4–9). i_{app} is often approximately linear with potential within ± 5 to 10 mV of E_{corr}, as in Fig. 2. The slope of this plot is $\Delta E/\Delta i$. When determined from a tangent to the E–i curve at E_{corr} as shown in Fig. 2, it defines the polarization resistance. Consequently, this method is often called the linear polarization method (LPR). The slope is independent of the degree of linearity (3), although the extent of the approximately linear E–i region can vary considerably among corroding systems, as will be discussed below.

The fact that the corrosion rate is inversely proportional to the polarization resistance is clearly seen by Eq. (3). Taking the logarithm of this equation, it is seen that log i_{corr} versus log R_p is linear with a slope of -1 and has the intercept log B[3].

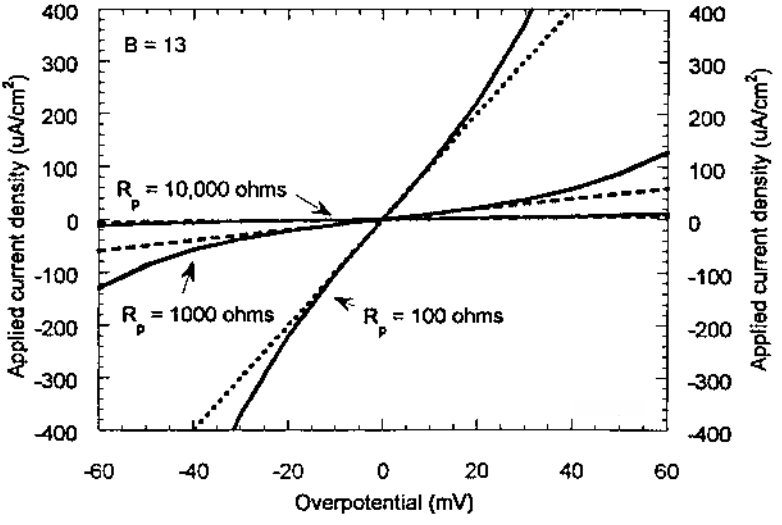

(a)

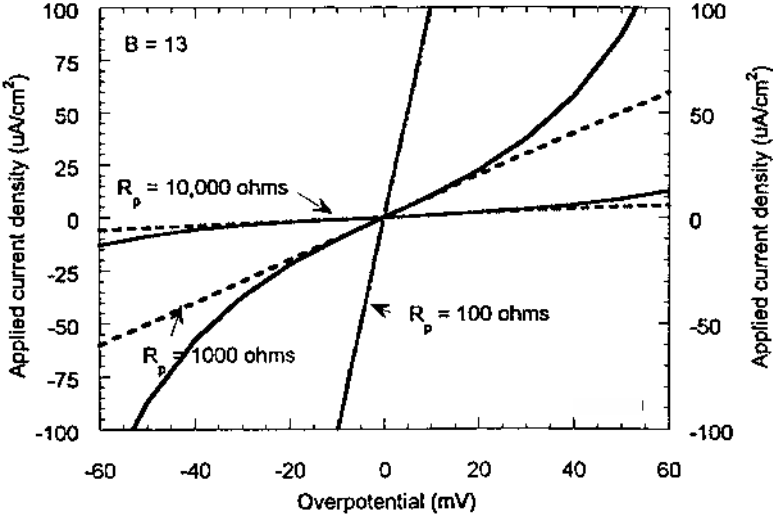

(b)

Figure 2 Hypothetical E–i polarization resistance data for hypothetical corroding interfaces with R_p = 100, 1000, and 10,000 ohms (assumed 1 cm^2) and $\beta_a = \beta_c$ = 60 mV/decade. The three cases produce corrosion current densities of 130.4, 13.0, and 1.3 μA/cm^2, respectively. Plots (a) and (b) of the same data provide different current scales to indicate the nonlinearity in each case. Plot (c) shows the linear relationship between $\log(R_p)$ and $\log(i_{corr})$. (From Ref. 8.)

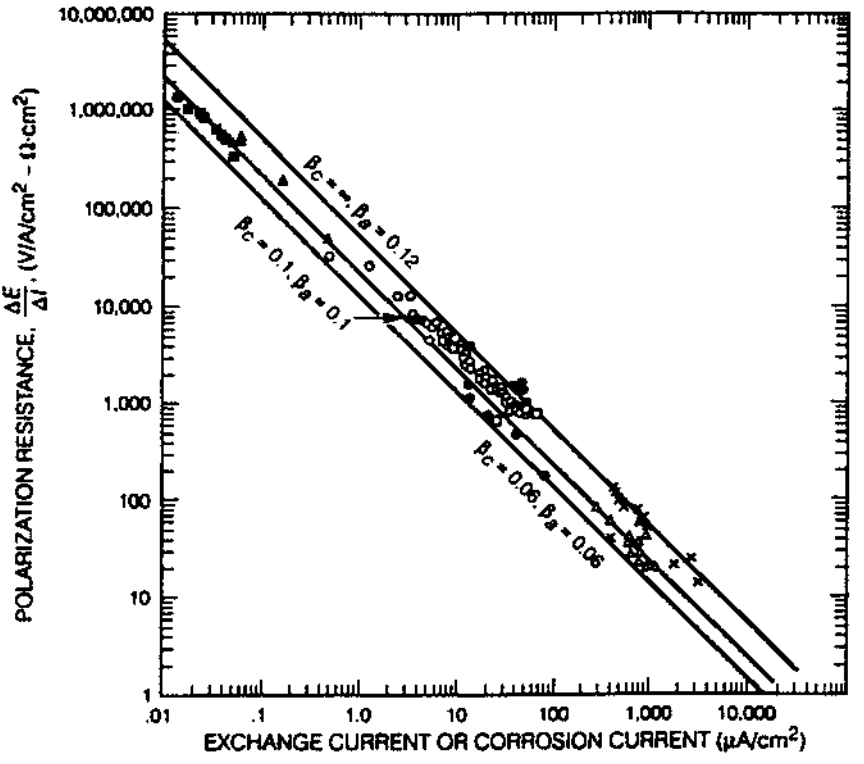

(c)

$$\log(R_p) = \log B - \log(i_{corr}) \tag{4}$$

Stern and Wiesert (8) confirmed such a relationship over a six-order-of-magnitude change in corrosion rate for corroding systems or exchange current density for reduction–oxidation systems*, as is illustrated in Fig. 2(c).

* This review focuses on corroding systems. However, the concept of polarization resistance applies equally well to reduction–oxidation systems. Here, the exchange current density, i_o, may be calculated from the polarization resistance, where R is the ideal gas constant, T is the temperature, and α_a and α_c are the anodic

$$R_p(\text{ohm-cm}^2) = \left[\frac{\Delta E}{\Delta i}\right]_{(E-E_{rev})\to 0} = \left(\frac{RT}{i_o F(\alpha_a + \alpha_c)}\right)$$

and cathodic multistep electron transfer coefficients, respectively, for the reduction–oxidation process.

C. Time Domain Methods for Determining the Polarization Resistance

ASTM standards D-2776 (9) and G-59 (10) describe standard procedures for conducting polarization resistance measurements. Potentiodynamic (11), potential step, and current-step methods (12,13) have all been described to determine the linear E–i behavior of an electrode near E_{corr}. The current step method has been cited to be faster than potentiodynamic methods and less susceptible to errors associated with drift in E_{corr}. This issue will be discussed below. Regardless of the method used, independent determination of β_a and β_c is still required.

Alternative techniques exploit nonlinearity at larger overpotentials. Note that nonlinearity invalidates Eq. (3). However, the nonlinearity, if treated properly, can enable determination of β_a and β_c without excessive polarization. The Oldham–Mansfeld method calculates i_{corr} from nonlinear E vs. i_{app} data obtained within ± 30 mV of E_{corr} without the need for high overpotential determination of β_a and β_c (14). Computerized curve fitting can exploit nonlinearity to calculate β_a and β_c from low overpotential data, avoiding the destructive nature of large overpotentials (15). The Mansfeld technique substitutes Eq. (3) into Eq. (1), eliminating i_{corr} (15). β_a and β_c are determined from the best fit of the resulting expression containing β_a and β_c as unknowns to a nonlinear plot of ΔE vs. $2.3 i_{app} R_p$. R_p is determined in the usual way from the slope of a linear tangent to the E vs. i_{app} data at E_{corr}. i_{corr} is subsequently determined from Eq. (3) for known values of R_p, β_a, and β_c. In this technique, elimination of i_{corr} enables determination of only two unknowns by fitting. Advancements in computerization enables a fit to Eq. (1), but this requires simultaneous determination of three unknowns. Consequently, extremely high quality E–$\log(i)$ data that is corrected for ohmic voltage error and does not contain other sources of overpotential (i.e., mass transport overpotentials) is required.

D. Electrochemical Impedance Methods for Determination of Polarization Resistance

The complications and sources of error associated with the polarization resistance method are more readily explained and understood after introducing electrical equivalent circuit parameters to represent and simulate the corroding electrochemical interface (1,16–20). The impedance method is a straightforward approach for analyzing such a circuit. The electrochemical impedance method is conducted in the frequency domain. However, insight is provided into complications with time domain methods given the duality of frequency and time domain phenomena. The simplest form of such a model is shown in Fig. 3a. The three parameters (R_p, R_s, and C_{dl}) that approximate a corroding electrochemical inter-

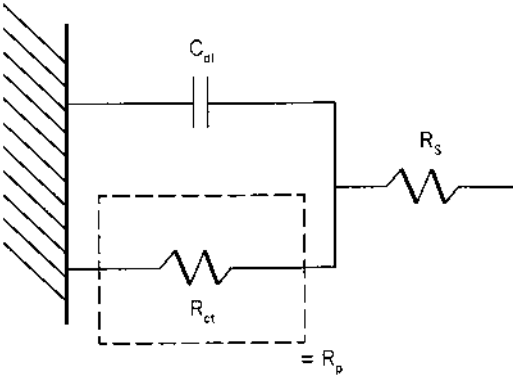

(a)

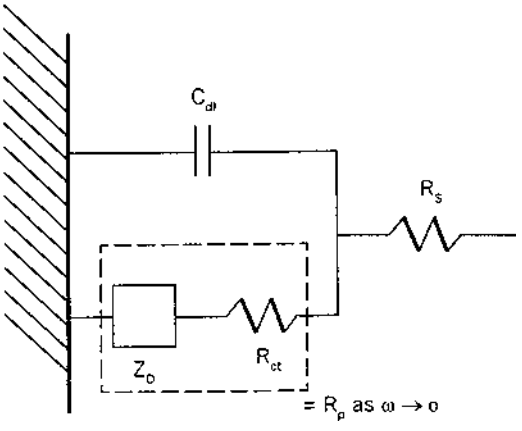

(b)

Figure 3 Electrical equivalent circuit model commonly used to represent an electrochemical interface undergoing corrosion. R_p is the polarization resistance, C_{dl} is the double layer capacitance, R_{ct} is the charge transfer resistance in the absence of mass transport and reaction intermediates, R_D is the diffusional resistance, and R_S is the solution resistance. (a) $R_p = R_{ct}$ when there are no mass transport limitations and electrochemical reactions involve no absorbed intermediates and nearly instantaneous charge transfer control prevails. (b) $R_p = R_D + R_{ct}$ in the case of mass transport limitations.

face are shown. Here R_s is the solution resistance, and C_{dl} is the double-layer capacitance that arises whenever an electrochemical interface exists. The algebraic sum of R_s and R_p is measured when a dc measurement is performed (e.g., zero ac frequency, long hold time during potential or current step, or slow scan rate approaching zero). This is because impedance associated with a capacitor approaches infinity as frequency approaches zero, and parallel electrical circuit elements are dominated by the element with the smallest impedance. Therefore the sum of R_s and R_p is measured at zero frequency. The true corrosion rate will be underestimated when R_s is appreciable. Conversely, any experiment conducted at too fast a voltage scan rate (short time, or too high an ac frequency) causes the algebraic sum of the ohmic resistance and the resultant frequency-dependent parallel impedance of the parallel resistive–capacitive network to be measured. This value will be lower than the sum of R_p and R_s determined at an infinitely slow scan rate or frequency because current leaks through the parallel capacitive element at higher scan rate owing to its low impedance at high frequency. This will usually result in an overestimation of the true corrosion rate. These complications in scan rate or current-step hold time can be overcome or at least detected more easily by using the electrochemical impedance method (1,16,20).

ASTM standard G 106 provides a standard practice for verification of algorithm and equipment for electrochemical impedance measurements (20). The standard also contains an appendix reviewing the technique. Typically a small-amplitude sinusoidal potential perturbation is applied to the working electrode at a number of discrete frequencies, ω. At each one of these frequencies, the resulting current waveform will exhibit a sinusoidal response that is out of phase with the applied potential signal by an amount depending upon the circuit parameters of the corroding interface and has a current amplitude that is inversely proportional to the impedance of interface. This electrochemical impedance, $Z(\omega)$, is the frequency-dependent proportionality factor that acts as a transfer function by establishing a relationship between the excitation voltage signal and the current response of the electrochemical system:

$$Z(\omega) = \frac{E(\omega)}{i(\omega)} \tag{5}$$

where E = the time-varying voltage across the circuit, $E = E_o \sin(\omega t)$, i = the time-varying current density through the circuit, $i = i_o \sin(\omega t + \theta)$, $Z(\omega)$ = the impedance (ohm-cm^2), and t = time (s).

$Z(\omega)$ is a complex-valued vector quantity with real and imaginary components whose values are frequency dependent:

$$Z(\omega) = Z'(\omega) + jZ''(\omega) \tag{6}$$

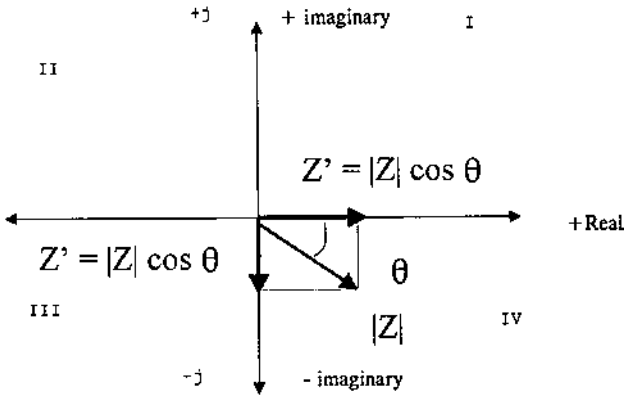

Figure 4 Cartesian coordinate system with imaginary j notation depicting an impedance vector $|Z|$ and its real and imaginary components Z' and Z'' as well as phase angle θ.

where $Z'(\omega)$ = the real component of impedance, $Z'(\omega) = |Z(\omega)|\cos(\theta)$, $Z''(\omega)$ = the imaginary component of impedance where $Z''(\omega) = |Z(\omega)|\sin(\theta)$, j^2 = the square of the imaginary number, or -1, $|Z(\omega)|$ = the impedance magnitude, where $|Z(\omega)| = (Z'(\omega)^2 + Z''(\omega)^2)^{1/2}$, and the phase angle $(\theta) = \tan^{-1} Z''(\omega)/Z'(\omega)$. An example of an impedance $Z(\omega)$ vector with real and imaginary (capacitive) components is shown in the complex plane plot in Fig. 4. The impedance vector indicated changes as a function of ω and is illustrated at a single frequency here.

The electrochemical impedance is a fundamental characteristic of the electrochemical system it describes. A knowledge of the frequency dependence of impedance for a corroding system enables a determination of an appropriate equivalent electrical circuit describing that system. Such a circuit is typically constructed from resistors and capacitors. Table 1 shows the transfer functions

Table 1 Linear Circuit Elements Commonly Used in Electrochemical Impedance

Circuit component	Impedance
Resistor (R)	$Z(\omega) = R$
Capacitor (C)	$Z(\omega) = -1/j\omega C$
Inductor (L)	$Z(\omega) = j\omega L$

for resistors, capacitors, and inductors. The capacitor can be a double layer capacitance, C_{dl}, alone, or a double layer capacitance and a pseudo-capacitance, C_θ, associated with an adsorbed intermediate, where q_F is the charge to form a fractional surface coverage, of such an intermediate.

$$C_T = \left(\frac{dq}{dE}\right)_T = \left(\frac{dt}{dE}\right)\left(\frac{dq_T}{dt}\right)_T = \frac{dq_T}{dE} \tag{7}$$

where $C_{dl} = dq_{dl}/dE$ and $C_\theta = dq_F/dE$. Figure 3a illustrates a simple equivalent electrical circuit model commonly used to represent an actively corroding metal. The following expression describes the impedance for that system:

$$Z(\omega) = R_s + \frac{R_p}{(1 + \omega^2 R_p^2 C^2)} - \frac{j\omega C R_p^2}{(1 + \omega^2 R_p^2 C^2)} \tag{8}$$

where $\omega = 2\pi f$, the frequency of the applied signal (rad/s), $f =$ the frequency of the applied signal (Hz), $C =$ the interfacial capacitance (F/cm^2). The complex plane, Bode magnitude, and phase plots resulting from a circuit such as is shown in Fig. 3a and described by Eq. (8) are shown for three different values of R_p in Fig. 5. It can be seen that at very low frequencies,

$$Z_{\omega\to 0}(\omega) = R_s + R_p \tag{9}$$

while at very high frequencies,

$$Z_{\omega\to\infty}(\omega) = R_s \tag{10}$$

Thus the determination of R_p is attainable in media of high resistivity because R_p can be mathematically separated from R_s by taking the difference between $Z(\omega)$ obtained at low and high ω ($R_p = Z_{\omega\to 0} - Z_{\omega\to\infty}$). In other words, determination of R_p can be achieved by subtracting the results of Eq. (10) from the results of Eq. (9). This is a particularly useful approach if R_s is nearly the same value as R_p, as shown in Fig. 6. This situation may result from either low conductivity environments or placement of the reference electrode far away from the working electrode. Note that corrosion rate determination in Eq. (3) requires knowledge of β_a and β_c, which are not obtained in the impedance experiment.

It should be noted that the presence of diffusion controlled corrosion processes does not invalidate the EIS method but does require extra precaution. In the case of a finite diffusional impedance added in series with the usual charge transfer parallel resistance shown in Fig. 3b, the frequency-dependent diffusional impedance can be described as (21)

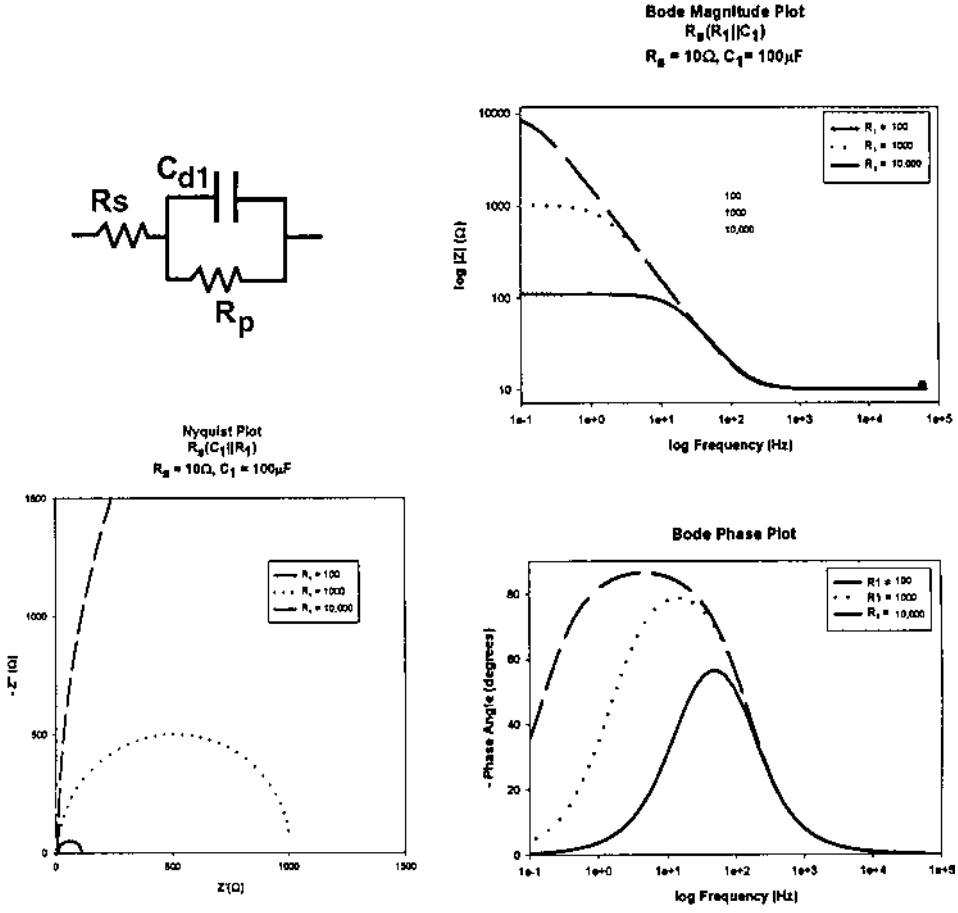

Figure 5 Nyquist, Bode magnitude and Bode phase angle plots for hypothetical corroding interfaces with $R_p = 10$, 100, or 1,000 ohms, $C_{dl} = 100$ μF, and $R_s = 10$ ohms using the electrical equivalent circuit model of Fig. 3a.

$$Z_D(\omega) = R_D\left[\frac{\tanh\sqrt{(j\,\omega s)}}{\sqrt{(j\omega s)}}\right] \tag{11}$$

Here, $s = l_{eff}^2/D$, where l_{eff} is the actual finite diffusion length and D is the diffusivity of the diffusing species. The value of $Z_D(\omega)$ approaches R_D as $\omega \to 0$. The low frequency required to obtain R_D depends on the value of s. The larger the value of s, the lower the frequency required. Therefore R_p, defined in Eq. (9) as $[\Delta E/\Delta i_{app}]$ as $\omega \to 0$, becomes the sum of the charge transfer controlled, R_{ct} and

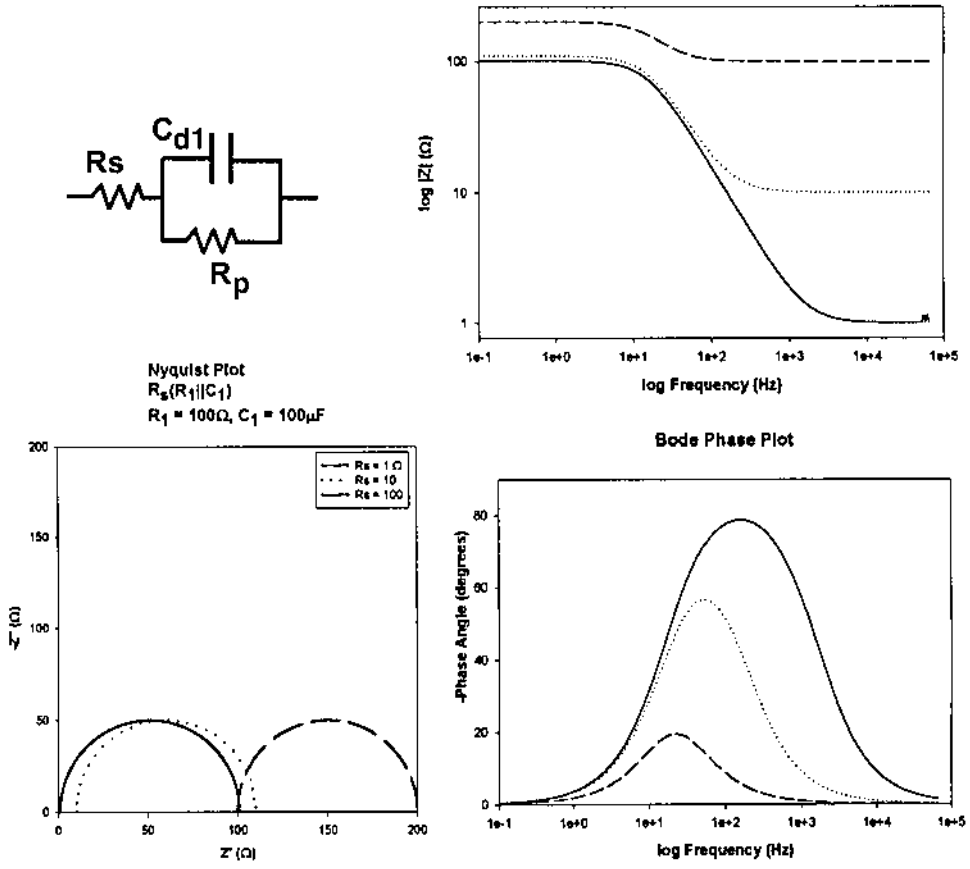

Figure 6 Nyquist, Bode magnitude and Bode phase angle plots for hypothetical corroding interfaces with R_p = 100 ohms, C_{dl} = 100 μF, and R_s = 1, 10, or 100 ohms using the electrical equivalent circuit model of Fig. 3a.

diffusion controlled, R_D, contributions to the polarization resistance, assuming that $R_D + R_{ct} \gg R_s$.

$$R_p = R_{ct} + R_D \tag{12}$$

A very low frequency or scan rate may be required to obtain R_p under such circumstances, as is illustrated in Fig. 7. Here an l_{eff} of 0.1 cm and a $D = 10^{-5}$ cm^2/s require that a frequency below 0.1 mHz be implemented to obtain R_p.

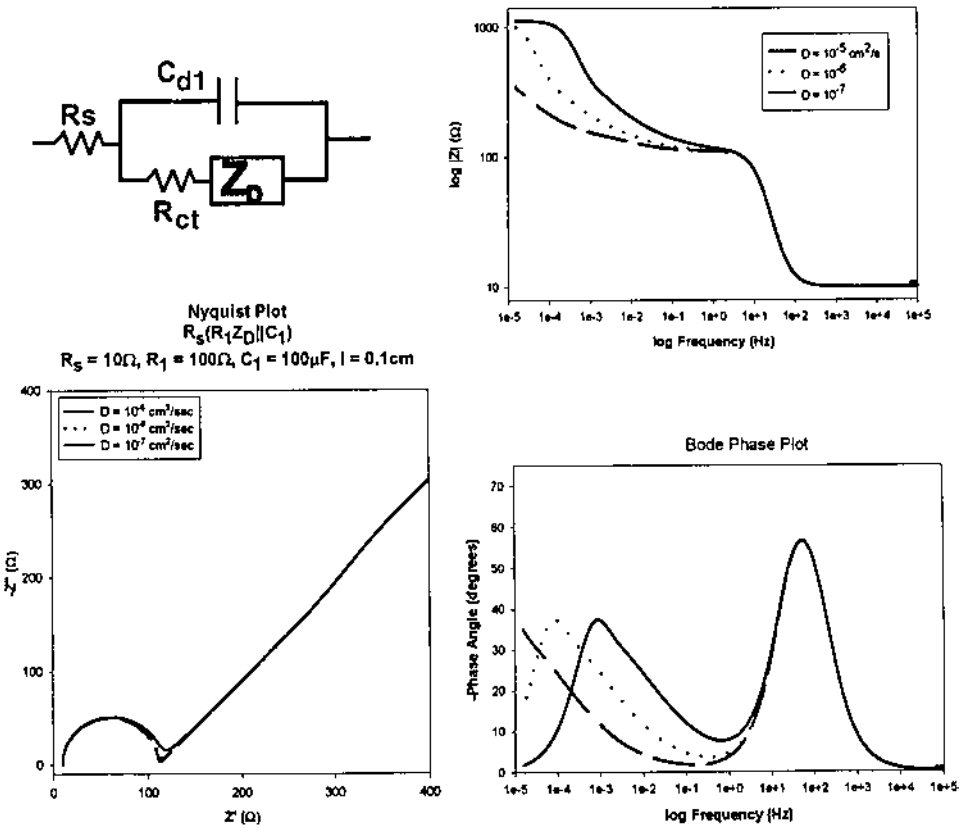

Figure 7 Nyquist, Bode magnitude and Bode phase angle plots for hypothetical corroding interfaces with $R_{ct} = 100$ ohms, $R_d = 1000$ ohms, $C_{dl} = 100$ μF, $R_s = 10$ ohms, $l_{eff} = 0.1$ cm, and $D = 10^{-5}$, 10^{-6}, and 10^{-7} cm^2/s using the electrical equivalent circuit model of Fig. 3b.

E. Complications with Polarization Resistance Measurement by the Linear Polarization Method

Error-producing complications related to the polarization resistance method and possible remedies are reported in the literature (14,15,22–27). The most common errors involve (1) invalidation of the results through oxidation of some other electroactive species besides the corroding metal in question, (2) a change in the open-circuit or corrosion potential during the time taken to perform the measurement, (3) use of ΔE that is too large, invalidating the assumption of a linear relationship between i_{app} and E required by Eq. (2) (i.e., $\Delta E/\beta < 0.1$), (4) too

fast a voltage scan rate or insufficient potential hold time, (5) ohmic solution resistance, and (6) current and potential distributions.

F. Oxidation or Reduction of Some Other Electroactive Species

If the E_{corr} of the corroding system is close to the reversible electrode potential of either the anodic or the cathodic reactions, as well as near the reversible electrode potential of any other redox process, then the corrosion rate will likely be overestimated. This situation can be experimentally ascertained by the use of any noncorroding, readily polarizable electrode, such as platinum, gold, or high-density graphite. These materials will assume a "redox" potential that is governed by the dominant parallel reduction–oxidation processes occurring in the system. If the corrosion potential of the corroding metal is very close to the "redox" potential of such an electrode, then E_{corr} may be close to a reversible electrode potential. The error in estimation of the corrosion rate depends on the exchange current density for the redox process, i_{corr}, β_a, β_c, and the difference in potentials between E_{corr} and the reversible electrode potential in question (27). A cyclic voltammogram on the platinum electrode may reveal the approximate reaction rate of any parallel redox process over the potential range of interest.

G. Deviations from Linearity Near the Open Circuit Potential

Deviations from linearity have been discussed in the literature (27–29). At issue is the question of when the range of ΔE is small enough so that the higher terms in the series expansion of Eq. (1) can be reasonably neglected. This requires that $\Delta E/\beta \ll 1$. Clearly, the extent of the E–i region, where Eq. (2) is a good approximation of Eq. (1), depends on the values of the Tafel parameters β_a and β_c. An approximately linear region can be restricted to ± 2 mV for low values of β_a and β_c and can be greater than 60 mV for high values. This curvature has been described mathematically by (27)

$$\left(\frac{\partial^2 i}{\partial E^2}\right) = i_{corr}\left(\frac{1}{(\beta_a/2.3)^2} + \frac{1}{(\beta_c/2.3)^2}\right) \tag{13}$$

Therefore, the extent of the curvature will depend on i_{corr}, which itself depends on B/R_p and is inversely proportional to the squares of β_a and β_c. Hence the curvature will be greater for smaller R_p, as indicated in Figs. 2 and 8, and smaller values of β_a and β_c. Obviously, the linear regions will differ for anodic versus cathodic polarization for differing values of β_a and β_c. Of course, the polarization resistance is always properly obtained from the tangent of the E–i data in the

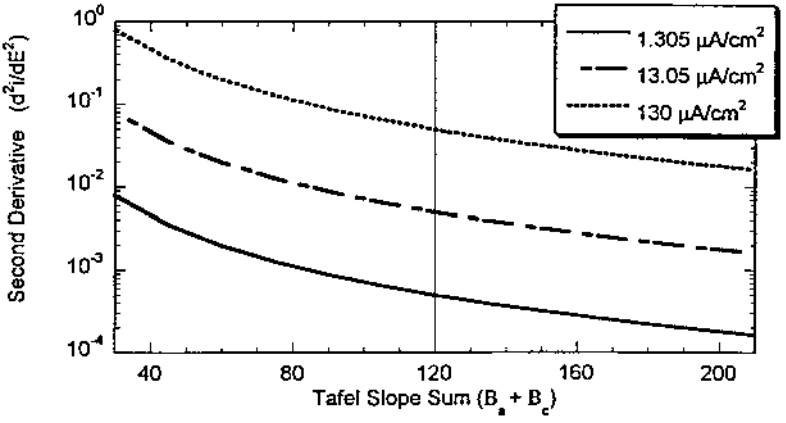

Figure 8 Second derivative of E–i data (d^2i/dE^2) versus ($\beta_a + \beta_c$) for i_{corr} = 1.305, 13.05, and 130.5 μA/cm^2, indicating that the curvature of E–i data is a function of corrosion rate and Tafel parameters.

vicinity of E_{corr}. Stated another way, there will always be finite curvature associated with the true governing electrode kinetic expression given by Eq. (1) when plotted as E vs. i, as is shown in Fig. 2. Since the E–i behavior of the corroding electrode will have a finite, albeit small, curvature, the presence of persistent linearity over a significant potential range may be a clue that ohmic voltage controls E–i behavior (27).

A second related issue is the asymmetry in the E–i response near E_{corr} for different values of β_a and β_c. Corrosion involves a cathodic electron transfer reaction that is different from the metal oxidation reaction. Therefore there is no fundamental reason why β_a and β_c should be equal, and they should be expected to differ. The extent of their difference defines the degree of asymmetry. Asymmetry matters because the extent of the region where Eq. (2) is a good approximation of Eq. (1) then differs for anodic and cathodic polarization (29). The errors in assuming ±10 mV linearity using both the tangent to the E–i data at E_{corr} and for +10 or −10 mV potentiostatic polarizations have been defined for different Tafel slopes (30).

H. Voltage Scan Rate, AC Frequency or Hold Time During Potential or Current Step

Capacitive effects cause hysteresis in small amplitude cyclic voltammogram current density–potential plots (16,31–34). Hysteresis in the current density-applied potential plot is brought about by combinations of high voltage scan rate, large

interfacial capacitances, and large polarization resistances. High capacitance multiplied by a rapid voltage scan rate causes a high capacitive current, which results in the hysteresis in cyclic E–i data. Attempting to determine R_p at too fast a scan rate can underestimate its true value as shown by Macdonald (31), leading to an overestimation of the corrosion rate. This error can be minimized by determining the polarization resistance at a slow scan rate, or extrapolating the results at several different slow scan rates to zero scan rate (31). Alternatively, one may take two or more current density measurements from potentiostatic data after long time periods near E_{corr} to minimize scan rate effects. However, cyclic voltammograms, potential steps, and current steps all represent the Fourier synthesis of sine waves, and therefore all require that adequate time be taken to perform each measurement, as will be shown below. This required time period depends on the R_pC time constant of the electrochemical interface for an electrode that does not involve mass transport controlled reactions.

The maximum scan rate allowed to obtain accurate measurement of the polarization resistance has been addressed in the literature (35). The governing principles are best understood through the concepts of impedance and the Bode magnitude plot for the simplified circuit shown in Fig. 5. Here the maximum applied frequency allowed to obtain $R_s + R_p$ from the low frequency plateau can be *approximated* by

$$f_{max} < f_{bp} = \frac{1}{2\pi C(R_s + R_p)} \tag{14}$$

where f_{bp} = an approximation of the lower breakpoint frequency (Hz) and f_{max} = the maximum test frequency (Hz). Thus it can be seen from Eq. (14) that increasing values of C, R_{sol}, or R_p dictate that a lower f_{max} is required to obtain $R_p + R_{sol}$ at $Z_{\omega\to 0}$ accurately (see Fig. 5). Capacitances may become larger than that expected from the double-layer capacitance alone in the presence of adsorption psuedo-capacitance. Such a psuedo-capacitance may be caused by an adsorbed intermediate with some fractional monolayer coverage. Corrosion of steel in concrete can complicate LPR measurements owing to very large apparent capacitances that may in fact represent mass transport control of oxygen reduction. One way that R_p may be increased is by passivity. Another is by diffusion controlled corrosion such that $R_p = R_{CT} + R_D$. A 1 mHz frequency is typically chosen as a reasonable initial choice of f_{max}, but it is obvious from Eq. (14) that either lower or higher frequencies may be required depending upon the circumstances. Since the magnitudes of C, R_s, and R_p are not known explicitly, a priori, prudence dictates that f_{max} be selected as one tenth of the estimated f_{bp}. Mansfeld and Kendig proposed that f_{max} determined by the impedance method defines the maximum voltage scan rate (V_{max}) for the potentiodynamic method (22). This derivation is

based on the assumption that the maximum voltage scan rate should not exceed the maximum rate of change of voltage with time during the sinusoidal voltage excitation at f_{max}:

$$V_{max} = \frac{\pi \Delta E_{pp} f_{max}}{10} \tag{15}$$

Here ΔE_{pp} is the peak-to-peak voltage excitation. Therefore V_{max} is 0.16 mV/s assuming a 10 mV peak-to-peak amplitude, for the equivalent circuit shown in Fig. 2 with $R_p = 1000\ \Omega$, $R_{sol} = 10\ \Omega$, and $C = 1000\ \mu F$. If ΔE is ± 5 mV, then the time required for one complete cyclic voltammogram at such a potential sweep rate is 125 seconds. However, for a slowly corroding electrode with the $R_{sol} + R_p = 10{,}010\ \Omega$, V_{max} becomes 0.0157 mV/s and the time required is 1250 seconds. Similarly, a frequency above the high-frequency breakpoint must be applied to obtain R_s:

$$f_{hf} \geq \frac{1}{2\pi C R_s} \tag{16}$$

Typically, f_{app} must be in the KHz range to determine R_s.

In separate but parallel efforts Gabrielli (32), Macdonald (31), and Townley (33) each discussed the choice of voltage scan rates for accurate R_p determination from small-amplitude cyclic voltammograms.

In these equations $a = R_s + R_p$, $b = R_s R_p C$, t is time, v = sweep rate, and $\tau = 1/R_s C + 1/R_p C$. Time in Eq. (19) can be equated to the sweep rate since $t = \Delta E_{pp}/v$. All three equations include a term that is independent of voltage scan rate and a second term that depends on voltage scan rate. The scan-rate-dependent term becomes negligible at low scan rates. Macdonald (31) and Townley (33) separately derived the current response of the standard three-element electrical equivalent circuit (Fig. 3a) to a small-amplitude triangular voltage excitation

$$\frac{1}{R_{app}} = \frac{1}{R_s + R_p} + \left(\frac{2R_p}{R_s(R_s + R_p)}\right)\left(\frac{1}{(1 + e^{a\Delta E_{pp}/vb})}\right) \tag{17}$$

(e.g., a potential sweep at fixed scan rate). The E–i response of this circuit to the triangular voltage excitation

$$\frac{1}{R_d} = \frac{1}{R_s + R_p} + \left(\frac{2R_p^2 C}{\Delta E(R_s + R_p)^2}\right)\left(\frac{(e^{a\Delta E_{pp}/vb} - 1)}{(e^{a\Delta E_{pp}/vb} + 1)}\right)v \tag{18}$$

is shown to be a complex function of circuit elements, ΔE_{pp}, and the voltage sweep rate. The results predict an

$$\frac{1}{R_{meas}} = \frac{1}{R_s + R_p} + \left(\frac{R_p}{R_s(R_s + R_p)}\right)e^{-t/\tau} \tag{19}$$

increase in current hysteresis and deviation of R_{meas} from $R_p + R_s$ at high scan rates, as is shown in Fig. 9a. Figures 9b and c show actual experimental results from a Cu–Ni alloy in flowing seawater. Macdonald characterized the E–i response by the diagonal resistance, R_d, the apparent resistance determined from the tangent to the curve at the end of the sweep before the forward and reverse sweeps reversal, R_{app}, and the hysteresis current. Townley (33) obtained R_{meas}, which is similar to the tangent resistance, R_{app}. A plot of experimental $1/R_d$ and $1/R_{app}$ data versus scan rate is shown in Fig. 9c for the Cu–Ni system. Macdonald (31) and Townley (33) both deduced that it is possible to determine $R_p + R_s$ from the tangent to the E–i curve at the end of both the forward and reverse sweeps at much higher scan rates than predicted by Eq. 15. The ideal scan rate maxima are shown in Figs. 10a and b for the same circuit parameters as examined above (i.e., $R_s = 10$ ohms, $R_p = 1000$ ohms, and $C = 10^{-3}$ F). Specifically, it is shown that $1/R_{meas}$ and $1/R_{app}$ approach the value $1/(R_s + R_p)$ at scan rates as high as 100 mV/s when the slope of the E–i plot is carefully taken at the very end of the forward or reverse voltage scan. However, accurate determination of $1/(R_s + R_p)$ from experimental $1/R_d$ values still requires a scan rate below 1 mV/s, which is in agreement with the predictions from Eq. 15. Unfortunately, the experimental case of Cu–Ni in seawater shows that a much lower scan rate is required in a real system (Figs. 9b and c). This problem is discussed further below.

The equivalence of R_{app} to $(R_s + R_p)$ at fast scan rates must be treated with caution in real corroding systems. Such an equivalence is only true for ideal fast charge transfer controlled corrosion processes and ideal double layer capacitances. The presence of either mass transport control or an adsorption pseudocapacitance caused by an adsorbed intermediate that participates in the corrosion process may complicate the results and the ability to use faster scan rates. The roles of adsorbed intermediates and mass transport in corrosion may not be observed at fast scan rates because the surface coverage and diffusional boundary layer does not have time to react and adjust to a very fast change in voltage. R_{ct} (Fig. 3b) is determined instead of R_p. Unfortunately, a sufficiently fast scan rate that "freezes in" an intermediate coverage may result in large capacitive currents as well as R_{app} and R_d values far below R_p. Indeed, Macdonald observed that an accurate value of $R_s + R_p$ was, in fact, not obtained from R_{app} or R_d values determined at fast scan rates for a corroding copper–nickel alloy in flowing seawater (Figs. 9b and c) (31). In contrast, a model like that of Fig. 3a for an ideal R_pC

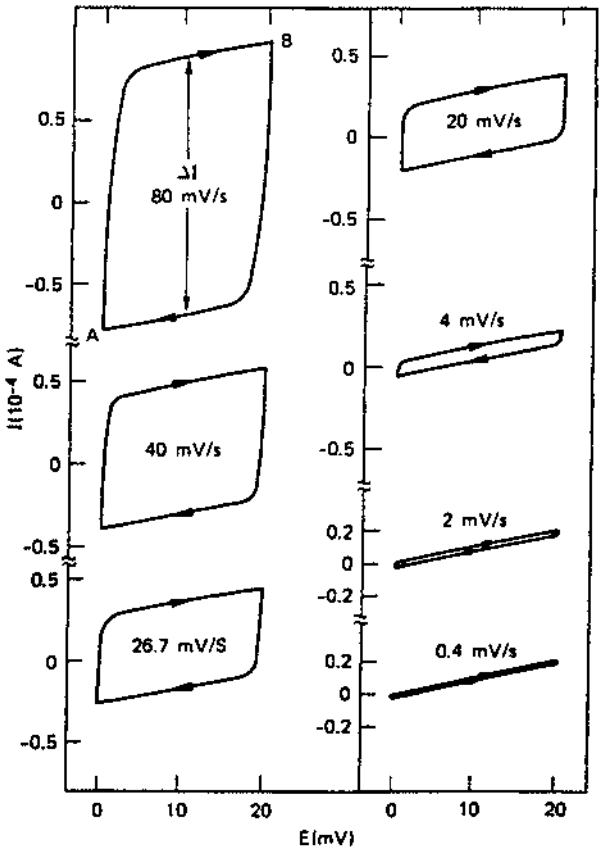

(a)

Figure 9 (a) Small-amplitude cyclic voltammograms depicting the E–i response for an electrical equivalent circuit of Fig. 3 with $R_p = 1000$ ohms, $C_{dl} = 1000$ μF, and $R_s = 10$ ohms when triangle voltage excitation waveform is applied to a corroding interface at various scan rates indicated. All results are for the circuit parameters listed above. (b) Experimental results for 90:10 Cu–Ni in flowing seawater showing cyclic voltammograms versus voltage scan rate. (c) Reciprocal values of R_d and R_{app} versus scan rate from experimental data for 90:10 Cu–Ni in seawater. (D. D. Macdonald. J. Electrochem. Soc. 125 (1978):1443. Reproduced by permission of the Electrochemical Society, Inc.)

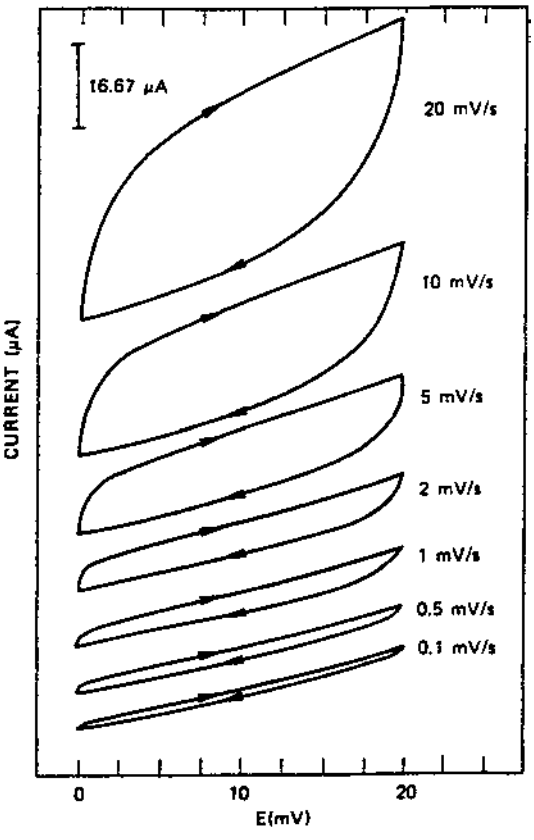

(b)

Figure 9 Continued

interface and Eqs. (17–19) suggest that 4–20 mV/s scan rates would be more than slow enough to obtain an R_{app} value that approaches R_p. Experimentally, this is not the case, as the corrosion rate would be overestimated from such data. In this system, O_2 reduction is mass transport controlled at the OCP of the Cu–Ni alloy, and adsorbed intermediates may also exist.

Jones and Greene (38) proposed that a current step method was attractive because of measurement speed and ability to contend with OCP drift during the time taken to conduct the measurement. For negligible R_s, it has been shown that the potential transient during a current step is given by

$$E_{app} = E_{corr} + i_{app}R_p(1 - \exp^{-t/R_pC}) \tag{20}$$

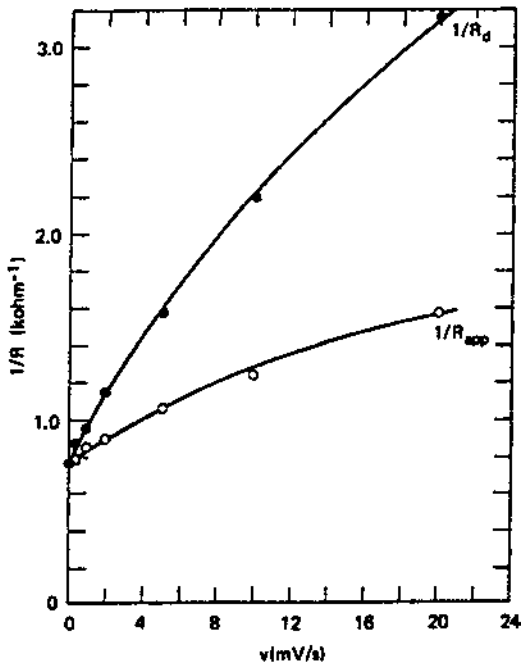

(c)

When $t \geq 4R_pC$, E_{app} reaches 98% of its value achieved at infinite time. Therefore the polarization resistance condition is reached when $t \geq 4R_pC$, or $\Delta E/i_{app} = R_p$. The time required to reach this condition is about 4 s for $R_p = 1000\ \Omega$, $R_s = 10\ \Omega$, and $C = 1000\ \mu F$. However, the time required for a slowly corroding electrode with $R_p = 10{,}000\ \Omega$ is about 40 s. Thus in comparison to polarization scans at the voltage scan rates predicted from Eq. (15), the time required for a single current step to approach steady state is much less than the time required to complete a low-amplitude cyclic voltammogram, given exactly the same electrical equivalent circuit parameters. It has also been argued that the measurement of overvoltages at selected times, after a series of small current steps, produces ΔE vs. i_{app} plots that develop linear slopes approximating the steady state conditions after incomplete short periods of decay (38).

Lastly it should be noted that the time or scan rate issue equally plagues time as well as frequency domain methods for obtaining R_p, since in the time domain measurement, the triangle waveform is simply the Fourier synthesis of a series of sinusoidal signal functions. However, voltage sweep, potential step, and impedance methods should all yield the same value of R_p when all the scan

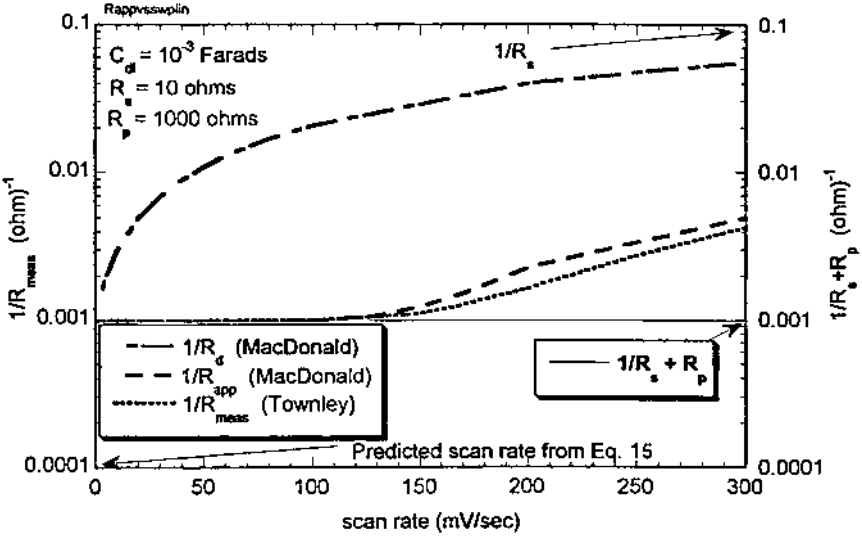

(a)

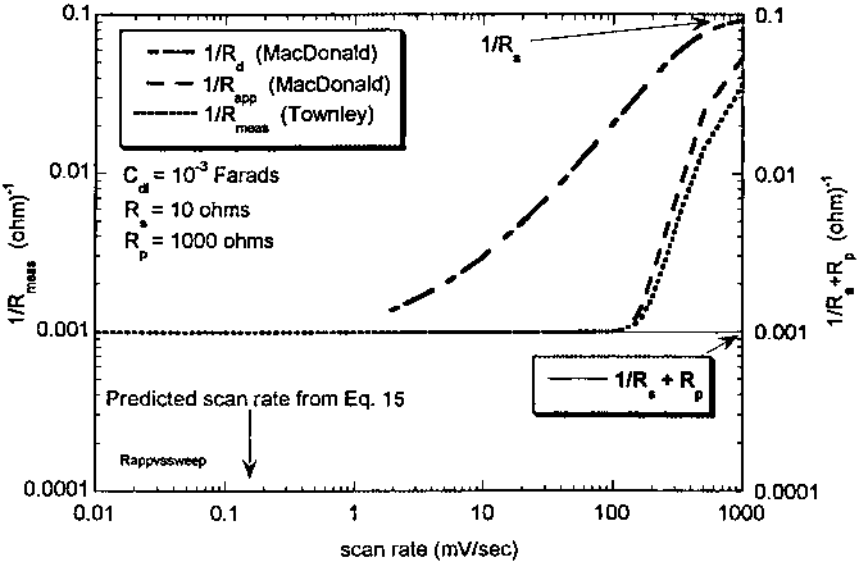

(b)

Figure 10 Relationship between measured R_{app}, R_d, and R_{meas} and scan rate using Eqs. (17), (18), and (19) for the circuit model of Fig. 3a with R_P = 1000 ohms, C_{dl} = 1000 μF, and R_s = 10 ohms The true impedance of the system at the limit of zero scan rate is R_s + R_p. The true impedance of the system at infinite scan rate is R_s. (a) Linear scale. (b) Logarithmic scale.

rate and AC frequency precautions given above are taken into consideration. This has been demonstrated by Syrett (39) in a study that produced R_p values that were independent of voltage excitation waveform.

I. Effect of Solution Resistance

Another frequently encountered complication is the need to correct polarization data for errors that arise from the contribution of solution resistance, R_s. Solution resistance contributes to a voltage error as well as a scan rate error (2). Since the applied potential is increased by an ohmic voltage component, an apparent value of polarization resistance is obtained that overestimates R_p by an amount equal to R_s. Consequently, the corrosion rate is underestimated.

J. Nonuniform Current and Potential Distributions to Polarization Resistance Probes

A dimensionless parameter known as the *Wagner* number is useful for qualitatively predicting whether a current distribution will be uniform or nonuniform (2,40,41). This parameter helps to answer the question, Which current distribution applies to my cell: primary, secondary or tertiary?

The Wagner parameter, W, is the ratio of the kinetic resistance to the ohmic resistance. The Wagner parameter is the ratio of the true polarization slope given by the partial derivative, $\partial E_{true}/\partial i_{app}$, evaluated at the overpotential of interest at constant pressure, temperature, and concentration, divided by the characteristic length and the solution resistance (2,40).

$$W = \left(\frac{\kappa}{L}\right)\left(\frac{\partial E}{\partial i}\right) \tag{21}$$

where κ (or $1/\rho$) is the specific solution conductivity $(\text{ohm-cm})^{-1}$ and L is a characteristic length (cm) or the dimension of "irregularity." Its value marks the transition from the primary to the secondary current distribution. When the Wagner number is much less than one, the ohmic component dominates, and current and potential distributions are governed primarily by cell geometry. When it is much larger than one, the kinetic component dominates and the resistance of the interface primarily governs the current flow from counterelectrode to working electrode. In practice, the primary current distribution is said to exist when $W < 0.1$ and the secondary current distribution exists if $W > 10^2$. We can take the partial derivative, $\partial E/\partial i$, of any analytical expression describing the interfacial

potential E_{true} as a function of i_{app} or obtain a polarization slope, R_p, from experimental E vs. i_{app} data. The partial derivative, $\partial E/\partial i$, has the units of Ω-cm^2. The solution resistance expressed in the same units is (κ/L). The resulting Wagner number in the low overpotential region where the linear E–i approximation is valid is

$$W = \frac{R_p}{R_s} \tag{22}$$

Thus the experimenter interested in estimating the current distribution regime pertinent to their polarization cell can estimate whether the primary or secondary current distribution applies from knowledge of R_p and R_s. The corrosion engineer can use this information in the following way. If the primary current distribution applies ($W < 0.1$), then current distributions are likely to be very nonuniform unless an ideal cell geometry leading to a uniform primary current distribution is used. Otherwise, errors in polarization resistance and other kinetic parameters are likely, because the electrode area actually undergoing polarization differs from the total area. Low scan rate data still gives $R_p + R_s$, but the area required to compute a true R_p value is uncertain.

Errors in polarization resistance from nonuniform primary or secondary current distributions have been documented (42). Data presented in the literature show examples of the extent of such errors (43). Positioning of the reference electrode at the center, at the edge, and at infinity with respect to the disk-shaped working electrode altered the apparent polarization resistance value by some amount relative to the true value. Placement at the edge is typical of flush-mounted probes. The source of difference between R_p and R_{eff} with position lies in that no single R_s value applies for all electrode positions. In other words, there is in fact a nonuniform ohmic potential drop over the disk. There can be large errors depending on reference electrode position (center, infinity, edge), conductivity, and resistance (43). When solution conductivity, κ, and R_{eff} are increased, the Wagner number becomes larger, indicating a more uniform current distribution and minimization of this source of error. Similarly, counter and reference electrode placement in low conductivity can alter solution resistance values and apparent polarization resistance values (44).

III. SUMMARY

The polarization resistance method, when performed properly, enables reliable determinations of instantaneous corrosion rates (45). Possible sources of error include violating linearity, high solution resistance, fast scan rates or inadequate

hold times, parallel redox reactions, and nonuniform current and potential distributions.

REFERENCES

1. J. O'M. Bockris, A. K. N. Reddy. Modern Electrochemistry 2. New York, Plenum Press, 1970.
2. E. Gileadi. Electrode Kinetics for Chemists, Chemical Engineers and Materials Scientists. VCH, 1993.
3. D. A. Jones. Principles and Prevention of Corrosion. New York, Macmillan, 1992.
4. M. Stern, R. M. Roth. J. Electrochem. Soc. 104 (1957):390.
5. M. Stern, A. L. Geary. J. Electrochem. Soc. 105 (1958):638.
6. M. Stern, A. L. Geary. J. Electrochem. Soc. 104 (1957):56.
7. I. Epelboin, C. Gabrielli, M. Keddam, H. Takenouti. In: Electrochemical Corrosion Testing, STP 727 (F. Mansfeld and U. Bertocci, eds.). ASTM, 1981, p. 150.
8. M. Stern, E. D. Weisert. Experimental observations on the relation between polarization resistance and corrosion rate. ASTM Proceedings 59, American Society for Testing and Materials, 1959, p. 1280.
9. Test methods for corrosivity of water in the absence of heat transfer (electrical methods), D Annual Book of ASTM Standards 03.02, ASTM, pp. 2776–2779.
10. Standard practice for conducting potentiodynamic polarization resistance measurements. ASTM Standard G-59, ASTM Annual/Book of Standards, ASTM.
11. F. Mansfeld. In: Electrochemical Techniques for Corrosion (R. Baboian, ed.). Houston, TX, NACE, 1977, p. 18.
12. D. A. Jones, N. D. Greene. Corrosion 22 (1966):198.
13. D. A. Jones. Corrosion 39 (1983):444.
14. K. B. Oldham, F. Mansfeld. Corros. Sci. 13 (1973):813.
15. F. Mansfeld. J. Electrochem. Soc. 120 (1973):515.
16. D. D. MacDonald, M. C. H. McKubre. In: Electrochemical Corrosion Testing, STP 727 (F. Mansfeld and U. Bertocci, eds.). ASTM, 1981, p. 110.
17. A. J. Bard, L. R. Faulkner. Electrochemical Methods: Fundamentals and Applications. John Wiley, 1980.
18. F. Mansfeld. Corrosion 36(5) (1981):301.
19. F. Mansfeld, M. W. Kendig, S. Tsai. Corrosion 38 (1982):570.
20. Practice for verification of algorithm and equipment for electrochemical impedance measurements. G 106 Annual Book of ASTM Standards 03.02, ASTM.
21. D. R. Franceschetti, J. R. Macdonald. Electroanal. Chem. 101 (1979):307.
22. F. Mansfeld, M. Kendig. Corrosion 37(9) (1981):556.
23. R. Bandy, D. A. Jones. Corrosion 32 (1976):126.
24. M. J. Danielson. Corrosion 36(No. 4) (1980):174.
25. J. C. Reeve, G. Bech-Nielsen. Corros. Sci. 13 (1973):351.
26. L. M. Callow, J. A. Richardson, J. L. Dawson. Br. Corrosion J. 11 (1976):132.
27. F. Mansfeld, K. B. Oldham. Corrosion Sci. 27 (1971):434.

28. S. Barnartt. Corros. Science 9 (1969):148.
29. R. L. Leroy. Corrosion 29 (1973):272.
30. F. Mansfeld. Corrosion 29 (1973):397.
31. D. D. MacDonald. J. Electrochem. Soc. 125 (1978):1443.
32. C. Gabrielli, M. Keddam, H. Takenouti, V. Kirk, F. Bourelier. Electrochem. Acta 24 (1979):61.
33. D. W. Townley. Corrosion 47 (1991):737.
34. D. D. Macdonald. J. Electrochem. Soc. 125 (1979):1977.
35. F. Mansfeld, M. Kendig. Corrosion 37 (1981):545.
36. S. R. Taylor, E. Gileadi. Corrosion 51 (1995):664.
37. K. Videm, R. Myrdal. Corrosion 53 (1997):734.
38. D. A. Jones, N. D. Greene. Corrosion 22 (1966):198.
39. B. Syrett, D. D. MacDonald. Corrosion 35 (1979):505.
40. J. Newman. Electrochemical Systems. Englewood Cliffs, NJ, Prentice Hall, 1973.
41. C. Wagner. J. Electrochem. Soc. 101 (1959):225.
42. W. C. Ehrhardt. In: The Measurement and Correction of Electrolyte Resistance in Electrochemical Cells. ASTM STP 1056 (Scribner, Taylor, eds.), (1990), pp. 5–26.
43. K. Nisancioglu. Corrosion J. 43 (1987):258.
44. M. A. Pech-Canul, A. A. Sagues, P. Castro. Corrosion J. 54(8) (1998):663.
45. J. R. Scully. Corrosion 56(2) (2000):199.

5
The Influence of Mass Transport on Electrochemical Processes

I. INTRODUCTION

In order to make a valid assessment of the thermodynamic tendency for corrosion to occur, the chemical potentials of all relevant species that participate in the reaction and their concentrations, as well as the system temperature and pressure, must be known. While thermodynamic prediction methods (i.e., Pourbaix diagrams) can be used to determine whether an electrochemical reaction can occur, information on electrochemical reaction rates is not provided.

The information required to predict electrochemical reaction rates (i.e., experimentally determined by Evans diagrams, electrochemical impedance, etc.) depends upon whether the reaction is controlled by the rate of charge transfer or by mass transport. Charge transfer controlled processes are usually not affected by solution velocity or agitation. On the other hand, mass transport controlled processes are strongly influenced by the solution velocity and agitation. The influence of fluid velocity on corrosion rates and/or the rates of electrochemical reactions is complex. To understand these effects requires an understanding of mixed potential theory in combination with hydrodynamic concepts.

In this chapter you will learn that proper assessment of mass transport controlled corrosion reactions requires knowledge of the concentration distribution of the reacting species in solution, certain properties of the electrolyte, and the geometry of the system. A rigorous calculation of mass transport controlled reaction rates requires detailed information concerning these parameters. Fortunately, many of the governing equations have been solved for several well-defined geometries.

This chapter is divided into two sections. The first will present some of the basic phenomenological observations regarding solution velocity effects and provide a framework for explaining them using mixed potential electrochemical theory. The concept of the limiting current density will be introduced. The second

section will review the mass transport correlations developed for the rotating disk and cylinder electrodes as well as the pipe and impinging jet geometries. Lastly, the effect of the fluid shear stress on protective surface films will be discussed. The emphasis of the chapter is on single-phase liquid systems. In cases where solid particles or bubbles interact with metallic surfaces to produce mechanical and electrochemical damage, the procedures discussed below must be modified or adjusted to account for these effects.

II. PHENOMENOLOGICAL OBSERVATIONS

Figure 1 qualitatively summarizes some of the effects of solution velocity on various mass transport controlled corrosion situations (1). The corrosion rate of bare metals is often observed to increase with solution velocity but becomes fixed at high solution velocities. This is an example of a situation where the cathodic reaction is under mass transport control until high solution velocities are reached. The anodic reaction is charge transfer controlled. At high velocity, both anodic and cathodic reactions are charge transfer controlled. The Evans diagram of Fig. 2 illustrates this phenomenon. Recall that the corrosion rate at open circuit (the corrosion potential) is defined by the point on the Evans diagram where the anodic and cathodic reaction rates are equal. By examining this point on the Evans diagram as a function of velocity, the trend shown in Fig. 1 can be established. It must be recognized that either the cathodic or anodic reaction can be the rate-limiting step in the overall corrosion process. The corrosion rate of many nonpassivating metals and alloys in neutral solutions is often determined by mass transport control of the cathodic reaction. One classic example of a mass transport controlled cathodic reaction is the oxygen reduction reaction on steel in aerated neutral sodium chloride solution (2,3). Here the low bulk oxygen concentration in room temperature aqueous solutions (typically 8 ppm = 0.25 mM/liter) limits the cathodic reaction rate on cathodically polarized structures. However, the supply of oxygen from the bulk solution to the reacting interface is enhanced by fluid flow. At fixed intermediate cathodic potentials the mass transport controlled reaction rate (vertical cathodic reaction line in Fig. 2) will continue to increase with increasing flow rate until charge transfer control is established. The transition to a velocity-independent cathodic reaction rate signifies the change from mass to charge transfer control.

It is useful now to describe the origins of the shape of the anodic and cathodic E–log i behaviors shown in Fig. 2. Note that the anodic reaction is linear on the E–log i plot because it is charge transfer controlled and follows Tafel behavior discussed in Chapter 2. The cathodic reaction is under ''mixed'' mass transport control (charge transfer control at low overpotential and mass transport control at high overpotential) and can be described by Eq. (1), which

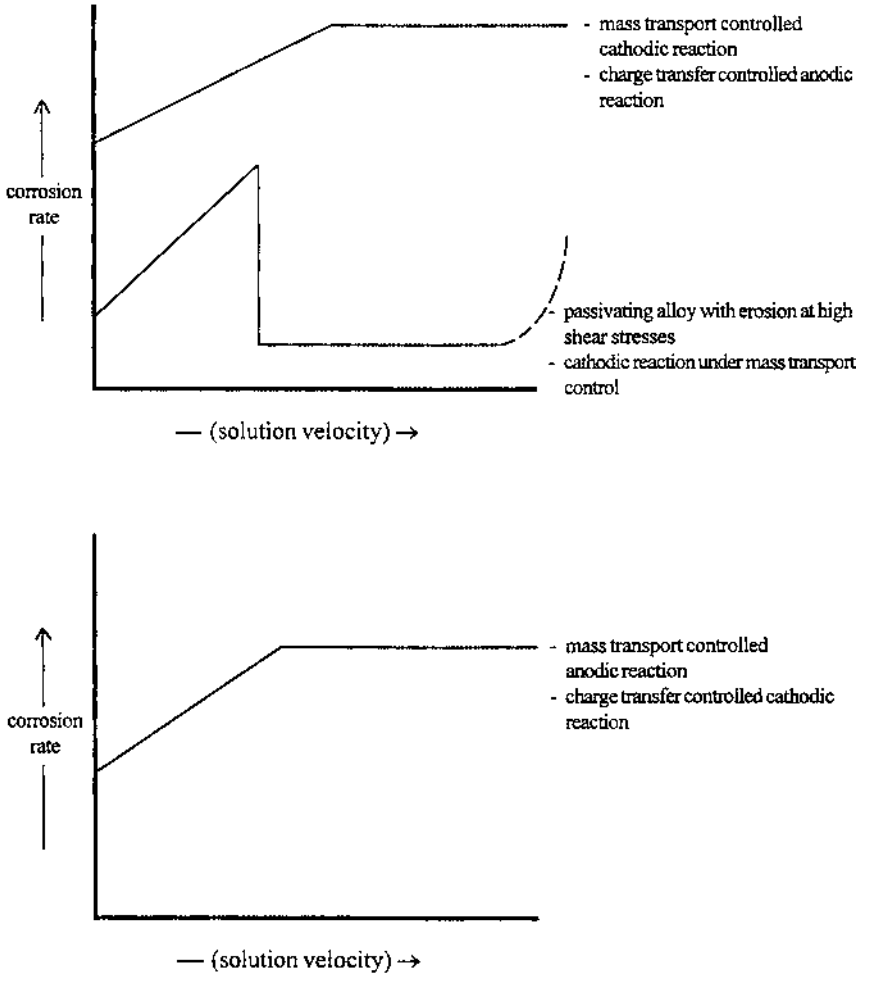

Figure 1 Phenomenological observations concerning the influence of solution velocity on metal corrosion rates.

can account for the vertical reaction line. The vertical line indicates that the mass transport controlled cathodic reaction rate is independent of applied potential. In this potential regime, the interfacial cathodic reaction rate is fast enough that the reacting species is depleted at the reacting surface. In order to maintain the reaction rate, diffusion of the reacting species through the electrolyte becomes the kinetic limitation. The cathodic reaction may be under ''mixed'' charged transfer

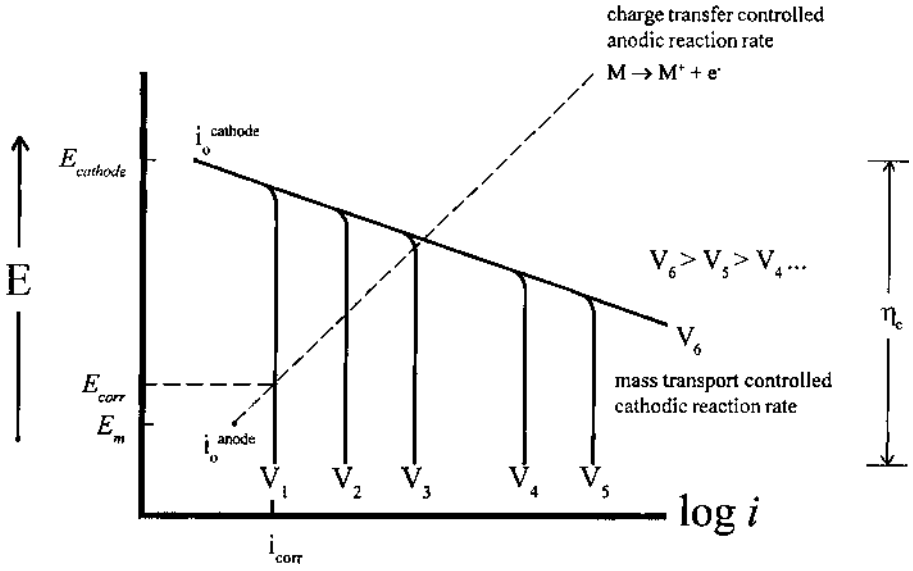

Figure 2 Evans diagram illustrating the influence of solution velocity on corrosion rate for a cathodic reaction under ''mixed'' charge transfer–mass transport control. The anodic reaction shown is charge transfer controlled.

mass transport or full mass transport control for many realistic corrosion situations, particularly if the cathodic reaction is O_2 reduction. The polarization behavior associated with mixed control can be described mathematically by the algebraic sum of the cathodic Tafel equation and the expression for mass transport control. The reaction becomes completely diffusion controlled at the limiting current density, i_L:

$$\eta_c = -\beta_c \log\left(\frac{i_{ca}}{i_o}\right) + \frac{2.3RT}{nF} \log\left(1 - \frac{i_{ca}}{i_L}\right) \tag{1}$$

where

i_{ca} = the true cathodic current density
i_L = the limiting current density defined by Fick's first law at steady state
n = the number of electrons consumed to complete the reduction reaction a single time
β_c = the cathodic Tafel slope
i_o = the exchange current density for the cathodic half cell reaction

and R, T, and F have their usual meanings.

As i_{app} approaches i_L, the cathodic overpotential, η_c, becomes very large and the cathodic reaction rate becomes independent of overpotential. For a completely mass transport limited cathodic reaction, the concentration of the reacting specie in solution, C_b, approached zero at the electrode interface and $i_{corr} = i_L$. This is shown at V_1 and V_2 in Fig. 2. The limiting current density is increased by increasing solution stirring or rotation rate, ω, in the case of a rotating cylinder or disk electrode. The corrosion rate would be increased.

An analogous situation can exist for the case of a charge transfer controlled cathodic reaction and a mass transport controlled anodic reaction. This can also account for a corrosion rate that increases with solution velocity but is independent of velocity at high velocities, as shown in Fig. 1. One example of a system exhibiting this behavior is rapidly corroding Fe in concentrated H_2SO_4. Slightly soluble $FeSO_4$ is precipitated and lowers the corrosion rate as it thickens to account for anodic mass transport control at low solution velocities (Fig. 3) (4,5). At extremely high velocities the reaction may become charge transfer controlled when bare Fe is exposed. This may occur as a result of elimination of the deposited sulfate deposit by rapid transport of dissolved $FeSO_4$ away from the interfacial region. Once all of the precipitated layer is removed, the anodic reaction rate cannot be increased further by additional stirring, and the anodic reaction rate,

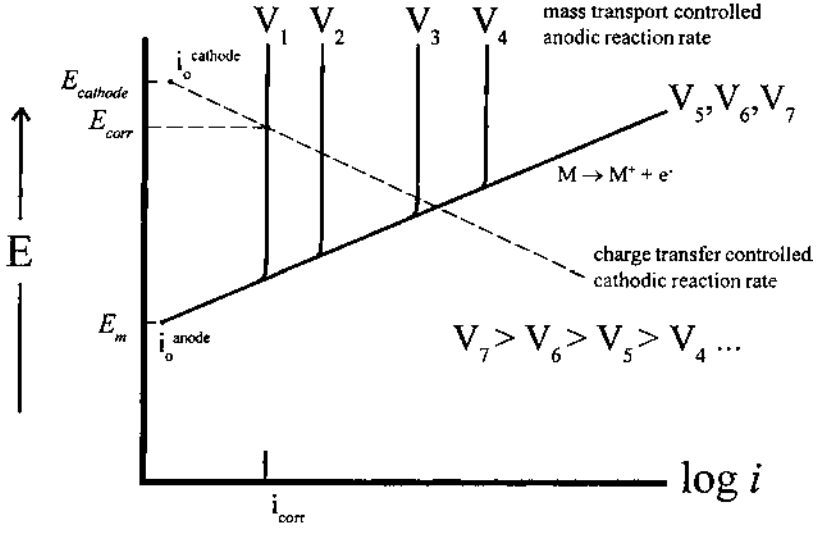

Figure 3 Evans diagram illustrating the influence of solution velocity on corrosion rate for an anodic reaction under ''mixed'' charge transfer–mass transport control. The cathodic reaction shown is charge transfer controlled. E_{corr} and i_{corr} at V_1 is shown.

and therefore the corrosion rate, becomes independent of velocity. It is useful now to describe the corresponding origins of the shape of the anodic and cathodic reaction lines on the Evans diagrams of Fig. 3. Note that the cathodic reaction is linear on the E–log i plot because it is charge transfer controlled and follows the Tafel behavior as discussed in Chapter 2. The anodic reaction is under mixed mass transport and charge transport control and can be described by and equations similar to that given by Eq. (1).

For passivating alloys, corrosion rate may at first be increased with velocity until the critical potential for passivation (e.g., the primary passive potential, E_{pp}) is exceeded. At this point the alloy becomes passivated, and the corrosion rate is much lower until extremely high shear stresses produce erosion corrosion (Fig. 1). An example of this is Fe–18Cr–8Ni alloys in concentrated H_2SO_4 + HNO_3 mixtures at elevated temperatures (1). Figure 4 provides an electrochemical description of this phenomenon using mixed potential theory. This Evans diagram illustrates an anodic reaction for an electrode that can be passivated above E_{pp} and a mass transport controlled cathodic reaction. Again, the interception of the anodic and cathodic reaction rates defines the corrosion potential.

A protective film may be physically removed at still greater velocities by high shear stresses. In fact, some Cu alloys have good corrosion resistance in seawater that is attributed to the formation of a protective oxychloride film. It has been theorized that high fluid velocities produce shear stresses that alter or

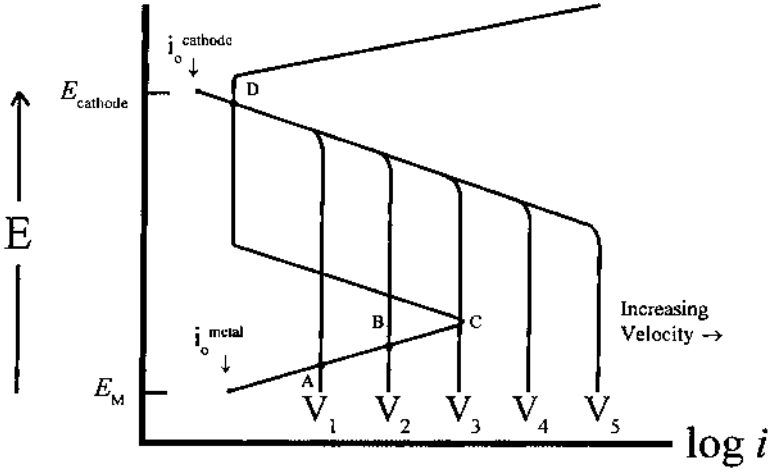

Figure 4 Evans diagram illustrating the influence of solution velocity on corrosion rate for a passivating electrode exhibiting an active–passive transition. The cathodic reaction shown is under ''mixed'' charge transfer–mass transport control.

strip off these films (5). Such behavior should be characterized by an abrupt increase in corrosion rate at a certain critical flow velocity. Such behavior has been observed for 316 stainless steel in a molten salt mixture at 493°C (7).

III. THEORETICAL ORIGINS OF THE LIMITING CURRENT DENSITY

Now let us discuss the origins of the limiting current density i_L introduced above and how it is affected by solution velocity. Recall that when the cathodic reaction is nearly mass transport limited, the concentration of the reacting specie (C_s) approaches zero at the electrode surface (Fig. 5). However, at a distance far away from the reacting electrode, the bulk concentration (C_b) is unaffected by the depletion of this reactant at the electrode surface. Near the electrode surface the concentration profile decreases with time and eventually reaches zero at the electrode surface. In this situation, the limiting c.d. defines the maximum rate at which the reaction can take place. The actual concentration profile is given by a curved line in Fig. 5, but for simplicity we will assume it to be a straight line as represented here by the dashed line. The distance from the electrode to the position where the dashed line crosses a horizontal line representing the bulk concentration defines the Nernst diffusion layer thickness, δ. δ is approximately 0.05 cm in un-

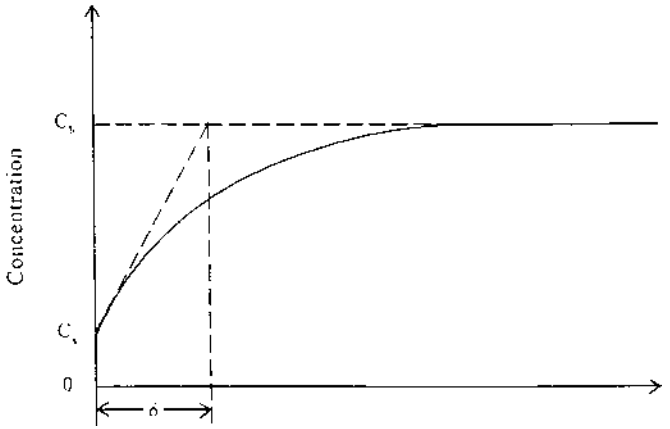

Figure 5 Schematic plot of cathodic specie concentration profile for a mass transport controlled cathodic reaction with the electrode–solution interface at the far left. The solid line represents the actual concentration profile. The dashed line from C_s to C_b represents an approximating linear concentration gradient. Its interception with the horizontal line representing C_b defines an approximation of the mass transport boundary layer.

stirred solution and 0.01 cm in lightly stirred solution. However, our objective will be to determine it precisely. The mass transport controlled reaction rate is given by Fick's first law under steady-state conditions. For the case of one-dimensional mass transport (8) this gives

$$J = -D * \frac{\Delta C}{\delta_d} (\text{moles/cm}^2 \times \text{s}) \tag{2}$$

where D is the diffusion coefficient for the reacting species and J is the flux. $\Delta C = C_b - C_s$, where C_b and C_s are the bulk and surface concentrations, respectively. The negative sign indicates that transport is in the direction of the negative of the concentration gradient for the cathodic reaction. In terms of electrochemical current density Eq. (2) may be rewritten as

$$i_L(\mu\text{A/cm}^2) = -JnF = -nFD * \frac{C_b - C_s}{\delta} \tag{3}$$

where $F = 96{,}487$ coulombs/equivalent and $n =$ equivalent/mole or the number of electrons transferred when the half cell reaction is completed a single time. In the case of anodic mass transport limitation, the concentration C_s becomes the saturation concentration for the sparingly soluble corrosion product forming on the metal surface. Note that the limiting current density in both cases is independent of the exact electrode material (of course, this is only true over a range of potentials where neither charge transfer control nor mixed control can be maintained). Can you think of a situation in which the properties of the electrode material might influence δ_d? (Hint: For a diffusion boundary layer established across a material-specific porous suface film.)

Either anodic or cathodic mass transport limited corrosion may be observed in numerous corrosion systems. Such phenomena may be simulated and investigated in the laboratory by establishing experimental conditions that match those in the field application. This is accomplished by equating i_L or δ_d in the laboratory to the same values present in the field. In this way the effect of fluid velocity or mass flow rate on the corrosion rate may be investigated. Similarly, the hydrodynamic conditions in the field must be matched by those in the laboratory. Procedures for establishing such correlations between field and laboratory measurements are described below.

IV. USE OF MASS TRANSPORT CORRELATIONS FOR UNDERSTANDING MASS TRANSPORT CONTROLLED CORROSION

The corrosion engineer concerned with mass transport controlled corrosion is interested in determining the limiting current density for a variety of geometries

and flow situations. Hundreds of mass transport correlations exist in the literature for various systems of interest to the corrosion engineer (4,9). For convenience most mass transport solutions are expressed in terms of dimensionless parameters. In this section we briefly review the typical dimensionless parameters utilized in the correlations presented below.

At low velocities between the metal and the solution, the solution flow is laminar, while at high velocities it is turbulent. The transition velocity depends on the geometry, flow rate, liquid viscosity, and surface roughness. The Reynolds number accounts for these effects and predicts the transition from laminar to fluid turbulent flow. The Reynolds number is the ratio of convective to viscous forces in the fluid. For pipes experiencing flow parallel to the centerline of the pipe (4,8):

$$\mathrm{Re} = \frac{V * d}{\nu} \text{ (unitless)} \tag{4}$$

where V is the solution velocity (cm/s), d is a characteristic length (cm), and ν is the kinematic viscosity (cm^2/s). The kinematic viscosity is equal to the fluid viscosity (μ) divided by its density (ρ). For rotating cylinders and disks an angular velocity terms is used instead, where $V = r\omega$. Here r is the radius of the disk or cylinder and ω is the rotation rate in units of radians per second. This results in a Reynolds number expression for the disk (4):

$$\mathrm{Re} = \frac{r^2\omega}{\nu} \text{ (unitless)} \tag{5}$$

The precise transition from laminar to turbulent flow occurs at different values of Re depending on geometry. Even in turbulent flow there exists a thin laminar hydrodynamic sublayer of thickness δ_h near the metal surface. If mass transport is also occurring at the surface, there will be a diffusional boundary layer of thickness δ_d. δ_h is a function of ν while δ_d is a function of D. The Schmidt number quantifies a relationship between these two parameters:

$$\mathrm{Sc} = \frac{\nu}{D} \text{ (unitless)} \tag{6}$$

For high Sc numbers a thin diffusion layer will be produced, and it will develop rapidly, since diffusional transport is slow.

The mass transfer coefficient, K, is defined as the ratio of the mass transport controlled reaction rate to the concentration driving force. The concentration driving force will depend on both turbulent and bulk convection. Bulk convection depends on molecular diffusivity, while the turbulent component depends on ''eddy'' diffusivity (4). The mass transfer coefficient considers the combination of the two transport mechanisms, empirically.

$$K = \frac{\text{rate of reaction}}{\text{concentration driving force}} \tag{7}$$

The concentration driving force is usually expressed as ΔC, and the limiting c.d. ($J = i_L/nF$, where J is given in units of moles/cm^2-s) describes the rate of reaction, under mass transport control.

$$K = \frac{J}{\Delta C} \tag{8}$$

Hence K can be determined by measuring J at different fixed ΔC values. Mass transfer rates are defined by the Sherwood number (Sh), which is given by (4)

$$\text{Sh} = \frac{Kd}{D} = \frac{i_L d}{nFD\,\Delta C} \tag{9}$$

where d is a characteristic dimension and D is the diffusion coefficient for the reacting species. However, dimensionless analysis shows that Sh is also a function of Re and Sc. These correlations are of the form (4,7,9)

$$\text{Sh} = \text{constant}\ \text{Re}^x \text{Sc}^y \tag{10}$$

where x often varies from 0.3 to 1 and y is about 0.33. Substitution of this expression for Sh into Eq. (9) and rearrangement shows that the limiting c.d. is given by the following expression for many mass transport correlations:

$$i_L = \text{constant}\,\frac{nFD\,\Delta C}{d}\,\text{Re}^x \text{Sc}^y \tag{11}$$

Here x and y will vary with the exact geometry.

It is worth mentioning again that not all reactions will exhibit complete mass transport control at all potentials. Complete mass transport control will only occur for extremely fast (reversible) charge transfer reactions and very slow mass transport rates. Charge transfer reactions occurring only at moderate rates will by under mixed control over a certain range of potentials. Here the total cathodic current density, i_{total}, will be equal to a combination of activation controlled current density and mass transport limiting current density. i_{total} is given as

$$\frac{1}{i_{\text{total}}} = \frac{1}{i_{\text{ac}}} + \frac{1}{i_L} \tag{12}$$

Here i_{ac} is the activation controlled current density occurring when transport to the interface is very fast. To clarify this equation, consider the two processes (activation and diffusion) to occur sequentially in the overall reaction sequence. Since they occur in series, the slowest rate will dominate the overall total rate.

V. MASS TRANSPORT CORRELATIONS FOR SELECTED GEOMETRIES OF INTEREST

This section describes selected mass transport correlations for laboratory devices such as the rotating disk and cylinder. These mass transport correlations may be used in order to establish the same mass transport conditions (diffusional boundary layer thicknesses) as those obtained in a pipe or under impinging flow. Essentially, the experimenter may vary the rotation rate and geometry of the cylinder or disk to ''dial in'' the same mass transport conditions as obtained in the field for pipes or impinging jets. The user should also verify that the same hydrodynamic conditions also exist through use of Reynolds numbers, as shown above.

A. The Rotating Disk Electrode

The rotating disk electrode (RDE) is an important system in electrochemistry. Axial followed by radial flow across the disk brings fresh solution to all points across the disk (Fig. 6). The surface is therefore uniformly accessible to reacting species. The RDE operates under laminar flow for $Re < 1.7 \times 10^5$. Flow is turbulent above 3.5×10^5 and is transitional in between (4). Thus the system is less practical for the study of corrosion under turbulent conditions but enjoys widespread use in research electrochemistry. For the rotating disk electrode, the laminar mass transport correlation obtained in the literature is given by Levich (10):

$$Sh = 0.621\, Re^{0.5}\, Sc^{0.33} \tag{13}$$

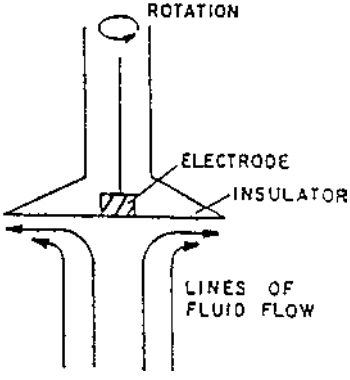

Figure 6 Cross-sectional view of the rotating disk electrode.

Recall that the limiting current density is given by

$$i_L = nF\,\Delta CK \tag{14}$$

and that K is given by

$$K = \mathrm{Sh} * \frac{D}{d} \tag{15}$$

so that

$$i_L = \frac{nFD\,\Delta C}{d}\,\mathrm{Sh} \tag{16}$$

or that

$$i_L = 0.621\,\frac{nFd\,\Delta C}{d}\,\mathrm{Re}^{0.5}\,\mathrm{Sc}^{0.33} \tag{17}$$

Moreover, it is easy to show that the limiting current density is expressed entirely in terms of readily obtained parameters: D, $\Delta C = C_b - C_s$, ω, and ν. Recall that $C_s = 0$ when the limiting c.d. is reached, yielding

$$i_L = 0.621\,nFD^{2/3}\,C_b\,\nu^{-1/6}\,\omega^{1/2} \tag{18}$$

Data is shown in Figs. 7a and 7b for oxygen reduction on carbon steel in room temperature 0.6M NaCl. i_L increases with $\omega^{0.5}$ as predicted. Hence if the corrosion rate is determined by the mass transport of oxygen to the disk surface to support oxygen reduction, then the corrosion rate will increase as a function of the rotation rate, ω, raised to the 0.5 power and linearly with dissolved oxygen concentration. The diffusion boundary layer thickness, δ_d, may be calculated from Fick's first law after i_L is determined. Recall that $\delta = nFDC_b/i_L$ for one dimensional diffusion at the steady state. This leads to the following expression for the diffusional boundary layer thickness:

$$\delta_d = 1.61\,D^{1/3}\,\nu^{1/6}\,\omega^{-1/2} \tag{19}$$

The boundary layer thickness decreases with increasing rotation rate as expected.

Figure 7 (a) Cathodic polarization data for a low carbon steel rotating disk electrode in 0.6 M NaCl with ambient aeration. Oxygen reduction limiting current densities are shown for the indicated rotation rates. (b) Plot of experimental limiting current density versus square root of the rotation rate, showing the experimental and predicted linear behavior.

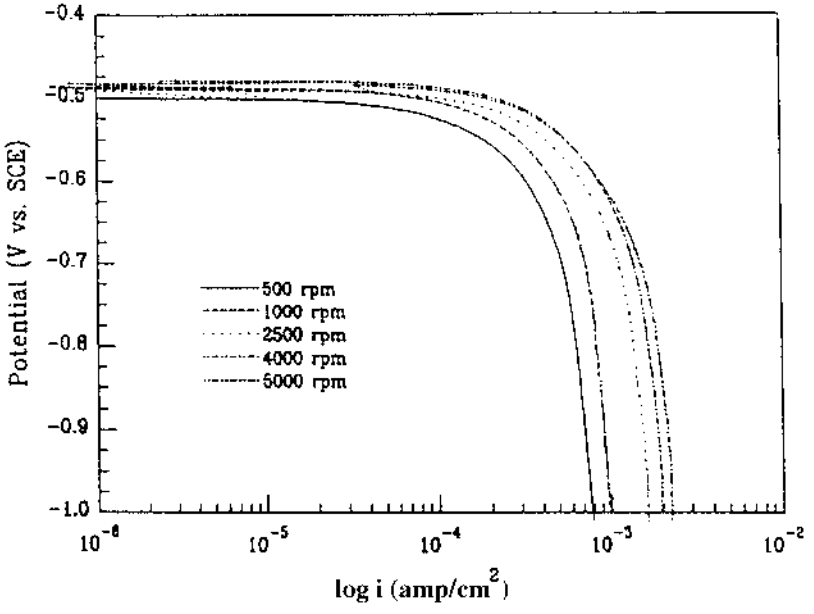
-0.4
-0.5
-0.6
-0.7
-0.8
-0.9
-1.0
Potential (V vs. SCE)
500 rpm
1000 rpm
2500 rpm
4000 rpm
5000 rpm
10^{-6}
10^{-5}
10^{-4}
10^{-3}
10^{-2}
log i (amp/cm^2)

(a)

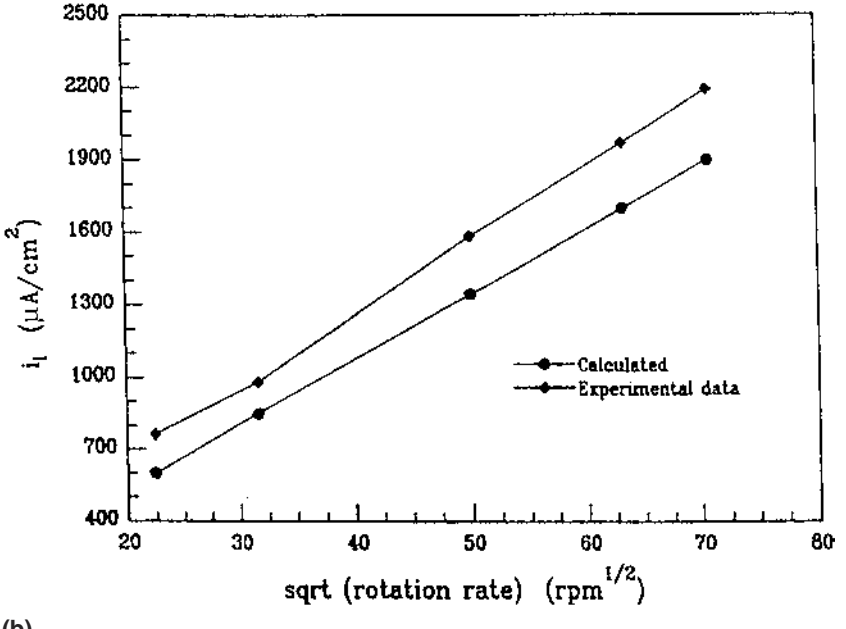
2500
2200
1900
1600
1300
1000
700
400
i_l (μA/cm^2)
Calculated
Experimental data
20
30
40
50
60
70
80
sqrt (rotation rate) (rpm$^{1/2}$)

(b)

B. The Rotating Cylinder Electrode

The rotating cylinder electrode (Fig. 8) is operated in the turbulent flow regime at Re $>$ 200, although flow can be complicated with vortexing until much higher Re, where true turbulence develops (4). A Re number $>$200 is readily achieved at modest rotation rates and cylinder diameters. Therefore the cylinder can be

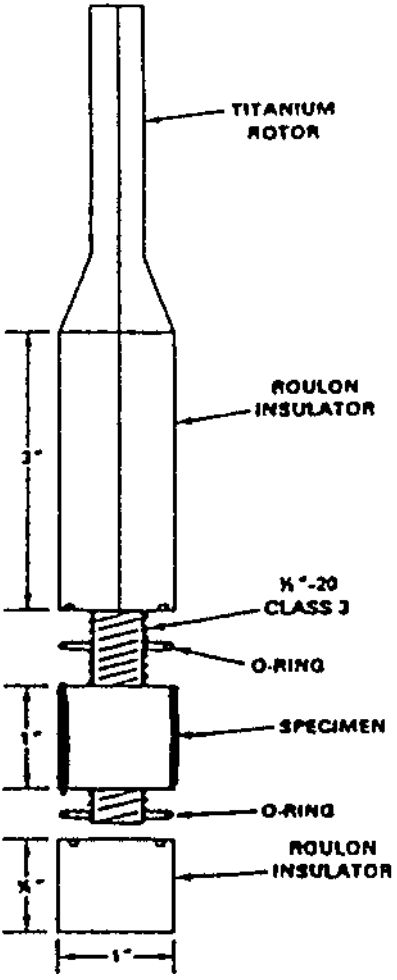

(a)

Figure 8 The rotating cylinder electrode. (a) Electrode specimen and mandrel shown as partially disassembled. (b) Typical laboratory setup for the RDE. (From Ref. 3.)

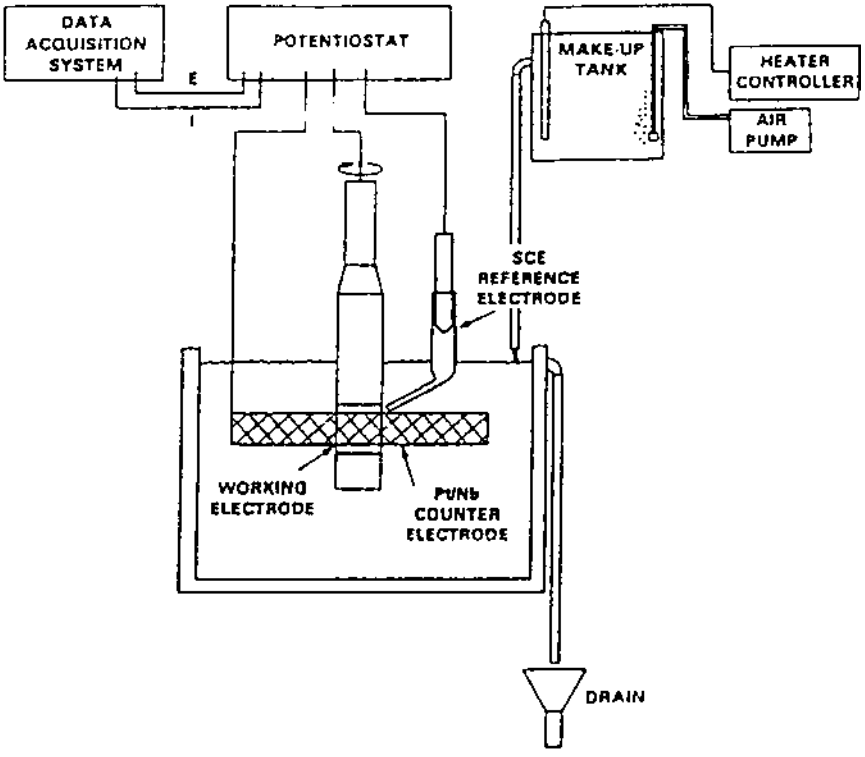

(b)

readily utilized by the corrosion engineer to simulate flowing corrosion conditions in turbulent pipes. For the smooth rotating cylinder electrode, the mass transport correlation is given by Eisenberg (11). However, surface roughening increases mass transport.

$$\mathrm{Sh} = 0.079\,\mathrm{Re}^{0.7}\,\mathrm{Sc}^{0.36} \tag{20}$$

This correlation is valid within the following range: $1000 < \mathrm{Re} < 100{,}000$ and $835 < \mathrm{Sc} < 11{,}490$. Recalling that the limiting current density is given by

$$i_l = nF\,\Delta C K \tag{21}$$

and that K is given by

$$K = \mathrm{Sh} * \frac{D}{d} \tag{22}$$

it is easy to show that the limiting current density can be expressed entirely in terms of very accesible parameters: D, ΔC, d, V, and ν, again, assuming that $C_s = 0$:

$$i_l = 0.079\, nFC_b\, (V)^{0.7}\, (D)^{0.64}\, (\nu)^{-0.34}\, (d)^{-0.3} \tag{23}$$

If the characteristic dimension is taken as the radius of the cylinder, r (recall that $V = r\omega$), throughout the calculation where $d = 2r$ we have

$$i_l = 0.064\, nFC_b\, (\omega)^{0.7}\, (D)^{0.64}\, (\nu)^{-0.34}\, (r)^{0.4} \tag{24}$$

Hence if the corrosion rate is determined by the mass transport of cathodic reactant to the cylinder surface, then the corrosion rate will increase as a function of the rotation rate raised to the 0.7 power and linearly with dissolved reactant concentration. Increasing the velocity by a factor of ten increases the corrosion rate by a factor of five. Figure 9a shows the cathodic polarization results obtained on a Ni-Cr-Mo-V alloy steel at five different rotation rates. Figure 9b illustrates that excellent agreement is obtained between the predicted limiting c.d. for oxygen reduction and those obtained experimentally. Silverman (12) has shown that the velocity of the rotating cylinder necessary to match the mass transport conditions for pipe flow, assuming the Eisenberg correlation applies, is given by

$$V_{cyl} = 0.11845 \left(\left(\frac{\rho}{\nu} \right)^{0.25} \left(\frac{d_{cyl}^{0.429}}{d_{pipe}^{0.179}} \right) \mathrm{Sc}^{-0.0857} \right) V_{pipe}^{1.25}$$

Useful velocity conversions in order to have equality of mass transport conditions between the rotating cylinder and the annulus and impinging jet are also reported by Silverman (12).

C. Flow in a Circular Tube or Pipe

Flow in circular tubes is of interest to many corrosion engineers. A large number of correlations exist for mass transport due to turbulent flow in a smooth straight pipe (4,9). The flow is transitionally turbulent at Re $\sim 2 \times 10^3$ and is fully turbulent at Re $\sim 10^5$ (4). The most frequently used expression for turbulent conditions at a straight tube wall is that given by Chilton and Colburn using the analogy from heat transfer (13):

Figure 9 (a) Cathodic polarization data for a Ni-Cr-Mo-V alloy steel rotating cylinder electrode in seawater with ambient aeration. Oxygen reduction limiting current densities are shown for the indicated rotation rates. (b) Plot of experimental limiting current density versus predicted limiting current density according to the Eisenberg correlation for selected rotation rates on different alloys. (From Ref. 3.)

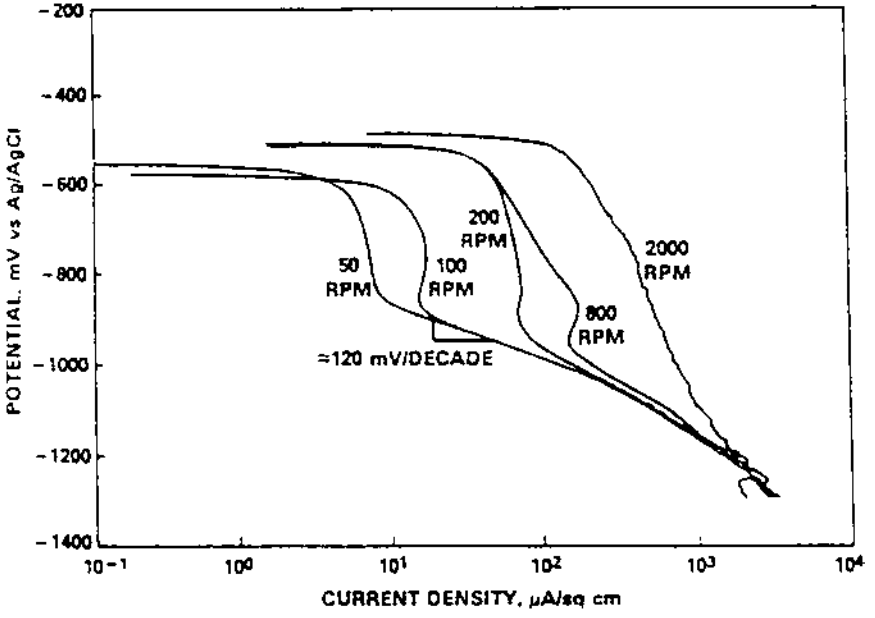
-200
-400
-600
-800
-1000
-1200
-1400
POTENTIAL, mV vs Ag/AgCl
50 RPM
100 RPM
200 RPM
800 RPM
2000 RPM
≈120 mV/DECADE
10⁻¹
10⁰
10¹
10²
10³
10⁴
CURRENT DENSITY, μA/sq cm

(a)

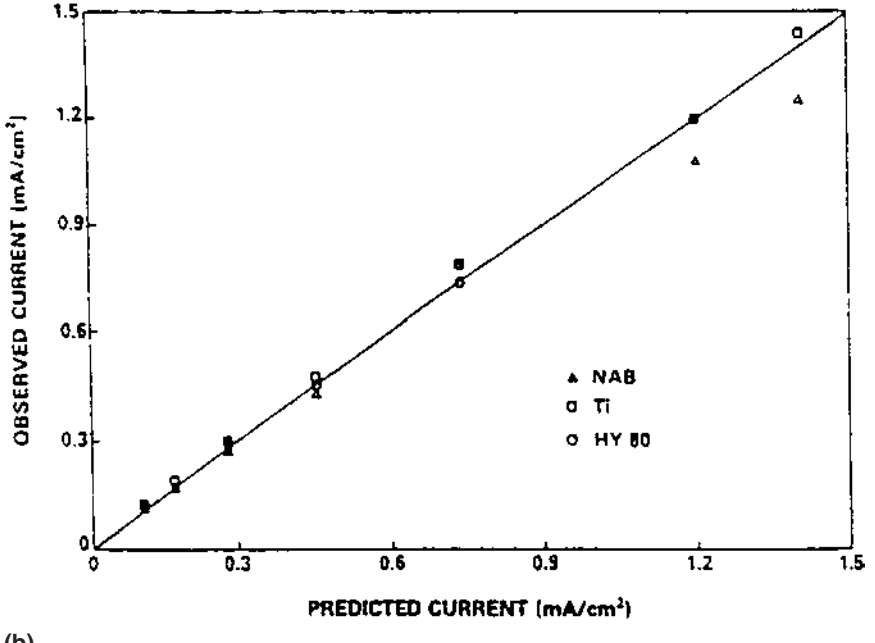
1.5
1.2
0.9
0.6
0.3
0
OBSERVED CURRENT (mA/cm²)
NAB
Ti
HY 80
0
0.3
0.6
0.9
1.2
1.5
PREDICTED CURRENT (mA/cm²)

(b)

$$\mathrm{Sh} = 0.023\,\mathrm{Re}^{0.8}\,\mathrm{Sc}^{0.33} \tag{26}$$

Recalling that the limiting current density is given by

$$i_l = nF\,\Delta CK \tag{27}$$

and that K is given by

$$K = \mathrm{Sh} * \frac{D}{d} \tag{28}$$

it is easy to show that the limiting current density is expressed entirely in terms of very familiar parameters: D, ΔC, d, V, and ν, where d is the pipe diameter:

$$i_l = 0.023\,nFC_b\,(V)^{0.8}\,(D)^{0.67}\,(\nu)^{-0.47}\,(d)^{-0.2} \tag{29}$$

Hence, if the corrosion rate is determined by the mass transport of cathodic reactant to the pipe surface, then the corrosion rate will increase as a function of the solution velocity raised to the 0.8 power and linearly with the dissolved reactant concentration. Note that at the same fluid velocity and reactant concentration, the limiting c.d. and hence the corrosion rate will be greater for pipes of smaller diameter. A similar relationship was proposed by Harriot and Hamilton (14) and applied by various investigators concerned with anodic mass transport controlled corrosion of ferrous piping materials (5,15).

$$\mathrm{Sh} = 0.0096\,\mathrm{Re}^{0.913}\,\mathrm{Sc}^{0.346} \tag{30}$$

It is logical to expect that enhanced mass transfer will occur at pipe entrances. Berger and Hae found the following relationship, where L is the length or distance from the entrance (4,16):

$$\mathrm{Sh} = 0.276\,\mathrm{Re}^{0.583}\,\mathrm{Sc}^{0.33}\,\frac{d^{0.33}}{L} \tag{31}$$

The establishment of nonentrance conditions was found to be a function of Reynolds number and flow regime (4,16). Expressions have also been utilized to describe the ''average'' limiting current density in the rectangular flow channel with plane parallel electrodes imbedded in opposite sides. Under laminar flow conditions, the current, potential, and concentration distributions have been calculated correlations and are reported in the literature (9). The complication with mass transport controlled processes in the rectangular channel is that the limiting c.d. is the greatest at the leading edge and varies with distance from the leading edge.

D. Flow from an Impingment Jet

If the incoming flow from a nozzle is at 90° to a planar metallic surface, then the flow impinges onto the metal surface and moves radially outward. The flow is redirected from being perpendicular to the planar surface to radial parallel to the surface. Mass transport solutions to this situation have been proposed and in general depend upon the ratio of vertical distance to nozzle diameter (H/d) and the radial position on the plate (x/d) as shown in Fig. 10. Chin and Tsang (4,17) showed that, for H/d between 0.2 and 6 and x/d between 0.1 and 1,

$$\mathrm{Sh} = 1.12\,\mathrm{Re}^{0.5}\,\mathrm{Sc}^{0.33}\left(\frac{H}{d}\right)^{-0.057} \tag{32}$$

for turbulent Reynolds numbers between 4000 and 16,000. Patrick proposed that mass transport in the wall jet region decreases with radial distance (4). The wall jet region begins at ~three to five nozzle diameters, and the following mass

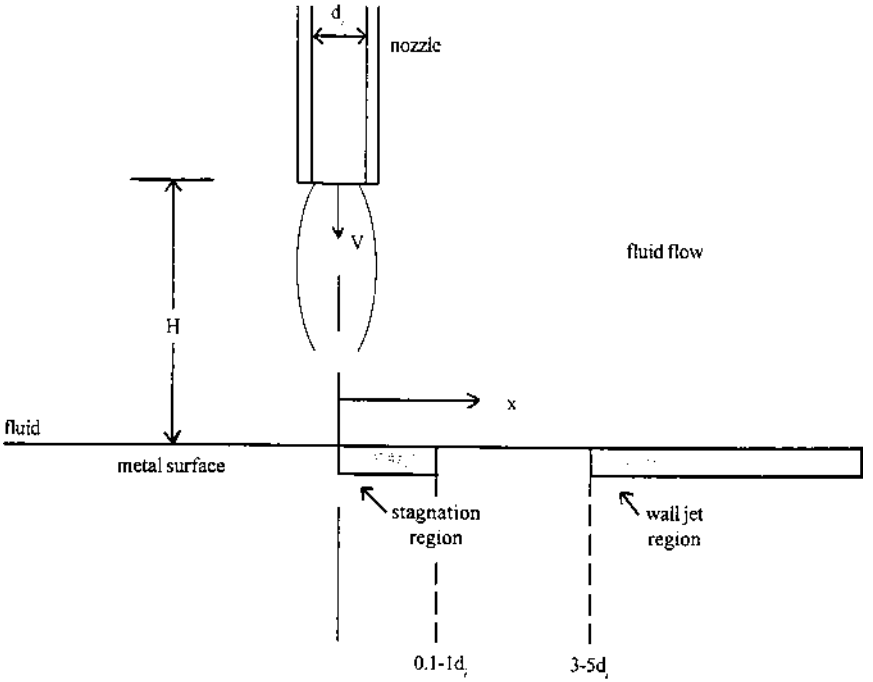

Figure 10 Schematic of the impinging fluid jet geometry showing various flow regions.

transport expression was found for $5120 < \mathrm{Re} \leq 13498$; $8 \leq x/d < 17$; $5 < h/d < 20$ (4):

$$\mathrm{Sh} = 1.14\,\mathrm{Re}^{0.82}\left(\frac{x}{d}\right)^{-1.05} \tag{33}$$

VI. THE CRITICAL SHEAR STRESS AS A MEANS TO SIMULATE THE EFFECTS OF FLUID FLOW IN CORROSION

For many years corrosion engineers have recognized that velocity controlled corrosion processes were significantly influenced by the gradient of the fluid velocity (creating a shear stress) as well as the reacting species concentration gradient with respect to the electrode surface instead of the absolute value of these parameters (7). These points are confirmed from consideration of two pipes of different diameters with the same fluid velocity. Clearly there will be different pressure drops and velocity gradients and therefore different shear stresses and mass transfer rates. A difference in velocity gradient occurs because of the boundary condition that the solution velocity approaches zero at the metal surface. Recall that the shear stress experienced by the metal surface is proportional to the gradient of fluid velocity with respect to the perpendicular distance away from the surface and the solution viscosity (8). This gradient will be larger for smaller diameter pipes operating at the same average velocity as larger pipes.

The mass transport correlations developed in the previous section are valid if the process controlling the corrosion rate is strictly the transport of a reacting specie to the electrode surface with no other influencing factors. On the other hand, it is possible to have a situation where fluid momentum transfer at the surface controls the corrosion rate. The shear stress induced by the fluid flow can strip off protective corrosion products or remove a protective corrosion-inhibiting film. Here the total metal loss rate is defined by the bare metal anodic reaction rate after mechanical stripping of the protective layer as well as by other factors such as purely mechanical erosion. The ''critical shear stress'' is the stress at which protective films are removed (6). However, it has been argued that even in cases of mass transport controlled corrosion it is useful to equate shear stresses in the laboratory to those in the field. This equality produces similar velocity gradients, similar hydrodynamic conditions, and thus similar Sherwood numbers, which contain mass transport coefficients. Hence, mass transfer can be linked to shear stress (12,15) as Silverman has reviewed relationships between mass transfer coefficients and wall shear stresses for the rotating cylinder, pipe, annulus,

and jet impingement (13). Indeed, Efird and coworkers recently found that shear stress was a useful correlating hydrodynamic parameter for the corrosion of steel under jet impingment (18). However, a shear mechanism of corrosion acceleration, per se, was not endorsed.

Hence it is useful for a variety of reasons to determine the shear stress on the electrode surface and to determine its variation with solution velocity. Laboratory tests must be able to apply the same shear stress as is obtained in the field (15). The idea then is to design the laboratory test so that the shear stress in the laboratory matches that present in the field application:

$$\tau_{lab} = \tau_{field} \tag{34}$$

However, it should be noted that equality of shear stresses in lab and field will not produce exact equality of mass transport coefficients owing to different dependencies on flow velocity, as shown below (15). Clearly, the flow regimes must be the same in the laboratory and in the field (e.g., both laminar or both turbulent).

A. The Rotating Disk Electrode

Flow is not uniform across the RDE. At high speeds the edges may be in turbulent flow, and the shear stress should vary with radial position. An average velocity or Re number value must be used in order to characterize flow. Consequently, the RDE is not favored for studying corrosion controlled by shear stresses.

B. The Rotating Cylinder Electrode

The rotating cylinder electrode utilized a specimen with a fixed diameter. Consequently, all points on the surface are exposed to the same surface velocity (excluding surface roughness effects). The RCE can be used to simulate flowing conditions present in other geometries if flow in those geometries is tangential to the electrode surface by using in the appropriate rotation rate. The surface shear stress* for the rotating cylinder is given as (15)

$$\tau \text{ (kg/m-s}^2) = \text{constant } \frac{f}{2} \rho \omega^2 r^2 \tag{35}$$

where f is the friction factor. The Re number and the surface roughness are important factors in determining the surface shear stress. For a smooth cylinder, $f/2$ is

* kg/m-s^2 is equivalent to N/m^2 or Pa, which is a shear stress term.

equal to $0.079\ \mathrm{Re}^{-0.30}$ (19). Substitution of this relationship gives the following expression for shear stress:

$$\begin{aligned}\tau\ (\mathrm{kg/m\text{-}s^2}) &= 0.079\ \mathrm{Re}^{-0.30}\ \rho\ \omega^2\ r^2 \\ &= 0.079\left(\frac{2r^2\ \omega\ \rho}{\mu}\right)^{-0.30}\ \rho\ \omega^2\ r^2\end{aligned} \tag{36}$$

Rearranging yields

$$\tau = 0.064\ (r^{1.4})\ (\omega^{1.7})\ (\rho^{0.7})\ (\mu^{0.3}) \tag{37}$$

where the shear stress is given in terms of the fluid density, ρ, the angular velocity, ω, the fluid viscosity, μ, and the cylinder radius, r. Note that the shear stress will increase as a function of the rotation rate raised to the 1.7 power. In contrast, the limiting current density increases with velocity raised to the 0.7 power for the RCE.

C. Flow in a Circular Pipe

The shear stress for flow in a pipe is given by the following expression, where all terms have their usual meaning (12,15,19):

$$\tau = \frac{f}{2}\rho\ V^2 \tag{38}$$

here the friction factor for a smooth tube is given by (19):

$$f = 0.079\ \mathrm{Re}^{-0.25} \tag{39}$$

for $2.3 \times 10^3 \leq \mathrm{Re} \leq 10^5$, or for $\mathrm{Re} \geq 10^5$, then (19):

$$f = 0.046\ \mathrm{Re}^{-0.2} \tag{40}$$

for $\mathrm{Re} \geq 10^5$. The former case yields the following relationship:

$$\tau = 0.040\ (V)^{1.75}\ (\mu)^{0.25}\ (d)^{-.25}\ (\rho)^{.75} \tag{41}$$

It was shown above that the limiting c.d. increases with velocity raised to the 0.8 power and the pipe diameter raised to the -0.2 power for piping corrosion rates that are controlled by mass transport. In contrast, it is evident that the shear stress increases with the fluid velocity raised to the 1.75 power and the pipe diameter raised to the -0.2 power. Thus equality of shear stress does not give equality of mass transfer rates. In both cases corrosion is enhanced in pipes of smaller diameter for the same solution velocity. Such a relationship can be rationalized based on the effect of pipe diameter on the thickness of the mass transport and hydrodynamic boundary layers for a given fixed geometry. Cameron and Chiu (19) have derived similar expressions for defining the rotating cylinder rotation rate required to match the shear stress in a pipe for the case of velocity-

influenced corrosion. In their derivation, pipe flow is defined in terms of volumetric flow rate. This form may be more convenient to the corrosion engineer.

An alternative version of the same expression describing flow-induced shear stresses for a circular pipe operating in the turbulent flow regime is described by the relation (6)

$$\tau \left(\frac{\text{force}}{\text{unit area}} \right) = \frac{fv^2\rho}{2g_c} \tag{42}$$

where g is a dimensional constant = 32.17 lb.-ft/(lb. force-s^2) and all other terms have their usual meanings. It is also evident from this expression that the shear stress increases with the fluid velocity raised to the 1.8 power and the pipe diameter raised to the -0.2 power, as shown above. Thus the shear stress is higher in smaller diameter pipes.

D. Impingment Jet

If the incoming flow from a nozzle is at right angles to a planar metallic surface, the flow impinges onto the metal surface and moves radially outward. The flow is redirected from being perpendicular to the planar surface to radial parallel to the surface at a distance of three to five nozzle diameters (wall jet region). The shear stress for the ''wall jet'' beyond the stagnation point has been given by Giralt and Trass (20,21) for $x/d > \sim$2-3 and Reynolds numbers in the range $2.4 \times 10^4 < \text{Re} < 1.25 \times 10^5$ (12):

$$\tau = 0.0447\, \rho\, V^2\, Re^{-0.182} \left(\frac{x}{d} \right)^{-2.0} \tag{43}$$

Here as before, the diameter of the nozzle is d, and x is the distance from the centerline of the jet as shown in Fig. 10.

E. Other Geometries

Silverman has defined a number of useful expressions that allow one to utilize the rotating cylinder method with a variety of practical geometries (12,15). Both shear stresses and mass transfer coefficients are included in the derivations described (12). Table 1 in NACE standard TM-0270-72 summarized the various features of experimental systems for studying flow induced corrosion (22).

VII. CORROSION AND EROSION

Many practical situations exist in which metal loss occurs from both erosion of a nonelectrochemical nature and corrosion phenomena. The question arises as to appropriate test methods. One suggestion has been to duplicate the test conditions

discussed above using the Sherwood number–Reynolds number correlations to calculate mass transfer coefficients (12). These calculated coefficients may then be compared to experimentally determined coefficients derived from mass loss. In this case of cavitation-induced corrosion, an ASTM standard exists that places the metal test specimen at the end of a vibrating transducer to generate bubble collapse in aqueous solutions (7,23).

REFERENCES

1. M. G. Fontana, N. D. Greene. Corrosion Engineering. McGraw-Hill, 18–21 (1978).
2. J. R. Scully, H. P. Hack, D. G. Tipton. Corrosion J. 42(8), 462–469 (1986).
3. R. Guanti, H. P. Hack. Determination of the best hydrodynamic parameter for modelling flow on cathodically polarized surfaces. Corrosion 1987, Paper No. 267, NACE, Houston, TX (1987).
4. B. Poulson. Corrosion Sci. 23(4), (1983).
5. B. T. Ellison, W. R. Schmeal. J. Electrochem. Soc. 125, 524 (1978).
6. K. D. Efird. Corrosion J. 33(1), 3 (1977).
7. S. W. Dean. Materials Performance 29(9), 61 (1990).
8. R. B. Bird, W. E. Stewart, E. N. Lightfoot. Transport Phenomena. John Wiley (1960).
9. J. R. Selman, C. W. Tobias. In: Advances in Chemical Engineering 10, 212 (1978).
10. V. G. Levich. Physico-Chemical Hydrodynamics. Prentice-Hall, Englewood Cliffs, NJ (1962).
11. M. Eisenberg, C. W. Tobias, C. R. Wilke. J. Electrochem. Soc. 101(6) (1954).
12. D Silverman. Corrosion J. 42–49 (1988).
13. T. H. Chilton, A. P. Colburn. Ind. Eng. Chem. 26, 1183 (1934).
14. P. Harriot, R. M. Hamilton. Chem. Eng. Sci. 20, 1023 (1965).
15. D. Silverman. Corrosion 1983, Paper No. 258, NACE, Houston, TX (1983).
16. T. K. Ross, D. H. Jones. J. Appl. Chem. 12, 314 (1962).
17. D. T. Chin, C. H. Tsang. J. Electrochem. Soc. 1461, 125 (1978).
18. K. D. Efird, E. J. Wright, J. A. Boros, T. G. Hailey. Corrosion, 992 (1993).
19. G. R. Cameron, A. S. Chiu. Electrochemical techniques for corrosion inhibitor studies. In: Electrochemical Techniques for Corrosion Engineering (R. Baboian, ed.), 183–189, NACE (1986).
20. F. Giralt, D. Trass. Can. J. Chem. Eng. 53, 505 (1975).
21. F. Giralt, D. Trass. Can. J. Chem. Eng. 54, 148 (1976).
22. Guidelines for conducting controlled velocity laboratory corrosion experiments. NACE Standard TM-0270-72.
23. ASTM Standard G-32. Standard method for cavitation erosion using vibratory apparatus. ASTM Volume 03.02, Wear and Erosion; Metal Corrosion, ASTM, Philadelphia, PA (1993).

6
Current and Potential Distributions in Corrosion

I. INTRODUCTION

A. Empirical Observations

Current and potential distributions are of great interest in cases where the anode and cathode are separated as in the case of cathodic protection, bimetal galvanic corrosion, pitting corrosion, crevice corrosion, stress corrosion, and local galvanic corrosion caused by the presence of inclusions, precipitate phases, or any other kind of surface heterogeneity (1–6). Moreover, current and potential distributions are of interest in laboratory or field two- and three-electrode polarization cells where errors in the measurement of electrode kinetics and polarization resistance may occur due to nonuniformity in current and potential distributions (1). In all of these situations, it is of great interest to understand the *local* electrochemical potential at the electrode interface (i.e., across the double layer), the local current density, and the possible errors in kinetic parameters (e.g., polarization resistance, Tafel slopes, etc.). On the other hand, current and potential distributions are *not* of great interest to the corrosion engineer in the case of freely corroding metals uniformly corroding, since local anodic and cathodic reactions occur at equal rates on the same surface, and balancing ionic current flow between anodes and cathodes occurs on a very local basis.

Let us begin with two common observations involving separated anodes and cathodes. The cathodic protection level obtained on metallic surfaces is often noted to vary with position. The metal is usually less well protected as the distance of the metal surface from the sacrificial or impressed current anode increases. Alternatively, the structure may be overprotected at positions close to the anode, leading to potentially embrittling hydrogen production. Similarly, it is well known that it is more difficult to plate metals electrolytically or "throw" current into corners or recesses, while exposed edges may receive a thicker plating deposit. The main explanation for this behavior is that the aqueous solution

Table 1 Resistivities of Some Metallic and Ionic Conductors at 20°C

Conductor	Resistivity (ohm-cm)	Conductivity $(\text{ohm-cm})^{-1}$
Copper wire	1.72×10^{-6}	0.58×10^{6}
Seawater	25	0.04
Soil	2500	0.0004

has a finite ionic conductivity, especially compared to the electrical conductivity of the metal. Note the significant differences in resistivity of metallic copper compared to seawater and soil as shown in Table 1.

The finite conductivity of aqueous solutions leads to an ohmic voltage "loss" or drop in the aqueous solution when ionic current flows between separated anodes and cathodes. This voltage drop consumes some of the total voltage driving force otherwise available to increase the overpotential at the electrode surface. Note that there may be other causes of local variations in electrochemical current and potential. For instance, the concentrations of reacting species in solution may vary locally, leading to local differences in conductivity and/or reaction rates. However, the main cause of current distributions is the separation (distance) between anodes and cathodes, irregular cell geometry, in combination with the finite conductivity of the electrolyte. These factors all affect the local overpotential that is achieved at the electrode surface of interest and ultimately affect the local galvanic corrosion rate or the cathodic protection level.

B. The Effect of Ohmic Resistance on Two- and Three-Electrode Cells

Finite electrolyte conductivities and ionic current flow lead to ohmic voltage components in electrochemical cells. It is constructive at this point to review the effects of ohmic voltage contributions to driven and driving cells in the case of uniform current distributions. It will be shown that for each type of cell, the ohmic resistance lowers the true overpotential at the electrode interface for a fixed cell voltage even in the case of a uniform current distribution at all points on the electrode.

The most typical cell arrangement for the corrosion engineer involves a three-electrode configuration with working, reference, and counter electrodes, as shown in Fig. 1. If we wish to polarize the working electrode to some applied potential, E_{app}, differing from the mixed potential, E_{corr}, in the presence of a finite solution resistance between our reference and working electrodes, then E_{app} is given by the following equation, where the terms have the same meanings as developed in earlier chapters:

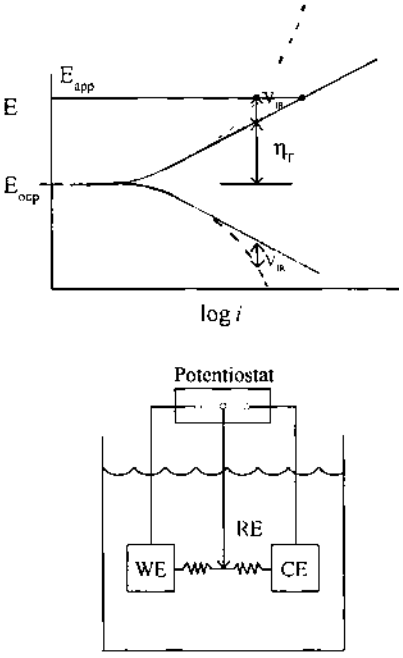

Figure 1 Influence of IR voltage error on E_{app} in a three-electrode polarization cell. E_{app} is increased for both anodic and cathodic polarization. A larger E_{app} than theoretical must be applied to achieve the same true overpotential, η_{true}. The resistors between the working electrode (WE), reference electrode (RE), and counter electrode (CE) signify the finite solution conductivity.

$$E_{app} = \eta_{true} + iR_{\Omega} + E_{corr} \tag{1}$$

Obviously, the E_{app} is increased by a finite value for nonzero R_{Ω} values. Note that the potential applied is greater than it would be in the absence of iR_{Ω} voltage for a fixed current density, but the true overpotential is less than it would otherwise be at fixed E_{app}. Said another way, a greater E_{app} must be applied to obtain the true overpotential desired. Recall that the applied overpotential is the sum of the true overpotential and the iR_{Ω} voltage drop (the product of the current density and the solution resistance) (2). The greater the product of these terms, the greater the chance that the true surface overpotential differs from the applied overpotential.

$$\eta_{app} = \eta_{true} + iR_{\Omega} \tag{2}$$

Here $\eta_{true} = E_{true} - E_{corr}$, and the product of I (A/cm^2) and R_{Ω} (ohm-cm^2) produces volts. Note that E_{true} is the exact local potential across the metal–solution interface

(i.e., the double layer measured with respect to a reference electrode) and not the potential of the metal itself. The engineer has only the option of controlling E_{app}, and consequently η_{app}, which equals $E_{app} - E_{corr}$. Hence if iR_Ω varies spatially over the surface, then it follows that E_{true} must vary spatially as well, even though the engineer maintains a single E_{app}. iR_Ω does not effect an anodic reaction and a cathodic reaction occurring on the same surface at equal and opposite rates. Therefore electrode geometry does not affect the uniform corrosion rate of a homogeneous metal or alloy, or electroless metal plating.

Similarly, for a galvanic couple (driving system) between two materials, A and B, of differing E_{corr}, the difference in E_{corr} values between A and B must equal the overpotentials on both the anode and the cathode as well as any IR voltage which is present.[1]

$$E^{A}_{corr} - E^{B}_{corr} = \sum\eta_{anode} + |\sum\eta_{anode}| + IR_\Omega \tag{3}$$

From this equation it can been seen that as the ohmic resistance increases, the remaining voltage driving force available to increase the overpotentials of the anode or cathode is diminished. Consequently smaller total current, I, flows through the cell. This is shown in Fig. 2, where in the absence of a finite R_Ω there is a single galvanic couple potential. A similar argument can be developed for the case of a driven two-electrode system.

C. Verification of Spatially Varying True Overpotentials

So far, we have discussed the effects of ohmic resistance for cells with completely uniform current distributions. That is, the distance, geometry, and ionic resistivity governed R_Ω term was assumed to be the same at all positions on the electrode surface. Consider the hypothetical cell in Fig. 3. Note that the top working electrode has the shape of a half-sinusoidal wave and is consequently further away from the flat counterelectrode at one position and closer at another. Therefore the solution path length varies, producing a large "effective" R_Ω at the position where the separation distance is greatest. Even though the same applied potential (E_{app}) on the working electrode may be "dialed in" from the potentiostat, using a reference electrode located at a fixed distance from the bottom flat electrode shown in Fig. 3, the true overpotential at the surface may differ owing to the position-dependent differences in R_Ω. It is apparent from Eq. (1) that the local value of η_{true} must be less for a given E_{app} if the product of i_{local} and R_Ω is greater, locally, at positions where the distance between the two electrodes is greater.

In the case of a nonpolarizable cell (e.g., small or zero η_{true} at any current

[1] In the case of galvanic corrosion, total current, I, is used instead of current density, i. The galvanic current associated with the anode must equal that from the cathode, or i^{*}_{A} area$_A$ = i^{*}_{B} area$_B$. In order for the last term in Eq. (3) to yield volts, R_Ω must have units of ohms.

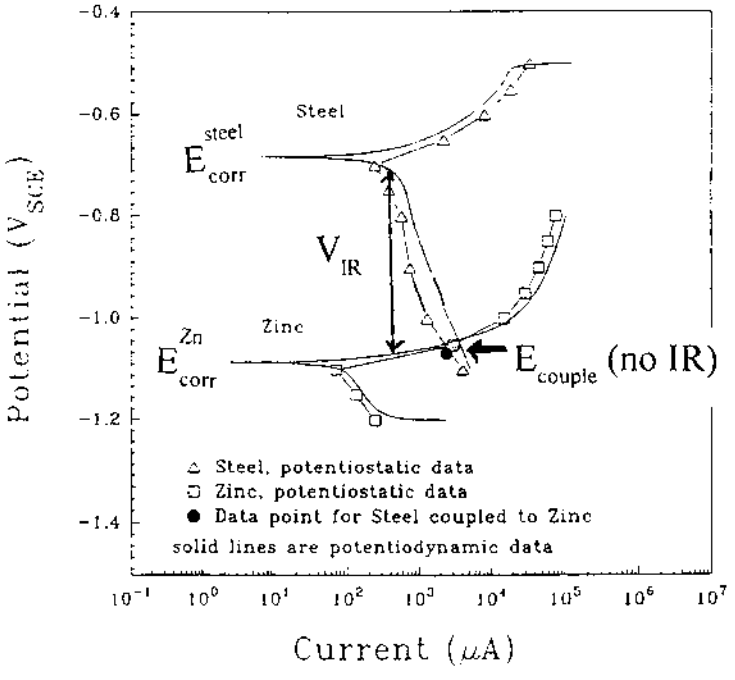

(a)

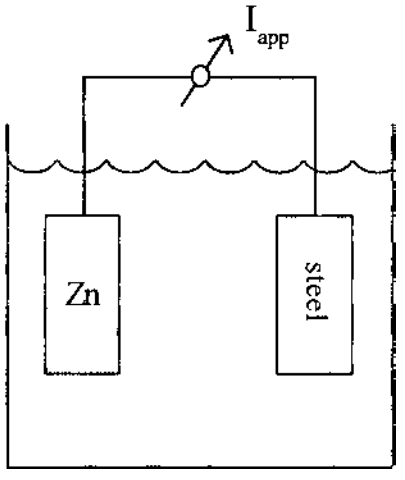

(b)

Figure 2 Influence of IR voltage error on galvanic corrosion. Increasing IR voltage error decreases the extent of anodic polarization of the anode and cathodic polarization of the cathode.

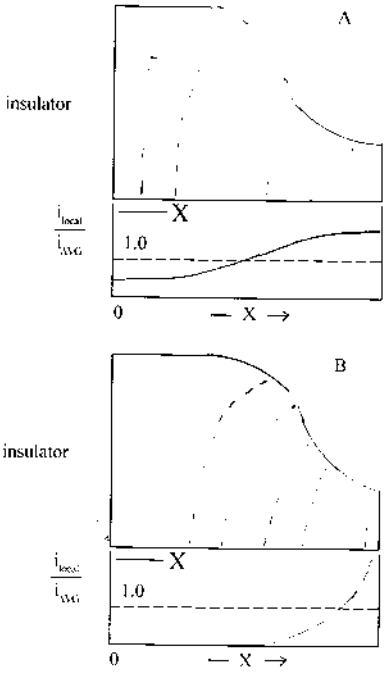

Figure 3 Sinusoidal two-electrode cell with insulating boundaries. In the primary current distribution, all current flow occurs at the peak in the sinusoid. For increasing ratios of R_p/R_Ω, the current uniformity increases.

density, I), the ohmic resistance, R_Ω will have controlling influence on the current distribution. For polarizable cells (e.g., η_{true} large at any current density, I) the effect of ohmic resistance may be negligible, as η_{true} is the dominant term in Eq. (1). This point will be developed and discussed further below.

D. Rules Used to Describe Isopotential and Current Lines

It is useful now to describe a few rules pertinent to current and potential distributions prior to discussing specific geometries (1).

1. Current lines are perpendicular to "isopotential lines" otherwise known as equipotential lines, which are lines of constant potential in two dimensions or surfaces of constant potential in three dimensions. Current lines do not terminate at insulating surfaces.

2. Isopotential lines or surfaces are perpendicular to insulator material surfaces because current cannot flow into the insulator.

3. Isopotential lines are parallel to the electrode surfaces for what is known as the primary current distribution (no interfacial electrode polarization, or zero polarization resistance). Said another way, the solution adjacent to an electrode surface is an equipotential surface (1). This primary current distribution applies to the case of extremely fast electrochemical reactions (e.g., nonpolarizable electrode reactions). This current distribution situation is only of interest to the corrosion engineer in cases where high current densities might be flowing (i.e., in relatively nonpolarizable cells).

4. Isopotential lines may vary with electrode position for the secondary and tertiary current and potential distributions, where interfacial polarization of various types is considered. The variation of local true potential across the electrochemical interface with electrode position is of great interest in galvanic corrosion, cathodic protection, etc., since this true potential drives electrochemical reactions.

These rules for the case of a flat electrode with an insulating edge at various angles are shown in Fig. 4. Note that the lines of constant potential or isopotential lines (solid) are perpendicular to the dotted lines, indicating the path taken by the current in the solution. The current density is greatest at positions where the current lines are crowded close together. The primary current distribution is a function of angle greater than or less than 90°. At angles greater than 90° between insulator and electrode, the primary current density approaches infinity. At angles

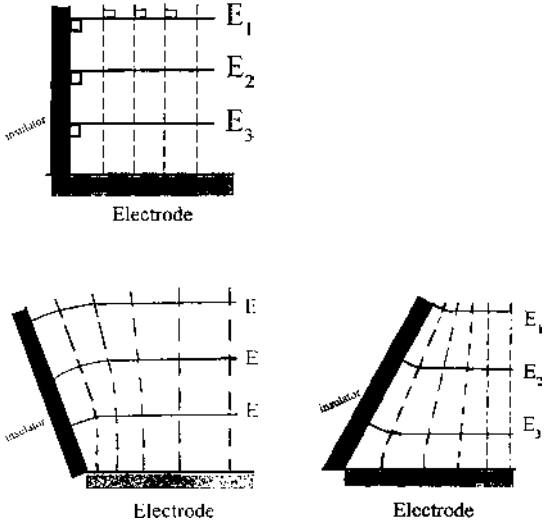

Figure 4 Primary current distribution rules applied to the case of a flush mounted electrode with an insulating edge of various angles.

less than 90° it approaches zero. Potential gradients are greatest where isopotential lines of widely different values are closest together. It will be shown below that the local current density is a function of the potential gradient. So, in order to proceed in understanding current distribution effects in corrosion, we must review the factors governing the magnitude of local current densities.

E. Theoretical Considerations Concerning Current Distributions

Ions can be transported through an electrochemical solution by three mechanisms. These are migration, diffusion, and convection. Electroneutrality must be maintained. The movement of ions in a solution gives rise to the flow of charge, or an ionic current. Migration is the movement of ions under the influence of an electric field. Diffusion is the movement of ions as driven by a concentration gradient, and convection is the movement due to fluid flow. In combination these terms produce differential equations with nonlinear boundary conditions (1).

Neglecting transport due to convection, or the existence of concentration gradients (these are valid assumptions for the bulk of the solution, far from surface boundary layers where concentrations might vary), the equations describing current flow in an electrolyte containing cations and anions reduce to the familiar Ohm's law. Unidirectional current between two parallel plates can be described by (1)

$$i = -\frac{\kappa \Delta E}{l} \tag{4}$$

where i is the current density (amps/cm^2), κ is the solution conductivity in units of ohms^{-1} cm^{-1}, $\Delta E/l = E_1 - E_2/l$ is the difference in potentials between any two isopotential lines separated by a distance, l, in one dimension, V/cm. The more general expression for one-dimensional current density is given by

$$i = -\kappa \nabla E \tag{5}$$

where ∇E is the gradient of the potential (a scalar quantity), so that in Cartesian coordinates $\nabla E = \partial E/\partial x + \partial E/\partial y + \partial E/\partial y$.[2] Hence the local current density will depend upon the gradient of potential in the solution. Note that the potential gradient in the metal itself will be close to zero for current densities typical in electrochemistry, since the high metallic conductivity precludes the possibility of potential gradients within the metal. (In extremely long pipelines, the resistance through the metal itself may come into play.) However, the potential gradient in solution can be considerable. Note the form of the equation above. It is similar

[2] It is also recognized that the divergence of the gradient in potential is zero, or $\nabla^2 E = 0$. This means that $\partial^2 E/\partial x^2 + \partial^2 E/\partial y^2 + \partial^2 E/\partial^2 = 0$.

to that describing the steady-state flux of a diffusing species discussed in Chapter 4 ($J_{ss} = Ddc/dx$), which states that the flux is proportional to the concentration gradient times a term describing the *mobility or ease of motion* of the diffusing species, D. In the case of migration, κ, the solution conductivity is *the ease of motion* term.

The notion of a potential and therefore a current distribution through a solution between two electrodes can be illustrated by the following examples.

We can apply these rules and the equations given above to describe the iR_Ω voltage associated with a rectangular "box" or prism-shaped cell. In this cell, the working and counterelectrodes are exposed on opposite parallel walls (Fig. 5), and the side walls are insulators. Ohm's law can be applied to describe the IR_Ω voltage across this cell if we apply a voltage between the WE and CE.

$$i = -\frac{\kappa \Delta E}{l} \tag{6}$$

The negative sign indicates that positive ions flow in the direction of the negative potential gradient. Note that the current density and current is the same at all positions across this cell, since the voltage gradient is linear across the cell (assuming that the conductivity is also the same at all positions).

The total current is (1)

$$I = iA = -\frac{A\kappa \Delta E}{l} \tag{7}$$

Rearranging this expression to solve for the ohmic voltage V_{IR}[3] and integrating from $x = 0$ to 1 where l is the total length of the cell yields

$$V_{IR} = -\frac{(Il)}{(A\kappa)} = -IR_\Omega \tag{8}$$

where $R_\Omega = l/A\kappa$, is given in units of ohms. As expected, the total ohmic voltage across the cell is influenced by $I = I/A$, l, the cell length, and is inversely proportional to solution conductivity, κ. This equation essentially is Ohm's law. The electrode area normalized resistance (ohm-cm^2) in such a cell is a linear function of the distance, l, and inversely proportional to the conductivity.

---

[3] In this chapter, E is used to represent any potential measurement that can be made versus a reference electrode. E_{app} and E_{corr} are measured relative to some reference electrode scale. The potential difference ΔE can also be measured at any two points in the electrolyte between separated anodes and cathodes. Two reference electrodes connected between a high impedance voltameter can make this measurement. Alternatively, the potential between the reference electrode and anode or cathode may be determined at any two points. ΔE is determined by taking the difference, which in this case eliminates the reference potential scale. V_{IR} is an absolute ohmic voltage (not referenced to any scale).

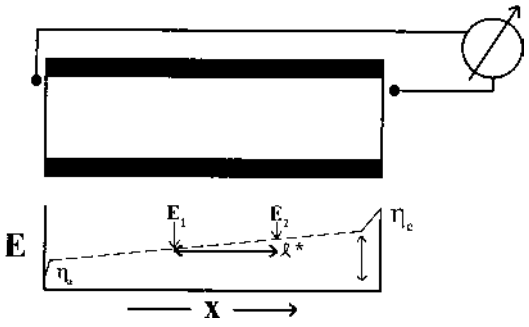

(a)

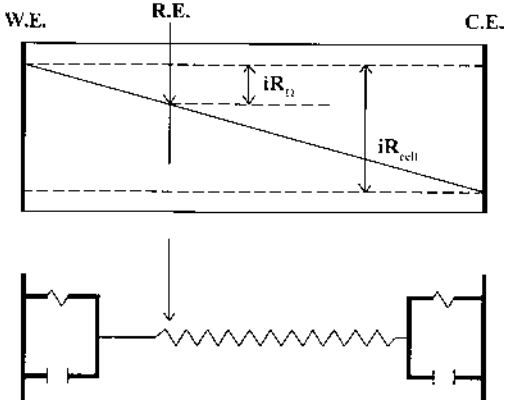

(b)

Figure 5 (a) Calculation of the local current density for flat parallel electrodes in a prismatic cell. (b) The ohmic voltage is shown to be a linear function of the distance from the working electrode. (From Ref. 6.)

$$R_\Omega = \frac{l}{\kappa} \tag{9}$$

If a reference electrode is inserted at a finite distance, l, from the working electrode, then the effective IR drop between WE and RE that contributes to error between η_{app} and η_{true} as given in Eq. (2) (6) is only the amount indicated by iR_Ω (Fig. 5b). Note that multiplication of Eq. (9) by the current density (amperes/cm^2) produces the correct units for voltage (volts). This is the amount by which the true potential of the interface differs from the applied potential, as indicated by Eq. (2).

The same derivation can also be developed for two concentric cylinders (1). Consider a cylinder of inner radius r_i, outer radius r_o, and a height of H (Fig. 6a). In this case the current distribution and thus the potential distribution will be completely homogeneous with regard to circumferential position on each concentric cylinder. The potential in solution and value of local current density will both vary radially, however.

Ohm's law for unidirectional current flow can be written in cylindrical coordinates as (1)

$$i = -\kappa\left(\frac{\partial E}{\partial r}\right) \tag{10}$$

Multiplying by electrode area produces (1)

$$I = 2\pi rHi = -2\pi rH\kappa\left(\frac{\partial E}{\partial r}\right) \tag{11}$$

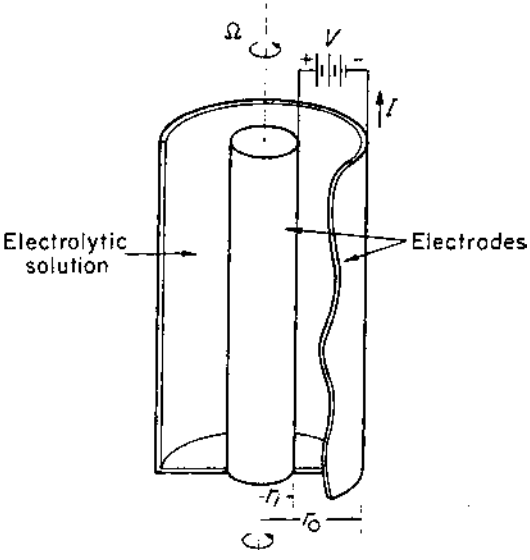

(a)

Figure 6 (a) Annular cell made from two concentric cylinders of height H, inner radius r_i, and outer radius r_o. (b) The ohmic voltage is a logarithmic function of radial distance. (c) Equipotential lines are concentric even in the primary current distribution. Note that the current density is greater on the inner electrode than on the outer electrode by an amount equal to the ratio of areas of the inner and outer electrodes. (From Ref. 1.)

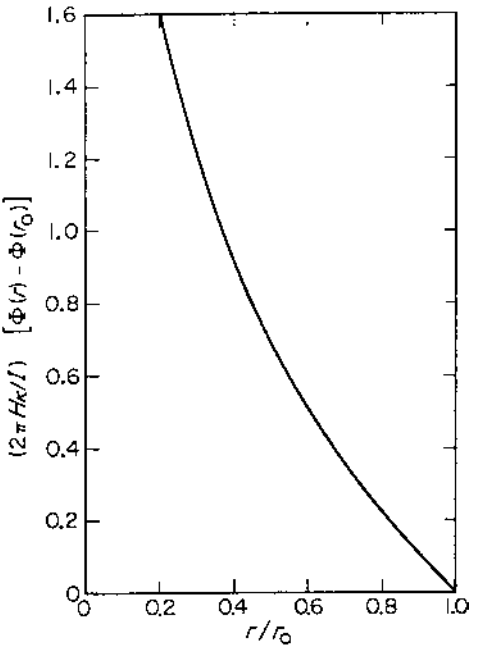

(b)

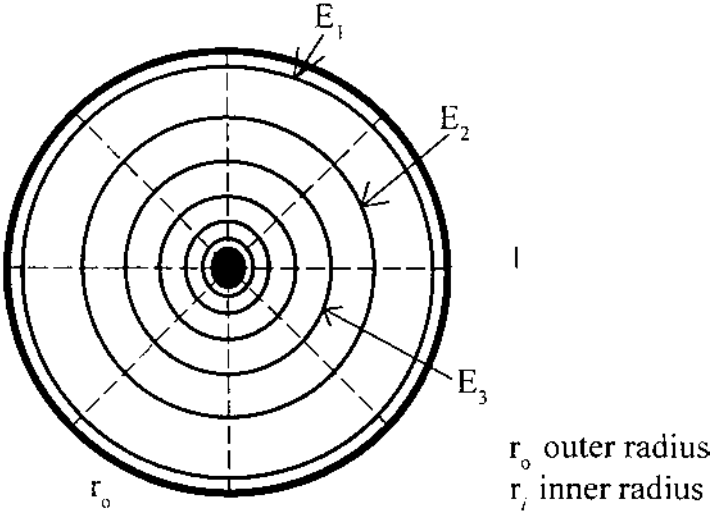

(c)

Figure 6 Continued

Rearranging this expression in terms of ∂E and integrating from r_i to r_o yields the ohmic voltage of the annular cell (1):

$$V_{IR} = \left(\frac{I}{2\pi H\kappa}\right) \ln\left(\frac{r_o}{r_i}\right) \tag{12}$$

Hence different isopotential lines of constant voltage increments in solution (actually cylindrical isopotential surfaces in 3D) vary logarithmically with respect to radial distance. Figure 6b illustrates the radial potential distribution as a function of radial distance. The isopotential lines and current lines are indicated in Fig. 6c looking down on such a cell. Note that the current density is greater on the inner cylinder in agreement with the logarithmic increase in the potential gradient, $\partial E/\partial r$, at the inner cylinder. The solution resistance (ohm-cm^2) is given by the following expression for $r_i < r < r_o$:

$$R_\Omega = \left(\frac{r}{\kappa}\right) \ln\left(\frac{r}{r_i}\right) \tag{13}$$

A simple rearrangement of this expression gives the solution resistance for a reference electrode placed a distance $d = r - r_i$ away from the inner cylinder with the outer cylinder at infinity (6).

F. Variation of Solution Resistance with Reference Electrode Position for Three Geometries

The variation of solution resistance with the distance, d, from the working electrode surface for three ideal electrode geometries, all with a uniform current distribution in the case of strictly one-dimensional migration or current flow (orthogonal to a planar electrode and radial to a cylindrical or spherical electrode, ignoring edge effects), is given below (6). These geometries include a flat working electrode in the parallel plate–rectangular cell arrangement, a cylinder, and a sphere. (See Table 2.) The expressions for solution resistance derive from the equations given above. Note again that the units of (ohm-cm^2) produce an ohmic voltage drop (volts) when multiplied by current density (A/cm^2). The motivation for using ohmic resistances in this form is that a corrosion engineer is always interested in current normalized to electrode area or current density.

G. Classification of Current Distribution Problems

Current distribution problems are often categorized according to the process that limits or determines the current and potential distribution (1,6).

Table 2 Solution Ohmic Resistance Versus Reference Electrode Distance

Working electrode geometry	R_Ω vs. WE–RE distance (Ω-cm^2)	
Planar	$R_\Omega = \frac{d}{\kappa}$	(14)
Cylindrical	$R_\Omega = \left(\frac{r}{\kappa}\right) \ln\left(1 + \frac{d}{r}\right)$	(15)
Spherical	$R_\Omega = \left(\frac{d}{\kappa}\right)\left(\frac{r}{r + d}\right)$	(16)

1. **The primary current distribution**: The current distribution is determined solely by the potential field in the solution. Hence the solution conductivity and geometry are the only factors considered, and the potential across the electrochemical interface is assumed to be negligible, such as when the electrode reactions are extremely fast (i.e., a nonpolarizable electrode).
2. **The secondary current distribution**: Both ohmic factors and charge transfer controlled overpotential kinetic effects are considered. The potential across the electrochemical interface can vary with position on the electrode.
3. **The tertiary current distribution**: Ohmic factors, charge transfer controlled overpotential effects, and mass transport are considered. Concentration gradients can produce concentration overpotentials. The potential across the electrochemical interface can vary with position on the electrode.

Many analytical numerical solutions appear in the literature for category 1 and 2, but few appear for 3 owing to its complexity (1). Consider for example the two-electrode half-sinusoidal cell shown in Fig. 3 with the irregular geometry (7). The current distribution can be described by replacing the solution and interfacial elements with resistors. For case 1, only solution resistances appear, and the resulting current density is extremely nonuniform. However, as the interfaces are replaced by larger and larger resistors to simulate slower charge transfer and mass transport, the current distribution becomes more uniform. This occurs primarily if the resistance of the interface is larger than the resistance of the solution. The resistance of the solution itself can be thought of as being determined by the specific resistivity of the electrolyte multiplied by the path length taken by the current and divided by the cross-sectional area for current flow. When the potential-dependent interfacial resistance becomes much larger than the solution resistance, the current will tend to spread out to minimize the cell voltage. This occurs because the incremental decrease in iR_Ω voltage, brought

about by minimizing the current path length by having all the current "crowd" the geometrically close electrode position, is more than offset by the much larger local true overpotential that results from crowding too much current to one area of the electrode. By plotting local current density divided by the average current density (i.e., total current/total area), the degree of nonuniformity can be seen as a function of electrode position (7).

H. Use of the Wagner Polarization Parameter to Estimate Qualitatively the Uniformity of Current Distribution

A dimensionless parameter known as the *Wagner* number is useful for qualitatively predicting whether a current distribution will be uniform or nonuniform (1,6,7). This parameter helps to answer the question, Which current distribution applies to my cell, primary, secondary, or tertiary?

The Wagner parameter may be thought of as the ratio of the kinetic resistance to the ohmic resistance. Hence when the Wagner number approaches numbers less than one, the ohmic component dominates the current distribution characteristics, and when it is much larger than one, the kinetic component dominates. In practice, the primary current distribution is said to exist when $W < 0.1$, and the secondary current distribution exists if $W > 10$ (6). The Wagner parameter is the ratio of the true polarization slope, $\partial E_{\text{true}}/\partial i$ (evaluated at the overpotential of interest) divided by the characteristic length and the solution resistance (1,6).

$$W = \left(\frac{\kappa}{L}\right)\left(\frac{\partial E}{\partial i}\right) \tag{17}$$

where κ (or $1/\rho$) is the specific solution conductivity (ohm-cm)$^{-1}$ and L is a characteristic length (cm), or the dimension of "irregularity." We can take the partial derivative, $\partial E/\partial I$, of any analytical expression describing the interfacial potential E_{true} as a function of I or obtain a polarization slope, R_{p}, from experimental E vs. I data. Such a slope can be evaluated at the average current density or at any pertinent applied current density. The partial derivative, $\partial E/\partial i$ has the units of Ω-cm^2. The solution resistance expressed in the same units is (κ/L). The resulting Wagner number is

$$W = \frac{R_{\text{p}}}{R_{\Omega}} \tag{18}$$

Thus the experimenter interested in estimating the current distribution "case" pertinent to their polarization cell can estimate whether the primary or secondary current distribution applies from knowledge of R_{p} and R_{Ω}.

The resulting Wagner numbers for various analytical expressions are shown

Table 3 Wagner Polarization Number Determination

Current distribution	Overpotential–current relationship $E = f(i)$	Polarization $\partial E/\partial i$ resistance term	Wagner number
Primary	. . .	. . .	κ/L
Secondary	$E = Bi$ (linear)	B	$\kappa B/L$
Secondary	$E = B'\ln(i/i_{corr})$ (Tafel)	B'/i	$\kappa B'/iL$
Tertiary	$E = [RT/nF]\ln(1 - i/i_l)$ (diffusion)	$(RT/nF) \cdot \left(\frac{1}{i_l - i}\right)$	$\kappa RT/[nF(i_l - i)L]$

in Table 3 for a number of current-overpotential cases. Note that a slightly different solution has been suggested.

The corrosion engineer can use this information in the following way. If the primary current distribution applies ($W < 0.1$), then current distributions are likely to be nonuniform unless one of the ideal cell geometries leading to uniform primary current distributions (discussed in Table 2) is used. In the former case, errors in polarization resistance and kinetic parameters are likely. In the latter case, η_{app} must still be corrected for iR_Ω, using the relationships given in Eq. (2) but the value of V_{IR} will be the same at all positions along the electrode surface.

II. CURRENT DISTRIBUTIONS FOR SELECTED GEOMETRIES OF INTEREST

Primary, secondary, and tertiary current distributions have been defined for selected geometries that are of practical interest to the corrosion engineer (2–6).

A. Current and Potential Distributions for the Rotating Cylinder Electrode

The rotating cylinder electrode with a concentric cylindrical counterelectrode is an ideal geometry for minimizing nonuniformity in current distribution. The current density will be completely uniform at all vertical positions around the full circumference of the inner cylinder, assuming little surface roughness (Fig. 6C) in the primary, secondary, and tertiary current distributions. However, this is only true for concentric cylinders that are of infinite length. For cylindrical samples of finite length, the current density will be greater at the top and bottom edges of the cylinders, except in the case of the tertiary current distribution. Here the current density will be nearly uniform at all locations.

B. Current and Potential Distributions for the Rotating Disk Electrode

The rotating disk electrode will have a uniform tertiary current distribution but an extremely nonuniform primary current distribution with the current density at the electrode edge approaching infinity (8–12). For a disk electrode of radius r_o, embedded in an infinite insulating plane with the counterelectrode far away, the primary current distribution is given by

$$\frac{i_{local}}{i_{avg}} = \frac{0.5}{(1 - (r/r_o))^{1/2}} \tag{19}$$

Since the isopotential lines are close together near the electrode edge, the gradient of the potential will be greater, and it follows from this that the local current density will be greater. This behavior is illustrated in Figs. 7a and b (1). In the secondary case, the current density will be greater at the electrode edge but not infinite. Figure 7c maps i_{local}/i_{avg} for various values of inverse Wagner numbers, $J = 1/W$ (1).

It is clear from the analysis of a disk electrode that when the electrode and insulator reside in the same plane (i.e., a flush mounted disk or plate), the primary current distribution is infinite at the electrode edge (13). Alternatively, the primary current distribution at the edge is zero if the angle between the insulator and the edge is less than 90°. The primary current distribution is not zero or infinite only when the angle is exactly 90°. This is shown in Fig. 4.

C. Current and Potential Distribution for the Flow Channel with Parallel Plates

The flow channel with parallel plates (Fig. 8a) will behave like the disk electrode in that it will have a uniform or nearly uniform tertiary current distribution but an extremely nonuniform primary current distribution (1,3,14–17). The tertiary current distribution may also be nonuniform if the reacting species is depleted at positions downstream from its upstream or leading edge. In the primary and secondary cases, the current density will be much greater at all electrode edges. Since the isopotential lines will bend so that they are closer together near the electrode edge, the gradient of the potential will be greater, and it follows from this that the local current density will be greater near such edges. A primary current distribution for two parallel plates of length L, mounted flush within insulating planes that are separated by a distance much greater than the plate length, has been given (3) by

$$\frac{i_{local}}{i_{avg}} = \frac{1}{\pi[(x/L) - (x/L)^2]^{1/2}} \tag{20}$$

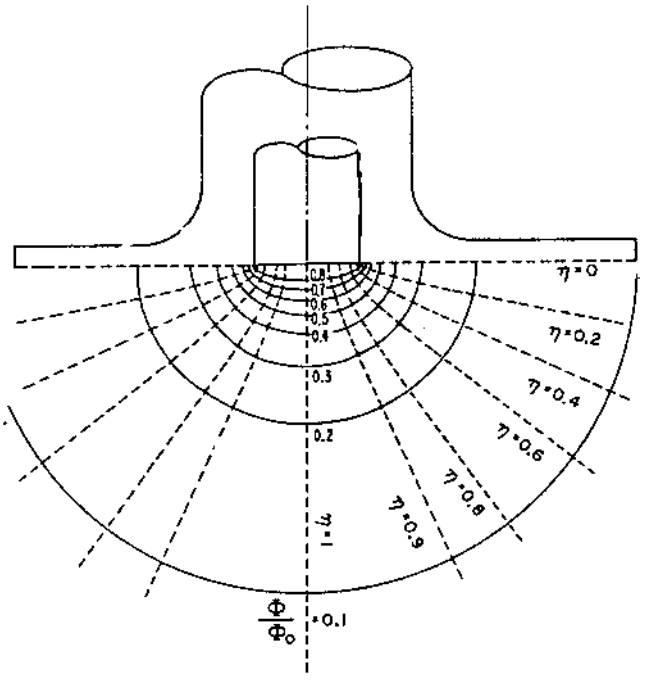

(a)

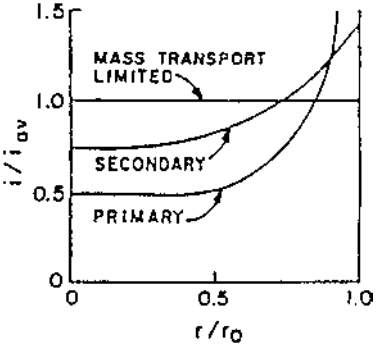

(b)

Figure 7 (a) Rotating disk electrode, flush mounted into an insulating plane. (b) Current distributions for primary, secondary, and tertiary cases as a function of radial position r/r_o. (c) Variation of i_{local}/i_{avg} as a function of r/r_o for various values of the reciprocal Wagner number ($J = 1/W$) for the case of linear polarization kinetics on the disk electrode. (From Refs. 1 and 9.)

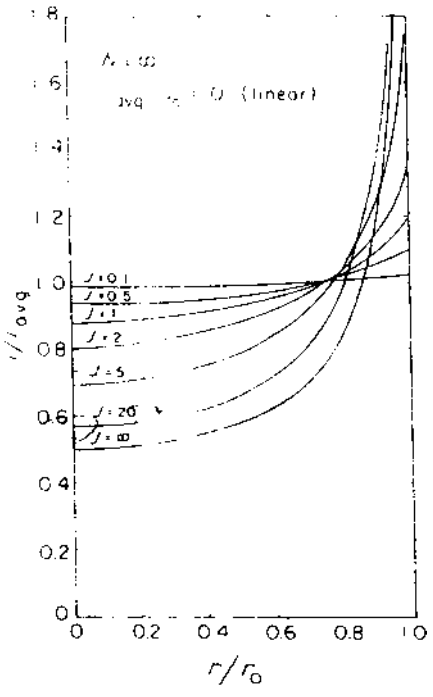

(c)

Here x is the distance along the plate starting at one of its edges. The distribution is very nonuniform, as it is infinite at the edges and only 64% of the average in the center of the electrode plate (3).

It should be mentioned that errors in both kinetic parameters and polarization resistance result from nonuniform primary or secondary current distributions during such measurements (3). Figure 9 shows examples of the extent of such errors (18). In this figure, R_{eff} is the "measured" polarization resistance from linear polarization or EIS corrected for the apparent value of R_Ω determined from current interruption or high-frequency impedance. R_p is the "true" value of the polarization resistance. The source of difference between R_p and R_{eff} lies in that no single R_Ω value applies for all electrode positions. That is, there is a nonuniform potential drop. Depending on reference electrode position (center, infinity, edge), there are large errors that represent the differences between R_{eff} and the true R_p. These errors decrease as R_{eff}, r_o, or conductivity κ or their combination become large (Fig. 9). When these parameters are large, the Wagner number becomes large, indicating a more uniform current distribution and minimization of this error.

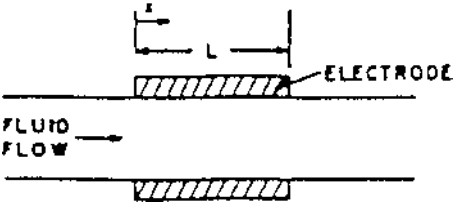

(a)

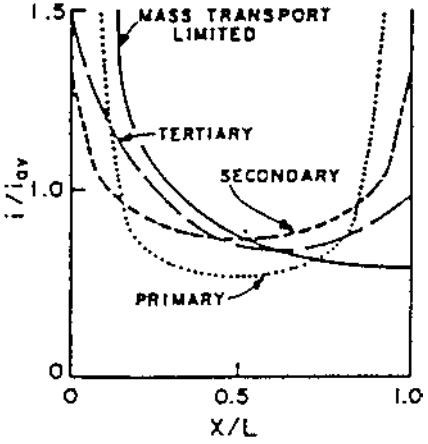

(b)

Figure 8 (a) Flow channel electrodes, flush mounted parallel to each other in insulating planes. (b) Current distributions for primary, secondary, and tertiary cases. (From Ref. 1.)

D. Two Parallel Cylinders

It is common in corrosion laboratories and in field corrosion monitoring probes to immerse two vertical rods parallel to one another in an electrolyte. In the lab, one of the rods consists of a high-density graphite counterelectrode while the other is a working electrode. A reference electrode may be placed in between the two rods. In the field, polarization resistance or electrochemical noise measurements are often made between two nominally identical rods that both consist of the material of interest. The primary current distribution is nonuniform with respect to circumferential position about each electrode when the distance between the two rods is small in comparison to the radius of the rod, Fig. 10a (16). Again, the value of R_Ω varies from where the rods face each other to where they

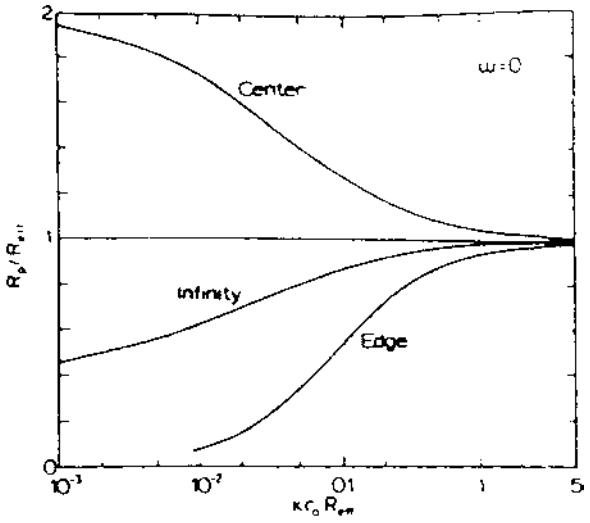

Figure 9 Calculated error in polarization resistance measured, R_{eff}, compared to true polarization resistance, R_p, on a disk electrode with the reference electrode at the center, edge, and infinity as a function of conductivity, κ, disk radius, r_o, and R_{eff}. (From Ref. 18.)

face away from each other. Therefore no single value of R_Ω can properly correct polarization data. Alternatively, when the distance of separation between the rods is great compared to their radius, then the local current becomes more uniform. Essentially, all of the current will not crowd to the portions of the surfaces facing each other when the distance required to spread out onto the rod surfaces facing away is small compared to the distance of rod separation, Fig. 10b (16). The transition from one regime to the other depends on the Wagner number.

E. Microelectrode Disk

The microelectrode disk embedded in an insulating planar surface is a useful arrangement for accessing high current densities without excessive ohmic resistances in low-conductivity environments. The reference electrode should be placed far away. The solution resistance expression for a spherical electrode can then be used, because ionic migration is hemispherical to an isolated disk in a flat insulating plane for a counterelectrode located at infinity. The ohmic resistance to a sphere has been given above in Table 2. In the limiting case, for large values of d ($d/r \gg 1$), when the reference electrode is placed far away from the microelectrode disk, is (6)

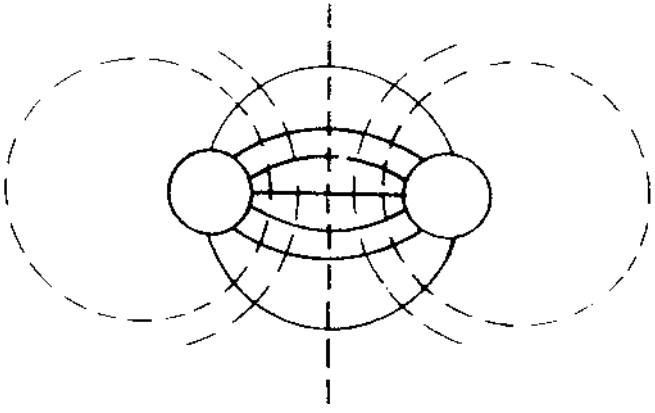

(a)

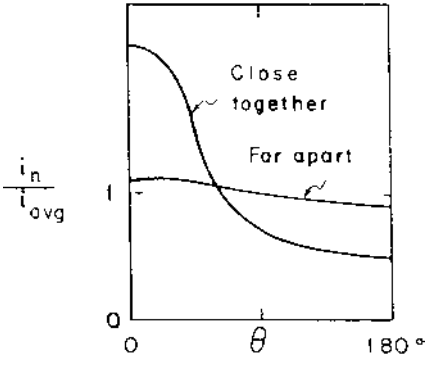

(b)

Figure 10 (a) Equipotential and current lines for two parallel cylinders in the primary current distribution. (b) i_{local}/i_{avg} as a function of electrode separation and angular position around the cylindrical electrodes. 0 degrees represents the horizontal position between the two electrodes. (From Ref. 16.)

$$R_\Omega = \frac{r_o}{\kappa} \tag{21}$$

Here r_o is the radius of the microelectrode disk. Note that R_Ω has been normalized to surface area, i.e., has units of Ω-cm^2. When this resistance is multiplied by current density, an ohmic voltage drop is determined. Note that the area normalized resistance decreases as the electrode disk is made smaller (6). Thus small

electrodes enable higher current densities to be accessed in low-conductivity environments.

III. CASE STUDIES

The geometries discussed above are relevant to laboratory scale experimental cells. The geometries discussed below are more appropriate for situations encountered in industry or practical application involving galvanic corrosion, cathodic protection, or field corrosion probes.

A. Polarization into a Recess or Crevice

A common situation of interest is the cathodic polarization of a recess or crevice. A related industrial geometry is a field probe electrode that is immersed under a film of electrolyte (18,19). This later case is similar to a crevice consisting of an insulator on one face and a metallic electrode on the opposite, parallel face. In the thin film situation, the insulator is the air–electrolyte interface. Nisancioglu and Pickering have independently modeled this situation (20–22). Nisancioglu considered a secondary current distribution solution for a metal embedded in an insulating plane of length $L_c - L_m$ (20) (Fig. 11A). The current and potential distribution is considered only in the x direction, because x is much greater than the crevice gap, h. The boundary conditions were as follows. There exists a current balance: the sum of all current in the walls equals the sum of all current in the solution. The local current density in the electrolyte in the horizontal direction, x, is i_x, where $i_x = -\kappa\, dE/dx$ such that $dE/dx = 0$ at $x = 0$, the end of the recess. The reaction kinetics are linear and uniform at all crevice sites, and there is no change in solution chemistry. It can be shown that the reciprocal of the Wagner polarization parameter, J, is given by (20)

$$J = \frac{L_m^2}{\kappa h(\partial\eta/\partial i)} \tag{22}$$

As J approaches infinity ($\partial\eta/\partial i$ approaching zero, or κ approaching zero), the primary current distribution is reached, and the current density is infinite at $x/L_m \rightarrow 1$. The current density is zero at all other x. As J approaches zero, the current distribution is uniform. In this expression, the polarization resistance $\partial\eta/\partial i$ is assumed to be position- and potential-independent. The true interfacial potential and local current distributions are given by

$$E(x) = E(s)\frac{\cosh(J^{0.5}x/L_m)}{\cosh(J^{0.5})} \tag{23}$$

and

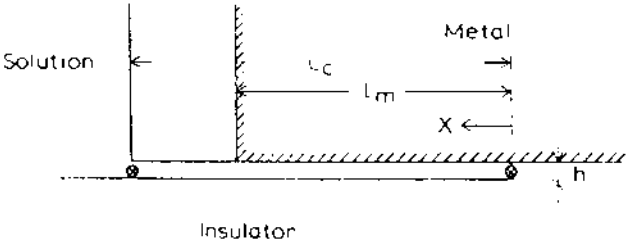

(a)

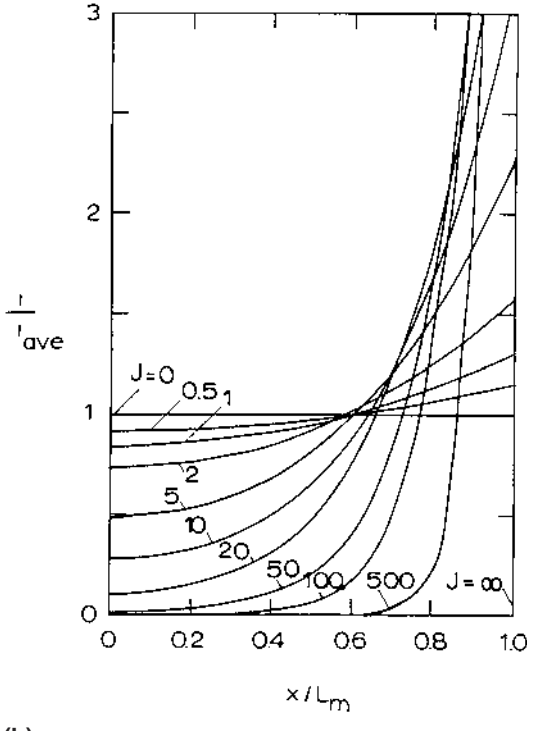

(b)

Figure 11 (a) Recess geometry where h is the crevice gap and x is the distance from the bottom of the recess. (b) i_{local}/i_{avg} for x/L_m. (From Ref. 20.)

$$i_{\text{local}} = i(\text{avg}) \frac{J^{0.5} \cosh(J^{0.5} x/L_{\text{m}})}{\sinh(J^{0.5})} \tag{24}$$

where $E(s)$ is the potential at the entrance to the crevice so that $E = E(s)$ at $x = L_{\text{m}}$. The current distribution for linear electrode kinetics (polarization resistance = $\partial\eta/\partial i$), assuming various values of J (Fig. 11b) is shown below. Note that lowering either the solution conductivity or the polarization resistance produces a less uniform current distribution with greater current densities at the mouth of the recess (for homogeneous electrode kinetics).

Ateya and Pickering have been concerned with the cathodic polarization of a crevice or recess (21,22). Note that while the term crack has been used, the crack half-angle is zero, which is not realistic for actual cracks. They focus on the situation where the external surface is either anodically or cathodically polarized for various metals. Active/passive electrodes and actively corroding metals have both been considered in these analyses.

B. Current and Potential Distributions at the Entrance to a Circular Pipe

The entrance to a circular pipe is an important engineering geometry. It is often necessary to attempt to protect cathodically the I.D. of the pipe using an anode located at the pipe entrance. The question arises as to how far the cathodic current can be "thrown" down the length of pipe. The engineer may also be confronted with a situation where he must choose between overprotecting the tube entrance with the undesirable possibility of hydrogen embrittlement versus the consequences of inadequately protecting the pipe I.D. at greater distances away. (An example of this type of arrangement is the cathodic protection of heat exchanger tube-sheets with an anode placed inside the water box at the end of the tube bundle.) Cathodic disbondment of any protective coatings on the structure near the anode may also be of concern.

Recall that the Wagner number depends on the solution conductivity, characteristic length, as well as the interfacial electrode characteristics. A solution has been given for the primary current distribution where the entire interior pipe surface (radius r_{o}) is uniformly cathodically protected to i_{w} and the pipe interface is considered to be nonpolarizable (16). The IR drop down the pipe to a distance, L, can be calculated so that the maximum tolerable potential drop from the entrance to the far end is known:

$$V_{\text{IR}} = \frac{i_{\text{w}} L^2}{r_{\text{o}} \kappa} \tag{25}$$

Again, the problem with such a primary current distribution solution is that the pipe–solution interface is assumed to be an equipotential surface. Instead, we

would like to know how the interfacial potential varies with distance down the pipe.

Therefore let us instead consider the more practical case of the tertiary current distribution. Based on the dependency of the Wagner number on polarization slope, we would predict that a pipe cathodically protected to a current density near its mass transport limited cathodic current density would have a more uniform current distribution than a pipe operating under charge transfer control. Of course the cathodic current density cannot exceed the mass transport limited value at any location on the pipe, as said in Chapter 4. Consider a tube that is cathodically protected at its entrance with a zinc anode in neutral seawater (4). Since the oxygen reduction reaction is mass transport limited, the Wagner number is large for the cathodically protected pipe (Fig. 12a), and a relatively uniform current distribution is predicted. However, if the solution conductivity is lowered, the current distribution will become less uniform. Finite element calculations and experimental confirmations (Fig. 12b) confirm the "qualitative" results of the Wagner number (4).

Consider, on the other hand, a galvanic couple between a tube (Cu-Ni) and a tube-sheet (Monel 400) where the reaction kinetics for both alloys are under charge transfer control (4). Here the Wagner number would be slightly greater than one. The resulting current distribution would be much less uniform, and the galvanic interaction would cease at the short distance away from the tube-sheet of a few tube diameters (Figs. 13a and b). However, after a corrosion film forms on the tube anode material, the anodic polarization slope becomes quite large, and the current is "thrown" further down the tube. Hence time effects can become very important.

C. Local Electrochemical Sites: Pits, Precipitates, or Inclusions

The current and potential distributions between pits, precipitates, and inclusions and the surrounding matrix are of great practical interest given that most materials are not microstructurally homogeneous and that pitting is a common issue for passive materials exposed to halides. The conductivity, potential differences, and polarization characteristics determine how far away the matrix will experience a galvanic interaction with the local site. Most solutions consider either the matrix or the local site to be nonpolarizable and thus to create an equipotential surface. Levich and Frumkin examined a disk-shaped cathode inclusion (23). Newman examined the same case except that the inclusion was considered to be the anode (24). Newman et al. examined the current and potential distribution in a hemispherical pit (25). An interesting variation of this issue is the question of the anodic polarization of an Al matrix by the presence of a cathodic precipitate phase. Cu-containing precipitate phases are common in age-hardened Al alloys

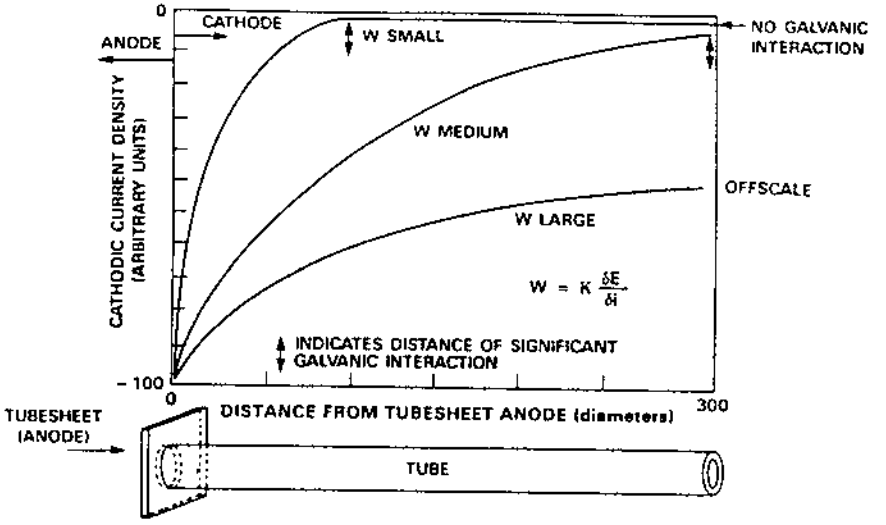

(a)

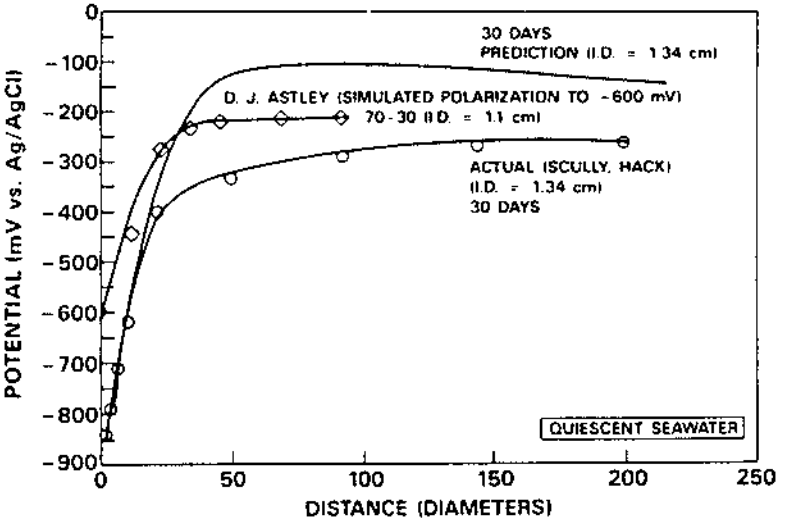

(b)

Figure 12 (a) Tube-tubesheet arrangement showing qualitative effect of Wagner number. (b) Finite element model predictions, analytical model predictions, and experimental verifications for 70-30 Cu-Ni tube coupled to anode grade zinc at the mouth of the tube in quiescent seawater. (From Ref. 4.)

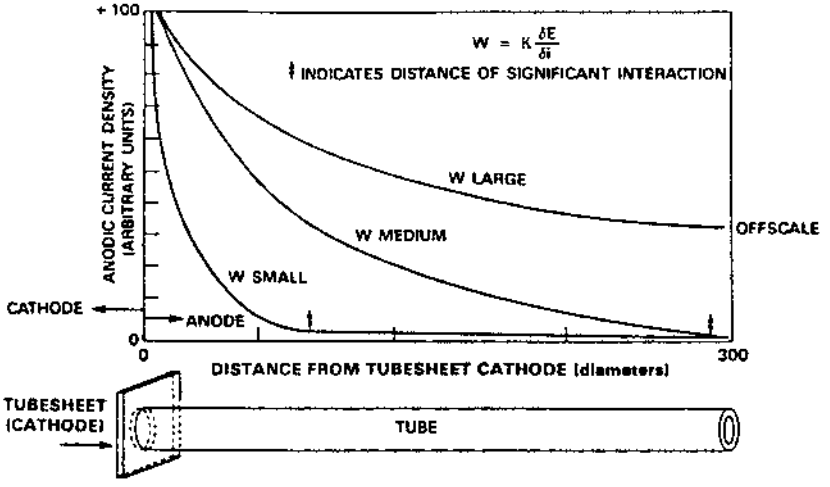
+100
0
ANODIC CURRENT DENSITY (ARBITRARY UNITS)
$W = K\frac{\delta E}{\delta i}$
INDICATES DISTANCE OF SIGNIFICANT INTERACTION
W LARGE
W MEDIUM
W SMALL
OFFSCALE
CATHODE
ANODE
0
300
DISTANCE FROM TUBESHEET CATHODE (diameters)
TUBESHEET (CATHODE)
TUBE

(a)

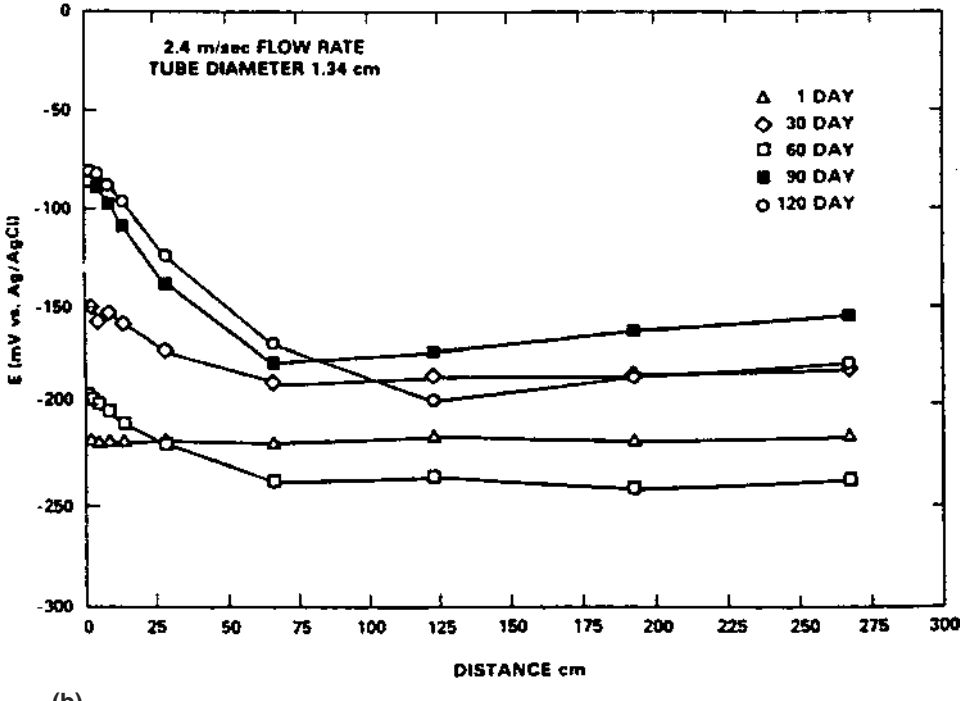
2.4 m/sec FLOW RATE
TUBE DIAMETER 1.34 cm
1 DAY
30 DAY
60 DAY
90 DAY
120 DAY
E (mV vs. Ag/AgCl)
0
-50
-100
-150
-200
-250
-300
0
25
50
75
100
125
150
175
200
225
250
275
300
DISTANCE cm

(b)

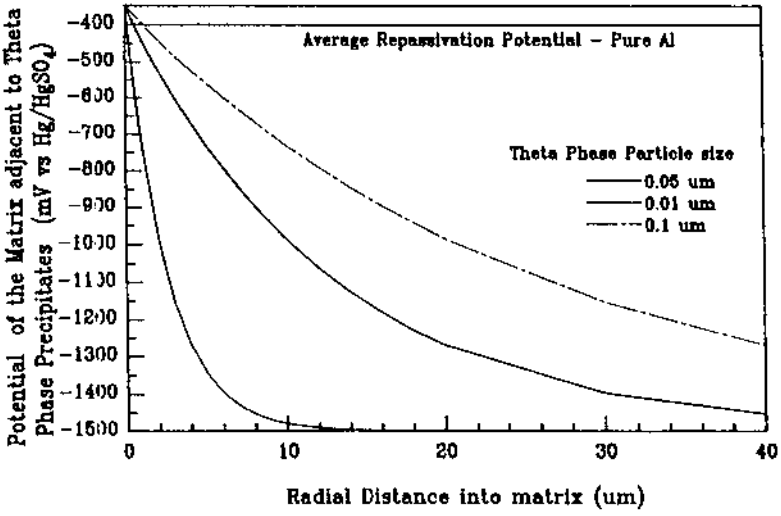

Figure 14 Potential distribution at the surface of the Al matrix near a theta phase precipitate assuming a nonpolarizable cathode site (Al_2Cu precipitate), polarizable passive Al matrix, and a dilute acidic solution. The effect of precipitate size is shown. (From Ref. 26.)

and they are well known to induce pitting. The extent of anodic polarization of the matrix to the more noble potential of the Cu-rich precipitate was of interest (26). The precipitate was assumed to be nonpolarizable, which was reasonable considering that fast cathodic reactions are possible on Cu-rich precipitates (26). The matrix was assumed to be polarizable, which also was reasonable considering that the matrix was passivated by Al_2O_3 prior to breakdown. The outcome was the extent of cathodic polarization of the matrix as a function of solution conductivity, the radius of the precipitate particle, the polarization resistance of the matrix, and the open circuit potentials of the matrix and particles. The size of the theta phase (Al_2Cu) particles governed the extent of anodic polarization of the adjacent matrix in a dilute acidic solution as shown in Fig. 14. Metastable pitting was observed only near precipitates, confirming the importance of local potentials.

Figure 13 Tube-tubesheet arrangement similar to Fig. 12 showing time effects on 90-10 Cu-Ni coupled to Monel 400 tubesheet in flowing seawater. The strong time effect on the potential distribution arises from a changing E_{corr} for the Monel 400 and increased kinetic resistance for the 90-10 Cu-Ni as oxide films thicken near the tube entrance. (From Ref. 4.)

Electrode roughness call also cause variations in current distributions (28). Penetration of current into pores may be limited if the solution resistance of pores is large relative to the polarization resistance.

REFERENCES

1. J. Newman. Electrochemical Systems. Prentice Hall, Englewood Cliffs, NJ, 1973.
2. H. P. Hack, P. J. Moran, J. R. Scully. In: The Measurement and Correction of Electrolyte Resistance in Electrochemical Cells (Scribner, Taylor, eds.). ASTM STP 1056, 5–26 (1990).
3. W. C. Ehrhardt. In: The Measurement and Correction of Electrolyte Resistance in Electrochemical Cells (Scribner, Taylor, eds.). ASTM STP 1056, 5–26 (1990).
4. J. R. Scully, H. P. Hack. In: Galvanic Corrosion (H. P. Hack, ed.). ASTM STP 978, ASTM, Philadelphia, 136–157 (1988).
5. G. A. Prentice, C. W. Tobias, J. Electrochem. Soc. 129, 72–78 (1982).
6. E. Gileadi. Electrode Kinetics for Chemists, Chemical Engineers, and Materials Scientists. VCH, 1993.
7. C. Wagner. J. Electrochem. Soc. 101, 225 (1959).
8. J. Newman. J. Electrochem. Soc. 113, 501 (1966).
9. J. Newman. J. Electrochem. Soc. 113, 1235 (1966).
10. L. Nanis, W. Kesselman. J. Electrochem. Soc. 118, 454 (1971).
11. B. Miller, M. I. Bellavance. J. Electrochem. Soc. 120, 42 (1973).
12. A. C. West, J. Newman. J. Electrochem. Soc. 136, 139 (1989).
13. W. H. Smyrl, J. Newman. J. Electrochem. Soc. 136, 132 (1989).
14. W. R. Parrish, J. Newman. J. Electrochem. Soc. 117, 43–48 (1970).
15. W. R. Parrish, J. Newman. J. Electrochem. Soc. 116, 169–172 (1969).
16. J. Newman. In: Localized Corrosion (R. W. Staehle, B. F. Brown, J. Kruger, A. Agarwal, eds.). NACE, Houston, TX, 1986, p. 45.
17. C. Wagner. J. Electrochem. Soc. 98, 116–128 (1951).
18. K. Nisancioglu. Corrosion 43, 258 (1987).
19. C. Fiaud, M. Keddam, A. Kadri, H. Takenouti. Electrochimica Acta 32, 445 (1987).
20. K. Nisancioglu. In: ASTM STP 1056, 61–77 (1990).
21. Ateya and Pickering. J. Electrochem. Soc. 122, 1018, (1975).
22. Ateya and Pickering. Corros. Science 37, 1443 (1995).
23. B. Levich, A. Frumkin. Acta Physiochimica U.R.S.S. 18, 325 (1943).
24. J. Newman. In: Advances in Localized Corrosion (H. Isaacs, U. Bertocci, J. Kruger, S. Smialowska, eds.). NACE 9, Houston, TX, 1990, p. 227.
25. J. Newman, D. N. Hanson, K. Vetter. Electrochmica Acta 22, 829 (1977).
26. J. R. Scully. In: Critical Factors in Localized Corrosion (G. S. Frankel, R. Newman, eds.). ECS PV 92-9, 1991, p. 144.
27. J. R. Scully, D. E. Peebles, A. D. Romig, Jr., D. R. Frear, C. R. Hills. Met. Trans. A, 22A, 2429 (1991).
28. C. B. Diem, B. Newman, M. E. Orazem. J. Electrochem. Soc. 135, 2524 (1988).

7
Development of Corrosion Models Based on Electrochemical Measurements

I. INTRODUCTION

Models to predict materials performance in industrial applications, or to assess the environmental consequences of some industrial activity, are a major immediate need. The requirement for such models is driven by environmental concerns, such as a desire to avoid groundwater contamination, and industrial concerns such as the necessity of reducing costs by extending plant lifetimes and operating efficiencies. Since many materials corrosion and mineral dissolution processes are electrochemical in nature, electrochemical techniques are commonly used in the study and development of solutions to these problems.

In many cases, the approach used has been mechanistically or empirically qualitative, with the primary purpose of developing immediate solutions to pressing environmental problems, or of improving plant maintenance and operating schedules and procedures. However, the need to preempt costly outages, extend plant lifetimes, or perform environmental assessments is leading to efforts to develop predictive models. The primary emphasis in this chapter is the development of such models and how electrochemical methods can be used in the process.

The problem and the required solution will dictate the experimental and modeling approach adopted. Many trade-offs driven by the need to balance economical operation against public/personnel safety must be made. When cost is the predominant driving force, engineering expediency leading to short-term solutions based only on qualitative assurances often dominate. Models for plant behavior must be based on accurate and realistic data to avoid unnecessary and costly shutdowns due to overly conservative predictions. Often, in this context, accurately measured but empirical data may be more valuable than a fundamen-

tal scientific understanding of the corrosion process. By contrast, when public/personnel safety is the primary concern, a more rigorous scientific and technical approach, one leading to longer term generic solutions, may be necessary, but inadequate databases can be compensated for by conservative model assumptions.

Figure 1 attempts to define the key stages in the development of corrosion models. Irrespective of whether the key concern is safety or operating efficiency, the steps involved in model development are common up to the point where data reliability must be accounted for (stage 8). At this juncture, the approaches deviate. When public/personnel safety is the key issue, one would adopt conservative assumptions (stage 9A) to cover the uncertainties that will inevitably permeate one's model. If plant efficiency is the key issue, then at this juncture it is necessary to refine one's data input by a combination of further experimentation and the careful consideration of information from plant inspection records (stage 9B).

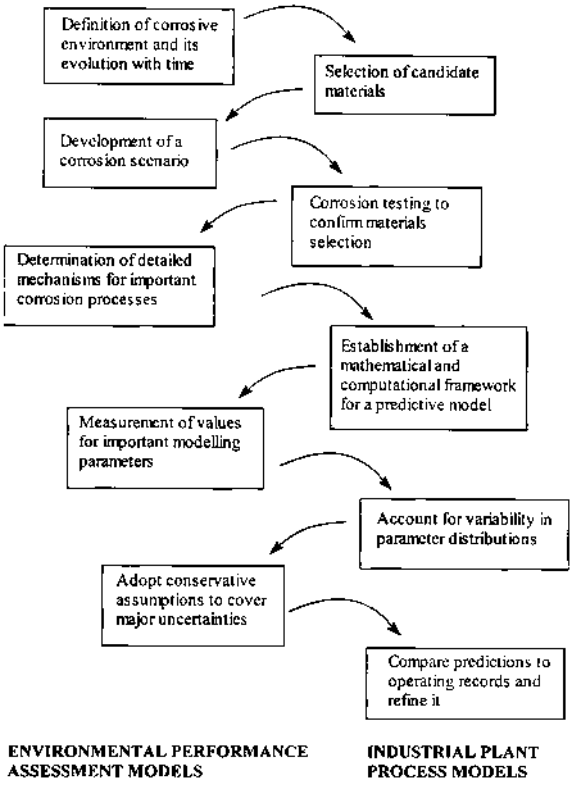

Figure 1 General modeling scheme.

Within this scheme, the application of electrochemical methods will be key in the determination of mechanism (stage 5) and the measurement of important modeling parameters (stage 6). It will be clear that the relevance of the latter is seriously reduced if the former is not addressed. This is because the influence of the simplifying assumptions that are always required in modeling would be unknown, and hence unquantifiable, if made in ignorance of a mechanistic understanding. Obviously, electrochemical methods also play a key role in the materials selection process (stage 2), but their discussion in this context is only briefly addressed toward the end of this chapter.

Most of the examples used in this chapter emphasize assessment models that can afford to incorporate conservative assumptions. Most deal with the environmental issue of nuclear waste disposal. This emphasis should not be taken to suggest that the literature is not replete with many other examples of valuable corrosion models. It is hoped that this chapter will encourage the reader to search for them.

II. THE EVOLUTION OF THE CORROSION PROCESS

Corrosion occurs when a material is exposed to an environment in which it is thermodynamically unstable. Generally, but not exclusively, materials degradation occurs under oxidizing conditions. Figure 2 illustrates the electrochemical driving force for corrosion under oxidizing conditions; it is defined as the difference between the equilibrium potential of the material in the environment of interest, $E^{e}_{M/M^{n+}}$, and the redox potential of the environment, $E^{e}_{Ox/Red}$. Evolution of the corrosion process with time could cause these potentials to change; i.e., the driving force for corrosion would not necessarily remain constant. Thus $E^{e}_{M/M^{n+}}$ would increase if dissolved corrosion product deposit with a more positive equilibrium potential, $E^{e}_{MOx/M}$, accumulated on the surface of the corroding material. A decrease in $E^{e}_{Ox/Red}$ would occur if available oxidant was consumed with time.

Determining the evolution of the corrosion process with time may require a significant amount of research, but at least a preliminary mechanistic understanding of the corrosion process is required before the development of a model to predict corrosion behavior can commence. Such preliminary understanding can be gained from a knowledge of the system corrosion potential, E_{CORR}, and how it changes with time.

The corrosion potential, E_{CORR}, adopted by the system will be dictated by the relative kinetics of the anodic material degradation process and the cathodic reduction kinetics of the oxidant. While E_{CORR} yields no quantitative information on the rate of the overall corrosion process, its value, and how it changes with time, is a good qualitative indication of the balance in corrosion kinetics and their evolution with time. Thus a knowledge of E_{CORR} and its comparison to ther-

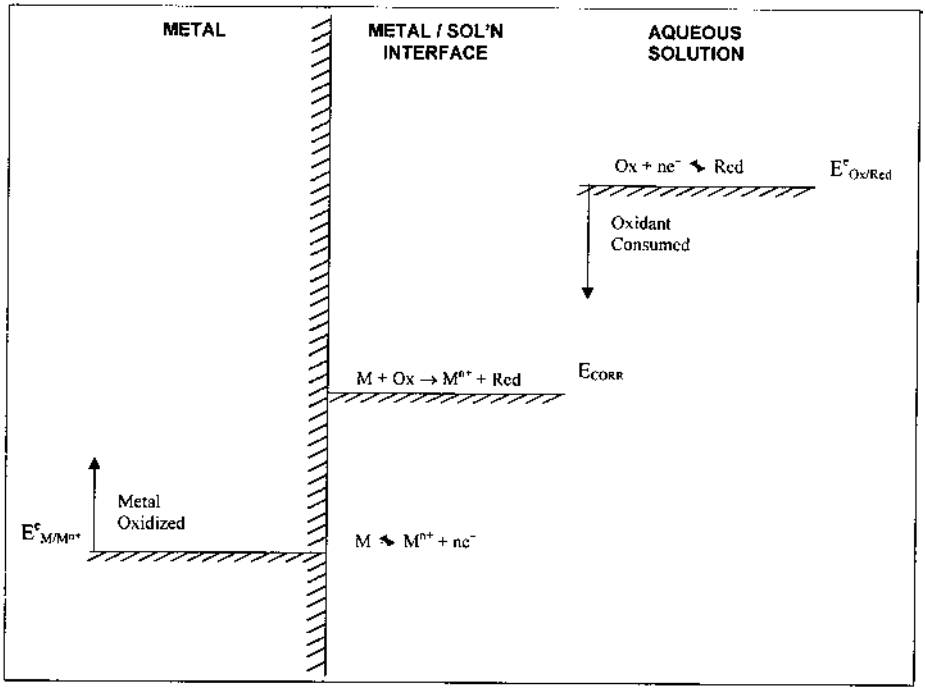

Figure 2 Electrochemical driving force for corrosion.

modynamic expectations (embodied in potential E^e–pH diagrams) provides a convenient reference point in model development. Also, the value of E_{CORR} and its proximity to breakdown (E_B) and repassivation potentials (E_R) is a key reference point in determining the probability of occurrence of localized corrosion processes.

A preliminary knowledge of which reaction steps could be key in determining the overall corrosion rate can be assessed by measurements of E_{CORR} as a function of important system parameters, e.g., oxidant concentration, solution composition, temperature. The proximity of E_{CORR} to either $E^e_{M/M^{n+}}$ or $E^e_{Ox/Red}$ can indicate which of the two half-reactions may be rate determining. This is illustrated in Fig. 3A, which shows an Evans diagram for the combination of a fast anodic reaction coupled to a slow cathodic one. The corrosion of iron or carbon steel in aerated neutral solution would be an example of such a combination. The anodic reaction requires only a small overpotential ($\eta = E^e_{M/M^{n+}} - E_{CORR}$) to sustain the corrosion current, I_{CORR}, compared to the much larger overpotential required to sustain the cathodic reaction at this current. The anodic reaction would

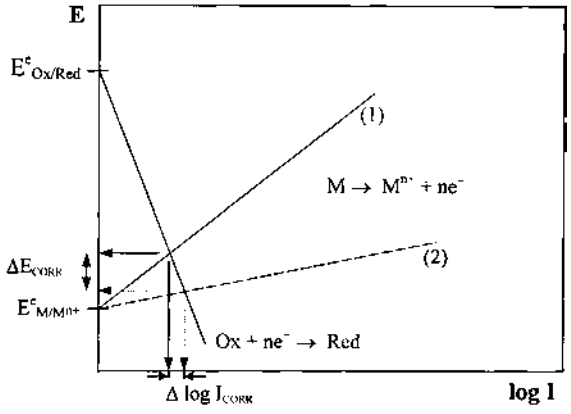

(A)

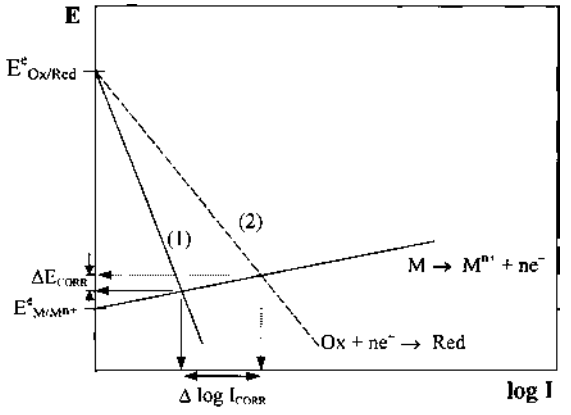

(B)

Figure 3 (A) Evans diagram illustrating the change in I_{CORR} and E_{CORR} for the increase in rate (from 1 to 2) of a fast anodic reaction coupled to a slow cathodic reaction. (B) Evans diagram for the same combination, illustrating the influence of a change in rate of the slow cathodic reaction (from 1 to 2).

be termed the potential-determining one. A change in the rate of the anodic reaction (line 1 to line 2 in Fig. 3A) exerts little influence on the corrosion rate but a measurable effect on E_{CORR}, whereas the opposite is true for a change in the cathodic reaction rate (line 1 to line 2 in Fig. 3B).

For many corroding systems, such a distinct separation in kinetics is not so readily obvious, but for those for which such a condition prevails, preliminary knowledge of this kind may greatly simplify the form of any predictive model

that might be developed. For the above example one might choose to model only the rate-determining cathodic half-reaction. If the corrosion process does not evolve with time, then the development of a corrosion model would be unnecessary, and a straightforward measurement of corrosion rate would suffice. However, for more complex situations, a knowledge of how the corrosion process evolves with time is essential to the development of a model. Again, a preliminary understanding of what parameters may dictate this temporal evolution can be obtained from E_{CORR} measurements.

In an environment with a constant redox condition (e.g., permanently aerated and/or constant pH), a condition not uncommon in industrial and environmental situations, E_{CORR} could shift in the positive direction for a number of reasons. Incongruent dissolution of an alloy could lead to surface ennoblement. Alternatively, as corrosion progresses, the formation of a corrosion product deposit could polarize (i.e., increase the overpotential, η, for) the anodic reaction as illustrated in the Evans diagram of Fig. 4. Polarization in this manner may be due to the introduction of anodic concentration polarization in the deposit as the rate of transport of dissolved metal species away from the corroding surface becomes steadily inhibited by the thickening of the surface deposit; i.e., the anodic half-reaction becomes transport controlled.

The introduction of transport effects due to the formation of corrosion product deposits would not necessarily be confined to one half-reaction. It is likely that transport of the oxidant to the corrosion site would also be polarized. Such an effect, coupled possibly to a consumption of the oxidant in the bulk environment, would make the evolution in E_{CORR} with time much more difficult to inter-

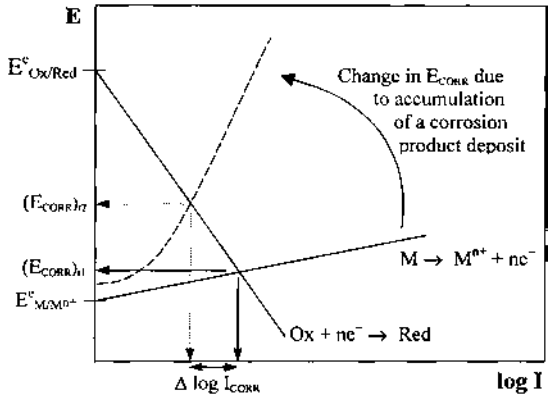

Figure 4 Evans diagram for the coupling of a fast anodic reaction to a slow cathodic reaction, illustrating the influence of the formation of a corrosion product deposit.

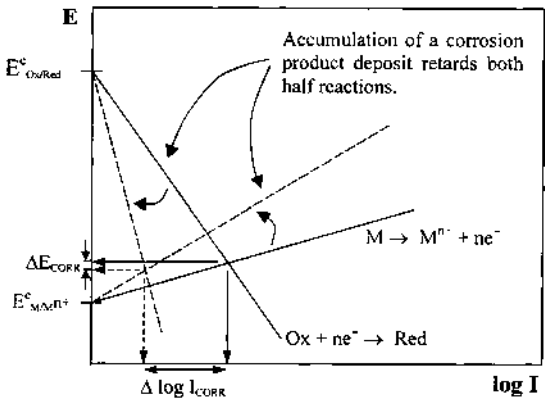

Figure 5 Evans diagram illustrating the influence on I_{CORR} and E_{CORR} of a corrosion product deposit that affects both the anodic and cathodic half-reactions. The solid lines are for no deposit; the dashed lines illustrate the changes in the presence of the deposit.

pret, as illustrated in the Evans diagram of Fig. 5. The shift in E_{CORR} anticipated due to anodic concentration polarization would be offset by a similar effect of the deposit on the cathodic half reaction. While its behavior may not be mechanistically definitive, the evolution of E_{CORR} with time does provide a qualitative template upon which to base the development of a corrosion model.

An example is shown in Fig. 6 for UO_2 (nuclear fuel) in the near neutral to slightly alkaline environment anticipated in a Canadian nuclear waste disposal vault. The E_{CORR}–time plot is schematic but is representative of that obtained in many laboratory experiments and is anticipated under waste disposal conditions. The reaction sequence was demonstrated for corrosion conditions by analyzing the surface composition of the fuel [using x-ray photoelectron spectroscopy (XPS)] as a function of the E_{CORR} achieved (1). The observed onset of surface oxidation around -0.3 V (vs. SCE) obviously matches thermodynamic expectations, as is indicated by the equilibrium stability zones (bottom right in Fig. 6) for various oxidized uranium phases. The equilibrium potential for an aerated solution environment is shown in the top right corner. The difference between upper and lower shaded areas defines the thermodynamic driving force for the corrosion process (as described in Fig. 2). In this case, E_{CORR} does not achieve a value conveniently close to either equilibrium potential, and the question of overall rate control cannot easily be decided. While the change in fuel surface composition as the steady-state E_{CORR} value $(E_{CORR})_{SS}$ is approached may be instructive, any model used to predict long-term fuel behavior under permanent disposal conditions must focus predominantly on the oxidative dissolution of

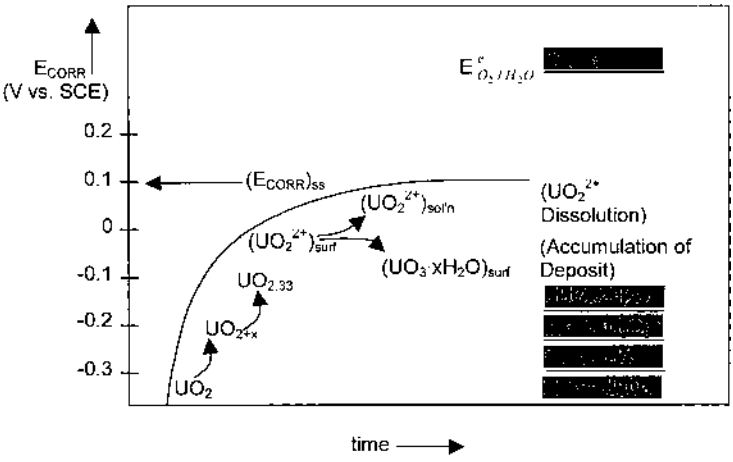

Figure 6 Schematic showing the evolution of E_{CORR} and the reactions occurring with time for the oxidation of nuclear fuel (UO_2) in neutral noncomplexing solution. The lines marked by uranium phases show the equilibrium potentials for the formation of discrete phases: $E^{e}_{O_2/H_2O}$ is the system redox potential for these conditions.

the oxidized fuel and the accumulation of corrosion product deposits (secondary phases); e.g., $UO_3 \cdot 2H_2O$ on the fuel surface. Once accumulated, these corrosion product deposits could maintain oxidizing conditions at the UO_2 fuel surface for a very long time even if all available oxidant is consumed; hence, $E^{e}_{O_2/H_2O}$ falls considerably. As indicated in the figure, a fall in E_{CORR} of ~300 mV from the steady-state value would be required before a $UO_3 \cdot 2H_2O$ deposit would become thermodynamically unstable. In the absence of oxidant, its removal to expose the underlying UO_2 surface would proceed by a chemical dissolution process in neutral solutions. This would be expected to be very slow. A combination of cyclic voltammetry and photothermal deflection spectroscopy was used to demonstrate that the onset of oxidation was accompanied by the onset of dissolution around −0.3 V, Fig. 7 (2). This knowledge of when dissolution commences/ceases is a key modeling parameter, since it provides a measured criterion for fuel stability.

III. DETERMINATION OF THE RATES OF CORROSION REACTIONS

Corrosion can be considered as a galvanic cell in which an anodic and cathodic half-reaction couple to yield the overall corrosion reaction, Fig. 8. The overall reaction proceeds at a rate I_{CORR} ($= I_A = |I_C|$) at the corrosion potential, E_{CORR}.

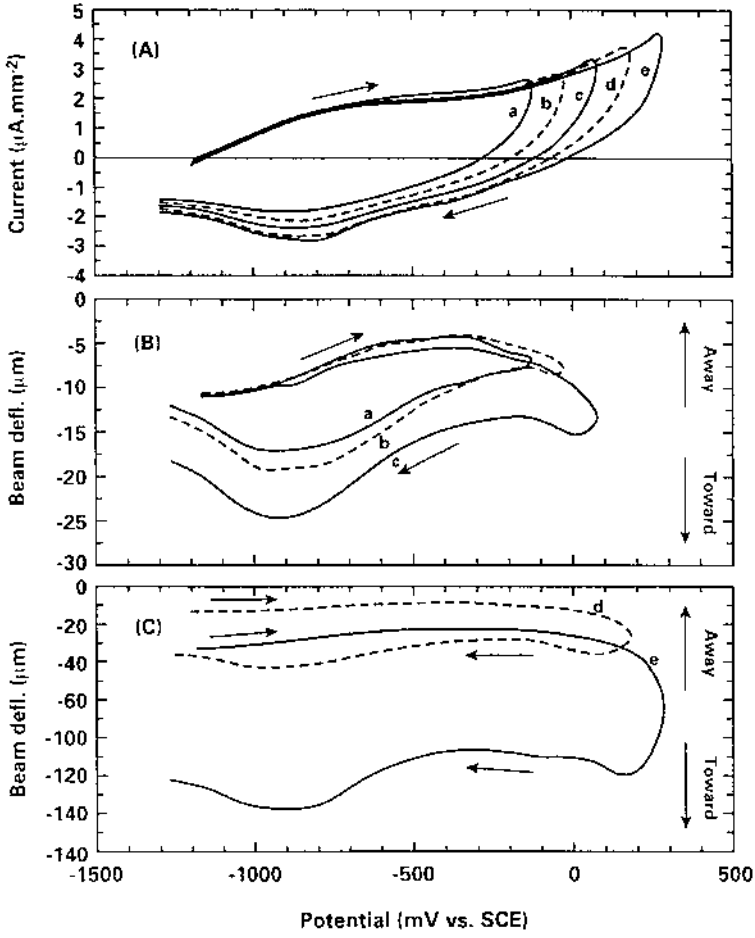

Figure 7 Electrochemical photothermal deflection spectroscopy experiment (0.5 mol · dm^{-3} Na_2SO_4; pH = 10.5, 20 $mV \cdot s^{-1}$), illustrating the detection of the onset of dissolution of nuclear fuel (UO_2); (A) voltammetric response for scans to various anodic potential limits; (B) and (C) probe beam deflection for each scan. The deflection of the probe beam is proportional to the dissolved uranium concentration, and deflection of the probe beam towards the electrode surface is an indication that dissolution is occurring (Reprinted from Ref. 2 with permission from Elsevier Science S.A.)

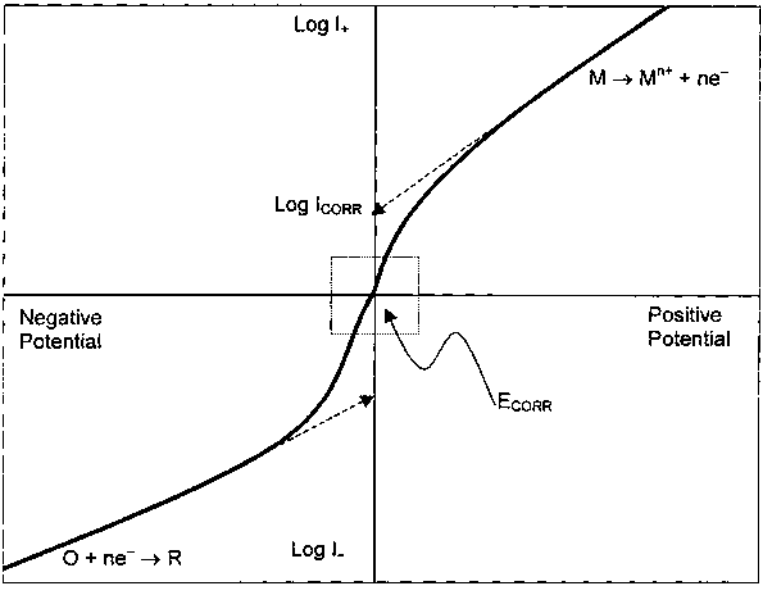

Figure 8 Current–potential relationship for a corrosion process, showing the separation of the anodic and cathodic half-reactions by polarization to positive and negative potentials, respectively.

However, since this corrosion reaction is short-circuited on the corroding surface, no current will flow in any external measuring circuit. Consequently, a direct electrochemical measurement of the corrosion current (convertible to corrosion rate by the application of Faraday's law) cannot be made. Despite this limitation, electrochemical techniques can be used to decouple the two half-reactions, thereby enabling each to be separately and quantitatively studied. This involves the determination of the current–potential relationships for each half-reaction. Subsequently, the behavior under electrochemically unperturbed (open-circuit or natural corrosion) conditions can be reconstructed by extrapolation of these relationships to E_{CORR}.

A. Active Corrosion Conditions

This process of electrochemically "deconstructing" the corrosion reaction provides a convenient experimental methodology for investigating active corrosion conditions and is illustrated schematically in Fig. 8. Each half-reaction should obey Butler–Volmer kinetics, in which the current increases exponentially [posi-

tively (anodic) or negatively (cathodic)] with applied potential. For a sufficiently large applied potential the two half-reactions are totally decoupled, and the individual Tafel relationships,

$$\log|I| = \log I_{CORR} \pm b(E_{CORR} - E_{APPLIED}) \quad (1)$$

can be determined. Extrapolation of these relationships to E_{CORR} (as illustrated in Fig. 8) then allows a determination of I_{CORR}.

This approach is experimentally intrusive, since large currents leading to irreversible surface damage can be sustained, particularly when recording the anodic relationship. By restricting the potential perturbation from E_{CORR} to $\sim \pm 10$ mV, such damage can be minimized and the current measured in the linear region around E_{CORR} (i.e., within the box in Fig. 8). This linear current–potential region arises because the exponential terms in the Butler–Volmer equation can be linearized for such small values of $E_{CORR} - E_{APPLIED}$. Under these conditions, the two half-reactions are only partially decoupled, and the measured current contains contributions from both. Techniques that utilize this approach to determine a charge transfer resistance (inversely proportional to I_{CORR}) are linear polarization (LP) and electrochemical impedance spectroscopy (EIS).

Despite the obvious advantage of these minimal perturbation techniques, their application requires a knowledge of Tafel slopes in order to convert the measured charge transfer resistances into corrosion currents/rates. In many applications, the use of LP and EIS is difficult or impossible, a modeling approach based on Tafel relationships is more appropriately or more easily applied. Their determination, however, is not always as simple as would initially appear. The currents that must be used in Tafel analyses are steady-state values free of contributions from solution transport. Also, if large currents are measured in resistive media [e.g., in dilute solutions with a high resistance, R_S, or on electrodes with a substantial bulk resistance, R_B (e.g., UO_2)], then the curves must be corrected for the distortion caused by IR_S and/or IR_B effects. Providing R_S (and/or R_B) is known, this second correction is readily made, and most modern electrochemical equipment is capable of making this correction using either a current interrupt or a feedback methodology.

The elimination of transport effects is not so readily achieved. One relatively simple procedure is to measure currents (I_m) as a function of electrode angular velocity (ω) using a rotating disc electrode. Currents free of diffusive transport effects (I_k) can then be obtained by application of the Koutecky–Levich equation,

$$I_m^{-1} = I_k^{-1} + B\omega^{-1/2} \quad (2)$$

where B is a constant. An example would be the anodic dissolution of Cu in strong chloride solutions, which has been shown to proceed via the two steps (2,3)

$$Cu + Cl^- \rightleftharpoons CuCl_{ad} + e \quad \text{(surface)} \quad (3)$$

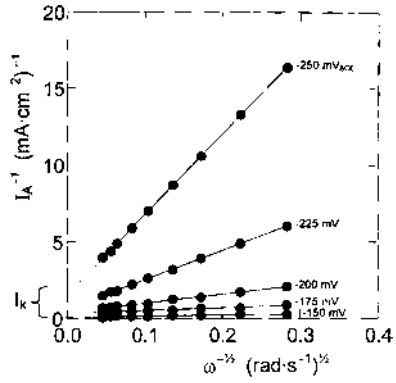

Figure 9 Use of the Koutecky–Levich equation to correct for diffusive transport effects on the anodic dissolution of Cu in 1 mol · dm^{-3} NaCl recorded on a rotating disk electrode.

$$CuCl_{ad} + Cl^- \rightleftharpoons Cu(Cl)_2^- \quad \text{(bulk)} \tag{4}$$

followed by the slow transport step,

$$Cu(Cl)_2^- \text{ (surface)} \rightarrow Cu(Cl)_2^- \text{ (bulk)} \tag{5}$$

The fit to the Koutecky–Levich equation, Fig. 9, demonstrates that the anodic dissolution of Cu occurs under mass-transport control, and extrapolation of these fits to $\omega^{-1/2} = 0$ yields kinetically controlled currents, I_k, free from transport effects and appropriately used in Tafel plots.

The Tafel expressions for both the anodic and the cathodic reaction can be directly incorporated into a mixed potential model. In modeling terms, a Tafel relationship can be defined in terms of the Tafel slope (b), the equilibrium potential for the specific half-reaction (E^e), and the exchange current density (I_0), where the latter can be easily expressed as a rate constant, k. An attempt to illustrate this is shown in Fig. 10 using the corrosion of Cu in neutral aerated chloride solutions as an example. The equilibrium potential is calculated from the Nernst equation; e.g., for the O_2 reduction reaction,

$$(E^e)_c = (E^o)_c - \frac{RT}{nF}\,\ell n\,\frac{[OH^-]^4}{p_{O_2}} \tag{6}$$

As indicated in the figure, extrapolation of one or both of the Tafel lines to E_{CORR} yields the condition

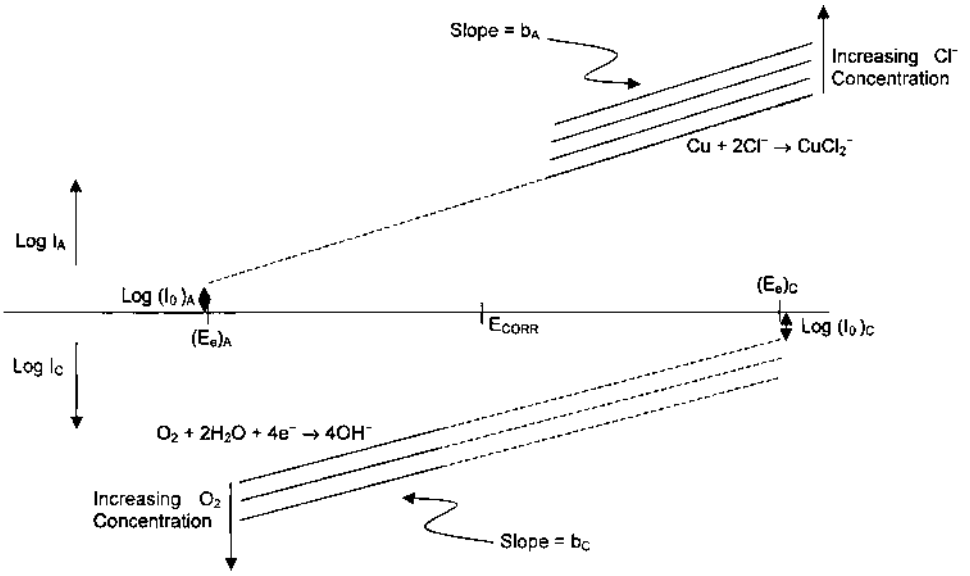

Figure 10 Schematic Tafel relationships showing the key parameters, E^e, I_0, and b, which define them. The sets of lines indicate the expected influence of concentration on the anodic and cathodic reactions.

$$\log I_A = \log|I_C| = \log I_{CORR} \tag{7}$$

and hence a value of the corrosion rate.

Also shown in Fig. 10 are additional lines indicating the influence of O_2 and Cl^- concentrations on the Tafel relationships. The lines allow the determination of reaction orders with respect to these reaction participants and yield the following expressions for the anodic and cathodic Tafel lines:

$$I_A = n_A F k_A [Cl^-]^2 \exp\{b_A(E - (E^e)_A)\} \tag{8}$$

$$I_C = n_C F k_C [O_2] \exp\{-b_C(E - (E^e)_C)\} \tag{9}$$

where n_A and n_C are the number of electrons involved in the anodic and cathodic reactions.

Implicit in these relationships is that both the anodic and the cathodic half-reactions are polarized far from their equilibrium potentials (i.e., $E - E^e$ is large) and hence are irreversible. For the O_2 reduction reaction this is inevitably so, but for reactive metals like Cu (and Fe, Zn) this may not be so.

This fact, and the more complicated two-step nature of the anodic reaction [via steps (3) and (4)], could be incorporated into the Tafel relationship to yield

$$I_A = n_A F(k_A)_f[Cl^-]^2 \exp\{b_A(E - (E^e)_A)\} - (k_b)_2[CuCl_2^-] \quad (10)$$

where $(k_b)_2$ is the rate constant for the reverse of reaction (4) and $(k_A)_f$ is a composite rate constant,

$$(k_A)_f = \frac{(k_f)_1}{(k_b)_1(k_f)_2} \quad (11)$$

with $(k_f)_1$ and $(k_b)_1$ being the forward and reverse electrochemical rate constants for reaction (3), and $(k_f)_2$ the forward rate constant for the chemical reaction (4). Obviously, the use of Eq. (10) as opposed to Eq. (8) would require a more detailed quantitative knowledge of the anodic reaction. A more extensive discussion of the details of this corrosion process has been given elsewhere (5).

It is worth emphasizing that the reaction orders measured for the individual half-reactions are not necessarily the same as those for the overall corrosion reaction. Manipulation of Eqs. (7) and (8) to yield an expression for I_{CORR} predicts a reaction order (n_{O_2}) with respect to O_2 (assuming $[Cl^-]$ constant) given by

$$n_{O_2} = b_C(b_A + b_C)^{-1} \quad (12)$$

i.e., the reaction order is determined by the Tafel slopes. Only when $b_A \ll b_C$ will $n_{O_2} \to 1$. Under these circumstances the cathodic half-reaction would be extremely polarized and totally rate determining [see Fig. 3 (A and B)]. The other extreme ($b_A \gg b_C$) would, of course, yield a corrosion rate independent of O_2 concentration, since the anodic reaction would be rate determining. This latter condition might be expected for the corrosion of passive metals or those whose corrosion is severely hindered by the presence of a corrosion product deposit.

Relationships such as that in Eq. (12) offer convenient means of testing the validity of mixed potential models by comparing electrochemically determined parameters (in this case, a reaction order based on measured Tafel slopes) to values measured by other means. One such example would be the corrosion of UO_2 (nuclear fuel) in aerated neutral solutions containing added carbonate (6). In the presence of carbonate, corrosion product deposits are avoided, since the UO_2^{2+} corrosion product is solubilized by complexation with the carbonate. Measured Tafel slopes yield a predicted reaction order of $n_{O_2} = 0.67$ with respect to O_2 for the overall corrosion reaction:

$$UO_2 + O_2 + 2CO_3^{2-} + 2H_2O \rightleftharpoons UO_2(CO_3)_2^{2-} + 4OH^- \quad (13)$$

This value is in excellent agreement with the range of values (0.69 to 0.74) measured in chemical dissolution experiments.

The determination of a Tafel slope for O_2 reduction illustrates some of the difficulties encountered in determining a value of this parameter and emphasizes the need for a thorough understanding of the reaction mechanism if the develop-

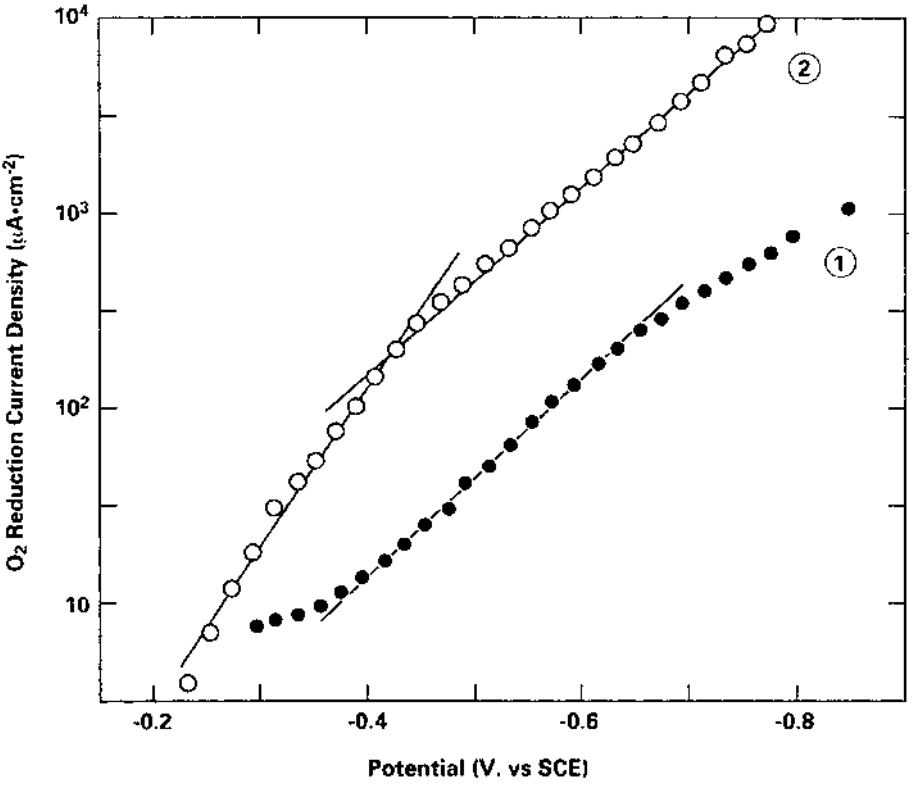

Figure 11 Transport- and IR-compensated O_2 reduction currents as a function of potential recorded on nuclear fuel (UO_2) in 0.1 mol · dm^{-3} $NaClO_4$ (pH = 9.5). The electrode was cathodically reduced before the experiment. (1) Data recorded from the most negative to the most positive potential, showing the behavior on a reduced UO_2 surface. (2) Data recorded from the most positive to the most negative potential after corrosion in aerated solution, illustrating the behavior on an oxidized UO_{2+x} surface.

ment of a justified model is to be achieved. The kinetics for this reaction change with the composition of the corroding surface. For example, O_2 reduction on UO_2 surfaces is accelerated if the surface is preoxidized as would be the case for the corrosion of UO_2 under oxidizing conditions. This is illustrated in Fig. 11, which shows the O_2 reduction current on reduced (UO_2) and oxidized (UO_{2+x}) surfaces. Not only is the current higher on the oxidized surface, but also the slope of the Tafel plot changes with potential, since the degree of oxidation of the surface (x in UO_{2+x}) changes with potential. The appropriate data to use in a model for UO_2

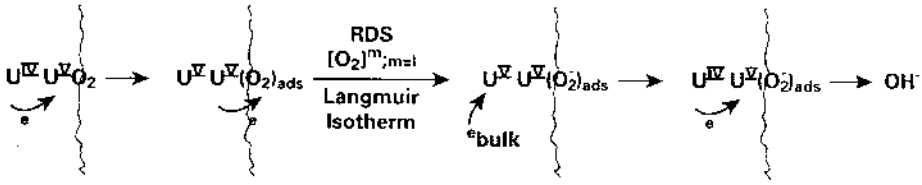

Figure 12 Schematic illustrating the mechanism of cathodic reduction of O_2 at donor–acceptor (U^{IV}/U^{V}) sites on UO_2 (nuclear fuel).

corrosion is that recorded on the oxidized surface in the potential range −0.2 to −0.4 V; i.e., closest to the natural corrosion conditions prevailing at E_{CORR}. This behavior is attributable to the fact that the breaking of the O—O bond during O_2 reduction on oxide surfaces requires catalysis by mixed oxidation states available in the surface of the oxide (7,8). This is illustrated in the schematic mechanism for O_2 reduction on UO_2 shown in Fig. 12. The presence of oxides on metal surfaces can similarly distort O_2 cathodic kinetics (9–11), making it difficult to specify a Tafel relationship.

In some situations the determination of Tafel relationships for anodic and cathodic reactions is extremely difficult and may be impossible. However, this does not necessarily disqualify the use of electrochemical methods to provide a database of corrosion rates for use in models. An example would be the determination of nuclear fuel (UO_2) corrosion rates in radiolytically decomposed water. In this case, the determination of Tafel slopes for the anodic dissolution of UO_2 in neutral to slightly alkaline solutions is achievable, as illustrated in Fig. 13 (6), which shows a series of such plots for solutions containing various amounts of dissolved carbonate. However, the cathodic half-reaction is the reduction of oxidants produced by the radiolytic decomposition of water. Depending on the nature of the radiation (α, β, γ), a range of reactive oxidants (predominantly $OH°/O_2^-$ for γ/β-radiation, and H_2O_2/O_2 for α-radiation) is produced in relatively small concentrations (12) at the radiation dose rates expected in fuel storage and disposal conditions. For γ-radiolysis, the extremely reactive radical species (OH°, O_2^-) appear to react with the fuel surface under diffusion controlled conditions. This dominance of diffusion control and the low concentrations make it impossible to determine a cathodic Tafel relationship. Alpha radiolysis is a high linear energy transfer form of radiation that deposits all its energy in a layer of solution ~25 μm thick adjacent to the fuel surface, a situation for which it is again impossible to measure a Tafel relationship.

However, a measurement of E_{CORR} in these environments is relatively simple. To obtain E_{CORR} as a function of γ-radiation dose rate it is simply necessary to

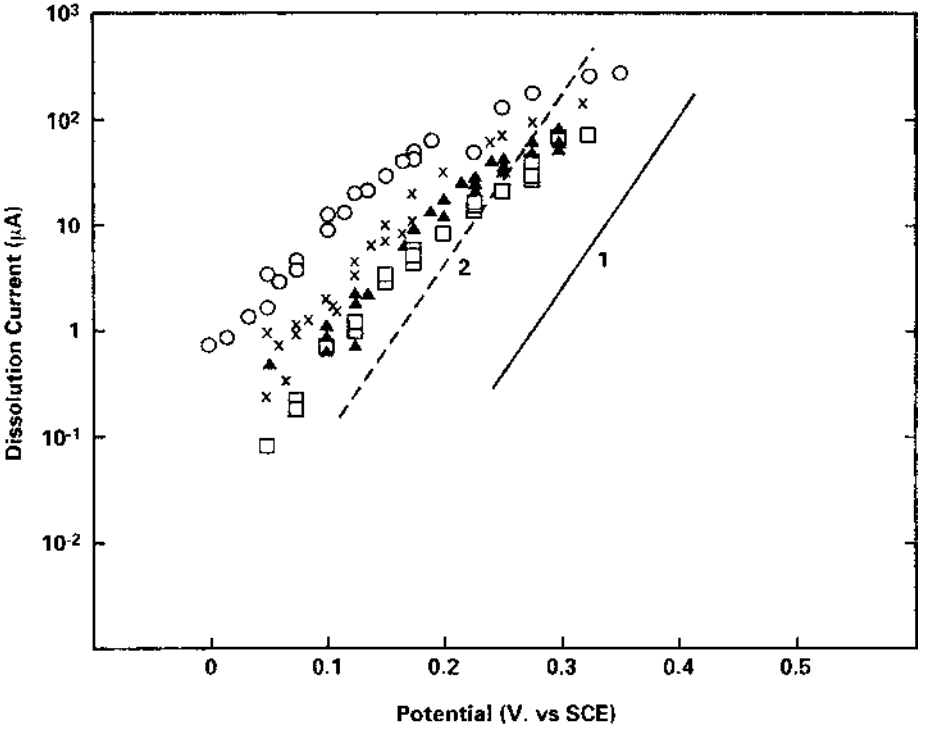

Figure 13 Electrochemically determined anodic dissolution currents recorded on a rotating nuclear fuel (UO_2) disk (ω = 16.7 Hz) in 0.1 mol · dm^{-3} $NaClO_4$ (pH = 9.5) containing various amounts of carbonate; (□) 0.005 mol · dm^{-3}; (▲) 0.01; (×) 0.05; (○) 0.1. Line 1 is the line that would fit the dissolution currents recorded with no carbonate present. Line 2 is a line of the same slope as line 1 shifted up two orders of magnitude in current.

conduct the measurement in a γ-cell (13). For measurements in α-radiolytically-decomposed water, the electrode is brought within 25 μm of a gold-plated α-source using a thin-layer electrochemical cell arrangement. Figure 14 shows the key electrode-source gap area of such a cell and illustrates the key reactions and features involved in this measurement. Since diffusive loss of oxidants from the periphery of the gap is possible (J_{O_2}, $J_{H_2O_2}$), it is necessary to model this geometric arrangement using finite difference methods and radiolysis codes to obtain a relationship between E_{CORR} and radiolytic oxidant concentration (14). This involves solving the radial reaction-diffusion equation

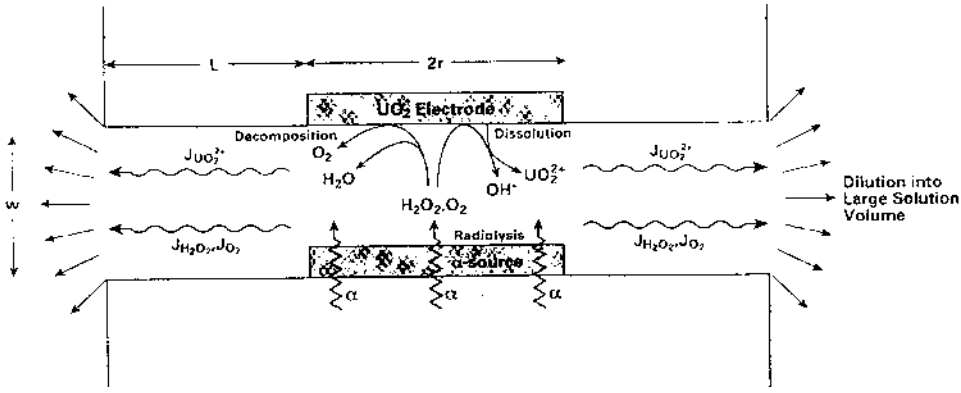

Figure 14 Schematic of the thin-layer electrochemical cell used to measure the influence of alpha radiolysis of water on the corrosion of nuclear fuel (UO_2).

$$\frac{\partial c_i}{\partial t} = \frac{D_i}{r}\frac{\partial}{\partial r}\left\{r\frac{\partial c_i}{\partial r}\right\} \tag{14}$$

for the many species, i, involved. Subsequently, an extrapolation of the anodic Tafel relationship to individual E_{CORR} values measured in the above manner can be used to produce a database of corrosion rates as a function of radiolytic oxidant concentration. This procedure is illustrated schematically in Fig. 15. As illustrated

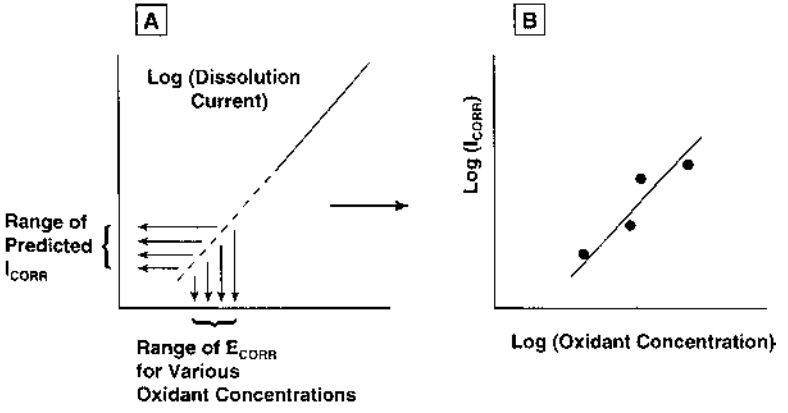

Figure 15 Procedure used to obtain a database of nuclear fuel (UO_2) corrosion rates (currents) (B) from a Tafel relationship for the anodic dissolution currents for UO_2 and a series of E_{CORR} values measured in radiolytically decomposed solutions (A).

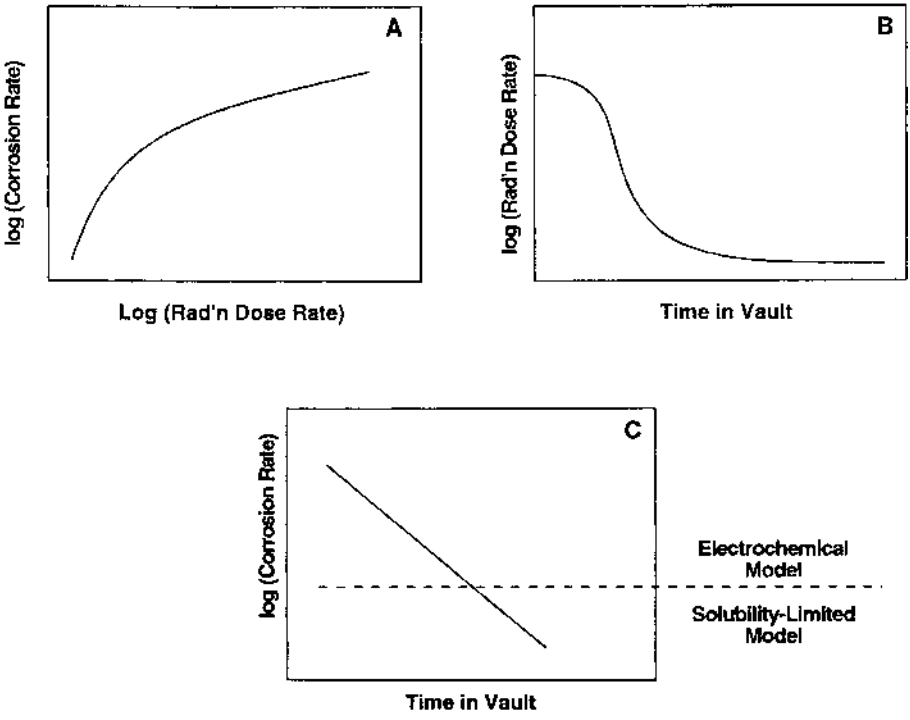

Figure 16 Illustration of the procedure used to evaluate fuel corrosion performance in a nuclear waste vault: (A) fuel corrosion rate as a function of radiation dose rate [from (B) in Figure 15]; (B) calculated radiation dose rate decay curve; (C) fuel corrosion rates as a function of time in a waste vault. The dashed line indicates that there is a limit to the acceptable extrapolation of rates determined electrochemically.

in Fig. 16, this database of rates can then be used with the easily calculable radiation decay characteristics of the fuel to predict the evolution of fuel corrosion rate as a function of time in a waste disposal vault.

B. Influence of Corrosion Product Deposits

Inevitably, corrosion is not a process that proceeds by straightforward, uncomplicated active dissolution, especially over extended exposure periods. Reactive materials (e.g., Fe, carbon steel, Cu, UO_2) corroding in neutral to slightly alkaline solutions ($4 < pH < 9$) when oxide/hydroxide solubilities are low, tend to accumulate corrosion product deposits.

These deposits will form at a rate determined by the material corrosion rate and the solubility of the deposit in the exposure environment. Predicting their rate of thickening and their ability to attenuate the corrosion rate of the substrate material could be a complicated procedure. The process involves at least one moving boundary (the material/deposit interface) and a knowledge of the evolution of deposit morphology, especially its porosity, as a function of increasing thickness. Also, the chemistry within the pores of a deposit is likely to differ from that of the general exposure environment and to involve diffusion gradients of various species such as dissolved metal cations, cathodic reagents (e.g., O_2), and pH. A detailed discussion of these features is beyond the scope of this chapter, but it is worth noting that a steady-state condition can evolve with extended exposure (15,16), and that key properties, such as porosity, would then be approximately constant.

For the sake of this discussion, it is assumed that the deposit is electrically insulating. This limits the available anodic and cathodic sites to the material surface at the base of the pores. If it is assumed that steady-state conditions exist within the deposit, then the only film parameter that changes as corrosion progresses will be its thickness. Ideally, the deposit can be considered to contain a uniform distribution of cylindrical pores, each of radius r_i and length l with the latter equivalent to the thickness of the film. The cross-sectional area of the pores will be $\sum \pi r_i^2$, their volume $\sum \pi r_i^2 l$, and the total volume of the deposit including pores, lA.

If the geometric surface area of the film is A, the total porosity of the deposit (ε) will be given by

$$\varepsilon = \sum_i \frac{\pi r_i^2}{A} \tag{15}$$

Consequently, the fraction of the fuel surface area exposed at the base of the pores is equal to ε. Since corrosion is confined to this exposed area, the rates of the interfacial anodic and cathodic reactions [i.e., Eqs. (7) and (8)] must be multiplied by this factor, ε, to account for the reduction in effective cross-sectional area. Figure 17 shows a schematic representation of this model.

This idealized model does not capture all of the essential details of corrosion deposits. As indicated in Fig. 17, the influence of local chemistry within the deposit (especially pH effects) is likely to separate the corrosion site (at the material/deposit interface) from the site at which the deposit forms (deposit/environment interface). Consequently, diffusion processes within the porous deposit must be involved if corrosion is to be sustained. Under simple steady-state conditions, diffusion can be treated simply using the Nernst diffusion layer approach; i.e., the flux, J, of a species dissolving in a pore will be given by

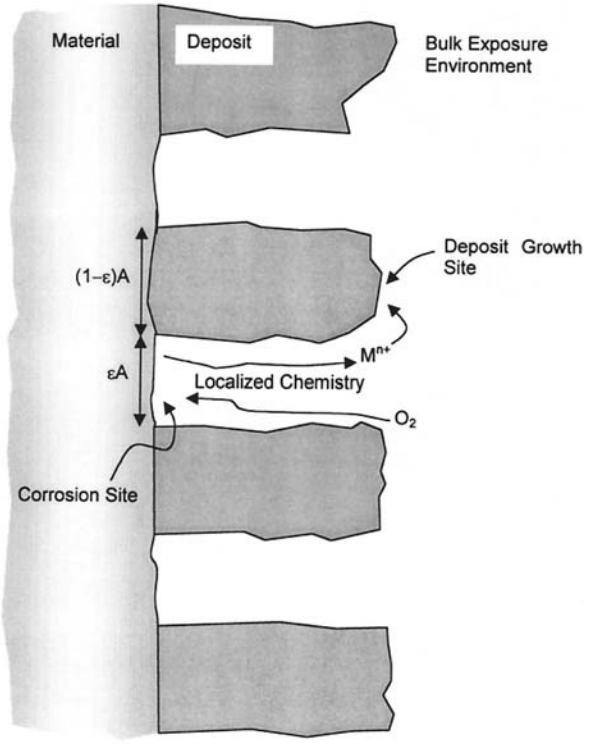

Figure 17 Schematic of an idealized corrosion product deposit on a corroding surface; l is the pore length, εA the fracture of the surface area exposed to the corrosion environment; $(1 - \varepsilon A)$ is the fraction of the surface blocked by corrosion product deposit.

$$J = D_{\text{eff}} \frac{\Delta c}{\Delta x} \sim D_{\text{eff}} \frac{\Delta c}{l} \tag{16}$$

where Δc is the difference in species concentration over the length of the pore, and the effective diffusion coefficient, D_{eff}, is the solution diffusion coefficient (D) attenuated by the porosity ($D_{\text{eff}} = \varepsilon D$). If we now accept a more general model, in which the corrosion product deposit is considered as a tortuous but continuous network of interconnected pores, Fig. 18, then the diffusion path length can be significantly greater than the film thickness, and the effective diffusion coefficient must be modified by a tortuosity factor (τ); i.e.,

$$D_{\text{eff}} = \varepsilon \tau D \tag{17}$$

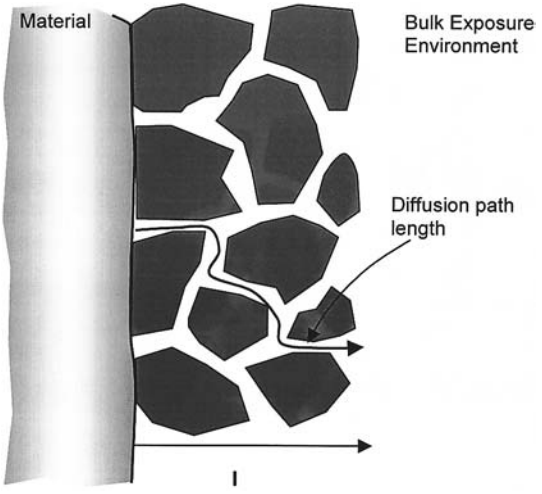

Figure 18 Schematic showing a corrosion product deposit composed of interconnected tortuous pores illustrating that the diffusion path length of dissolved species or dissolved oxidant through the deposit is greater than the thickness of the deposit.

Thus the key parameters influencing the corrosion rate under deposits will be the deposit porosity, which determines the available surface area of material for corrosion, and the deposit tortuosity, which along with porosity will modify the fluxes of diffusing species within pores. Readers interested in a more extensive discussion are referred to other sources (17). Here we concentrate on a brief discussion of electrochemical methods of investigating the properties of deposits as a basis for eventual modeling.

A primary methodology for investigating such processes is impedance spectroscopy (EIS). The interpretation of EIS data using equivalent circuits can yield a substantial amount of information on the properties of evolving films, and many detailed studies have been published (18,19). Here we attempt only to capture the essential features of such analyses. It should be noted before proceeding that, as with many electrochemical techniques, EIS records only a general surface response and does not yield site-specific information. For the present application, this means that EIS may successfully detect low-impedance pathways associated with pores but cannot differentiate easily between a large number of narrow pores and a small number of larger ones; i.e., it cannot on its own provide an accurate measure of deposit porosity. Microscope, metallographic and mercury porosimetry (20) measurements are necessary complements.

Figure 19 (A to E) shows a collection of potential EIS responses and possi-

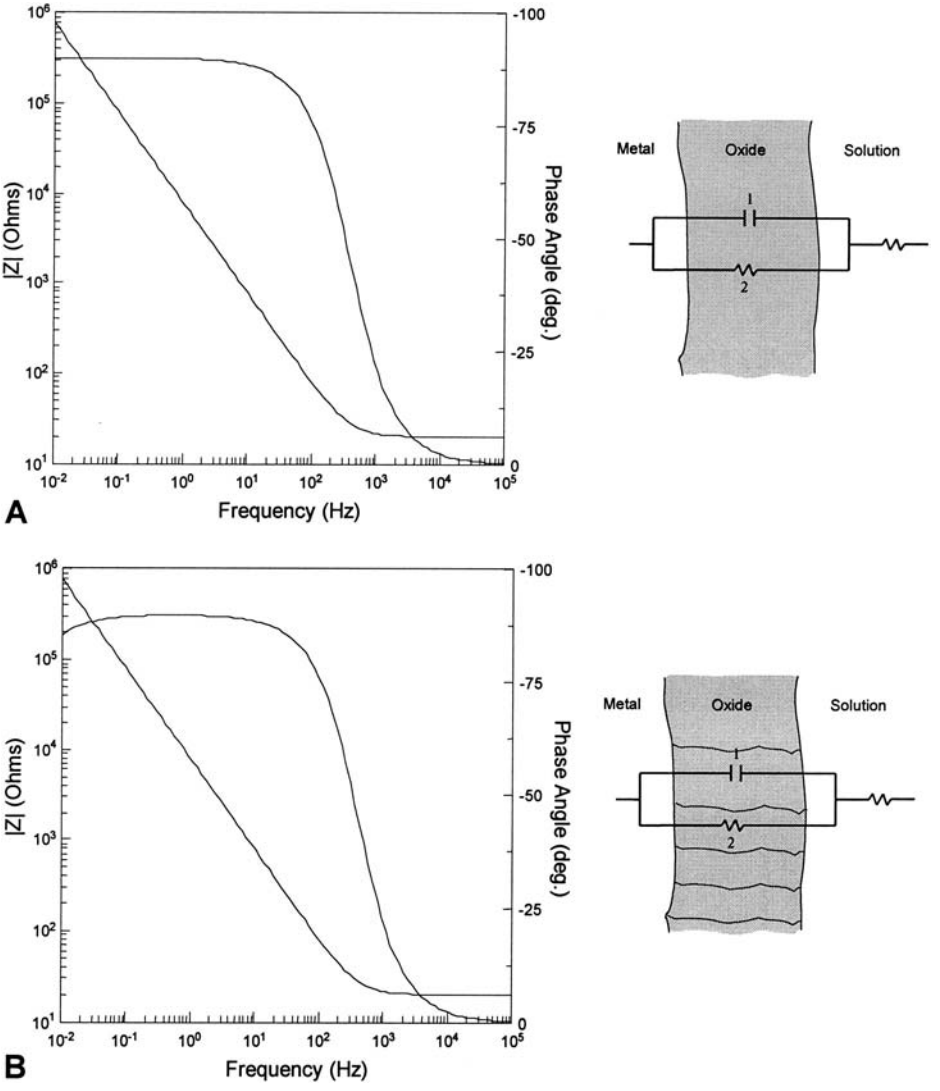

Figure 19 Schematic Bode plots from EIS measurements and equivalent circuits that could be used to fit them for various possible corrosion product deposit structures: (A) nonporous deposit (passive film); (B) deposit with minor narrow faults such as grain boundaries or minor fractures; (C) deposit with discrete narrow pores; (D) deposit with discrete pores wide enough to support a diffusive response (to the a.c. perturbation) within the deposit; (E) deposit with partial pore blockage by a hydrated deposit: (1) oxide capacitance; (2) oxide resistance; (3) bulk solution resistance; (4) interfacial capacitance; (5) polarization resistance; (6) pore resistance; (7) Warburg impedance; (8) capacitance of a hydrated deposit.

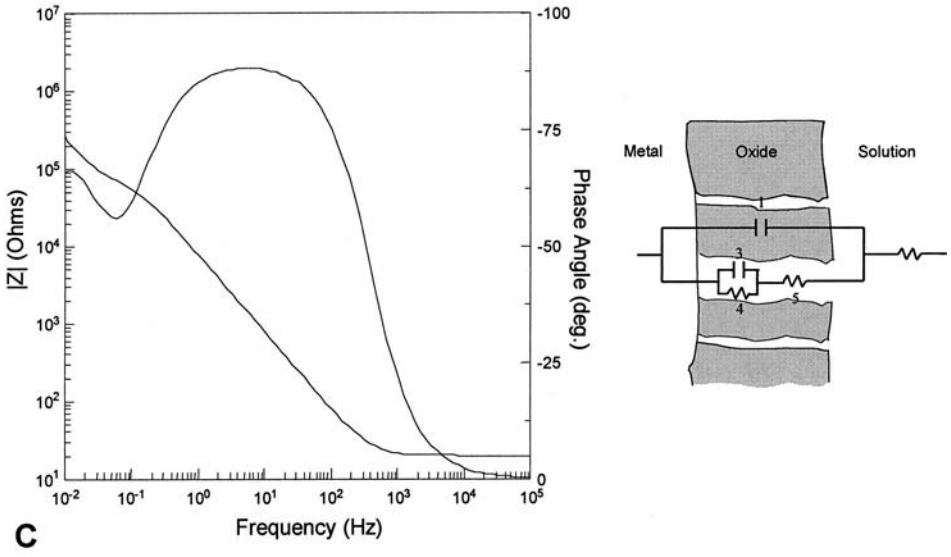

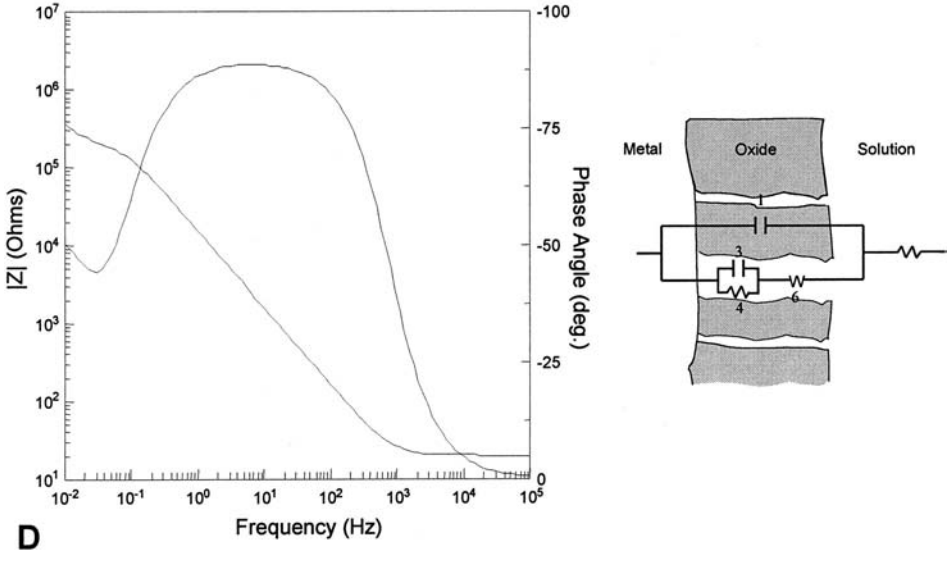

Figure 19 Continued

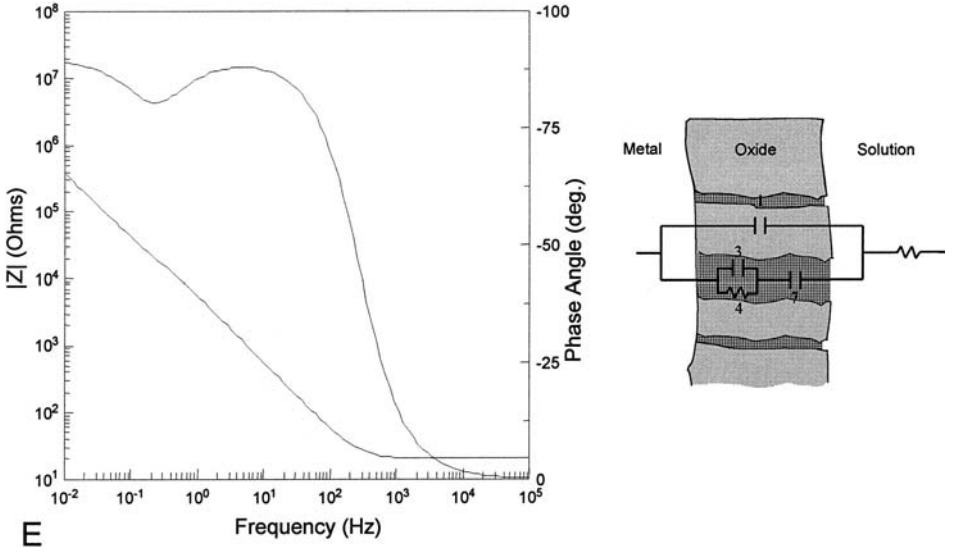

ble equivalent circuits that could be used to interpret them in terms of deposit properties. The key features in the spectra illustrating the influence of the deposit on the corrosion process are to be found at the low-frequency ends of the spectra. For a nonporous deposit, the response and simple parallel circuit shown in Fig. 19A would be expected. Since $R_F \sim 10^6$ ohm $\cdot$ cm^{-2}, the deposit effectively acts as a capacitor. Such a deposit is unlikely, and a system yielding this kind of response can be considered passive, since corrosion at the material/deposit interface could only be sustained by film dissolution/corrosion at the oxide/solution interface. Passivity is dealt with in the next section.

Deposits with extremely low porosities or an interconnected network of fine crystalline grain boundaries would be expected to show some loss of phase shift at low frequencies (i.e., a less than fully capacitative response) as the real resistance of the flaws becomes detectable, Fig. 19B. The value of R_F obtained is inversely proportional to the corrosion rate.

Eventually, as pores increase in size, additional equivalent circuit elements are required to account for the detection of these pores as discrete time constants in the low frequency end of the spectrum, Fig. 19C. As frequencies are scanned to lower values in recording the EIS spectrum, the frequency at which the decrease in phase shift (i.e., a decrease in absolute value of the phase angle) commences provides an indication of either the number density of fine pores or the dimensions of a smaller number of larger pores. The value of the pore resistance (R_{PORE}) is a more direct indication of pore dimension. The interfacial capaci-

tance (C_I) approaches values anticipated for the double-layer capacitance at the material/solution interface but could be significantly increased if adsorbed intermediates are involved in the interfacial corrosion process [e.g., $Fe(OH)_{ads}$ in carbon steel corrosion or $(UO_2HCO_3)_{ads}$ in nuclear fuel corrosion]. The interfacial resistance, R_I, is the system polarization resistance and is inversely related to the corrosion rate. Since both anodic and cathodic reactions occur at the base of pores in the deposit, R_I cannot distinguish which of these two reactions is of overriding importance in determining the corrosion rate. An attempt to separate the response of these reactions using EIS has been published (21).

For wider pores it becomes possible to detect the influence of diffusive transport within the pores. Under these circumstances, the use of the Warburg impedance (Z_w) is required to fit the data, where

$$Z_w = \sigma\omega^{-1/2}(1 - j) \tag{18}$$

and σ (ohm $s^{1/2}$) is the Warburg impedance coefficient. When diffusion is the dominant (rate controlling) process, the log $|Z|$ vs. log f (frequency) plot will approach a slope of -0.5 and a phase angle (θ) of -45 degrees as $\omega \rightarrow 0$. Inevitably, diffusion is not totally dominant, and control of the corrosion process at the base of the pore will be partially controlled by interfacial kinetics. For this situation, the slope of log $|Z|$ against log f will change with frequency in the rage 0 to -0.5, and θ will change with frequency over the range 0 to -45 degrees, as illustrated in Fig. 19D.

The final section of Fig. 19, E, shows the EIS response anticipated if the accumulation of hydrated deposits were to partially reseal the pores. These deposits tend to act like a capacitor, C_H. Such an EIS response would be anticipated in complex environments (e.g., ones containing a number of anions) or in pores with complex chemistry (e.g., containing large gradients in pH and/or metal cation complexants). It is clear from the Bode plots in Fig. 19 that distinguishing between possible behaviors is not simple.

Many of these approaches have been used in mixed potential models to predict the behavior of copper nuclear waste containers in a compacted clay environment (22), and to predict the corrosion rate of nuclear fuel inside these containers once they have failed and water allowed to contact the nuclear fuel (UO_2) wasteform (6). The container is lined with a carbon shell liner to give it mechanical integrity. Consequently, when the container floods with water on failure,* two corrosion processes are possible, corrosion of the UO_2 wasteform (conservatively assumed to be unprotected by the Zircalloy cladding within which it is encapsulated) and corrosion of the carbon steel liner. The reaction scheme underlying

* This is an example of a conservative assumption permissible in such a performance assessment model. In reality, a narrow aperture failure in the copper shell would allow only a very slow entry of water into the container.

this model is shown in Fig. 20. The two interfacial corrosion processes are linked by the aqueous environment, a scenario that introduces the possibility that each corrosion process can interfere with the other. Interconnecting diffusion processes makes a wide range of adsorption, desorption, solution redox, and precipitation processes possible (6). Fuel corrosion will be driven by the alpha radiolytic production of the oxidants H_2O_2 and O_2 and carbon steel corrosion by reaction with water. A key potential interaction that could suppress fuel corrosion is the scavenging of the radiolytic oxidants (H_2O_2, O_2) by Fe^{2+} formed by carbon steel corrosion reactions (k_4, k_5).

The model solves a set of 10-one-dimensional reaction–diffusion equations for the ten key species involved in corrosion processes [UO_2^{2+}, $UO_2(CO_3)_2^{2-}$, $UO_3 \cdot 2H_2O$, CO_3^{2-}, O_2, H_2O_2, Fe^{2+}, $(Fe^{II})_{ppt}$, $(U^{IV})_{ppt}$, $(UO_2^{2+})_{ads}$],

$$\varepsilon \frac{\partial c_i}{\partial t} = \frac{\partial}{\partial x}\left\{\tau\varepsilon D_i \frac{\partial c_i}{\partial x}\right\} + \varepsilon \sum_{j=1}^{10} R_j \tag{19}$$

where R_j represents the chemical reactions occurring in the system; the diffusion coefficient, D_i, is modified to take into account that the species will, on occasion, be diffusing within the porous corrosion product layers on the two corroding surfaces. The boundary conditions within this model are the electrochemical expressions, similar in form to those shown in Eqs. (8) and (9) above, for those species involved in anodic and cathodic reactions at the fuel and carbon steel surfaces.

The fuel corrosion rate is given by

$$I_{CORR} = \sum_i I_{Anod} = I_{UO_2^{2+}} + I_{UO_2(CO_3)_2^{2-}} \tag{20}$$

The two anodic reactions on the fuel surface are

$$UO_2 \xrightarrow{k_A} UO_2^{2+} + 2e \tag{21}$$

$$UO_2 + 2CO_3^{2-} \xrightarrow{k_B} UO_2(CO_3)_2^{2-} + 2e \tag{22}$$

The fuel corrosion potential, E_{CORR}, is computed from the relationship

$$\Sigma I_{Anod} + \Sigma I_{Cath} = 0 \tag{23}$$

which applies only at E_{CORR} and can be expanded to yield

$$\{I_{UO_2^{2+}} + I_{UO_2(CO_3)_2^{2-}} + (I_{H_2O_2})_A\} + (I_{O_2} + (I_{H_2O_2})_C\} = 0 \tag{24}$$

An anodic and cathodic current is included for H_2O_2 since electrochemical experiments indicate that this species may be catalytically decomposed by the fuel surface:

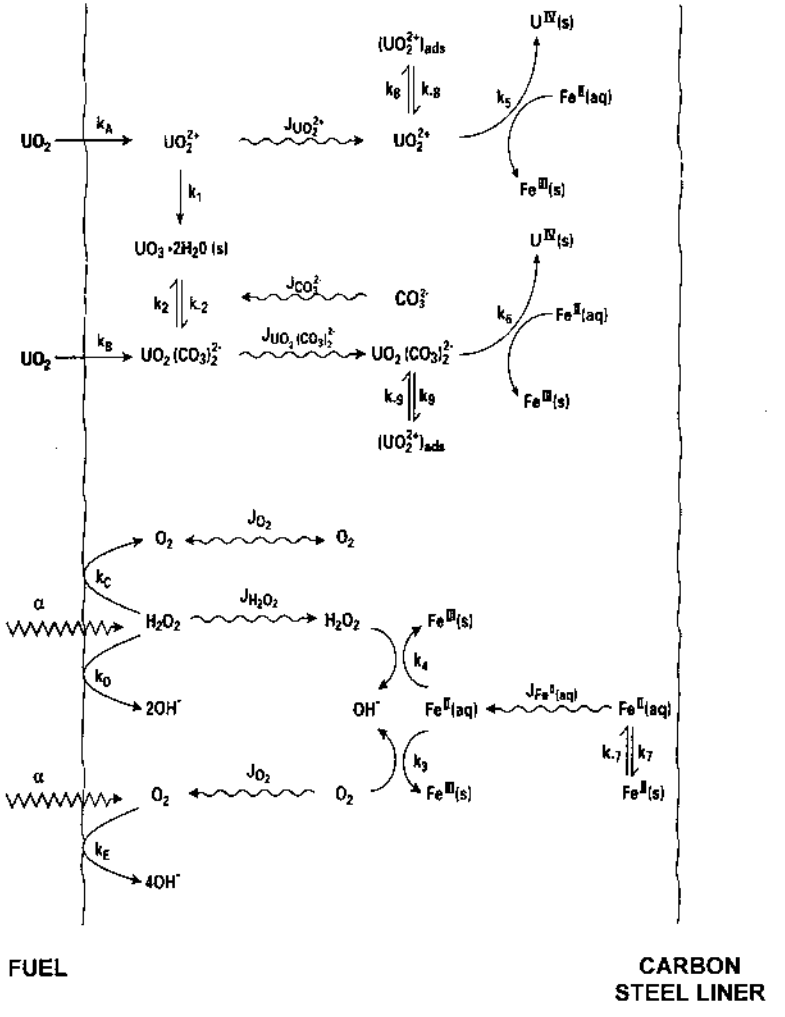

Figure 20 The reaction scheme considered for nuclear fuel (UO_2) corrosion inside a failed (flooded) carbon-steel-lined nuclear waste container.

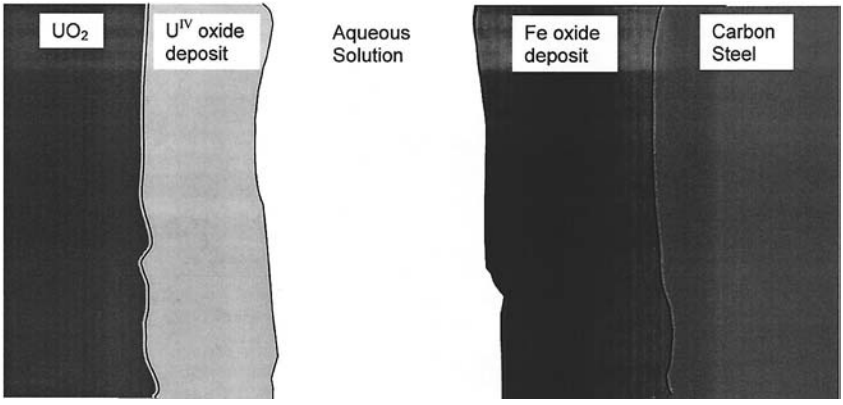

Figure 21 Schematic illustrating the one-dimensional array of layers considered in the mixed potential model of nuclear fuel corrosion in a failed (flooded) nuclear waste container.

$$2H_2O_2 \rightarrow O_2 + 2H_2O \tag{25}$$

The diffusion–reaction equations are solved using finite-difference techniques employing a multilayer spatial grid to account for the corrosion product deposits present on the fuel and carbon steel surfaces, Fig. 21. For further details the reader is referred to more extensive discussions published elsewhere (6,23).

Other examples of such mixed potential models include that developed by Macdonald and Urquidi-Macdonald to predict water radiolysis effects in thin condensed water layers on metal surfaces (24), and the models of Marsh and Taylor (25), and Kolar and King (22) to predict the corrosion of carbon steel and copper waste containers surrounded by a low permeability material such as clay.

C. Passive Conditions

Most modern industrial materials are designed to be passive; i.e., covered by an adherent, chemically inert, and pore-free oxide that is highly insoluble in aqueous solutions and hence dissolves at an extremely slow rate. Examples would be modern stainless steels, nickel-chromium-molybdenum, and titanium alloys. The concept of passivity is often defined by reference to the polarization curve for metals and alloys in aggressive acidic solutions, Fig. 22. This curve defines the potential regions within which the alloy would be expected to corrode actively or passively.

In the passive region, values of the passive corrosion rate could be obtained from a polarization curve, though there is no guarantee that it would represent

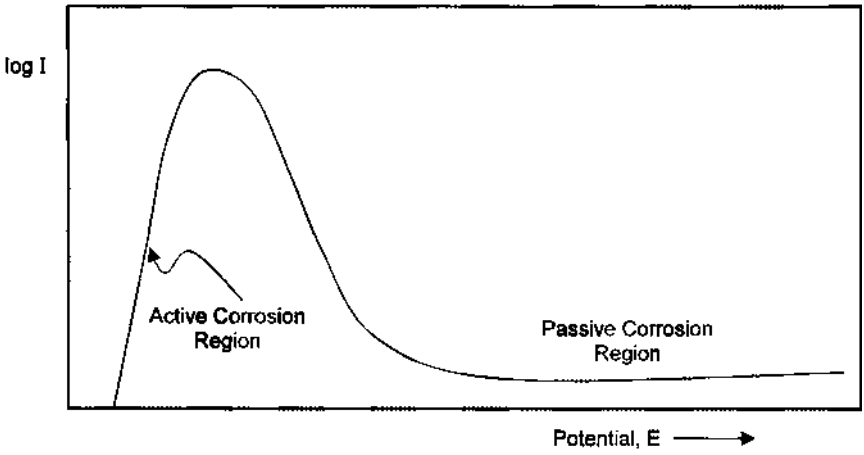

Figure 22 Schematic anodic polarization curve indicating active and passive corrosion regions.

the true passive corrosion rate under steady-state conditions. A more reliable value could be obtained by potentiostating the material in the passive region and recording the passive current only after steady-state conditions were achieved. In this manner the transient changes in film composition and/or defect density induced by rapidly enforced film growth are complete, and the film is more representative of that expected under natural corrosion conditions. In these applications there is no need to model the corrosion processes. However, for the specialized application of nuclear waste disposal, when maintenance of passivity over 10^5 years is required, it is necessary to consider how passivity may evolve over long time periods, especially when changes in exposure environment (e.g., salinity and temperature) may change. Under these circumstances, passive corrosion may not be as simple a process as initially envisaged.

An example would be the long term passive corrosion of titanium. Over observable time periods the passive oxide film on titanium grows via either a direct logarithmic or an inverse logarithmic growth law (24,25). Under these conditions, the rapid development of an electric field in the oxide would prevent the ionic conduction (of Ti^{4+} and/or O^{2-}) necessary to sustain film growth. To all intents and purposes, film growth would effectively stop. However, crystallization, a process that seems inevitable over long exposure periods, would introduce a high density of grain boundaries along which ionic conduction to sustain film growth could be facilitated. Under these conditions, passive film growth is effectively the same as the thickening of a corrosion product deposit, as was discussed above. A difference between the two processes might be that, in the case of

passive film growth, the original pore-free passive layer could survive as a thin barrier layer of constant thickness, while film growth led to a thickening of an outer recrystallized layer. This is the commonly accepted view of passivity (26). If these conditions prevailed, the electric field in the barrier layer would remain constant and, assuming the recrystallized layer exerted no retarding influence on continued growth, a linear film growth process (and hence a constant corrosion rate) would be maintained. This scenario is represented in Fig. 23A.

A second possibility is that a linear corrosion rate could also be maintained by the finite dissolution rate of the film in the environment. For this situation, the rate of film thickening would eventually be counterbalanced by the rate of film dissolution, leading to both a constant film thickness and a constant corrosion

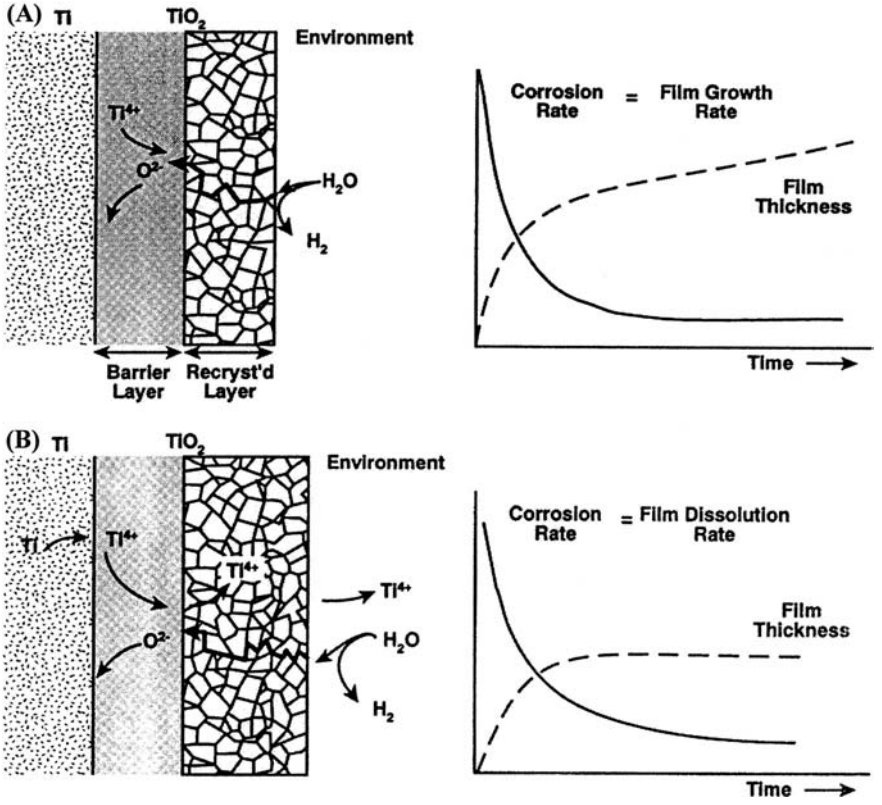

Figure 23 Various reaction scenarios for the passive corrosion of titanium alloys: (A) linear oxide film growth due to film recrystallization; (B) linear film growth kinetics maintained by film dissolution.

rate, Fig. 23B. A complication with this second process is that film growth and dissolution may not proceed uniformly across the surface and that a transition from slow passive film growth to a more rapid growth of a corrosion product deposit could occur. If the dual exposure of metal and oxide occurs, then the galvanic coupling of metal dissolution and oxide dissolution may become possible, a process likely to be facilitated by the development of local acidity within these local pores, Fig. 17. Such processes are well documented for reactive metals such as Fe and carbon steel (27), and they help to explain the thick film formation in situations such as the development of tubercles in water pipe systems (28). While theoretically possible with metals like titanium, such a process is only likely under reducing acidic conditions and will not be considered further here.

The direct electrochemical measurement of such low corrosion rates is difficult and limited in accuracy. However, electrochemical techniques can be used to establish a database against which to validate rates determined by more conventional methods (such as weight change measurements) applied after long exposure times. Blackwood et al. (29) used a combination of anodic polarization scans and open circuit potential measurements to determine the dissolution rates of passive films on titanium in acidic and alkaline solutions. An oxide film was first grown by applying an anodic potential scan to a preset anodic limit (generally 3.0 V), Fig. 24, curve 1. Subsequently, the electrode was switched to open-circuit and a portion of the oxide allowed to chemically dissolve. Then a second anodic

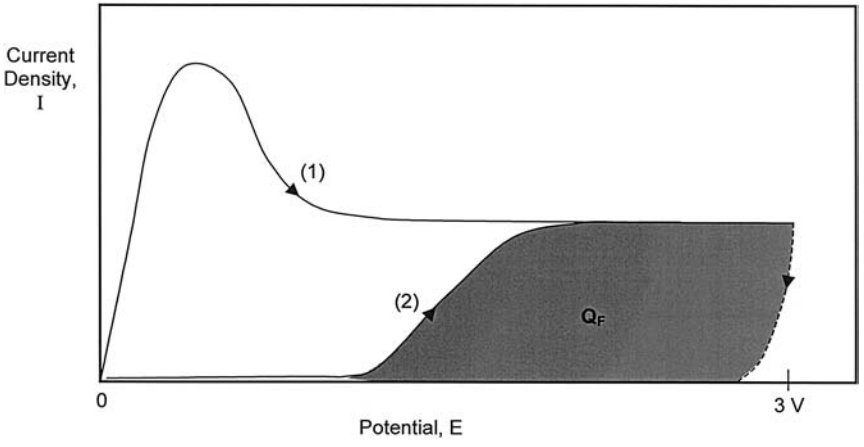

Figure 24 Schematic polarization curve showing the anodic film reformation technique for determining passive oxide dissolution rates; (1) original anodic polarization scan to grow the oxide film; (2) second anodic polarization scan to regrow the oxide dissolved on open circuit. Q_F is the charge lost in open-circuit dissolution between the two scans.

scan was performed from the open-circuit potential attained to the same anodic limit, Fig. 24, curve 2. The charged passed in reforming the oxide (Q_F in Fig. 24) is a direct measure of the amount of film dissolved on open circuit. This charge divided by the time spent on open circuit yields a value for the passive film dissolution rate. Since these authors also determined a pH dependence for the oxide dissolution process, it was then possible to extrapolate these rates to more neutral environments. A comparison of these extrapolated rates to those obtained by other nonelectrochemical techniques yielded a gratifyingly close agreement, thereby strengthening the justification for the use of the latter values in corrosion models.

Based on measurements of this kind, the lifetimes of titanium nuclear waste containers under Canadian waste disposal conditions have been modeled (30). Since these conditions are expected to be anoxic, the passive corrosion of titanium will be driven by a very slow reaction with water, leading to the possibility of hydrogen adsorption into the metal:

$$\begin{aligned} \mathrm{Ti} + 2\mathrm{H_2O} &\rightarrow \mathrm{TiO_2} + 2\mathrm{H} \\ &\rightarrow \mathrm{TiO_2} + f_{\mathrm{H}}(2\mathrm{H})_{\mathrm{abs}} + (1 - f_{\mathrm{H}})\mathrm{H_2} \end{aligned} \tag{26}$$

where f_H is the fractional efficiency for H absorption into the metal, the remaining fraction being lost to the environment as evolved H_2. Hydrogen absorbed in this fashion will precipitate in the metal as titanium hydrides (TiH_x ($1 < x < 2$)) and, once a critical hydrogen level is achieved, render the material potentially susceptible to hydrogen-induced cracking (HIC).

Since these hydrides are thermodynamically stable in the metal, the passive oxide can only be considered as a transport barrier, not as an absolute barrier. Various electrochemical techniques including EIS and photoelectrochemical measurements have been used to identify the mechanism by which the TiO_2 may be rendered permeable to hydrogen, and to identify the conditions under which absorption is observable (31). These determinations show that H absorption into the TiO_2 (and hence potentially into the metal) occurs under reducing conditions when redox transformations ($Ti^{IV} \rightarrow Ti^{III}$) in the oxide commence. However, the key measurement, if H absorption is to be coupled to passive corrosion, is that of the absorption efficiency.

A measurement of f_H can be achieved electrochemically (32). Under galvanostatic (constant current) cathodic conditions, the fractional efficiency of hydrogen absorption is the ratio of the amount of hydrogen produced electrochemically to the amount absorbed by the metal, as is illustrated in Fig. 25. While this appears to be a very simple direct measurement, it has the normal problems associated with an accelerated electrochemical measurement, including the need to demonstrate that the parameter measured electrochemically will retain the same value under the much slower natural corrosion conditions.

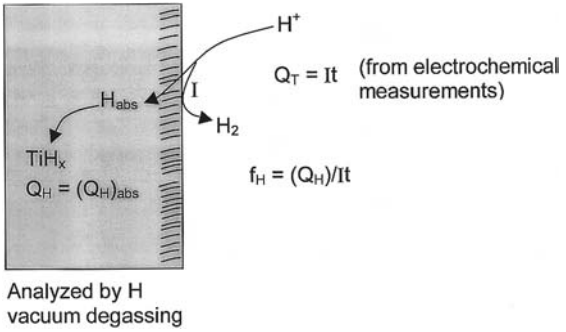

Figure 25 Schematic illustrating the galvanostatic method of determining the hydrogen absorption efficiency of titanium.

Using a constant corrosion rate multiplied by the adsorption efficiency measured as described above, the rate of hydrogen absorption into the metal was calculated, and susceptibility to HIC was assumed to be established once a critical hydrogen concentration (H_C) was reached. A more detailed discussion of this simple conservative model, including a description of the determination of H_C from mechanical experiments, is described elsewhere (33). The conservatism in the model arises from the assumption that all the hydrogen absorbed is retained by the metal rather than released by oxidation as the corrosion process proceeds through the metal. As was emphasized in the introduction, such a conservatism is acceptable in a model where safety is the primary requirement. The approach described would be too conservative for an industrial service model.

D. Localized Corrosion Processes

When one is dealing with localized corrosion processes, the tendency is experimentally to determine or model whether a particular process can occur in a specific environment; i.e., to determine the susceptibility. Such procedures are invaluable in materials selection, and the use of electrochemical methods is an integral part of these efforts. However, in some environments it is injudicious to assume that localized corrosion will not occur. One example would be SCC in nuclear reactor heat exchangers and other components. In other applications, the need to minimize materials costs leads to the selection of materials for which there is no guarantee of immunity to localized corrosion. For such applications there is a strong need for models that will predict how fast such processes will propagate once they are initiated and what kind and extent of damage will accumulate.

Local corrosion sites are typified by (1) local chemistries that are commonly only loosely related to the bulk exposure environment, (2) the separation of anodic and cathodic sites, and (3) the localization of corrosion damage sites (i.e., within pits, crevices, and cracks). Since, within a local corrosion site, the reactive surface area to available solution volume can be very large, extreme environments (in terms of concentration, concentration gradients, pH) are often encountered. For the same geometric reasons, these environments are difficult to characterize. Extremely high corrosion current densities can be sustained within the local site by the presence of much lower cathodic current densities over a much larger available surface area outside the corrosion site. Finally, the existence of ionic and concentration gradients between the local corrosion site and the external environment introduces complex transport scenarios.

Many models exist to predict the conditions within these sites (e.g., 34,35). However, if the primary need is to determine the extent of corrosion damage (e.g., the depth of corrosion penetration), these models are not sufficient. Generally, electrochemical techniques contain no spatial information, since the current measured is the sum of currents from all individual corrosion sites. In the case of pitting, this limitation is being slowly erased as scanning techniques capable of spatial resolution are being developed. However, the ability to resolve local corrosion sites within fixed occluded areas such as cracks and crevices remains minimal.

The generally applied electrochemical procedure to predict when localized corrosion can initiate is to compare the system corrosion potential (E_{CORR}) with the breakdown (E_B) and/or repassivation potential (E_R) measured in a polarization experiment. This procedure is illustrated schematically in Fig. 26 for pitting or crevice corrosion. The shaded areas associated with E_B and E_R indicate the range of values (usually normally distributed) associated with these two parameters. Defining these distributions is a major need in reducing the uncertainties inherent in predicting the probability of occurrence of localized corrosion. A good example of the electrochemical and statistical approaches to achieve this goal has recently been published by Kehler et al. (36). An example of a polarization curve to record E_B and E_R for the Ni-Cr-Mo alloy C-276 in high-temperature saline solution is shown in Fig. 27 (37).

Figure 26 shows that known values of E_B and E_R, coupled to a knowledge of how E_{CORR} evolves with exposure time, allow the specification of the duration of the period of propagation of localized corrosion. The difference between the two periods A and B is a measure of the uncertainty in the duration of propagation due to the distribution in the repassivation potential. The use of E_R, as opposed to E_B, to specify the period of localized corrosion is conservative, and the efficacy of relying on this parameter in safety assessment models has been demonstrated by Sridhar et al. (38). These authors also showed that the value of E_R decreases as the extent of corrosion damage sustained during the propagation period in-

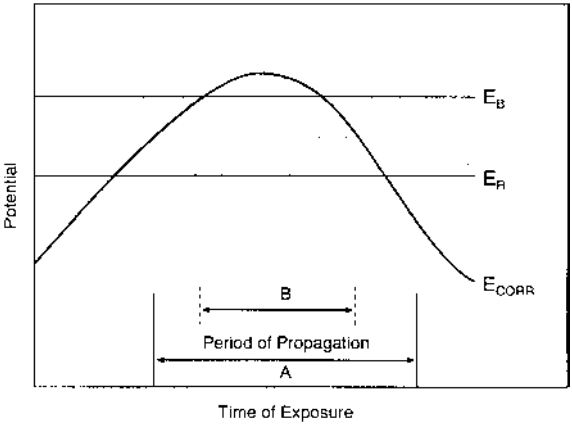

Figure 26 Illustration of the period of propagation of localized corrosion (pitting) as defined by the relative values of E_{CORR} and the breakdown (E_B) and repassivation potentials (E_R). The shaded areas associated with E_B and E_R illustrate the uncertainties in the values of these two parameters.

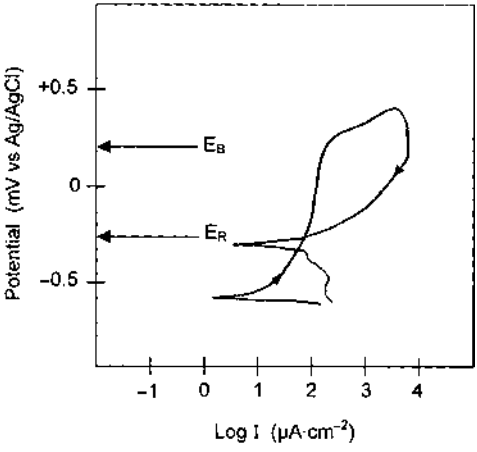

Figure 27 Anodic polarization scan recorded on a creviced specimen of the Ni-Cr-Mo alloy C276 in 0.59 mol · dm^{-3} NaCl at 150°C at a scan rate of 0.8 mV · s^{-1}.

creases. This highlights the dangers inherent in relying on E_R values measured under dynamic polarization conditions. More appropriately, the time should be taken to measure these values potentiostatically over a sufficient time period that they are uninfluenced by the extent of localized corrosion damage.

Attempts to determine the extent of corrosion damage during the propagation period are also fraught with difficulties. A substantial amount of evidence exists to show that electrochemically grown pits obey the empirical growth law

$$d = kt^n \tag{27}$$

where d is the maximum depth of penetration, k is a pit growth constant, and the time exponent n empirically incorporates the penetration limiting features of the localized process (38, and references therein). The maximum pit depth is the key depth determining first failure. Simple theoretical developments show that this relationship does represent pit growth under either diffusion or IR control (40).

A source of doubt in such analyses is whether the depths of the pits grown electrochemically are representative of those expected under natural conditions and therefore appropriate to extrapolate to longer times in predictive models. The data shown for pitting of carbon steel, sketched in Fig. 28, show that they are not. Clearly, growth is accelerated under potentiostatic electrochemical conditions, and the extrapolation of pit depths seriously overestimates the predicted pit depths after long exposure times. This is not surprising, since the use of a

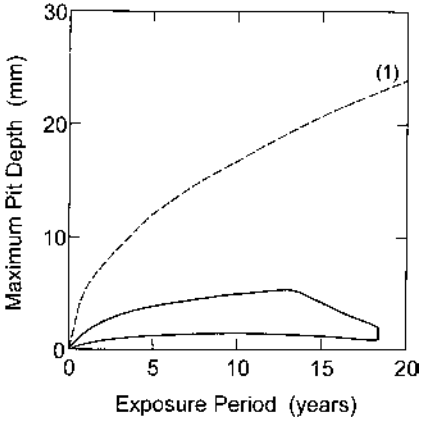

Figure 28 Illustration of the problems encountered when trying to produce a database of pit depths in an accelerated electrochemical experiment. The shaded area shows the range of pit depths on naturally corroded steel specimens in a range of soil types. (1) Predicted pit depth evolution based on potentiostatically grown pits. (Data schematically reproduced from Ref. 50.)

potentiostat will override the natural stifling features inherent in pit growth by allowing no limit on the pits' demand for sustaining current. As emphasized by Shoesmith et al. (41) and Laycock and Newman (42), limitations on the supply of current by the external cathodic reaction and chemical/geometric features within the pit can lead to the stifling/repassivation of pits at shallower depths than would be predicted based on electrochemical measurements. For this reason care must be taken in using the depths of electrochemically grown pits in predictive models. Consequently, whenever possible, models to predict the evolution of pit depths have relied on the statistical evaluation of naturally grown pit populations (43–45). Unfortunately, such extensive databases are not commonly available.

For the stochastic process of pitting, this limitation on the application of electrochemical methods is difficult to avoid. For crevice corrosion, however, the localized corrosion sites are confined within a well-defined occluded site and hence are more easily simulated in an electrochemical experiment. By coupling an artifically creviced electrode through a zero resistance ammeter to a large planar counterelectrode of the same material, it is possible electrochemically to monitor the propagation of crevice corrosion without the use of a potentiostat. By making the coupled cathode area much bigger than the creviced area, the small anode/large cathode characteristic of a natural crevice is achieved. Also, the influence of the available cathodic area on the crevice corrosion process can be simulated by varying the anode-to-cathode ratio. If a reference electrode is included in the same cell and connected via a high-impedance voltameter to the creviced electrode, it is possible simultaneously to monitor both the crevice potential and the crevice current. If these electrodes are sealed into a pressure vessel, experiments of this kind can be conducted at high temperatures (up to ~270°C) of industrial relevance (13).

For some materials (e.g., nickel alloys), the current is a direct measure of the rate of crevice propagation. For systems such as titanium alloys, however, internal cathodic reactions are also possible, as is illustrated in Fig. 29. This figure shows schematically the important electrochemical and chemical reactions occurring within the creviced area and on the coupled counterelectrode. This system will be used to illustrate the information that can be obtained from this galvanic coupling technique and how it can then be used directly in the development of models.

Once crevice propagation is underway, the reduction of O_2 on the coupled cathode drives metal dissolution, which only occurs within the acidified occluded area of the crevice. Hydrolysis of dissolved cations leads to the formation of a $TiO_2 \cdot 2H_2O$ deposit that tightens the crevice, and to the generation of protons, which further suppress the pH. As a consequence, the metal dissolution is further accelerated by proton reduction within the crevice, leading to both the evolution of hydrogen and the absorption of hydrogen into the metal. This absorbed hydro-

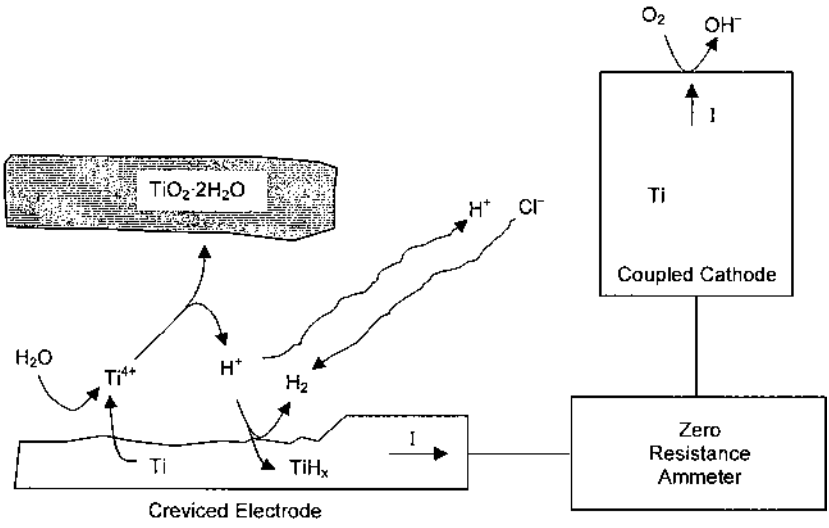

Figure 29 Schematic showing the important electrochemical/chemical reactions occurring inside a creviced titanium electrode and on a Ti cathode coupled to the creviced electrode through a zero resistance ammeter.

gen leads to the precipitation of titanium hydrides. The key feature of the proton reduction reaction is that the current generated is short-circuited within the crevice. Hence this internal contribution to crevice propagation is undetectable electrochemically; i.e., it does not contribute to the current measured by the ammeter (Fig. 29). This dual cathode response introduces a second potential failure mode for Ti under crevice conditions. The first is, of course, penetration of the wall thickness by metal dissolution. This second mode is hydrogen-induced cracking as a consequence of H absorption and TiH_x formation in the presence of tensile stresses.

Figure 30 shows the general form of the crevice current (I_C), creviced electrode potential (E_C), and the potential of a planar electrode (E_P) monitored in the same experiment for comparison. The form of these parameters represents the behavior observed for experiments conducted within a sealed pressure vessel containing a fixed charge of oxygen. Consequently, an experiment conducted at constant temperature will capture the crevice behavior from initiation, through propagation, to repassivation as the O_2 within the vessel is consumed. Initiation is indicated by a separation between E_p and E_C as E_C drops accompanied by the onset of I_C. As propagation proceeds, E_C remains low as expected for active crevice conditions, while I_C increases as crevice propagation spreads within the crevice and then falls as the available O_2 is consumed. E_p remains positive, while

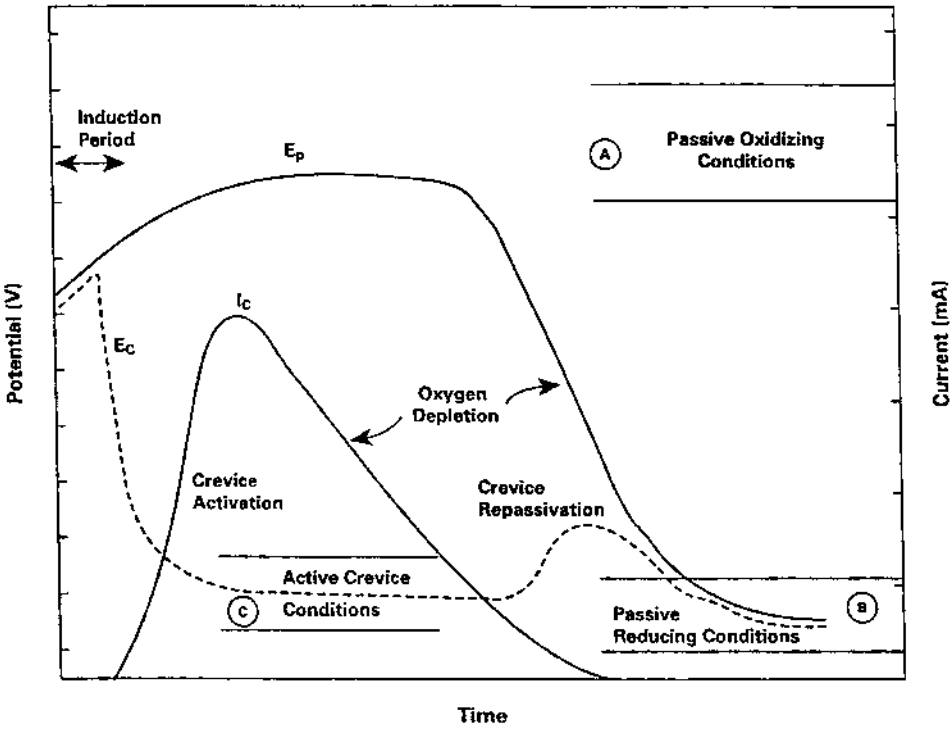

Figure 30 The general form of the crevice current (I_C), crevice potential (E_C), and planar electrode potential (E_P) measured using a galvanic coupling technique. (A) Range of planar electrode (corrosion) potentials (E_P) measured for passive corrosion under oxidizing conditions; (B) range of E_P values measured for passive corrosion under anoxic conditions; (C) range of crevice potentials (E_C) measured during active crevice propagation.

passive oxidizing conditions prevail on the planar electrode, but begins to fall as O_2 is depleted. The onset of repassivation is marked by a fall in I_C to zero and an equalizing of the E_C and E_p values. This equalization often involves a slight rise in E_C as I_C approaches zero. In the example shown, repassivation does not occur until all available O_2 is consumed and passive reducing conditions are established. For more crevice-resistant materials, such as Ti-12, on which propagation is limited by materials properties, E_C rises to meet E_p while passive oxidizing conditions still prevail.

Many features and much mechanistic detail on crevice corrosion can be determined using this technique (46). Here the discussion is concentrated on the

determination of those parameters that will enable us to develop a predictive model for the crevice corrosion process.

Since I_C is a measure of the rate of crevice propagation supported by O_2 reduction on the coupled cathode, the total amount of O_2 consumed (Q_C) can be found from

$$Q_C = \int_{t_I}^{t} I_C \cdot dt \tag{28}$$

where t_1 is the time of initiation. To determine the total crevice propagation rate we must also determine the rate of internally supported propagation (i.e., by H^+ reduction). This rate cannot be monitored continuously in the electrochemical experiment and must be determined from weight change (W) measurements on a series of specimens from experiments of different duration. A parameter $g = W/Q_C$ can be defined as the ratio of the total extent of crevice propagation to that supported only by O_2 reduction, from which the total rate of propagation (R_{CC}) can be evaluated,

$$W = gQ_C = \int_{t_I}^{t} R_{CC} \cdot dt \tag{29}$$

The parameter g has been determined, from this kind of investigation, to be ~5 and constant; i.e., ~80% of propagation is supported internally by proton reduction (47) under rapid propagation conditions. Since only the internal cathodic reaction supports hydrogen absorption, the rate of hydrogen absorption (R_{HA}) can be defined by

$$R_{HA} = f_H(R_{CC} - I_C) = f_h I_C \frac{W - Q_C}{Q_C} \tag{30}$$

where f_h is the fraction of the hydrogen produced that is absorbed by the metal. This efficiency was determined by measuring the hydrogen content of the crevice volumetrically after vacuum degassing and found to be ~0.15 and independent of propagation rate (32,33). Since this value was obtained by postexamination of the crevice, it is an overall efficiency and may disguise a variation in efficiency as propagation proceeds.

Since metallographic examination of the crevice shows the hydrogen concentrates within a surface hydride layer within the crevice (32,33), continuing propagation will oxidatively dissolve this layer as well as promote absorption. Consequently, we would expect the hydrogen concentration to achieve a steady-state value as propagation progresses, and eventual failure will be by wall penetration, not HIC. Thus it is necessary to connect the extent of propagation (Q_C, W) to the maximum depth of wall penetration (P_w). This can be done using metallographic and image analysis techniques (48) for a series of crevices that have

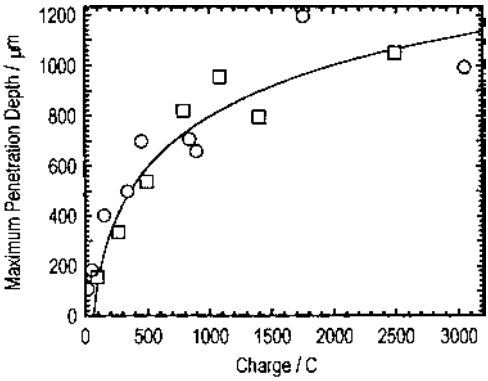

Figure 31 Maximum penetration depths measured on Ti-2 specimens crevice corroded in 0.27 mol · dm^{-3} NaCl at 100°C (□) and 150°C([1]) for various amounts of oxygen consumed.

propagated for different durations (t) and hence extent (Q_C). Figure 31 shows the relationship between P_W and Q_C determined for two temperatures. The interesting feature is that while the propagation rate is much faster at 150°C than at 100°C, the depth of penetration is independent of this rate and apparently dependent only on the amount of O_2 consumed. This greatly simplifies the eventual model development, since only one damage function (P_w vs. Q_C) is required.

The electrochemical and supplementary procedures described above have been used to develop a model to predict the extent of corrosion damage sustained by Canadian nuclear waste containers constructed from different titanium alloys. As noted in Fig. 1, before model development can begin it is necessary to specify the exposure environment and how it will evolve with time. As shown schematically in Fig. 32, within a waste vault the temperatures will be initially high but will decrease with time as the heat-producing radioactivity within the fuel decays. Also, the initially high O_2 concentration, trapped within the vault on sealing, will decrease with time as it is consumed by the corrosion process and/or scavenged by oxidizable minerals or organics in the backfill materials compacted around the container. As a consequence of this evolution in environmental conditions, two distinct periods can be defined (Fig. 32): an early warm oxidizing period lasting, at most, up to a few hundred years, and a longer term cool nonoxidizing period, which would prevail indefinitely. Intuitively therefore, crevice corrosion would be most likely to initiate and propagate using the warm oxidizing period, but to repassivate eventually as cooler nonoxidizing conditions are established.

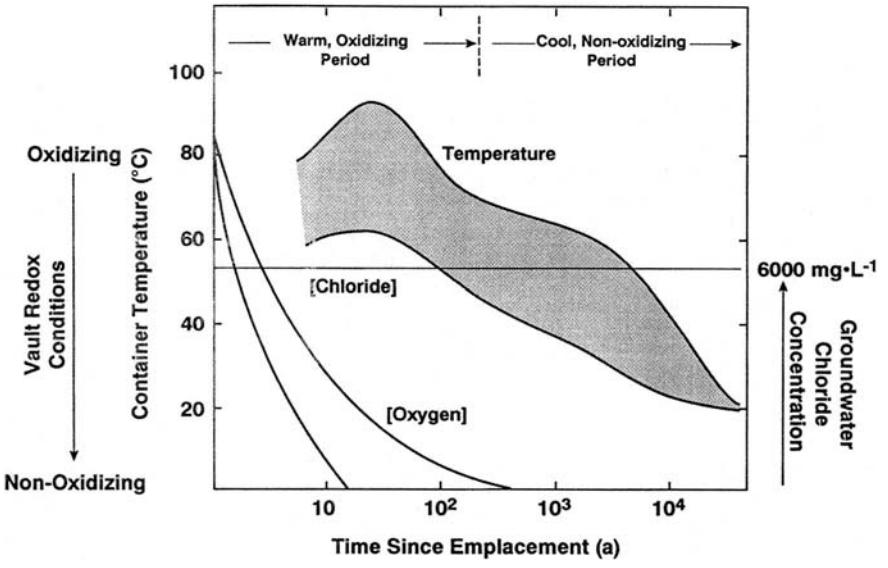

Figure 32 Expected evolution of the key environmental parameters within a Canadian nuclear waste vault. The shaded area for temperature illustrates the distribution of waste container cooling profiles within the waste vault. The two profiles for decaying O_2 concentration represent the range of estimated profiles for $[O_2]$ being consumed by reaction with minerals and organic matter within the vault.

To capture this evolution in a model requires that relationships between propagation rate (R_{CC} or I_C) and O_2 concentration and temperature be determined. This can be achieved in the galvanic coupling experiment by activating a crevice and then changing the O_2 concentration or temperature and recording I_C as a function of these two parameters. The results of such experiments have been published elsewhere (49), and the relationship for O_2 concentration is shown in Fig. 33. Once O_2 reaches a sufficiently low concentration, I_C drops to zero; i.e., repassivation occurs. This enables us to specify a repassivation criterion based on a critical O_2 concentration ($[O_2]_P$) as noted in the figure. A similar dependence of I_C (and hence R_{CC}) on temperature was determined.

Based on this information and these relationships a model framework can now be developed, Fig. 34. The four primary inputs to the model are the crevice propagation rate as a function of O_2 concentration and temperature (A and B), a knowledge of the time-evolution of temperature and oxygen concentration within the waste vault (C), and a transport model for the flux of O_2 to the container

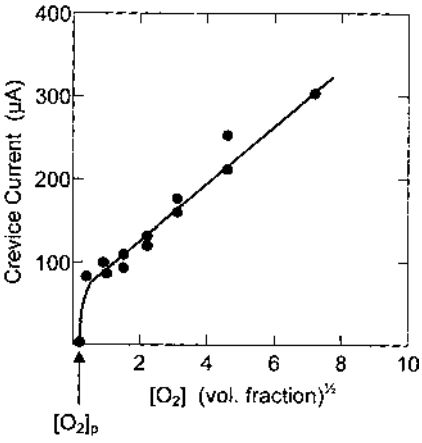

Figure 33 Crevice current (I_C) recorded on a creviced Ti-2 electrode in 0.27 mol · dm^{-3} NaCl (95°C) as the volume fraction of O_2 in the pressure vessel was changed. This volume fraction could easily be converted to a dissolved concentration: $[O_2]_p$ is the volume fraction when the crevice repassivated.

surface (D). This last input is necessary since the container would be placed in a compacted clay environment through which diffusive transport of O_2 would be very slow ($D_{eff} = 10^{-7}$ cm^2 · s^{-1}). One arbitrary feature of the model is that the creviced area and anode-to-cathode area would have to be specified.

The combination of these inputs would lead to a prediction of the rate of crevice propagation with time, and using $[O_2]_{CRIT}$, a repassivation time could be specified (E). Integration of this relationship yields a measure of the total extent of crevice propagation as a function of time (F). Then, using the experimentally

Figure 34 The steps involved in determining the depth of container wall penetration under Canadian nuclear waste disposal conditions using data obtained in an electrochemical galvanic coupling experiment. (A) Crevice propagation rate ($R'_{CC} \propto I_C$) as a function of temperature (T); (B) R_{CC} as a function of O_2 concentration $[O_2]$; (C) calculated evolution of container surface temperatures and vault O_2 concentrations with time in the vault; (D) flux of O_2 (J_{O_2}) to the container surface as a function of time; (E) predicted evolution of R_{CC} up to the time of repassivation (i.e., at $[O_2]_p$); (F) total extent of crevice corrosion damage expressed as the total amount of O_2 consumed (Q) up to the time of repassivation; (G) experimentally determined maximum depth of wall penetration (P_w) as a function of O_2 consumed (Q); (H) predicted maximum value of P_w up to the time of repassivation (t_p).

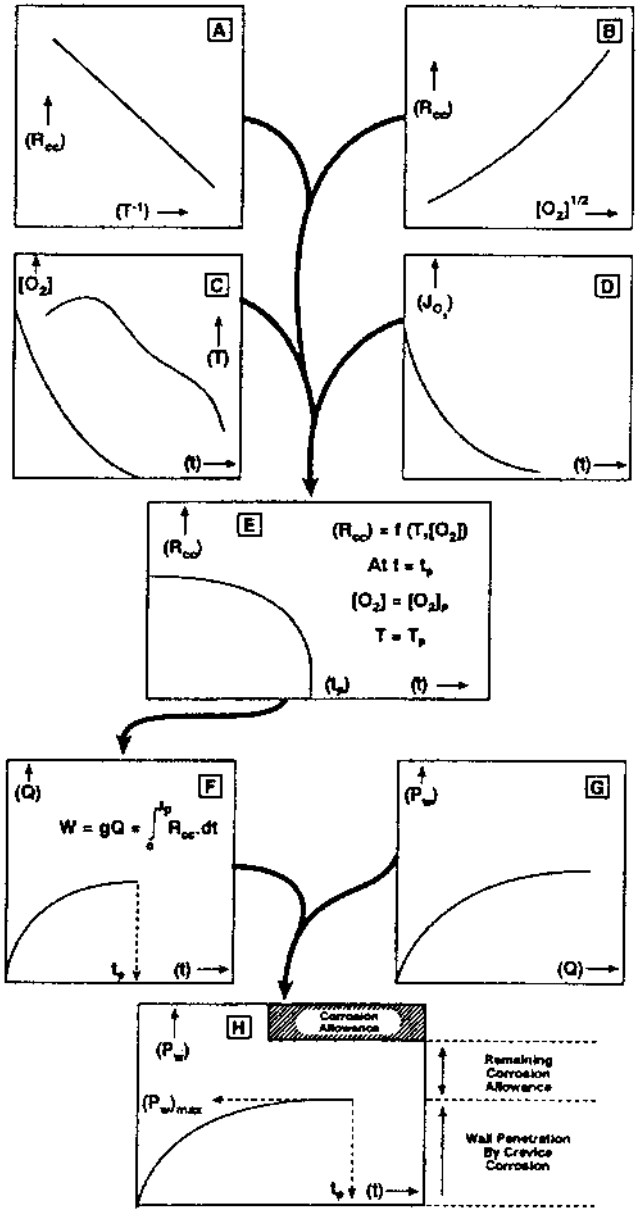
A
(R_{cc})
(T^{-1})
B
(R_{cc})
$[O_2]^{1/2}$
C
$[O_2]$
(T)
(t)
D
(J_{O_2})
(t)
E
(R_{cc})
$(R_{cc}) = f(T, [O_2])$
At $t = t_p$
$[O_2] = [O_2]_p$
$T = T_p$
(t_p)
(t)
F
(Q)
$W = gQ = \int_0^{t_p} R_{cc}.dt$
t_p
(t)
G
(P_w)
(Q)
H
Corrosion Allowance
(P_w)
$(P_w)_{max}$
t_p
(t)
Remaining Corrosion Allowance
Wall Penetration By Crevice Corrosion

determined damage function (P_w as a function of the amount of O_2 consumed) (G), the extent of wall penetration as a function of exposure time can be calculated (H). Comparison of this depth of penetration [$(P_w)_{max}$] to the available corrosion allowance is then a measure of the extent of container damage.

The modeling scheme outlined in Fig. 34 indicates only one path to failure: penetration by loss of wall thickness. However, propagation is accompanied by absorption of hydrogen into the alloy, and even though repassivation may eventually occur, the material is left with an increased inventory of hydrogen. While propagation persists, metallographic examination of corroded specimens show that the majority of absorbed hydrogen resides in a surface hydride layer (33). Once repassivation has occurred, this inventory of hydrogen will diffuse into the metal at a rate determined by temperature. Thus, under the eventually prevailing passive corrosion conditions, there are two sources for the accumulation of hydrogen in the bulk of the material, as illustrated in Fig. 35.

The maximum inventory of hydrogen absorbed during crevice propagation could be calculated by integration of Eq. (30), and all the terms in this equation can be evaluated from data gathered in galvanic coupling experiments. However this is likely to overestimate significantly the hydrogen content of the crevice corroded specimen, since it does not account for the fraction of the surface hydride redissolved as crevice propagation continues. Consequently, a direct experimental measurement of hydrogen content (by vacuum degrassing and volumetric analysis) provides a more accurate measure.

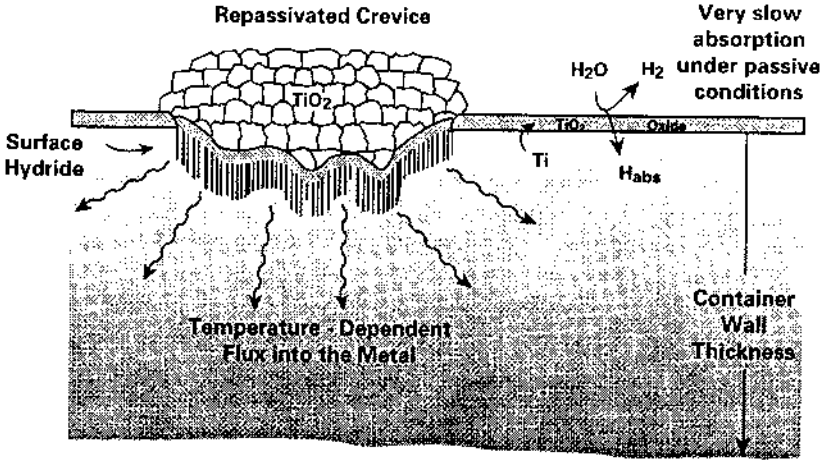

Figure 35 Schematic showing the process of hydrogen absorption into titanium under passive corrosion conditions after a period of crevice corrosion.

What is clear from these analyses is that the avoidance of crevice corrosion will delay eventual container failure significantly, irrespective of whether it occurs by wall penetration or by HIC. With this is mind, the galvanic coupling technique (along with the associated analytical methods outlined above) can be used to compare qualitatively the crevice corrosion performance of a series of titanium alloys. Figs. 36A and B compare the parameter (I_C, E_C, E_p) values ob-

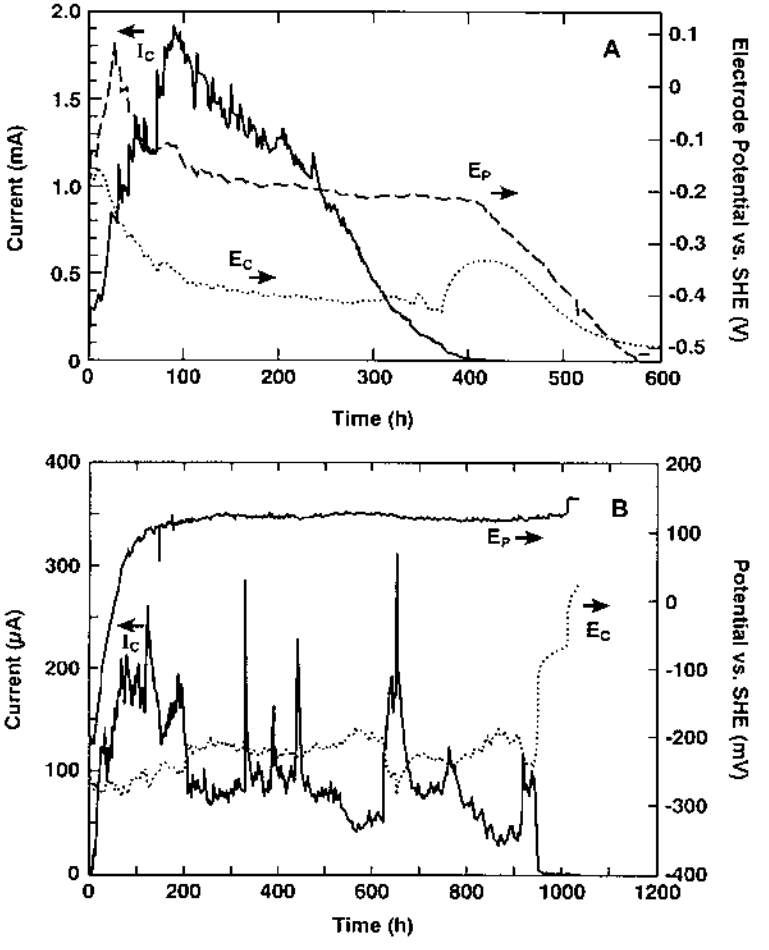

Figure 36 Values of the parameters, I_C (crevice current), E_C (crevice potential), and E_p (planar potential) recorded in galvanic coupling experiments at 125°C in 0.27 mol · dm^{-3} NaCl: (A) Ti-2 (commercially pure alloy); (B) Ti-12 (0.8 wt% Ni + 0.3 wt% Mo).

tained for Ti-2 and Ti-12 (containing 0.8 wt% Ni and 0.3 wt% Mo to resist crevice corrosion). As expected for Ti-2, propagation proceeds at high currents until available O_2 is consumed, and repassivation is only observed once passive reducing conditions [$E_p \sim -500$ mV (see Fig. 30)] are established. By contrast, propagation on Ti-12 progresses at much lower currents, and repassivation occurs while oxidizing conditions still prevail [$E_p \sim 100$ mV (see Fig. 30)]. Based on the results from this galvanic coupling technique, the crevice corrosion resistance of a series of alpha titanium alloys is summarized in Fig. 37 (Ti-16 contains ~0.06 wt% Pd). A more extensive discussion of the results of these experiments is given elsewhere (46).

This understanding provides not only a basis for materials selection (improved resistance to crevice corrosion must be balanced against materials costs) but also a basis for predicting the possible loss of wall thickness for a range of

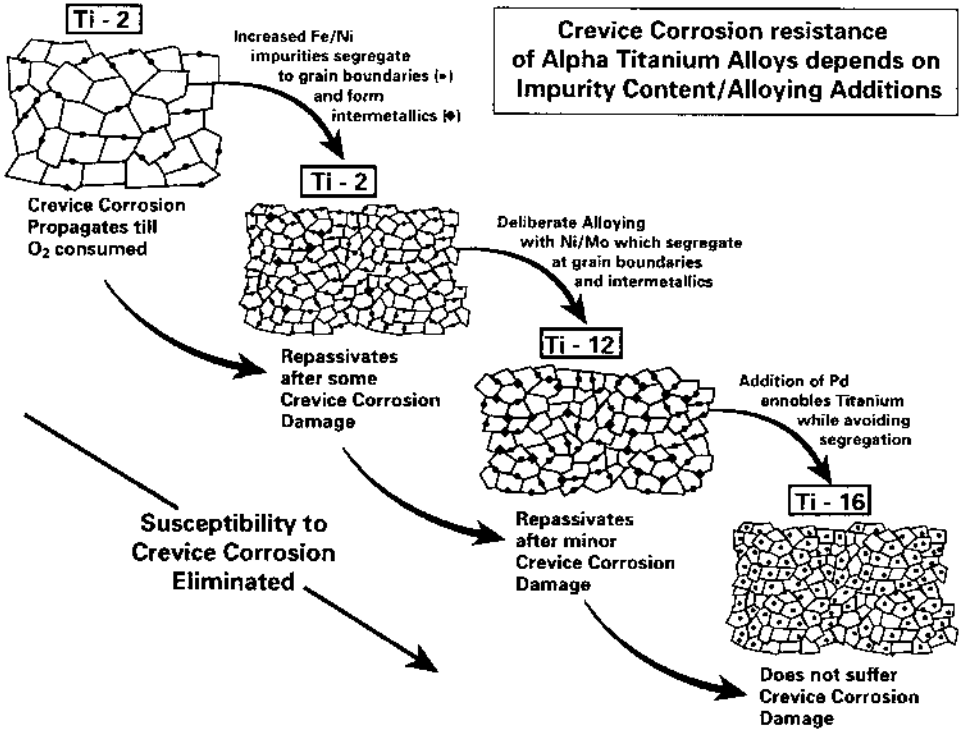

Figure 37 Schematic illustrating the improvement in crevice corrosion behavior as the composition and microstructure of a series of α-Ti alloys are changed.

materials due to an early period of crevice propagation. Again, more extensive discussions are given elsewhere (30).

IV. SUMMARY

A general scheme for the development of corrosion models based on electrochemical principles has been described, and a number of examples for active, passive, and localized corrosion has been given. This chapter is by no means comprehensive, and a search of the scientific and technical literature will unearth many additional examples. The value in using electrochemical methods both to develop understanding of the corrosion process and to measure the values of specific modeling parameters is obvious. However, their application alone would not provide all the elements and parameter values required for the development of corrosion models, so the use of supplementary techniques is necessary. It is necessary also to keep in mind that electrochemical techniques inevitably accelerate the corrosion process one is interested in. Consequently, the scaling of electrochemically determined parameter values to the rates and time periods of interest in the corrosion process to be modeled should be undertaken carefully and with a full knowledge of the limitations involved.

REFERENCES

1. D. W. Shoesmith, W. H. Hocking, B. M. Ikeda, F. King, J. J. Noël. Can. J. Chem. 75 (1997):1566.
2. J. D. Rudnicki, R. E. Russo, D. W. Shoesmith. J. Electroanal. Chem. 372 (1994): 63.
3. C. Deslouis, B. Tribollet, G. Mengoli, M. M. Musiani. J. Appl. Electrochem. 18 (1988):374, 384.
4. F. King, C. D. Litke, S. R. Ryan. General corrosion of copper nuclear waste containers. Paper 119, Corrosion 92, NACE International, Houston, TX (1992).
5. F. King, C. D. Litke, M. J. Quinn, D. M. LeNeveu, Corr. Sci. 37 (1995):833.
6. D. W. Shoesmith, F. King. Ontario Power Generation Report No.: 06819-REP-01200-0038 R00 (1998).
7. E. J. M. O'Sullivan, E. J. Calvo. In: Comprehensive Chemical Kinetics (R. G. Compton, ed.), Vol. 27. Elsevier, Amsterdam, Chap. 3 (1987).
8. V. A. Presnov, A. M. Trunov, Elektrokhimiya 11 (1975):71, 77.
9. F. King, M. J. Quinn, C. D. Litke. Atomic Energy of Canada Ltd. Report, AECL-11061, COG-94-123 (1994).
10. E. J. Calvo, D. J. Schiffrin. J. Electroanal. Chem. 243 (1988):171.
11. M. Stratmann, J. Muller. Corrosion Science 36 (1994):327.

12. H. Christensen, S. Sunder, D. W. Shoesmith. Atomic Energy of Canada Ltd. Report, AECL-11102, COG-93-488 (1994).
13. B. M. Ikeda, M. G. Bailey, C. F. Clarke, D. W. Shoesmith. Atomic Energy of Canada Ltd. Report, AECL-9568 (1989).
14. J. C. Wren, S. Sunder, D. W. Shoesmith. Ontario Power Generation Report No: 06819-REP-01200-0054 R00 (1999).
15. J. R. Park, D. D. Macdonald. Corrosion Science 23 (1983):295.
16. R. J. Finch, E. C. Buck, P. A. Finn, J. K. Bates. Mat. Res. Soc. Symp. Proc. Vol. 556, Materials Research Society, Warrendale, PA, 431 (1999).
17. F. King, M. Kolar, D. W. Shoesmith. Modelling the effects of porous and semipermeable layers on corrosion processes. Paper 380, Corrosion 96, NACE International, Houston, TX (1996).
18. Electrochemical Impedance: Analysis and Interpretation (J. R. Scully, D. C. Silverman, M. W. Kendig, eds.). ASTM STP 1188 ASTM, Philadelphia, PA (1983).
19. Electrochimica Acta, EIS'98 Proceedings—impedance spectroscopy (O. R. Mattos, ed.), 44 (24) (1999).
20. S. Stroes-Gascoyne, J. Betteridge, F. King. Ontario power generation report. No: 06819-REP-01200-10017-R00 (2000).
21. S. Turgoose, R. A. Cottis. In Ref. 17, p. 173.
22. M. Kolar, F. King. Atomic energy of Canada ltd. report. AECL-11473, COG-95-521 (1997).
23. F. King, M. Kolar. Ontario power generation report. No: 06819-REP-01200-10005 R00 (1999).
24. D. D. MacDonald, M. Urquidi-Macdonald. Corrosion 46 (1990):380.
25. G. P. Marsh, K. J. Taylor. Corrosion Science 28 (1988):289.
26. D. D. Macdonald. J. Electrochem. Soc. 139 (1992):3434.
27. M. J. Pryor, U. R. Evans. J. Chem. Soc. (1950):1259.
28. A. Kuch. Corrosion Science 28 (1988):221.
29. D. J. Blackwood, L. M. Peter, D. E. Williams. Electrochimica Acta 33 (1988):1143.
30. D. W. Shoesmith, F. King, B. M. Ikeda. Atomic energy of Canada ltd. report, AECL-10972, COG-94-534 (1995).
31. D. W. Shoesmith, B. M. Ikeda. Atomic energy of Canada ltd. report, AECL-11709, COG-95-557-I (1997).
32. J. J. Noël, M. G. Bailey, J. P. Crosthwaite, B. M. Ikeda, S. R. Ryan, D. W. Shoesmith. Atomic energy of Canada ltd. report, AECL-11608, COG-96-249 (1997).
33. D. W. Shoesmith, J. J. Noël, D. Hardie, B. M. Ikeda. Corrosion Reviews 18 (2000): 331.
34. J. W. Oldfield, W. H. Sutton. British Corrosion Journal 13 (1978):13, 104.
35. H. W. Pickering. In: Proceedings of the Research Topical Symposium on Localized Corrosion (G. S. Frankel and J. S. Scully, eds.) Corrosion 2001, NACE International, Houston, TX (2001):103.
36. B. E. Kehler. Crevice corrosion electrochemistry of alloys 625 and C22. M.Sc. thesis, University of Virginia (2001).
37. D. W. Shoesmith, M. G. Bailey, B. M. Ikeda. The localized corrosion of alloy 276 in hot aqueous sodium chloride solutions typical of those expected under Canadian

nuclear waste disposal conditions. Nickel Development Institute (NiDI), Toronto (1996).
38. N. Sridhar, D. S. Dunn, C. S. Brossia, G. A. Cragnolino. In: Proceedings of the Research Topical Symposium on Localized Corrosion (G. S. Frankel and J. R. Scully, eds.). Corrosion 2001, NACE International, Houston, TX (2001):1.
39. D. W. Shoesmith, M. Kolar. In: Alternative approaches to assessing the performance and suitability of Yucca Mountain for spent fuel disposal. EPRI Report TR-108732, Chap. 5 (1998).
40. K. J. Vetter, H. H. Strehblow. In: Proceedings of the Conference on Localized Corrosion, NACE International, Houston, TX (1974):240.
41. D. W. Shoesmith, B. M. Ikeda, F. King. In: Modelling Aqueous Corrosion (K. R. Trethewey, P. R. Roberge, eds.). Kluwer Academic Press, Dordrecht, Germany (1994):201.
42. N. J. Laycock, R. C. Newman. In: Proceedings of the Research Topical Symposium on Localized Corrosion (G. S. Frankel, J. R. Scully, eds.). Corrosion 2001, NACE International, Houston, TX (2001):165.
43. F. King, D. M. LeNeveu. In: Nuclear Waste Packaging, FOCUS'91. American Nuclear Society, LaGrange Park, IL (1992):253.
44. G. P. Marsh, I. D. Bland, K. J. Taylor. British Corrosion Journal 23 (1998):157.
45. S. F. Mughabghab, T. M. Sullivan. Waste Management 9 (1989):239.
46. J. J. Noël, D. W. Shoesmith, B. M. Ikeda. In: Proceedings of the Research Topical Symposium on Localized Corrosion (G. S. Frankel, J. R. Scully, eds.). Corrosion 2001, NACE International, Houston, TX (2001):65.
47. B. M. Ikeda, M. G. Bailey, M. J. Quinn, D. W. Shoesmith. In: Application of Accelerated Corrosion Tests to Service Life Prediction of Materials (G. Cragnolino, N. S. Sridhar, eds.). ASTM, Philadelphia, PA (1994):126.
48. M. J. Quinn, B. M. Ikeda, D. W. Shoesmith. Atomic energy of Canada ltd. report, AECL-10966 (1993).
49. D. W. Shoesmith, B. M. Ikeda, M. G. Bailey, M. J. Quinn, D. M. LeNeveu. Atomic energy of Canada ltd. report, AECL-10973 (1994).
50. G. P. Marsh, K. J. Taylor, A. H. Harker. SKB Technical report 91-62. SKB, Stockholm, Sweden (1991).

8

The Use of Electrochemical Techniques in the Study of Surface Treatments for Metals and Alloys

I. OVERVIEW

Electrochemical methods are used in many different ways to assess the effectiveness of corrosion inhibitors and coatings for metals and alloys. In this chapter, several important cleaning, inhibition, and coating technologies are described including passivation, conversion coating, anodizing, and organic coating. The use of electrochemical methods for determining the effectiveness of these corrosion protection methods is the focus of this discussion. Methods based on the use of DC polarization and electrochemical impedance are presented. Electrochemical impedance spectroscopy (EIS) has matured greatly over the past 20 years as a tool in corrosion protection research and has proved to be one of the most useful electrochemical characterization techniques presently available. This chapter concludes with a presentation of some of the newest electrochemical measurement techniques. These techniques have developed in research laboratories over the past 10 years. They hold promise for the study of coatings and corrosion inhibition but have only been applied on a selective basis so far.

II. DESCALING AND PASSIVATION OF STEELS AND STAINLESS STEELS

A. Overview of Descaling and Passivation

Steels and stainless steels develop oxides scales during hotworking, annealing, or welding that lower corrosion resistance or paint adhesion. Scales are removed using chemical means, mechanical means, or combinations of both. Within the trade, chemical descaling is often referred to as pickling. In the case of stainless

and semistainless alloys, additional chemical treatments, commonly referred to as passivation processes, are used to ensure maximum resistance to pitting and crevice corrosion by enriching the adherent oxide film with Cr (1), and preferentially dissolving inclusions that serve as pit initiators (2).

Pickling of carbon and alloy steels is usually carried out in sulfuric acid solutions ranging in concentration from 3 to 40%, depending on the alloy type and product form (3,4). Baths are operated at 60° to 100°C, and processing times range from tens of seconds to 30 minutes or more. Contact times greater than 30 minutes are not common as the risk for surface etching increases. Steel rod and wire are often pickled using a 1 to 20 s immersion in hot hydrochloric acid solutions with concentrations of 6 to 15% by weight at temperatures of 75° to 95°C, or chloride additions to sulfuric acid baths are sometimes used to accelerate the descaling action (5). Other acid cleaning treatments are used to remove not only oxide scale but also dirt, oils, and other contaminants from the steel surface. The use of mineral acids such as phosphoric acid is common in this regard (6). For structures too large for treatment by immersion, pickling pastes have been developed (7).

The more corrosion resistant 300 and 400 series stainless steels are normally pickled in nitric acid, or HF-accelerated nitric acid mixtures. Solutions are operated at temperatures ranging from 70° to 90°C, and contact times of 2 to 20 minutes are typical (3).

B. Traditional Techniques to Assess Effectiveness of Descaling and Passivation

Most descaling and passivation processes for steels were developed prior to the widespread use of electrochemical techniques. As a result, a variety of visual and chemical tests are widely used for determining the surface cleanliness. Chemical tests have also been established to verify the presence of a robust oxide film on austenitic and ferritic stainlesses (8). These methods are very simple to conduct in a manufacturing environment, but they are qualitative in nature and rely strongly on the judgment of the inspector. Outside of the laboratory, electrochemical methods have not been widely used to evaluate cleanliness of carbon and alloy steels after pickling. Nevertheless, they are well suited for this purpose and have been examined in considerable detail in laboratory studies.

C. Electrochemical Techniques for Assessing Effectiveness of Descaling and Passivation

Austenitic stainless steels are generally regarded as being spontaneously passive in aerated, near-neutral aqueous solutions, but surface treatment has a significant

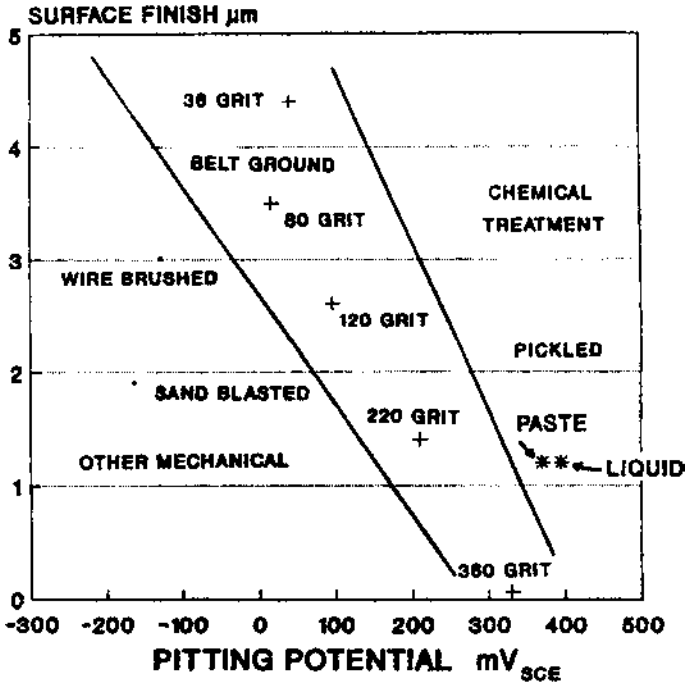

Figure 1 Surface finish versus pitting potential for 316 stainless steel subject to various surface treatments. (From G. E. Coates. Materials Perf., Aug. 1990, p. 61.)

effect on pitting and crevice corrosion resistance. Figure 1 shows a compilation of pitting potentials for various surface treatments on 316 stainless steel (9). This figure illustrates the beneficial effects of polishing and chemical treatment on the resistance to localized corrosion and suggests that measurement of pitting potential is a good electrochemically derived parameter for assessing surface cleanliness.

In principle, rinsing austenitic stainlesses in aerated water after pickling should be sufficient to induce passivation most of the time. But further treatment by dipping in nitric acid or nitric–hydrofluoric acid mixtures is common practice because it decontaminates the surface, further stabilizes the passive film, and ensures passivity (10). Acid dipping helps remove contamination in the alloy's surface such as slag inclusions from welding and residual iron from machining and grinding. Surface roughness, MnS inclusions, oxide inclusions and Cr-depleted surfaces will also serve to destabilize passivity. In service, these factors lead to unexpected red rusting, pitting, and crevice corrosion. In laboratory tests,

these effects increase the metastable pitting rate, lower the pitting potential, lower the critical pitting temperature, and lower the resistance to crevice corrosion, as has been shown in several studies discussed below.

Suter et al. have developed a microelectrochemical cell that uses glass capillaries drawn down to tens of micrometers in diameter (11–14) (Fig. 2). Capillary ends can be precisely positioned on an alloy surface enabling electrochemical measurements to be made at microstructurally relevant length scales. Using this technique, the effect of MnS inclusions on the pitting activity of stainless steels has been studied directly. When smaller and smaller capillaries are used to measure polarization curves, the pitting potential is observed to increase substantially. In a 0.003% S austenitic stainless steel the pitting potential, E_{pit}, in 1 M NaCl increases from about +0.300 to V_{sce} to a value more positive than the oxygen evolution potential when the capillary tip diameter was reduced from 100 to 50 μm (Fig. 3). The increase in E_{pit} occurs because as the cell size decreases, the number of inclusions sampled decreases, thereby reducing the number of defect sites available for pit initiation. This finding is in agreement with conventional understanding articulated by Crolet, who states that the effectiveness of a given

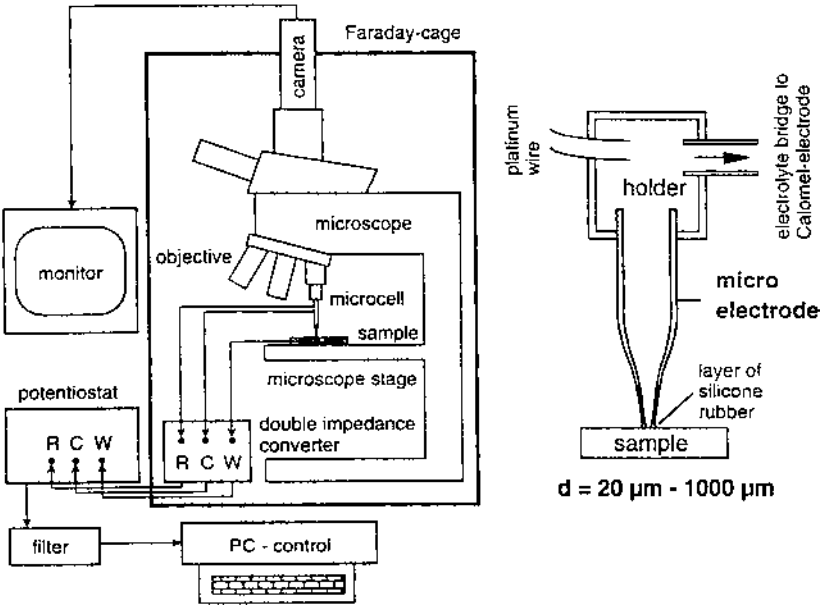

Figure 2 Schematic illustration of the experimental apparatus for the microcapillary electrochemical cell. (From T. Suter, T. Peter, H. Bohni. Mater. Sci. Forum, 192–194, 25 (1995).)

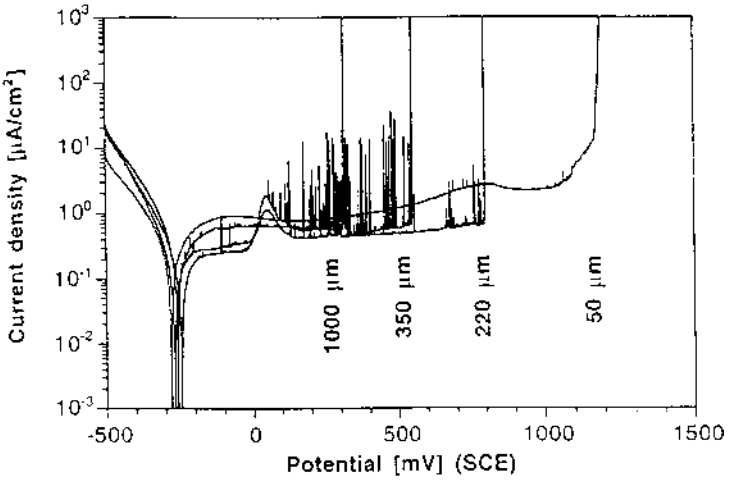

Figure 3 Potentiodynamic polarization curves from a 0.003% S austentic stainless steel measured in 1 M NaCl with capillaries of differing size. (From T. Suter, T. Peter, H. Bohni. Mater. Sci. Forum, 192–194, 25 (1995).)

passivation treatment is determined to a large extent by the effectiveness of MnS inclusion removal (10).

Other researchers have investigated the effects of Cr enrichment in the oxide film during nitric acid passivation (15–17). Cr enrichment during passivation has been observed in XPS measurements. However, on the basis of electrochemical measurements, it is not clear that Cr enrichment has as profound an effect on pitting resistance as the removal of inclusions. Hultquist examined the effect of nitric and nitric–hydrochloric acid passivation on pitting and crevice corrosion of Mo-bearing 316 stainlesses. XPS showed that the various passivation treatments examined resulted in Cr+Fe+Ni ratios in the oxide of 40 to 60%. Stepwise potentiodynamic polarization of samples with artificial crevices showed that the crevice corrosion initiation potential scaled linearly with oxide film Cr content. Conversely, the E_{pit} measured on boldly exposed surfaces did not scale with the oxide film Cr content, which led the authors to conclude that Cr enrichment is more important in determining crevice corrosion resistance and that inclusion removal is more important in determining pitting resistance.

Wallinder et al. examined passivation of 316L using electrochemical impedance spectroscopy (EIS), potentiodynamic polarization, and x-ray photoelectron spectroscopy (XPS) techniques to examine the relationships between corrosion resistance and surface chemistry after passivation treatments (17). The

effects of variables including contact time, temperature, HNO_3 concentration, and surface finish on surface composition and electrochemical behavior in 0.5% H_2SO_4 solutions were systematically studied. EIS measurements showed that passivated surfaces exhibited a single but broadly dispersed time constant that was modeled using a parallel constant phase element (CPE)–resistor network in series with a solution resistance. The magnitude of the film resistance and the capacitance extracted from the CPE showed regular dependencies on variables such as surface finish, acid concentration, and passivation time. Film thicknesses were estimated from capacitance measurements, and thickness values were compared to those derived from XPS data. Findings from this study led the authors to conclude that improved corrosion resistance was due to a high Cr content and increased thickness in the passive film.

Hong et al. examined the effect of nitric acid passivation on type 430 ferritic stainless steel using potentiodynamic polarization, EIS, and Auger electron spectroscopy (AES) (18). Passivation treatments were carried out on wet polished surfaces by immersion for 60 minutes in nitric acid solutions ranging from 1 to 61% at 50°C. Pitting potential and the magnitude of the total impedance were positively correlated with surface Cr concentration. In response to this study,

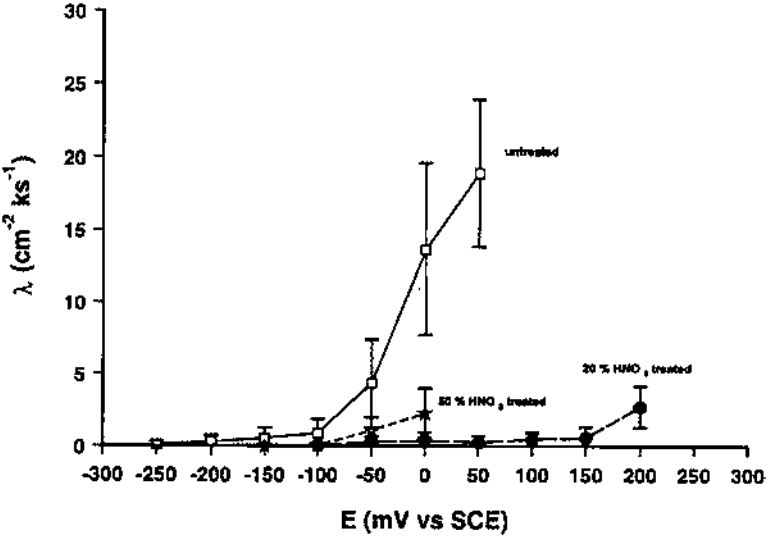

Figure 4 Metastable pitting rate (λ) for 316 stainless steel in 1 M NaCl solution as a function of potential for untreated samples and samples passivated with 20% or 50% nitric acid for 1 hour. (From J. S. Noh, N. J. Laycock, W. Gao, D. B. Wells. Corrosion Sci. 42, 2069 (2000).)

Crolet remarked that causality does not always follow from correlation of results from electrochemical tests and results from surface analysis (19). Strictly speaking, the effect of inclusion removal on pitting potential cannot be distinguished from effects due to Cr surface enrichment.

Noh et al. characterized pitting potentials and metastable pitting transients collected during potentiodynamic polarization of passivated 316 stainless steel immersed in deaerated 1 M NaCl solutions at 70°C (20). Passivation treatments were carried out for 1 hour at ambient temperatures on surfaces polished to 600 grit in HNO_3 solutions ranging in concentration from 0.65 to 25 wt%. MnS inclusions were removed to certain extents at all concentrations of HNO_3, but the Cr concentration in the surface film, measured as a Cr:Fe peak height ratio by XPS, achieved a maximum at about 25%. This peak height ratio was about four to five times that measured on the grit polished but unpassivated sample. A maximum in E_{pit} was also recorded on samples passivated in the 25 wt% solution, suggesting a relation to the oxide film Cr content, though it was also pointed out that the correlation between E_{pit} and Cr:Fe ratio is not a linear one, suggesting the influence of other factors, such as inclusions, in determining E_{pit}. Nitric acid passivation was shown to decrease metastable pitting rates and decrease the probability of a metastable pit becoming stable. Figure 4 shows the metastable pitting rate as a function of applied potential in 1 M NaCl solution. These results were interpreted as indicating a reduction in the number of available pitting sites due to the passivation treatment.

III. INHIBITION BY SOLUBLE CHROMATE

A. Overview of Chromate Inhibition

The various simple chromate anions including chromate, CrO_4^{2-}, dichromate, $Cr_2O_7^{2-}$, and bichromate, $HCrO_4^-$, have all been reported to be potent corrosion inhibitors when they are present as soluble species in solution. Chromate is an effective inhibitor for Al, Fe, Mg, Cd, Sn, and many other metals and alloys. The specific form of the anion present in solution depends on its concentration and solution pH (21). Because evidence of corrosion inhibition has been detected over very wide ranges of soluble Cr(VI) ion concentration and pH, each of these species appears to possess inhibiting properties.

Recently, the mechanism of corrosion protection by soluble chromate inhibitors has been the subject of active research, which has attempted to understand and replicate its inhibiting functions with less toxic chemical substances. In this section, some recent findings on chromate corrosion inhibition are reviewed, particularly as they pertain to corrosion of light metals, with a focus on the use of techniques that are useful for studying mechanisms of inhibition.

Chromates are particularly effective inhibitors, and there appear to be several components to inhibition. Chromate in solution inhibits metal dissolution and oxygen reduction reactions. It also slows metastable pitting, the transition to stable pitting, and, when present in sufficient concentration, the growth stage of pitting and crevice corrosion.

Electrochemical techniques alone cannot reveal all the relevant aspects of chromate inhibition, and key characterization experiments involving surface analysis, solution analysis, or other techniques are required to help understand inhibition. For this reason, several useful nonelectrochemical techniques are also discussed. These techniques provide a means for examining the effects of inhibition under free corrosion conditions where electrochemical methods are not well suited for measuring corrosion rate.

B. Chromates and Anodic Inhibition

In polarization experiments using solutions containing mixtures of chromates and attacking ions like chloride, evidence for anodic inhibition of aluminum by chromates is derived from elevation of the pitting potential and reduction in passive current density (22–24). In these solutions, the pitting potential will depend on alloy type, pH, and degree of aeration. Most significantly though, the pitting potential depends on the chromate:chloride activity ratio (Fig. 5). Data from Kaesche for aerated near-neutral solutions suggest that the pitting potential begins to be ennobled when the chromate:chloride ratio exceeds about 0.1 to 1.0 (23). Bohni and Uhlig have reported pitting inhibition efficiencies that are based on complete suppression of pitting and are therefore somewhat more conservative because greater chromate:chloride ratios are indicated (22).

1. Effect of Chromates on Metastable Pitting

In near-neutral dilute chloride solutions, concentrations of chromate, less than those suggested by Kaesche, have been observed to increase the pitting potential. Figure 6a shows anodic polarization curves from high purity Al wire loop electrodes in deaerated 1.0 mM chloride solutions (25). Additions of 25 to 50 μM of sodium chromate were shown to elevate the pitting potential by hundreds of millivolts and reduce the passive current density by about a factor of 2.

This elevation was attributed to the effect of chromate on metastable pitting. Figure 6b shows plots or current density versus time for high purity Al wire loop electrodes potentiostatically polarized to $-0.500\ V_{sce}$ in the same solutions as those shown in Fig. 6a. As the chromate concentration is increased from 0 to 25 μM, and then from 25 to 50 μM, the metastable pit nucleation rate (events per unit time) diminishes, as does the magnitude of individual events (event peak current). The presence of chromate appears to decrease the metastable pit growth

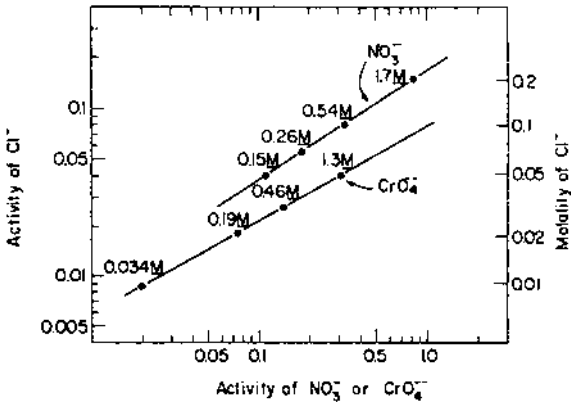

(a)

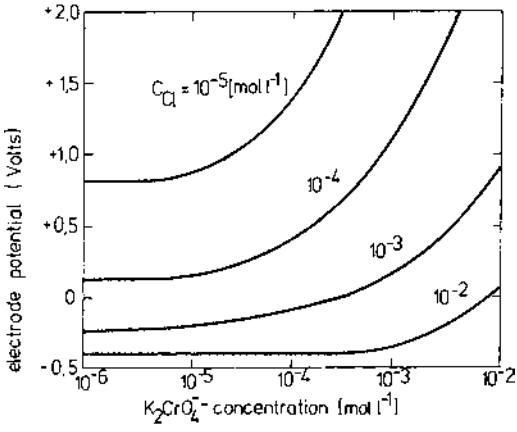

(b)

Figure 5 (a) Minimum activity of $NaNO_3$ or Na_2CrO_4 required to inhibit pitting in 99.99% Al in aerated NaCl solutions. (b) Dependence of the pitting potential of Al on the chloride : chromate ratio. (From (a) H. Bohni, H. H. Uhlig. J. Electrochem. Soc. 119, 906 (1969). (b) H. Kaesche. Localized Corrosion III, p. 516, NACE, Houston, TX (1971).)

rate and the apparent pit current density compared to chromate-free chloride solutions. These factors combine to decrease the probability that metastable pits will stabilize to form propagating pits.

The use of the wire loop electrode technique is important in these studies, as it is one means of ensuring against crevice attack that might compromise the integrity of the experimental findings. In such experiments, the working electrode

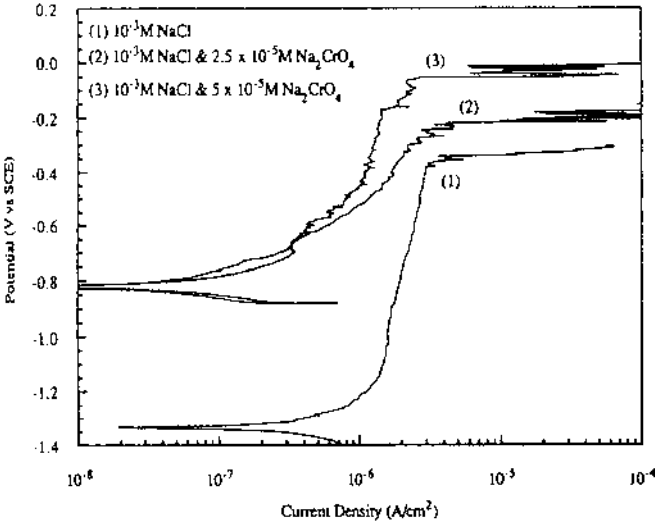

Figure 6 (a) Anodic polarization curves showing the effect of CrO_4^{2-} on the pitting potential of pure Al wire loop electrodes in deaerated 1 mM NaCl solution. (b) Time records show in the effect of CrO_4^{2-} on metastable pitting activity during potentiostatic polarization at -0.500 V_{sce} in 1 mM NaCl solution. The inset shows the cumulative number of metastable pitting events shown as events/cm^2 versus exposure time. (From S. T. Pride, J. R. Scully, J. L. Hudson. J. Electrochem. Soc. 141, 3028 (1994).)

consists of a thin wire loop, a portion of which is immersed below the level of the electrolyte. There is no gasket or seal required, and the opportunity for crevice formation is minimized. Care is taken to avoid plastically deforming the wire, which may localize dissolution. While it is possible to use a straight wire electrode, the presence of a cut end may be a region of high plastic deformation or have asperities or recesses that may affect the electrochemical response. The looped wire configuration exposes only the length of the wire, which is much more nearly all in the same surface condition. Local effects at the water line, where the loop is submerged, may develop, especially in aerated solutions where a differential aeration cell may occur. Solution deaeration may be used to minimize this effect, but if deaeration is accomplished by bubbling a gas into the electrolyte, care must be taken to isolate the electrode from ripples on the solution surface that may cause variations in the submerged electrode area.

2. Pit Growth in Thin Films

The thin film pitting technique has been used to examine the influence of chromate on pit growth kinetics. Thin film pitting is a nonelectrochemical technique for assessing pit growth kinetics in thin film metallizations. In films that are sufficiently thin (1000 nm or less), pits initiate, very rapidly penetrate to the inert substrate under the metallization, and then propagate radially outward. Pit growth can be recorded by measuring the rate of change of the pit radius, dr/dt, using a video recording system (Fig. 7a and b). Pit depth is fixed by the film thickness, and pitting propagates in a two-dimensional fashion. Knowing the thin film thickness and the pit wall velocity, Faraday's law can be used to make a nonelectrochemical determination of pit dissolution kinetics:

$$i = \frac{\rho nF}{M} \cdot \frac{dr}{dt} \tag{1}$$

In this expression, i is current density, ρ is density, n is the number of electron equivalents per mole of dissolved metal, M is the atomic weight of the metal, F is Faraday's constant, r is pit radius, and t is time. The advantage of this technique is that a direct determination of the dissolution kinetics is obtained. A direct determination of this type is not possible by electrochemical methods, in which the current recorded is a net current representing the difference between the anodic and the cathodic reaction rates. In fact, a comparison of this nonelectrochemical growth rate determination with a comparable electrochemical growth rate determination shows that the partial cathodic current due to proton reduction in a growing pit in Al is about 15% of the total anodic current (26).

In experiments aimed at measuring pit and crevice growth kinetics, chromate is not a potent anodic inhibitor (27). The growth of film pits in Al films is not slowed unless high chromate:chloride ratios exist. The addition of 0.05

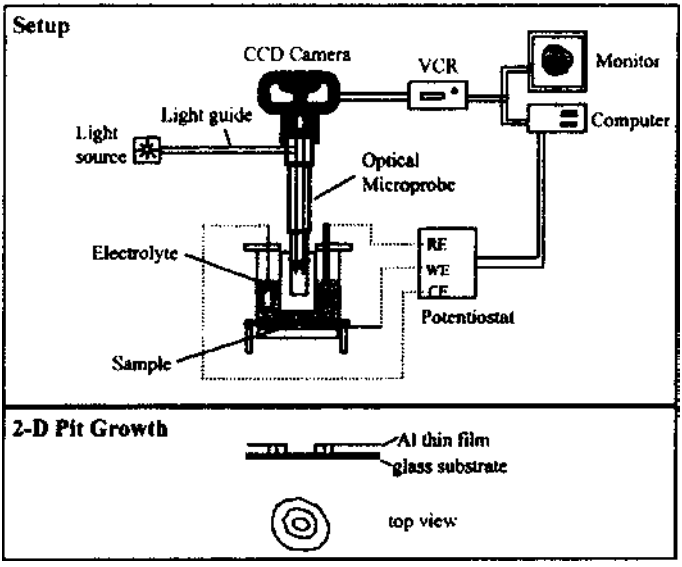

(a)

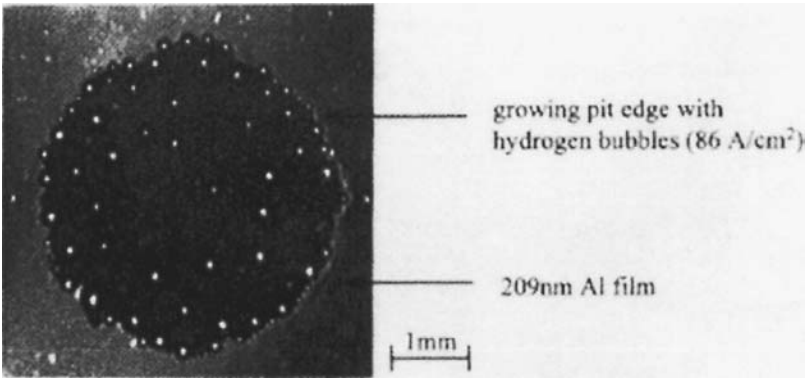

(b)

Figure 7 (a) Schematic drawing of the thin film pit experimental apparatus. (b) An optical micrograph of a 2D thin film pit growing in an Al film at $-0.450\ V_{sce}$ in aerated 1.0 M NaCl solution. (From A. Sehgal, D. Lu, G. S. Frankel. J. Electrochem. Soc. 145, 2834 (1998).)

M $Na_2Cr_2O_7$ to aerated 1.0 M NaCl solution has virtually no effect on the pit polarization curve compared to a dichromate-free solution. Additions of 0.5 M $Na_2Cr_2O_7$ increase the repassivation potential by about 90 mV, while a 2.0 M $Na_2Cr_2O_7$ addition nearly stops pit propagation. The concentrations of dichromate required to inhibit thin film pit growth are consistent with those proposed by Kaesche (23) but are much greater than those required to slow metastable pitting in bulk Al samples.

3. Pit Growth in Metal Foils

The foil penetration technique is another nonelectrochemical technique for assessing the growth stage of pitting and intergranular corrosion (24). In this technique, metal foils with thicknesses ranging from 50 to 200 μm are exposed to an attacking electrolyte in a cell configuration like that shown in Fig. 8a and b. The sample is exposed to solution through a gasketed port that prevents crevice corrosion. The sample may also be made the working electrode (WE) in a three-electrode cell configuration for potential- or current-controlled experiments. A detection circuit is incorporated into the cell design to record the time at which the sample is perforated by localized corrosion. The detection scheme involves the use of a metal foil (e.g., Cu) separated from the back side of the WE electrode metal foil by wettable filter paper. The WE and Cu electrode are connected, and the Cu foil is held at +12 V with respect to the WE. During the experiment, the resistance is measured between the WE and the Cu foil. The measurement circuit is open when the paper is dry, but it closes when corrosion perforates the WE and wets the filter paper with electrolyte. Once the circuit is closed, the time is recorded, and an accurate determination of the time required to penetrate the WE is made. Using this technique, penetration times can be collected in experiments where the environmental conditions or the WE thickness is varied in a systematic fashion.

Hunkeler and Bohni used this approach to show that pit growth in Al foils occurred under ohmic control (24). It was also shown that nitrate and chromate inhibitors, added to the electrolyte after pit initiation, inhibited pit growth kinetics; though the effect due to chromate additions was small. Several other inhibitors added to solution increased pit growth kinetics, since their primary influence was in decreasing the solution resistance.

More recently, this technique has been used to examine the effect of dichromate additions on the stable growth of pitting and intergranular corrosion in high-strength Al alloys (28). Figure 8c shows the average foil penetration time for 220 μm thick 2024-T3 (Al-4.4Cu-1.5Mg-.06 Mn) foils potentiostatically polarized to $-0.550\ V_{sce}$ in oxygen-sparged 1.0 M NaCl solution containing different concentrations of dichromate. In these experiments the 2024-T3 foils were polarized 0.3 V above the pitting potential for a few seconds to initiate pit growth and

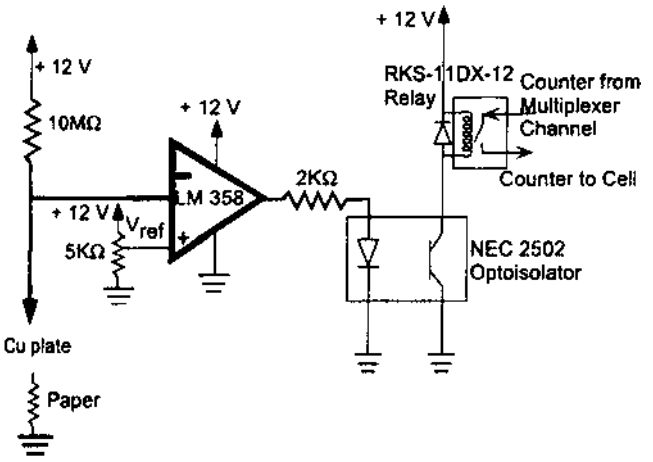
+ 12 V
10MΩ
+ 12 V
LM 358
2KΩ
+ 12 V
V_{ref}
5KΩ
+ 12 V
RKS-11DX-12
Relay
Counter from
Multiplexer
Channel
Counter to Cell
NEC 2502
Optoisolator
Cu plate
Paper

(a)

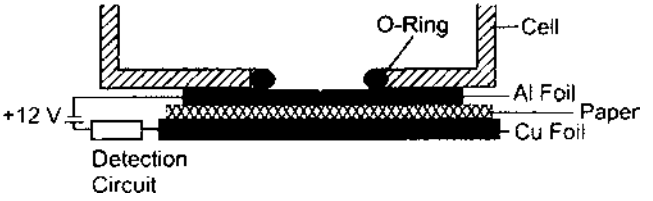
O-Ring
Cell
Al Foil
Paper
Cu Foil
+12 V
Detection
Circuit

(b)

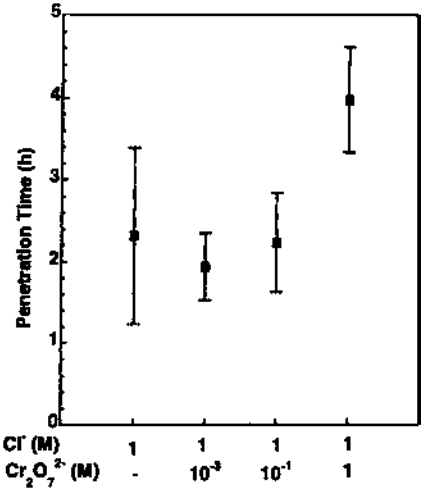
Penetration Time (h)
0
1
2
3
4
5
Cl⁻ (M) 1 1 1 1
$Cr_2O_7^{2-}$ (M) - 10^{-3} 10^{-1} 1

(c)

ensure that the time to penetrate that was recorded reflected the pit propagation only. These data show that there is no increase in the penetration time for dichromate additions up to 0.1 M. A 1.0 M addition of dichromate about doubled the penetration time, showing that the anodic inhibition localized kinetics is modest and requires about a 1:1 ratio of dichromate to chloride, as was suggested by the data of Kaesche (23).

4. Pit and Crevice Growth Studies with Artificial Crevice Electrodes

Artificial pits and crevice electrodes can be formed by embedding wires or thin foils in an insulating material leaving an exposed wire or foil edge. As the wire or foil dissolves and the interface recedes, a one-dimensional pit or crevice forms. Normally, the entire interfacial area is active, which facilitates determination of dissolution rates, and pit or crevice current density. Modeling the effects of mass transfer are straightforward as the pit or crevice grows only in one dimension. If a transparent mounting medium is used, the recession rate of the wire or foil can be measured optically to make a nonelectrochemical determination of the dissolution rate possible.

These techniques have been used to study pitting reaction control mechanisms in stainless steel (29,30), iron (31), and nickel (32). The effect of bulk solution flow on pit dissolution rates for Fe, Ti, and Al have also been made (33). Interrogation of artificial crevice chemistries by x-ray absorption techniques has also been reported (30,34,35).

Artificial crevice electrodes have been used to study the effect of dichromate on active dissolution of aluminum. In these experiments, 50 μm thick commercially pure Al foils were placed between thin plastic sheets and mounted in epoxy. This assembly was fixed against a square cell that accommodated counter and reference electrodes and a trap that allowed for H_2 gas collection. A schematic illustration of this cell and electrode is shown in Fig. 9 (36). Crevice corrosion growth experiments were conducted in aerated 0.1 M NaCl solution with additions of either 0.01 or 0.1 M $Na_2Cr_2O_7$. Artificial crevice growth experiments were conducted under potentiostatic polarization at potentials ranging from 0 to

Figure 8 (a) Schematic illustration of the experimental apparatus used in the foil penetration technique. (b) A schematic of the detection circuit used to determine the time of penetration of the sample foil. (c) Average foil penetration times from replicate experiments for a 216 μm thick 2024-T3 foil potentiostatically polarized to -0.550 V_{sce} in actively oxygenated 1.0 M NaCl solutions containing different concentrations of dichromate ion. The bars represent one standard deviation. (From A. Sehgal, G. S. Frankel, B. Zoofan, S. Rokhlin. J. Electrochem. Soc. 147, 140 (2000).)

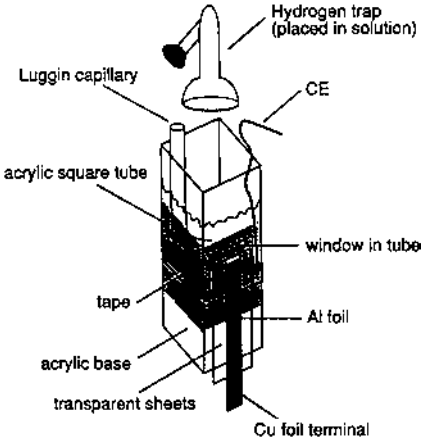

Figure 9 A schematic illustration of the artificial crevice cell. (From E. Akiyama, G. S. Frankel. J. Electrochem. Soc. 146, 4095 (1999).)

1 V_{sce} for 2 hour time intervals. In these experiments, it is possible to analyze the following charge balance:

$$Q_{net} = Q_{anodic} - Q_{cathodic} = Q_{anodic} - (Q_{H2} + Q_{chromate}) \quad (2)$$

Here, Q_{net} is the charge supplied by the potentiostat during the course of the experiment. Q_{anodic} is the charge evolved by metal dissolution. This is determined using Faraday's law and measurement of the volume of foil dissolved during the experiment. $Q_{cathodic}$ consists of two components Q_{H2}, cathodic charge due to hydrogen reduction, which is determined by gas collection, and $Q_{chromate}$, the charge due to chromate-to-chromic reduction. The analysis assumes that oxygen reduction does not contribute significantly to $Q_{cathodic}$, Q_{net}, Q_{anodic}, and Q_{H2}, which are all determined by direct measurement, while $Q_{chromate}$ can be estimated by difference. This allows experiments to be systematically characterized to assess any possible inhibiting effect due to the presence of chromate.

Figure 10 shows the effect of applied potential in the range of 0.0 to +1.0 V_{sce} on the various charge components in 0.1 M NaCl solution and 0.1 M NaCl solutions with additions of 0.01 and 0.1 M $Na_2Cr_2O_7$ (28). The data for charge components are scattered but do not indicate a strong inhibiting effect due to the addition of dichromate to solution. With increasing dichromate concentration, the total cathodic charge increased, presumably due to an increased contribution from dichromate reduction. In a related fashion, the total anodic charge also appeared to increase with increasing dichromate concentration. Analysis of the crevice solution conductivity during ohmically limited crevice growth showed that

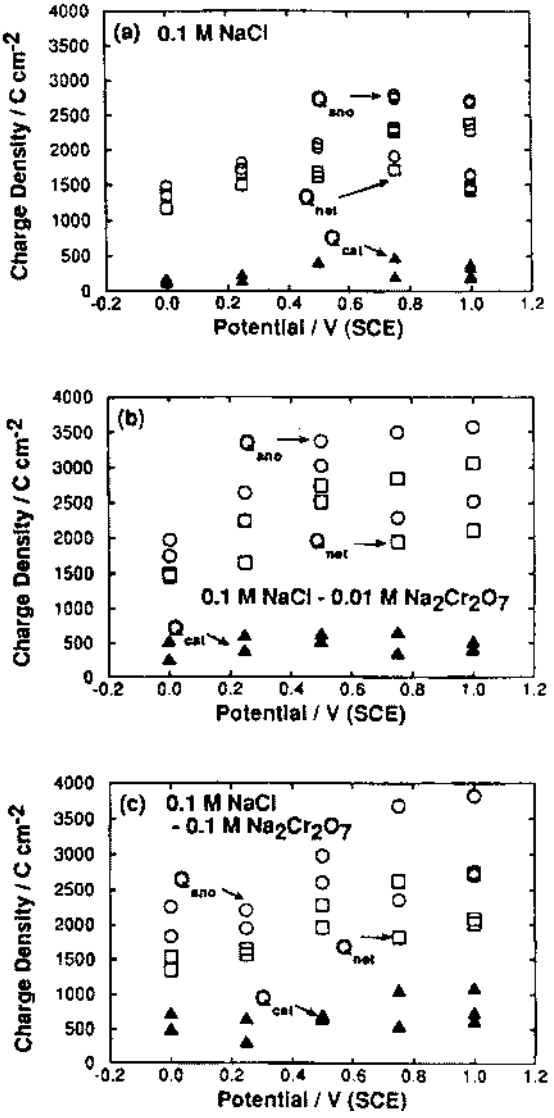

Figure 10 The effect of applied potential on the various charge components arising from electrochemical activity in artificial crevice experiments conducted for different dichromate concentrations and different dichromate : chloride concentration ratios: (a) 0.1 M NaCl. (b) 0.1 M NaCl plus 0.01 M $Na_2Cr_2O_7$, (c) 0.1 M NaCl plus 0.1 M $Na_2Cr_2O_7$. (From E. Akiyama, G. S. Frankel. J. Electrochem. Soc. 146, 4095 (1999).)

the crevice solution conductivity was not a simple function of the bulk solution dichromate concentration. As a result, a systematic effect of increased solution conductivity on Q_{anodic} is not evident.

Dichromate does not function as an anodic inhibitor during crevice propagation in these experiments. Dichromate is not expected to be an inhibitor at the applied potentials used here, but estimates of the potential drop place the bottom of the crevice at a potential ranging from -0.5 to -0.8 V_{sce}. In this potential range, anodic inhibition might be expected, provided the chromate:chloride ratio is sufficiently large.

Kendig has argued that in experiments conducted under potential control, the cathodic reaction is displaced to the counter electrode (37). This may allow more acidic conditions to develop on the electrode surface than might be expected under natural conditions where the cathodic reaction must be supported on the corroding surface. Crevice pH values are normally observed to be in the 3 to 4 range for crevices in Al alloy samples immersed in a bulk environment and can become slightly alkaline if they are isolated from a bulk environment. Kendig has speculated that in potential controlled experiments, the pH is much lower if there is no cathodic activity in the crevice. Chromate anions become increasingly protonated with decreasing pH. For total dissolved chromium concentrations in the millimolar range, Cr^{6+} is present predominantly as fully protonated H_2CrO_4. In 10 mM chromic acid solutions at pH 2, an 1100 Al sample polarized to -0.500 V_{sce} exhibits a dissolution current that is about 1% of that measured in a chromic acid-free solution. In pH 1 solutions, the current ratio increases to about 10%, and at pH 0, it is 100%. Although the chloride–chromate ratio in these experiments was not held constant, these results suggest that part of the loss in inhibition efficiency with decreasing pH is attributable to increased speciation of Cr^{6+} to noninhibiting H_2CrO_4.

Overall, these results indicate that chromates inhibit corrosion by elevating the pitting potential on aluminum with respect to the corrosion potential, which decreases the probability for the formation of stable pits. In general a chromate chloride concentration ratio in excess of 0.1 is necessary to observe significant anodic inhibition.

C. Chromates and Cathodic Inhibition

Chromates are excellent inhibitors of oxygen reduction in near neutral and alkaline solutions. In these environments, they can stifle corrosion by suppressing this cathodic partial reaction. The inhibition mechanism appears to involve reduction of Cr(VI) to Cr(III) at a metal surface and formation of Cr(III)-O-substrate metal bonds (38). This surface complex is likely to be substitutionally inert and a good blocker of oxygen reduction sites, as suggested by the exceedingly small water exchange rate constant for the first coordination sphere of Cr^{3+} (39).

1. Chromate Inhibition and Cathodic Polarization

Chromate is a very powerful cathodic inhibitor even at low chromate:chloride ratios. In cathodic polarization curves collected for 2024-T3 in a base solution of oxygen-sparged 1.0 M $Na_2Cr_2O_7$, the oxygen reduction reaction rate is reduced by about an order of magnitude (at $-0.800V_{sce}$) by the addition of 10^{-5} M $Na_2Cr_2O_7$ (28) (Fig. 11). In similar experiments where 0.3% H_2O_2 was added as a cathodic depolarizer, 10^{-4} M dichromate additions had no effect on the oxygen reduction reaction rate, but additions of 10^{-3} M chromate reduced the cathodic reaction rate by an order of magnitude. The results of these experiments show that chromate inhibits the cathodic reaction at chromate:chloride concentration ratios of 10^{-5}. This value is much lower than the 0.1 to 1.0 ratio required to observe increases in the pitting potential during anodic polarization experiments (23). The curves in Fig. 11 also suggest that hydrogen and water reduction are inhibited at the lowest measured potentials. Sometimes the cathodic polarization response of Al alloys is compromised by cathodic corrosion In Cu-bearing alloys this may lead to Cu surface enrichment and enhancements in the cathodic kinetics. However, the data of Fig. 11 suggest that dichromate is potent enough to inhibit cathodic kinetics and suppress cathodic corrosion even at very large cathodic overpotentials.

2. The Split Cell and Related Experiments

The split cell is similar to the classic differential aeration cell (40). Corrosion kinetics are studied by measuring the current flowing between two physically separated working electrodes. The electrodes may reside in the same cell exposed to the same electrolyte (single cell), or they may be segregated in different compartments separated by a porous frit that allows ionic conduction but restricts mixing of the cell contents (split cell). Current flow between the two electrodes can be measured using a zero resistance ammeter. The potential difference between electrodes, or between an electrode and a reference electrode, may be made using a high impedance voltmeter. A schematic illustration of these cell arrangements are show in Fig. 12 (41). In experiments conducted with dissimilar electrode materials, one electrode will be become the net anode, while the other will become the net cathode. By properly pairing electrode materials and area ratios it is possible to simulate the galvanic interactions among microstructural elements in heterogeneous alloys and examine the action of chromates on local anodic and cathodic regions. In the split cell arrangement, the environments may be varied to examine separately the effect of solution chemistry on the anodic or cathodic parts of a corrosion process.

Ramsey et al. used split cell experiments to study the effect of chromates on inhibition of the anodic and cathodic reactions using Cu, Al, and Al alloy 2024-T3 in near-neutral chloride solutions (41). Split cell experiments involving

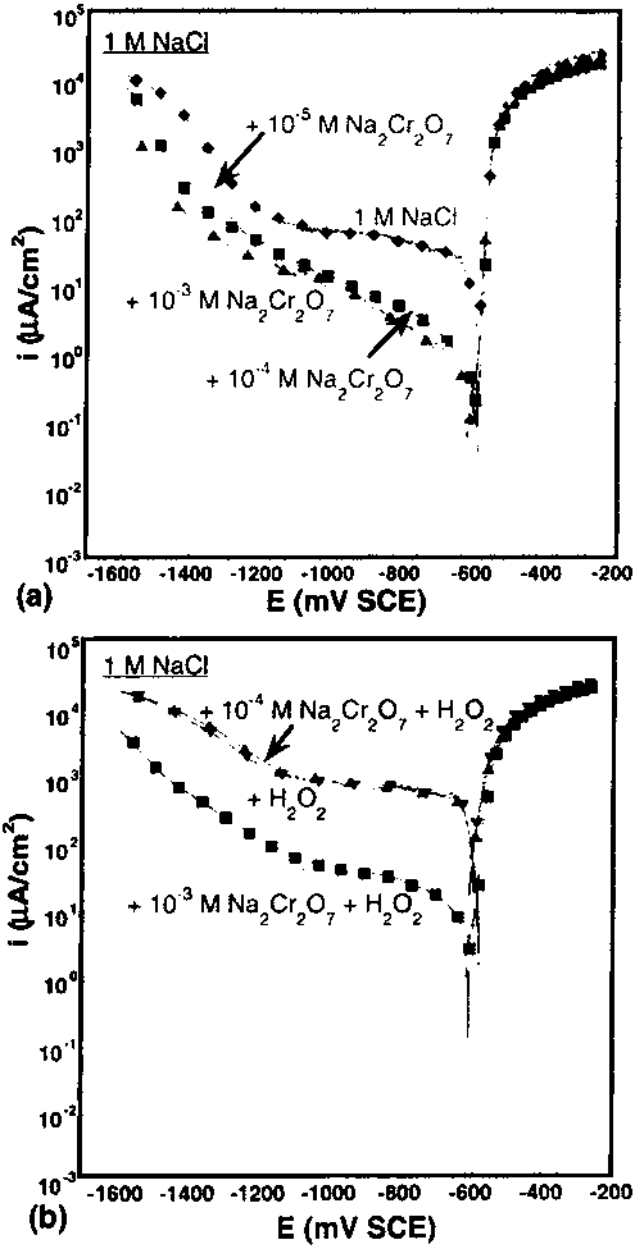

Figure 11 Cathodic polarization curves on 2024-T3 in actively oxygen-sparged 1 M NaCl solution with (a) dichromate additions and (b) 0.3 vol% peroxide and dichromate additions. (From A. Sehgal, G. S. Frankel, B. Zoofan, S. Rokhlin. J. Electrochem. Soc. 147, 140 (2000).)

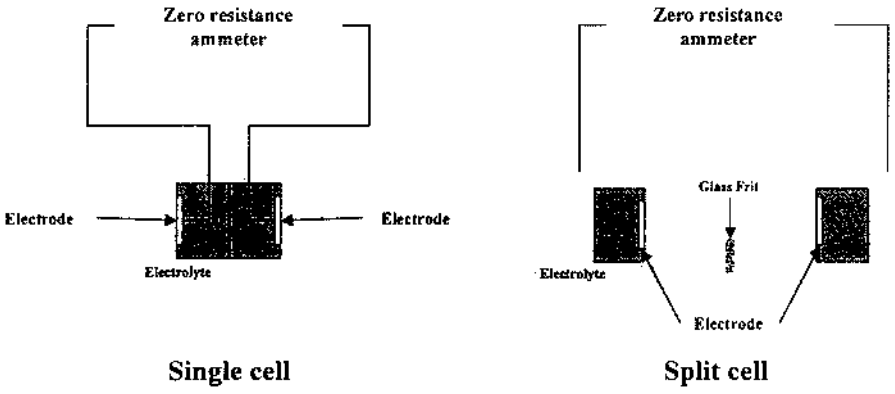

Figure 12 Schematics of single- and split-cell apparatus. (Courtesy of W. J. Clark, J. D. Ramsey, R. L. McCreery, G. S. Frankel, Ohio State University.)

Al and Cu electrodes strongly segregated anodic and cathodic reactions. And although they are idealized models of microstructural features in Al–Cu alloys (42), they are relevant to microgalvanic coupling in high-strength Al alloys. Figure 13 shows plots of galvanic couple current and couple potential versus time showing the effect of 50 mM $K_2Cr_2O_7$ additions (0.1 M chromate) to aerated 100 mM NaCl solutions (41). When dichromate is added to the cell compartment containing the Al (or Al alloy 2024), there is no detectable reduction in the galvanic current flowing, and only a very small change in the couple potential is observed. Since the cathodic reaction proceeds unimpeded in the other compartment of the cell, this result suggests that there is very little effect of dichromate on the anodic reaction, consistent with Kaesche's findings (23). However, when dichromate is added to the cell compartment containing the Cu, which supports oxygen reduction, there is a sharp transient increase in the couple current followed by a rapid decrease to low steady-state values. This is attributed to chromate reduction to insoluble $Cr(OH)_3$, which forms an insulating film on the Cu electrode surface and restricts the reduction reaction and limits the couple current. This shows that the overall corrosion process is under cathodic reaction control and that dichromate is a potent cathodic inhibitor at this concentration ratio.

3. Rotating Disk Electrode (RDE) Experiments

Corrosion of Al alloys often occurs under conditions in which the primary cathodic reaction is oxygen reduction. In cathodic polarization experiments, this reaction appears to be under mass-transfer control at potentials near the open

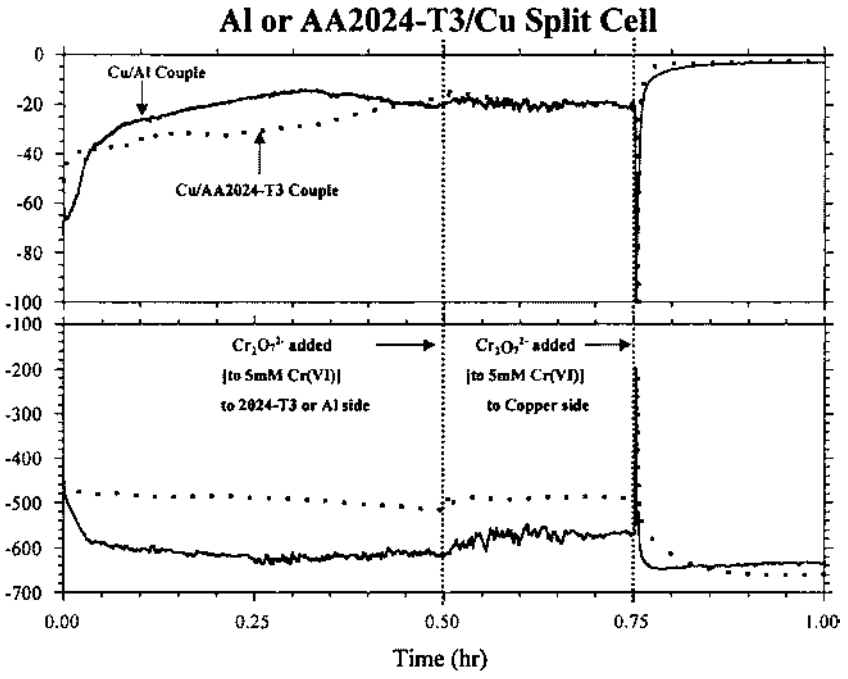

Figure 13 Behavior of a split cell containing a Cu electrode in one compartment and either Al or 2024-T3 in the other. Both compartments were open to air but not actively aerated. $K_2Cr_2O_7$ was added as indicated to a total chromate content of 5 mM. (From W. J. Clark, J. D. Ramsey, R. L. McCreery, G. S. Frankel. J. Electrochem. Soc., in review, June, 2001.)

circuit potential of many engineering alloys. The rotating ring disk electrode approach enables study of transport controlled reactions under well controlled experimental conditions and has been used to separate direct and indirect effects of chromate on the suppression of oxygen reduction on Al alloys (43).

The RDE consists of a disk electrode embedded in an insulating rod material as shown in Fig. 14 (44). The composite electrode can be rotated about its axis, which causes electrolyte to be drawn up against, and forced outwards across, the face of the metal disk electrode, as shown in Fig. 15 (45). The convection and diffusion equations that describe solution flow in this situation have been rigorously established making this experimental approach a powerful one for the study of the effects of forced convection of electrochemical reactions.

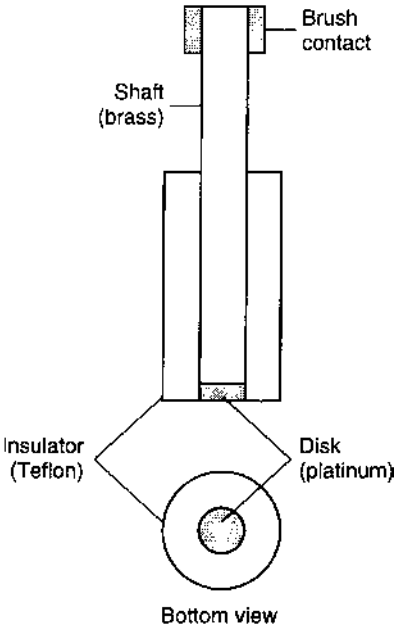

Figure 14 Schematic illustration of the composite electrode used in RDE experiments. (From A. J. Bard, L. E. Faulkner. *Electrochemical Methods: Fundamentals and Applications*. 2d ed. John Wiley, New York, 2001, p. 335.)

In the present case, the Levich equation describes the reaction rate for a mass-transfer limited reaction in an RDE experiment. The Levich equation is

$$i_l = 0.62nFAD_O^{2/3}\omega^{1/2}\nu^{-1/6}C_O^* \quad (3)$$

The limiting reaction rate expressed as a current density depends on the electrode area, A, angular velocity, ω, the kinematic viscosity, ν, the concentration of reactant in solution, C_o^* and its diffusion coefficient, D_o.

Figure 16 shows the steady-state limiting current density, i_{lim}, for the oxygen reduction reaction (ORR) on pure Al, pure Cu, and an intermetallic compound phase in Al alloy 2024-T3 whose stoichiometry is $Al_{20}Cu_2(Mn,Fe)_3$ after exposure to a sulfate–chloride solution for 2 hours (43). The steady-state i_{lim} values for the Cu-bearing materials match the predictions of the Levich equation, while those for Al do not. Reactions that are controlled by mass transport in the solution phase should be independent of electrode material type. Clearly, this is not the case for Al, which suggests that some other process is rate controlling.

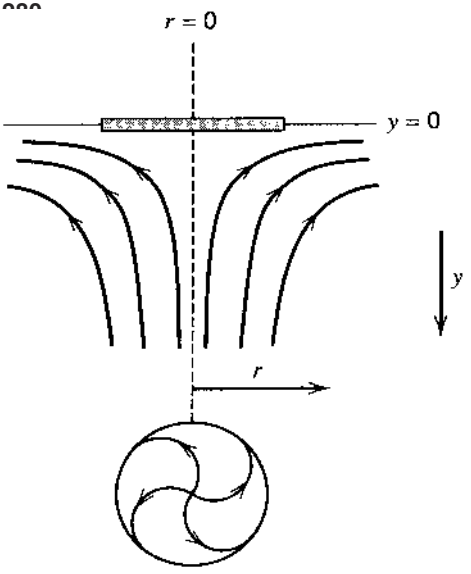

Figure 15 Representation of steady-state electrolyte flow past the electrode disk in RDE experiments. (From A. J. Bard, L. E. Faulkner. *Electrochemical Methods: Fundamentals and Applications*, 2d ed. John Wiley, New York, 2001, p. 337.)

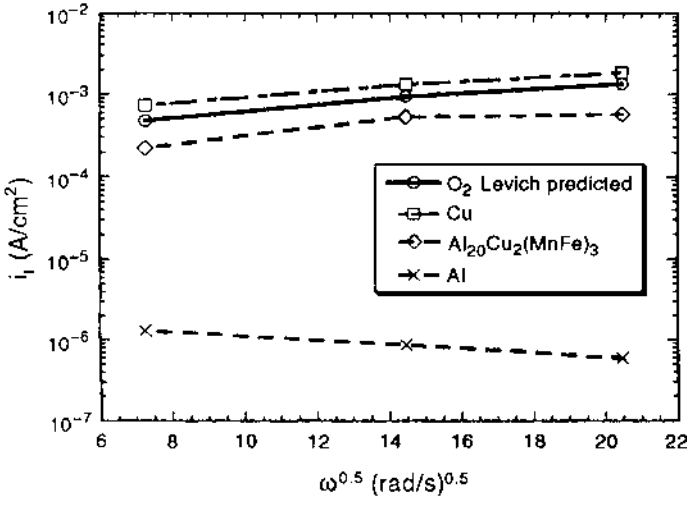

Figure 16 Limiting current densities for oxygen reduction on rotating disks for pure Cu, $Al_{20}Cu_2(Mn,Fe)_3$, and pure Al in 0.1 M Na_2SO_4 + 0.005 M NaCl under ambient aeration. The Levich prediction assumes a dissolved oxygen concentration of 6 ppm (1.8×10^{-4} M). (From G. O. Ilevbare, J. R. Scully. Corrosion 57, 134 (2001).)

In this case, it is likely that electron transfer is sluggish through the Al oxide film on the pure Al electrode, and this limits the rate at which the ORR can be sustained. The high ORR rate on the Cu-bearing materials was attributed to corrosion and surface roughening that increased the area capable of supporting the ORR. In the case of the intermetallic compound, dealloying may also have contributed to the increase in active surface area.

A different situation is observed when these same materials are exposed to a chromate-bearing sulfate–chloride solution prior to RDE measurement. In this case, transport-limited ORR rates were lower than the Levich prediction, but not as low as the ORR rates on pure Al, as shown in Fig. 17. RDE measurements of the ORR on Au, which is not susceptible to roughening in chromate–sulfate–chloride solutions, showed no change due to prior exposure. On the basis of these results, chromate appeared to suppress corrosion during the pretreatment phase, thereby limiting the extent of surface roughening and any increase in active surface area. The important finding from these studies for Al–Cu alloys is that the limitation in surface roughening of Cu-bearing intermetallics in Al–Cu alloys limits the development of large catalytically active surface to support the ORR. This in turn contributes to improved resistance to corrosion.

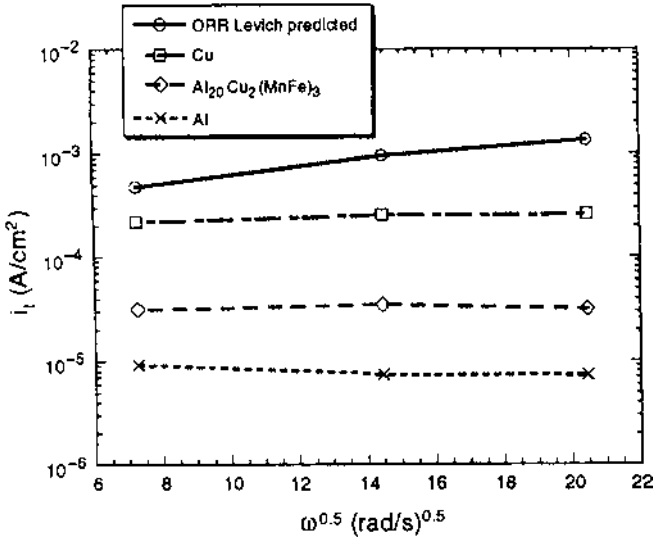

Figure 17 Limiting current densities for oxygen reduction on rotating disks for pure Cu, $Al_{20}Cu_2(Mn,Fe)_3$, and pure Al in 0.1 M Na_2SO_4 + 0.005 M NaCl + 0.0062 M Na_2CrO_4 + 0.0038 M H_2CrO_4 at pH 6 under ambient aeration. The Levich prediction assumes a dissolved oxygen concentration of 6 ppm (1.8×10^{-4} M). (From G. O. Ilevbare, J. R. Scully. Corrosion 57, 134 (2001).)

IV. CONVERSION COATINGS

A. Overview of Conversion Coatings

Conversion coatings are formed on metal surfaces to enhance adhesion of subsequently applied paints and adhesives and to provide temporary or modest permanent increases in corrosion resistance. In the broadest sense, conversion coatings can be divided into three categories: chromate conversion coatings, phosphate conversion coatings, and a less well-defined and still emerging class of environmentally friendly conversion coatings that contain little or no phosphate or chromate. Conversion coatings are usually formed by immersing or spraying an aqueous solution that activates a metal surface, dissolves any existing surface oxide, and replaces it with a thin mixed metal oxide coating.

In terms of processing, conversion coatings are distinct from anodized coatings because no externally applied voltage or current is needed to the substrate to accomplish coating formation. In terms of properties, conversion coatings are distinct from anodized coatings because they are much less corrosion resistant and much more susceptible to inadequate coverage or improper coating formation due to substrate composition and metallurgical heterogeneity. Conversion coatings are usually much softer than anodized coatings, especially when they are first formed.

Conversion coating thicknesses range from 0.1 to nearly 10 μm. Most commonly, they are in the 1 to 2 μm range. The coatings may be largely amorphous or polycrystalline. They do not possess regular arrays of pores and are not generally known to have a duplex structure (inner barrier layer and outer porous layer) like anodized coatings.

Chromate conversion coatings are used widely on aluminum alloys as a pretreatment for painting, though in some applications, where noncondensing atmospheric exposure is expected, they may be used as the primary means of corrosion protection. Chromate conversion coatings are used on magnesium, cadmium, and zinc, and on galvanized steel to suppress the formation of white rust.

Phosphate conversion coatings have long been used in the automotive industry to prepare steel surfaces for painting. Owing to the increasing use of aluminum in automobiles and the desire to maintain simple and cost-effective surface finishing facilities, phosphate conversion is now being used to prepare Al alloy sheet for painting. A detailed review on chromate and phosphate conversion coatings can be found in Ref. 46.

Phosphate conversion coatings are formed on metal surfaces by immersion in aqueous phosphate solutions. These coatings are primarily intended to promote the adhesion of subsequently applied paints. Phosphate coatings typically consist of a compact mass of hydrated metal phosphate crystallites; $M_3(PO_4)_2nH_2O$. They differ from CCCs in that they are crystalline, do not attempt to provide

complete surface coverage of the metal, and provide lower levels of corrosion resistance.

Chromate- and phosphate-free coating chemistries are currently the subject of intensive research and development. Chromates are toxic and carcinogenic to humans. Phosphate discharged into aquatic environments leads to accelerated eutrophication. The challenge for environmentally friendly replacement coating chemistries is to duplicate the ease of application and high performance of chromate and phosphate coatings without using or producing hazardous chemical substances. Reviews on the status of Cr-free coatings development can be found in Refs. 47–50.

For many years, evaluation of conversion coatings was carried out using cabinet exposure testing (51) or spot testing (52). Over the past 20 years, and especially since the introduction of electrochemical impedance spectroscopy to corrosion research, electrochemical techniques have been used with increasing regularity to assess corrosion resistance of conversion coatings. Phosphate coatings are not usually as corrosion resistant as chromate coatings, but electrochemical techniques are used to estimate the extent of phosphate surface coverage. As the use of electrochemical techniques has increased, effort has been directed towards characterizing the corrosion behavior of traditional chromate-based coatings using modern electrochemical methods to establish a performance baseline defined in terms of results from electrochemical experiments.

B. Electrochemical Testing of Conversion Coatings

1. Anodic Polarization

In general, small passive current densities and increases in pitting potential are regarded as evidence for anodic inhibition in anodic polarization experiments. However, in aerated chloride solutions, chromate conversion coated alloys do not exhibit strong reductions in passive current or elevations in pitting potential. In fact, it is not uncommon for conversion coated aluminum alloys to exhibit no passive region at all in aerated solutions with chloride concentrations greater than 0.1 M. This has been interpreted as a lack of anodic inhibition by CCCs. However, test electrode areas are usually on the order of square centimeters and contain many metallurgical and surface defects that readily initiate pits. Given that pitting is a defect-dominated process, pits will initiate at the weakest site no matter how robust the remainder of the coating. In this sense, anodic polarization measures only the strength of the weakest point in the sample. This is unlike cabinet exposure testing, or electrochemical impedance methods, where the evaluation more or less accounts for the behavior of the entire sample surface.

The effect of defect mediation of coating breakdown in anodic polarization experiments can be observed in polarization experiments conducted with arrays

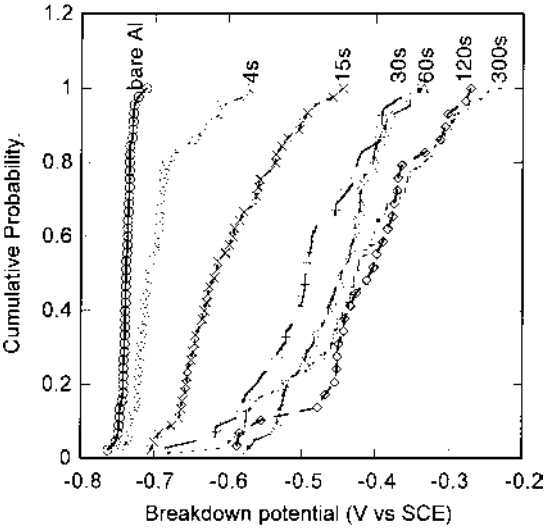

Figure 18 Effect of immersion time on CCC breakdown distributions determined in 0.5 M NaCl solution. CCCs formed on high purity Al wire electrodes. (From W. Zhang, B. Hurley, R. G. Buchheit. J. Electrochem Soc., submitted, June, 2001.)

of small, nominally identical electrodes. Figure 18 shows distributions of pitting potentials measured in 0.5 M NaCl solution on 500 μm diameter Al electrodes arranged in an array (53). Entire arrays were chromate conversion coated for different lengths of time, removed, aged in air for 24 hours, and then immersed in 0.5 M NaCl and polarized potentiodynamically until pitting was detected. This plot shows that as the immersion time in the conversion coating bath increases, the distribution of the pitting potential shifts to more positive potentials, clearly indicating anodic inhibition. These pitting potential distributions reflect the behavior of large area measurements, where some regions of the surface break down more readily than others.

For phosphate coatings, anodic polarization techniques have been used to assess the uncoated metal surface area. Integration of metal oxidation peaks in the $i–V$ curves from cyclic voltammetry and comparison to integrated peak areas determined from reference samples with known surface coverages give such indications (54–56). However, the metal oxidation process and the interpretation of the electrochemical response may be significantly altered by the fact that metal dissolution occurs at the bases of pores, where local chemistry may differ significantly compared to the bulk. Polarization resistance measurements have also been explored as a means for determining the exposed surface area (57). In the proper

environment, the corrosion rate of the metal will be proportional to the exposed area. This approach has the advantage that the coated surface is never driven very far from its steady-state open circuit potential and that the coating is not heavily damaged during the measurement.

2. Cathodic Polarization

Conversion coatings are electronically resistive and do not support reduction reactions that depend on electron transfer through the coating. In near-neutral aqueous solutions oxygen reduction is transport limited on bare metals and occurs at a rate of about 10^{-5} A/cm^2. For an intact conversion coating, oxygen reduction occurs under mixed reaction control at much lower rates, and it is a straightforward matter to distinguish between bare and conversion coated surfaces on the basis of cathodic polarization. Defective or damaged conversion coatings will support reduction reactions at higher rates, and it is possible to rank the corrosion resistance of certain types of conversion coatings on the basis of their ability to inhibit oxygen reduction. In many conversion coatings, the only meaningful component of corrosion resistance is the ability to inhibit the cathodic portion of the corrosion process.

For phosphate coatings, the magnitude of the limiting current density is used as a measure of exposed surface area (58). Like anodic polarization methods though, this method must be used with care, as chemistry changes and restricted transport occurs in pore spaces where the reduction reaction occurs. Alkaline dissolution of the phosphate coating may also occur after extended cathodic polarization, which damages the coating and increases the exposed metal area.

3. Tests for Self-Healing

One of the most noteworthy components of chromate coating corrosion protection is active corrosion protection or self-healing. Self-healing refers to the ability of a coating to resist localized corrosion in locations where it has suffered minor amounts of mechanical or chemical damage; or where the original coating did not form completely. It has long been speculated that chromium–chromate coatings possess this property, because they can leach chromate into an attacking solution, which is transported to the site of attack to stifle corrosion. The self-healing effect appears to be very pronounced for primer paint coatings containing high fractions of sparingly soluble chromate pigment, but the effect also seems to be present in chromate conversion coatings (CCCs).

A simple cell, termed the simulated scratch cell, has been devised that can check for the key elements in the self-healing of CCCs (59). This cell, shown in Fig. 19, consists of two metal surfaces, normally several square centimeters in area, opposing one another and separated by several millimeters. One metal surface is conversion coated, while the other is left bare to simulate a defect or

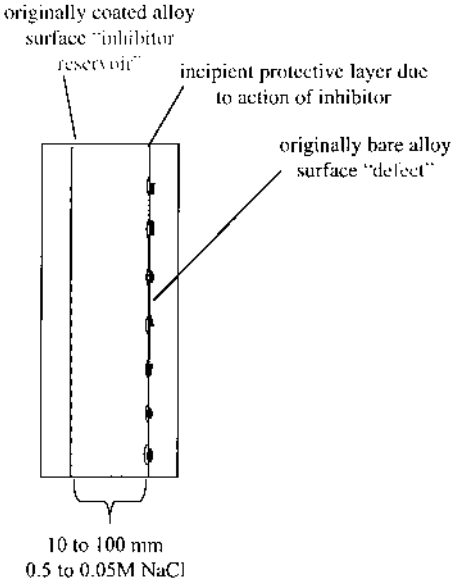
originally coated alloy
surface "inhibitor
reservoir"
incipient protective layer due
to action of inhibitor
originally bare alloy
surface "defect"
10 to 100 mm
0.5 to 0.05M NaCl

(a)

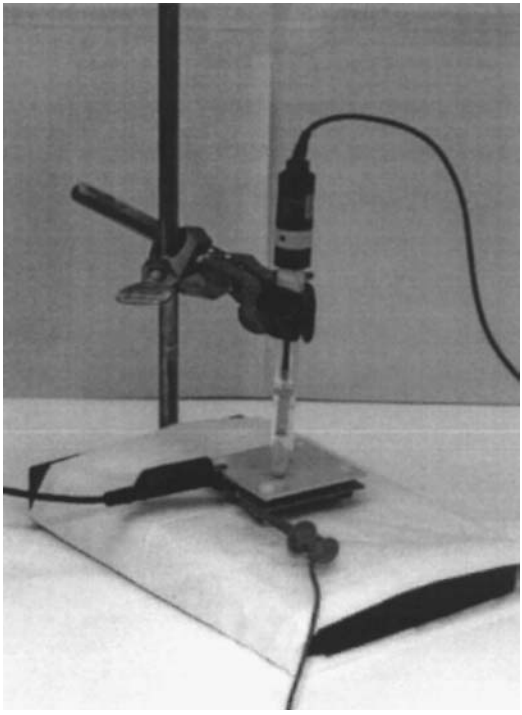

(b)

"scratch." The two metal surfaces are separated by a gap of several millimeters, which is filled with an attacking electrolyte like a dilute chloride solution. The cell may be equipped with a counter and reference electrode and either the coated or defect sides of the cell can be interrogated using electrochemical methods.

Using this cell constructed with bare and conversion coated 2024-T3 and filled with a solution of 0.1 M NaCl, an accelerated chromium–chromate conversion coating was examined for evidence of self-healing (59). Over a span of 48 hours, the polarization of the originally bare surface was found to increase by two orders of magnitude, while the pitting potential increased 60 mV. Raman spectroscopy on the surface showed that CCC-like chromate products had formed near pits. In ex situ solution chemistry determinations, chromate release was verified by placing a droplet of solution on a conversion coated surface. Over a 48 hour period, a chromate concentration of 35 ppm was found to have developed. All together, these results confirmed anecdotal reports of self-healing derived from the performance of scribed conversion coated panels in cabinet exposure testing.

Simulated scratch cells have been used to show that hydrotalcite conversion coatings containing Ce(VI) can also be self-healing (60). Conversion coatings were made by first forming a hydrotalcite coating on 2024-T3 and 6061-T6 substrates and then immersing the coated substrates in a solution consisting of 10 g/L $Ce(NO_3)_3$ + 3 mL/L 30 vol% H_2O_2. The alkaline conditions of the coating induced precipitation of sparingly soluble Ce(VI) hydrated oxides. Simulated scratch cells were constructed using this coating and a bare 2024-T3 sample as the scratch. The gap solution in these experiments was 0.5 M NaCl. Bare surfaces were exposed in the simulated scratch cell and then tested for changes in corrosion resistance ex situ in a 0.05 M NaCl solution. Results from these experiments and other comparative experiments are shown in Fig. 20. The plot shows that the corrosion resistance of the bare surface exposed to the Ce sealed hydrotalcite coating exhibited a much greater corrosion resistance than a sample exposed to Ce coating containing primarily Ce(III) or a sample exposed to another uncoated alloy surface. Solution analysis showed that Ce was released by Ce(IV) coatings, and that Ce precipitated on the bare surface, primarily at Cu-rich inclusions in the alloy.

Evidence for self-healing is not detected in identical experiments with lanthanum sealed hydrotalcite coatings. La does not have a soluble tetravalent oxide

Figure 19 (a) Cross section schematic of the simulated scratch cell. (b) Photograph of an artificial scratch cell modified to make in situ electrochemical measurements to test for self-healing by conversion coatings. (From Zhao, McCreery, Frankel. J. Electrochem. Soc. 145, 2258 (1998).)

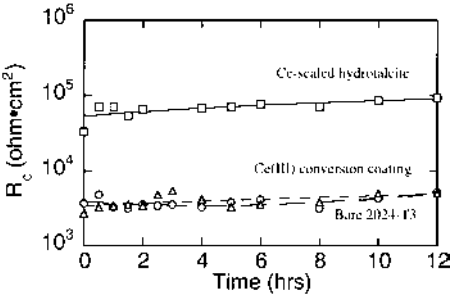

Figure 20 Coating resistance versus time for bare 2024-T3 surfaces exposed to Ce sealed hydrotalcite, a Ce(III) conversion coating, and bare 2024-T3 in the simulated scratch cell. R_c was determined ex situ during immersion in 0.05 M NaCl solution. The plot indicates an elevated resistance to corrosion for the sample exposed to the Ce sealed hydrotalcite coating. (From S. B. Mamidipally, P. Schmutz, R. G. Buchheit. Corrosion, 58, 3, 2001.)

like Ce. Therefore, once it is precipitated on the hydrotalcite surface, it is not easily released to aid in self-healing. Overall, these results show that self-healing is not limited to chromate conversion coatings.

C. Electrochemical Impedance Spectroscopy (EIS)

1. Overview of the Technique

EIS has become an important method of characterizing inorganic coating of all types and the basis of the technique is briefly introduced here. For details on EIS measurements, hardware, data analysis, data presentation, and applications the reader is referred to the materials presented in Refs. 61–64.

EIS uses small periodic signals to perturb an electrode surface and measure an electrochemical response that can be analyzed to gain information on corrosion mechanisms and corrosion kinetics. In corrosion experiments, it is common to apply a 10 to 50 mV sinusoidal voltage signal to a corroding electrode interface and measure the resulting current signal occurring at the same excitation frequency. The voltage and current signals are related by the impedance in a form that is analogous to Ohm's law:

$$Z(\omega) = \frac{V(\omega)}{I(\omega)} \tag{4}$$

The term $Z(\omega)$ is known as the complex impedance and accounts for the relationship between the amplitudes of the voltage and current signals as well as the phase shift between them. The measurement is spectroscopic because the com-

plex impedance is measured over a domain of discrete frequencies. For corrosion studies, the high-frequency end of the measurement domain is determined by the frequency required to short the interfacial capacitance. Under these conditions, only the cell solution resistance will be contained in the complex impedance. For bare metals, conversion coated metals, the interfacial capacitance is shorted at frequencies ranging from 5 to 20 kHz. For anodized coatings, excitation frequencies of 50 to 100 kHz may be required. The coating capacitance for organic coatings cannot be shorted at frequencies accessible to EIS measurement systems, which is normally about 100 kHz for commercial EIS systems. As the frequency is lowered, interfacial resistances and reactances will contribute to the complex impedance. Electrochemical and diffusional processes associated with corrosion are detected at frequencies between about 10 and 10^{-6} Hz. However, it is rare that measurements are made below about 10^{-3} Hz owing to the instability of corroding metal surfaces.

EIS measurements on corroding surfaces are usually made using two or three electrode cell configurations. A potentiostat is used to control the potential between the working and reference electrodes and measure the current flow between the counter and working electrodes. A frequency generator is required to provide the periodic excitation signal. An impedance analyzer is also required to measure the complex impedance. Frequency response analyzers or lock-in amplifiers may be used for this purpose. Integrated systems that contain all the necessary electronic hardware for conducting EIS measurements are commercially available. The measurement hardware is controlled by a personal computer, which runs software that coordinates the execution of the experiment, logs the data, and provides graphical and numerical analysis of the EIS spectra.

In corrosion studies, EIS data are graphically presented in complex plane plots and Bode plots. Examples of these plots are shown in Fig. 21 (65). In complex plane plots, the complex impedance at each frequency is located according to its real and imaginary components. At each frequency, the magnitude of the complex impedance is equal to the length of the vector drawn to the point from the plot origin. The phase angle is defined as the angle the impedance magnitude vector makes with the real axis. Capacitive responses, like those associated with intact barrier coatings, are represented by straight or nearly straight lines that fall along the imaginary axis. Charge transfer processes, like those associated with pitting, usually trace out partial or complete semicircular arcs in the complex plane. Diffusional processes take on a variety of forms depending on the precise nature of the process. In severely pitted conversion coated samples, diffusion is characterized by a tail extending from the right-hand side of a semicircular arc.

In Bode plots the log of the impedance magnitude and the phase angle are plotted versus the log of the applied frequency. Capacitive responses are characterized by regions of the curve that take on slopes of about -1 in the Bode magnitude plot and have phase angles approaching -90 degrees. Charge transfer

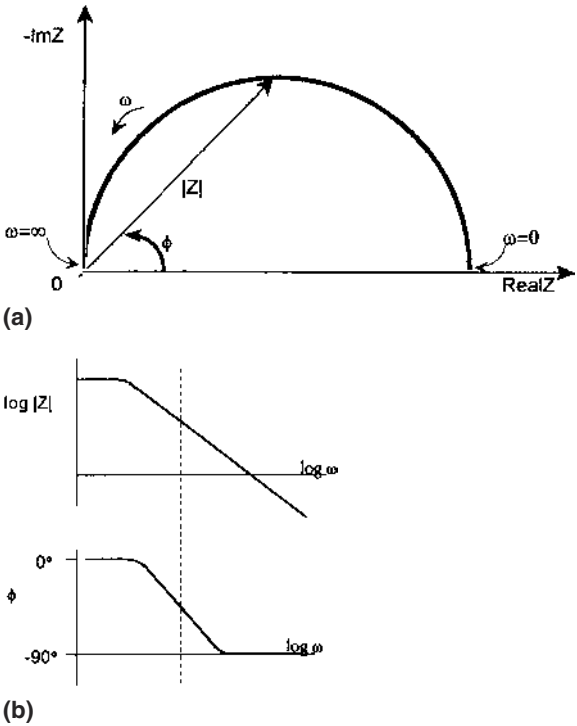

Figure 21 Common graphical representations of EIS data in corrosion studies. (a) Complex plane plot. (b) Bode magnitude and Bode phase angle plots. (From Gamry, EIS Manual, pp. 2–3, 2–5.)

processes have sigmoidally shaped Bode magnitude plots. At the highest and lowest measured frequencies the impedance is primarily resistive in nature, and the Bode magnitude plots are flat. These two regions are separated at intermediate frequencies by a region, where the capacitive response of the electrode is predominant. In Bode phase angle plots, the phase angle is near 0° at high and low frequencies and is near −90° at intermediate frequencies. At the lowest measured frequencies where diffusional processes tend to dominate the impedance response, the Bode magnitude often increases slowly with decreasing frequency and takes on an $\omega^{-1/2}$ to $\omega^{-1/4}$ frequency dependence.

2. EIS and Conversion Coatings

Historically, conversion coatings have been evaluated by exposure testing, usually in a 5% salt fog. Corrosion resistance of conversion coated panels is deter-

mined by visual inspection after some predetermined exposure period. Usually the extent of corrosion damage is evaluated against some established metric such as number of pits per unit area visible to the unaided eye. Coated samples are normally given a pass or a fail ranking. This type of test is simple and is relevant to certain types of service conditions. It can also be very useful for process in quality control. However, exposure durations of 100 to 1000 hours may be required for discriminating results to develop, and the results are based on visual inspection, which is subjective. During exposure, samples will fade, stain, pit, and form corrosion product deposits. A means of quantifying the distribution of corrosion type and intensity has not been widely accepted. Normally, it is a simple matter to distinguish between coatings that provide little corrosion protection from those that offer superior protection. However, no good scheme has arisen to distinguish among coatings of intermediate (but useful) corrosion protection that fail the salt spray test but provide substantially different levels of corrosion resistance.

For these reasons, EIS has been explored as an alternative proof test for evaluation of conversion coatings. In these tests, conversion coated surfaces are exposed to an aggressive electrolyte for some period of time during which coating damage will accumulate. An impedance spectrum is collected and evaluated using a suitable equivalent circuit model and complex nonlinear last-squares fitting.

EIS has several advantages for evaluations of conversion coatings. First, it is a small-signal technique, and the electrode is never polarized very far away from its corrosion potential as the measurement is made. Second, EIS can be very quantitative as it yields both kinetic and mechanistic information about the corrosion process taking place on the sample. The interfacial capacitance can be shorted at frequencies as low as 10 kHz. As a result, meaningful characterizations of the corrosion response can often be obtained from spectra collected between 10 kHz and 10 mHz. This can be completed in a matter of minutes with currently available commercial measuring equipment. Although nearly all conversion coatings yield a nondiscriminating capacitive response immediately upon immersion in an aggressive solution (e.g., 0.5 M NaCl), pitting damage will begin to occur in a number of hours. As a result, discriminating results can be obtained in less then one day using EIS, whereas several days or more are required for exposure testing.

3. Equivalent Circuit Analysis

Equivalent circuit analysis is well suited for analysis of EIS measurements of conversion coatings and is the primary method for interpreting EIS spectra from conversion coated metal surfaces. A widely accepted generalized equivalent circuit model for the EIS response of pitted conversion coatings is shown in Fig. 22a (66,67). Several related models discussed below are also shown. In the gener-

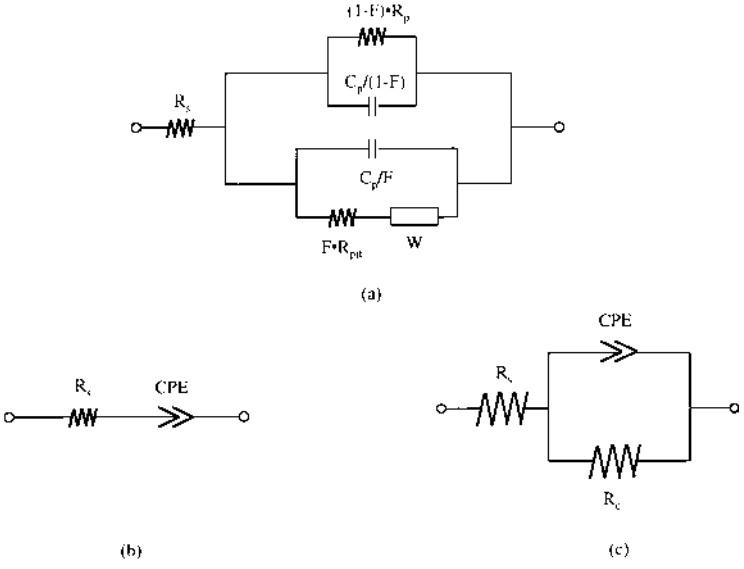

Figure 22 Equivalent circuit models for conversion coatings. (a) Generalized model for pitting conversion coated surfaces, adapted from Ref. (b) Model for a barrier conversion coating. (c) Model for the early stages of CCC breakdown.

alized model, R_p and C_p refer to the specific resistance and capacitance of the conversion coating. R_{pit} and C_{pit} refer to the pit resistance and capacitance. The element labeled W is present to account for any diffusional processes, such as those that may be present in severely degraded coatings, or coatings that are naturally porous. When a conversion coating with good barrier properties degrades, the fraction of the surface area covered by pits, F, increases. This shorts the impedance associated with the conversion coating.

For coatings with no pitting, the generalized model must be amended to account for that fact that all current must flow through the barrier coating. The coating resistivity, R_p, is on the order of 100 to 1000 $M\Omega \cdot cm^2$ and behaves essentially as an open circuit under near-DC conditions (f = 0). The EIS response over the typically measured frequency domain is that of a constant phase element (CPE) in series with a solution resistance (Fig. 22b).

A CPE is a nonphysical circuit element whose characteristic is a constant phase shift over a wide range of frequencies. The impedance of this element is (68)

$$Z_{CPE}(\omega) = \frac{1}{C(j\omega)^{\alpha}} \tag{5}$$

On a complex plane plot, a CPE exhibits a straight line whose angle is $\pi/2 \cdot \alpha$ ($1 < \alpha < -1$) with respect to the real axis. In a Bode magnitude plot a straight line response like that of a capacitor is obtained. The slope deviates from an ideal value of -1 as α decreases below 1.

As exposure time to an aggressive environment increases, conversion coating begins to break down. The conversion coating impedance is shorted by pits, which typically have smaller resistivities and larger specific capacitances than the intact conversion coating. In the early stages of coating breakdown, diffusion in pits, represented in the generalized model, is not significant. Usually, a single time constant EIS response is observed. In this case, the measured capacitance consists of contributions from the coating and the pits:

$$C_c = C_p(1 - F) + C_{pit}(F) \tag{6}$$

where C_c is the composite capacitance and the other symbols refer to elements described in the generalized model. This composite capacitance is usually nonideal and can be modeled in an equivalent circuit using a CPE (Fig. 22c). For pitting conversion coatings, α, which is a measure of nonideality in the capacitance, typically ranges from 0.7 to 0.95.

The composite resistance, R_c, is

$$\frac{1}{R_c} = \frac{(1 - F)}{R_p} + \frac{F}{R_{pit}} \tag{7}$$

Since $R_p \gg R_{pit}$

$$\frac{1}{R_c} \approx \frac{F}{R_{pit}} \tag{8}$$

This leads to a very simple single time constant model that accounts for the EIS response for conversion coatings in the early stages of breakdown (Fig. 22c).

For coatings that are inherently porous, or have suffered extensive pitting, the generalized model in Fig. 22a describes the EIS response. Degraded conversion coatings often exhibit one or two time constants in addition to a diffusional impedance.

A common way to rank the performance of coatings is to compute the total impedance from equivalent circuit modeling or to use the magnitude of the impedance at the DC limit. So while the EIS response becomes increasingly complicated as pitting initiates and propagates, the magnitude of the impedance typically falls with increasing exposure time. Table 1 give typical values of the total impedance of various coated and passivated substrates.

Table 1 Coating Resistance Ranges for Various Surface Treatments and Substrates

Coating	"Coating Resistance" $M\Omega \cdot cm^2$
Bare Al alloys	0.005
Sputter-deposited high purity Al	0.5–1.0
Poor conversion coatings	0.1–1.0
Good conversion coatings	1–5
Sealed anodized coatings	10
Painted surfaces	>10

4. Continuum Reaction Analysis

The continuum reaction approach has been used to examine film formation on Al under modestly anodizing conditions (69). In the continuum reaction approach, the entire electrochemical reaction mechanism is written explicitly. Rate equations for the various steps in the electrochemical process are developed. Changes in surface coverages that affect the mechanism are usually accounted for using appropriate adsorption isotherms. Diffusional, migrational, and convective components of mass transfer are expressed in terms of diffusivities, solution conductivies, and viscous properties. A comprehensive description of the various elements in the reaction mechanism are defined and subject to mass and charge balance. An overall rate equation describing the behavior of the net current response is then constructed and linearized to eliminate exponential terms. Polarization dependencies are incorporated for activation controlled and electromigration controlled processes. A term describing a periodic (usually sinusoidal) voltage perturbation is inserted into the equation, and the expression is rearranged to extract the impedance transfer function, which is now defined in terms of kinetic and physical parameters rather than a network of equivalent passive circuit elements. This approach has been used best in analyzing dissolution and passivation in well-behaved systems such as iron in sulfuric acid (70–72). Continuum reaction analysis is a very powerful method for understanding the contributions of faradaic reactions, adsorption, passivation, and transport to the EIS response. However, developing the transfer function requires precise knowledge of the corrosion process. Ancillary data such as reaction rate constants and transport characteristics are also required to construct a comprehensive and meaningful expression for the impedance function. Often these data do not exist in sufficient detail. For these reasons, the continuum reaction approach has not been widely used in the analysis of EIS data for conversion coated surfaces.

5. Nonparametric Analysis

The total equivalent resistance of a corroding surface may be estimated by integration of the imaginary component of the impedance over the measured frequency domain according to

$$R_c = \frac{2}{\pi} \int_{\omega_{lo}}^{\omega_{hi}} Z''(\omega) d \ln \omega \tag{9}$$

where $Z''(\omega)$ is the imaginary component of the impedance, and ω is the radial frequency ($2\pi f$). ω_{hi} and ω_{lo} refer to the limits of the frequency range used in the experiment.

This expression was originally used to estimate the polarization resistance for actively corroding metals whose impedance response was a well-behaved semicircular arc in the complex plane (73), but can be used in certain situations to estimate the equivalent resistance of conversion coated metal surfaces. Equation (9) is derived from the Kramers–Kronig transforms and subject to the conditions that limit their use (74–78). These conditions include

Causality: The measured response is due only to the applied perturbation and does not contain contributions from spurious sources.

Linearity: The relation between the applied perturbation and the measured response is linear.

Stability: The system is stable to the extent that it returns to its original condition after the perturbation is removed.

Finiteness of the impedance function: The impedance must be finite valued at $f \to 0$ and $f \to \infty$, and the impedance must be continuous and finite valued at intermediate frequencies.

This method of estimating R_c is useful when it can be applied, since the determination is not based on any presumed model of the corrosion damage process or any of the assumptions that come with assignment of an equivalent circuit model. This method is particularly helpful when there is more than one time constant in the spectrum, or the impedance spectrum is particularly complicated. Caution is warranted however. This method of estimation can be in serious error for samples with large capacitance-dominated low-frequency impedances. As a general rule, for this estimation method to be reasonably accurate, the impedance function must exhibit a clear DC limit, or a diffusional response that can be modeled by a constant phase element in equivalent circuit analysis (75).

D. Use of EIS for Evaluation of Conversion Coatings: Examples

EIS is very sensitive to the conversion coating breakdown process, and changes in coating corrosion protection can be recognized in graphical representations of

the data; the accumulation of damage can be tracked using equivalent circuit modeling. However, standardized methods for evaluating conversion coatings by EIS do not yet exist.

Intact barrier conversion coatings behave as capacitors that yield distinctive Bode plots. An example of this is shown in Fig. 23 for Ce/Mo passivated Al 6061-T6 exposed to 0.5 M NaCl solution (79). At high frequencies, the interfacial capacitance is shorted, and only the solution resistance is measured. At frequencies below about 10^4 Hz, a pure capacitive response is obtained. This is characterized by a large negative phase shift in the Bode phase angle plot and a straight line with a slope of about -1 in the Bode magnitude plot. These are the indications of high corrosion resistance. This coating is particularly resistant under these conditions, and does not exhibit signs of breakdown after exposures as long as 30 days.

Passivation of Al alloys surfaces in Ce, La, and Y chloride solutions might be expected to produce similar levels of corrosion protection because they all belong to the lanthanide series in the periodic table and share similar chemical characteristics. Examination of surfaces passivated in solutions of each of these salts shows that this is not the case. Figure 24 shows Bode plots for Al 6061-

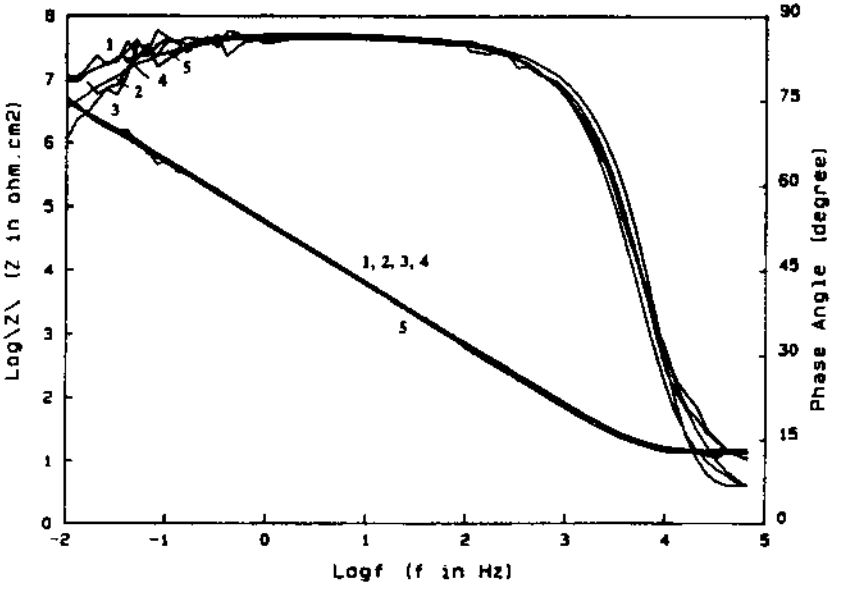

Figure 23 Bode plots for Ce/Mo passivated 6061-T6 exposed to 0.5 M NaCl solution. Curve 1, 6 h; curve 2, 1 d; curve 3, 7 d; curve 4, 14 d; curve 5, 30 d. This plot illustrates the EIS response of a very protective conversion coating. (From F. Mansfeld, V. Wang, H. Shih. J. Electrochem. Soc. 138, L74 (1991).)

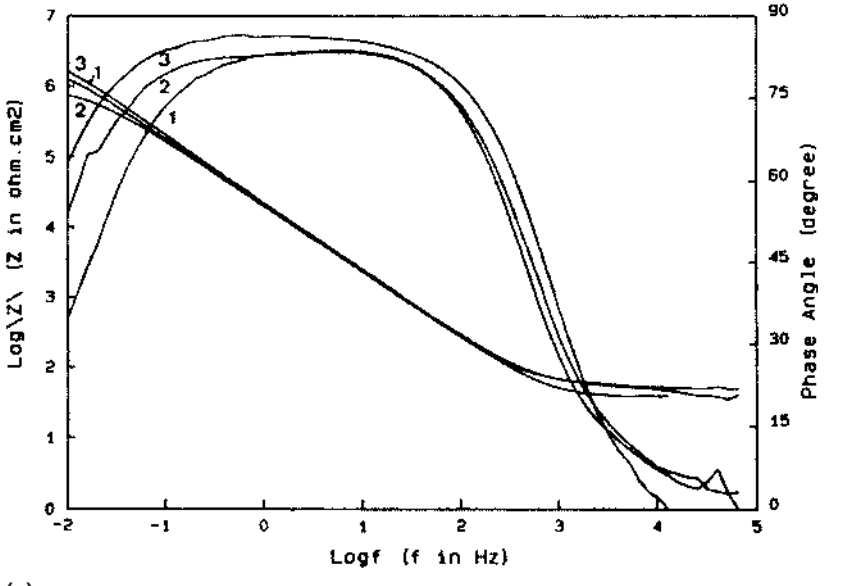

(a)

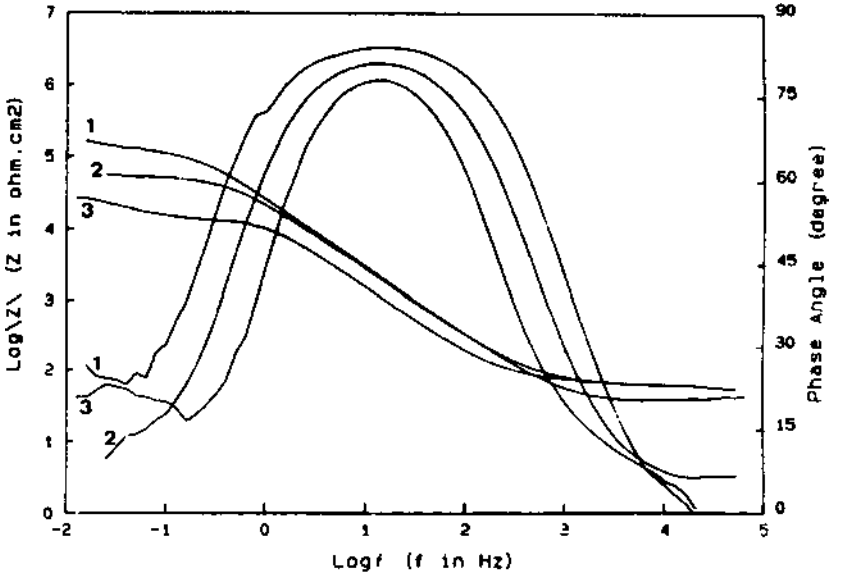

(b)

Figure 24 Bode magnitude plots for $CeCl_3$-, $LaCl_3$-, and YCl_3-passivated 6061-T6 exposed to 0.5 M NaCl solution. (a) $CeCl_3$-passivated samples exposed for 7 d (curve 1), 15 d (curve 2), and 60 d (curve 3). (b) $LaCl_3$-passivated sample (curve 1), YCl_3-passivated sample (curve 2), and bare alloy (curve 3). (From H. Shih, F. Mansfeld. p. 180, ASTM STP 1134, ASTM, Philadelphia, PA (1992).)

T6 passivated in $CeCl_3$ (Fig. 24a) and $LaCl_3$ and YCl_3 (Fig. 24b), which were then exposed to 0.5 M NaCl solution (80). The $CeCl_3$-passivated samples exhibit capacitive behavior. These coatings are not as corrosion resistant as those shown in Fig. 23 and begin to exhibit a low-frequency breakpoint (phase angle = 45°) just above 10 mHz in some cases. The $LaCl_3$- and YCl_3-passivated samples have much smaller capacitive regions across the frequency domain and distinct-low frequency breakpoints, which result in well-defined DC limits in the magnitude of the impedance. Overall, these DC limits are one to two orders of magnitude smaller than the impedance of the $CeCl_3$-passivated surfaces measured at the same frequency. This type of EIS response is characteristic of modest levels of corrosion protection, easily distinguished from the response of more corrosion resistant coatings.

Using the generalized equivalent circuit model for conversion coated surfaces shown in Fig. 22, it is possible to track the time-dependent changes in the resistances and capacitances of the intact coating and evolving pits. Figure 25 shows representative Bode plots for $CeCl_3$-passivated and bare Al 7075-T6 immersed in 0.5 M NaCl solution (81). Spectra like these were collected over 35

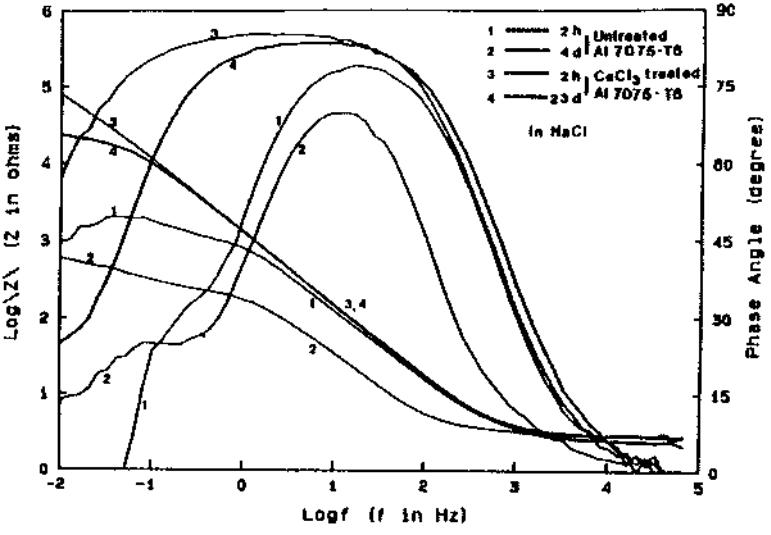

(a)

Figure 25 (a) Bode plot for $CeCl_3$-treated 7075-T6 during immersion in 0.5 M NaCl solution. (b) Results of the equivalent circuit modeling of the EIS data from Fig. 25 using the generalized equivalent circuit model in Figure 22a. (From F. Mansfeld, S. Lin. S. Kim. H. Shih. Corrosion 45, 615 (1989).)

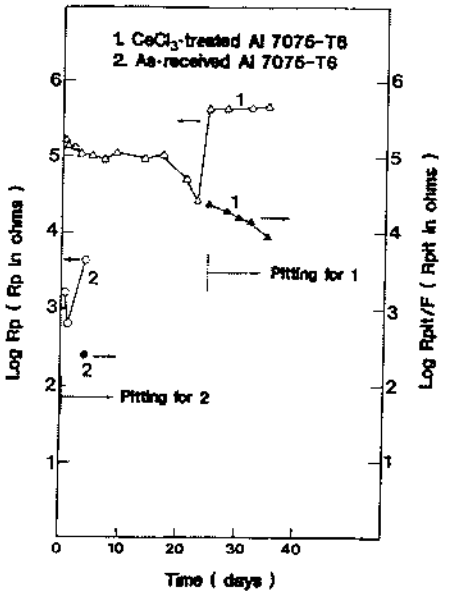

(b)

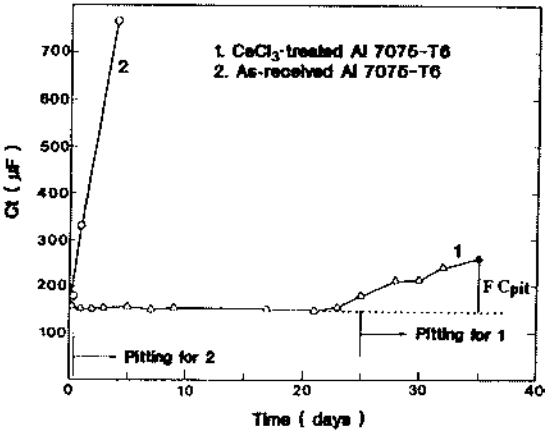

(c)

days and analyzed using the generalized equivalent circuit model. Figure 25b shows the variation in coating and pit resistances versus time, and Fig. 25c shows the variation in coating and pit capacitances. For the $CeCl_3$-passivated sample, the coating resistance R_p is more or less constant over the course of the experiment. Pitting damage does accumulate, but the total pitted area never exceeds a

few parts per thousand and does not contribute to any increase in R_p. After 25 days, a new low frequency time constant appears indicating the appearance of pits. In this case, owing to the small pit area fraction, pit resistance does decrease as pit area increases. For the uncoated sample, the total resistance is comparatively low, and pitting initiates very early in the experiment.

Capacitance is also a sensitive indicator of the onset of pitting. In Fig. 25c a significant pit capacitance increase is detected at 25 days, at the onset of pitting. Capacitance increases dramatically at the outset of the exposure period for the unprotected sample as widespread pitting progresses. Capacitance measurements in particular are good early indicators of pitting in conversion coated samples because increases in sample capacitance usually precede any visual indication of pitting.

E. Relation Between EIS and Salt Spray Exposure

The use of EIS for evaluating conversion coatings has grown considerably since the late 1980s. EIS methods clearly enable conversion coated metals to be evaluated more quickly and quantitatively than exposure test methods such as salt spray. As a research tool, EIS provides important information on corrosion kinetics and mechanisms. EIS-based coating evaluations also appear to be significant from a practical perspective, as they give indications of corrosion resistance that appear to scale with those provided by exposure testing.

To understand more completely the relationship between coating corrosion resistance determined by EIS and that determined by salt spray, 33 different conversion coatings applied to five different Al alloy substrates were evaluated by both methods (82). The data were then evaluated to determine if a correlation existed. A variety of chromate and chromate-free coatings were included in the evaluation representing a wide range in corrosion resistance (83). Coatings were applied to cast 356 (Al-7.0Si), 2024-T3 (Al-4.4Cu-1.5Mg-0.6Mn), 3003 (Al-1.2Mn), 6061-T6 (Al-1.0Si-0.6Mg), and 7075-T6 (Al-5.6Zn-2.5Mg-1.6Cu). Salt spray testing was carried out in accordance with ASTM B117 (84), which directs that coated samples be exposed in a chamber to a 5% salt fog at 95°F. Five replicate samples from each unique coating–substrate combination were evaluated. The samples were visually inspected for evidence of corrosion after 24, 48, 96, and 168 hours. Based on the inspection, samples were assigned a fail ranking if five or more isolated pits were identified. Otherwise, the samples were given a pass ranking.

For the EIS evaluation, samples were exposed to an aerated 0.5 M NaCl solution for 24 h under free corrosion conditions. During this time, some amount of corrosion damage occurred that normally manifested itself as pitting. Replicate EIS spectra were collected from each sample between 10 kHz and 10 mHz using a 10 mV sinusoidal voltage perturbation. During the 24 h exposure period, sam-

ples pitted to greater or lesser extent determined by the protectiveness of the coating. The EIS spectra were fitted to the equivalent circuit model in Fig. 22c, which describes the EIS response of a small number of small area pits on an otherwise passive surface. The model was able to fit the EIS data well except for organically sealed paintlike coatings that gave a strongly capacitive response, and coatings with little corrosion resistance where the EIS response was dominated by diffusional impedance. Numeric parameters describing the spectra were the solution resistance, the coating resistance, R_c, and the magnitude of the impedance and exponent term from the CPE.

A qualitative sensitivity analysis indicated that R_c scaled best with the salt spray pass–fail data. For each sample–coating combination, the average R_c value was treated as an independent random variable, and the fraction of the five replicate samples that earned a passing rating in salt spray was treated as the relative dependent variable. The mean rank method was then used to develop a probabilistic description of the tendency for a given substrate–coating combination to exhibit a passing salt spray result (85,86). From the paired EIS and salt spray data, graphical depictions of the relationship between R_c and the probability of achieving a passing salt spray result were constructed. Figure 26 shows a plot of the cumulative passing frequency (CPF), which is the measure of the tendency to pass the salt spray test, versus R_c measured by EIS for coatings applied to 2024-

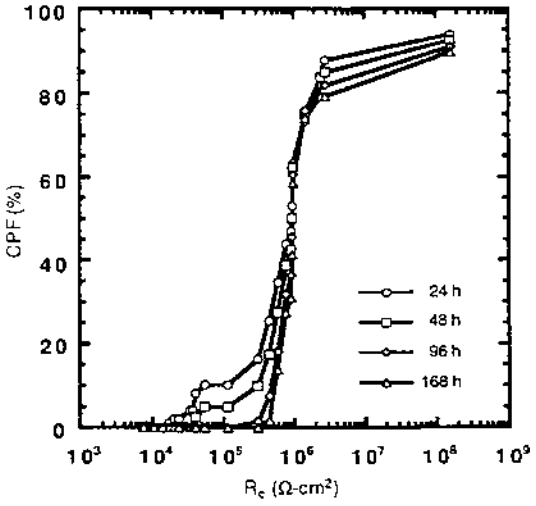

Figure 26 Plot of the CPF versus R_c for chromate and chromate-free conversion coatings on 2024-T3 substrates. (From R. G. Buchheit, M. Cunningham, H. Jensen, M. W. Kendig, M. A. Martinez. Corrosion 54, 61 (1998).)

T3 substrates (82). In general, as R_c increases, the chances of achieving a passing result in salt spray increase, as might be expected. Individual panels must either pass or fail, so a CPF of 80% or greater applied to five panels suggests that more than four of the five panels would pass the test, or essentially five panels would pass. Therefore samples with R_c values corresponding to a CPF of 80% or greater are expected to exhibit passing behavior in salt spray testing at the proper inspection interval. Table 1 shows the R_c values corresponding to the 80% CPF for the five different alloys examined in this study, showing that these values range from 2 to 20 $M\Omega \cdot cm^2$. The threshold R_c value for 2024-T3 is about 2.4 $M\Omega \cdot cm^2$, which agrees well with a threshold value of 2 $M\Omega \cdot cm^2$, which has been suggested as a critical value for achieving a salt spray result in another study (87).

Figure 26 also shows that there is a set of data that exhibit R_c values that range from 0.01 to 0.5 $M\Omega \cdot cm^2$, but have a 0% CPF at 168 h. This suggests that EIS has the ability to discriminate quantitatively among coating performances with more sensitivity than salt spray testing. While these coatings do not perform well in ASTM B117 salt spray, these differences in corrosion protection may be important to know for other applications or environments.

Overall, this analysis suggests that results from EIS do give indications of coating corrosion resistance that scale with the indications of salt spray testing in many cases. EIS also provides some important advantages including greater discriminating power, a more quantitative description of corrosion protection, and a more rapid measurement.

V. ANODIZED SURFACES

A. Overview of Anodization

Anodization involves thickening of oxide layers on metals through application of a voltage or current to a metal surface that is immersed in a suitable electrolyte. Anodization is used to improve the corrosion resistance, abrasion resistance, paint adhesion, and adhesive bonding characteristics of Al, Mg, Ti, and their alloys. Anodizing can be accomplished in a range of solutions. The use of nitric, phosphoric, chromic, and sulfuric oxalic acids is common. Anodic oxide films are divided into two categories: (1) thin barrier layers with high dielectric strength and (2) thick duplex films, which consists of an inner barrier layer and a thick porous outer layer (88,89).

The growth of barrier layers on Al occurs under conditions where oxide film dissolution is negligible. Film growth has been described quantitatively by a high field conduction model involving transport of both Al^{3+} cations and O^{2-} or OH^- anions (90,91). Al^{3+} cations are transported to the film/electrolyte interface, react with water, and participate in film growth. O^{2-} and OH^- anions are

transported to the film/substrate interface where they react with the metal substrate to contribute to film growth. The film growth constant for Al is generally reported to be in the range of 12 to 14 Å/V (92). Anions present in the anodizing solution may also be incorporated into the barrier film and affect its subsequent electronic and barrier properties (93–95).

The thickness of structure of anodized layers depends on the solution chemistry and the magnitude of the current or voltage that is applied. Anodized layer thicknesses range from about 5 to 50 μm depending on the substrate type and anodization conditions. Anodized surfaces often possess excellent corrosion resistance. Further increases in corrosion resistance can be imparted by the use of various sealing treatments that plug pores in the layer by precipitation, or react with the pore walls. Electrochemical methods are well suited for studying the corrosion resistance of anodized surfaces and anodized and sealed surfaces. In particular, electrochemical impedance spectroscopy (EIS) is well suited for determining the characteristics of anodized layers and the effects of sealants and their breakdown in aggressive environments.

Porous-type coatings exhibit a duplex structure consisting of an inner barrier layer and a crystalline outer layer that consists of a regularly spaced array of pores in certain cases. As with barrier film formation, Al^{3+} cation and O^{2-} and OH^{-} anion transport occurs during anodization, but in this case Al^{3+} is ejected into solution instead of participating in film formation. The Al^{3+} then reprecipitates on the previously existing barrier layer leading to the formation of a porous outer layer (89,96).

During anodization, it is possible to monitor current or voltage and relate these to coating characteristics. Figure 27 is a schematic illustration of the voltage versus time response and representative cross sections of porous films, which form on aluminum in sulfuric acid solution (97). Initially, sample voltage increases rapidly, and a barrier film consisting of amorphous aluminum oxide and perhaps some excess aluminum ions is formed. At later stages, a porous outer layer consisting of interpenetrating oxide and voids forms, resulting in a bilayered or duplex structure. This outer layer thickens to a terminal value that is established by solution chemistry applied current and voltage and the material.

Porous coatings may be sealed to improve their properties. Sealing involves precipitation of solids in the intercrystalline spaces or regular pores that exist in porous coatings. Sealing is accomplished by contacting coatings with steam, water vapor, or boiling water. A wide range of inorganic sealing solutions are known. Noteworthy among these are chromates, silicates and nickelous solutions. Organic sealing solutions include triethanolamine and tannins. Coatings may also be sealed with a range of lacquers, waxes and oils. Wernick et al. review in some detail the sealing of anodic coatings on aluminum, and further details can be obtained in their review (46).

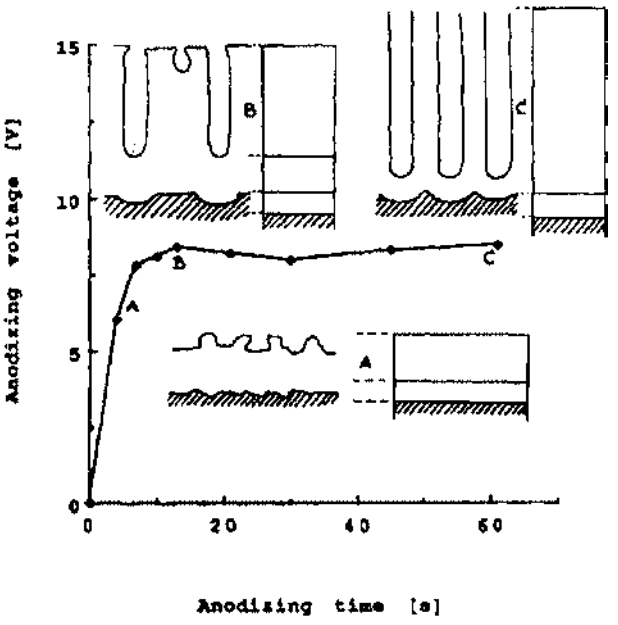

Figure 27 Schematic illustration of the film formation morphology across the anodization voltage–time response for Al in sulfuric acid. In this environment, porous anodic films form. (From J. De Laet, H. Terryn, J. Vereecken. Electrochim Acta 41, 7/8, 1151 (1996).)

B. Measurement Methods

1. Single-Frequency Admittance Measurements

Single-frequency admittance measurements, sometimes reported as capacitance and dissipation factor measurements, can be made on anodized surfaces at frequencies between 0.5 and 50 kHz. At these frequencies, electrochemical processes with time constants ranging from about 10^{-3} to 10^{-6} s can be detected in the admittance response, and it is generally agreed that pore filling due to sealing can be studied effectively using admittance techniques. Various interpretations of the admittance of anodic films, particularly in the 1 to 10 kHz regime, have been developed.

The admittance in this region is modeled using either a film capacitance in series with the solution resistance or a parallel resistance and capacitance, which is in series with the solution resistance. This is treated as a parallel R–C combination whose magnitude, expressed as an impedance, is given by

$$|Z| = \left|\left(\frac{Z_R Z_C}{Z_R + Z_C}\right)\right| = \left(\frac{R^2}{1 + (\omega RC)^2}\right)^{1/2} \tag{10}$$

The loss factor, δ, which is a comparative measure of the resistive and reactive components of the admittance, is also used to characterize the response

$$\tan \delta = \frac{Z_R}{Z_C} = \frac{R}{(\omega C)^{-1}} = \omega RC \tag{11}$$

Admittance measurements were used extensively prior to the widespread use of impedance spectroscopy in the 1980s. Capacitance bridge methods are typically used, though this limits the lower bound on the measured frequency to several hundred hertz. Corrosion processes, whose time constants are normally measured at or below 1 Hz, cannot be directly interrogated with this method.

There are two general interpretations for the admittance characteristics of barrier anodic films (98). The first interpretation is based on film conduction mechanisms, either electronic or ionic, and the influence of solution ions on the oxide film lattice defect structure on conduction behavior. The second is based on the behavior of preexisting defects in anodic films and the effects of attacking or passivating solutions.

Pryor and coworkers used capacitance bridge methods to determine admittance characteristics at single frequencies ranging from 1 to 100 kHz associated with the interaction of electrolytes with passive and barrier anodic films on aluminum. Results were interpreted in the context of changes, occurring prior to the onset of localized corrosion, in bulk conduction characteristics associated with oxide film thickness changes, or changes in the defect structure that affected conduction mechanism (99–101). For example, exposure of 260 Å anodic barrier films on aluminum to 1.0 M sodium chloride solution resulted in a decrease in the resistance at 1 kHz, but no change at 100 kHz, indicating a decrease in film ionic resistance, but no change in film electronic resistance. A substitution of Cl^- for O^{2-} in the anodic film oxide lattice, which increased the concentration of n-type carriers in the film, contributed to conduction at lower frequencies but not at higher frequencies. F^- and OH^- were also thought to induce similar effects though formation of a crystalline oxyfluoride phase in fluoride solution, which complicated the interpretation of the data. Exposure of anodic films to sulfate solutions induced no change in either the ionic or the electronic resistivity of anodic films. It was proposed that the sulfate anion does not exchange with oxide ions in the lattice of the film and did not affect the charge carrier concentration. Measurements made while films were thinned by chemical dissolution in chromate solutions produced variations in admittance that were used to characterize film electrical properties as a function of film depth.

The admittance response at 1 kHz has also been interpreted in terms of the behavior at residual defects in anodic films. This interpretation is based on electron optical characterization, which shows that anodic films contain a distribution of preexisting defects associated with substrate inclusions and mechanical flaws (96,102). In aggressive environments, pits nucleate from these defects and propagate into the metal substrate. In this model, pits are distinct from anodic film flaws, and both can contribute to the measured admittance. Measurements of anodic films exposed to chloride solutions showed that the dissipation factor increased with time, but the capacitance remained nearly constant. Under these conditions, pit propagation at a flaw led to a pit area increase, which increased the resistive component of the admittance, resulting in an increased dissipation factor, but no increase in the capacitance. Measurements at 100 kHz were reflective of the electric double layer and not the components of the oxide film.

During exposure to chromate solutions, defects in the anodic film heal, and there is some thinning of the barrier layer. Under these conditions, the characteristic response in a 1 kHz admittance measurement is a slight increase in the capacitance and dissipation factor. An anodic film with an intentional defect will show an increase in capacitance due to flaw healing.

Single-frequency or limited-frequency range capacity measurements have been used to collect information about the time dependence in the resistive and reactive characteristics of anodic films (103).

2. EIS

EIS is well suited for characterizing anodized films and has been used to study the formation and characteristics of barrier and duplex coatings. EIS has also been used widely to study the sealing of anodized films. As with conversion coatings, equivalent circuit modeling is a powerful tool for analyzing EIS spectra obtained from anodized surfaces. Barrier layers formed early in the anodization process behave much like intact passive layers in EIS measurements. The response obtained is that of an imperfect capacitor or CPE. An example of CPE behavior for a barrier film is given in Fig. 28, which shows Bode magnitude and phase angle plots for a barrier layer on Al formed by galvanostatic polarization in ammonium tartarate (97). It is evident from the phase angle information that even a CPE does not fully represent barrier layer behavior. The two minima in the phase angle data are due to two time constants, which may originate with a duplex film or from the presence of residual flaws (96).

Figure 28 also shows data from a duplex film consisting of an inner barrier layer and an unsealed outer porous layer. Superposition of this data set with a data set from a sample with the barrier layer only suggests that the resistance of

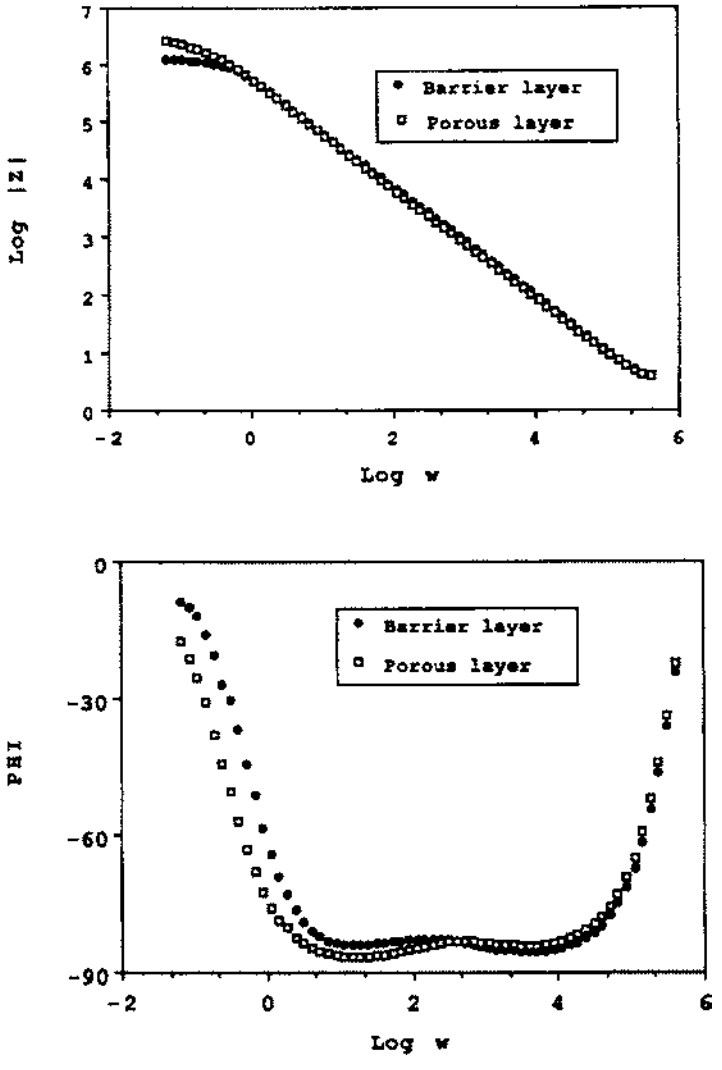

Figure 28 EIS spectra of the porous film formed at 360 s in 20% sulfuric acid at a current density of 400 A/m^2, and a barrier film formed in 3% ammonium tartarate at a current density of 88 A/m^2. (From J. DeLaet. H. Terryn, J. Vereecken. Electrochim. Acta 41, 1155 (1996).)

the porous layer is very small. As a result, neither the resistance nor the capacitance of the porous layer can be detected in the EIS response.

C. Sealing of Anodic Films

Porous anodic films can be sealed by immersion in aqueous solutions to increase the protection of the underlying substrate. For anodized coatings on Al alloys, sealing can be accomplished by immersion in boiling water or hot or cold metal salt solutions. Contact times are usually on the order of tens of minutes. Sealing of porous anodic films on Al in boiling water involves the formation of hydrated oxide material in the topmost regions of the pores that results in plugging. With time, the new deposit may crystallize, and the void space in the intermediate layer of the coating reorganizes. Admittance measurements can be used to track changes in coatings due to sealing, but EIS measurements are usually more informative because they are conducted over a larger frequency range, which enables changes in the porous layer to be distinguished from changes occurring in the barrier layer.

Figure 29a shows a cross section of a pore and an explicit equivalent circuit model superimposed on it (104). In this model, the EIS response of the barrier layer is represented by the parallel combination of the barrier layer resistance and capacitance. The pore walls are also represented by a parallel resistance and capacitance, which is in series with the barrier layer R–C network. The pore solution resistance and bulk solution resistances are represented as indicated. Sealing does not involve any electrochemical reactions, so parameters representing faradaic processes are not required. In unsealed coatings, only the impedance of the barrier layer is significant, and the model reduces to the R–C combination associated with the barrier layer. As sealing progresses and the pores plug, changes in the EIS response can be accounted for using a parallel R–C combination that accounts for the contributions of the pore walls and pore solution resistance (Fig. 29b). In some cases, porous layer capacitance is small compared to the resistance, and its contribution to the EIS response is negligible. This results in a further simplification of the equivalent circuit model (Fig. 29c). In this case, the sealed anodized layer exhibits single-time-constant barrier behavior.

Figure 30 shows Bode magnitude and Bode phase angle plots for EIS measurements of a 5 μm thick porous coating sealed in hot water for various lengths of time (104). These measurements were interrupted, meaning that the sample was removed from the sealing bath and placed into cold water (20°C) for measurement and then returned to the sealing bath for further treatment. The unsealed coating exhibits a single-time-constant response due to the capacitance of the barrier layer. As sealing proceeds, a second time constant emerges at high frequencies owing to processes associated with surface film precipitation and pore plugging. Figure 31 shows variation in the characteristic coating resistances and

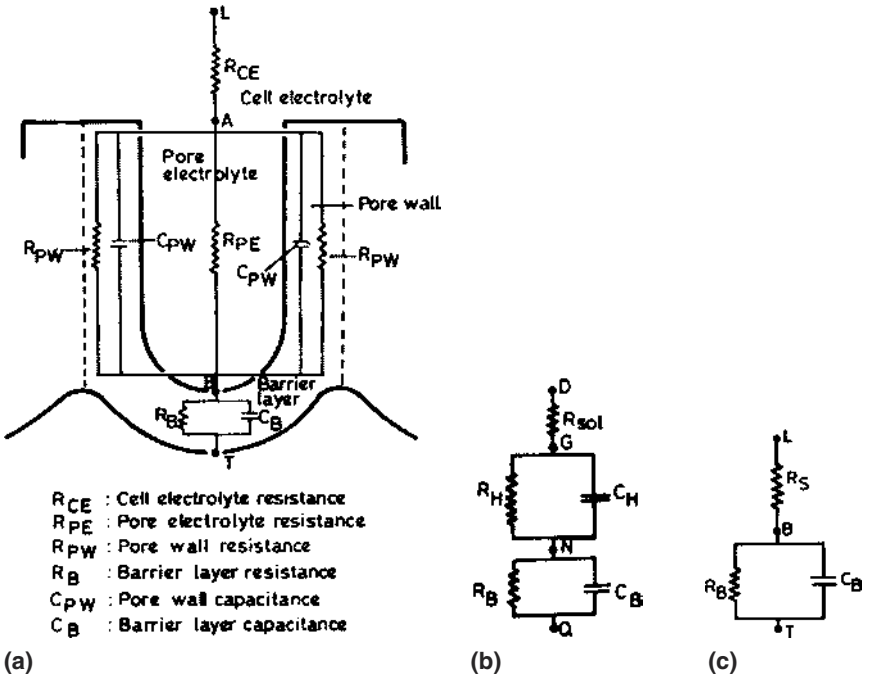

Figure 29 (a) Explicit equivalent circuit model for an unsealed porous anodized film superimposed on a single pore cross section. (b) A simplified equivalent circuit model representing the impedance response from the barrier and porous layer. In this case, RH and CH represent the impedance of the porous layer. (c) The equivalent circuit model for a fully sealed layer, which yields only a single time-constant barrier response. (From J. L. Dawson, G. E. Thompson, M. B. H. Ahmadun. p. 255, ASTM STP 1188, ASTM, Philadelphia, PA (1993).)

capacitances as a function of sealing time over the course of 5 minutes (104). R_s increases initially and then stabilizes owing to the formation of a precipitated alumina layer on top of the porous coating. After an induction period, R_H increases and C_H decreases. The increase in resistance of the porous layer is due to shrinking of the pore volume and filling with a more resistive gel material. C_H decreases owing to the same geometric change in pore volume and the displacement of water ($\varepsilon = 80$) with a lower dielectric constant hydrated alumina get ($\varepsilon \rightarrow 10$). The induction time observed in these experiments is believed to represent the length of time required to exceed the solubility product for the pore-filling gel. In many cases R_B and C_B do not change with sealing, because the barrier layer does not thin or thicken, and compositional and structural changes

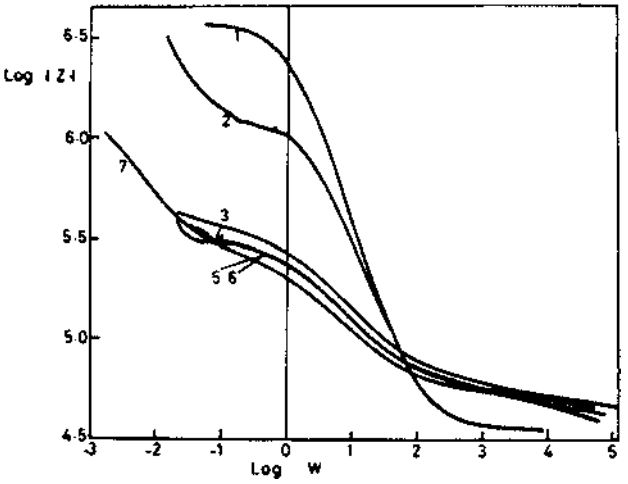

(a)

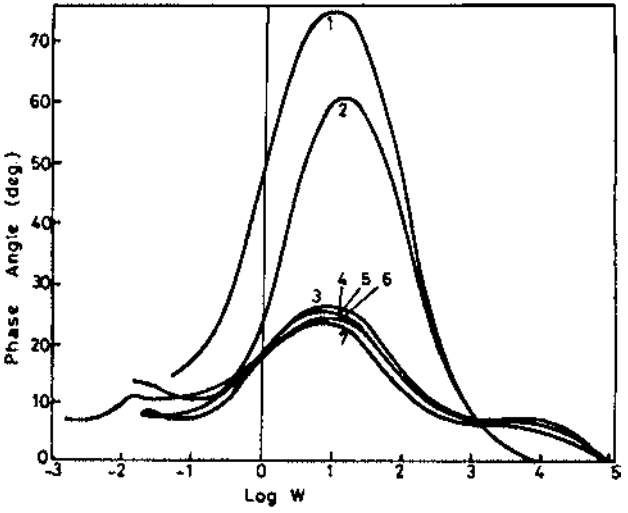

(b)

Figure 30 Bode magnitude and phase angle plots of a 5 μm thick sulfuric acid anodized film subject to sealing in hot water. Measurements were made on an interrupted basis in cold water. Immersion times are (1) 0 s, (2) 30 s, (3) 60 s, (4) 90 s, (5) 120 s, (6) 180 s, (7) 300 s, (From J. L. Dawson, G. E. Thompson, M. B. H. Ahmadun. p. 255. ASTM STP 1188. ASTM, Philadelphia, PA (1993).)

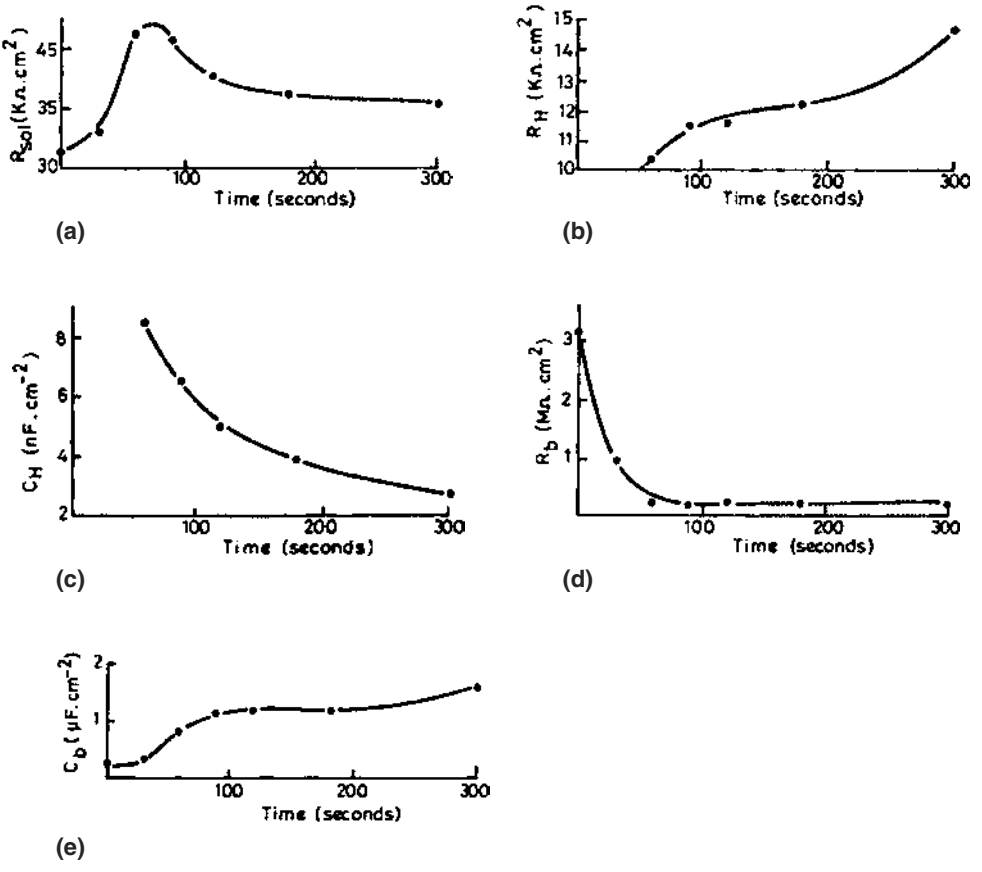

Figure 31 Time-dependent changes in equivalent circuit model element values due to interrupted sealing. (a) Solution resistance, R_s, (b) porous layer resistance, R_H, (c) porous layer capacitance, C_H, (d) barrier layer resistance, R_b, (e) barrier layer capacitance, C_b. (From J. L. Dawson, G. E. Thompson, M. B. H. Ahmadun. p. 255, ASTM STP 1188, ASTM, Philadelphia, PA (1993).)

do not occur that alter the electrical resistivity or dielectric properties of the layer. In this example, R_B decreases and C_B increases, indicating barrier film thinning. This leads to an overall decrease in the impedance of the film, which seems contrary to the primary intent of sealing. This observation has been interpreted as thinning due to attack by acid from the anodizing bath trapped in the pore volume. It has also been suggested that these measurements are sensitive to the gel formation process and that the known improvement in corrosion resistance

by sealing is achieved when this gel crystallizes after the sample is removed from the sealing bath.

D. Breakdown of Anodic Films

Breakdown of anodic films is yet another phenomenon for which EIS is well suited. Equivalent circuit analysis has been used to analyze EIS spectra from corroding anodized surfaces. While changes in anodic films due to sealing are detected at higher frequencies, pitting is detected at lower frequencies. Film breakdown leads to substrate dissolution, and equivalent circuit models must be amended to account for the faradaic processes associated with localized corrosion.

For the case of breakdown of sealed anodized surfaces, two closely related equivalent circuit models exist (105,106). Figure 32a shows a representation of a duplex surface film in which the outer layer has broken down to expose the inner barrier layer. This type of model represents passivated pits, or defect sites that may have formed some type of protective layer that differs from that on other portions of the surface (107,108). The fractional area of the intact surface is denoted by θ and the defective area by $1 - \theta$. The corresponding equivalent circuit model is also shown in Fig. 32a. In this model, one leg of the circuit accounts for the impedance response through the intact duplex film and is represented by two R–C networks arranged in series. The subscripts L1 and L2 refer to the individual layers in the duplex film. Each parameter is normalized by the surface coverage term θ. The second leg of the circuit accounts for the impedance response of the defective area. R_b and C_b are the barrier layer resistance and capacitance, and $R_{\Omega,por}$ is the solution resistance in the defects. The resistance of the bulk solution is denoted by R_Ω. Each of these terms is normalized by the sample defect area $(1 - \theta)$. Simulated Bode magnitude and phase angle plots for this equivalent model are shown in Fig. 32b. In the high-frequency regions denoted by 1, 2, and 3, the effect of decreasing surface coverage of the intact film is evident. As the intact area falls, the magnitude of the capacitive impedance decreases, and the resistive plateau associated with the outer layer resistance is

Figure 32 (a) The equivalent circuit model and physical model for a passive pit in a duplex film. EC and IC refer to electronic conductor and ionic conductor, respectively, in the physical model. (b) Simulated Bode plots of the equivalent circuit in (a), where $R_{\Omega,por}$ is equal to zero. Simulation parameters are $R_{L2} = 10^5\ \Omega$, $C_{L2} = 10^{-9}$ F, $C_{L1} = 5 \times 10^{-7}$F, $R_{sol} = 20\ \Omega$, and θ = (1) 1, (2) 0.95, (3) 0.5, R_{L1}/θ = (4) $10^8\ \Omega$, (5) $10^7\ \Omega$, (6) $10^6\ \Omega$. (From (a) K. Juttner, W. J. Lorenz, W. Paatsch. Corrosion Sci. 29, 279 (1989). (b) J. Hitzig, K. Juttner, W. J. Lorenz, W. Paatsch. J. Electrochem. Soc. 133, 887 (1986).)

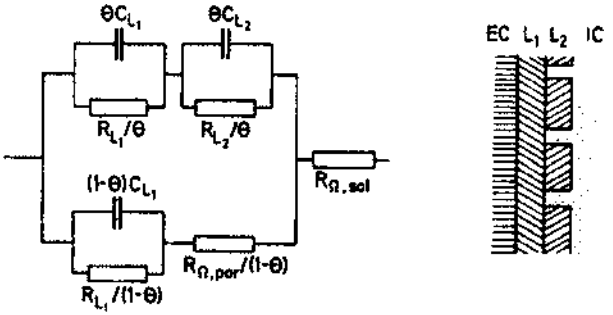
θC_L1
θC_L2
R_L1/θ
R_L2/θ
(1-θ)C_L1
R_Ω,sol
R_Ω,por/(1-θ)
R_L1/(1-θ)
EC L1 L2 IC

(a)

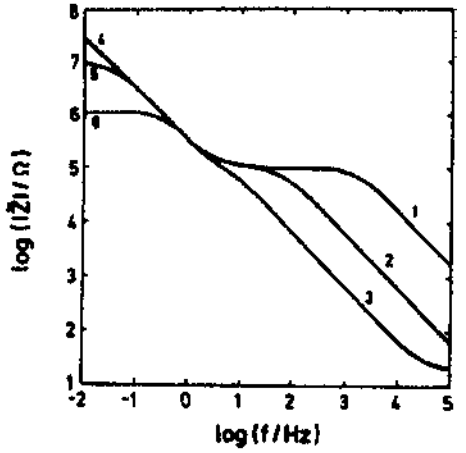
log (|Z|/Ω)
log (f/Hz)
1
2
3
4
5
6

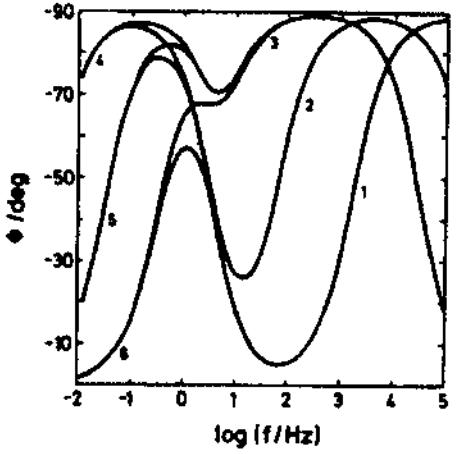
φ /deg
log (f/Hz)
1
2
3
4
5
6

(b)

resolved less distinctly. Eventually, the solution resistance is resolved at the highest frequencies. At low frequencies denoted by 4, 5, and 6, the effect of decreasing the barrier layer resistance for a fixed surface coverage θ is shown. As R_b decreases from 10^8 to 10^6 ohms, a low-frequency plateau becomes evident, and the DC limit of the impedance decreases in direct relation to R_b. In this example, $R_{\Omega,por}$ is assumed to be zero.

Actively pitting surfaces are represented by analogous physical and equivalent circuit models shown in Fig. 33a. The main difference in these models is that the substrate is exposed at the base of the pits and active dissolution is occurring. The area-specific capacitance and resistance take on values consistent with metal dissolution, e.g., tens of μF/cm^2 for the double layer capacitance, C_{dl}, and 10^2 to 10^3 ohm · cm^2 for faradaic resistance Z_{SR}. Simulated Bode magnitude and phase angle plots for increasing defect area, and for the case where $R_{\Omega,por}$ is zero, are shown in Fig. 33b. As the defect area increases, the impedance in the high-frequency capacitive region decreases, and the resistive plateau associated with the porous layer resistance is less clearly resolved. Although Z_{SR} is taken to be 10^5 ohms in this example, the DC limit associated with this impedance ranges from about 5×10^7 ohms to 10^6 ohms due to defect area normalization. Overall as the defect area increases, the DC limit decreases, making this parameter useful for the evaluation of pitting damage.

The essential characteristics of the EIS response from simulated Bode plots can be detected in spectra collected from real anodized samples (109). Figure 34 shows Bode plots from chromic acid anodized and sulfuric acid anodized surfaces exposed to aerated 0.5 M NaCl for various lengths of time. As predicted by the simulated spectra, the main changes in the Bode magnitude plot due to pitting occur at frequencies below about 1 Hz. The effects of pitting on the Bode phase angle plot are detectable as frequencies as high as 10^4 Hz for unsealed sulfuric acid anodized surfaces.

To track the progression of corrosion damage accumulation on anodized surfaces it is often desirable to use more simplified analysis approaches, especially when many replicate samples are to be examined. Since the effects of sealing are confined to the highest measured frequencies and those due to corro-

Figure 33 (a) The equivalent circuit model and physical model for an active pit in a duplex film. EC and IC refer to electronic conductor and ionic conductor, respectively, in the physical model. (b) Simulated Bode plots of the equivalent circuit in (a) where $R_{\Omega,por}$ is equal to zero. Simulation parameters are $R_{L2} = 10^5\ \Omega$, $C_{L2} = 10^{-9}$ F, $R_{L1} = 10^{25}\ \Omega$, $C_{L1} = 5 \times 10^{-7}$ F $Z_{SR} = 10^5\ \Omega$, $C_{dl} = 3 \times 10^{-5}$ F, $R_{sol} = 20\ \Omega$, and θ = (1) 1, (2) 0.999, (3) 0.99, (4) 0.92. (From (a) K. Juttner, W. J. Lorenz, W. Paatsch. Corrosion Sci. 29, 279 (1989). (b) J. Hitzig, K. Juttner, W. J. Lorenz, W. Paatsch. J. Electrochem. Soc. 133, 887 (1986).)

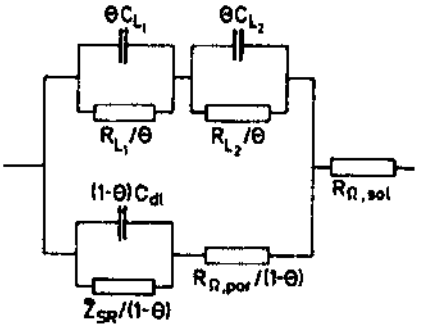
ΘC_L1
ΘC_L2
R_L1/Θ
R_L2/Θ
(1-Θ)C_dl
R_Ω,sol
R_Ω,por/(1-Θ)
Z_SR/(1-Θ)

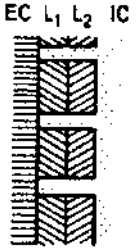
EC L1 L2 IC

(a)

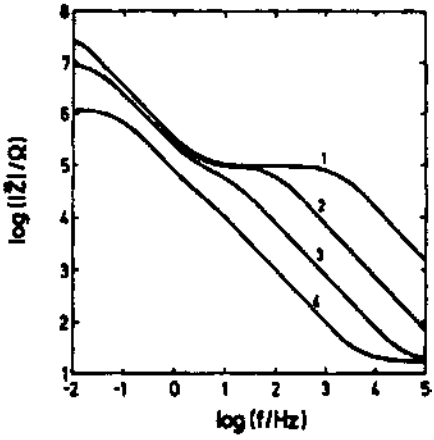
log (|Z|/Ω)
log (f/Hz)
1
2
3
4

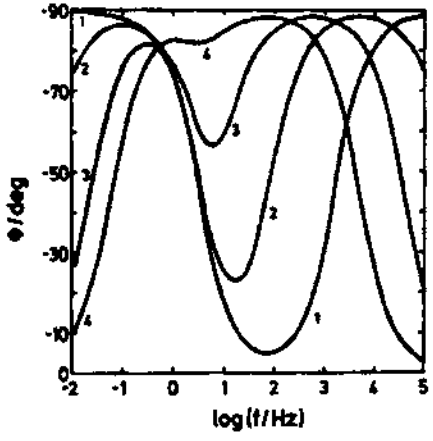
φ/deg
log (f/Hz)
1
2
3
4

(b)

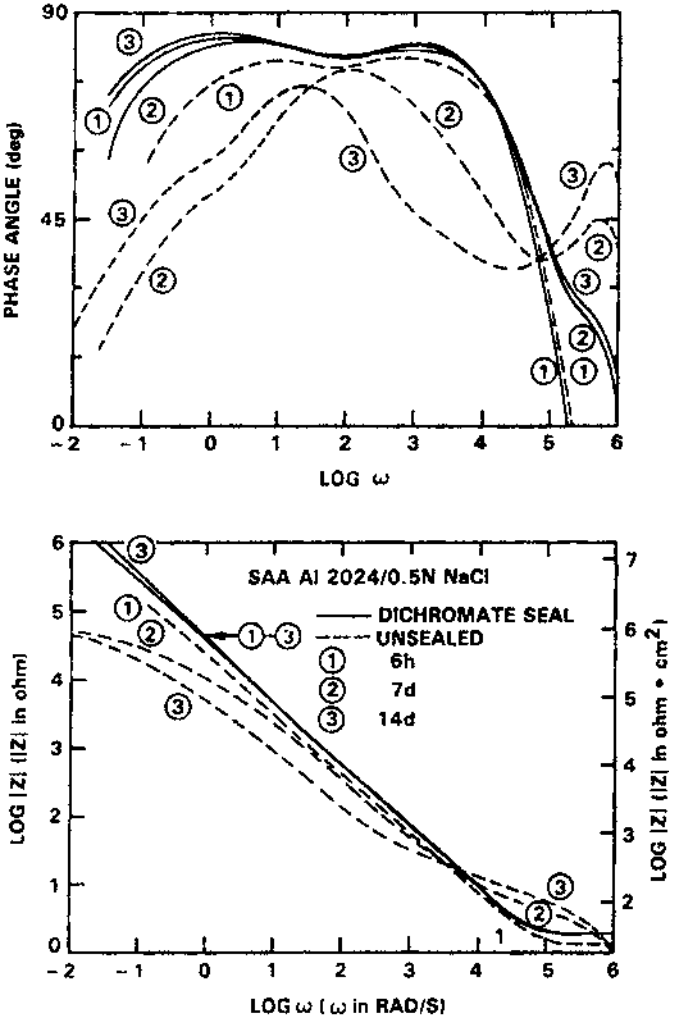

Figure 34 Bode plots of EIS data determined in aerated 0.5 M NaCl solution for sealed and unsealed sulfuric acid anodized Al alloy 2024. (From F. Mansfeld, M. W. Kendig. Corrosion 41, 490 (1985).)

sion at low frequencies, it is possible to use the DC limit in the impedance spectra to assess corrosion damage.

There are indications that the magnitude of the DC limit measured in an impedance experiment correlates with the performance of anodized surfaces in cabinet exposure tests. On this basis, it is possible to define a damage function, D, as the logarithm of the ratio of the impedance, taken at 0.1 Hz at zero exposure time, to that at some exposure time, t (109).

$$D = \log \left. \frac{Z_0}{Z_t} \right|_{0.1Hz} \tag{12}$$

At this frequency, the magnitude of the impedance will decrease with increasing exposure time, so the damage function should increase with time. In principle, this measurement could be made using a single-frequency admittance-type approach, but collection of the spectrum at higher frequencies than 0.1 Hz can be made with little additional measurement time penalty.

VI. ORGANIC COATINGS

A. Overview of Organic Coatings

There is a wide range of organic coatings and adhesives that are applied to metals for corrosion protection. Organic coatings provide barrier protection by isolating the metal substrate from the environment, and they do not support electron transfer well because the are very resistive. As a result, electrochemical activity is all but impossible on undegraded organic coatings. Some coatings contain active inhibitors, like sparingly soluble chromate pigments. Chromate leached into an attacking electrolyte is transported to coating defects, where it acts to stifle corrosion. Such coatings are said to be actively protecting or self-healing.

Many electrochemical methods are of limited utility for studying the processes leading to organic coating degradation. In the early stages of coating breakdown, the interfacial impedance is exceedingly large and cannot be measured by a potentiostat. However, as the coating degradation process proceeds, the interfacial impedance falls to levels that can be effectively measured by EIS. For this reason, EIS has been particularly effective for quantitatively evaluating the progress of organic coating degradation and metallic corrosion that occurs as a result.

It is convenient to consider the corrosion of polymer coated metals as a process that consists of several distinct stages:

Defect formation
Uptake and transport of water through the coating

Coating–substrate decohesion and formation of a condensed electrolyte at the interface
Substrate corrosion

Defects may exist in the coating as a result of imperfections arising at the time of coating application. These defects may include entrained dust, dirt, moisture, oil or grease, lack of surface coverage, or lack of adhesion on the substrate. Mechanical defects may occur owing to abrasion or impact. Chemical defects may arise by exposure to acids or solvents. Defects may also arise from elevated temperature exposure or exposure to light (UV damage). The defect structure in an organic coating system is important because it determines the course of subsequent corrosion damage. The second stage in the degradation process is water uptake and transport. Water uptake is aided by a molecular level defect specific to organic coatings commonly known as pore space. Pore space generally refers to open space between polymer chains or molecules in the polymer film. In many coatings, this pore space allows the uptake and transport of water and ions that leads to coating degradation and corrosion. Pore space is a natural consequence of coating curing and is usually unavoidable, though some polymer coatings have very low water permeabilities. In aggressive environments, electrolyte may penetrate through defects and result in the loss of adhesion. Loss of adhesion may spread laterally from a defect site. Alternatively, loss of adhesion may occur under mechanically intact coatings when electrolyte condenses at the metal-film interface to form a blister. Once an aggressive electrolyte has made contact with the metallic substrate, corrosion is likely.

B. Measurement Methods

1. Direct Current (DC) Electrochemical Methods

DC electrochemical methods are not well suited for characterizing the breakdown of polymer coated metals for several reasons. First, coating breakdown is defect mediated; the results from measurement to measurement are irreproducible. Measurements of a surface-averaged response are much more suitable for this reason (e.g., EIS or exposure test methods). Second, organic coatings are electrically resistive, and high potential drops develop across organic films when DC voltages are applied to the interface. This reduces the driving force for electrochemical reactions at the coating–metal interface. Often the extent of this potential drop is uncharacterized, which clouds the interpretation of the resulting data. Third, as with all large signal DC measurements, application of a large polarization drives the electrode far from the steady state and from the conditions under which corrosion naturally occurs. Additionally, application of high potentials may also lead to irreversible changes in the polymer structure, especially if dielectric breakdown is induced.

2. EIS

EIS is considerably more effective for the study of organic coating breakdown. It is sensitive to each of the four main stages of the coating breakdown process, and it can also be used in situ. Degradation of organic coatings occurs over the span of days and months (or longer) and is slow compared to the typical impedance spectrum collection times. As a result, EIS measurements can be used to measure changes in organic coating degradation in real time. Typically, the overall process of coating degradation and corrosion is analyzed using an equivalent circuit modeling approach, but first it is important to address instrument limitations.

Instrument limitations must be considered in the measurement of organic coatings because their resistivities are large, $10^{12}\ \Omega \cdot$ cm or more. The input resistance of common potentiostats is usually not more than 10^{11} to 10^{12} ohms, and if the cell resistance approaches or exceeds the input resistance of the potentiostat, a significant fraction of the applied signal will pass across the input impedance and not the cell impedance. In these cases the collected data do not reflect just the impedance of the electrochemical interface, which is a fundamental assumption in almost all data analyses. In fact, the potentiostat input impedance in parallel with the stray capacitance associated with the potentiostat measuring leads will be obtained.

Measurement leads used to connect to the electrochemical cell contribute measured capacitance. Lead capacitance between the potentiostat and the electrometer is normally accounted for in the potentiostat calibration, but stray capacitance associated with the leads and connections to the cell may not. Moreover, this capacitance may change with time: the leads age, and the connections become oxidized. Uncompensated capacitance may also exist within the measurement circuitry of the potentiostat itself. These uncompensated capacitances impose a practical lower limit on the coating capacitance that can be measured.

A convenient check for the input impedance and stray capacitance can be obtained by making an impedance measurement with the leads not connected to anything. The resulting data can be analyzed to estimate the input impedance and the stray capacitance using a parallel R–C network or by graphical analysis of the Bode magnitude plot. The Bode magnitude plot is especially useful because it graphically illustrates the measurement limitations of an EIS system in the lower frequency regions. Figure 35 is a Bode magnitude plot of just such a measurement made with commercial equipment. Analysis of the data using an equivalent circuit model consisting of a parallel combination of the input resistance and the stray capacitance indicates an input resistance of 2×10^{9} ohms and a stray capacitance of 2×10^{-10} F.

Measurement of calibrated capacitors can also be used to determine instrument limitations. Figure 36 shows a plot of the variation in measured capacitance versus known capacitance for a commercial impedance analyzer system (110).

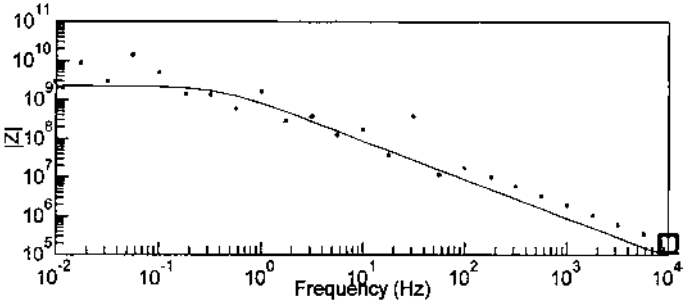

Figure 35 Bode magnitude plot for a "leads unconnected" measurement with a commercial electrochemical impedance system. Analysis of the data enable an estimate of the potentiostat input impedance ($2 \times 10^9\ \Omega$) and the stray capacitance (2×10^{-10} F).

The empirically derived error from all sources in the measured capacitance is greater than 10% for capacitances less than about 1 nF. Therefore acceptable determinations of coating capacitance can only be made for capacitances greater than about 1 nF. One simple strategy for increasing the measured coating capacitance above a measurement sensitivity threshold is to increase the electrode area. Using estimates for the relative permittivity and coating thickness, it is possible

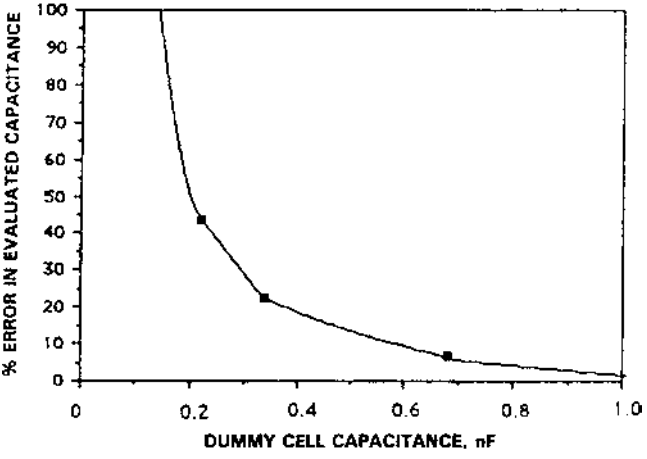

Figure 36 Error in the observed capacitance as a function of the value of the known capacitance. This illustrates the limit of an impedance measurement system. (From M. Kendig, J. Scully. Corrosion 46, 23 (1990).)

to estimate the electrode area required to bring the coating capacitance into a measurable range. If the expression for coating capacitance is

$$C = \frac{\varepsilon\varepsilon_0 A}{t} \tag{13}$$

and the relative permittivity for organic coatings ranges from 3 to 4, to obtain nanofarad sensitivity the electrode area must be

$$A > 10^{-9}\left(\frac{t}{\varepsilon\varepsilon_o}\right) > 4000t \tag{14}$$

where t is the coating thickness in cm, ε is the relative permittivity of the coating, and ε_o is the permittivity constant. For a 10 μm thick coating, an electrode area of 4 cm^2 is sufficient to exceed sensitivity constraints. However, for a 500 μm coating (20 mils), an electrode area of 200 cm^2 is necessary.

C. Coating Degradation

1. Defects in Coatings

The range of unintentional defects that can be present in polymer coatings was listed earlier. However, polymer coatings often contain intentionally added solid particulate in the form of fillers, pigments, and extenders. These solid particles may constitute defects in some cases. An example of the inorganic particulate distribution in an automotive paint is shown in Fig. 37. This figure shows a mixture of intentionally added metal flake and unwanted dirt and dust. The extent to which these particulates constitute breakdown-initiating defects can be determined from EIS measurements conducted shortly after immersion in an aggressive electrolyte. The most protective coatings exhibit purely capacitive behavior and retain that behavior for long periods of time during exposure to near neutral molar chloride solutions. The presence of serious defects can be inferred if a resistive component detected at the lowest measured frequencies is detected immediately, or shortly after exposure to an aggressive electrolyte.

EIS can also detect defects arising from lack of adhesion at adhesively bonded surfaces (111). The presence of such defects produces pronounced changes in the character of the data presented either in complex plane plots or in Bode plots. Figure 38 illustrates the measurement configuration and provides examples of EIS data for defective and defect-free samples. Studies have shown that the presence of defects is readily revealed and that the geometry of the defects and their spatial extent can be inferred from a detailed analysis of EIS spectra.

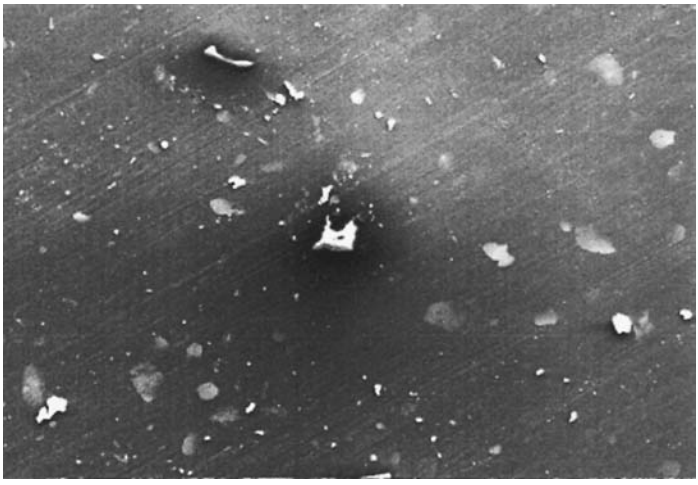

Figure 37 Scanning electron micrograph of metal flake paint for trucks showing entrained dirt and intentionally added metal flakes. The particulate material in this micrograph averages several micrometers in diameter.

2. Ingress of Electrolyte

Electrolytes will penetrate through defects to the coating–metal interface. They will also penetrate through pore space in many types of coatings. Water residing in the pore space changes the effective dielectric constant of the film in a way that can be detected by measurement of film capacitance (112,113). The capacitance method for determining water uptakes has considerable advantage over traditional gravimetric methods. It is also possible to determine water diffusivity, equilibrium constant, and dielectric constant. Capacitance measurements are particularly sensitive to water uptake because the dielectric constant for water ($\varepsilon = 80$) is at least four times greater than that of a typical organic coating. For low volume fractions of water in polymer, the water volume fraction is given by the Brasher–Kingsbury equation (114).

$$\phi = \frac{\log\,(C_t/C_o)}{\log\,80} \tag{15}$$

In this expression, φ is the volume fraction of water, C_t is the capacitance after some exposure time *t,* C_o is the capacitance of a "dry" film, which is usually measured at the outset of an exposure experiment. The relative permittivity of water at 25°C is reflected in the denominator of the expression. This expression applies only when water is homgeneously dispersed in the polymer, no water–

(a)

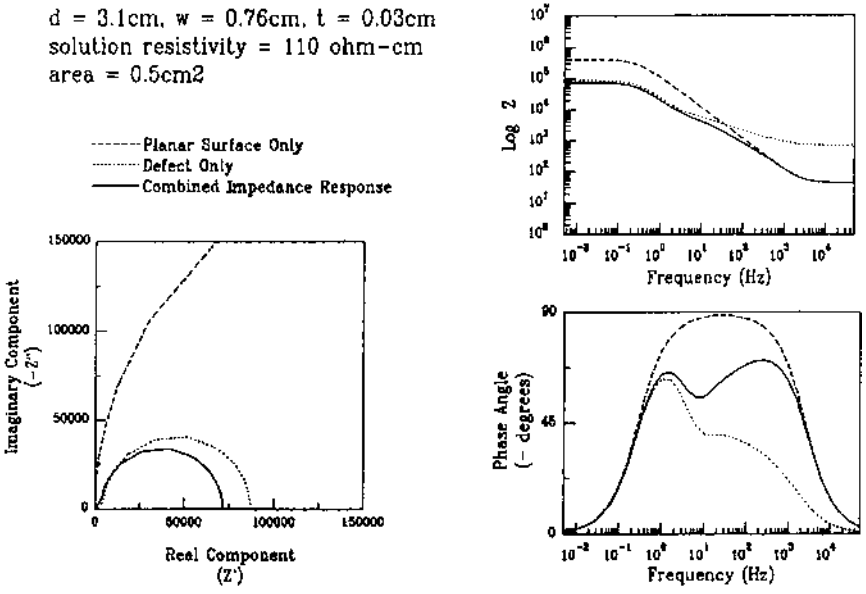

(b)

Figure 38 (a) Schematic illustration of moisture ingress into an edge-exposed defect. (b) Theoretical impedance response of a defect-containing laminate specimen. (From G. R. T. Schueller, S. R. Taylor. ASTM STP1188. p. 328, ASTM, Philadelphia, PA (1993).)

polymer chemical interactions occur, the absolute water content in the polymer is low, and there is negligible swelling of the polymer due to water uptake. Strictly speaking, this expression is only valid for binary water–polymer systems. However, it has been applied to the characterization of water uptake in multicomponent paints with apparent success (115,116).

Figure 39 is an example of water uptake for polyester coated steel immersed in a NaCl solution. In this example one coating was subject to 100 h of UV exposure prior to immersion (112). Both coatings absorb water at fast rates during the first 200 minutes of immersion, but the UV-exposed sample accomodates

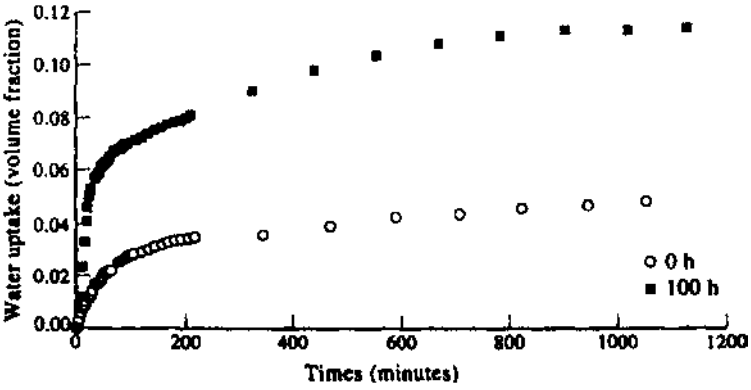

Figure 39 Water uptake trend for a polyester coated galvanized steel immersed in sodium chloride solution, before and after about 100 h of UV irradiation. (From P. L. Bonora, F. Deflorian, L. Fedrizzi. Electrochim. Acta 41, 1073 (1996).)

more than twice as much water at steady state owing to the UV-induced damage to the polymer. The ability to detect water uptake is significant because this is often a prelude to corrosion (112).

3. Loss of Adhesion and Corrosion of the Substrate

With increased exposure time to an aggressive environment, ionic conduction pathways through the coating short the coating capacitance, and a resistive impedance develops. Once electrolyte contacts bare metal, faradaic reactions occur and corrosion is underway. Several equivalent circuit models are commonly used to analyze EIS data from degraded organic coatings. Examples of common equivalent circuits are shown in Fig. 40 (110,117). In these models, the impedance response of intact areas of the coating is represented by a capacitor, C_c. There is a coating resistance, but it is usually too large to measure. The impedance response at defects varies from sample to sample but falls into three general categories, which distinguish the models in Fig. 40. In all models, R_{po} represents the pore resistance, which is the ionic resistance to current flow between the bulk electrolyte and the metal–film interface. This pathway exists through microscopic pores at defects, and through the pore space containing water and ions in the polymer film. The further distinction between models I and II depends on the impedance behavior at low frequencies. In the case where the spectrum achieves a DC limit (equivalent to $R_\Omega + R_{po} + R_t$), localized corrosion occurs under charge transfer control, and model I applies. In cases where the Bode plots indicate a $\omega^{-1/2}$ or $\omega^{-1/4}$ dependence, localized corrosion is under diffusion control and model II applies.

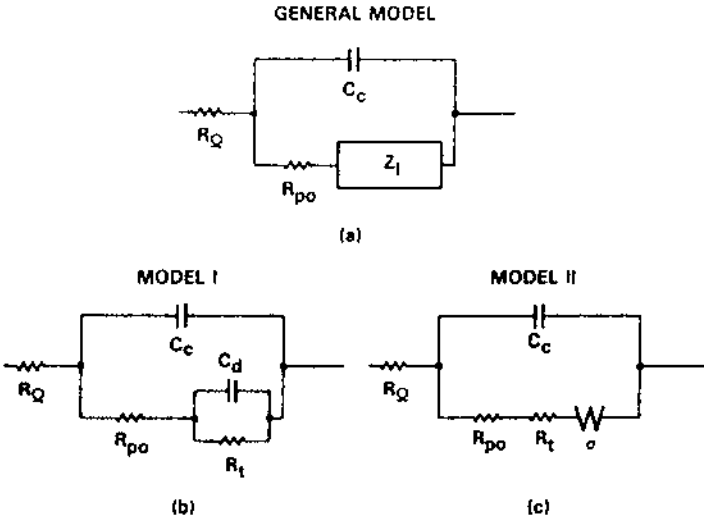

Figure 40 Equivalent circuit models for analyzing impedance data from degraded polymer coated metals. (a) General model. (b) Model I: for coatings with defects corroding under activation control. (c) Model II: for coatings with defects corroding under diffusion control. (From F. Mansfeld, M. W. Kendig, S. Tsai. Corrosion 38, 478 (1982) and M. Kendig, J. Scully. Corrosion 46, 22 (1990).)

Figure 41 shows an equivalent circuit model and resulting simulated EIS data in Bode plot format for a failed organic coating (110). At high frequencies, the response is due to the capacitance associated with the coating, C_c, and a solution resistance is usually not observed. At intermediate frequencies, a resistive plateau is observed in the Bode magnitude plot, which is equal to the sum of the solution resistance and the pore resistance, $R_{po} + R_\Omega$. At lower frequencies, a second capacitive region is found corresponding to the capacitance associated with corrosion at defects, C_d. At the lowest frequencies, a DC limit is observed, and the magnitude of the resistance is equal to $R_t + R_{po} + R_\Omega$. The phase angle information indicates two distinct time constants in this example, although separation as clear as this is not normally the case in experimental situations.

As organic coatings degrade, regular changes in the EIS data occur that signal the initiation and propagation of coating breakdown and substrate corrosion. Figure 42 shows Bode magnitude and phase angle plots for an epoxy resin–based coating on phosphated steel substrates exposed to 0.5 M NaCl solution (118). Initially, the coating exhibits quasi-ideal capacitive behavior associated with an intact coating. However, with increasing exposure time, a two-time constant response emerges indicating coating breakdown as shown in Fig. 41. With

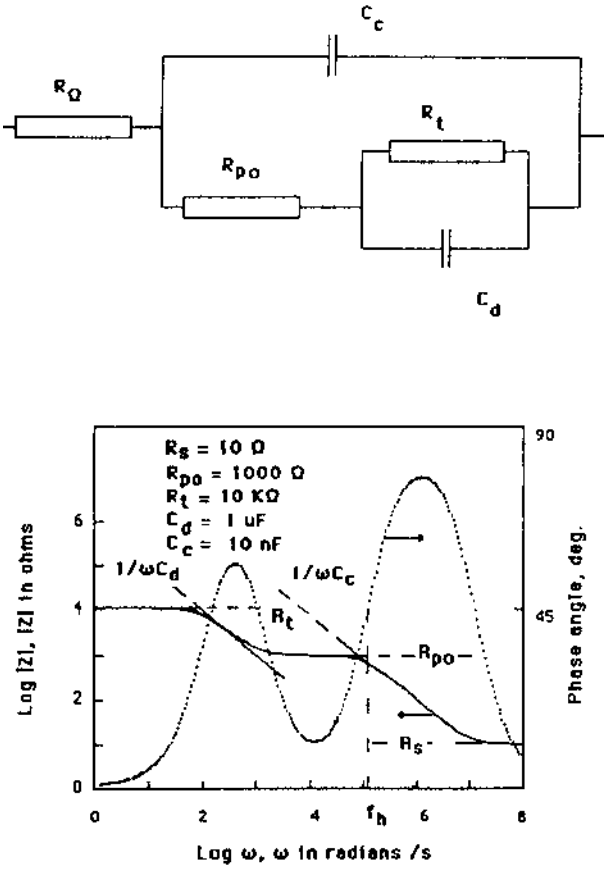

Figure 41 Example of simulated EIS data from the equivalent circuit model shown with circuit element values indicated in the plot. (From M. Kendig, J. Scully. Corrosion 46, 22 (1990).)

increasing exposure time, the DC limit falls as the extent of corrosion progresses. These types of regular changes in the EIS data with increasing exposure time suggest the possibility of using EIS quantitatively to track the progress of corroded surface area.

a. The Breakpoint Frequency Method. Experimental observations of polymer coated metals exposed to aggressive solutions for increasing lengths of time typically show decreases in R_{po} and R_p and increases in C_{dl}. These regular

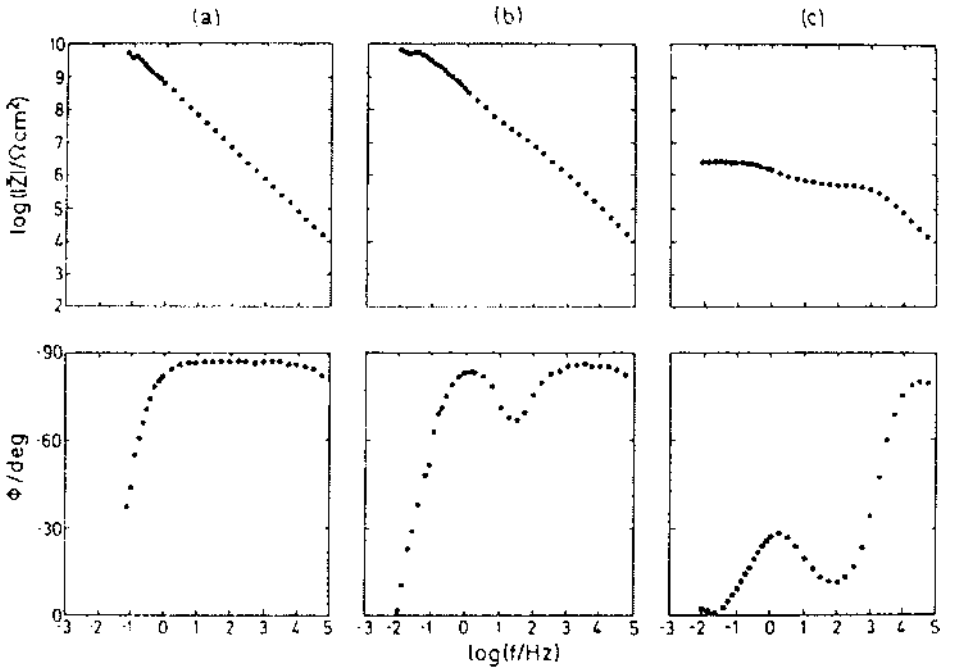

Figure 42 Bode plots of an epoxy-resin-based coating on phosphated steel exposed to 0.5 M NaCl solution. (a) Quasi-ideal coating. (b) Sample exposed for 1 hour. (c) Sample exposed for 48 h. (From J. Titz, G. H. Wagner, H. Spahn, M. Ebert, K. Juttner, W. J. Lorenz. Corrosion 46, 221 (1990).)

changes are consistent with an increase in the delaminated area associated with underfilm corrosion. Although the charge transfer resistance and double layer capacitance values scale with defect area, the values for these elements must be extracted from the low-frequency part of the EIS spectrum. In many experimental situations, measurements at low frequency are complicated by signal instability, mixed reaction control, or changes in the specific interfacial resistance and capacitance associated with the accumulation of corrosion products (119). To circumvent these difficulties, the breakpoint frequency method was developed to make estimates of the delaminated area from high-frequency EIS data, which are not affected by these factors (119–122). This method was based on analysis of the value of the frequency (the breakpoint) separating coating capacitance–dominated response (higher frequencies) from resistive response due to the sum of the pore resistance and solution resistance (lower frequencies). The location of

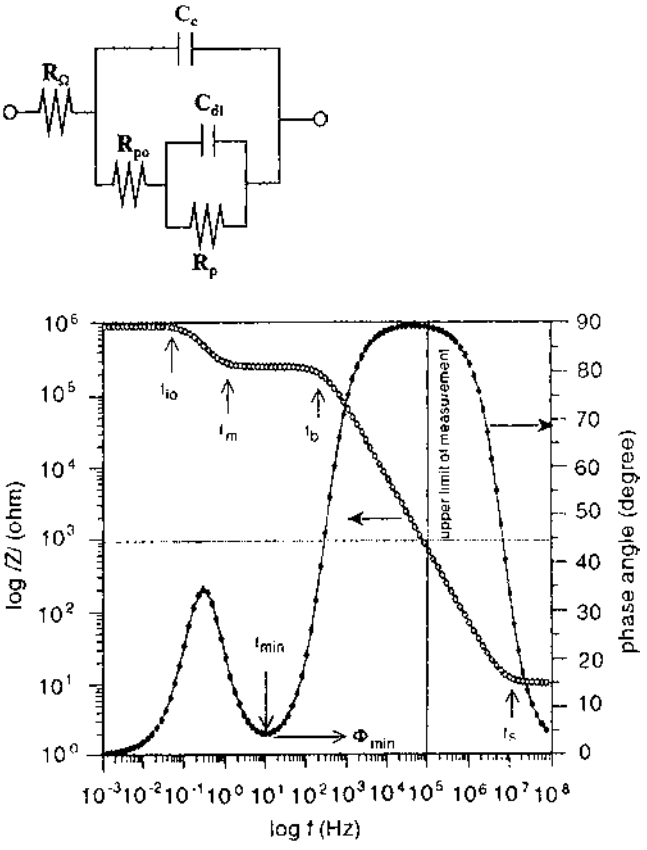

Figure 43 Equivalent circuit model for a degraded polymer coating on a metal substrate and the corresponding EIS data presented in Bode plot format. The breakpoint frequency is indicated as f_b in the plot. (From C. H. Tsai, F. Mansfeld. Corrosion 49, 726 (1993).)

the breakpoint frequency in Bode plots is shown in Fig. 43. An equivalent circuit model with labeled circuit parameters and the corresponding simulated EIS data are also indicated.

The breakpoint frequency analysis assumes that the pore resistance R_{po}, the polarization resistance of the defect, R_p, and the double layer capacitance in the defects, C_{dl}, scale with the area of substrate–coating delamination, A_d by

$$R_{po} = \frac{R_{po}^0}{A_d} \tag{16}$$

$$R_p = \frac{R_p^0}{A_d} \tag{17}$$

$$C_{dl} = C_{dl}^0 A_d \tag{18}$$

In these expressions, $R_{po}^o = \rho t$ (ohm-cm^2), and R_p^o (ohm-cm^2) and C_{dl}^o (μF/cm^2) are characteristic (area-specific) values that do not change with time; t is coating thickness, and ρ is coating resistivity, which must also be time-independent. Furthermore, the coating capacitance, C_c, is given by

$$C_c = C_c^0 A \tag{19}$$

where A is the area of the intact coating. At the breakpoint frequency the magnitude of the impedance from the resistive plateau is equal to the magnitude of the impedance from the coating capacitance,

$$R_{po} + R_s = \frac{1}{\omega C_c} \tag{20}$$

Assuming that $R_{po} \gg R_s$, which is usually the case in chloride solutions like seawater,

$$R_{po} = \frac{1}{2\pi f_b C_C} \tag{21}$$

and upon rearranging,

$$f_b = \frac{1}{2\pi R_{po} C_C} \tag{22}$$

If it is assumed that

$$R_{po} = \frac{\rho t}{A_d} \tag{23}$$

and

$$C_C = \frac{\varepsilon\varepsilon_o(A - A_d)}{t} \tag{24}$$

and that total electrode area, A, is much greater than the delaminated area, A_d (e.g., $A_d < 1\%$), the breakpoint frequency is

$$f_b = \frac{1}{2\pi\varepsilon\varepsilon_o\rho} \cdot \frac{A_d}{A} \tag{25}$$

The practical consequence of this analysis is that the breakpoint frequency is directly proportional to the delaminated area, and can be monitored with a fast

high-frequency EIS measurement. It must be stressed that this analysis assumes that ρ and ε are independent of thickness and do not change with exposure time. It must also be recognized that this analysis is subject to the assumption that the delaminated area is a small fraction of the total area under analysis.

Figure 44 shows the variation in f_b for different defect area fractions. The value of f_b ranges from 10^3 to 10^5 Hz for defect area percentages of 0.001 to 0.05%, respectively (119). The ability to measure small defect area fractions is compromised by incomplete resolution of the resistive plateau, which occurs when R_{po} is large and C_{dl} is small; f_b measurements are also limited at high frequencies by the use of potentiostatic control. This normally imposes an upper limit of 10^5 Hz. A further limitation occurs for thick coatings whose capacitive response shifts the breakpoint to low frequencies where it is difficult to identify confidently and may fall in a range where the EIS data are affected by electrode

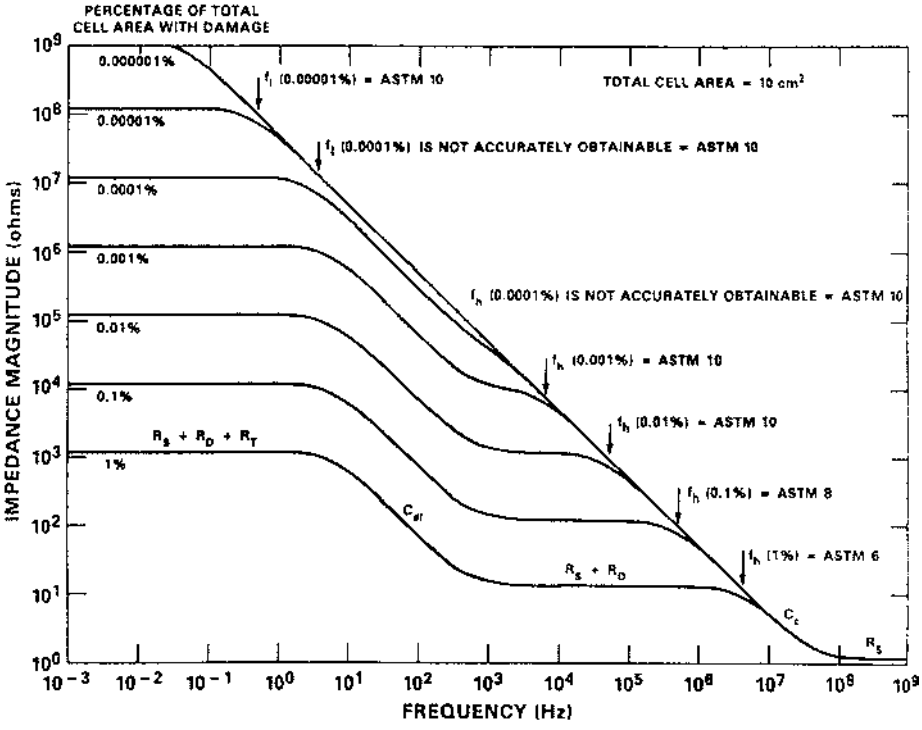

Figure 44 Effect of defect area percentage on impedance magnitude behavior of a coated steel. Total cell area assumed is 10 cm². (From H. P. Hack, J. R. Scully. J. Electrochem. Soc. 138, 33 (1991).)

instability. To avoid these complications, other parameters such as the low-frequency breakpoint (119) and the phase angle minimum (122) have been investigated for determining the delaminated area.

The theoretical underpinning of the breakpoint frequency method has also been challenged (123,124). This stems from the definition of R_{po} and the resistance of free-standing polymer films to ionic conduction. The somewhat unsatisfying definition of R_{po} is that it represents the ionic resitance of the polymer film, but only in areas where delamination has occurred. In other locations on the surface, R_{po} is essentially infinite. The ionic resistance of free-standing films can be measured directly and is found to be large, about 10^7 ohm $\cdot$ cm^2, and independent of exposure time in aggressive solutions. If R_{po} does not vary with exposure time, and the coating capacitance is assumed not to vary with time, then no variation in f_b should be possible according to Eq. (22). Therefore it has been argued that R_{po} really represents the resistance to ionic current flow within growing defects. Since this resistance is a function of several variables including local chemistry variation, defect geometry, and accumulation of corrosion product, the direct relationship between f_b and A_d indicated by Eq. (25) is in doubt.

Despite inherent assumptions and objections to the breakpoint frequency method, experiments show that there is general agreement between f_b and delaminated area (119). Figure 45 shows the relationship between f_b and the estimated delamination area for opaque and transparent epoxy coatings on steel. The figure supports the positive relationship between f_b and delaminated area indicated by Eq. (25), but the scatter in the relationship is relatively large, suggesting that sample-to-sample variation and frequency dispersion in the EIS data may affect the determination of f_b for any specific amount of delamination.

b. Life Prediction. From a practical perspective, EIS characterization of polymer coated metal degradation may be most useful for rapidly assessing the protectiveness of a coating and making a service life prediction. EIS is sensitive to damage accumulation in its earliest stages in controlled laboratory testing. These tests can be carried out easily and rapidly, and it is easy to imagine EIS-based methods being used to make many individual measurements in a short period of time. However, it is not well established if the result of such tests can be used to predict service life. For this reason, there has been great interest in determining if short-term EIS data are related to long-term exposure performance.

An example of the use of EIS measurements to make long-term corrosion predictions for polymer coated metals is shown in Fig. 46 (110). In this plot, the ASTM D610 and D714 visual rankings of corrosion damage after 550 days of exposure in simulated seawater are plotted against a protection index, $\Phi(f)$, determined after only 10 days of exposure. The damage protection index is determined from the breakpoint frequency, f_b, as

$$\phi(f) = 10^{-2} \log f_b \tag{26}$$

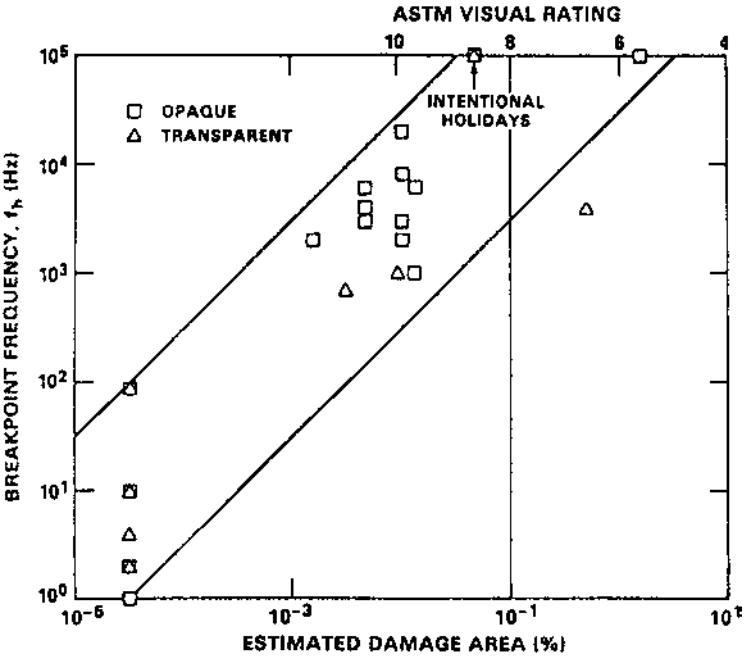

Figure 45 Relationship between the breakpoint frequency and the estimated active area for opaque and transparent epoxy coatings on steel. (From H. P. Hack, J. R. Scully. J. Electrochem. Soc. 138, 33 (1991).)

On the vertical axis, high ASTM rating numbers correspond to lower amounts of visual corrosion damage, with 10 indicating no visible damage. $\Phi(f)$ does not discriminate well among coatings with the best performance, but it does separate coatings with inferior performance (ASTM rating <7) after 550 days of exposure. This example illustrates the possibility of making gross distinctions among coating performance for long-term exposures.

It is also desirable to have predictive tests that are rapid and are grounded by benchmarking with older exposure-based tests. Rapid validated tests are necessary for quality control and lot release inspection. Often the results of such tests are needed within hours. Cabinet exposure testing that requires days or weeks is obviously impractical.

To determine if short-term electrochemical test results were related to longer term salt spray exposure results, a two-part test was conducted, and results were correlated to results from salt spray testing. The first part of the test involved measurement of impedance immediately upon exposure and after 24 hours of

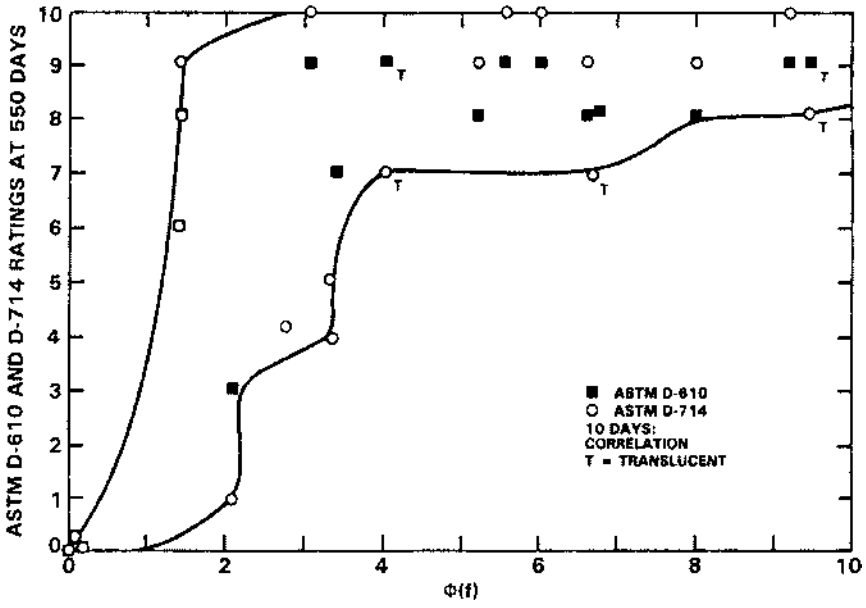

Figure 46 Correlation between the protection index, $\Phi(f)$, determined after 10 days exposure to 0.5 M NaCl and the ASTM D 610 visual rating determined after 550 days exposure. (From M. Kendig, J. Scully. Corrosion 46, 22 (1990).)

exposure to aerated 0.5 M NaCl solution. Coating capacitance was extracted from the data for estimation of water uptake using the Brasher–Kingsbury equation [Eq. (15)]. The corrosion resistance of the coated metal at 24 hours was also determined. Cathodic disbondment comprised the second evaluation. In this test, intersecting scribes were made through the coating to expose bare metal. The sample was then exposed to 0.5 M NaCl solution and then cathodically polarized at $-1.05V_{sce}$ for 24 hours. After exposure, the sample was removed from solution, and loose coating was removed from the surface. The area exposed was measured and used in the subsequent correlation. Other identically coated samples were subject to salt spray exposure until failure. Several different failure criteria were invoked. The failure time was taken as either

1. The time required for paint pullback from a scribe to exceed 3 mm
2. The time required for the ASTM D610 visual rating to drop below 9
3. The average time for criteria 1 and 2

Analysis showed that time to failure (TTF) did not correlate well with the results of the EIS or the cathodic disbondment individually. However, when the

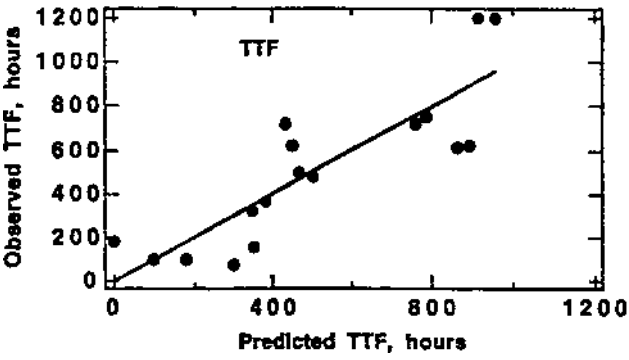

Figure 47 Relation between observed salt spray TTF and TTF predicted from the regression model in Eq. (15). (From M. Kendig, S. Jeanjaquet, R. Brown, F. Thomas. J. Coat. Tech. 68, 39 (1996).)

results of both tests were included in the analysis, a good correlation was obtained. The empirical relationship between TTF (according to criterion 3) and the electrochemical results was found to be

$$\text{TTF} = -804.5 = 109.4 \log R_{\text{cor}} - 118.7 \log\left(\frac{dx}{dt}\right) \tag{27}$$

In this expression, TTF is measured in hours, the corrosion resistance of the painted metal is taken as the charge transfer resistance of the actively corroding metal surface in ohm · cm^2, and dx/dt is the delaminated area from cathodic disbondment measured in mm^2. Figure 47 shows the relationship between the observed and the predicted TTF based on Eq. (27). While the data are somewhat scattered, a strong positive correlation between prediction and observation is indicated, supporting the idea that short-term electrochemical characterization is relatable to longer term performance in cabinet exposure testing. This kind of benchmarking information is crucial for the introduction and regular use of electrochemical methods for routine industrial testing.

VII. NEW TECHNIQUES

A. Scanning Reference Electrode Technique (SRET)

On a freely corroding electrode surface, ionic currents flow in solution between local anodic and cathodic sites. A spatially varying potential field is associated with ionic current flow so that the potential field lines and lines of current flux

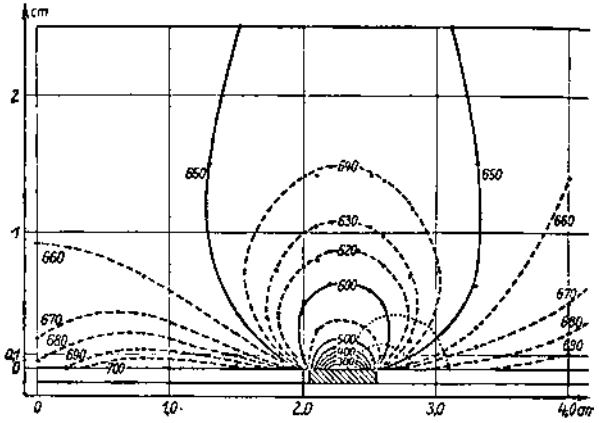

Figure 48 The potential distribution associated with a Pt cathode on a Zn anode in 0.05 M HCl, showing the measured normal variation in the potential field. (From H. S. Isaacs. In: Localized Corrosion. p. 158, NACE, Houston, TX (1974).)

always intersect normally, as is depicted in the simple cross sectional schematic of small anode surrounded by a larger cathode (Fig. 48) (125). The relationship between the current density flowing through solution and potential field is given by

$$i = \frac{1}{\rho} \cdot \frac{\partial V}{\partial l} \tag{28}$$

where i is the current density in solution (A/cm^2), ρ is the solution resistivity ($\Omega \cdot$ cm), and $\partial V/\partial l$ is the gradient of the voltage field in the direction of current flow (V/cm). The largest gradients of the voltage field exist near the electrode surface. By scanning a reference electrode near the corroding surface and measuring its potential with respect to a reference electrode positioned far away (centimeters), it is possible to measure the near surface potential variation in either a one-dimensional line scan mode or a two-dimensional mapping mode.

The experimental apparatus normally consists of a drawn glass capillary microreference electrode that minimizes screening between anodic and cathodic sites, an apparatus for rastering the microreference electrode across the corroding electrode surface in a systematic manner, high-impedance voltmeters, and the necessary data recording devices. A representative schematic of the apparatus is shown in Fig. 49 (125). The sensitivity and resolution of the measurement depend on the diameter of the tip of the microreference electrode, the standoff distance

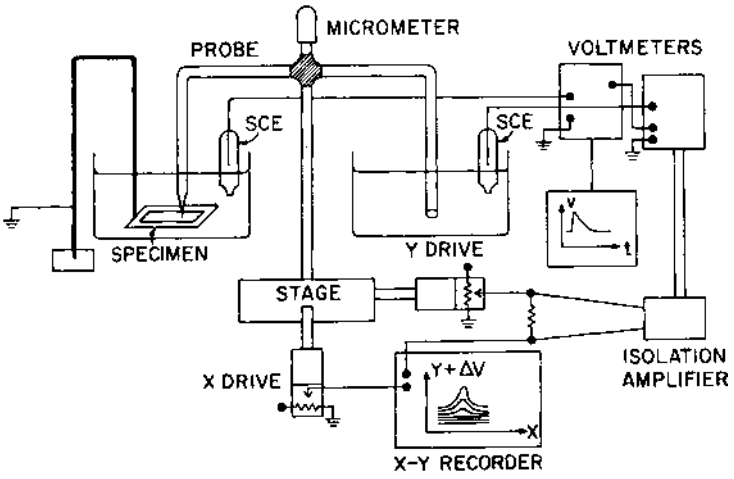

Figure 49 Schematic illustration of the scanning reference electrode probe apparatus used by Isaacs. (From H. S. Isaacs. In: Localized Corrosion. p. 158, NACE, Houston, TX, 1974.)

between the microreference and the surface, the scan rate, and the solution resistivity. In measurements of weldments in carbon steels in line scan mode using a 75 μm reference electrode tip scanned at 50 mm/min in a synthetic seawater, millivolt potential resolution and millimeter spatial resolution can be achieved (126). Potential field maps collected on pitting 304 stainless steel using a 250 μm diameter microreference tip and a scan rate of 75 mm/min in 0.4 M $FeCl_3$ solution adjusted to a pH of 0.9 yielded 0.3 mV resolution and millimeter spatial resolution (127)

It is also possible to scan a pair of reference or pseudoreference electrodes separated by a small, fixed distance of a few micrometers to measure the local potential field gradient, $\partial v/\partial l$, and estimate the local current density from Eq. (48) (128). This is a slightly more sophisticated measurement because the anodic or cathodic character of local sites can be determined from the polarity of the current, and the intensity of the attack can be estimated from the current density flowing in solution. The difficulty with this arrangement is that the potential difference between two closely spaced reference electrodes in a conductive solution is usually less than 1 microvolt. The stability of reference electrodes is on the order of microvolts, and thus it often exceeds the magnitude of the potential difference signal. This imposes a fundamental limitation on the usefulness of this technique.

B. Scanning Vibrating Electrode Techniques (SVET)

To overcome the limitations associated with the poor signal-to-noise ratio in the paired reference electrode measurement scheme, the scanning vibrating electrode technique was developed. In this technique, a single pseudoreference electrode is subject to a small periodic mechanical perturbation that induces an electrical oscillation of known amplitude. The peak-to-peak AC voltage measured by the tip is equal in magnitude to the potential gradient in solution over the distance of travel of the oscillation amplitude. The current density in the direction of the electrode oscillation can be calculated from Eq. (28). To eliminate noise interference, the signal from the oscillating tip is extracted using a lock-in amplifier, which is tuned to measure the signal only at the oscillation frequency of the vibrating tip. It is also possible to superimpose two orthogonal mechanical oscillations on the pseudoreference electrode. If the imposed oscillations are of different frequencies, each signal can be separately measured using lock-in detection, and the directional components of current flow can be resolved. The vibrating tip can be scanned across the corroding surface to identify anode and cathode locations, the current density, and the current density vectors in solution. This enables direct measurement of the progress and intensity of local corrosion processes on a site-by-site basis.

An example of the use of SVET in studies of Ce corrosion inhibitors is found in the work of Aldykewicz et al. (129). Figure 50 shows a representative schematic illustration of the apparatus used in these experiments. The vibrating probe consisted of a 5 μm diameter Pt–Ir wire tipped with platinum black at the sensing end of the wire. The diameter of the tip at the sensing end of the wire was about 20 μm. The wire was attached to two piezo crystals that were capable of inducing mutually orthogonal oscillations in the wire at different frequencies. Lock-in detection of the AC voltage signal from the tip was capable of resolving current densities normal and horizontal to the sample surface, although this was not exploited in this particular study. The vibrating tip was rastered over the surface at a standoff distance of about 150 μm using a programmed stepper motor with a 2.5 μm step size. Areas with dimensions of about 1000×1500 μm were scanned in several minutes. In a 12 mM NaCl solution with a solution resistivity of 830 $\Omega \cdot$ cm, a current density resolution of 2 $\mu A/cm^2$ was possible. Spatial resolution in these experiments is difficult to specify, as it depends on the intensity and spacing of active areas, which are not easily controlled in real materials. However, areas on corroding Al alloy surfaces that were sufficiently active and separated appeared to be detectable with approximately 10 μm spatial resolution. Assuming that the current density in solution due to pit dissolution is uniform across an imaginary hemispherical surface around the pit, the pit current can be determined from the peak current density in solution, which is measured over

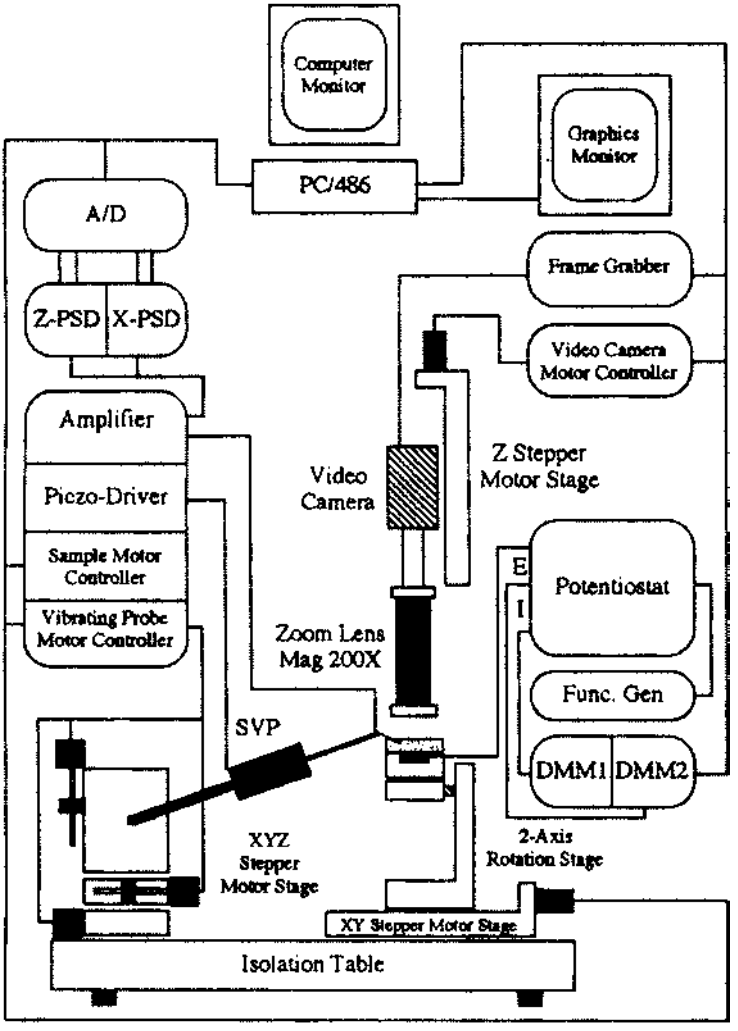

Figure 50 Schematic illustration of the 2D scanning vibrating probe system used by Aldykewicz, et al. (From A. J. Aldykewicz, H. S. Isaacs, A. J. Davenport. J. Electrochem. Soc. 142, 3342 (1995).)

the center of the pit at a standoff distance equal to the radius of the hemisphere,

$$i_{\text{pit}} = (2\pi h^2) j_{\text{measured}} \tag{29}$$

In this expression, i_{pit} is the pit current density, j_{measured} is the measured current density in solution due to the vibrating probe, and h is the standoff distance, which is equal to the radius of the hemisphere of uniform current density surrounding the pit. A pit current of 3 nA is possible given a current density measurement sensitivity of 2 $\mu A/cm^2$.

In addition to the constraints mentioned above, active areas must be sufficiently long-lived and nearly fixed in position for detection by SVET. This is not normally a problem in the study of coatings where the location of active areas are often fixed by existing or emergent coating defects. However, some pitting phenomena, especially metastable pitting, may not be detected well by this technique.

Aldykewicz et al. used SVET to study the inhibiting effects of $CeCl_3$ on localized corrosion of 2024-T3 (Al-4.4Cu-1.5Mg-0.6Mn). Current density maps were made for samples exposed to 12 mM NaCl and 4 mM $CeCl_3$ solutions over several hours. Figure 51 shows current density maps from this study. Discrete and intense sites of anodic activity were detected, but intense cathodes were not. This suggests that anodic activity is very focussed, while the cathodic reaction is supported at a lower rate over a much larger surface area. At short times, the anodic activity is more intense in the presence of $CeCl_3$ and NaCl, but after 2 hours of exposure, the number and intensity of sites is vastly diminished in the Ce-bearing solution, which was taken as an indication of its ability to inhibit corrosion.

Locally intense anodes and cathodes can be observed in current density maps made in the vicinity of scribes in galvanized steel surfaces in chloride solutions (130). Figure 52 shows a time series of current density maps in the scribe regions of a hot dip galvanized surface during exposure to aerated 0.01 M NaCl solution. Cathodic regions corresponding to exposed steel in the scribe and anodic regions are due to local Zn dissolution. Galvanic coupling, which is the origin of sacrificial protection in this system, is highly localized, and interacting anodes and cathodes are separated by only tens of micrometers.

C. Local Electrochemical Impedance Spectroscopy (LEIS)

LEIS techniques spatially resolve changes in impedance (or admittance) at a single frequency, or collect impedance spectra over a range of frequencies at a single location (131,132) Traditional EIS measurements contain contributions from corroding and noncorroding regions of the surface, but LEIS permits interrogation of locally corroding sites directly (133). In these measurements, a two-element

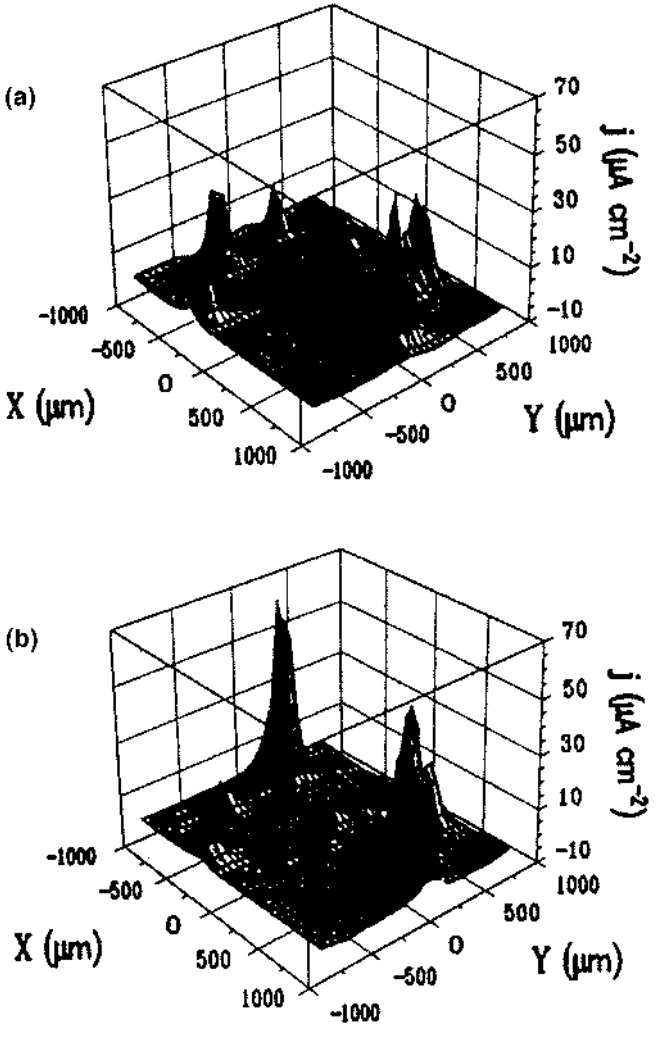

Figure 51 Measured current density flowing normal to the electrode surface at a height of 150 μm above 2024-T3 in 12 mM NaCl after immersion for (a) 0 and (b) 2 h. (From A. J. Aldykewicz, H. S. Isaacs, A. J. Davenport. J. Electrochem. Soc. 142, 3342 (1995).)

Figure 52 Normal current density distribution over a scribed electrogalvanized steel sample in 0.01 M NaCl as a function of time: (a) 15 min, (b) 1 h, (c) 2 h. (From H. S. Isaacs, A. J. Aldykewicz, D. Thierry, T. C. Simpson. Corrosion 52, 163 (1996).)

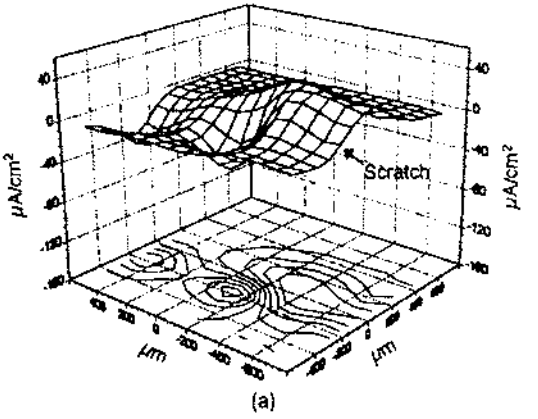

(a)

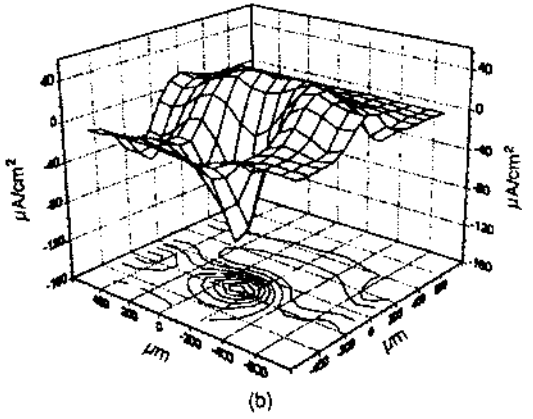

(b)

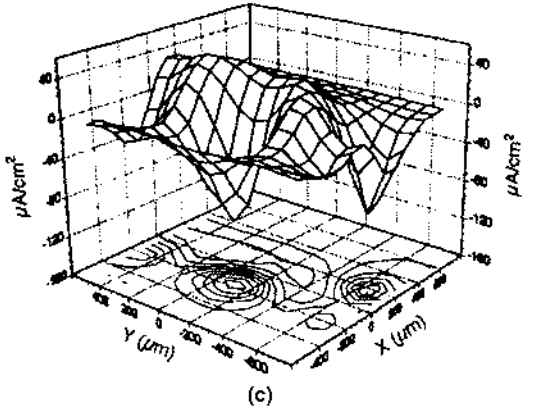

(c)

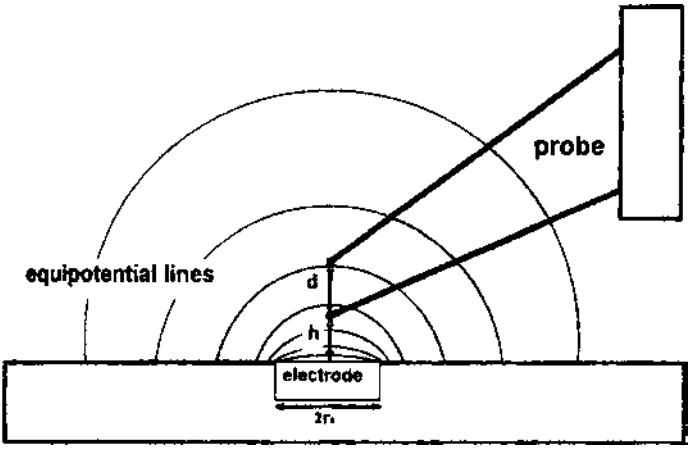

Figure 53 Schematic illustration of the pseudoreference electrode pair used to make LEIS measurements. In this diagram, *d* refers to the electrode separation and *h* refers to the height of the probe from the working electrode surface. (From F. Zou, D. Thierry, H. S. Isaacs. J. Electrochem. Soc. 144, 1957 (1997).)

pseudoreference electrode is used to measure the normal component of the AC current density in solution as a function of signal frequency and/or position over a coated metal surface. An example of the two-element electrode used to make this type of measurement is shown in Fig. 53 (134).

In LEIS measurements, the working electrode is under potential control in a three-electrode cell. The pseudoreference electrode pair is then brought close to the sample surface to measure the local AC current density. A key assumption behind LEIS is that in the potential field near a working electrode surface, the AC solution current density is proportional to the local electrode impedance, and at any given measurement frequency, ω, the current density in solution is

$$i(\omega) = \frac{\Delta V(\omega) \cdot \sigma}{l} \tag{30}$$

where $i(\omega)$ is the current density in solution, $\Delta V(\omega)$ is the AC voltage drop that is measured between the two pseudoreference electrodes, ρ is the solution conductivity, and l is the separation distance between the pseudoreference electrodes. The magnitude of the local impedance is then

$$|Z(\omega)|_{\text{local}} = \frac{V(\omega)}{i(\omega)} = \frac{V(\omega)_{\text{applied}}}{V(\omega)_{\text{probe}}} \cdot \frac{l}{\rho} \tag{31}$$

Here, $|Z(\omega)|_{local}$ is the magnitude of the local impedance, $V(\omega)_{applied}$ is the magnitude of the voltage between the working electrode and a distant reference electrode, and $V(\omega)_{probe}$ is the AC voltage drop measured by the pseudoreference electrode pair. Again, it is implicitly assumed that the current density measured in solution is equal to the current density at the electrode surface.

The pseudoreference probe electrode sizes that have been used to study coatings have ranged from 100 to about 250 μm in diameter, with vertical offsets between the probe elements of about 1 mm. The probe pair is usually brought to within a few hundred micrometers of the surface for measurement. The impedance of the probe pair is usually quite large, and the voltage signal small. Therefore it is necessary to amplify the probe signal before it is applied to the frequency response analyzer. For mapping, the probe pair is rastered using a high-precision x–y stepper motor system. Vibration isolation of the entire apparatus is important for proper measurement.

Spatial resolution of 30 to 40 μm has been demonstrated, but submillimeter spatial resolution of the impedance variation is typical in studies on coated metals. The probe is able to resolve variations at distances equal to the size of the probe or larger. The probe size may be decreased to increase spatial resolution, but this strategy is limited by a corresponding increase in the probe impedance, which reduces AC signal sensitivity. Current flow in an electrolyte will spread radially from a localized site in a manner determined primarily by the solution conductivity. Therefore the probe–working electrode separation distance will also affect spatial resolution. The apparent size of impedance variation is also frequency-dependent. At high excitation frequencies, the current distribution is altered because the interfacial impedance is shorted by capacitive charge transfer. It is also possible that the directional components of current flow are frequency dependent. LEIS is usually conducted to detect the component of current flow normal to the working electrode surface. Should the magnitude of the component flowing parallel to the surface change with frequency, impedance variations may shrink or grow in their spatial extent as a function of measurement frequency. Additional details on the effects of probe configuration, separation, solution conductivity, and excitation frequency on spatial resolution of the impedance variation can be found in result presented by Thierry (134).

Taylor et al. conducted LEIS in a mapping mode to characterize the spatial variation in the admittance associated with various types of intentionally formed defects on organically coated metal surfaces (135). The LEIS probe used in these experiments consisted of chloridized silver wires to form Ag|AgCl reference electrodes. Excitation frequencies between 100 and 1000 Hz were used for mapping admittance. The precise frequency used was selected to maximize the admittances differences observed. Admittance mapping resolved differences due to millimeter-sized defects associated with adsorbed machine oil, underfilm NaCl

deposits, and arrays of pinhole defects. These findings are significant because subtle defects that lead to corrosion are detectable before corrosion is observed visually. Admittance mapping was also found to be sensitive to underfilm corrosion. Figure 54 shows the admittance map taken over two parallel scribes made in a 10 μm thick polymer coating on an aluminum substrate. The figure shows that the extent of the admittance variation is considerably wider than the width of the scribe. This region was found to correspond to a region where corrosion had propagated laterally away from the scribe defect.

Admittance mapping by LEIS has also been used on naturally formed defects on polymer coated metals (136,137). Al alloy 2024-T3 coated with polyvinyl chloride/polyvinyl acetate and polyurethane-based polymer films will form blisters when immersed in dilute chloride or sulfate solutions for several days. Two different types of blisters were found to evolve that were distinguishable in LEIS mapping. Black blisters, named for their color, were round defects 1 to 2 mm in diameter. Red defects were irregularly shaped and ranged from 1 to 7 mm in diameter. The admittance response from each of these defects was substantially different, as shown in Figure 55. Black defects exhibited a comparatively low admittance indicating a low rate of corrosion, while red defects exhibited a high admittance and a greater rate of corrosion. These findings correlated well with local measurements, which showed symptoms of aggressive local attack including high metal cation concentrations, high chloride ion concentrations, low pH, hydrogen evolution, and active open circuit potentials. These symptoms were not found to the same extent in black defects. These findings show that LEIS is a sensitive indicator of localized corrosion intensity in film defects, and can distinguish the severity of defects occurring on the same sample.

In another study, LEIS was used to show that subtle differences in Al alloy surfaces due to mechanical surface treatment produced different admittance responses (136). Regions of high admittance were found to exist in bands that were associated with surface deformation. The admittance response was found to correlate well with local determinations of the pitting potential. On average, high admittance regions exhibited a pitting potential that was 150 mV more negative than the pitting potential on other regions of the surface.

Another method of spatially resolving variations in impedance involves constructing regular arrays of small cells on a sample surface and performing conventional EIS measurements in them on a serial basis (138). This method does not require any special measurement equipment beyond that needed for conventional EIS measurement. However, as the cell size and working electrode area is reduced, the measured current will be reduced to the point where noise and instrument current resolution become factors. These factors limit how small a cell can be and determine the spatial resolution of the technique. This technique has been used to examine the changes in the EIS response on coil coated galva-

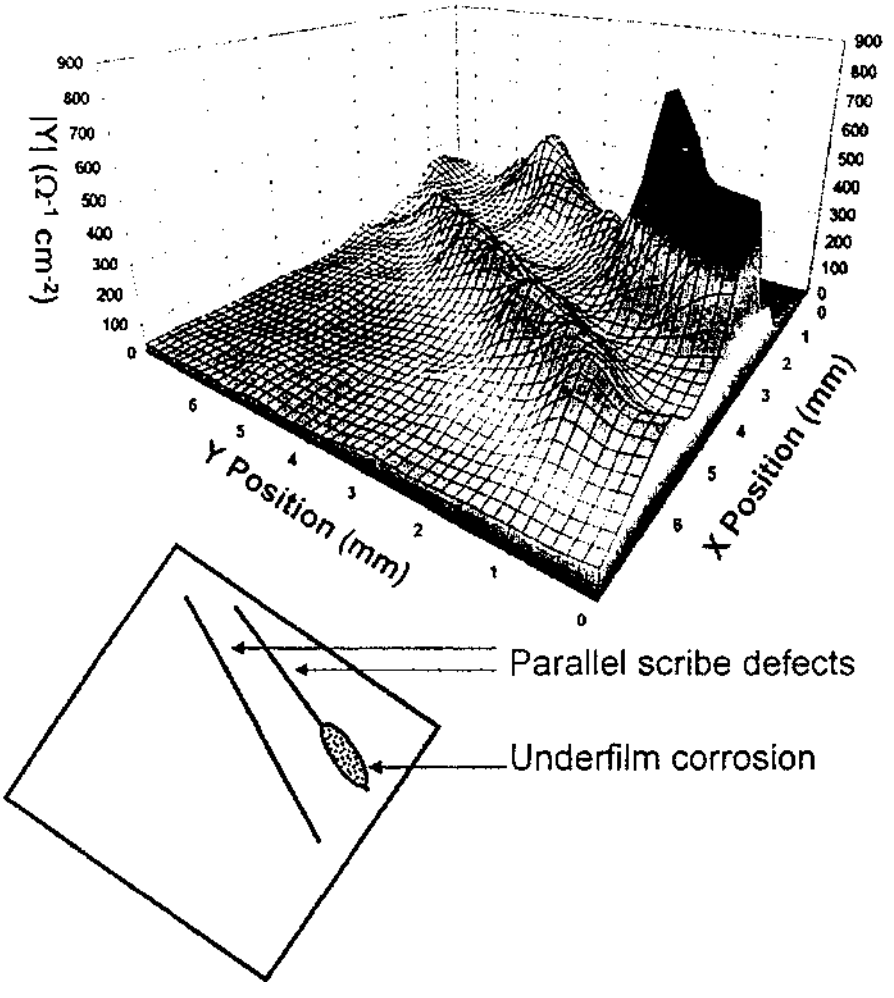

Figure 54 LEIS admittance map of two scribe marks on 10 μm thick polyvinyl chloride/polyvinyl acetate coating on Al alloy 5182 (Al-2.5 Mg) after exposure to 3.5 wt% NaCl for 24 h. The map was collected using a 15 mV amplitude voltage perturbation at 500 Hz. Underfilm corrosion is occurring in association with the rightmost scribe, as indicated by the extended high admittance region located approximately at $x = 2$, $y = 1$. (From M. W. Wittmann, R. B. Leggat, S. R. Taylor. J. Electrochem. Soc. 146, 4071 (1999).)

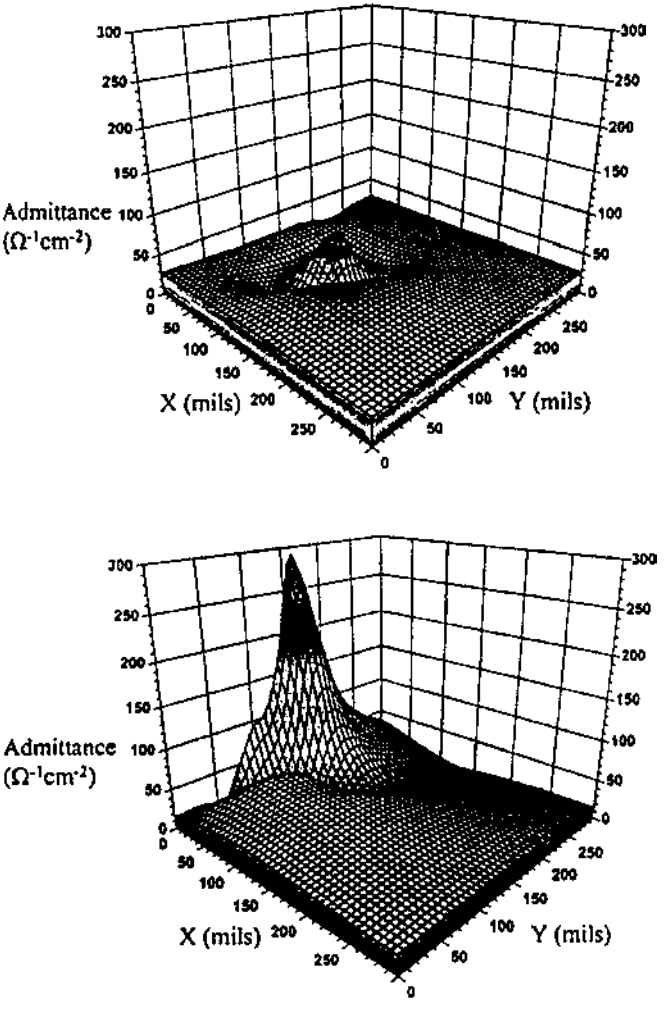

Figure 55 Comparison of LEIS admittance maps for red (right) and black (left) defects under a vinyl coating on 2024-T3 after 35 h exposure to 0.6 M NaCl. The large admittance peak for the red defect indicates aggressive local corrosion. (From A. M. Miersch, J. Yuan, R. G. Kelly, S. R. Taylor. J. Electrochem. Soc. 146, 4449 (1999).)

nized steel after corrosion testing. Rows of cylindrical cells 8 mm in diameter were glued to painted surfaces 2 mm apart from one another. Cell centers were located 6, 20, and 34 mm away from the cut edge of the coil. Prior to the local EIS characterization, the coil coated samples were exposed to cyclic exposure in simulated acidified rain solution. Local EIS was conducted in each cell, and the results were fitted to an equivalent circuit model. Results suggested that corrosion at the cut edge undercutting the paint was detectable by local EIS.

A single vibrating platinum wire pseudoreference electrode has been used in another variant of the local impedance technique (139). In a demonstration experiment, a 250 μm diameter Fe wire was inserted into a 316 stainless steel sample to form a galvanic couple. The composite electrode was immersed in a 0.1 M Na_2SO_4 solution, and a 0.2 μA DC current with a 3 μA current perturbation, whose frequency was swept between 0.1 and 1000 Hz, was applied between the stainless steel and the Fe wire. A Pt/Ir needle with a 15 μm diameter Pt black tip was vibrated mechanically at 266 Hz normal to the sample surface with a 15 μm amplitude. The probe signal was influenced by both the mechanical and the current oscillations and contained both local potential and local current information. To extract and separate the useful information, the probe signal was amplified and filtered using phase-sensitive detection. From this information, the local impedance was computed yielding a depressed semicircular arc in the complex plane at frequencies between 0.1 and about 100 Hz. An interfacial capacitance of about 80 $\mu F/cm^2$ was estimated from the data, which was generally consistent with the capacitance of actively corroding iron. This technique is a distinct variant of the local impedance technique because the local impedance is defined by the ratio of the local current density to the local potentials rather than by the local current density to the global potential as was the case in LEIS.

D. Electrochemical Noise (ECN)

Electrochemical noise consists of low-frequency, low-amplitude fluctuations of current and potential due to electrochemical activity associated with corrosion processes. ECN occurs primarily at frequencies less than 10 Hz. Current noise is associated with discrete dissolution events that occur on a metal surface, while potential noise is produced by the action of current noise on an interfacial impedance (140). To evaluate corrosion processes, potential noise, current noise, or both may be monitored. No external electrical signal need be applied to the electrode under study. As a result, ECN measurements are essentially passive, and the experimenter need only ''listen'' to the noise to gather information.

Potential noise is measured by collecting the potential versus time record between a noisy corroding electrode and a noiseless reference electrode using a high-impedance digital voltmeter (DVM). This is essentially a measurement of

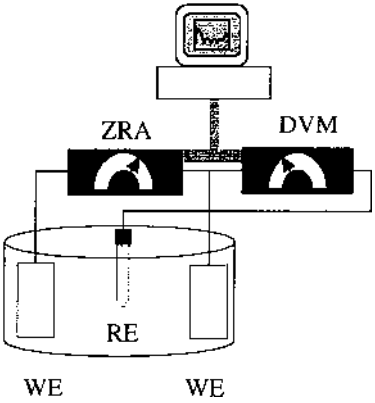

Figure 56 Schematic illustration of an ECN measurement system.

the open circuit potential. Measurement of current noise is made using a zero resistance ammeter (ZRA) connecting two identical working electrodes immersed in the same electrolyte. Potential and current noise can also be measured simultaneously by connecting working electrodes through a ZRA and measuring the potential of one electrode against a reference electrode using a DVM. In these types of measurements, the current and potential noise can be made simultaneously, and are said to be correlated (141). Usually, the measurement of correlated data is orchestrated by computer. A schematic illustration of the apparatus for making correlated noise measurements is shown in Fig. 56. General purpose DVMs and ZRAs are usually unsuitable for electrochemical noise measurements because the magnitude of the signals is quite small. However, commercial systems, including both hardware and software, are available for making correlated noise measurements.

Electrochemical noise can be characterized by some common statistical parameters including the mean, the variance, and the standard deviation. In particular, the standard deviation, σ, is used as a measure of the amplitude of the variation in the noise signal. Skew and kurtosis sometimes give indications of the form of corrosion occurring (140). For unfiltered digitized noise data in a time record, the noise resistance, R_n, is

$$R_n = \frac{\sigma_V}{\sigma_I} \tag{32}$$

where R_n is the noise resistance in ohms, and σ_V and σ_I are the standard deviation

in the potential and current noise signals, respectively (142). This definition assumes that potential noise arises due to the action of current noise across the interfacial impedance. R_n, as it is used in corrosion studies, is based on simple statistical evaluation of noise signals, and an equally simple Ohm's law formalism. However, a widely accepted fundamental, first-principles derivation of the noise resistance has not yet emerged (143,144).

Determination of R_n does not require that the current and potential signal be correlated. However, if measurements are made at different times, they should be made with similar working electrodes and similar exposure conditions. R_n values have been used to assess the degradation of organically coated metals. In these studies, R_n data appeared to correlate with the film resistance (impedance magnitude at low frequency) values determined from EIS (145), or with visual inspection of painted samples subject to various cabinet exposures (146).

In the case of general corrosion, R_n can be used in the Stern–Geary equation to estimate corrosion rate:

$$i_{corr} = \frac{1}{R_n} \cdot \frac{b_a b_c}{2.3(b_a + b_c)} \tag{33}$$

In this expression, b_a and b_c refer to the appropriate anodic and cathodic Tafel constants. Comparison of weight loss data collected as a function of exposure time determined from R_n, R_p from EIS, and gravimetric measurements of mild steel exposure to 0.5 M H_2SO_4 are often within a factor of two. This suggests that use of R_n in the Stern–Geary equation may be appropriate for the estimation of corrosion rate (147–150). However, R_n measurements may underestimate corrosion rates. R_p is often measured at effective frequencies of 10^{-2} Hz or less in linear polarization or EIS measurements, while R_n is measured at 1 Hz or greater. An example of this is provided in Fig. 57, which shows the corrosion rate of carbon steel in 3% NaCl solution as a function of exposure time determined by EIS, linear polarization, noise resistance, and direct current measurement with a ZRA. Among these data, the corrosion rates determined by noise resistance are consistently the lowest.

Correlated noise data can be transformed to the frequency domain using a fast Fourier transform (FFT) or the maximum entropy method (MEM) (151) A spectral noise impedance, $R_{sn}(f)$, can then be calculated (152):

$$R_{sn}(f) = \frac{E_n(f)}{I_n(f)} \tag{34}$$

and

$$R_{sn}(f) = |R(f)| = \sqrt{(R_{Re}^2 + R_{Im}^2)} \tag{35}$$

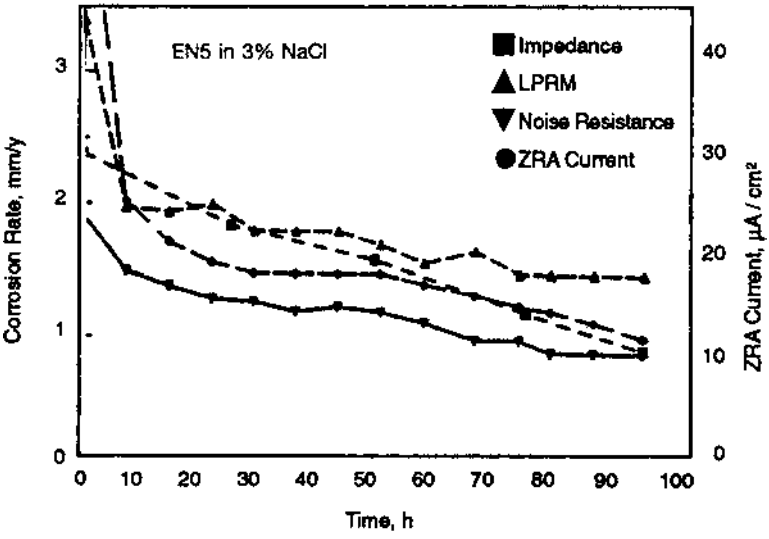

Figure 57 Corrosion rate of carbon steel in 3% sodium chloride solution as a function of exposure time. (From J. L. Dawson. p. 3, Electrochemical Noise Measurements for Corrosion Applications, ASTM STP 1277. ASTM, Philadelphia, PA (1996).)

In this expression, E_n and I_n are the magnitude of the potential and current noise at any given frequency, f. R_{Re} and R_{Im} are the real and imaginary components of R_{sn}. Plots of spectral noise impedance versus frequency resemble Bode magnitude plots of EIS data as shown in Fig. 58. Meaningful phase angle information is not usually obtained, as this is not preserved by the MEM transform, and data are usually of insufficient quality for accurate phase information to be obtained from the FFT.

The spectral noise resistance, determined from the DC limit in a spectral noise impedance plot, is defined as

$$R_{sn}^{0} = lim_{f \to 0} \left\{ R_{sn}(f) \right\} \tag{36}$$

which is equal to the magnitude of the impedance at the DC limit, provided that instrumentation is sufficiently sensitive to very small currents.

Noise resistance monitoring has been used to track the long-term degradation of marine coatings under laboratory exposures (153), and remotely under natural exposure conditions (154). In studies of epoxy and alkyd coatings on steel

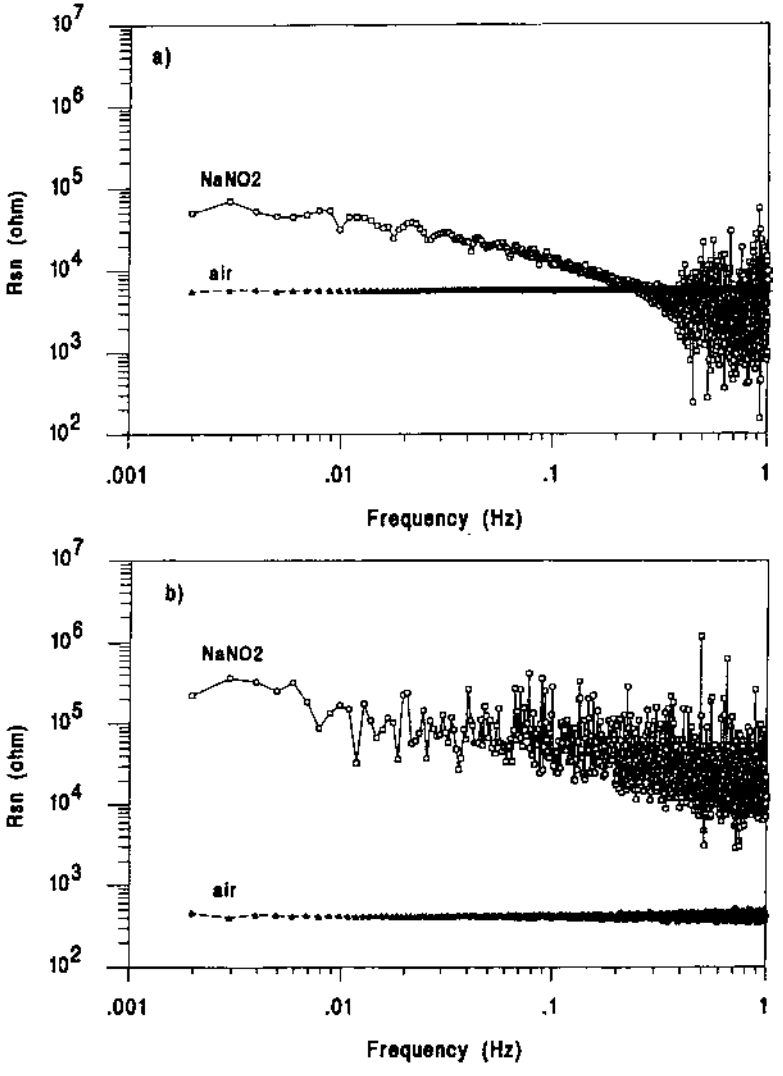

Figure 58 Frequency dependence of the spectral noise resistance, R_{sn}, for iron in aerated, and aerated and inhibited 0.5 M NaCl after exposure for (a) 1 h and (b) 24 h. (From F. Mansfeld, H. Xiao. p. 59, Electrochemical Noise Measurements for Corrosion Applications, ASTM STP 1277. ASTM, Philadelphia, PA (1996).)

substrates exposed to chloride solutions or natural seawater, there appeared to be good qualitative correlation between the noise resistance, R_n, and the spectral noise resistance, R^o_{sn} (141,155). Additionally, these two parameters were observed to exhibit the same time-dependent trends as the pore resistance, R_{po}, and the polarization resistance, R_p, determined from EIS experiments carried out over the same exposure time interval.

Power spectra estimation can be carried out with correlated ECN data. Data are plotted in power spectral density (PSD) plots, which show the power of a noise signal over frequencies that range from $1/T$, where T is the sampling period, to the maximum sampling rate. Normally data are plotted as the logarithm of the power using units of V^2/Hz or A^2/Hz versus the logarithm of frequency. PSD plots have three characteristics: the roll-off slope, which is observed at the high-frequency regime, the DC limit at the lowest frequency, and the roll-off frequency, which separates the two regimes (156). The overall shape of the PSD may give an indication of the shape and duration of individual current or potential transients, and their distribution in time (157). The roll-off slope itself may indicate the nature of the corrosion process. A slope of -2 may indicate a Gaussian process characteristic of general corrosion, a slope of -1 is consistent with a diffusion-controlled process, and a slope of 0 indicates a stochastic or Poisson process, which is characteristic of localized corrosion (158). As a result, PSD analysis can discriminate among different types of corrosion.

Under the proper conditions there are important relations among the PSDs, the noise resistance, and the spectral noise resistance that make PSD measurement useful in corrosion studies (159–161). The variance of a random signal, x, is the integral of its PSD in the frequency domain:

$$\sigma_x^2 = \int_0^{+\infty} \Psi_x(f)\, df \tag{37}$$

where $\Psi_x(f)$ is the PSD of the signal. Therefore the noise resistance, R_n, can be determined from the integration of the potential and current PSDs as

$$R_n = \frac{\sigma_V}{\sigma_I} = \left(\frac{\int_{f_{min}}^{f_{max}} \Psi_V(f) df}{\int_{f_{min}}^{f_{max}} \Psi_I(f) df} \right)^{1/2} \tag{38}$$

where f_{min} is the inverse of measurement time length and f_{max} is one-half of the maximum sampling rate. The voltage and current PSDs are also related to the spectral noise resistance:

$$R_{sn}(f) = \left(\frac{\Psi_V(f)}{\Psi_I(f)} \right)^{1/2} \tag{39}$$

When the current and voltage PSDs decrease faster than $1/f$, R_n and $R_{sn}(f)$ are related via the voltage and current PSDs as

$$R_n = \left(\frac{\int_{f_{min}}^{f_{max}} \Psi_I(f) R_{sn}^2(f)\, df}{\int_{f_{min}}^{f_{max}} \Psi_I(f)\, df} \right)^{1/2} \tag{40}$$

If $R_{sn}(f)$ is frequency-independent in the range of f_{max} to f_{min}, then R_n will equal R_{sn}. If the spectral noise resistance is equal to the magnitude of the impedance, which is reasonable at low frequencies, then

$$R_n = R_{sn}(0) = |Z(0)| \tag{41}$$

Area normalization of ECN data is not as straightforward as with other type of electrochemical data (140). Current and potential noise may scale differently with electrode area. For example, if it is considered that the mean current is the sum of contributions from discrete events across the electrode surface, then the variance associated with the mean value will be proportional to the electrode area. The standard deviation of the current noise, σ_I, a measure of current amplitude, will then scale as the square root of the area. If is assumed that potential noise originates from current noise acting on the interfacial impedance, then σ_E will scale with the inverse root of the area. Therefore it is inappropriate to normalize current and potential noise by electrode area linearly. On the contrary, area normalization of noise resistance does appear to be appropriate. This is so because the potential and current noise have a constant relationship with one another. As a result, it is appropriate to report noise resistance in units of $\Omega \cdot cm^2$, remembering that the total area for normalization is given by the sum of the areas on both working electrodes.

A fundamental assumption in the interpretation of current noise from correlated noise data is that the two working electrodes in a working electrode pair are sufficiently identical that they have the same polarization resistance and the same mean current (162). In corrosion studies, this is sometimes not the case. Often one electrode is slightly more passive than the other in the pair. The more passive electrode develops into a net cathode, while the other electrode activates and becomes a net anode. The working electrode pair now behaves like a galvanic couple, and this asymmetry invalidates noise data. Another type of electrode asymmetry develops with coated metals. In this case, corrosion occurs at widely separated defects in the coating. In high-quality coatings, the areal density of defects is very small and the spacing between them is very large. Any given working electrode may only have one or two defects, and if a sample containing a defect is paired with one that does not have a defect, the working electrode pair will be asymmetric, thereby invalidating the noise data.

REFERENCES

1. T. Sydberger. Werkstoffe und Korrosion, 1981, 32 p. 119.
2. M. A. Streicher. J. Electrochem. Soc., 1956. 103 p. 375.
3. R. M. Hudson, R. J. Joniec, S. R. Shatynski. Pickling of Iron and Steel. In: Metals Handbook, Vol. 5, 1987, ASM International Materials Park, OH.
4. B. Gaur, T. B. Singh, D. D. N. Singh. Corrosion, 1996. 52(2) p. 154.
5. Ed. E. H. Phelps. The Making Shaping and Treating of Steel. 1971, U.S. Steel Corp. Pittsburgh, PA. p. 802.
6. A. H. Tuthill. Advance Materials and Processes, 1992 (December) p. 34.
7. J. Pilznienski. Acid Cleaning of Iron and Steel, in Metals Handbook Vol. 5. 1987, ASM International Materials Park, OH.
8. ASTM A380-99, "Standard Practice for Cleaning, Descaling and Passivation of Stainless Steel Parts, Equipment and Systems", in Annual Book of ASTM Standards. 1999, ASTM, Philadelphia, PA.
9. G. E. Coates. Materials. Perf., 1990 (August) p. 61.
10. J. Crolet, L. Seraphin, R. Tricot. Mem. Sci. Rev. Met., 1977. 74 p. 647.
11. H. Bohni, T. Suter, A. Schreyer. Electrochim. Acta, 1995. 40(10) p. 1361.
12. H. Bohni, T. Suter, A. Schreyer. Electrochim. Acta, 1997. 42(20–22) p. 3275.
13. T. Suter, T. Peter, H. Bohni. Mater. Sci. Forum, 1995. 192–194 p. 25.
14. T. Suter, H. Bohni. Electrochim. Acta, 1998. 43(19–20) p. 2843.
15. G. Hultquist, C. Leygraf. Corrosion, 1980. 36(3) p. 126.
16. K. Asami, K. Hashimoto. Corrosion Sci., 1979. 19 p. 1007.
17. D. Wallinder. J. Pan, C. Leygraf and A. Delblanc-Bauer, Corrosion Sci., 1999. 41 p. 275.
18. T. Hong, T. Ogushi, M. Nagumo. Corrosion Sci., 1996. 38 p. 881.
19. J. L. Crolet. Corrosion Sci., 1997. 39 p. 1137.
20. J. S. Noh, N. J. Laycock. W. Gao and D. B. Wells, Corrosion Sci., 2000. 42 p. 2069.
21. C. F. Baes, Jr., R. E. Mesmer. Hydrolysis of Cations. 1986, Robert E. Krieger, Malabar, FL. p. 220.
22. H. Bohni, H. H. Uhlig. J. Electrochem. Soc., 1969. 116 p. 906.
23. H. Kaesche. Pitting Corrosion of Aluminum and Intergranular Corrosion of Al Alloys. in Localized Corrosion. 1971. Williamsburg, VA NACE, Houston, TX.
24. F. Hunkeler, H. Bohni. Corrosion, 1981. 37 p. 645.
25. S. T. Pride, J. R. Scully, J. L. Hudson. J. Electrochem. Soc., 1994. 141 p. 3028.
26. G. S. Frankel. Corrosion Sci., 1990. 30 p. 1203.
27. A. Sehgal, D. Lu, G. S. Frankel. J. Electrochem. Soc., 1998. 145 p. 2834.
28. A. Sehgal, G. S. Frankel, B. Zoofan, S. Rokhlin. J. Electrochemc. Soc., 2000. 147 p. 140.
29. J. W. Tester, H. S. Isaacs. J. Electrochem. Soc., 1975. 122 p. 1438.
30. H. S. Isaacs, J.-H. Cho, M. L. Rivers, S. R. Sutton. J. Electrochem. Soc., 1995. 142 p. 1111.
31. R. T. Beck. J. Electrochem. Soc., 1982. 129 p. 2412.
32. P. Heimgartner, H. Bohni. Corrosion, 1985. 41 p. 715.

33. T. R. Beck. Corrosion, 1977. 33 p. 9.
34. G. S. Frankel, A. G. Schrott, A. J. Davenport, H. S. Isaacs, C. V. Jahnes, M. A. Russak. J. Electrochem. Soc., 1994. 141 p. 83.
35. G. S. Frankel, A. J. Davenport, H. S. Isaacs, A. G. Schrott, C. V. Jahnes, M. A. Russak. J. Electrochem. Soc., 1992. 139 p. 1812.
36. E. Akiyama, G. S. Frankel. J. Electrochem. Soc., 1999. 146 p. 4095.
37. M. W. Kendig and R. G. Buchheit. Surface Conversion of Aluminum and Ferrous Alloys for Corrosion Resistance. In Proceedings of the Research Topical Symposium CORROSION/2000. 2000 NACE International.
38. L. Xia, R. L. McCreery. J. Electrochem. Soc., 1998. 145 p. 3083.
39. A. Cusanelli, U. Frey, D. T. Richens, A. E. Merbach. J. Am. Chem. Soc., 1996. 118 p. 5265.
40. D. A. Jones. In: Principles and Prevention of Corrosion. 1992, Prentice Hall, Englewood Cliffs, NJ. p. 190.
41. W. J. Clark, J. D. Ramsey, R. L. McCreery. J. Electrochem. Soc., 2002, 149 (to be published).
42. R. G. Buchheit, P. F. Hlava, B. McKenzie, G. Zender. J. Electrochem. Soc., 1997. 144 p. 2628.
43. G. O. Ilevbare, J. R. Scully. Corrosion, 2001. 57 p. 134.
44. A. J. Bard, L. E. Faulkner. Electrochemical Methods: Fundamental and Applications, 2nd ed. 2001, John Wiley, New York. p. 355.
45. A. J. Bard, L. E. Faulkner. In Electrochemical Methods: Fundamentals and Applications, 2nd ed. 2001, John Wiley, New York. p. 337.
46. S. Wernick, R. Pinner, P. G. Sheasby. The Surface Treatment and Finishing of Aluminum and Its Alloys. 5th ed. 1987, Metals Park, OH. ASM International.
47. S. M. Cohen. Corrosion, 1995. 51 p. 71.
48. B. W. R. Hinton. Metal Finishing, 1991. 89(9) p. 55.
49. B. W. R. Hinton. Metal Finishing, 1991. 89(10) p. 15.
50. R. L. Twite, G. P. Bierwagen. Progress in Org. Coat., 1998. 33 p. 91.
51. MIL-C-5541E, "Chemical Conversion Coatings on Aluminum and Aluminum Alloys." 1990, NAEC Lakehurst, NJ.
52. G. D. Cheever. J. Paint Technol., 1969. 41 p. 259.
53. W. Zhang, B. Hurley, R. G. Buchheit. J. Electrochem. Soc., 2002, 149 (to be published).
54. A. Losch, J. W. Schultze, H.-D. Speckmann. Appl. Surf. Sci., 1991. 52 p. 29.
55. E. Klusmann, U. Konnig, J. W. Schultze. Materials and Corrosion, 1995. 46 p. 83.
56. K. Kiss, M. Coll-Palagos. Corrosion, 1987. 43 p. 8.
57. N. Satoh. Surface and Coating Tech., 1988. 34 p. 331.
58. R. W. Zurilla, V. Hospadaruk. SAE Technical Paper No. 780187, 1978.
59. J. Zhao, G. Frankel, R. L. McCreery. J. Electrochem. Soc., 1998. 145 p. 2258.
60. S. B. Mamidipally, P. Schmutz, R. G. Buchheit. Corrosion, 2002, 58, p. 3.
61. J. R. Macdonald, ed. Impedance Spectrocopy Emphasizing Solid Materials and Systems. 1987, New York, John Wiley.
62. F. Mansfeld. Corrosion, 1981. 36 p. 301.

63. M. W. Kendig, E. M. Meyer, G. Lindberg, F. Mansfeld. Corrosion Sci., 1983. 23 p. 1007.
64. F. Mansfeld, M. W. Kendig, S. Tsai. Corrosion, 1982. 38 p. 570.
65. Gamry Instruments, Inc., EIS Manual. p. p. 2.
66. F. Mansfeld, H. Shih. J. Electrochem. Soc., 1988. 135 p. 906.
67. F. Mansfeld, S. Lin, S. Kim, H. Shih. Corros. Sci., 1987. 27 p. 997.
68. J. R. Macdonald. Solid State Ion., 1984. 13 p. 147.
69. J. H. DeWit, H. J. W. Lenderink. Electrochim. Acta, 1996. 41 p. 1111.
70. H. Schweickert, W. J. Lorenz, H. Friedburg. J. Electrochem. Soc., 1980. 127 p. 1693.
71. I. Epelboin, C. Gabrielli, M. Deddam, H. Takenouti. Electrochim. Acta, 1975. 20 p. 913.
72. M. Keddam, O. R. Mattos, H. Takenouti. J. Electrochem. Soc., 1981. 128 p. 257.
73. M. Kendig, F. Mansfeld. Corrosion, 1983. 39 p. 466.
74. D. D. Macdonald, M. Urquidi-Macdonald. J. Electrochem. Soc., 1985. 132 p. 2316.
75. H. Shih, F. Mansfeld. Corrosion, 1989. 45 p. 325.
76. J. M. Esteban, M. E. Orazem. J. Electrochem. Soc., 1991. 138 p. 67.
77. M. M. Jaksic, J. Newman. J. Electrochem. Soc., 1986. 133 p. 1097.
78. M. Urquidi-Macdonald, S. Real, D. D. Macdonald. J. Electrochem. Soc., 1986. 133 p. 2018.
79. F. Mansfeld, V. Wang, H. Shih. J. Electrochem. Soc., 1991. 138 p. L74.
80. H. Shih, F. Mansfeld. ASTM STP 1134. 1992, ASTM Philadelphia, PA. p. 180.
81. F. Mansfeld, S. Lin, S. Kim, H. Shih. Corrosion, 1989. 45 p. 615.
82. R. G. Buchheit, M. Cunningham, H. Jensen, M. W. Kendig, M. A. Martinez. Corrosion, 1998. 54 p. 61.
83. "Alternatives to Chromium for Metal Finishing." National Center for Manufacturing Sciences, Ann Arbor, MI.
84. Standard Practice for Operating Salt Spray (Fog) Apparatus. In: Annual Book of Standards. 1999, ASTM Philadelphia, PA. p. 1.
85. W. Nelson. In: Accelerated Testing Statistical Models, Test Plans, and Data Analyses. 1990, John Wiley, New York. p. 115.
86. D. M. Himmelblau. In: Process Analysis by Statistical Methods. 1970, John Wiley, New York. p. 27.
87. M. W. Kendig, S. Jeanjaquet, M. Cuinningham. Replacement for Chromate Conversion Coating and Anodization. 1993.
88. G. E. Thompson, Y. Xu, P. Skeldon, K. Shimizu, G. C. Wood. Phil. Mag. B, 1987. 55 p. 651.
89. Y. Xu, G. E. Thompson, G. C. Wood, B. Bethune. Corrosion Sci., 1987. 27 p. 83.
90. L. Young. Anodic Oxide Films. 1971, London, Academic Press.
91. P. Skeldon, K. Shimizu, G. E. Thompson, G. C. Wood. Thin Solid Films, 1985. 123 p. 127.
92. J. E. Norman. Corros. Sci., 1977. 17 p. 39.
93. D. J. Sharp, J. K. G. Panitz. J. Electrochem. Soc., 1980. 127 p. 1412.

94. G. D. Davis, T. S. Sun, J. S. Ahearn, J. D. Venables. J. Materials Sci., 1982. 17 p. 1807.
95. H. Konno, S. Kobayashi, H. Takahashi, M. Nagayama. Corrosion Sci., 1982. 22 p. 913.
96. G. E. Thompson, Y. Xu, P. Skeldon, K. Shimizu, G. C. Wood. In Advances in Localized Corrosion. 1990, NACE Houston, TX. p. 47.
97. J. De Laet, H. Terryn, J. Vereecken. Electrochim. Acta, 1996 p. 1151.
98. D. A. Vermilyea. J. Electrochem. Soc., 1968. 115 p. 177.
99. M. A. Heine, M. J. Pryor. J. Electrochem. Soc., 1967. 114 p. 1001.
100. M. A. Heine, D. S. Keir, M. J. Pryor. J. Electrochem. Soc., 1965. 112 p. 24.
101. A. F. Beck, M. A. Heine, D. S. Keir, D. Van Rooyen, M. J. Pryor. Corrosion Sci., 1962. 2 p. 133.
102. K. Shimizu, G. E. Thompson, G. C. Wood. Electrochim. Acta, 1982. 27 p. 245.
103. T. A. Libsch. J. Electrochem. Soc., 1974. 121 p. 400.
104. J. L. Dawson, G. E. Thompson, M. B. H. Ahmadun. In: ASTM STP 1188. 1993, ASTM Philadelphia, PA. p. 255.
105. J. Hitzig, K. Juttner, W. J. Lorenz. J. Electrochem. Soc., 1986. 133 p. 887.
106. K. Juttner, W. J. Lorenz. Corros. Sci., 1989. 29 p. 279.
107. N. Xu, G. E. Thompson, J. L. Dawson, G. C. Wood. Corros. Sci., 1993. 34 p. 461.
108. N. Xu, G. E. Thompson, J. L. Dawson, G. C. Wood. Corros. Sci., 1993. 34 p. 479.
109. F. Mansfeld, M. W. Kendig. Corrosion, 1985. 41 p. 490.
110. M. Kendig, J. Scully. Corrosion, 1990. 46 p. 22.
111. G. R. T. Schueller, S. R. Taylor. In: Electrochemical Impedance Analysis and Interpretation. 1993, ASTM, Philadelphia, PA. p. 328.
112. P. L. Bonora, F. Deflorian, L. Fedrizzi. Electrochim. Acta, 1996. 41 p. 1073.
113. F. Bellucci, L. Nicodemo. Corrosion, 1993. 49 p. 235.
114. D. M. Brasher, A. H. Kingsbury. J. Appl. Chem., 1954. 4 p. 62.
115. R. E. Touhsaent, Jr., H. Leidheiser. Corrosion, 1972. 28 p. 435.
116. H. Leidheiser, M. W. Kendig. Corrosion, 1976. 32 p. 69.
117. F. Mansfeld, M. W. Kendig, S. Tsai. Corrosion, 1982. 38 p. 478.
118. J. Titz, G. H. Wagner, H. Spahn, M. Ebert, K. Juttner, W. J. Lorenz. Corrosion, 1990. 46 p. 221.
119. H. P. Hack, J. R. Scully. J. Electrochem. Soc., 1991. 138 p. 33.
120. S. Haruyama, T. M. Asari, T. Tsuru. In: Proc. Symp. on Corrosion Protection by Organic Coatings. 1987. The Electrochemical Society, Pennington, NJ.
121. R. Hirayama, S. Haruyama. Corrosion, 1991. 47 p. 952.
122. F. Mansfeld, C. H. Tsai. Corrosion, 1991. 47 p. 958.
123. M. W. Kendig, S. Jeanjaquet, J. Lumsden. In: Electrochemical Impedance Analysis and Interpretation. 1994, ASTM Philadelphia, PA. p. 407.
124. M. W. Kendig. Corrosion, 1991. 47 p. 964.
125. H. S. Isaacs. In: Localized Corrosion. 1974, NACE Houston, TX. p. 158.
126. V. S. Voruganti, D. DeGeer, H. B. Luft, S. A. Bradford. Corrosion, 1991. 47 p. 343.
127. H. S. Isaacs. In: in Localized Corrosion. 1974 Houston, TX. p. 158.

128. I. L. Rosenfeld, I. S. Danilov. Corrosion Sci., 1967. 7 p. 129.
129. A. J. Aldykewicz, H. S. Isaacs, A. J. Davenport. J. Electrochem. Soc., 1995. 142 p. 3342.
130. H. S. Isaacs, A. J. Aldykewicz, D. Thierry, T. C. Simpson. Corrosion, 1996. 52 p. 163.
131. R. S. Lillard, J. Kruger, W. S. Tait, P. J. Moran. Corrosion, 1995. 51 p. 251.
132. R. S. Lillard, P. J. Moran, H. S. Isaacs. J. Electrochem. Soc., 1992. 139 p. 1007.
133. I. Annergren, D. Thierry, F. Zou. J. Electrochem. Soc., 1997. 144 p. 1208.
134. F. Zou, D. Thierry, H. S. Isaacs. J. Electrochem. Soc., 1997. 144 p. 1957.
135. M. W. Wittmann, R. B. Leggat, S. R. Taylor. J. Electrochem. Soc., 1999. 146 p. 4071.
136. R. B. Leggat, S. R. Taylor. Corrosion, 1999. 55 p. 984.
137. A. M. Miersch, J. Yuan, R. G. Kelly, S. R. Taylor. J. Electrochem. Soc., 1999. 146 p. 4449.
138. I. Dehri, R. L. Howard, S. B. Lyon. Corrosion Sci., 1999. 41 p. 141.
139. E. Bayet, F. Huet, M. Keddam, K. Ogle, H. Takenouti. J. Electrochem. Soc., 1997. 144 p. L87.
140. R. A. Cottis. Corrosion, 2001. 73 p. 265.
141. H. Xiao, F. Mansfeld. J. Electrochem. Soc., 1994. 141 p. 2332.
142. A. N. Rothwell, D. A. Eden. CORROSION/92, 1992. Paper no. 223. Houston, TX.
143. G. P. Bierwagen. J. Electrochem. Soc., 1994. 141 p. L155.
144. F. Huet. J. Electrochem. Soc., 1995. 142 p. 2861.
145. C.-T. Chen, B. S. Skerry. Corrosion. 47 p. 598.
146. D. J. Mills, G. P. Bierwagen. Materials Perf., 1995. 34 p. 33.
147. J. L. Dawson. In: in Electrochemical Noise Measurement, ASTM STP 1277. 1996, American Society for Testing and Materials, Philadelphia, PA. p. 3.
148. D. L. Reichert. In: Electrochemical Noise Measurement, ASTM STP 1277. 1996, ASTM, Philadelphia, PA. p. 79.
149. R. G. Kelly, M. E. Inman, J. L. Hudson. In: Electrochemical Noise Measurement, ASTM STP 1277. 1996, American Society for Testing and Materials, Philadelphia, PA. p. 101.
150. V. Brusamarello, A. Lago, C. V. Franco. Corrosion, 2000. 56 p. 273.
151. L. Beaunier, J. Frydman, C. Gabrielli, F. Huet, M. Keddam. In: Electrochemical Noise Measurement, ASTM STP 1277. 1996, ASTM Philadelphia, PA. p. 114.
152. F. Mansfeld, H. Xiao. In: Electrochemical Noise Measurement, ASTM STP 1277. 1996, ASTM, Philadelphia, PA. p. 59.
153. G. P. Bierwagen, C. S. Jeffcoate, S. Balbyshev, J. Li, D. E. Tallman, D. J. Mills. Progress in Org. Coat., 1996. 29 p. 21.
154. F. Mansfeld, H. Xiao, L. T. Han, C. C. Lee. Progress in Org. Coat., 1997. 30 p. 89.
155. F. Mansfeld, L. T. Han, C. C. Lee. J. Electrochem. Soc., 1996. 143 p. L286.
156. R. Mansfeld, H. Xiao. J. Electrochem. Soc., 1993. 140 p. 2205.
157. U. Bertocci, F. Huet, B. Jaoul, P. Rousseau. Corrosion, 2000. 56 p. 675.
158. D. A. Eden. J. Electrochem. Soc., 1994. 141 p. 1402.

159. U. Bertocci, C. Gabrielli, F. Huet, M. Keddam, and P. Rousseau. J. Electrochem. Soc., 1997. 144 p. 37.
160. U. Bertocci, C. Gabrielli, F. Huet, M. Keddam. J. Electrochem. Soc., 1997. 144 p. 31.
161. F. Mansfeld, C. C. Lee. J. Electrochem. Soc., 1997. 144 p. 2068.
162. A. Aballe, A. Abutista, U. Bertocci, F. Huet. Corrosion, 2001. 57 p. 35.

9
Experimental Procedures

LABORATORY I

PART A: GALVANIC SERIES AND REFERENCE ELECTRODES

A. Objective

In this laboratory, you will construct a number line for reference electrode conversions, measure the corrosion potentials of several alloys in a salt water solution, construct a galvanic series with two different reference electrodes, and convert the two galvanic series to the NHE scale to determine if they agree (as they should). This lab will demonstrate some of the concepts discussed in Chapter 2.

B. Experimental Procedure

1. When you enter the laboratory, first check that you have the following:

A container of 3.5 wt% NaCl in water with five electrodes already immersed
A saturated calomel reference electrode (SCE)
A mercury/mercurous sulfate (Hg/Hg_2SO_4) reference electrode
A voltmeter

The five electrodes in solution will be AISI 1020 carbon steel, tin graphite, an aluminum alloy, and 303 stainless steel. The SCE has a potential of $+0.241$ V_{NHE}, whereas the Hg/Hg_2SO_4 has a potential of $+0.400$ V_{SCE}.

2. Construct a number line with units of volts vs. NHE and indicate the position of the SCE on it. Next, measure the potential of the Hg/Hg_2SO_4 electrode relative to the SCE in the salt solution with the voltmeter. Remember that, in this case, the SCE is the reference electrode, so it should be connected to the negative lead (or common) of the voltmeter. Convert the Hg/Hg_2SO_4 potential vs. SCE to the proper potential vs. NHE. Now, using the number line to help

you, indicate the position of the Hg/Hg_2SO_4 reference electrode on the number line.

3. Measure the open circuit potential of each of the five electrodes relative to the SCE and record these values in the table provided under Results. Convert each of these to the NHE scale with the help of the number line. Now, measure the corrosion potential of each of the five electrodes relative to the Hg/Hg_2SO_4 and record these values in the table. Convert each of these to the NHE scale with the help of the number line. Compare the values of each of the electrodes vs. NHE as determined by the two different reference electrodes. It should not make any difference which reference electrode was used, as a reference electrode is simply a reference point or benchmark.

4. A standard electrode potential series consists of equilibrium potentials, not corrosion potentials as you have been measuring in this laboratory. These potentials are usually referenced to NHE but could be referenced to any reference electrode system. How would you convert a standard electrode potential series from V_{NHE} to V_{SCE}?

5. Note the potentials of the graphite and the aluminum alloy that you determined. If these two are connected with an electrical contact, their potentials should move toward each other. Further, since the solution is relatively conductive, and assuming that the electrical lead connecting them was highly conductive, they would come to the same potential. Therefore connect the leads of the two electrodes together and connect them both to the positive (or V) lead of the voltmeter. Measure the potential of this galvanic couple relative to one of the reference electrodes and confirm that the couple potential does indeed rest somewhere in between the corrosion potentials of the two materials.

C. Results

Potential of Hg/Hg_2SO_4 relative to SCE:

Material	E_{corr} (V_{SCE})	E_{corr} (V_{NHE})	E_{corr} (V_{Hg/Hg_2SO4})	E_{corr} (V_{NHE})

Potential of 7075-T76 aluminum coupled to graphite: _____

Number lines:

(vs. NHE)

_____

(vs. SCE)

_____

D. Sample Results

Potential of Hg/Hg_2SO_4 relative to SCE: 0.400 V

Material	E_{corr} (V_{SCE})	E_{corr} (V_{NHE})	E_{corr} ($V_{Hg/Hg2S04}$)	E_{corr} (V_{NHE})
Graphite	0.227	0.468	−0.189	0.468
303 SS	−0.375	−0.134	−0.771	−0.134
Tin	−0.650	−0.409	−1.049	−0.409
1020 steel	−0.702	−0.461	−1.103	−0.461
AA 7075	−0.778	−0.537	−1.180	−0.537

LABORATORY I

PART B: POLARIZATION CURVES

In this experiment, polarization curves for carbon steel and copper in 3.5 wt% NaCl will be determined. From these data, the corrosion rates will be estimated for the individual metals freely corroding in solution and for the metals electrically coupled in solution as would be the case for an immersed, riveted connection, for example.

A. Background

Potentiostatic polarization is widely used to determine the steady-state corrosion behavior of metals and alloys as a function of potential in environments of interest. This technique involves holding a specimen's surface at a series of constant potentials versus a reference electrode, and then measuring the current necessary to maintain each of the applied potentials. From this dependence of the current on the applied potential of the sample, a number of parameters important for understanding the corrosion behavior of the material in the environment (such as i_{corr}, b_a, and b_c) can be determined as pointed out in Chapter 2.

It is important to remember that the measured current is the applied current, defined as

$$i_{app} = i_a - i_c \tag{1}$$

where

i_{app} = applied current
i_a = total anodic current
i_c = total cathodic current

Thus at potentials close to the corrosion potential, i_{app} is very small, since i_a and i_c are very close in magnitude. Note that this is true even if i_a and i_c are themselves large in magnitude. However, at large anodic overpotentials, i_a is much larger than i_c, and therefore i_{app} approaches i_a. Conversely, at large cathodic overpotentials, i_c is much larger than i_a, and i_{app} approaches i_c. By determining the Tafel slopes of the reaction in these regions, an estimate of the corrosion rate can be performed by Tafel extrapolation as demonstrated in Chapter 2. In addition, the "hidden" portions of the anodic and cathodic lines can also be estimated by continuing the Tafel lines back to the reversible potentials of the reactions. In this way, an estimate of the oxidation rate of the material can be made at any given cathodic protection potential. This estimate can be of great importance where information on the level of cathodic protection necessary to reduce the corrosion rate of a material must be made in a short time. As was pointed out in Chapter 2 and will be seen in this experiment, care must be taken in interpreting the results of extrapolating the behavior to service times longer than the duration of the experiment.

The importance of area ratios in discussing galvanic corrosion cannot be overemphasized. Because charge (and therefore current) is conserved, our analysis of the galvanic couple of copper and steel will focus on studying E vs. log I (current) plots rather than the more traditional E vs. log i (current density) plots. Because the specimens will have different geometric areas, it will be important to keep this in mind during the analysis section of the laboratory session. By plotting the data initially in the E vs. log I format, the "natural" coordinate system

of galvanic corrosion, an understanding of the system behavior can be obtained. When the materials are coupled, they will come to the same potential and will pass a current of the same magnitude through their exposed surfaces. The current densities will, of course, be different if the specimens have different exposed areas. However, because current is conserved, it is from this vantage point that the analysis must begin. After determining the corrosion current for each specimen at their respective open circuit potentials and at the couple potential, a corrosion current density and then a penetration rate can be calculated knowing the exposed areas and material properties (density, molecular weight, number of electrons transferred, etc.) through the use of Faraday's law, as discussed in Chapter 1.

USEFUL INFORMATION

Areas of Working Electrodes

Carbon steel: 3.8 cm^2

Copper: 2.8 cm^2

Atomic Mass of Materials

Carbon steel: 55.85 g/mol

Copper: 63.55 g/mol

Density

Carbon steel: 7.8 g/cm^3

Copper: 8.96 g/cm^3

Dissolution Reactions

$Cu \rightarrow Cu^{2+} + 2e^-$

$Fe \rightarrow Fe^{2+} + 2e^-$

B. Experimental Procedure

There are two types of potentiostat setups in the laboratory, and each requires a different procedure to perform a potentiostatic polarization. Determine which type of potentiostat (PAR 273 or VersaStat) is at your station and use the appro-

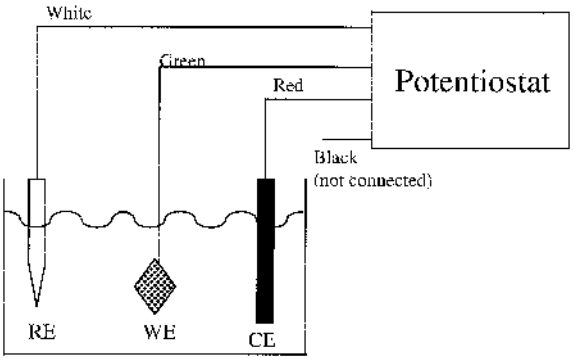

RE = Reference Electrode (SCE) connected to white pin connector
WE = Working Electrode
CE = Counter Electrode (Graphite Rod) connected to red lead

Figure 1 The wiring diagram for connecting the experimental cell electrodes to the potentiostat.

priate procedure described below. If you have trouble identifying the type of potentiostat ask a lab assistant to figure it out.

1. To apply a potential using the VersaStat or PAR 273 potentiostat:
   a. Connect the working electrode (green lead) to the sample to be polarized (either the carbon steel or copper). Connect the counter electrode (red lead) to the graphite rod. Use the calomel electrode as the reference and connect it to the white Reference jack on the electrometer.
   b. Turn the VersaStat or PAR 273 power ON. For the VersaStat make sure the potentiostat/galvanostat toggle switch is in the potentiostat position.
   c. Turn the VersaStat cell on by pressing the button labeled "Cell Switch" until the red light comes on. For the PAR 273, press the "Cell Enable" button. This button should now display the word ON.

NOTE: THE CELL IS NOW "HOT." DO NOT TOUCH ANY LEAD WITHOUT TURNING THE CELL OFF. IT IS TURNED OFF BY PUSHING THE CELL SWITCH SO THAT THE WORD *OFF* IS DISPLAYED.

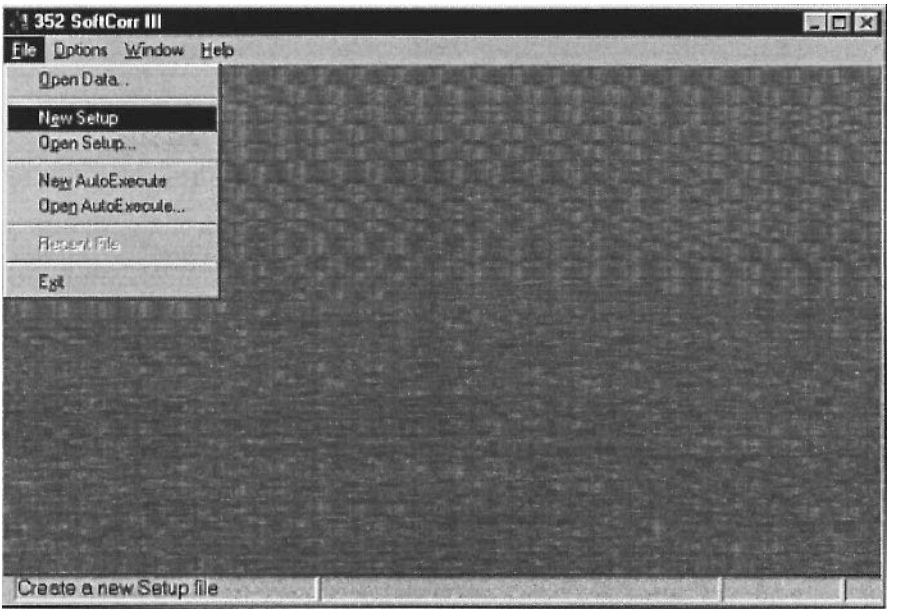

Figure 2 The opening window for PARC 352 SoftCorr III. Begin a new experimental setup by choosing New Setup.

d. Both the VersaStat and the PAR 273 are controlled by the accompanying computer and PAR 352 software. Select **NEW SETUP** (or type "e") from the **FILE** menu to begin a new experimental setup.
e. Select the **POTENTIOSTATIC** option under the **TECHNIQUE** menu.
f. Enter the potential to be applied by clicking on the **INITIAL POT**. Dialog box. At the prompt enter a potential from Table 1 from the following "Results and Data Analysis Section."
g. To run the experiment select the **RUN** option by clicking on the button or by pressing "R". If the prompt **Save Data, Results &/or Labels? Pstat #1** appears, choose NO. Once the potential is applied, the current, potential, and time will appear in the upper left-hand corner of the computer screen. Wait for a stable current and record on the worksheet. This process will take about 5 minutes at each potential. If, at the end of 5 minutes, the current has not stabilized, take a reading and move to the next potential.
h. Stop the experiment after the current has been recorded by selecting **STOP** (press "S") under the **EXPERIMENT** menu.

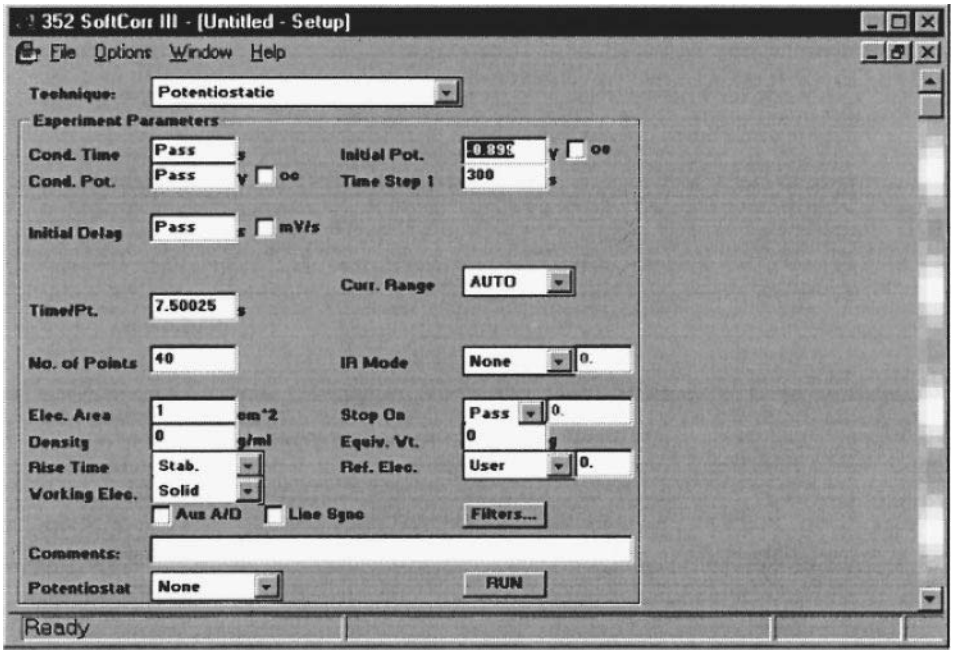

Figure 3 The experimental setup window showing the potentiostatic technique option.

i. A graph of current vs. time will appear on the screen. Current values may be obtained by selecting **CURVE CURSOR** under the **CURVE** option of the **VIEW** menu and recording the final value shown at the bottom of the screen. Values may also be obtained from the data table at the far right side of the window. The table can be accessed by selecting **DATA TABLE** under the **VIEW** menu.

j. Return to the setup menu by closing the data file; choose **CLOSE** under the **FILE** menu. To apply the next potential repeat steps **e** through **h**.

k. After all potentials for a given specimen have been applied, turn the potentiostat cell off by pressing the "cell switch" so that the word OFF is displayed.

2. Measure the short-circuit current between the steel and copper. This current measured represents the current that would flow between the two materials if they were in electrical contact with one another in the saltwater environment.

   a. Connect one specimen to the CE and RE leads and the other to the working electrode lead.

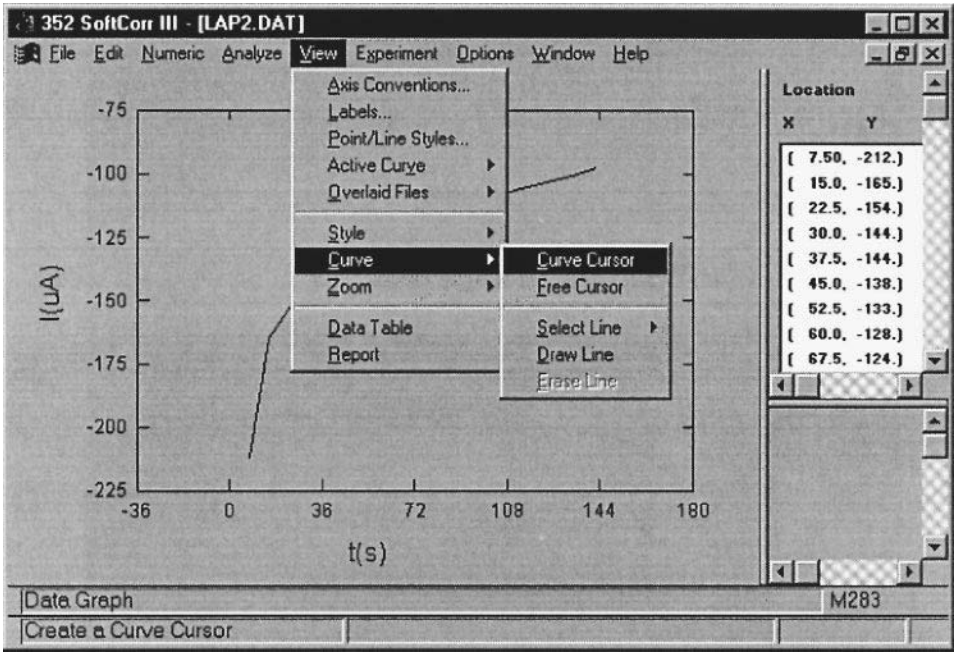

Figure 4 A potentiostatic scan on steel. Data can be viewed from the graph and curve cursor or from the data table.

b. Apply zero volts between the working and reference electrodes.
c. The applied current is the short circuit current. Record the result.

3. Measure the potential of the couple versus the SCE reference electrode.
   a. **MAKE SURE THE POTENTIOSTAT IS NOT "HOT."** For the 273 press the "CELL ON" and "CELL ENABLE" buttons so that they are unlit. For the VersaStat push the "CELL SWITCH" so that the word OFF is displayed.
   b. Use a wire with alligator clips to electrically connect the steel to the copper.
   c. Use the digital voltmeter (DVM) to measure the potential of the couple vs. the SCE reference electrode and record the result.

C. Results and Data Analysis

Areas of working electrodes:

Copper: _____ cm^2 E_{corr} = _____ V_{SCE}

Carbon steel: _____ cm^2 E_{corr} = _____ V_{SCE}

Table 1 Potential-Current Data from Polarization Experiment

Carbon steel		Copper	
Potential (V vs SCE)	Current	Potential (V vs SCE)	Current
−0.900		−0.500	
−0.850		−0.450	
−0.800		−0.400	
−0.750		−0.350	
−0.700		−0.300	
−0.675		−0.250	
−0.650		−0.225	
−0.625		−0.200	
−0.600		−0.175	
		−0.150	

E_{couple} = _____ V_{SCE} I_{couple} = _____ μA

D. Analysis

From the plots of E vs. log I for steel and zinc that you have generated:

I_{corr}(Carbon steel) = _____ μA I_{corr}(Copper) = _____ μA

i_{corr}(Carbon steel) = _____ μA/cm^2 i_{corr}(Copper) = _____ μA/cm^2

Corr. rate (Carbon steel) in mpy:

Corr. rate (Copper) in mpy:

From the Nernst equation calculate the reversible potential for copper in a neutral solution containing 10^{-6} mol/L Cu^{2+}. Plot this value on your E vs. log I curve.

E_r(Cu/Cu^{2+}): _____ mV (vs. SCE)

From the direct coupling of the steel and copper:

i_{couple}(Carbon steel) = _____ μA/cm^2 i_{couple}(Copper) = _____ μA/cm^2

Corr. rate (Carbon steel) in mpy: _____

From extrapolation of the cathodic portion of the copper to E_{couple}:

$I_{Fe/Fe++}(E = E_{couple})$ = _____ μA

$i_{Fe/Fe++}(E = E_{couple})$ = _____ μA/cm^2

Corr. rate of steel at E_{couple} (in mpy): _____

$$\text{RECALL: MPY} = \frac{0.129 * Ai}{nD}$$

A = atomic weight
i = corrosion rate ($\mu A/cm^2$)
D = density (g/cm^3)

E. Questions

1. What are the anodic and cathodic reactions observed for each electrode material?
2. Calculate the corrosion rate for the carbon steel when it is coupled to the copper. Express the results in both $\mu A/cm^2$ and mpy.
   Assume that
   a. The self-corrosion of the anode is negligible.
   b. The galvanic current measured is due solely to the oxidation of the anode.
   c. Your measurements reflects the steady-state condition.
   d. All corrosion is electrochemical (e.g., there is no appreciable grain fall-out).
3. Which of the assumptions in question 2 do you think is the best? Which is the worst?
4. Prove that when coupled to steel the corrosion rate of copper is zero. Assume that the concentration of copper ions in solution is 10^{-6}.
5. Estimate the corrosion rate of the copper under freely corroding conditions and when it is coupled to the steel by extrapolating the anodic portion of the copper polarization curve to E_{couple}. Compare these oxidation rates. Why can't either rate be measured directly?
6. Compare values of E_{couple} and I_{couple} for a 1:1 cathode-to-anode area ratio to the values calculated with a 1000:1 copper-to-steel area ratio. What is the dissolution rate of copper at this area ratio?
7. An interesting exercise is to try to generate Evans diagrams for the copper and steel (mostly Fe) from theoretical data (i.e., reversible potentials, exchange current densities, Tafel slopes, expected limiting currents, etc.) and compare to the experimental data obtained.

F. Significant Observations

Figure 5 and Table 3 show typical data for the specimens studied. These data can be compared with those experimentally generated to get an idea of the degree of variability. It should be noted that very few experimental variables, such as degree of aeration, surface finish, or temperature, were controlled to any great

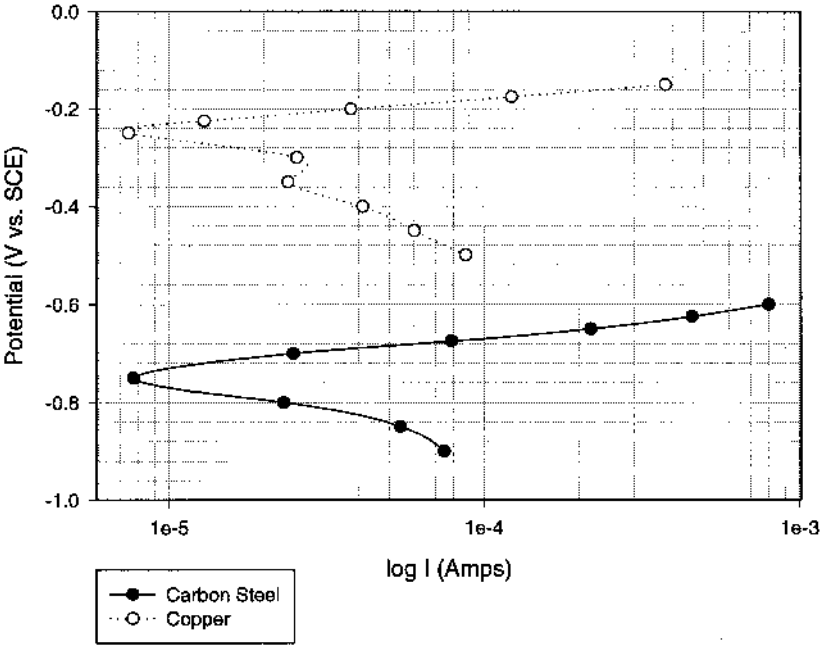

Figure 5 Sample polarization curves for copper and steel samples.

extent in these experiments. In general, such variables (and others) should be considered in the experimental design in order to make the testing as relevant as possible to the service conditions of interest.

There are a number of significant observations which should have been made during this experiment. First, the relative corrosion potentials of the steel and the copper should be noted. These would be the potentials that would be included in a galvanic series of materials in 3.5% NaCl, if that were our intention. Simply on this basis, it can be seen that while steel has the possibility of acting as a sacrificial anode for copper, copper cannot do so for steel. In addition, the potentials are well separated in this environment (approximately 0.4 V), giving further evidence that, for most kinetic schemes found experimentally, there is a significant driving force available to reduce the corrosion rate of copper by coupling to steel. With respect to the E_{corr} measurements made in this experiment, the short period of time used to allow for attainment of steady state must be kept in mind when trying to extrapolate the behavior found to service conditions. It is usually feasible to allow longer exposure times before conducting the polarization experiments in order to develop a situation at the interface that is more relevant.

Table 2 Sample Potential-Current Data from Polarization Experiment

Carbon Steel		Copper	
Potential (V vs SCE)	Current	Potential (V vs SCE)	Current
−0.900	−7.46e-5	−0.500	−87.6e-6
−0.850	−5.42e-5	−0.450	−60.0e-6
−0.800	−2.3e-5	−0.400	−41.2e-6
−0.750	7.71e-6	−0.350	−23.8e-6
−0.700	2.47e-5	−0.300	−25.4e-6
−0.675	7.88e-5	−0.250	7.44e-6
−0.650	2.19e-4	−0.225	1.29e-5
−0.625	4.58e-4	−0.200	3.78e-5
−0.600	8.04e-4	−0.175	1.23e-4
		−0.150	3.78e-4

E_{couple} = _____ V_{SCE} I_{couple} = _____ μA

In analyzing the polarization data, it can be seen that the cathodic reaction on the copper (oxygen reduction) quickly becomes diffusion controlled. However, at potentials below −0.4 V, hydrogen evolution begins to become the dominant reaction, as seen by the Tafel behavior at those potentials. At the higher anodic potentials applied to the steel specimen, the effect of uncompensated ohmic resistance (IR_{ohmic}) can be seen as a "curving up" of the anodic portion of the curve.

Finally, the increase in the corrosion rate of the steel and the reduction of the corrosion rate of the copper upon coupling can be easily seen in the results; they demonstrate the usefulness of cathodic protection and the detrimental effect of improper control of galvanic couple corrosion.

G. Results and Data Analysis

Areas of working electrodes:

Copper: 2.8 cm^2 E_{corr} = −264 V_{SCE}

Carbon steel: 3.8 cm^2 E_{corr} = −684 V_{SCE}

H. Analysis

From the plots of E vs. log I for steel and zinc that you have generated:

I_{corr}(Carbon steel) = 32 μA I_{corr}(Copper) = 24 μA

i_{corr}(Carbon steel) = 8.42 μA/cm^2 i_{corr}(Copper) = 8.6 μA/cm^2

Corr. rate (Carbon steel) in mpy: 3.88

Corr. rate (Copper) in mpy: 3.93

From the direct coupling of the steel and copper:

i_{couple}(Carbon steel) = 2.62 μA/cm^2 i_{couple}(Copper) = 3.56 μA/cm^2

Corr. rate (Steel) in mpy: 1.20

From extrapolation of the cathodic portion of the copper to E_{couple}:

$I_{Fe/Fe++}(E = E_{couple})$ = 2.8e2 μA

$i_{Fe/Fe++}(E = E_{couple})$ = 73.7 μA/cm^2

Corr. rate of steel at E_{couple} (in mpy): 34.3

$$\text{RECALL: MPY} = \frac{0.129 * Awi}{nD}$$

Aw = atomic weight
i = corrosion rate (μA/cm^2)
D = density (g/cm^3)

LABORATORY II

LOCALIZED CORROSION

A. Objective

The goals of this laboratory session are to introduce you to potentiodynamic polarization measurements for the determination of localized susceptibility, demonstrate the effect of the presence of non-Cl^- ions on pitting, and present examples of metastable pitting (one type of "electrochemical noise").

B. Experimental Procedure

Cell connections for all tests are as follows (see Fig. 6):

1. Green lead: connect to the working electrode (302SS wire loop).
2. Red lead: connect to the counter electrode (graphite).
3. Black lead: not connected.
4. RE pin connector: connect to the reference electrode (SCE).

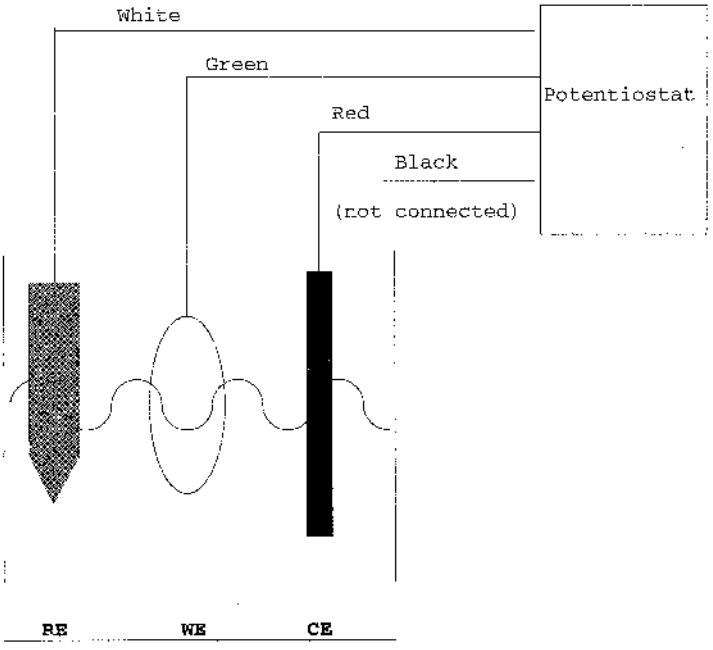

Figure 6 Cell connections for Lab II.

You have been provided with five 302 stainless steel wire loops and strips of 600 grit sand paper. Prior to each test, lightly polish the loops to remove any dirt and oil that may be present due to handling. Do not touch the loop with your hands; use disposable gloves. This is very important!

Test 1: Cyclic Polarization of 302SS in 1000 ppm (0.017 M) NaCl

In this first experiment you will run a standard cyclic polarization curve on stainless steel.

1. Partially immerse one loop into 1.5 L of 1000 ppm NaCl solution. This loop will serve as the working electrode. Do not immerse the entire loop. Make sure that the windings do not enter the solution.
2. Select FILE, NEW SETUP from the top of the window. Press the arrow next to TECHNIQUE and select ECORR VS. TIME. Set TIME STEP 1 to "**300**" seconds and TIME/PT. to "**1**" second. Your setup window should look like the

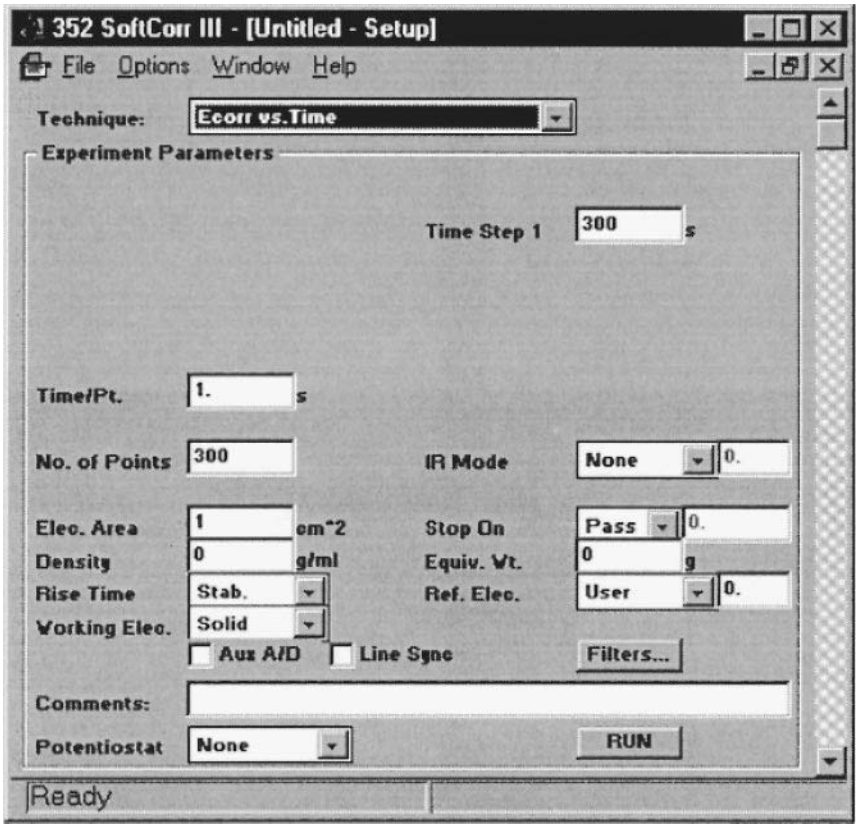

Figure 7 Example of screen setup to measure open circuit.

one shown in Fig. 7. Select the RUN button. Record the final value for the potential in the table provided. You will know the scan is completed when the words DATA GRAPH appear in the lower left corner of the window.

3. Select FILE, NEW SETUP from the top of the window. Press the arrow next to TECHNIQUE and select CYCLIC POLARIZATION. You will now have on display the setup menu for the experiment.
   a. Select INITIAL POT. and enter "**−.300**" (this will begin the scan at −0.300V vs SCE).
   b. Select VERTEX 1 POT. and enter "**0.1**."
   c. Select FINAL POT. and enter "**0.050**." Click on the box next to OC so that a check mark appears. This means that the current is measured versus the open circuit.

d. Select I THRESHOLD and enter "**2e-3**" A/cm^2.
e. Select SCAN RATE and enter "**1**" mV/s.
f. Add the appropriate information for the Density ("**7.94**" g/cc), Equiv. Wt. ("**25**"), Elec. Area ("**0.4**" cm^2) and Ref. Elec ("**SCE**"). The setup window should look like the one in Fig. 8 below.
g. Switch the Cell Enable Key "ON" on the potentiostat. Select RUN and the experiment will start. "SETTING UP EXPERIMENT" and then "RUNNING EXPERIMENT" will appear on the lower left corner of the window. (This scan will take approximately half an hour.)
h. The end of the experiment is indicated by the signal "DATA GRAPH" on the lower left corner. Press the Cell Enable Switch to "OFF." Select FILE, SAVE to save the data as a "**.dat**" file.

4. From the resulting curve, determine E_{bd}, E_{repass}, and i_{pass}. (See Fig. 14 at the end of this write-up.)

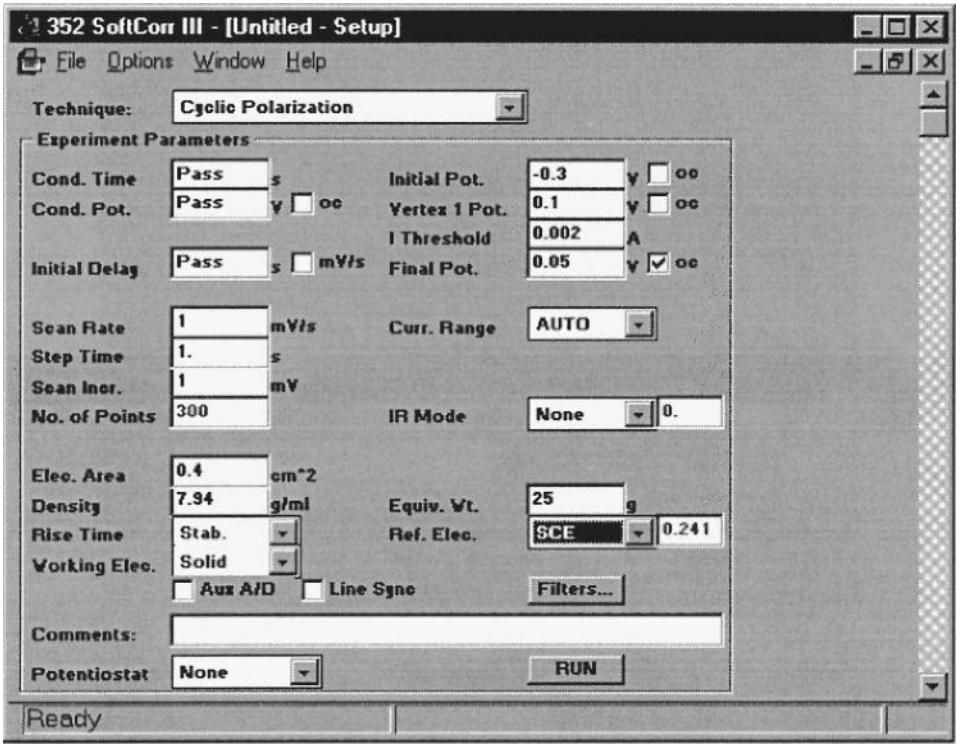

Figure 8 Example of screen setup to run cyclic polarization as in Test 1.

Test 2: Determination of E_{repass} Using Electrochemical Scratch

From an engineering perspective, the repassivation potential is a more important parameter than the potential for pit nucleation. We want to know the potential below which pits will not grow. This is analogous in theory to measuring K_{IC} or K_{ISCC} in mechanical and SCC testing. One way to test this is to produce a completely bare surface that is dissolving rapidly, and determine at what potential it can repassivate. An easy way to do this is what may be termed an "electrochemical scratch."

1. Partially immerse a **new** polished loop (working electrode) in 1000 ppm NaCl. Do not use the loop from the previous experiment.

2. Select FILE, NEW SETUP from the top of the window. Press the arrow next to TECHNIQUE and select ECORR VS. TIME. Set TIME STEP 1 to "**300**" seconds and TIME/PT. to "**1**" second. Select the RUN button. Record the final value for the potential in the table provided.

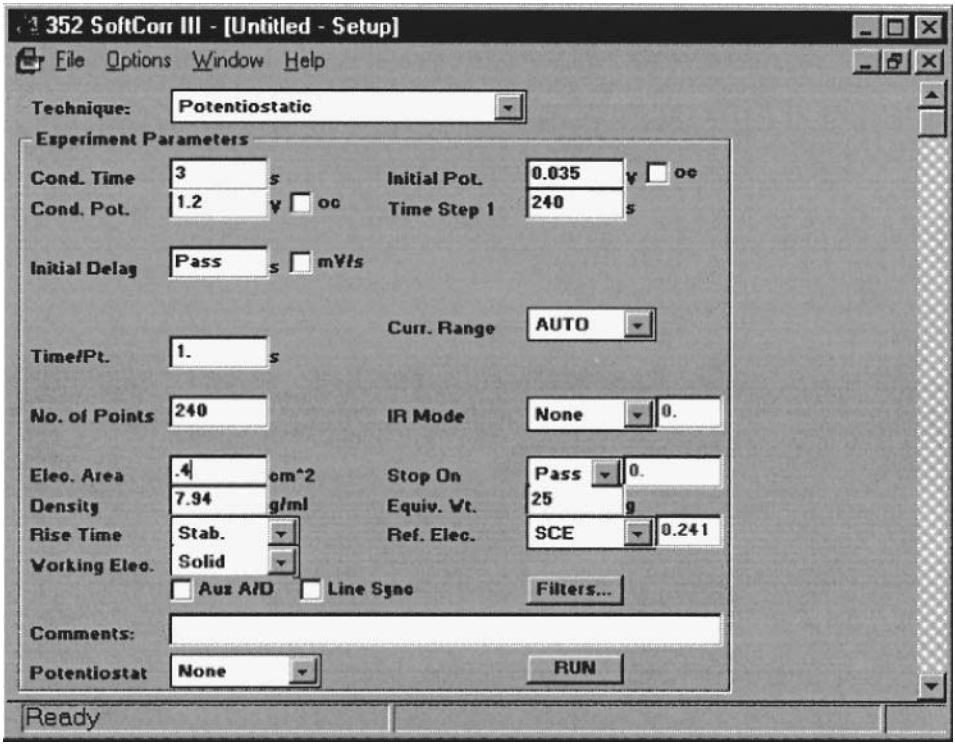

Figure 9 Example of screen setup to run potentiostatic holds as in tests 2 and 3.

3. Using the POTENTIOSTATIC technique, you will sequence through a series of increasing applied potentials while monitoring the current.

4. Perform the following:

a. Select FILE, NEW SETUP from the top of the window. Press the arrow next to TECHNIQUE.

b. Select POTENTIOSTATIC from the menu.

c. You will now see the setup sheet for the potentiostatic experiment. Select INITIAL POT. and enter "**0.035**" to apply +35 mV vs SCE to the sample.

d. Select TIME STEP 1 and enter "**240**" seconds.

e. Select TIME/PT. and enter "**1**" second.

f. Select COND. POT. and enter "**1.2**" V.

g. Select COND. TIME and enter "**3**" seconds.

h. Add appropriate information for Density, Equiv. Wt., and Ref. Elec. (See 3f in Test 1) The setup window should look like the one in Fig. 9.

i. Press the Cell Enable Switch to "ON."

j. Select RUN. Click on DISPLAY to view the progress of the experiment.

k. Save the data using FILE, SAVE.

l. Go to the MAIN Menu to GRAPH the data.

m. If the current is observed to be rising after 240 seconds, you can stop the experiment. If not, go to the FILE Menu and select SETUP. Change INITIAL POT. by +0.05 V and repeat steps 4j through 4m. Observe the current in each case. Record the last potential for which the current was not rising after 240 seconds.

n. Press the Cell Enable Switch to "OFF."

Test 3: Potentiostatic Holds on 302SS—Metastable Pitting

In class, we discussed metastable pitting, and you may have seen some indications of it in some of the previous tests. The easiest way to see metastable pits is to perform potentiostatic holds at potentials just below the pitting potential. In order to reduce our background current, as well as provide a baseline, we will first grow the passive film at a low potential before moving it to a potential where metastable pitting can be observed. Finally, we will polarize just above the pitting potential to see the induction time and the similarity between metastable and stable pits.

1. Partially immerse a fresh wire loop electrode in 1000 ppm NaCl solution.

2. Perform the following:

a. Select FILE, NEW SETUP from the top of the window. Press the arrow next to TECHNIQUE.

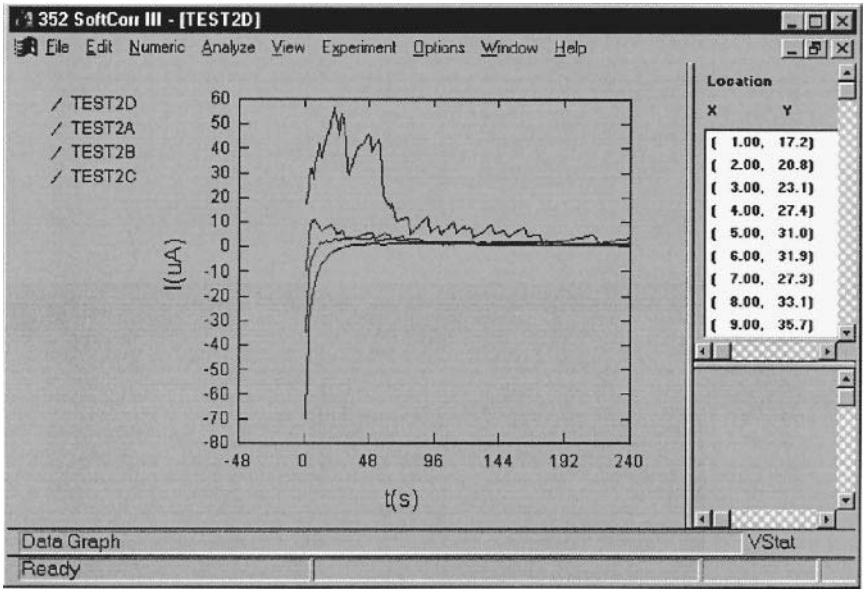

Figure 10 Data obtained in test 2 showing potentiostatic holds at four different potentials after electrochemical scratch.

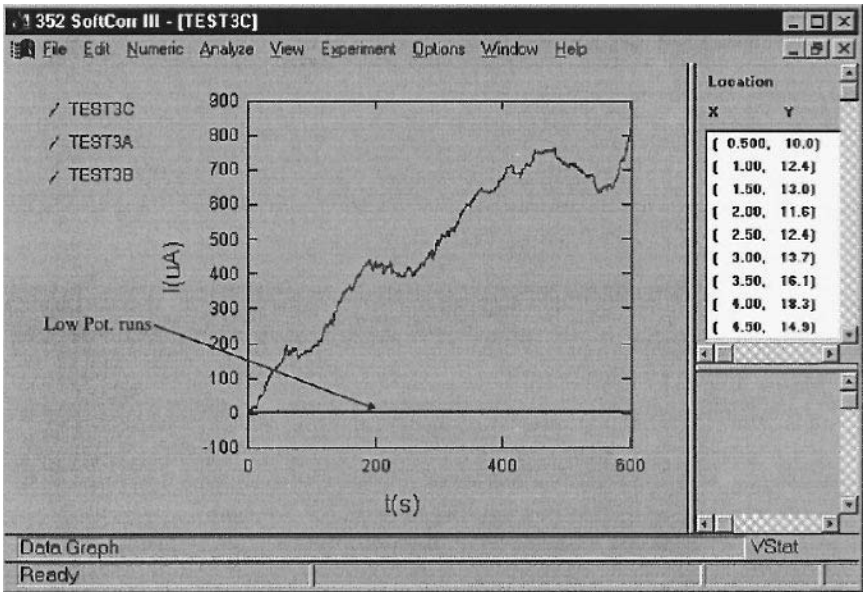

Figure 11 Data obtained from potentiostatic holds in test 3. This shows the final run where active pitting occurs.

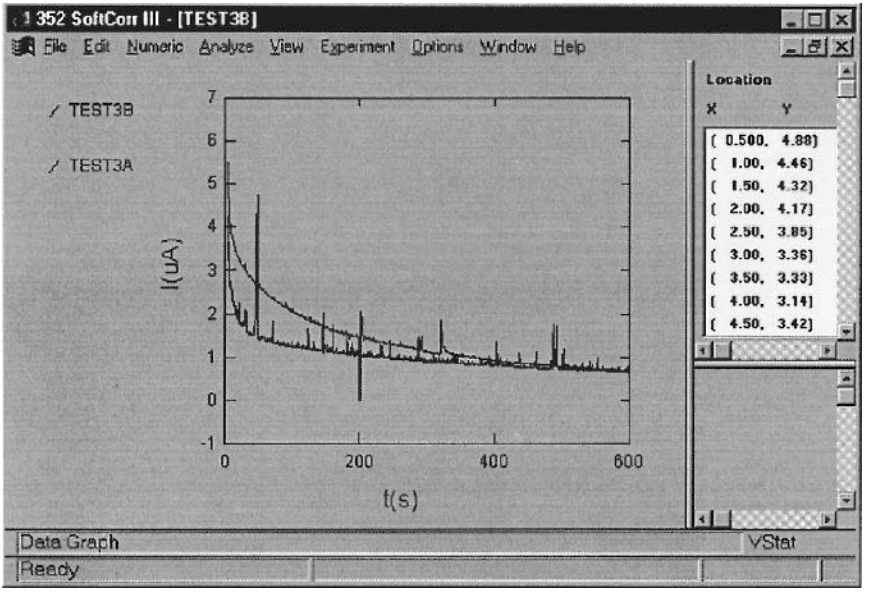

Figure 12 Data from the first two potentiostatic holds in test 3 showing metastable pitting.

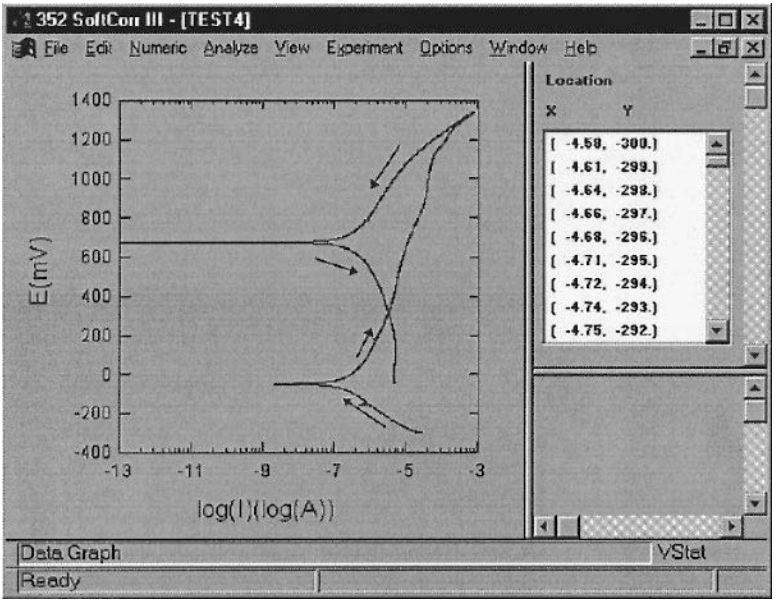

Figure 13 Data from test 1 taken in 1000 ppm NaCl + 9650 ppm Na2SO4. Sample is 302SS and scan rate is 2.5 mV/sec. Arrows indicate scan direction.

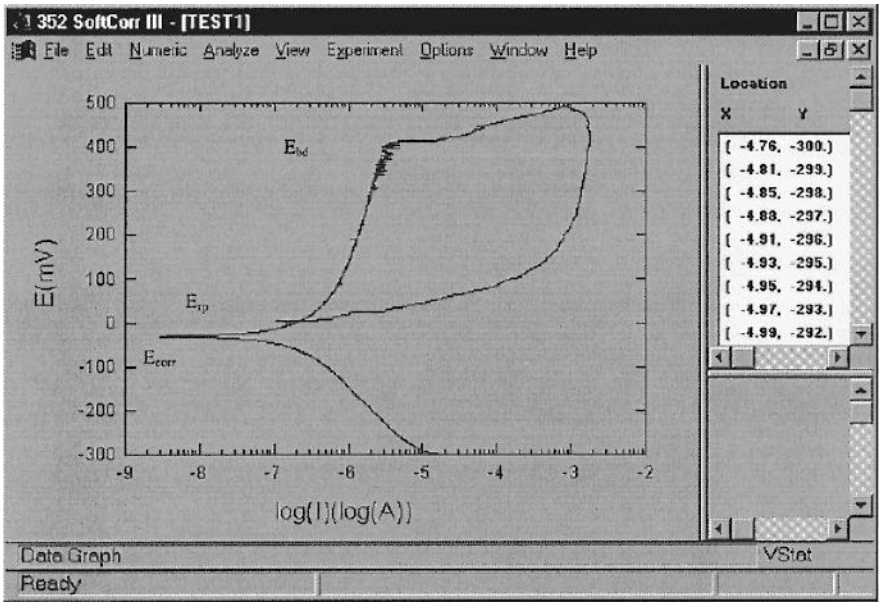

Figure 14 Data from test 1 taken in 1000 ppm NaCl. Sample is 302SS and scan rate is 1.0 mV/sec.

b. Select POTENTIOSTATIC.
c. Select TIME STEP 1 and enter "**1200**" seconds. Select TIME/PT. and enter "**1**" second. Select INITIAL POT. and enter "**0.00**" volts. Make sure that there is no condition potential or condition time entered.
d. Add the appropriate information for Density, Equiv. Wt, Elec. Area, and the Ref. Elec. as given in 3f of Test 1. Save the setup by selecting FILE, SAVE and entering a file name **(.set)**.
e. Press the Cell Enable Switch to ON to activate the Cell. After the run is complete, save the data (SAVE option under FILES Menu, "**.dat**" form).
f. Click on FILE, OPEN, and the file name for your setup. Change Initial Pot. to "**0.250**" V and TIME STEP 1 to "**600**" seconds. Run the experiment as in 2e.
g. Repeat the experiment (see 2f) for Initial Pot. = "**0.350**" V.
h. Repeat the test (see 2f) for Initial Pot. = "**0.450**" V. Stop the experiment when the current reaches 200 $\mu A/cm^2$. Press the Cell Enable Switch to OFF to deactivate the cell.

Test 4: Cyclic Polarization of 302SS in 1000 ppm (0.017 M) NaCl + 9650 ppm (0.068 M) Na_2SO_4

The fourth experiment shows the effect of supporting electrolyte. The aggressive local chemistry cannot develop because sulfate dominates the transport into any incipient pits.

1. Partially immerse a new wire loop in the 1000 ppm NaCl + 9650 ppm Na_2SO_4 solution. Use the counterelectrode to completely mix the solution.
2. Select FILE, NEW SETUP from the top of the window. Press the arrow next to TECHNIQUE and select ECORR VS. TIME. Set TIME STEP 1 to "**300**" seconds and TIME/PT. to "**1**" second. Select the RUN button. Record the final value for the potential in the table provided.
3. Follow the instructions in Test 1, steps 3a through 3g, with the exception of changing the SCAN RATE from 1 mV/s to "**2.5**" mV/s.
4. From the resulting curve, determine E_{bd}, E_{rp}, and i_{pass}.

C. Significant Observations

These tests focused on the determination of a materials resistance to localized (pitting) corrosion. To accomplish this goal, three types of electrochemical experiments were conducted (cyclic polarization, electrochemical scratch, and potentiostatic holds) to measure several key parameters associated with pitting corrosion. These parameters were the breakdown potential, E_{bd}, the repassivation potential, E_{rp}, and the passive current density, i_{pass}.

The initially cathodic current in test 2 is due to the reduction of the oxygen evolved during the pulse portion of the test. When the voltage is pulsed to 1.2 volts, oxygen is evolved. When the potential is held at the lower voltages, the solution closest to the interface is now saturated. The total current is cathodic while this oxygen is reduced.

Two main points should be remembered from this lab. First, the breakdown potential is not necessarily the best measurement of pitting resistance. This is because pitting can occur at potentials below E_{bd}, as was demonstrated by metastable pitting in test 4. E_{bd} corresponds to the potential for stable pit growth and propagation only. Pits can nucleate, however, at any potential above the repassivation potential. Secondly, the effects that additional anions have on the pitting behavior is concentration dependent and not mass dependent.

D. Results

For examples of data scans generated during each test, see Figs. 14, 10, 12, 11, and 13.

Test no.	E_{corr} (mV_{SCE})	E_{bd} (mV_{SCE})	E_{rp} (mV_{SCE})	i_{pass} $\mu A/cm^2$
1	−50	400	10	0.9
2	−50	550	N/A	N/A
3	−50	N/A	N/A	N/A
4	−50	None	None	0.5

Conversion: 1 $\mu A/cm^2 = 10^{-6}$ A/cm^2.

For Test 3, you have to decide which peaks to count as pitting events.

Potential	Number of metastable pits in 10 min	Nucleation frequency (events/s/cm^2)
0V	4	0.017
0.25V	12	0.050

LABORATORY III

ELECTROCHEMICAL IMPEDANCE SPECTROSCOPY AND POLARIZATION RESISTANCE MEASUREMENTS

A. Objective

In this experiment, corrosion rates will be estimated via the Stern–Geary relationship by measuring the polarization resistance, R_p. This parameter will be measured in two ways: via conventional polarization resistance (PR) measurements and via electrochemical impedance spectroscopy (EIS). In addition, the errors in corrosion rate estimation introduced by the use of a finite scan rate and the presence of uncompensated ohmic resistance will be demonstrated.

B. Background

There are many situations where a nondestructive estimation of corrosion rate is necessary. However, electrochemical processes are inherently nonlinear, making this task more difficult. Recall that many electrochemical processes have current–voltage relationships that follow Butler–Volmer kinetics, which for a corroding electrode would be expressed as

$$i = i_{corr}\left(\exp\frac{\eta}{b_a} - \exp\frac{\eta}{b_c}\right) \tag{2}$$

where η is the overpotential, b_a is the anodic Tafel slope, and b_c is the cathodic Tafel slope. This equation indicates that unless the overpotentials are small compared to the Tafel slopes, large, potentially damaging currents will be generated upon polarization of the material. However, for small overpotentials (usually on the order of 10 to 15 mV), the Butler–Volmer equation can be linearized. This was done by Stern and Geary [JECS, 104, 56 (1959)] to arrive at the following relationship:

$$i_{corr} = \frac{b_a b_c}{(b_a + b_c)R_p} \tag{3}$$

where R_p is the polarization resistance. The polarization resistance is found to be inversely proportional to the corrosion rate (the equation was developed upon the assumption that both anodic and cathodic processes are under activation control). Therefore, by determining the polarization resistance of a material in an environment, the corrosion rate can be estimated, assuming a knowledge of the Tafel slopes (a more complete discussion of this can be found in the Significant Observations section). Two of the most widely used methods for determining R_p are polarization resistance and electrochemical impedance spectroscopy. The two techniques are explained in detail in Chapter 4. Briefly, both impose small amplitude perturbations of the potential and measure the current necessary to attain such perturbations. While the PR measurements utilize a slow voltage ramp, EIS measurements utilize a sinusoidal voltage waveform over a wide range of frequencies. The goal of both techniques is to evaluate the opposition of the electrochemical interface to the passage of current, which in many cases is inversely related to the rate of the oxidation of the material. However, before using the R_p determined experimentally to estimate corrosion rate, complications due to scan rate and uncompensated solution or ohmic resistance must be taken into account. In order to explain the importance of these errors, the Randles equivalent circuit is helpful (see Appendix 1).

The effect of too high a scan rate is due to the existence of the interfacial capacitance, whereas the effect of uncompensated ohmic resistance is the result of the solution resistance between the working electrode surface and the point in solution at which the reference electrode senses this potential. These effects are explained in more detail below.

C. Scan Rate

The impedance of a capacitor is inversely proportional to the frequency of the oscillation of the voltage field across it. An equivalent way to state the same property is that the current through a capacitor is directly proportional to the time derivative of the potential field across it.

$$i_{\text{capacitor}} = C\frac{dV}{dt} \tag{4}$$

Thus the importance of using a slow scan rate in the PR measurements (or equivalently, measuring down to a low frequency in the EIS measurements) can be seen. At very slow sweep rates, dV/dt is small, so the current through the capacitor is small. Therefore the impedance of the RC combination is only R_p. As the scan rate is increased, the fraction of current that flows through the capacitor increases, and the measured impedance falls, since the parallel combination of the resistor and capacitor will have a smaller impedance than the resistor alone. This effect will cause an underestimation of R_p and hence an overestimation of the corrosion rate.

D. Uncompensated Ohmic Resistance

The effect of uncompensated ohmic resistance is to overestimate R_p, and hence to underestimate the corrosion rate. Reference to the Randles circuit in Appendix 1 shows that if a slow enough scan rate is used, so that the capacitor effectively acts as an open circuit (i.e., its impedance is very high, hence the current allowed through it is very low), the impedance value actually measured is $R_p + R_\Omega$. This is true in all cases, even in conductive electrolytes. Because this effect increases the impedance measured over that which is of interest, its magnitude, relative to R_p, is of interest. In conductive solutions, R_Ω may be very small, but it is never zero. In more resistive media, such as soil, R_Ω may be a significant fraction of, or even greater than, R_p, and will then introduce large errors in the corrosion rate calculations if the low-frequency limit of the impedance is used as R_p without correction for the effects of R_Ω. Hence it is always important to correct one's data for the effect. At this point, one advantage of EIS over PR measurements is obvious. EIS measurements, when conducted over a wide frequency range, can be used to determine the values of R_Ω, the sum of R_Ω and R_p, and C_{dl}. The disadvantage is that the EIS measurements usually take more time and require more sophisticated equipment.

The goals of this lab are to acquaint the student with the following effects: the effect of reference electrode placement on R_Ω, the effect of scan rate on R_p measurements, and the effect of R_Ω on R_p measurements.

E. Experimental Procedures

Part A: Polarization Resistance

1. The Type 303SS samples are already in the solutions (0.01 M H_2SO_4 + 0.02 M HCl) and have equilibrated for approximately 12 hours. The instrumentation has been turned on and warmed up.

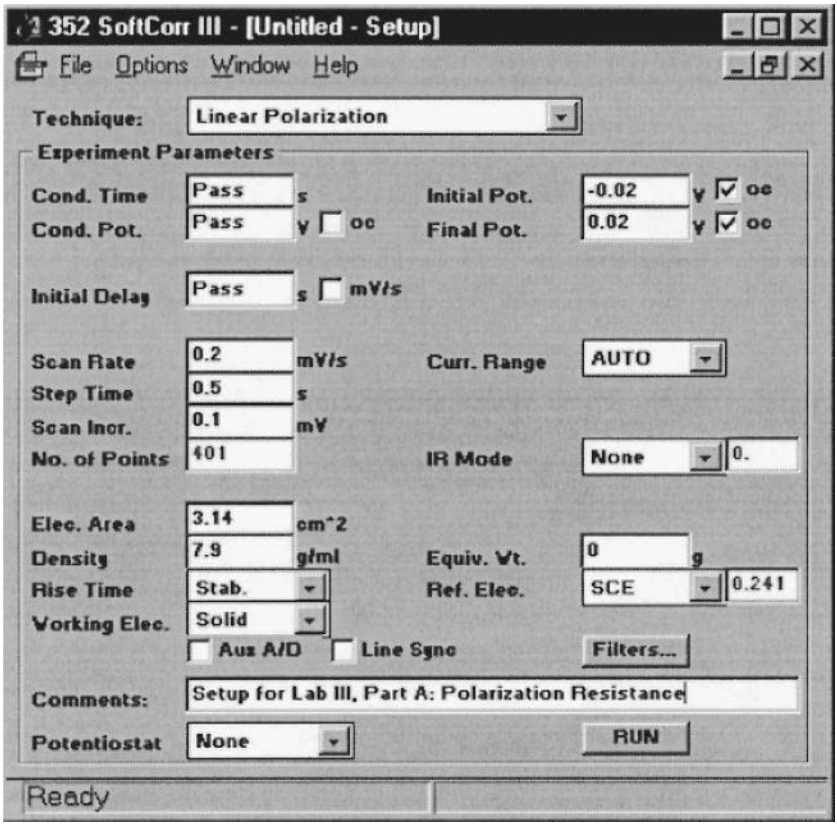

Figure 15 PAR 352 SoftCorr III Linear Polarization experimental setup window.

2. Make sure the cell enable switch is turned off. Connect the cell cables to the cell: green lead to the working electrode, red lead to the counter electrode, and the reference to the white pin jack. If a dummy cell is being connected, attach the leads as indicated in step 3 below.

a. To set up a new experiment select **FILE, NEW SETUP** from the opening window.
b. Select **LINEAR POLARIZATION** from the **Technique** combo box.
c. Use the default settings, except for the scan rate (see below), to run the experiment.
d. Add the appropriate information for the working electrode density and area. (D = 7.9 g/cm^3, area = 3.14 cm^2)
e. Enter the appropriate Reference Electrode (SCE).

f. Enter the appropriate scan rate from #3 below.
g. Press the Cell Enable Switch on the potentiostat to enable the cell or if a VersaStat is being used press the Cell On button.
h. Select **RUN** to start the experiment.
i. When finished with the scan, press the Cell Enable Switch to disconnect the cell.
j. After each experiment is complete, save the data by selecting **FILE** then **SAVE AS**. Enter a name for the data file and press RETURN.

3. There are four polarization resistance experiments that need to be run. Two are experiments on dummy cells, and two are experiments on real cells. For the dummy cell experiments, use the dummy cell labeled Polarization Resistance. For the actual cell experiments, use the 303SS immersed in the acidified chloride solution. Repeat steps 2a through 2f for each experiment.

a. Attach the working (green) lead at WE and the counter lead (red) at CE.
   1. Expt #1—Attach the reference cable to B; scan rate is to be 0.2 mV/s.
   2. Expt #2—Attach the reference cable to B; scan rate is to be 10 mV/s.
b. For the 303SS in acidified chloride experiments, attach the green lead to the working electrode, the red lead to the counterelectrode (graphite rod), and the reference to the white pin jack.
   1. Expt #3—Move the reference electrode close to but not touching the working electrode; use a scan rate of 0.2 mV/s.

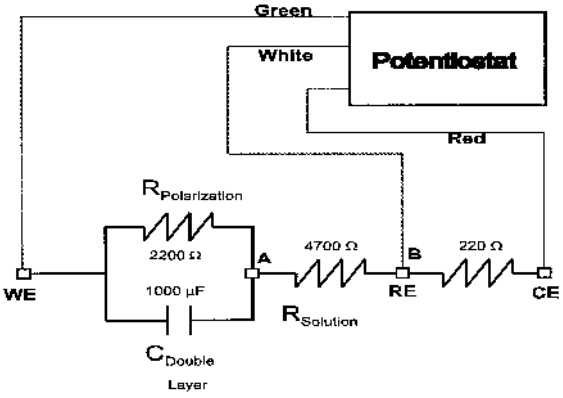

Figure 16 Wiring diagram for dummy cell with reference electrode (RE) at point B.

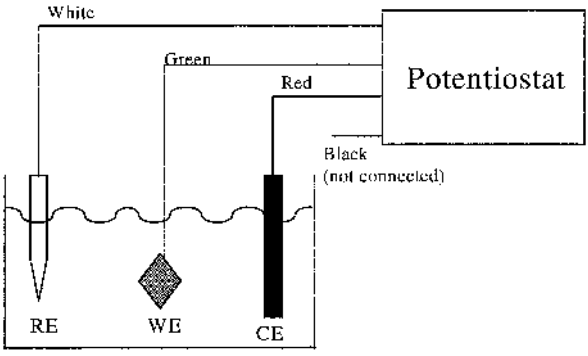

RE = Reference Electrode (SCE) connected to white pin connector
WE = Working Electrode
CE = Counter Electrode (Graphite Rod) connected to red lead

Figure 17 Experimental wiring diagram for the 303SS in acidified chloride environment.

2. Expt #4—Move the reference electrode far from the working electrode; use a scan rate of 0.2 mV/s.

4. Data Analysis

For each experiment,

a. Select **FILE, OPEN** from the initial window. Recall the appropriate data file.
b. Select **ANALYZE** to perform a polarization resistance calculation.
c. Press "R" from the pull-down menu or select **Rp CALC** with the mouse. The calculation is done automatically. Record the value for R_p. (See Fig. 18).
d. Select **FILE, SAVE** to resave the data with the calculated results.
e. Repeat steps 4a through 4g for each experiment just performed.

Part B: Electrochemical Impedance Spectroscopy

1. Use PAR 398 Electrochemical Impedance Spectroscopy software. If you are unsure how to access this software ask a lab assistant for help.

2. The following four experiments will be run in this laboratory:

a. Dummy Cell (labeled EIS) with working electrode (green) at WE and counterelectrode (red) at CE (see Fig. 20 for wiring diagram).
   1. With RE attached to B, run 100 kHz to 0.1 Hz.

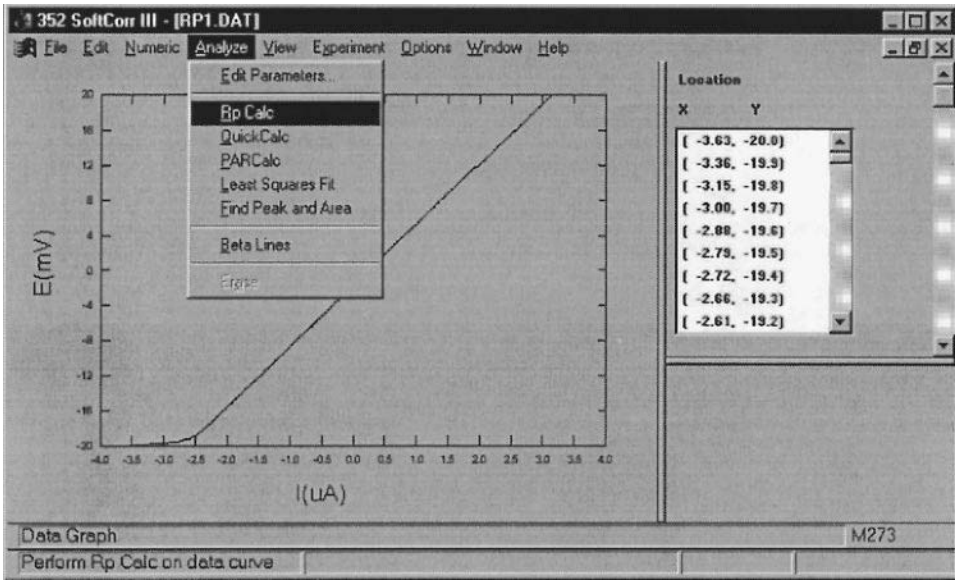

Figure 18 PAR 352 SoftCorr III window displaying selections for a R_p calculation.

2. With RE attached to A, run 10 kHz to 10 Hz. This scan is run to see the change in the ohmic resistance only, so you will not see a full semicircle.

b. 303 Stainless steel in 0.01 M H_2SO_4 + 0.02 M HCl (see Fig. 17 for wiring diagram).
   1. With RE far from WE, run 100 kHz to 0.1 Hz.
   2. With RE close to but not touching WE, run 10 kHz to 10 Hz. This scan is run to see the change in the ohmic resistance only, so you will not see a full semicircle.

3. To run experiments from 100 kHz to 0.1 Hz use the following procedure:
   a. From the Main Menu select **SETUP**.
   b. Select **NEW TECHNIQUE** and then select **SINGLE SINE EIS** $Z(f)$.
   c. Set **INITIAL FREQUENCY** to 100 KHz. Set **FINAL FREQUENCY** to 0.1 Hz. Change the **AC AMPLITUDE** to 20 mV rms. For the remaining options use the default settings.
   d. Now press the Cell Enable switch to enable the cell and select **RUN**.
   e. The data can be viewed during the experiment in several forms. To

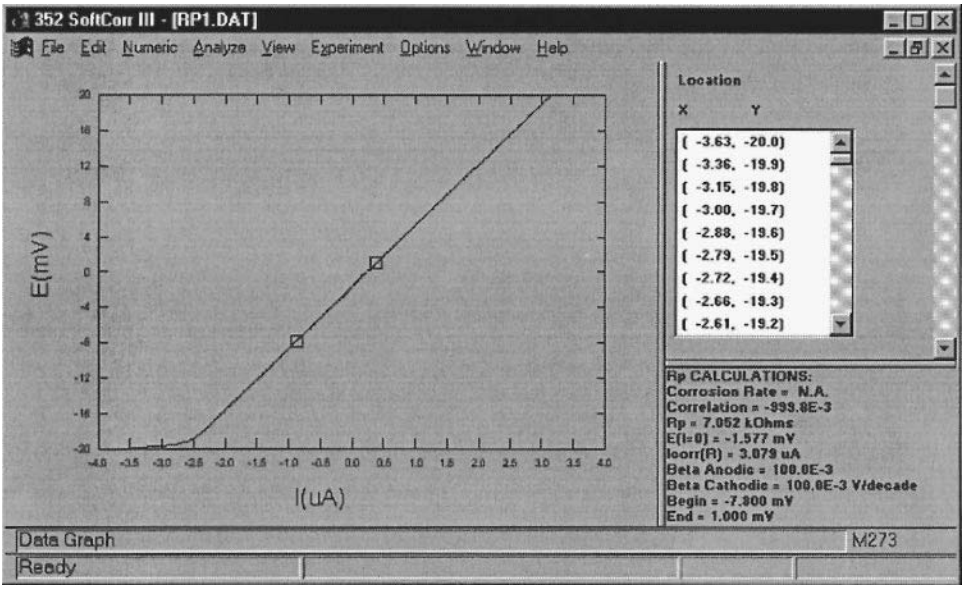

Figure 19 Typical PAR 352 SoftCorr III window after a R_p calculation has been performed.

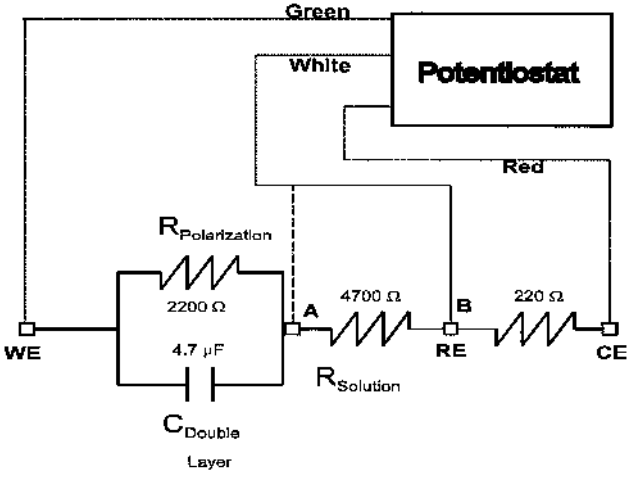

Figure 20 Wiring diagram for EIS dummy cell with the reference electrode (RE) at points A or B.

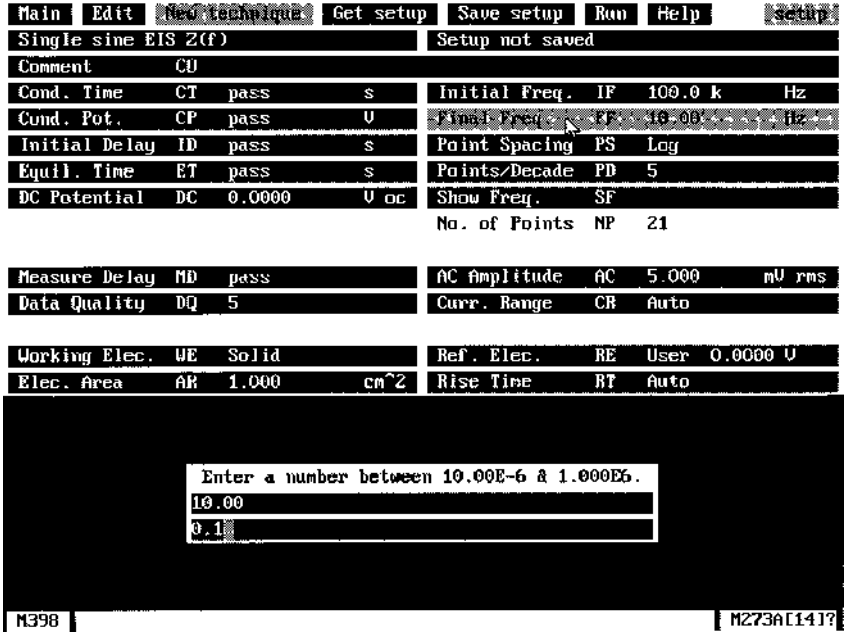

Figure 21 PAR M398 Single Sine experiment setup.

select the format for viewing, select the **TO**...option from the top banner.

f. Once the experiments are complete, the message "After Run" will appear in the top right corner of the screen. To view both sets of data, select **MAIN** from the banner. Next select **FILES**, and choose the **GET DATA** option. Enter the name of the data file for the Single Sine Experiment (O1) and press RETURN.

g. Next, press the ESC key and select **GRAPH** from the banner. Select **STYLE** from the banner to choose the format in which the data is presented. In this case, you will want the data in the Nyquist format. To select this, type "5."

h. To obtain a printout of the data, select **MAIN** from the banner. Next select **FILE** from the banner and choose the **PRINT/PLOT DATA** option.

4. To run experiments from 10 kHz to 10 Hz use the following procedure:

a. From the Main Menu select **SETUP**.

b. Select **NEW TECHNIQUE** and then select **SINGLE SINE EIS** *Z(f)*.

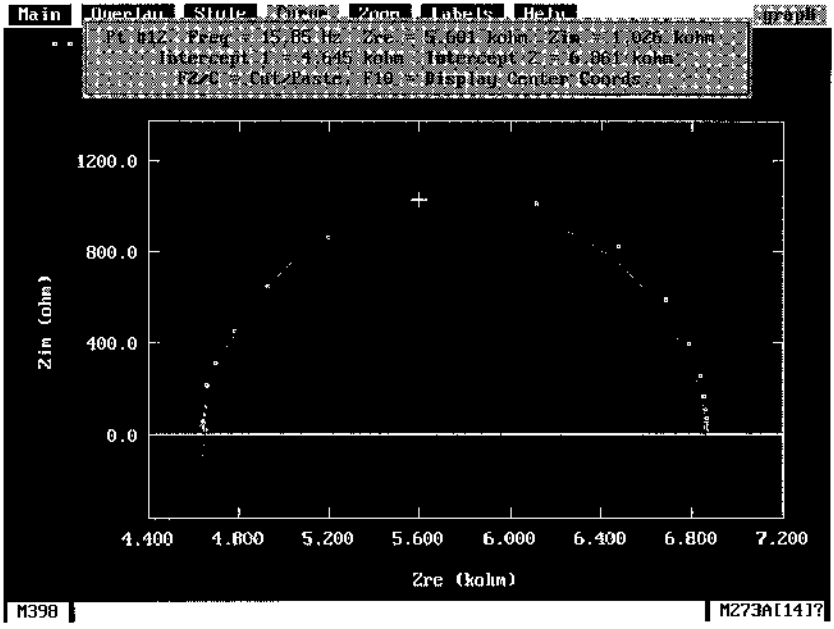

Figure 22 An example of the semicircle fit function of the PAR M398 EIS software.

c. Set **INITIAL FREQUENCY** to 10 KHz. Set **FINAL FREQUENCY** to 10 Hz. Change the **AC AMPLITUDE** to 20 mV rms. For the remaining options use the default settings.
d. Now press the Cell Enable switch to enable the cell and select **RUN**.

5. Data analysis to determine R_p, R_Ω, and C_{dl}.

a. From the Main Menu select **GRAPH**, **CURVE**, **SEMICIRCLE FIT**.
b. Use the mouse buttons or "B" and "E" (begin and end) to select point limits on the semicircle. (One point should be a high value of the real impedance while the other point should be a low value of the real impedance.)
c. Press **F-10** to display the real impedance intercepts. Intercept 1 is equivalent to R_Ω. Intercept 2 is equivalent to $R_\Omega + R_P$.
d. From this same screen the frequency at the maximum value of the imaginary impedance can be determined. Move the cursor until you have reached the maximum value of the imaginary impedance (top of semicircle). Record the frequency value. Use Appendix 1 to calculate C_{dl}.

F. Results and Data Analysis

1. Polarization Resistance

Dummy cell

R_p (measured) (Ω)

RE at "B," scan rate = 0.2 mV/s _____

RE at "B," scan rate = 10 mV/s _____

Experimental cell

R_p (measured) (Ω)

RE close to WE, scan rate = 0.2 mV/s _____

RE far from WE, scan rate = 0.2 mV/s _____

2. Electrochemical Impedance Spectroscopy

Dummy cell

R_Ω with RE at B = _____

R_Ω with RE at A = _____

R_p = _____ C_{dl} = _____

Experimental cell

R_Ω with RE close = _____

R_Ω with RE far = _____

R_p = _____ C_{dl} = _____

G. Questions

1. For the dummy cell polarization resistance experiments, calculate the percentage error in R_p at 0.2 mV/s and 10 mV/s.

2. Compare the R_p values from EIS to those obtained from PR measurements. Give reasons for any differences.

3. Based upon the EIS measurements, what would be the maximum scan rate that could be used without having appreciable capacitive current?

4. Explain why errors resulting from the presence of appreciable ohmic resistance are usually more severe than those that result from the use of too fast a scan rate.

H. Significant Observations

This set of experiments has focused on the use of two nondestructive electrochemical techniques to measure polarization resistance and thereby estimate the corrosion rate. In addition, the effects of scan rate and uncompensated ohmic resistance were studied. Three main points should have been made by this lab: (1) Uncompensated ohmic resistance is always present and must be measured and taken into account before R_p values can be converted into corrosion rates, otherwise an overestimation of R_p will result. This overestimate of R_p leads to an underestimate of corrosion rate, with the severity of this effect dependent upon the ratio R_p/R_Ω. (2) Finite scan rates result in current shunted through the interfacial capacitance, thereby decreasing the observed impedance and overestimating the corrosion rate. (3) Both of these errors can be taken into account by measuring R_Ω via EIS or current interruption and by using a low enough scan rate as indicated by an EIS measurement in order to force the interfacial capacitance to take on very large impedance values in comparison to R_p.

It should be pointed out that an exact knowledge of the Tafel slopes is often unnecessary, because in the normal range of values experienced in electrochemical systems, the effect on the corrosion rate of wide changes in Tafel constants is small as compared to equivalent changes in R_p. To prove this to yourself, range the Tafel slopes from 40 to 200 mV/decade to find out what combinations give more than a factor of 2 from the value of 100 mV/decade.

Finally, the basic equivalence of the two measuring techniques should be appreciated. Although there are many ways to approach such a comparison, the following simplified explanation will, we hope, give a more intuitive feeling for the relationship between EIS and PR measurements. As stated above, both techniques rely on the frequency dependence of the impedance of the double-layer capacitance in order to determine the polarization resistance. EIS uses low frequencies to force the capacitor to act like an open circuit. PR measurements use a slow scan rate to do the same thing. To make comparisons, the idea of "equivalent scan rate" is useful. Suppose that a particular electrochemical system requires EIS measurements to be made down to 1 mHz in order to force 99% of the current through R_p. What would the equivalent scan rate be for PR measurements? A frequency of 1 mHz corresponds to a period of 1000 s. If the sine wave is

approximated by a sawtooth wave of the same period and 10 mV peak-to-peak amplitude such as would be typical in PR measurements, this frequency corresponds to 0.02 mV/s:

$$\frac{20\ \text{mV}}{\text{cycle}} \times \frac{1\ \text{cycle}}{1000\ \text{s}} = 0.02\ \text{mV/s}$$

The ASTM standard for PR measurements stipulates that a scan rate of 6 V/h (0.167 mV/s) be used. For a 10 mV p–p scan, this corresponds to an "equivalent frequency" of 8 mHz. While there are many corrosion systems in which this is a low enough frequency to resolve R_p ($+R_\Omega$), there are also many cases where it is not. In these cases, the estimates of the corrosion rate will be overestimates, as pointed out in the section on scan rate effects.

I. Results and Data Analysis

Part A: Polarization Resistance

Dummy cell

	R_p (measured) (Ω)
RE at "B", scan rate = 0.2 mV/s	7052
RE at "B", scan rate = 10 mV/s	5245

Experimental cell	R_p (measured) (Ω)
RE close to WE, scan rate = 0.2 mV/s	57.48
RE far from WE, scan rate = 0.2 mV/s	80.63

Part B: Electrochemical Impedance Spectroscopy

Experimental cell

R_Ω with RE close = 8.852 ohms

R_Ω with RE far = 23.42 ohms

$R_p = 88.46 - 23.42 = 65.04$ ohms

$$C_{dl} = \frac{1}{0.1 \times 2\pi \times 65.04}$$

$$C_{dl} = 2.44 \times 10^{-2}\ \text{F}$$

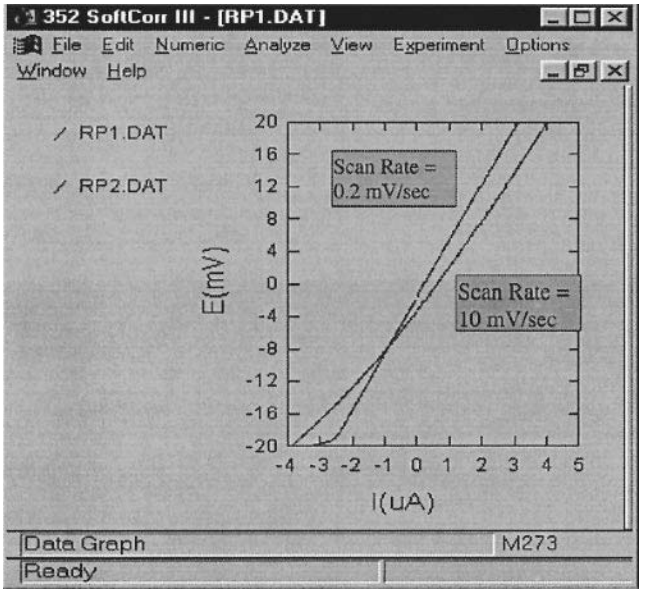

Figure 23 Linear polarization curves from the dummy cell showing the influence of scan rate.

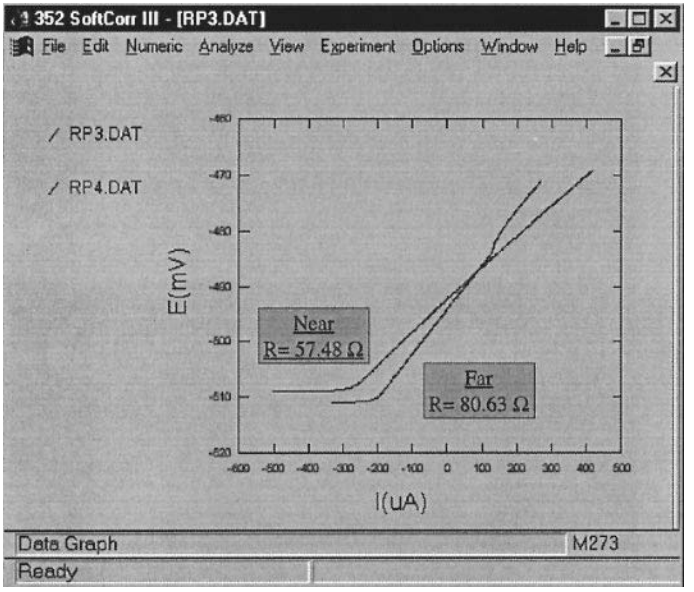

Figure 24 Linear polarization of 303SS in an acidified chloride environment showing the influence of solution resistance.

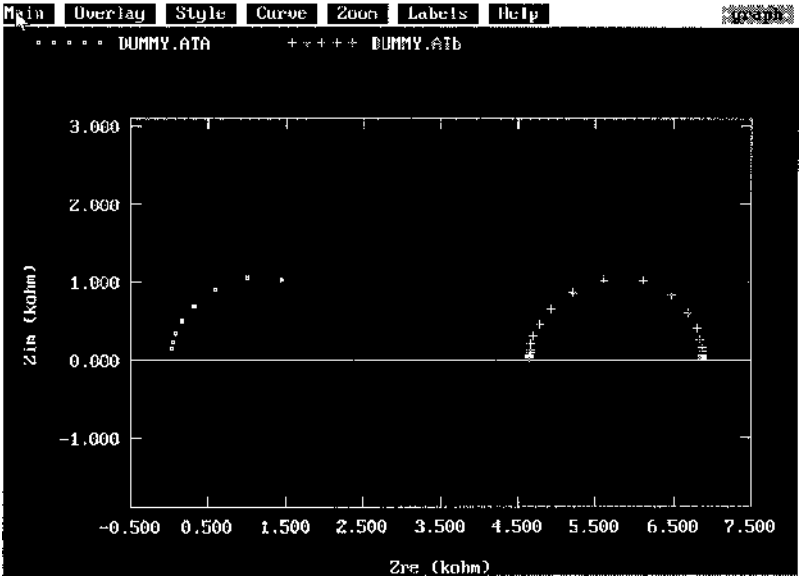

Figure 25 EIS results of dummy cell simulating two different solution resistances. At point A no solution resistance is simulated. At point B a solution resistance of 4700 Ω is simulated.

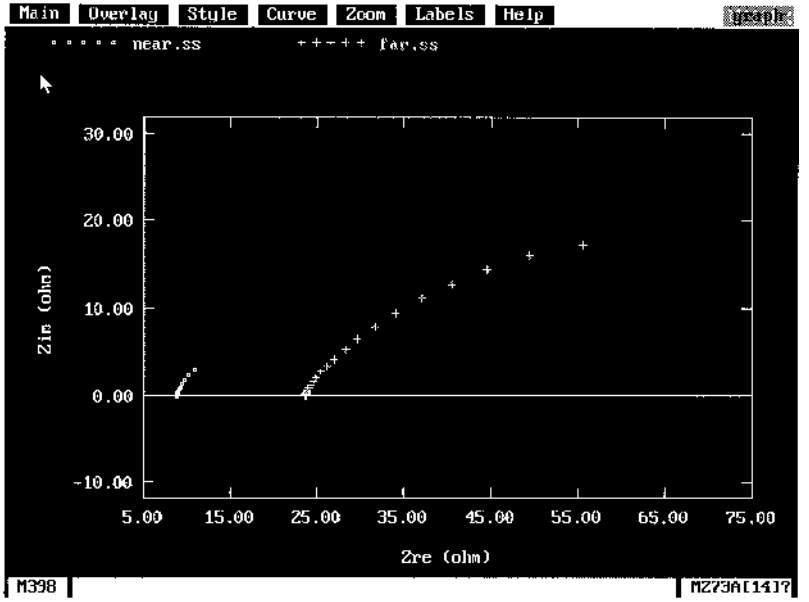

Figure 26 EIS results of 303SS in an acidified chloride environment showing the influence of solution resistance.

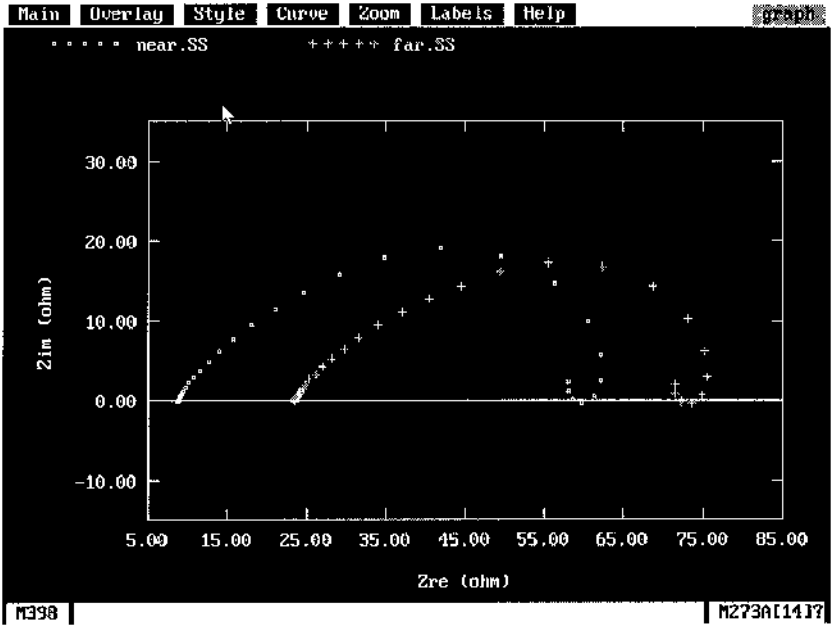

Figure 27 EIS data shown in Fig. 26 scanned to very low frequencies.

Dummy cell

R_Ω with RE at B = 1.248 ohms

R_Ω with RE at A = 4645 ohms

$R_p = 6861 - 4645 = 2216$ ohms

$$C_{dl} = \frac{1}{15.85 \times 2\pi \times 2216}$$

$$C_{dl} = 4.5 \times 10^{-6}\ \text{F} = 4.5\ \mu\text{F}$$

J. Data Analysis

A. Polarization resistance

Dummy cell

	R_p (measured) (Ω)
RE at "B", scan rate = 0.2 mV/s	7052

RE at "B", scan rate = 10 mV/s 5245

Experimental cell

R_p (measured) (Ω)

RE close to WE, scan rate = 0.2 mV/s 57.48

RE far from WE, scan rate = 0.2 mV/s 80.63

B. Electrochemical impedance spectroscopy

Dummy cell

R_Ω with RE at B = 1.248 ohms

R_Ω with RE at A = 4645 ohms

$R_p = 6861 - 4645 = 2216$ ohms

$$C_{dl} = \frac{1}{15.85 \times 2\pi \times 2216}$$

$$C_{dl} = 4.5 \times 10^{-6}\ \text{F} = 4.5\ \mu\text{F}$$

Experimental cell

R_Ω with RE close = 8.852 ohms

R_Ω with RE far = 23.42 ohms

$R_p = 88.46 - 23.42 = 65.04$ ohms

$$C_{dl} = \frac{1}{0.1 \times 2\pi \times 65.04}$$

$$C_{dl} = 2.44 \times 10^{-2}\ \text{F}$$

APPENDIX 1: CALCULATION OF THE DOUBLE LAYER CAPACITANCE

For the Randles circuit:

The total impedance of this circuit is

$$Z_{total} = R_s + \left(\frac{1}{R_p} + j\omega C_{dl}\right)^{-1} = R_S + \frac{R_p}{1 + j\omega R_p C_{dl}}$$

where

R_s	denotes the solution resistance
R_p	denotes the polarization resistance
ω	denotes frequency
C_{dl}	denotes the double layer capacitance
j	denotes imaginary number

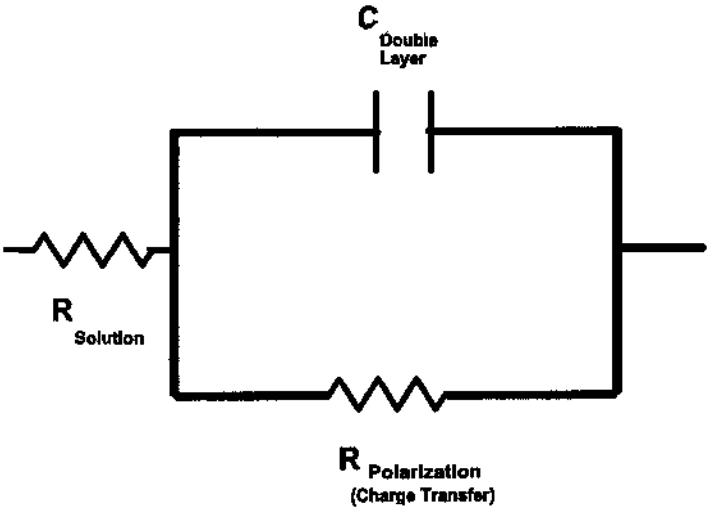

Figure 28 Randles' circuit that serves as an electrical analog of the corroding interface.

Multiplying by the complex conjugate and rearranging into the real and imaginary components, we obtain

$$Z_{\text{total}} = Z_{\text{real}} + Z_{\text{imaginary}}$$

$$Z_{\text{total}} = \frac{R_s(1 + \omega^2 R_p^2 C_{dl}^2) + R_p}{1 + \omega^2 R_p^2 C_{dl}^2} - \frac{j\omega R_p C_{dl}}{1 + \omega^2 R_p^2 C_{dl}^2}$$

Using the Nyquist Plot to Find C_{dl}

Define $\omega_{max,Nyq}$ as the frequency at which the imaginary component of the impedance has its largest value.

Find $\omega_{max,Nyq}$ by taking the derivative of the imaginary impedance component with respect to ω and setting equal to zero.

$$\frac{\partial Z_j}{\partial \omega} = \frac{\partial}{\partial \omega}\left(\frac{-j\omega R_p C_{dl}}{1 + \omega^2 R_p^2 C_{dl}^2}\right)$$

$$= \frac{-jR_p C_{dl}(1 + \omega^2 R_p^2 C_{dl}^2) - j\omega R_p C_{dl}(2\omega R_p^2 C_{dl}^2)}{(1 + \omega^2 R_p^2 C_{dl}^2)^2}$$

$$= \frac{-jR_p C_{dl}(1 - \omega^2 R_p^2 C_{dl}^2)}{(1 + \omega^2 R_p^2 C_{dl}^2)}$$

Setting the derivative equal to zero, we obtain

$$0 = (1 - \omega^2_{\max,\mathrm{Nyq}} R_\mathrm{p}^2 C_\mathrm{dl}^2)$$

$$C_\mathrm{dl} = \frac{1}{\omega_{\max,\mathrm{Nyq}} R_\mathrm{p}}$$

Using the Bode Plot to Find C_{dl}

Define $\omega_{\max,\mathrm{Bode}}$ as the frequency at which the phase angle has the highest magnitude. (This is the frequency at which the ratio of the imaginary impedance component to the real impedance component is maximum.) Note: The frequency selected for $\omega_{\max,\mathrm{Bode}}$ is not the same as the frequency selected using the Nyquist plot.

Find $\omega_{\max,\mathrm{Bode}}$ by taking the derivative of this ratio with respect to ω and setting equal to zero.

$$\frac{\partial(Z_\mathrm{j}/Z_\mathrm{r})}{\partial\omega} = \frac{\partial}{\partial\omega}\left(\frac{-j\omega R_\mathrm{p}^2 C_\mathrm{dl}}{R_\mathrm{s} + R_\mathrm{p} + \omega^2 R_\mathrm{s} R_\mathrm{p}^2 C_\mathrm{dl}^2}\right)$$

$$= \frac{-jR_\mathrm{p}^2 C_\mathrm{dl}(R_\mathrm{s} + R_\mathrm{p} + \omega^2 R_\mathrm{s} R_\mathrm{p}^2 C_\mathrm{dl}^2) - j\omega R_\mathrm{p}^2 C_\mathrm{dl}(2\omega R_\mathrm{s} R_\mathrm{p}^2 C_\mathrm{dl}^2)}{(R_\mathrm{s} + \mathrm{R_p} + \omega^2 R_\mathrm{s} R_\mathrm{p}^2 C_\mathrm{dl}^2)^2}$$

$$= \frac{-jR_\mathrm{p}^2 C_\mathrm{dl}(R_\mathrm{s} + R_\mathrm{p} - \omega^2 R_\mathrm{s} R_\mathrm{p}^2 C_\mathrm{dl}^2)}{(R_\mathrm{s} + R_\mathrm{p} + \omega^2 R_\mathrm{s} R_\mathrm{p}^2 C_\mathrm{dl}^2)^2}$$

Setting the derivative equal to zero, we obtain

$$0 = (R_\mathrm{s} + R_\mathrm{p} - \omega^2_{\max,\mathrm{Bode}} R_\mathrm{s} R_\mathrm{p}^2 C_\mathrm{dl}^2)$$

$$C_\mathrm{dl} = \frac{1}{\omega_{\max,\mathrm{Bode}} R_\mathrm{p}}\left(\frac{R_\mathrm{s} + R_\mathrm{p}}{R_\mathrm{s}}\right)^{1/2}$$

$$C_\mathrm{dl} = \frac{1}{\omega_{\max,\mathrm{Bode}} R_\mathrm{p}}\left(1 + \frac{R_\mathrm{p}}{R_\mathrm{s}}\right)^{1/2}$$

APPENDIX 2: IMPEDANCE MEASUREMENTS IN DETAIL

Impedance measurements performed with PAR M398 software in conjunction with a potentiostat and a lock-in amplifier or frequency response analyzer are obtained using one or both of two techniques, depending on the frequency range

of interest. The lower frequency range (5 Hz and lower) is collected using a multisine technique, while the upper frequency range (5 Hz to 100 kHz) is collected using a single sine technique. For the experiments performed in this laboratory from 100 kHz to 0.1 Hz it is necessary to use both techniques, whereas the experiments from 10 kHz to 10 Hz can be performed using only the single sine technique. The auto execute mode is most convenient for collecting data over both frequency ranges, as the data can be automatically merged into one data file and collected in a single, automated experiment.

Single Sine Technique

The single sine technique is used to acquire data over the frequency range 5 Hz to 100 kHz when a LIA is used and 50 μHz to 100 kHz when a FRA is used. To access the single sine technique from the main menu select **SETUP**, then select **NEW TECHNIQUE** from the banner. Select the Single Sine option. The options from the single sine technique that were specified in this lab are discussed in the following paragraphs.

Initial Frequency

This option allows the user to specify the frequency at which the impedance measurements will begin. The value entered must be between 5 Hz and 100 kHz (LIA) or between 50 μHz and 100 kHz (FRA). In this lab 100 kHz and 10 kHz were used for initial frequencies.

Final Frequency

This option allows the user to specify the frequency at which the impedance measurements will terminate. The value must fall in the same range stated for **Initial Frequency**. For the LIA stations, the limit was set to 5 Hz for the scans ranging from 100 kHz to 0.1 Hz, and the frequencies below 5 Hz were collected using the multisine technique. For the FRA stations, 0.1 Hz was entered. For experiments ranging from 10 kHz to 10 Hz, the multisine technique was not required for either FRA or LIA stations, and this parameter was set to 10 Hz.

Points/Decade

This parameter specifies how many data points will be collected over each decade of frequencies, a decade being defined as an order of magnitude base 10 (i.e., 1 to 10 Hz, 1000 to 100,000 Hz, etc). The program allows values from 0 to 20 to be entered. In laboratory work it is customary to collect between 5 and 15 data points per decade. In this laboratory 10 data points per decade were collected.

AC Amplitude

This option allows the user to define the amplitude of the AC perturbation applied to the system for determination of impedance response. The AC signal is usually a small voltage signal in the range of 5 to 20 mV for typical applications. Small values perturb the system to a lesser degree and do not disturb the steady state as much as large values. Thus smaller AC signals are "less destructive" than larger values. However, larger values may be able to increase the signal-to-noise ratio observed in the system response. These basic ideas demonstrate the tradeoffs in selecting an AC amplitude.

DC Potential

This parameter specifies the potential upon which the AC signal is imposed. Oftentimes, to maintain the steady state of the system, the DC potential is selected as 0 mV vs. open circuit. However, the response of a system can be evaluated over a potential range by running successive experiments with different DC potentials. Thus the impedance response of a system could be mapped to a potentiodynamic polarization curve by specifying various DC potentials defined by the polarization curve. In all experiments performed in this laboratory, the DC potential was set to 0 mV versus open circuit.

Condition Time

This parameter defines the length of time that the system will be held at a potential defined by **Condition Potential**. A condition time may be useful to study systems at potentials away from open circuit. By applying the desired potential for a length of time before the experiment is run, the system is allowed to stabilize before the data is collected. In the lab #3 experiments, this value is set to zero vs. open circuit, since the samples are already at a steady-state open circuit potential.

Condition Potential

This option allows the user to specify a potential at which the sample will be held for a period of time defined by **Condition Time**. Normally this potential would be set to the same value as **DC potential**. Using **Condition Time** and **Condition Potential** allows the system to stabilize at an applied potential before data collection is initiated. Remember that a system does not immediately attain a stable response to an applied potential (lab #1 part B).

Open Circuit Delay

This option allows the user to specify a length of time prior to the impedance experiment during which the system will remain under free corrosion conditions.

Note that this option precludes using a condition potential and vice versa. This option is useful if it is known that the system requires a significant time to stabilize under open circuit conditions. Thus the software can be told to wait a specified amount of time before initiating the impedance scan.

Multisine Technique (5×10^{-5} −5 Hz)

The multisine technique is used to acquire data over the frequency range 5×10^{-5} Hz to 5 Hz. To access the multisine technique from the main menu select **SETUP**, and then select **NEW TECHNIQUE**. Select the Multisine option. The options from the multisine technique that were specified in this lab are discussed in the following paragraphs. Although the multisine technique commonly only provides one or two decades of information out of a total of six or seven, the data from this frequency range is significant, as they often give insight into the polarization resistance and thus the corrosion rate of the material.

Initial Frequency

This option allows the user to specify the frequency at which the impedance measurements will begin. The value entered must be between 50 μHz and 100 mHz.

Final Frequency

The final frequency is automatically determined by setting the initial frequency. The value of the final frequency is **Initial Frequency** multiplied by 113.

Points/Decade

This parameter specifies how many data points will be collected over each decade of frequencies, a decade being defined as an order of magnitude base 10 (i.e., 1 to 10 Hz, 1000 to 100,000 Hz, etc). The program allows values from 0 to 20 to be entered. In laboratory work it is customary to collect between 5 and 15 data points per decade. In this laboratory 10 data points per decade were collected.

AC Amplitude

This option allows the user to define the amplitude of the AC perturbation applied to the system for determination of impedance response. The AC signal is usually a small voltage signal in the range of 5 to 20 mV for typical applications. Small values perturb the system to a lesser degree and do not disturb the steady state as much as large values. Thus smaller AC signals are “less destructive” than larger values. However, larger values may be able to increase the signal-to-noise ratio observed in the system response. These basic ideas demonstrate the tradeoffs in selecting an AC amplitude.

DC Potential

This parameter specifies the potential upon which the AC signal is imposed. Oftentimes, to maintain the steady state of the system, the DC potential is selected as 0 mV vs. open circuit. However, the response of a system can be evaluated over a potential range by running successive experiments with different DC potentials. Thus the impedance response of a system could be mapped to a potentiodynamic polarization curve by specifying various DC potentials defined by the polarization curve. In all experiments performed in this laboratory, the DC potential was set to 0 mV versus open circuit.

Condition Time

This parameter defines the length of time that the system will be held at a potential defined by **Condition Potential**. A condition time may be useful to study systems at potentials away from open circuit. By applying the desired potential for a length of time before the experiment is run, the system is allowed to stabilize before the data is collected. In the lab #3 experiments, this value is set to zero vs. open circuit since the samples are already at a steady-state open circuit potential.

Condition Potential

This option allows the user to specify a potential at which the sample will be held for a period of time defined by **Condition Time**. Normally this potential would be set to the same value as **DC potential**. Using **Condition Time** and **Condition Potential** allows the system to stabilize at an applied potential before data collection is initiated. Remember that a system does not immediately attain a stable response to an applied potential (lab #1 part B).

Open Circuit Delay

This option allows the user to specify a length of time prior to the impedance experiment during which the system will remain under free corrosion conditions. Note that this option precludes using a condition potential and vice versa. This option is useful if it is known that the system requires a significant time to stabilize under open circuit conditions. Thus the software can be told to wait a specified amount of time before initiating the impedance scan.

LABORATORY IV

PART A: CURRENT DISTRIBUTION

A. Objective

The objective of the current distribution lab is to explore the influence of electrode geometry, solution conductivity, and electrode polarization characteristics on ca-

thodic current–potential distributions. The influence of these three parameters will be assessed experimentally by potential mapping techniques. The geometry chosen represents a 2D simulation of a 3D tube–tubesheet heat exchanger. Students will potentiostatically polarize the entrance to the tube–tubesheet arrangement to −1.0 V vs. SCE and determine the potential distribution as a function of position down the tube. Solution conductivity will be varied to show its effect on the resulting potential distribution. The component of current density parallel to the center line of the tube will be calculated.

B. Approach

The student will apply an impressed cathodic current to the entrance of the tube–tubesheet arrangement using a potentiostat in the conventional three-electrode arrangement with a counterelectrode (CE) and *controlling* reference electrode (RE). These electrodes will be placed at a distance from the tube–tubesheet arrangement as illustrated in Fig. 29. The working electrode (WE) consists of 304 stainless steel, the RE is a saturated calomel electrode (SCE), and the two test

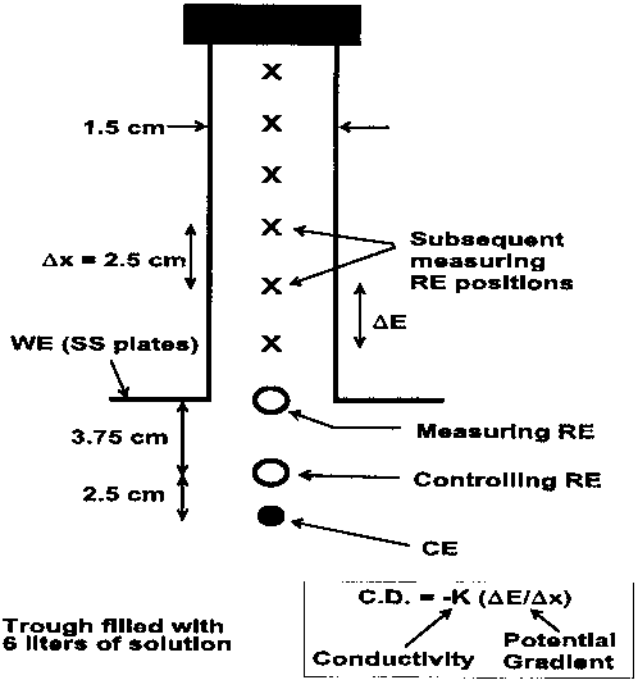

Figure 29 Tube–tubesheet simulation schematic.

solutions are 0.06 M NaCl and 0.6 M NaCl. For this experiment the PAR 352 SoftCorr III software will be utilized to apply the potentiostatic polarization required.

Two basins are provided, the first containing 6 liters of 0.06 M NaCl and the second containing 6 liters of 0.6 M NaCl. The WE samples should not be completely immersed. Ensure that the stainless steel sheets are in the grooves of the Plexiglas provided.

Prior to applying a potential of −1.0 V, the open circuit potential will be monitored. Verify with the second "*measuring* RE" (connected to the WE through a digital voltmeter) that the open circuit potential is approximately the same no matter where the measuring RE is placed with respect to the WE surface. Cell connections, shown in Fig. 30 are as follows:

PAR 273 electrometer:

1. Green lead: connect to stainless steel working electrode.
2. Red lead: connect to graphite counter electrode.
3. Black lead: not connected.
4. RE pin connector: connect to controlling RE.
5. Toggle switch: toggle to ext. cell.

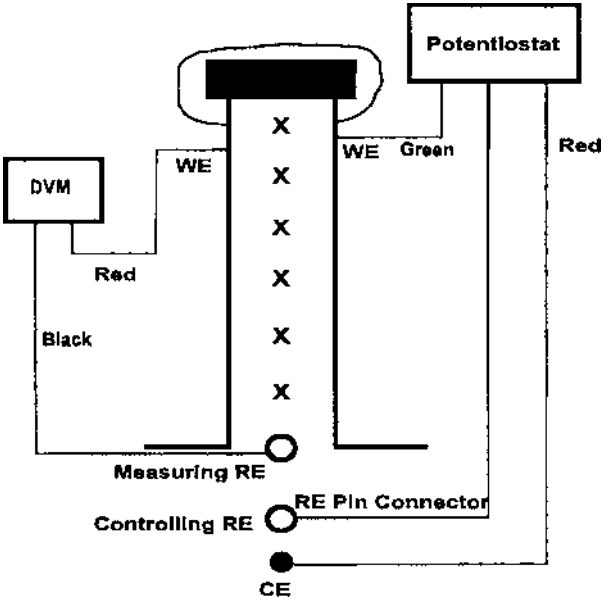

Figure 30 Wiring diagram for tube-tubesheet.

Digital voltmeter (DVM):

1. Ground lead (black): connect to measuring RE.
2. Positive lead (red): connect to steel WE.

NOTE: Before touching anything other than the 'measuring reference"turn the cell OFF and press the cell enable switch to disconnect the cell from the potentiostat.

Experimental Procedure

Setup the experiment using PAR 352 SoftCorr III software:

a. From the main menu of the software select FILE.
b. Select NEW SETUP.
c. Select POTENTIOSTATIC from the Technique combo box.
d. Set the INITIAL POT to "−1.0" volts. The potentiostat will apply −1 V vs. the RE.
e. Select the TIME STEP and set to "3600" seconds.
f. Set the TIME/POINT to "5" seconds.
g. Set the REFERENCE ELECTRODE TO "SCE". Figure 31 shows the POTENTIOSTATIC Technique combo box after setup.
h. Press the Cell Enable Switch on the potentiostat to activate the cell.
i. Press RUN to start the experiment.

Section 1

After activating the cell to apply the cathodic potential, the system should be allowed to stabilize for 5 minutes. This stabilization can be observed by noting the stability of the current displayed on the monitor or the potential monitored by the measuring RE (read from the DVM).

After the system stabilizes, measure the potential at the various marked positions down the length of the tube using the second measuring RE. Leave the PSTAT on while making measurements with the measuring RE. Allow 2 minutes before recording the value on the data sheet provided. Take care to keep the basin stable; solution flow can affect the measurements.

Record the cell current (I_{cell}) from the PAR 273 front panel or the Versastat monitor. Also record the cell voltage (V_{cell}) by using the DVM to measure the potential between the WE and CE (to do this you must temporarily connect the black DVM lead to the CE).

When you have completed all of the measurements outlined above, stop the potentiostatic hold by selecting EXPERIMENT from the menu bar and selecting

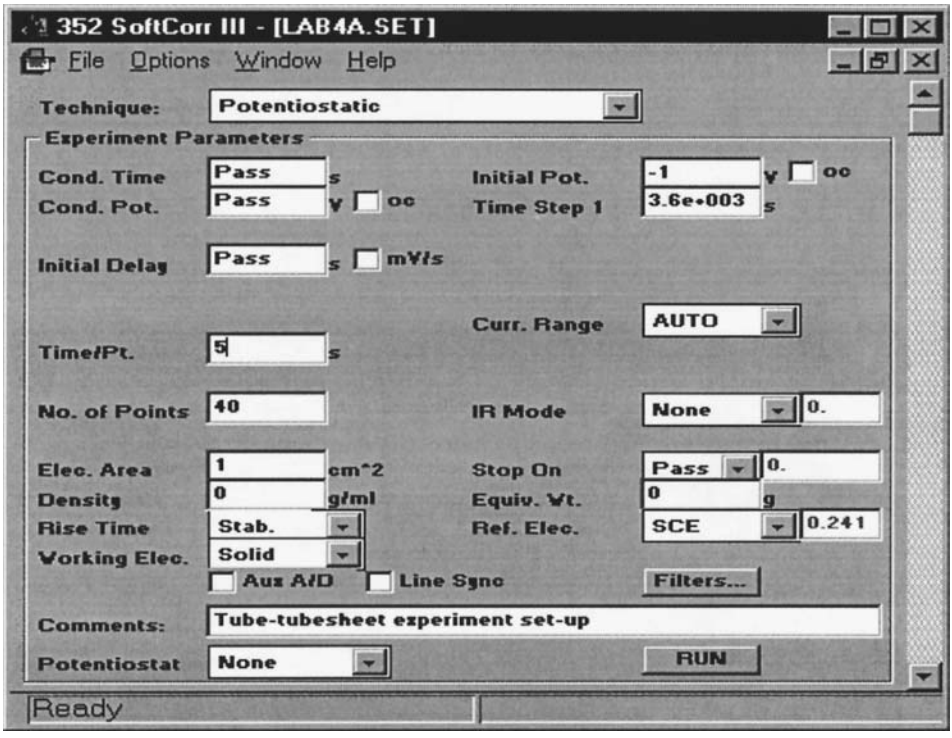

Figure 31 PARC 352 SoftCorr III Potentiostatic technique combo box.

STOP. Deactivate the cell by pressing the Cell Enable switch. Do not save the data file.

Section 2

Move the Plexiglas support, CE, and WEs to the second basin and repeat the above experiment. IF YOU ARE PART OF THE SECOND GROUP, IT IS IMPORTANT TO RINSE THE ELECTRODES WITH DISTILLED WATER WHEN MOVING THE SETUP FROM THE 0.6 M TO THE 0.06 M SOLUTION TO AVOID CONTAMINATION FROM THE MORE CONCENTRATED SOLUTION. As before, apply a potential of −1.0 vs. *controlling* RE using the controlling RE/CE arrangement described previously and allow it to stabilize for 5 minutes. Measure the potential at the various marked positions down the length of the tube using the measuring RE, allowing 2 minutes before recording the measurement on the data sheet provided. Record the cell current from the PAR

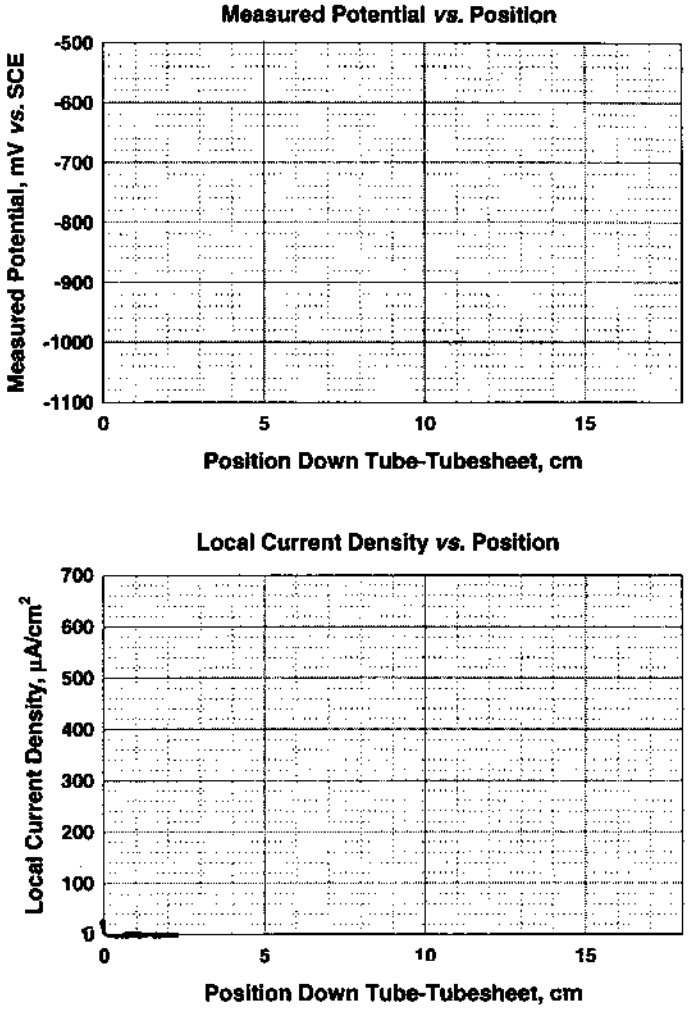

Figure 32 Measured potential versus position.

273 front panel or the Versastat monitor. Also record the cell voltage (V_{cell}) by using the DVM to measure the potential between the WE and CE (to do this you must temporarily connect the black DVM lead to the CE).

When you have completed all of the measurements outlined above, stop the potentiostatic hold by selecting EXPERIMENT from the menu bar and selecting

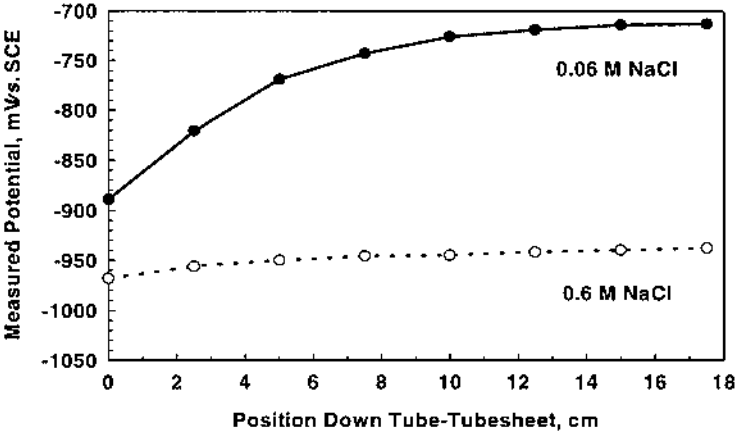

Figure 33 Measured potentials for simulated tube–tubesheet experiment.

STOP. Deactivate the cell by pressing the Cell Enable switch. Do not save the data file.

Analysis

Plot the measured potential versus position for each test solution on the graphs provided. For each solution, determine the component of applied current density parallel to the center line of the tube as a function of position by calculating the

Table 3 Potential and Current Distribution Data for 0.06 M NaCl

Position (cm)	Potential (mV)	Potential grad. (mV/cm)	Current density (mA/cm^2)	Current density ($\mu A/cm^2$)
0.0	−889	29.60	0.1717	171.68
2.5	−821	27.20	0.1578	157.76
5.0	−769	20.80	0.1206	120.64
7.5	−743	10.40	0.0603	60.32
10.0	−726	6.80	0.0394	39.44
12.5	−719	2.80	0.0162	16.24
15.0	−714	2.00	0.0116	11.60
17.5	−713	0.40	0.0023	2.32

Table 4 Potential and Current Distribution Data for 0.6 M NaCl

Position (cm)	Potential (mV)	Potential grad. (mV/cm)	Current density (mA/cm^2)	Current density ($\mu A/cm^2$)
0.0	−968	8.53	0.4250	424.96
2.5	−956	4.80	0.2390	239.04
5.0	−950	2.40	0.1195	119.52
7.5	−946	1.60	0.0797	79.68
10.0	−945	0.40	0.0199	19.92
12.5	−942	1.20	0.0598	59.76
15.0	−940	0.80	0.0398	39.84
17.5	−938	0.80	0.0398	39.84

potential gradient (difference between two successive potentials divided by 2.5 cm) at each position and multiplying the result by the solution conductivity (provided). Plot current density as a function of position. Sample data are provided in Tables 3 and 4 for the two solutions of different concentration. Figures 33 and 34 show the measured potentials and calculated current densities, respectively. Calculate the cell power in each case by multiplying $V_{cell} \times I_{cell}$. Describe qualitatively the effect of solution conductivity on the results.

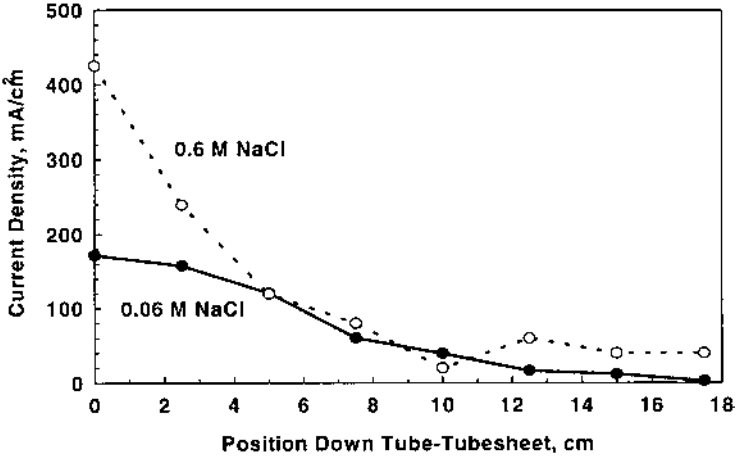

Figure 34 Calculated current density for simulated tube–tubesheet experiment.

Current Distribution Experiment

Sample Data Sheet

Solution concentration: 0.06 M NaCl
Conductivity: 0.0058 $(\text{ohm-cm})^{-1}$
Applied potential: −1.0 V
Tube diameter: 1.5 cm
Cell voltage (V_{cell}) (WE-CE):
Cell current (I_{cell}) from 273 display or Versastat monitor:
Cell power ($V_{cell}I_{cell}$):

	Reference position (cm)	Potential (mV)	Potential gradient (mV/cm)	Current density (mA/cm^2)*	Current density ($\mu A/cm^2$)
0		−1000			
1	0		_____ mV/3.75 cm = _____ mV/cm		
2	2.5		_____ mV/2.5 cm = _____mV/cm		
3	5		_____ mV/2.5 cm = _____ mV/cm		
4	7.5		_____ mV/2.5 cm _____ mV/cm		
5	10		_____ mV/2.5 cm = _____ mV/cm		
6	12.5		_____ mV/2.5 cm = _____ mV/cm		

7	15		_____ mV/2.5 cm = _____ mV/cm		
8	17.5		_____ mV/2.5 cm = _____mV/cm		

* mV/cm × 1/ohm-cm = mA/cm^2
1 μA = 10^{-3} mA

Current Distribution Experiment

Sample Data Sheet

Solution concentration: 0.6 M NaCl.
Conductivity: 0.0498 (ohm-cm)$^{-1}$
Applied potential: −1.0 V
Tube diameter: 1.5 cm
Cell voltage (V_{cell}) (WE-CE):
Cell current (I_{cell}) from 273 display or Versastat monitor:
Cell power ($V_{cell}I_{cell}$):

	Reference position (cm)	Potential (mV)	Potential gradient (mV/cm)	Current density (mA/cm^2)*	Current density (μA/cm^2)
0		−1000			
1	0		_____ mV/3.75 cm = _____ mV/cm		
2	2.5		_____ mV/2.5 cm = _____mV/cm		
3	5		_____ mV/2.5 cm = _____ mV/cm		

	Reference position (cm)	Potential (mV)	Potential gradient (mV/cm)	Current density (mA/cm^2)*	Current density ($\mu A/cm^2$)
4	7.5		_____ mV/2.5 cm = _____ mV/cm		
5	10		_____ mV/2.5 cm = _____ mV/cm		
6	12.5		_____ mV/2.5 cm = _____ mV/cm		
7	15		_____ mV/2.5 cm = _____ mV/cm		
8	17.5		_____ mV/2.5 cm = _____mV/cm		

* $mV/cm \times 1/ohm\text{-}cm = mA/cm^2$
$1\ \mu A = 10^{-3}$

LABORATORY IV

PART B: MASS TRANSPORT EFFECTS

A. Objective

The objective of the mass transport lab is to explore the effect of controlled hydrodynamics on the rate at which a mass transport controlled electrochemical reaction occurs on a steel electrode in aqueous sodium chloride solution. The experimental results will be compared to those predicted from the Levich equation. The system chosen for this experiment is the cathodic reduction of oxygen at a steel electrode in neutral 0.6 M NaCl solution. The diffusion-limited cathodic current density will be calculated at various rotating disk electrode rotation rates and compared to the cathodic polarization curve generated at the same rotation rate.

B. Approach

A cathodic potentiodynamic scan will be conducted on an AISI 1020 steel rotating disk electrode (RDE) that has been polished to a 600 grit finish. The electrolyte consists of 2 liters of 0.6 M NaCl, the counterelectrode is a graphite rod, and an SCE will be used for the reference electrode. Make the connections shown below with the cell off, taking care to keep all leads away from the moving parts. Ensure that electrical contact is made between the RDE and the rotator using the DVM.

Cell connections, shown in Fig. 35, are as follows:

1. Green lead: connect to steel working electrode.
2. Red lead: connect to graphite counter electrode.
3. Black lead: connect the cell ground to rotator.
4. RE pin connector: connect to controlling RE.
5. Toggle switch: toggle to ext. cell.

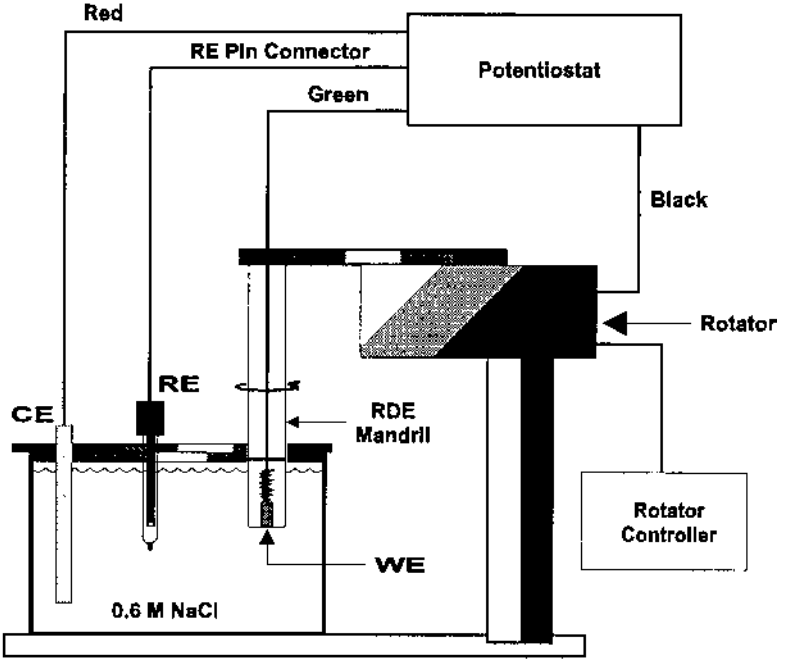

Figure 35 Wiring diagram for rotating disk electrode.

Your results will depend upon the length of time the sample is exposed to the electrolyte prior to the scan, so it is best to *set up the software before immersing the sample*. After setting up the software to step g shown below, lower the electrode the rest of the way; continue with step h and start the experiment. Do not lower the electrode more than 1.5″ below the water line; *the seam between the mantle and the sample shank should not be immersed*.

C. Experimental Procedure

Set up the experiment using PAR 352 SoftCorr III software:

a. From the main menu, select FILE, then select NEW SETUP.
b. Select POTENTIODYNAMIC from the Technique combo box.
c. For INITIAL DELAY enter "300" to monitor the open circuit potential for 300 seconds.
d. Select INITIAL POTENTIAL, enter "0", and click on the box beside OC so that an "X" appears in the box. This setting will start the cathodic scan at 0 volts vs. open circuit.
e. Select FINAL POTENTIAL and enter "−1.0" to get −1 volts vs. the RE. (Make sure that there is no "X" in the box beside OC on the FINAL POTENTIAL line or else the experiment will terminate at −1 V vs. OCP!)
f. Select SCAN RATE and enter "5" mV/s.
g. Add the appropriate information for the REFERENCE ELECTRODE, DENSITY, EQUIVALENT WEIGHT, and the AREA (see the experimental data sheet below). The completed setup for the potentiodynamic test technique is shown in Fig. 36.
h. For the first test set the rotation speed to 500 rpm. Turn the rotator on and press the cell enable switch to activate the cell. Lower RDE into solution. Select RUN to begin the experiment. Because the open circuit potential is near −500 mV vs. SCE, the 500 mV cathodic scan should take approximately 100 seconds.
i. When the experiment is finished, save the data to a file by selecting FILE and SAVE. Note the open circuit potential and the limiting cathodic current density. Figure 37 shows a typical cathodic scan under diffusion limited conditions.
j. Close the current window which shows the last cathodic scan performed.
k. Press the Cell Enable switch to disconnect the cell.

Following each cathodic scan, but before repeating the experiment at a different rotation rate, the WE should be polished on the 600 grit paper provided. A small

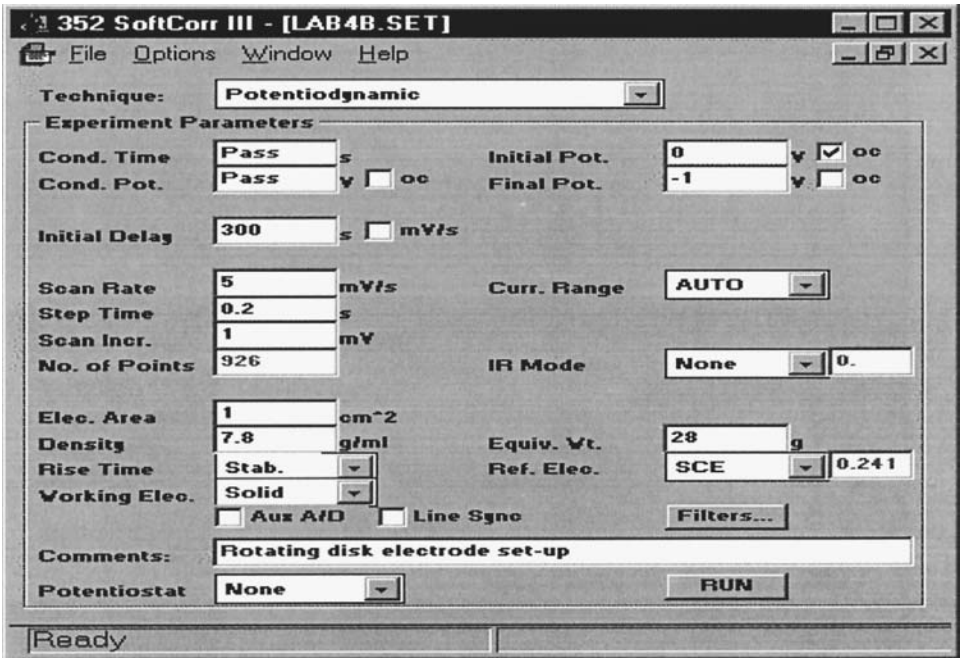

Figure 36 PARC 352 SoftCorr III Potentiodynamic technique combo box window.

spring is inserted into the threaded back of the RDE to establish electrical contact between the RDE and the rotator; when removing the RDE from the mandrel to polish the electrode surface *be careful not to dislodge and lose it*. Before running the experiment, again ensure that electrical contact is made between the rotator and the RDE with the DVM. Repeat steps *h through k* above at rotation rates of 2500 and 5000 rpm, respectively. Press RUN from the POTENTIOSTATIC experiment to start the test using the setup from the previous scan.

Figure 38 shows typical data for this experiment. To overlay the three cathodic scans, open each data file using the FILE, OPEN DATA command. From VIEW select OVERLAID FILES and select the files.

D. Analysis

Calculate the diffusion-limited current density that is expected for each rotation rate assuming a dissolved oxygen concentration of 6–8 ppm (see experimental data sheet for calculation procedure).

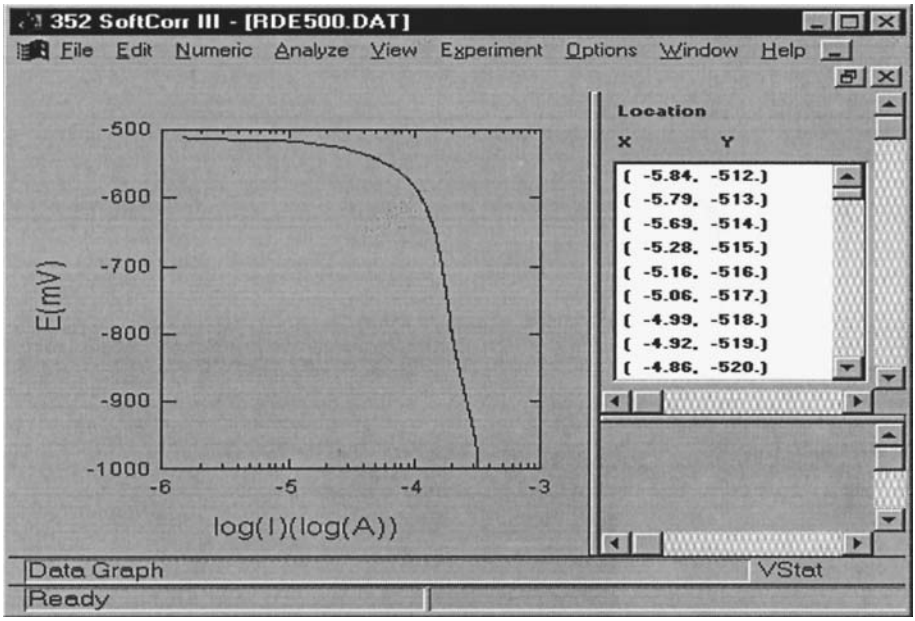

Figure 37 Cathodic polarization of carbon steel RDE in 0.6 M NaCl at 500 rpm.

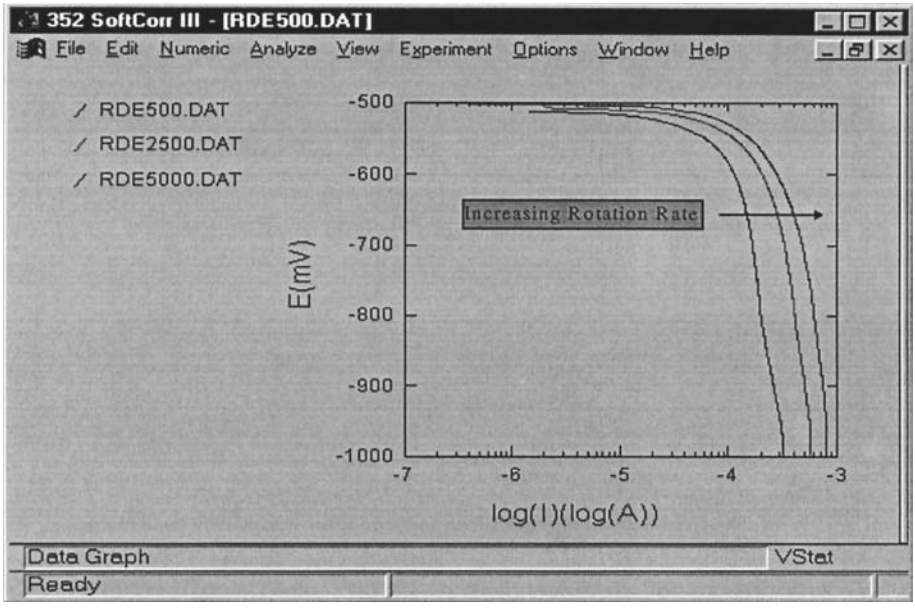

Figure 38 Cathodic polarization scans for rotating disk electrode experiment.

1. Why is the open circuit potential more positive when the rotation rate is increased? (Hint: use mixed potential theory to prove that it should be!)
2. How does the calculated limiting C.D. compare to the actual? What additional factors may account for any differences?
3. What is the effect of increasing surface roughness and corrosion product layer thickness on results?
4. What is wrong with the assumption of purely one-dimensional diffusion? It turns out that a small-diameter rotating disk may be more appropriately described by hemispherical diffusion. The limiting current density in the hemispherical case is greater than that in the linear case by a factor that remains constant with time and rotation rate. This situation is in fact observed in Fig. 39, which compares the experimental data to the predicted results assuming 1D diffusion. (See Bard and Faulkner. *Electrochemical Methods–Fundamentals and Applications*, pp. 136–146.)

Experimental Data Sheet

Density:	7.8 g/cm^3
Equivalent weight:	28 g/mole-equiv
Electrode area:	PAR rotators = 1 cm^2
	Pine rotators = 0.317 cm^2

Rotation rate(rpm)	OCP (mV vs. SCE)	Exp. limiting C.D. (μA/cm^2)	Calc. limiting C.D. (μA/cm^2)
500 rpm			
2500 rpm			
5000 rpm			

The Levich equation:

$$i_l = 0.62\, nFD^{2/3}\, C_b\, \nu^{-1/6}\, \omega^{1/2}$$

For oxygen reduction:

$D = 1.9 \times 10^{-5}$ cm^2/s
$n = 4$ equiv/mole
$C_b =$ 6–8 ppm = [(6–8 mg/liter)*(1 liter/10^3 cm^3)]/(32×10^3 mg/mole)
$= 0.22 \times 10^{-6}$ moles/cm^3
$F = 96487$ coulombs/equiv
$\nu = 1.0 \times 10^{-2}$ cm^2/sec

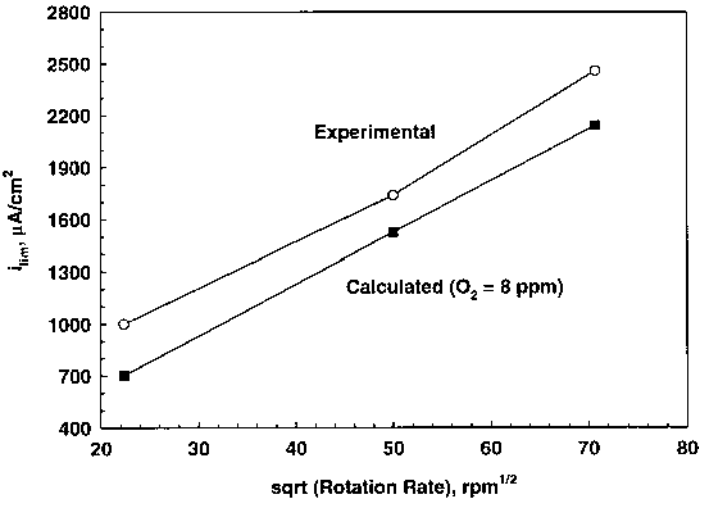

Figure 39 Experimental and calculated diffusion-limited current densities for RDE experiment.

Rewriting the Levich equation in a more abbreviated and convenient form:

$$i_l = K\,\omega^{1/2}$$

where $K = 80.7 \times 10^{-6}$ coulombs/cm^2-s$^{1/2}$ and ω is in units of radians/s.

When rpm are expressed in units of radians/s the resulting units for i_l are coulombs/cm^2-s. Recognizing that 10^{-6} coulombs/s is equivalent to microamperes, it is easy to determine the theoretical limiting current density in μA/cm^2 from the abbreviated form of the Levich equation.

Hence at 50 rpm:

$$\omega = (50 \text{ rev/min})*(1 \text{ min}/60 \text{ s})*(2 \text{ rad/rev} = 5.24 \text{ rad/s}$$

and

$$i_l = 185\ \mu\text{A/cm}^2$$

You should be able to calculate a theoretical "predicted" limiting current density for each rpm selected; the results are shown in Fig. 39.

Index